REVIEWS IN COMPUTATIONAL CHEMISTRY
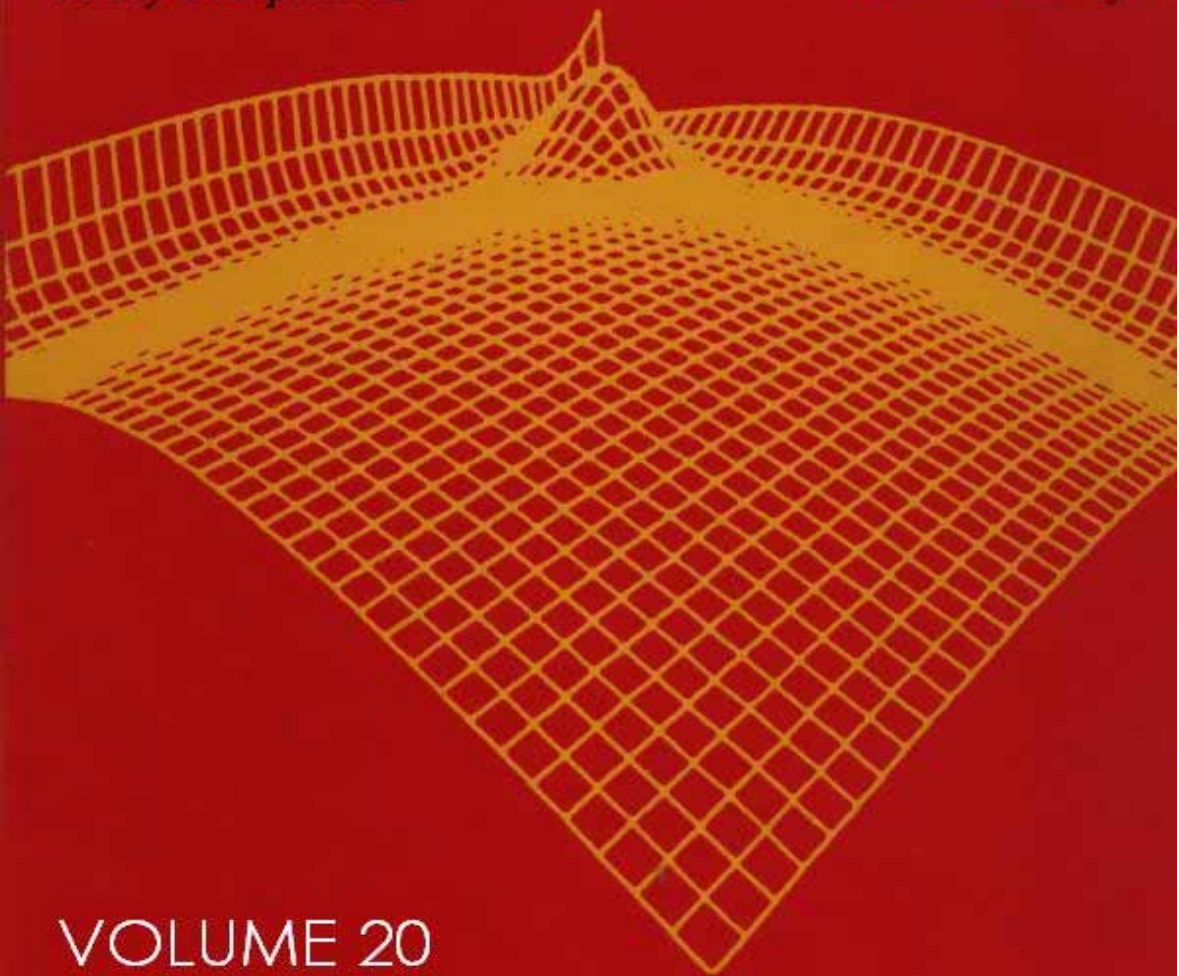
Kenny B. Lipkowitz   *Donald B. Boyd*

VOLUME 20

Reviews in Computational Chemistry Volume 20

Reviews in Computational Chemistry Volume 20

Edited by

Kenny B. Lipkowitz, Raima Larter, and Thomas R. Cundari

Editor Emeritus

Donald B. Boyd

⟨W⟩ WILEY-VCH

Kenny B. Lipkowitz
Department of Chemistry
Ladd Hall 104
North Dakota State University
Fargo, North Dakota 58105-5516, USA
kenny.lipkowitz@ndsu.nodak.edu

Raima Larter
Department of Chemistry
Indiana University-Purdue University
    at Indianapolis,
402 North Blackford Street
Indianapolis, Indiana 46202-3274, USA
rlarter@nsf.gov

Thomas R. Cundari
Department of Chemistry
University of North Texas
Box 305070
Denton, Texas 76203-5070, USA
tomc@unt.edu

Donald B. Boyd
Department of Chemistry
Indiana University-Purdue University
    at Indianapolis
402 North Blackford Street
Indianapolis, Indiana 46202-3274, USA
boyd@chem.iupui.edu

Preface

Our goal over the years has been to provide tutorial-like reviews covering all aspects of computational chemistry. In this, our twentieth volume, we present six chapters covering a diverse range of topics that are of interest to computational chemists. When one thinks of modern quantum chemical methods there is a proclivity to think about molecular orbital theory (MOT). This theory has proved itself to be a useful theoretical tool that allows the computation of energies, properties and, nowadays, dynamical aspects of molecular and supramolecular systems. Molecular orbital theory is, thus, valuable to the average bench chemist, but that bench chemist invariably wants to describe chemical transformations to other chemists in a parlance based on the use of resonance structures. So, an orbital localization scheme must be used to convert the fully delocalized MO results to a valence bond type representation that is consonant with the chemist's working language. One of the great merits of valence bond theory (VBT) is its intuitive wave function. So, why not use VBT? If VBT is the lingua franca of most synthetic chemists, shouldn't those chemists be relying on the VBT method more than they now do, and, if they do not, how can those scientists learn about this quantum method? In Chapter 1, Professors Sason Shaik and Philippe Hiberty provide a detailed view of VBT vis-à-vis MOT, its demise, and then its renaissance; in short they give us a history lesson about the topic. Following this, they outline the basic concepts of VBT, describe the relationship between MOT and VBT, and provide insights about qualitative VBT. Comparisons with other quantum theories and with experiment are made throughout. The VB state correlation method for electronic delocalization is defined and the controversial issue of what makes benzene have its D_{6h} structure is discussed. Aspects of photochemistry are then covered. The spin Hamiltonian VBT and ab initio VB methods are also described and reviewed, which provides a compelling historical account of VBT along with a tutorial and a review. It uses a parlance that is consistent with the way synthetic chemists naturally speak, and it contains insights concerning the many uses of this vibrant field of quantum theory from two veteran VB theorists.

Most chemists solving problems with quantum chemical tools typically work on a single potential energy surface. There are many chemical transformations,

however, where two or more potential energy surfaces need to be included to describe properly the event that is taking place as is the case, for example, in photoisomerizations. In many examples of photoexcitation, nonradiative internal conversion processes are followed that involve the decay of an excited state having the same multiplicity as the lower electronic state. In other processes, however, a nonradiative decay path can be followed where, say, a singlet state can access a triplet state. How one goes about treating such changes in spin multiplicity is a daunting task, to both novice and seasoned computational chemists alike. Professors Nikita Matsunaga and Shiro Koseki provide a tutorial on the topic of modeling spin-forbidden reactions in Chapter 2. The authors describe for the novice the importance of the minimum energy crossing point (MEXP) and rationalize how spin–orbit coupling provides a mechanism for spin-forbidden reactions. An explanation of crossing probabilities, the Fermi golden rule, and the Landau–Zener semiclassical approximation are given. Methodologies for obtaining spin–orbit matrix elements are presented including, among others, the Klein–Gordon equation, the Dirac equation, the Foldy–Wouthuysen transformation, and the Breit–Pauli Hamiltonian. With this background the authors take the novice through a tutorial that explains how to locate the MEXP. They describe programs available for modeling spin-forbidden reactions, and they then provide examples of such calculations on diatomic and polyatomic molecules.

Chapter 3 continues the theme of quantum chemistry and the excited state. In this chapter, Professor Stefan Grimme provides a tutorial explaining how best to calculate electronic spectra of large molecules. Great care must be taken in the interpretation of electronic spectra because significant reorganization of the electronic and nuclear coordinates occurs upon excitation. Even for medium-sized molecules, the density of states in small energy regions can be large, which leads to overlapping spectral features that are difficult to resolve (experimentally and theoretically). Other complications arise as well and the novice computational chemist can become overwhelmed with the many decisions that are needed to carry out the calculations in a meaningful manner. Professor Grimme addresses these challenges in this chapter by first introducing and categorizing the types of electronic spectra and types of excited states, and then explaining the various theoretical aspects associated with simulating electronic spectra. In particular, excitation energies, transition moments, and vibrational structure are covered. Quantum chemical methods used for computing excited states of large molecules are highlighted with emphases on CI, perturbation methods, and time-dependent Hartree–Fock and density functional theory (DFT) methods. A set of recommendations that summarize the methods that can (and should) be used for calculating electronic spectra are provided. Case studies on vertical absorption spectra, circular dichroism, and vibrational structure are then given. The author provides for the reader a basic understanding of which computational methodologies work while alerting the reader to those that do not. This tutorial imparts to the novice many years of experience by Professor Grimme about pitfalls to avoid.

In Chapter 4, Professor Raymond Kapral reviews the computational techniques used in simulating chemical waves and patterns produced by certain chemical reactions such as the Belousov–Zhabotinsky reaction. He begins with a brief discussion of the different length and time scales involved and an explanation for the usual choice of a macroscopic modeling approach. The finite difference approach to modeling reaction-diffusion systems is next reviewed and illustrated for a couple of simple model systems. One of these, the FitzHugh–Nagumo model, exhibits waves and patterns typical of excitable media. Kapral goes on to review other modeling approaches for excitable media, including the use of cellular automata and coupled map lattices. Finally, mesoscopic modeling techniques including Markov chain models for the chemical dynamics of excitable systems are reviewed.

Chapter 5 by Professors Costel Sârbu and Horia Pop on Fuzzy Logic complements previous contributions to this series on Neural Networks (Volume 16) and Genetic Algorithms (Volume 10). Like the other artificial intelligence techniques, fuzzy logic has seen increasing usage in chemistry in the past decade. Here, for the first time, the many different techniques that fall within the arena of fuzzy logic are organized and presented. As delineated by the authors, fuzzy logic is ideally suited for those areas in which imprecise or incomplete measurements are an issue. Its primary application has been the mining of large data sets. The fuzzy techniques discussed in this chapter are equally suited for achieving an effective reduction of the data in terms of either the number of objects (by clustering of data) or a reduction in dimensionality. Additionally, cross-classification techniques make it possible to simultaneously cluster data based on the objects and the characteristics that describe them. In this way, the characteristics that are responsible for two objects belonging to the same (or different) chemical families can be probed directly. In either case, fuzzy methods afford the ability to probe relationships among the data that are not apparent from traditional methods. An eclectic assortment of examples from the literature of fuzzy logic in chemistry is provided, with special emphasis on a subject near and dear to the heart of all chemists—the periodic table. Through the application of fuzzy logic, the chemical groups evident since the time of Mendeleev emerge as the techniques evolve from being crisp to increasingly fuzzy. Professors Sârbu and Pop show how the different fuzzy classification schemes can be used to unearth relationships among the elements that are not evident from a quick perusal of standard periodic tables. Other areas of application include analysis of structural databases, toxicity profiling, structure–activity relationships (SAR) and quantitative structure–activity relationships (QSAR). The chapter concludes with a discussion about interfacing of fuzzy set theory with other soft computing techniques.

The final chapter in this volume (Chapter 6) covers a topic that has been of major concern to computational chemists working in the pharmaceutical industry: Absorption, Metabolism, Distribution, Excretion, and Toxicology (ADME/Tox) of drugs. The authors of this chapter, Dr. Sean Ekins and Professor Peter Swaan, an industrial scientist and an academician, respectively,

provide a selective review of the current status of ADME/Tox covering several intensely studied proteins. The common thread interconnecting these different classes of proteins is that the same computational techniques can be applied to unravel the intricacies of several individual systems. The authors begin by describing the concerted actions of transport and metabolism in mammalian physiology. They then delineate the various approaches used to model enzymes, transporters, channels, and receptors by describing, first, classical QSAR methods and, then, pharmacophore models. Specific programs that are used for the latter include Catalyst, DISCO, CoMFA, CoMSIA, GOLPE, and ALMOND, all of which are described in this chapter. The use of homology models are also explained. Following this introductory section on techniques, the authors review examples of ADME/Tox studies beginning with Transporter Systems, proceeding to Enzyme Systems, and then to Channels and Receptors. Seventeen different case studies are presented to illustrate how the various modeling techniques have been used to evaluate ADME/Tox. A set of "Ten Commandments" that are applicable to many ADME/Tox properties as well as bioactivity models is given for the novice computational chemist. A prognostication of future developments completes the chapter.

We invite our readers to visit the *Reviews in Computational Chemistry* website at http://www.chem.ndsu.nodak.edu/RCC. It includes the author and subject indexes, color graphics, errata, and other materials supplementing the chapters. We are delighted to report that the Google search engine (http://www.google.com/) ranks our website among the top hits in a search on the term "computational chemistry". This search engine has become popular because it ranks hits in terms of their relevance and frequency of visits. We are also pleased to report that the Institute for Scientific information, Inc. (ISI) rates the *Reviews in Computational Chemistry* book series in the top 10 in the category of "general" journals and periodicals. The reason for these accomplishments rests firmly on the shoulders of the authors whom we have contacted to provide the pedagogically driven reviews that have made this ongoing book series so popular. To those authors we are especially grateful.

We are also glad to note that our publisher has plans to make our most recent volumes available in an online form through Wiley InterScience. Please check the Web (http://www.interscience.wiley.com/onlinebooks) or contact reference@wiley.com for the latest information. For readers who appreciate the permanence and convenience of bound books, these will, of course, continue.

We thank the authors of this and previous volumes for their excellent chapters.

<div align="right">

Kenny B. Lipkowitz
Fargo, North Dakota
Raima Larter
Indianapolis, Indiana
Thomas R. Cundari
Denton, Texas
December 2003

</div>

Contents

**6. Development of Computational Models for Enzymes,
Transporters, Channels, and Receptors Relevant to ADME/Tox   333**
Sean Ekins and Peter W. Swaan

Contributors

Sean Ekins, GeneCo, 500 Renaissance Drive, Suite 106, St. Joseph, MI 49085, USA.
(Electronic mail: ekinssean@yahoo.com)

Stefan Grimme, Theoretische Organische Chemie, Organisch-Chemisches Institut der Universität Münster, Correnstrasse 40, D-48149 Münster, Germany. (Electronic mail: grimmes@uni-muenster.de)

Philippe C. Hiberty, Laboratoire de Chimie Physique, Groupe de Chimie Thérique, Université de Paris-Sud, 91405 Orsay, Cedex France.
(Electronic mail: philippe.hiberty@lcp.u-psud.fr)

Raymond Kapral, Chemical Physics Theory Group, Department of Chemistry, University of Toronto, Toronto, Ontario M5S 3H6, Canada.
(Electronic mail: rkapral@gatto.chem.utoronto.ca)

Shiro Koseki, Department of Material Sciences, College of Integrated Arts and Sciences, Osaka Prefecture University, 1-1, Gakuen-cho, Sakai 599-8531, Japan. (Electronic Mail: shiro@ms.cias.osakafu-u.ac.jp)

Nikita Matsunaga, Department of Chemistry and Biochemistry, Long Island University, 1 University Plaza, Brooklyn, NY 11201 USA.
(Electronic mail: nikita.matsunaga@liu.edu)

Horia F. Pop, Babeş-Bolyai University, Faculty of Mathematics and Computer Science, Department of Computer Science, 1, M. Kogalniceanu Street, RO-3400 Cluj-Napoca, Romania. (Electronic mail: hfpop@cs.ubbcluj.ro)

Costel Sârbu, Babeş-Bolyai University, Faculty of Chemistry and Chemical Engineering, Department of Analytical Chemistry, 11 Arany Janos Street, RO-3400 Cluj-Napoca, Romania. (Electronic mail: csarbu@chem.ubbcluj.ro)

Sason Shaik, Department of Organic Chemistry and Lise Meitner-Minerva Center for Computational Chemistry, Hebrew University, 91904 Jerusalem, Israel. (Electronic mail: sason@yfaat.ch.huji.ac.il)

Peter Swaan, Department of Pharmaceutical Sciences, University of Maryland, HSF2, 20 Penn Street, Baltimore, MD 21201 USA.
(Electronic mail: pswaan@rx.umaryland.edu)

Contributors to Previous Volumes

Volume 1 (1990)

David Feller and **Ernest R. Davidson,** Basis Sets for Ab Initio Molecular Orbital Calculations and Intermolecular Interactions.

James J. P. Stewart, Semiempirical Molecular Orbital Methods.

Clifford E. Dykstra, Joseph D. Augspurger, Bernard Kirtman, and **David J. Malik,** Properties of Molecules by Direct Calculation.

Ernest L. Plummer, The Application of Quantitative Design Strategies in Pesticide Design.

Peter C. Jurs, Chemometrics and Multivariate Analysis in Analytical Chemistry.

Yvonne C. Martin, Mark G. Bures, and **Peter Willett,** Searching Databases of Three-Dimensional Structures.

Paul G. Mezey, Molecular Surfaces.

Terry P. Lybrand, Computer Simulation of Biomolecular Systems Using Molecular Dynamics and Free Energy Perturbation Methods.

Donald B. Boyd, Aspects of Molecular Modeling.

Donald B. Boyd, Successes of Computer-Assisted Molecular Design.

Ernest R. Davidson, Perspectives on Ab Initio Calculations.

Volume 2   (1991)

Andrew R. Leach, A Survey of Methods for Searching the Conformational Space of Small and Medium-Sized Molecules.

John M. Troyer and **Fred E. Cohen,** Simplified Models for Understanding and Predicting Protein Structure.

J. Phillip Bowen and **Norman L. Allinger,** Molecular Mechanics: The Art and Science of Parameterization.

Uri Dinur and **Arnold T. Hagler,** New Approaches to Empirical Force Fields.

Steve Scheiner, Calculating the Properties of Hydrogen Bonds by Ab Initio Methods.

Donald E. Williams, Net Atomic Charge and Multipole Models for the Ab Initio Molecular Electric Potential.

Peter Politzer and **Jane S. Murray,** Molecular Electrostatic Potentials and Chemical Reactivity.

Michael C. Zerner, Semiempirical Molecular Orbital Methods.

Lowell H. Hall and **Lemont B. Kier,** The Molecular Connectivity Chi Indexes and Kappa Shape Indexes in Structure–Property Modeling.

I. B. Bersuker and **A. S. Dimoglo,** The Electron-Topological Approach to the QSAR Problem.

Donald B. Boyd, The Computational Chemistry Literature.

Volume 3   (1992)

Tamar Schlick, Optimization Methods in Computational Chemistry.

Harold A. Scheraga, Predicting Three-Dimensional Structures of Oligopeptides.

Andrew E. Torda and **Wilfred F. van Gunsteren,** Molecular Modeling Using NMR Data.

David F. V. Lewis, Computer-Assisted Methods in the Evaluation of Chemical Toxicity.

Volume 4   (1993)

Jerzy Cioslowski, Ab Initio Calculations on Large Molecules: Methodology and Applications.

Michael L. McKee and **Michael Page,** Computing Reaction Pathways on Molecular Potential Energy Surfaces.

Robert M. Whitnell and **Kent R. Wilson,** Computational Molecular Dynamics of Chemical Reactions in Solution.

Roger L. DeKock, Jeffry D. Madura, Frank Rioux, and **Joseph Casanova,** Computational Chemistry in the Undergraduate Curriculum.

Volume 5   (1994)

John D. Bolcer and **Robert B. Hermann,** The Development of Computational Chemistry in the United States.

Rodney J. Bartlett and **John F. Stanton,** Applications of Post-Hartree–Fock Methods: A Tutorial.

Steven M. Bachrach, Population Analysis and Electron Densities from Quantum Mechanics.

Jeffry D. Madura, Malcolm E. Davis, Michael K. Gilson, Rebecca C. Wade, Brock A. Luty, and **J. Andrew McCammon,** Biological Applications of Electrostatic Calculations and Brownian Dynamics Simulations.

K. V. Damodaran and **Kenneth M. Merz Jr.,** Computer Simulation of Lipid Systems.

Jeffrey M. Blaney and **J. Scott Dixon,** Distance Geometry in Molecular Modeling.

Lisa M. Balbes, S. Wayne Mascarella, and **Donald B. Boyd,** A Perspective of Modern Methods in Computer-Aided Drug Design.

Volume 6   (1995)

Christopher J. Cramer and **Donald G. Truhlar,** Continuum Solvation Models: Classical and Quantum Mechanical Implementations.

Clark R. Landis, Daniel M. Root, and Thomas Cleveland, Molecular Mechanics Force Fields for Modeling Inorganic and Organometallic Compounds.

Vassilios Galiatsatos, Computational Methods for Modeling Polymers: An Introduction.

Rick A. Kendall, Robert J. Harrison, Rik J. Littlefield, and Martyn F. Guest, High Performance Computing in Computational Chemistry: Methods and Machines.

Donald B. Boyd, Molecular Modeling Software in Use: Publication Trends.

Eiji Ōsawa and Kenny B. Lipkowitz, Appendix: Published Force Field Parameters.

Volume 7 (1996)

Geoffrey M. Downs and Peter Willett, Similarity Searching in Databases of Chemical Structures.

Andrew C. Good and Jonathan S. Mason, Three-Dimensional Structure Database Searches.

Jiali Gao, Methods and Applications of Combined Quantum Mechanical and Molecular Mechanical Potentials.

Libero J. Bartolotti and Ken Flurchick, An Introduction to Density Functional Theory.

Alain St-Amant, Density Functional Methods in Biomolecular Modeling.

Danya Yang and Arvi Rauk, The A Priori Calculation of Vibrational Circular Dichroism Intensities.

Donald B. Boyd, Appendix: Compendium of Software for Molecular Modeling.

Volume 8 (1996)

Zdenek Slanina, Shyi-Long Lee, and Chin-hui Yu, Computations in Treating Fullerenes and Carbon Aggregates.

Volume 18 (2002)

Geoff M. Downs and John M. Barnard, Clustering Methods and Their Uses in Computational Chemistry.

Hans-Joachim Böhm and **Martin Stahl,** The Use of Scoring Functions in Drug Discovery Applications.

Steven W. Rick and **Steven J. Stuart,** Potentials and Algorithms for Incorporating Polarizability in Computer Simulations.

Dmitry V. Matyushov and **Gregory A. Voth,** New Developments in the Theoretical Description of Charge-Transfer Reactions in Condensed Phases.

George R. Famini and **Leland Y. Wilson,** Linear Free Energy Relationships Using Quantum Mechanical Descriptors.

Sigrid D. Peyerimhoff, The Development of Computational Chemistry in Germany.

Donald B. Boyd and **Kenny B. Lipkowitz,** Appendix: Examination of the Employment Environment for Computational Chemistry.

Volume 19 (2003)

Robert Q. Topper, David L. Freeman, Denise Bergin and Keirnan R. LaMarche, Computational Techniques and Strategies for Monte Carlo Thermodynamic Calculations, with Applications to Nanoclusters.

David E. Smith and **Anthony D. J. Haymet,** Computing Hydrophobicity.

Lipeng Sun and William L. Hase, Born–Oppenheimer Direct Dynamics Classical Trajectory Simulations.

Gene Lamm, The Poisson–Boltzmann Equation.

CHAPTER 1

Valence Bond Theory, Its History, Fundamentals, and Applications: A Primer[a]

Sason Shaik* and Philippe C. Hiberty[†]

*Department of Organic Chemistry and Lise Meitner-Minerva Center for Computational Chemistry, Hebrew University 91904 Jerusalem, Israel
[†]Laboratoire de Chimie Physique, Groupe de Chimie Théorique, Université de Paris-Sud, 91405 Orsay Cedex, France

INTRODUCTION

The new quantum mechanics of Heisenberg and Schrödinger have provided chemistry with two general theories of bonding: valence bond (VB) theory and molecular orbital (MO) theory. The two were developed at about the same time, but quickly diverged into rival schools that have competed, sometimes fervently, in charting the mental map and epistemology of chemistry. Until the mid-1950s, VB theory dominated chemistry; then, MO theory took over while VB theory fell into disrepute and was soon almost completely abandoned. From the 1980s onward, VB theory made a strong comeback and has ever since been enjoying a renaissance both in qualitative applications of

---

[a]This review is dedicated to Roald Hoffmann—A great teacher and a friend.

the theory and the development of new methods for computational implementation.[1]

One of the great merits of VB theory is its visually intuitive wave function, expressed as a linear combination of chemically meaningful structures. It is this feature that made VB theory so popular in the 1930s–1950s, and, ironically, it is the same feature that accounts for its temporary demise (and ultimate resurgence). The comeback of this theory is, therefore, an important development. A review of VB theory that highlights its insight into chemical problems and discusses some of its state-of-the-art methodologies is timely.

This chapter is aimed at the nonexpert and designed as a tutorial for faculty and students who would like to teach and use VB theory, but possess only a basic knowledge of quantum chemistry. As such, an important focus of the chapter will be the qualitative wisdom of the theory and the way it applies to problems of bonding and reactivity. This part will draw on material discussed in previous works by the authors. Another focus of the chapter will be on the main methods available today for ab initio VB calculations. However, much important work of a technical nature will, by necessity, be left out. Some of this work (but certainly not all) is covered in a recent monograph on VB theory.[1]

A STORY OF VALENCE BOND THEORY, ITS RIVALRY WITH MOLECULAR ORBITAL THEORY, ITS DEMISE, AND EVENTUAL RESURGENCE

Since VB has achieved a reputation in some circles as an obsolete theory, it is important to give a short historical account of its development including the rivalry of VB and MO theory, the fall from favor of VB theory, and the reasons for the dominance of MO theory and the eventual resurgence of VB theory. Part of the historical review is based on material from the fascinating historical accounts of Servos[2] and Brush.[3,4] Other parts are not published historical accounts, but rational analyses of historical events, reflecting our own opinions and comments made by colleagues.

Roots of VB Theory

The roots of VB theory in chemistry can be traced to the famous paper of Lewis "*The Atom and The Molecule*",[5] which introduces the notions of electron-pair bonding and the octet rule.[2] Lewis was seeking an understanding of weak and strong electrolytes in solution, and this interest led him to formulate the concept of the chemical bond as an intrinsic property of the molecule that varies between the covalent (shared-pair) and ionic situations. Lewis' paper predated the introduction of quantum mechanics by 11 years, and constitutes

the first formulation of bonding in terms of the covalent–ionic classification. It is still taught today and provides the foundation for the subsequent construction and generalization of VB theory. Lewis' work eventually had its greatest impact through the work of Langmuir who articulated Lewis' model and applied it across the periodic table.[6]

The overwhelming support of the chemistry community for Lewis' idea that electron pairs play a fundamental role in bonding provided an exciting agenda for research directed at understanding the mechanism by which an electron pair could constitute a bond. The nature of this mechanism remained, however, a mystery until 1927 when Heitler and London traveled to Zurich to work with Schrödinger. In the summer of the same year they published their seminal paper, *Interaction between Neutral Atoms and Homopolar Binding*,[7,8] in which they showed that the bonding in H_2 can be accounted for by the wave function drawn in **1**, in Scheme 1. This wave function is a super-
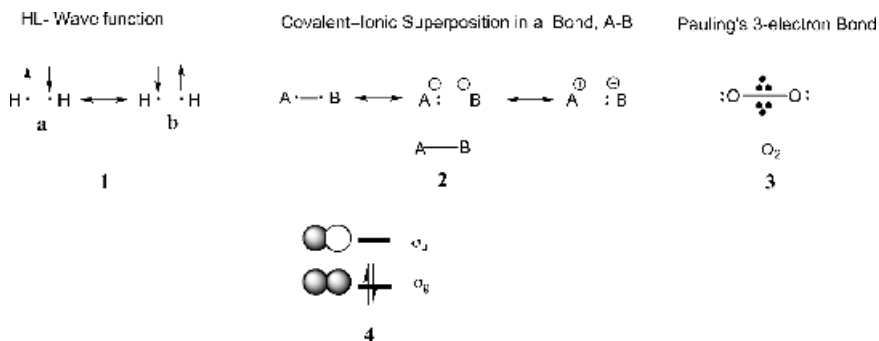
Scheme 1

position of two covalent situations in which one electron is in the spin up configuration (α spin), while the other is spin down (β spin) [form (**a**)], and vice versa in the second form (**b**). Thus, the bonding in H_2 was found to originate in the quantum mechanical "resonance" between the two situations of spin arrangement required to form a singlet electron pair. This "resonance energy" accounted for $\sim$75% of the total bonding of the molecule, and thereby suggested that the wave function in **1**, which is referred to henceforth as the HL (Heitler–London) wave function, can describe the chemical bonding in a satisfactory manner. This "resonance origin" of bonding was a remarkable insight of the new quantum theory, since prior to that time it was not obvious how two neutral species could bond.

The notion of resonance was based on the work of Heisenberg,[9] who showed that, since electrons are indistinguishable particles then, for a two-electron system, with two quantum numbers n and m, there exist two wave

functions that are linear combinations of the two possibilities of arranging these electrons, as shown in Eq. [1].

$$\Psi_A = (1/\sqrt{2})[\phi_n(1)\phi_m(2) + \phi_n(2)\phi_m(1)] \qquad \text{[1a]}$$

$$\Psi_B = (1/\sqrt{2})[\phi_n(1)\phi_m(2) - \phi_n(2)\phi_m(1)] \qquad \text{[1b]}$$

As demonstrated by Heisenberg, the mixing of $[\phi_n(1)\phi_m(2)]$ and $[\phi_n(2)\phi_m(1)]$ led to a new energy term that caused splitting between the two wave functions Ψ_A and Ψ_B. He called this term "resonance" using a classical analogy of two oscillators that by virtue of possessing the same frequency resonate with a characteristic exchange energy. In the winter of 1928, London extended the HL wave function and formulated the general principles of covalent or homopolar bonding.[8,10] In both this and the earlier paper[7,10] the authors considered ionic structures for homopolar bonds, but discarded their mixing as being too small. In London's paper,[10] the ionic (so-called polar) bond is also considered. In essence, HL theory was a quantum mechanical version of Lewis' shared-pair theory. Even though Heitler and London did their work independently and perhaps did not know of the Lewis model, the HL wave function described precisely the shared pair of Lewis. In fact, in his landmark paper, Pauling points out that the HL[8] and London's later treatments are "entirely equivalent to G.N. Lewis's successful theory of shared electron pair…".[11]

The HL wave function formed the basis for the version of VB theory that became very popular later, but was also the source of some of the failings that were to later plague VB theory. In 1929, Slater presented his determinant method.[12] In 1931, he generalized the HL model to n-electrons by expressing the total wave function as a product of $n/2$ bond wave functions of the HL type.[13] In 1932, Rumer[14] showed how to write down all the possible bond pairing schemes for n-electrons and avoid linear dependencies between the forms, which are called canonical structures. We shall hereafter refer to the kind of VB theory that considers only covalent structures as VBHL. Further refinement of the new bonding theory between 1928 and 1933 were mostly quantitative,[15] focusing on improvement of the exponents of the atomic orbitals by Wang, and on the inclusion of polarization functions and ionic terms by Rosen and Weinbaum.

The success of the HL model and its relation to Lewis' model, posed a wonderful opportunity for the young Pauling and Slater to construct a general quantum chemical theory for polyatomic molecules. They both published, in the same year, 1931, several seminal papers in which they each developed the notion of hybridization, the covalent–ionic superposition, and the resonating benzene picture.[13,16–19] Especially effective were Pauling's papers that linked the new theory to the chemical theory of Lewis, and that rested on an encyclopedic command of chemical facts. In the first paper,[18] Pauling presented the electron-pair bond as a superposition of the covalent HL form and the two

possible ionic forms of the bond, as shown in **2** in Scheme 1, and discussed the transition from covalent to ionic bonding. He then developed the notion of hybridization and discussed molecular geometries and bond angles in a variety of molecules, ranging from organic to transition metal compounds. For the latter compounds, he also discussed the magnetic moments in terms of the unpaired spins. In the second paper,[19] Pauling addressed bonding in molecules like diborane, and odd-electron bonds as in the ion molecule H_2^+ and dioxygen, O_2, which Pauling represented as having two three-electron bonds, as shown in **3** in Scheme 1. These two papers were followed by more papers, all published during 1931–1933 in the *Journal of the American Chemical Society*, and collectively entitled "*The Nature of the Chemical Bond*". This series of papers allowed one to describe any bond in any molecule, and culminated in Pauling's famous monograph[20] in which all structural chemistry of the time was treated in terms of the covalent–ionic superposition theory, resonance theory, and hybridization theory. The book, published in 1939, was dedicated to G.N. Lewis, and, in fact, the 1916 paper of Lewis is the only reference cited in the preface to the first edition. Valence bond theory is, in Pauling's view, a quantum chemical version of Lewis' theory of valence. In Pauling's work, the long sought for Allgemeine Chemie (Generalized Chemistry) of Ostwald was, thus, finally found.[2]

Origins of MO Theory and the Roots of VB–MO Rivalry

At the same time that Slater and Pauling were developing their VB theory,[17] Mulliken[21–24] and Hund[25,26] were working on an alternative approach, which would eventually be called molecular orbital (MO) theory. The actual term (MO theory) does not appear until 1932, but the roots of the method can be traced to earlier papers from 1928,[21] in which both Hund and Mulliken made spectral and quantum number assignments of electrons in molecules, based on correlation diagrams of separated to united atoms. According to Brush,[3] the first person to write a wave function for a molecular orbital was Lennard-Jones in 1929, in his treatment of diatomic molecules. In this paper, Lennard-Jones shows with facility that the O_2 molecule is paramagnetic, and mentions that the VBHL method runs into difficulties with this molecule.[27] In MO theory, the electrons in a molecule occupy delocalized orbitals made from linear combinations of atomic orbitals (LCAO). Drawing **4**, Scheme 1, shows the molecular orbitals of the H_2 molecule; the delocalized σ_g MO should be contrasted with the localized HL description in **1**.

The work of Hückel in the early 1930s initially received a chilly reception,[28] but eventually Hückel's work gave MO theory an impetus and developed into a successful and widely applicable tool. In 1930, Hückel used Lennard-Jones' MO ideas on O_2, applied it to C=X (X = C, N, O) double bonds and suggested the concept of σ–π separation.[29] With this novel treatment, Hückel ascribed the restricted rotation in ethylene to the π-type orbital.

Equipped with this facility of σ–π separability, Hückel solved the electronic structure of benzene using both VBHL theory and his new Hückel MO (HMO) approach, the latter giving better "quantitative" results, and hence being preferred.[30] The π-MO picture, **5** in Scheme 2, was quite unique in the sense that it viewed the molecule as a whole, with a σ-frame dressed by π-electrons that occupy three completely delocalized π-orbitals. The HMO picture also allowed Hückel to understand the special stability of benzene.
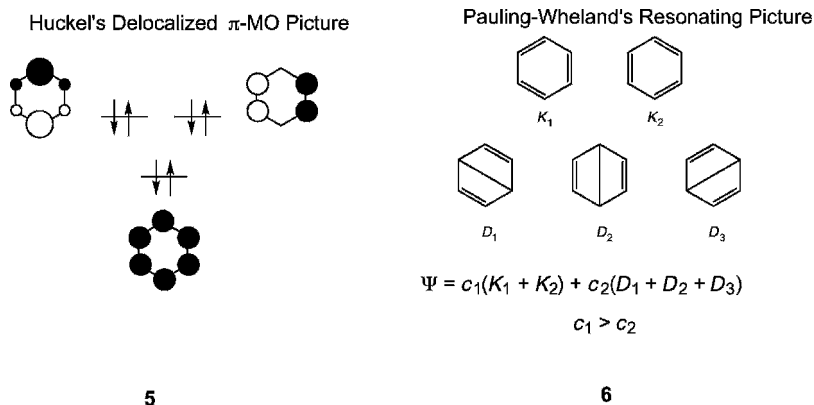
Scheme 2

Thus, the molecule was found to have a closed-shell π-component and its energy was calculated to be lower relative to three isolated π bonds in ethylene. In the same paper, Hückel treated the ion molecules of C_5H_5 and C_7H_7 as well as the molecules C_4H_4 (CBD) and C_8H_8 (COT). This allowed him to understand why molecules with six π-electrons have special stability, and why molecules like COT or CBD either do not possess this stability (COT) or had not yet been synthesized (CBD). Already in this paper and in a subsequent one,[31] Hückel begins to lay the foundations for what will become later known as the "Hückel Rule", regarding the special stability of "aromatic" molecules with $4n + 2$ π-electrons.[3] This rule, its extension to "antiaromaticity", and its articulation by organic chemists in the 1950–1970s would become a major cause of the acceptance of MO theory and rejection of VB theory.[4]

The description of benzene in terms of a superposition (resonance) of two Kekulé structures appeared for the first time in the work of Slater, as a case belonging to a class of species in which each atom possesses more neighbors than electrons it can share.[16] Two years later, Pauling and Wheland[32] applied the VBHL theory to benzene. They developed a less cumbersome computational approach, compared with Hückel's previous VBHL treatment,

using the five canonical structures, in **6** in Scheme 2, and approximated the matrix elements between the structures by retaining only close neighbor resonance interactions. Their approach allowed them to extend the treatment to naphthalene and to a great variety of other species. Thus, in the VBHL approach, benzene is described as a "resonance hybrid" of the two Kekulé structures and the three Dewar structures; the latter had already appeared before in Ingold's idea of mesomerism. In his book, published for the first time in 1944, Wheland explains the resonance hybrid with the biological analogy of mule = donkey + horse.[33] The pictorial representation of the wave function, the link to Kekulé's oscillation hypothesis, and the connection to Ingold's mesomerism, all of which were known to chemists, made the VBHL representation very popular among practicing chemists.

    With these two seemingly different treatments of benzene, the chemical community was faced with two alternative descriptions of one of its molecular icons. Thus began the VB–MO rivalry that continues to the twenty-first century. The VB–MO rivalry involved many prominent chemists (to mention but a few names, Mulliken, Hückel, J. Mayer, Robinson, Lapworth, Ingold, Sidgwick, Lucas, Bartlett, Dewar, Longuet-Higgins, Coulson, Roberts, Winstein, Brown, etc.). A detailed and interesting account of the nature of this rivalry and the major players can be found in the treatment of Brush.[3,4] Interestingly, as early as the 1930s, Slater[17] and van Vleck and Sherman[34] stated that since the two methods ultimately converge, it is senseless to quibble about the issue of which one is better. Unfortunately, however, this rational attitude does not seem to have made much of an impression.

The "Dance" of Two Theories: One Is Up, the Other Is Down

    By the end of World War II, Pauling's resonance theory had become widely accepted while most practicing chemists ignored HMO and MO theories. The reasons for this are analyzed by Brush.[3] Mulliken suggested that the success of VB theory was due to Pauling's skill as a propagandist. According to Hager (a Pauling biographer) VB theory won out in the 1930s because of Pauling's communication skills. However, the most important reason for its dominance is the direct lineage of VB-resonance theory to the structural concepts of chemistry dating from the days of Kekulé. Pauling himself emphasized that his VB theory is a natural evolution of chemical experience, and that it emerges directly from the concept of the chemical bond. This has made VB-resonance theory appear intuitive and "chemically correct". Another great promoter of VB-resonance theory was Ingold who saw in it a quantum chemical version of his own "mesomerism" concept (according to Brush, the terms resonance and mesomerism entered chemical vocabulary at the same time, due to Ingold's assimilation of VB-resonance theory; see Brush,[3] p. 57). Another very important reason for the early acceptance of VB theory is the facile

qualitative application of this theory to all known structural chemistry of the time (in Pauling's book[20]) and to a variety of problems in organic chemistry (in Wheland's book[33]). The combination of an easily applicable general theory and its good fit to experiment, created a rare credibility nexus. By contrast, MO theory seemed diametrically opposed to everything chemists had thought was true about the nature of the chemical bond. Even Mulliken admitted that MO theory departs from "chemical ideology" (see Brush,[3] p. 51). And to complete this sad state of affairs, in this early period MO theory offered no visual representation to compete with the resonance hybrid representation of VB-resonance theory. For all these reasons, by the end of World War II, VB-resonance theory dominated the epistemology of chemists.

By the mid-1950s, the tide had started a slow turn in favor of MO theory, a shift that gained momentum through the mid-1960s. What caused the shift is a combination of factors, of which the following two may be decisive. First, there were the many successes of MO theory: the experimental verification of Hückel's rules;[28] the construction of intuitive MO theories and their wide applicability for rationalization of structures (e.g., Walsh diagrams) and spectra [electronic and electron spin resonance (ESR)]; the highly successful predictive application of MO theory in chemical reactivity; the instant rationalization of the bonding in newly discovered exotic molecules like ferrocene,[35] for which the VB theory description was cumbersome; and the development of widely applicable MO-based computational techniques (e.g., extended Hückel and semiempirical programs). The second reason, on the other side, is that VB theory, in chemistry, suffered a detrimental conceptual arrest that crippled the predictive ability of the theory and started to lead to an accumulation of "failures". Unlike its fresh exciting beginning, in its frozen form of the 1950–1960s, VB theory ceased to guide experimental chemists to new experiments. This lack of utility ultimately led to the complete victory of MO theory. However, the MO victory over VB theory was restricted to resonance theory and other simplified versions of VB theory, not VB theory itself. In fact, by this time, the true VB theory was hardly being practiced anymore in the mainstream chemical community.

One of the major registered "failures" of VB theory is associated with the dioxygen molecule, O_2. Application of the Pauling–Lewis recipe of hybridization and bond pairing to rationalize and predict the electronic structure of molecules fails to predict the paramagneticity of O_2. By contrast, MO theory reveals this paramagneticity instantaneously.[27] Even though VB theory does not really fail with O_2, and Pauling himself preferred, without reasoning why, to describe it in terms of three-electron bonds (**3** in Scheme 1) in his early papers[19] (see also Wheland's description on p. 39 of his book[33]), this "failure" of Pauling's recipe has tainted VB theory and become a fixture of the common chemical wisdom (see Brush[3] p. 49, footnote 112).

A second example concerns the VB treatments of CBD and COT. The use of VBHL theory leads to an incorrect prediction that the resonance energy

of CBD should be as large as or even larger than that of benzene. The facts (that CBD had not yet been made and that COT exhibited no special stability) favored HMO theory. Another impressive success of HMO theory was the prediction that due to the degenerate set of singly occupied MOs, square CBD should distort to a rectangular structure, which provided a theoretical explanation for the ubiquitous phenomena of Jahn-Teller and pseudo-Jahn-Teller effects, amply observed by the community of spectroscopists. Wheland analyzed the CBD problem early on, and his analysis pointed out that inclusion of ionic structures would probably change the VB predictions and make them identical to MO.[33,36,37] Craig showed that VBHL theory in fact correctly assigns the ground state of CBD, by contrast to HMO theory.[38,39] Despite this mixed bag of predictions on properties of CBD, by VBHL or HMO, and despite the fact that modern VB theory has subsequently demonstrated unique and novel insight into the problems of benzene, CBD and their isoelectronic species, the early stamp of the CBD story as a failure of VB theory still persists.

The increasing interest of chemists in large molecules as of the late 1940s started making VB theory impractical, compared with the emerging semiempirical MO methods that allowed the treatment of larger and larger molecules. A great advantage of semiempirical MO calculations was the ability to calculate bond lengths and angles rather than assume them as in VB theory.[4] Skillful communicators like Longuet–Higgins, Coulson, and Dewar were among the leading MO proponents, and they handled MO theory in a visualizable manner, which had been sorely missing before. In 1951, Coulson addressed the Royal Society Meeting and expressed his opinion that despite the great success of VB theory, it had no good theoretical basis; it was just a semiempirical method, he said, of little use for more accurate calculations.[40] In 1949, Dewar's monograph, *Electronic Theory of Organic Chemistry*,[41] summarized the faults of resonance theory, as being cumbersome, inaccurate, and too loose: "it can be played happily by almost anyone without any knowledge of the underlying principles involved". In 1952, Coulson published his book *Valence*,[42] which did for MO theory, at least in part, what Pauling's book[20] had done much earlier for VB theory. In 1960, Mulliken won the Nobel Prize and Platt wrote, "MO is now used far more widely, and simplified versions of it are being taught to college freshmen and even to high school students".[43] Indeed, many communities took to MO theory due to its proven portability and successful predictions.

A decisive defeat was dealt to VB theory when organic chemists were finally able to synthesize transient molecules and establish the stability patterns of $C_8H_8^{2-}$, $C_5H_5^{-,+}$, $C_3H_3^{+,-}$ and $C_7H_7^{+,-}$ during the 1950–1960s.[3,4,28] The results, which followed Hückel's rules, convinced most of the organic chemists that MO theory was right, while VBHL and resonance theories were wrong. From 1960–1978, C_4H_4 was made, and its structure and properties as determined by MO theory challenged initial experimental determination of a square structure.[3,4] The syntheses of nonbenzenoid aromatic compounds

like azulene, tropone, and so on, further established Hückel's rules, and high-lighted the failure of resonance theory.[28] This era in organic chemistry marked a decisive down-fall of VB theory.

In 1960, the 3rd edition of Pauling's book was published,[20] and although it was still spellbinding for chemists, it contained errors and omissions. For example, in the discussion of electron deficient boranes, Pauling describes the molecule $B_{12}H_{12}$ instead of $B_{12}H_{12}^{2-}$ (Pauling,[20] p. 378); another example is a very cumbersome description of ferrocene and analogous compounds (on pp. 385–392), for which MO theory presented simple and appealing descrip-tions. These and other problems in the book, as well as the neglect of then-known species like $C_5H_5^{-,+}$, $C_3H_3^{+,-}$, and $C_7H_7^{+,-}$, reflected the situation that, unlike MO theory, VB theory did not have a useful Aufbau principle that could predict reliably the dependence of molecular stability on the num-ber of electrons. As we have already pointed out, the conceptual development of VB theory had been arrested since the 1950s, in part due to the insistence of Pauling himself that resonance theory was sufficient to deal with most pro-blems (see, e.g., p. 283 in Brush[4]). Sadly, the creator himself contributed to the downfall of his own brainchild.

In 1952, Fukui published his Frontier MO theory,[44] which went initially unnoticed. In 1965, Woodward and Hoffmann published their principle of conservation of orbital symmetry, and applied it to all pericyclic chemical reactions. The immense success of these rules[45] renewed interest in Fukui's approach and together formed a new MO-based framework of thought for chemical reactivity (called, e.g., ''giant steps forward in chemical theory'' in Morrison and Boyd, pp. 934, 939, 1201, and 1203). This success of MO theory dealt a severe blow to VB theory. In this area too, despite the early cal-culations of the Diels–Alder and $2 + 2$ cycloaddition reactions by Evans,[46] VB theory missed making an impact, in part at least because of its blind adherence to simple resonance theory.[28] All the subsequent VB derivations of the rules (e.g., by Oosterhoff in Ref. 90) were ''after the fact'' and failed to reestablish the status of VB theory.

The development of photoelectron spectroscopy (PES) and its applica-tion to molecules in the 1970s, in the hands of Heilbronner, showed that spec-tra could be easily interpreted if one assumes that electrons occupy delocalized molecular orbitals.[47,48] This further strengthened the case for MO theory. Moreover, this served to lessen the case for VB theory, because it describes electron pairs that occupy localized bond orbitals. A frequent example of this ''failure'' of VB theory is the PES of methane, which shows two different ionization peaks. These peaks correspond to the a_1 and t_2 MOs, but not to the four C—H bond orbitals in Pauling's hybridization theory (see a recent paper on a similar issue[49]). With these and similar types of arguments VB theory has eventually fallen into a state of disrepute and become known, at least when the authors were students, either as a ''wrong theory'' or even a ''dead theory''.

The late 1960s and early 1970s mark the era of mainframe computing. By contrast to VB theory, which is difficult to implement computationally (due to the non-orthogonality of orbitals), MO theory could be easily implemented (even GVB was implemented through an MO-based formalism—see later). In the early 1970s, Pople and co-workers developed the GAUSSIAN70 package that uses "ab initio MO theory" with no approximations other than the choice of basis set. Sometime later density functional theory made a spectacular entry into chemistry. Suddenly, it became possible to calculate real molecules, and to probe their properties with increasing accuracy. This new and user-friendly tool created a subdiscipline of "computational chemists" who explore the molecular world with the GAUSSIAN series and many other packages that sprouted alongside the dominant one. Calculations continuously reveal "more failures" of Pauling's VB theory, for example, the unimportance of $3d$ orbitals in bonding of main group elements, namely, the "verification" of three-center bonding. Leading textbooks hardly include VB theory anymore, and when they do, they misrepresent the theory.[50,51] Advanced quantum chemistry courses teach MO theory regularly, but books that teach VB theory are virtually nonexistent. The development of user friendly ab initio MO-based software and the lack of similar VB software seem to have put the last nail in the coffin of VB theory and substantiated MO theory as the only legitimate chemical theory of bonding.

Nevertheless, despite this seemingly final judgment and the obituaries showered on VB theory in textbooks and in public opinion, the theory has never really died. Due to its close affinity to chemistry and utmost clarity, it has remained an integral part of the thought process of many chemists, even among proponents of MO theory (see comment by Hoffmann on p. 284 in Brush[4]). Within the chemical dynamics community, moreover, the usage of the theory has never been eliminated, and it exists in several computational methods such as LEPS (London–Eyring–Polanyi–Sato), BEBO (bond energy bond order), DIM (diatomics in molecules), and so on, which were (and still are) used for the generation of potential energy surfaces. Moreover, around the 1970s, but especially from the 1980s and onward, VB theory began to rise from its ashes, to dispel many myths about its "failures" and to offer a sound and attractive alternative to MO theory. Before we describe some of these developments, it is important to go over some of the major "failures" of VB theory and inspect them a bit more closely.

Are the Failures of VB Theory Real Ones?

All the so-called failures of VB theory are due to misuse and failures of very simplified versions of the theory. Simple resonance theory enumerates structures without proper consideration of their interaction matrix elements (or overlaps). It will fail whenever the matrix element is important as in the case of aromatic versus antiaromatic molecules, and so on.[52] The hybridization

bond-pairing theory assumes that the most important energetic effect for a molecule is the bonding, and hence one should hybridize the atoms and make the maximum number of bonds—henceforth "perfect pairing". The perfect-pairing approach will fail whenever other factors (see below) become equal to or more important than bond pairing.[53,54] The VBHL theory is based on covalent structures only, which become insufficient and require inclusion of ionic structures explicitly or implicitly (through delocalization tails of the atomic orbitals, as in the GVB method described later). In certain cases, like that of antiaromatic molecules, this deficiency of VBHL makes incorrect predictions.[55] Next, we consider four iconic "failures", and show that some of them tainted VB in unexplained ways.

1. **The O_2 "Failure":** It is doubtful that this so-called failure can be attributed to Pauling himself, because in his landmark paper,[18] he was very careful to state that the molecule does not possess a "normal" state, but rather one with two three-electron bonds (**3** in Scheme 1). Also see Wheland on page 39 of his book.[33] We also located a 1934 *Nature* paper by Heitler and Pöschl[56] who treated the O_2 molecule with VB principles and concluded that "the $^3\Sigma_g^-$ term ... [gives] the fundamental state of the molecule". It is not clear to us how the myth of this "failure" grew, spread so widely, and was accepted so unanimously. Curiously, while Wheland acknowledged the prediction of MO theory by a proper citation of Lennard-Jones' paper,[27] Pauling did not, at least not in his landmark papers,[18,19] nor in his book.[20] In these works, the Lennard-Jones paper is either not cited,[19,20] or is mentioned only as a source of the state symbols[18] that Pauling used to characterize the states of CO, CN, and so on. One wonders about the role of animosity between the MO and VB camps in propagating the notion of the "failures" of VB to predict the ground state of O_2. Sadly, scientific history is determined also by human weaknesses. As we have repeatedly stated, it is true that a naive application of hybridization and the perfect pairing approach (simple Lewis pairing) without consideration of the important effect of four-electron repulsion would fail and predict a $^1\Delta_g$ ground state. As we shall see later, in the case of O_2, perfect pairing in the $^1\Delta_g$ state leads to four-electron repulsion, which more than cancels the π-bond. To avoid the repulsion, we can form two three-electron π-bonds, and by keeping the two odd electrons in a high-spin situation, the ground state becomes $^3\Sigma_g^-$ that is further lowered by exchange energy due to the two triplet electrons.[53]

2. **The C_4H_4 "Failure":** This is a failure of the VBHL approach that does not involve ionic structures. Their inclusion in an all-electron VB theory, either explicitly,[55,57] or implicitly through delocalization tails of the atomic orbitals,[58] correctly predicts the geometry and resonance energy. In fact, even VBHL theory makes a correct assignment of the ground state of cyclo butadiene (CBD), as the $^1B_{1g}$ state. By contrast, monodeterminantal MO

theory makes an incorrect assignment of the ground state as the triplet $^3A_{2g}$ state.[38,39] Moreover, HMO theory succeeded for the wrong reason. Since the Hückel MO determinant for the singlet state corresponds to a single Kekulé structure, CBD exhibits zero resonance energy in HMO.[36]

3. **The $C_5H_5^+$ "Failure":** This is a failure of simple resonance theory, not of VB theory. Taking into account the sign of the matrix element (overlap) between the five VB structures shows that singlet $C_5H_5^+$ is Jahn–Teller unstable, and the ground state is, in fact, the triplet state. This is generally the case for all the antiaromatic ionic species having $4n$ electrons over $4n + 1$ or $4n + 3$ centers.[52]

4. **The "Failure" associated with the PES of methane (CH_4):** Starting from a naive application of the VB picture of CH_4, it follows that since methane has four equivalent localized bond orbitals (LBOs), the molecule should exhibit only one ionization peak in PES. However, since the PES of methane shows two peaks, VB theory "fails"! This argument is false for two reasons. First, as has been known since the 1930s, LBOs for methane or any molecule, can be obtained by a unitary transformation of the delocalized MOs.[59] Thus, both MO and VB descriptions of methane can be cast in terms of LBOs. Second, if one starts from the LBO picture of methane, the electron can come out of any one of the LBOs. A physically correct representation of the CH_4^+ cation would be a linear combination of the four forms that ascribe electron ejection to each of the four bonds. One can achieve the correct physical description, either by combining the LBOs back to canonical MOs,[48] or by taking a linear combination of the four VB configurations that correspond to one bond ionization.[60,61] As shall be seen later, correct linear combinations are $^2A_1$ and $^2T_2$, the latter being a triply degenerate VB state.

We conclude that those who reject VB theory cannot continue to invoke "failures", because a properly executed VB theory does not fail, just as a properly done MO-based calculation does not "fail". This notion of VB "failure" that is traced back to the VB–MO rivalry in the early days of quantum chemistry should now be considered obsolete, unwarranted, and counterproductive. A modern chemist should know that there are two ways of describing electronic structure, and that these two are not contrasting theories, but rather two representations of the same reality. Their capabilities and insights into chemical problems are complementary and the exclusion of either one of them undermines the intellectual heritage of chemistry. Indeed, theoretical chemists in the dynamics community continued to use VB theory and maintained an uninterrupted chain of VB usage from London, through Eyring, Polanyi, to Wyatt, Truhlar, and others in the present day. Physicists, too, continued to use VB theory, and one of the main proponents is the Nobel Laureate P.W. Anderson, who developed a resonating VB theory of superconductivity. And, in terms of the focus of this chapter, in mainstream chemistry too, VB

theory is beginning to enjoy a slow but steady renaissance in the form of modern VB theory.

Modern VB Theory: VB Theory Is Coming of Age

The renaissance of VB theory is marked by a surge in the following two-pronged activity: (a) creation of general qualitative models based on VB theory, and (b) development of new methods and software that enable applications to moderate-sized molecules. Below we briefly mention some of these developments without pretence of creating an exhaustive list.

A few general qualitative models based on VB theory started to appear in the late 1970s and early 1980s. Among these models we count also semiempirical approaches based, for example, on Heisenberg and Hubbard Hamiltonians,[62–70] as well as Hückel VB methods,[52,71–73] which can handle well ground and excited states of molecules. Methods that map MO-based wave functions to VB wave functions offer a good deal of interpretive insight. Among these mapping procedures we note the half-determinant method of Hiberty and Leforestier,[74] and the CASVB methods of Thorsteinsson et al.[75,76] and Hirao and co-worker.[77,78] General qualitative VB models for chemical bonding were proposed in the early 1980s and the late 1990s by Epiotis et al.[79,80] A general model for the origins of barriers in chemical reactions was proposed in 1981 by Shaik, in a manner that incorporates the role of orbital symmetry.[52,81] Subsequently, in collaboration with Pross[82,83] and Hiberty,[84] the model has been generalized for a variety of reaction mechanisms,[85] and used to shed new light on the problems of aromaticity and antiaromaticity in isoelectronic series.[57] Following Linnett's reformulation of three-electron bonding in the 1960s,[86] Harcourt[87,88] developed a VB model that describes electron-rich bonding in terms of increased valence structures, and showed its occurrence in bonds of main group elements and transition metals.

Valence bond ideas have also contributed to the revival of theories for photochemical reactivity. Early VB calculations by Oosterhoff and co-workers[89,90] revealed a possible general mechanism for the course of photochemical reactions. Michl and co-workers[91,92] articulated this VB-based mechanism and highlighted the importance of "funnels" as the potential energy features that mediate the excited-state species back into the ground state. Recent work by Robb and co-workers[93–96] showed that these "funnels" are conical intersections that can be predicted by simple VB arguments, and computed at a high level of sophistication. Similar applications of VB theory to deduce the structure of conical intersections in photoreactions were done by Shaik and Reddy[97] and recently generalized by Zilberg and Haas.[98]

Valence bond theory enables a very straightforward account of environmental effects, such as those imparted by solvents and/or protein pockets. A major contribution to the field was made by Warshel who created an empirical VB (EVB) method. By incorporating van der Waals and London interactions

using a molecular mechanics (MM) method, Warshel created the QM(VB)–MM method for the study of enzymatic reaction mechanisms.[99–101] His pioneering work inaugurated the now emerging QM–MM methodologies for studying enzymatic processes. Hynes and co-workers,[102–104] showed how to couple solvent models to VB and create a simple and powerful model for understanding and predicting chemical processes in solution. Shaik[105,106] showed how solvent effects can be incorporated in an effective manner in the reactivity factors that are based on VB diagrams.

All in all, VB theory is seen to offer a widely applicable framework for thinking about and predicting chemical trends. Some of these qualitative models and their predictions are discussed in the Application sections.

In the 1970s, a stream of nonempirical VB methods began to appear and were followed by many applications of accurate calculations. All these methods divide the orbitals in a molecule into inactive and active subspaces, treating the former as a closed-shell and the latter by a VB formalism. The programs optimize the orbitals, and the coefficients of the VB structures, but they differ in the manners by which the VB orbitals are defined. Goddard et al.[107–110] developed the generalized VB (GVB) method, which uses semilocalized atomic orbitals (having small delocalization tails), employed originally by Coulson and Fisher for the H_2 molecule.[111] The GVB method is incorporated now in GAUSSIAN and in most other MO-based software. Somewhat later, Gerratt, Raimondi, and Cooper developed their VB method known as the spin coupled (SC) theory and its follow up by configuration interaction using the SCVB method,[112–114] which is now incorporated in the MOLPRO software. The GVB and SC theories do not employ covalent and ionic structures explicitly, but instead use semilocalized atomic orbitals that effectively incorporate all the ionic structures, and thereby enable one to express the electronic structures in compact forms based on formally covalent pairing schemes. Balint-Kurti and Karplus[115] developed a multistructure VB method that utilizes covalent and ionic structures with localized atomic orbitals (AOs). In a later development by van Lenthe and Balint-Kurti[116,117] and by Verbeek and van Lenthe,[118,119] the multistructure method is referred to as a VB self-consistent field (VBSCF) method. In a subsequent development, van Lenthe, Verbeek, and co-workers[120,121] generated the multipurpose VB program called TURTLE, which has recently been interfaced with the MO-based program GAMESS-UK. Matsen,[122,123] McWeeny,[124] and Zhang and co-workers[125,126] developed their spin-free VB approaches based on symmetric group methods. Subsequently, Wu et al.[127,128] extended the spin-free approach, and produced a general purpose VB program called the XIAMEN-99 package. Soon after, Li and McWeeny[129] announced their VB2000 software, which is also a general purpose program, including a variety of methods. Another package incorporating multiconfigurational VB (MCVB) methods, called CRUNCH and based on the symmetric group methods of Young, was written by Gallup et al.[130,131] During the early 1990s, Hiberty et al.[132–137] developed the breathing orbital

VB (BOVB) method, which also utilizes covalent and ionic structures, but in addition allows them to have their own unique set of orbitals. This method is now incorporated into the programs TURTLE and XIAMEN-99. Very recently, Wu et al.[138] developed a VBCI method that is akin to BOVB, but which can be applied to larger systems. The recent biorthogonal VB method (bio-VB) of McDouall[139] has the potential to carry out VB calculations on systems with up to 60 electrons outside the closed shell. And finally, Truhlar and co-workers[140] developed the VB-based multiconfiguration molecular mechanics method (MCMM) to treat dynamical aspects of chemical reactions, while Landis and co-workers[141] introduced the VAL–BOND method that predicts the structures of transition metal complexes using Pauling's ideas of orbital hybridization. In the section dedicated to VB methods, we mention the main software and methods that we used, and outline their features, capabilities, and limitations.

This plethora of acronyms for VB software starts to resemble that which accompanied the ascent of MO theory. While this may sound like good news, certainly it is also a call for systematization much like what Pople and co-workers enforced on computational MO terminology. Nonetheless, at the moment the important point is that the advent of many good VB programs has caused a surge of applications of VB theory to problems ranging from bonding in main group elements to transition metals, conjugated systems, aromatic and antiaromatic species, and even excited states and full pathways of chemical reactions, with moderate to very good accuracies. For example, a recent calculation of the barrier for the identity hydrogen exchange reaction, $H + H–H' \rightarrow H–H + H'$, by Song et al.[142] shows that it is possible to calculate the reaction barrier accurately with just eight classical VB structures! Valence bond theory is coming of age.

BASIC VB THEORY

Writing and Representing VB Wave Functions

VB Wave Functions with Localized Atomic Orbitals

We illustrate the theory by using, as an example, the two-electron/two-center (2e/2c) bond. A VB determinant is an antisymmetrized wave function that may or may not also be a proper spin eigenfunction. For example, $|a\bar{b}|$ in Eq. [2] is a determinant that describes two spin-orbitals a and b having one electron each; the bar over the b orbital indicates a β spin, while its absence indicates an α spin:

$$|a\bar{b}| = \frac{1}{\sqrt{2}}\{a(1)b(2)[\alpha(1)\beta(2)] - a(2)b(1)[\alpha(2)\beta(1)]\} \qquad [2]$$

The parenthetical numbers *1* and *2* are the electron indices. By itself this determinant is not a proper spin-eigenfunction. However, by mixing with $|\bar{a}b|$ two spin-eigenfunctions will result, one having a singlet coupling as shown in Eq. [3], the other possessing a triplet coupling in (Eq. [4]); in both cases the normalization constants are omitted for the time being.

$$\Psi_{HL} = |a\bar{b}| - |\bar{a}b| \tag{3}$$

$$\Psi_{T} = |a\bar{b}| + |\bar{a}b| \tag{4}$$

If *a* and *b* are the respective AOs of two hydrogen atoms, Ψ_{HL} in Eq. [3] is just the historical wave function used in 1927 by Heitler and London[7] to treat the bonding in the H_2 molecule, hence the subscript descriptor HL. This wave function displays a purely covalent bond in which the two hydrogen atoms remain neutral and exchange their spins (the singlet pairing is represented, henceforth by the two dots connected by a line as shown in **7** in Scheme 3).

$$\text{H} \bullet \!\!-\!\!\bullet \text{H} \qquad \text{H}\!\uparrow \ \uparrow\!\text{H} \qquad \text{H}^- \ \text{H}^+ \qquad \text{H}^+ \ \text{H}^-$$

$$\textbf{7} \qquad\qquad \textbf{8} \qquad\qquad \textbf{9} \qquad\qquad \textbf{10}$$

Scheme 3

The state Ψ_{T} in Eq. [4] represents a repulsive triplet interaction (see **8** in Scheme 3) between two hydrogen atoms having parallel spins. The other VB determinants that one can construct in this simple two-electron/two-center 2e/2c case are $|a\bar{a}|$ and $|b\bar{b}|$, corresponding to the ionic structures **9** and **10**, respectively. Both ionic structures are spin-eigenfunctions and represent singlet situations. Note that the rules that govern spin multiplicities and the generation of spin-eigenfunctions from combinations of determinants are the same in VB and MO theories. In a simple two-electron case, it is easy to distinguish triplet from singlet eigenfunctions by factoring the spatial function out from the spin function: the singlet spin eigenfunction is antisymmetric with respect to electron exchange, while the triplet is symmetric. Of course, the spatial parts behave in precisely the opposite manner. For example, the singlet is $\alpha(1)\beta(2) - \beta(1)\alpha(2)$, while the triplet is $\alpha(1)\beta(2) + \beta(1)\alpha(2)$ in Eqs. [3] and [4].

While the H_2 bond was considered as purely covalent in Heitler and London's paper[7] (Eq. [3] and Structure **7** in Scheme 3), the exact description of H_2 or any homopolar bond ($\Psi_{VB\text{-full}}$ in Eq. [5]) involves a small contribution from the ionic structures **9** and **10**, which mix by configuration interaction (CI) in the VB framework. Typically, and depending on the atoms that are bonded, the weight of the purely covalent structure is $\sim$75%, while the ionic structures

share the remaining 25%. By symmetry, the wave function maintains an average neutrality of the two bonded atoms (Eq. [5]).

$$\Psi_{\text{VB-full}} = \lambda(|a\bar{b}| - |\bar{a}b|) + \mu(|a\bar{a}| + |b\bar{b}|) \quad \lambda > \mu \qquad [5a]$$

$$H_a-H_b \approx 75\%(H_a\bullet-\bullet H_b) + 25\%(H_a^- H_a^+ + H_b^+ H_b^-) \qquad [5b]$$

For convenience, and to avoid confusion, we shall symbolize a purely covalent bond between A and B centers as A•—•B, while the notation A—B will be employed for a composite bond wave function like the one displayed in Eq. [5b]. In other words, A—B refers to the "real" bond while A•—•B designates its covalent component (see **2** in Scheme 1).

VB Wave Functions with Semilocalized AOs

One inconvenience of using the expression $\Psi_{\text{VB-full}}$ (Eq. [5]) is its relative complexity compared to the simpler HL function (Eq. [3]). Coulson and Fischer[111] proposed an elegant way of combining the simplicity of Ψ_{HL} with the accuracy of $\Psi_{\text{VB-full}}$. In the Coulson–Fischer (CF) wave function, Ψ_{CF}, the two-electron bond is described as a formally covalent singlet coupling between two orbitals φ_a and φ_b, which are optimized with freedom to delocalize over the two centers. This is exemplified below for H_2 (dropping once again the normalization factors):

$$\Psi_{\text{CF}} = |\varphi_a \overline{\varphi_b}| - |\overline{\varphi_a} \varphi_b| \qquad [6a]$$

$$\varphi_a = a + \varepsilon b \qquad [6b]$$

$$\varphi_b = b + \varepsilon a \qquad [6c]$$

Here a and b are purely localized AOs, while φ_a and φ_b are delocalized AOs. In fact, experience shows that the Coulson–Fischer orbitals φ_a and φ_b, which result from the energy minimization, are generally not very delocalized ($\varepsilon < 1$). As such they can be viewed as "distorted" orbitals that remain atomic-like in nature. However minor this may look, the slight delocalization renders the Coulson–Fischer wave function equivalent to the VB-full (Eq. [5]) wave function with the three classical structures. A straightforward expansion of the Coulson–Fischer wave function leads to a linear combination of classical structures in Eq. [7].

$$\Psi_{\text{CF}} = (1 + \varepsilon^2)(|a\bar{b}| - |\bar{a}b|) + 2\varepsilon(|a\bar{a}| + |b\bar{b}|) \qquad [7]$$

Thus, the Coulson–Fischer representation keeps the simplicity of the covalent picture while treating the covalent–ionic balance by embedding the effect of the ionic terms in a variational way through the delocalization tails. The Coulson–Fischer idea was later generalized to polyatomic molecules and gave rise to the

generalized valence bond (GVB) and spin-coupled (SC) methods, which were mentioned in the introductory part and will be discussed later.

VB Wave Functions with Fragment Orbitals

Valence bond determinants may involve fragment orbitals (FOs) instead of localized or semilocalized AOs. These fragment orbitals may be delocalized (e.g., like some MOs of the constituent fragments of a molecule). The latter option is an economical way of representing a wave function that is a linear combination of several determinants based on AOs, just as MO determinants are linear combinations of VB determinants (see below). Suppose, for example, that one wanted to treat the recombination of the $CH_3^{\bullet}$ and $H^{\bullet}$ radicals in a VB manner. First, let ($\varphi_1 - \varphi_5$) be the MOs of the $CH_3^{\bullet}$ fragment (φ_5 being singly occupied), and b the AO of the incoming hydrogen. The covalent VB function that describes the active C–H bond in our study just couples the φ_5 and b orbitals in a singlet way, as expressed in Eq. [8]:

$$\Psi(H_3C\bullet\text{---}\bullet H) = |\varphi_1\overline{\varphi_1}\varphi_2\overline{\varphi_2}\varphi_3\overline{\varphi_3}\varphi_4\overline{\varphi_4}\,\varphi_5\overline{b}| - |\varphi_1\overline{\varphi_1}\varphi_2\overline{\varphi_2}\,\varphi_3\,\overline{\varphi_3}\varphi_4\overline{\varphi_4}\,\overline{\varphi_5}b| \quad [8]$$

Here, $\varphi_1 - \varphi_4$ are fully delocalized on the CH_3 fragment. Even the φ_5 orbital is not a pure AO, but may involve some tails on the hydrogens of the fragment. It is clear that this option is conceptually simpler than treating all the C–H bonds in a VB way, including the ones that remain unchanged in the reaction.

Writing VB Wave Functions Beyond the 2e/2c Case

Rules for writing VB wave functions in the polyelectronic case are just intuitive extensions of the rules for the 2e/2c case discussed above. First, let
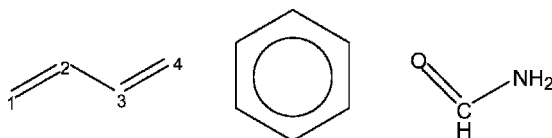
11   **12**   **13**

Scheme 4

us consider butadiene, structure **11** in Scheme 4, and restrict the description to the π system.

Denoting the π AOs of the C_1–C_4 carbons by a, b, c, and d, respectively, the fully covalent VB wave function for the π system of butadiene displays two singlet couplings: one between a and b, and one between c and d. It follows that the wave function can be expressed in the form of Eq. [9], as a product of the bond wave functions.

$$\Psi(\mathbf{11}) = |(a\overline{b} - \overline{a}b)(c\overline{d} - \overline{c}d)| \quad [9]$$

Upon expansion of the product, one gets a sum of four determinants as in Eq. [10].

$$\Psi(\mathbf{11}) = |a\bar{b}c\bar{d}| - |a\bar{b}\bar{c}d| - |\bar{a}bc\bar{d}| + |\bar{a}b\bar{c}d| \qquad [10]$$

The product of bond wave functions in Eq. [9], involves so-called perfect pairing, whereby we take the Lewis structure of the molecule, represent each bond by a HL bond, and finally express the full wave function as a product of all these pair-bond wave functions. As a rule, such a perfect-pairing polyelectronic VB wave function having n bond pairs will be described by 2^n determinants, displaying all the possible 2×2 spin permutations between the orbitals that are singlet coupled.

The above rule can readily be extended to larger polyelectronic systems, like the π system of benzene **12**, or to molecules bearing lone pairs like formamide, **13**. In this latter case, using *n, c*, and *o*, respectively, to refer to the π AOs of nitrogen, carbon, and oxygen, the VB wave function describing the neutral covalent structure is given by Eq. [11]:

$$\Psi(\mathbf{13}) = |n\bar{n}c\bar{o}| - |n\bar{n}\,\bar{c}o| \qquad [11]$$

In any one of the above cases, improvement of the wave function can be achieved by using Coulson–Fischer orbitals that take into account ionic contributions to the bonds. Note that the number of determinants grows exponentially with the number of covalent bonds (recall, this number is 2^n, n being the number of bonds). Hence, 8 determinants are required to describe a Kekulé structure of benzene, and the fully covalent and perfectly paired wave function for methane is made of 16 determinants. This shows the benefit of using FOs rather than pure AOs as much as possible, as has been done above (Eq. [8]). Using FOs to construct VB wave functions is also appropriate when one wants to fully exploit the symmetry properties of the molecule. For example, we can describe all the bonds in methane by constructing group orbitals of the four Hs. Subsequently, we can distribute the eight bonding electrons of the molecule into these FOs as well as into the *2s* and *2p* AOs of carbon. Then we can pair up the electrons using orbital symmetry-matched FOs, as shown by the lines connecting these orbital pairs in Figure 1. The corresponding wave function can be written as follows:

$$\Psi(CH_4) = |(2s\overline{\varphi_s} - \overline{\varphi_s}2s)(2p_x\overline{\varphi_x} - \overline{\varphi_x}2p_x)(2p_y\overline{\varphi_y} - \overline{\varphi_y}2p_y)(2p_z\overline{\varphi_z} - \overline{\varphi_z}2p_z)| \qquad [12]$$

In this representation, each bond is a delocalized covalent two-electron bond, written as a HL-type bond. The VB method that deals with fragment orbitals

$\Psi'_{VB}\{CH_4\}$
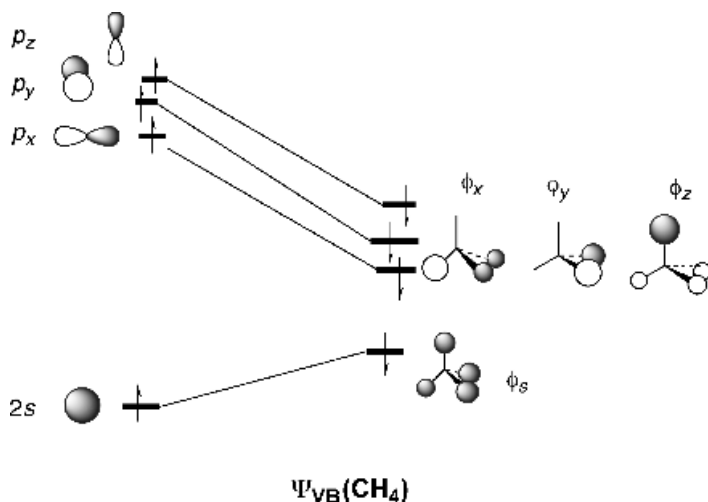
Figure 1 A VB representation of methane using delocalized FOs. Each line that connects the orbitals is a bond pair. The total wave function is given in Eq. 12.

(FO–VB) is particularly useful in high-symmetry cases such as ferrocene and other organometallic complexes.

Pictorial Representation of VB Wave Functions by Bond Diagrams

Since we argue that a bond need not necessarily involve only two AOs on two centers, we must provide an appropriate pictorial representation of such a bond. A possibility is the bond diagram in Figure 2, which shows two spin-paired electrons in general orbitals φ_1 and φ_2, with a line connecting these orbitals. This bond diagram represents the wave function in Eq. [13]

$$\Psi_{bond} = |\varphi_1 \overline{\varphi_2}| - |\overline{\varphi_1} \varphi_2| \qquad [13]$$

where the orbitals can take any shape; it can involve two centers with localized AOs, or two Coulson–Fischer orbitals with delocalization tails, or FOs that span multiple centers.
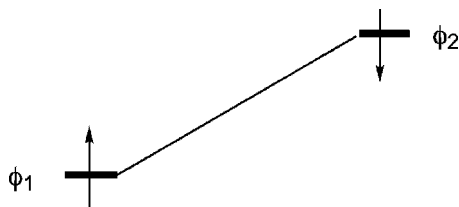
Figure 2 A bond diagram representation of two spin-paired electrons in orbitals ϕ_1 and ϕ_2. The bond pair is indicated by a line connecting the orbitals.

The Relationship between MO and VB Wave Functions

We now consider the difference between the MO and VB descriptions of an electronic system, at the simplest level of both theories. As we shall see, in the cases of one-electron, three-electron, and four-electron interactions between two centers, there is no real difference between the two theories, except for a matter of language. However, the two theories do differ in their description of the two-electron bond. Let us consider, once again, the example of H_2, with its two AOs *a* and *b,* and examine first the VB description, dropping normalization factors for simplicity.

As has been stated already, at equilibrium distance the bonding is not 100% covalent, and requires an ionic component to be accurately described. On the other hand, at long distances the HL wave function is the correct state, as the ionic components necessarily drop to zero and each hydrogen carries one electron away through the homolytic bond breaking. The HL wave function *dissociates correctly,* but is quantitatively inaccurate at bonding distances. Therefore, the way to improve the HL description is straightforward: simply mixing Ψ_{HL} with the ionic determinants and optimizing the coefficients variationally, by CI. One then gets the wave function $\Psi_{VB-full}$, in Eq. [5a] above, which contains a major covalent component and a minor ionic one.

Let us now turn to the MO description. Bringing together two hydrogen atoms leads to the formation of two MOs, σ and σ^* (bonding and antibonding, respectively); see Eq. [14].

$$\sigma = a + b \qquad \sigma^* = a - b \qquad [14]$$

At the simple MO level, the ground state of H_2 is described by Ψ_{MO}, in which the bonding σ MO is doubly occupied. Expansion (see Appendix for details) of this MO determinant into its AO determinant constituents leads to Eq. [15]:

$$\Psi_{MO} = |\sigma\overline{\sigma}| = (|a\overline{b}| - |\overline{a}b|) + (|a\overline{a}| + |b\overline{b}|) \qquad [15]$$

It is apparent from Eq. [15] that the first half of the expansion is just the Heitler–London function Ψ_{HL} (Eq. [3]), while the remaining part is ionic. It follows that the MO description of the two-electron bond will always be half-covalent, half-ionic, irrespective of the bonding distance. Qualitatively, it is already clear that in the MO wave function, the ionic weight is excessive at bonding distances, and becomes an absurdity at long distances, where the weight of the ionic structures should drop to zero in accord with homolytic cleavage. The simple MO description *does not dissociate correctly* and this is the reason why it is inappropriate for the description of stretched bonds as, for example, those found in transition states. The remedy for this poor description is CI, specifically the mixing of the ground configuration, σ^2, with the diexcited one, σ^{*2}. The reason this mixing resizes the covalent versus

ionic weights is the following: If one expands the diexcited configuration, Ψ_D, into its VB constituents (for expansion technique, see Appendix A.1), one finds the same covalent and ionic components as in Eq. [15], but coupled with a negative sign as in Eq. [16]:

$$\Psi_D = |\sigma^*\overline{\sigma^*}| = -(|a\overline{b}| - |\overline{a}b|) + (|a\overline{a}| + |b\overline{b}|) \qquad [16]$$

It follows that mixing the two configurations Ψ_{MO} and Ψ_D with different coefficients as in Eq. [17] will lead to a wave function Ψ_{MO-CI} in which the covalent and ionic components have

$$\Psi_{MO-CI} = c_1|\sigma\overline{\sigma}| - c_2|\sigma^*\overline{\sigma^*}| \qquad c_1, c_2 > 0 \qquad [17]$$

unequal weights, as shown by an expansion of Ψ_{MO-CI} into AO determinants in Eq. [18]:

$$\Psi_{MO-CI} = (c_1 + c_2)(|a\overline{b}| - |\overline{a}b|) + (c_1 - c_2)(|a\overline{a}| + |b\overline{b}|) \qquad [18a]$$
$$c_1 + c_2 = \lambda \qquad c_1 - c_2 = \mu \qquad [18b]$$

Since c_1 and c_2 are variationally optimized, expansion of Ψ_{MO-CI} should lead to exactly the same VB function as $\Psi_{VB-full}$ in Eq. [5], leading to the equalities expressed in Eq. [18b] and to the equivalence of Ψ_{MO-CI} and $\Psi_{VB-full}$. The equivalence also includes the Coulson–Fischer wave function Ψ_{CF} (Eq. [6]) which, as we have seen, is equivalent to the VB-full description.

$$\Psi_{MO} \neq \Psi_{HL} \quad \Psi_{MO-CI} \equiv \Psi_{VB-full} \equiv \Psi_{CF} \qquad [19]$$

To summarize, the simple MO treatment describes the bond as being too ionic, while the simple VB level (Heitler–London) defines it as being purely covalent. Both theories converge to the right description when CI is introduced. The accurate description of two-electron bonding is half-way between the simple MO and simple VB levels; elaborated MO and VB levels become equivalent and converge to the right description, in which the bond is mostly covalent but has a substantial contribution from ionic structures.

This equivalence clearly indicates that the MO–VB rivalry, discussed above, is unfortunate and senseless. VB and MO are not two diametrically different theories that exclude each other, but rather two representations of reality that are mathematically equivalent. The best approach is to use these two representations jointly and benefit from their complementary insight. In fact, from the above discussion of how to write a VB wave function, it is apparent that there is a spectrum of orbital representations that stretches between the fully local VB representations through semilocalized CF orbitals, to the use of delocalized fragment orbitals VB (FO–VB), and all the way to the fully

delocalized MO representation (in the MO–CI language). Based on the problem at hand, the best representation from this spectrum should be the one that gives the clearest and most portable insight into the problem.

Formalism Using the Exact Hamiltonian

Let us turn now to the calculation of energetic quantities using exact VB theory by considering the simple case of the H_2 molecule. The exact Hamiltonian is of course the same as in MO theory, and is composed in this case of two core terms and a bielectronic repulsion:

$$H = h(1) + h(2) + 1/r_{12} + 1/R \qquad [20]$$

where the h operator represents the attraction between one electron and the nuclei, r_{12} is the interelectronic distance and R is the distance between the nuclei and accounts for nuclear repulsion. In the VB framework, some particular notations are traditionally employed to designate the various energies and matrix elements:

$$Q = \langle |a\overline{b}| |H| |a\overline{b}| \rangle = \langle a|h|a \rangle + \langle b|h|b \rangle + \langle ab|1/r_{12}|ab \rangle \qquad [21]$$

$$K = \langle |a\overline{b}| |H| |b\overline{a}| \rangle = \langle ab|1/r_{12}|ab \rangle + 2S\langle a|h|b \rangle \qquad [22]$$

$$\langle (|a\overline{b}|)|(|b\overline{a}|) \rangle = S^2 \qquad [23]$$

Here Q is the energy of a single determinant $|a\overline{b}|$, K is the spin exchange term which will be dealt with later, and S is the overlap integral between the two AOs a and b.

The energy Q has an interesting property: It is quasiconstant as a function of the interatomic distance, from infinite distance to the equilibrium bonding distance R_{eq} of H_2. It corresponds to the energy of two hydrogen atoms when brought together without exchanging their spins. Such a pseudo-state (which is not a spin-eigenfunction) is called the "quasi-classical state" of H_2 (Ψ_{QC} in Fig. 3), because all the terms of its energy have an analogue in classical (not quantum) physics. Turning now to real states, that is, spin-eigenfunctions, the energy of the ground state of H_2, in the fully covalent approximation of HL, is readily obtained.

$$E(\Psi_{HL}) = \frac{\langle (|a\overline{b}| - |\overline{a}b|)|H|(|a\overline{b}| - |\overline{a}b|) \rangle}{\langle (|a\overline{b}| - |\overline{a}b|)|(|a\overline{b}| - |\overline{a}b|) \rangle} = \frac{Q+K}{1+S^2} \qquad [24]$$

Plotting the $E(\Psi_{HL})$ curve as a function of the distance now gives qualitatively correct Morse curve behavior (Fig. 3), with a reasonable bonding energy, even if a deeper potential well can be obtained by allowing further mixing with the
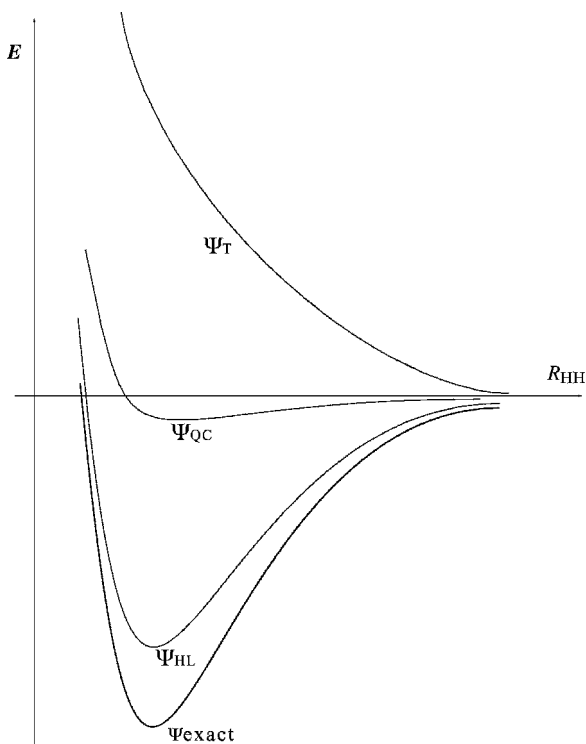
Figure 3 Energy curves for H_2 as a function of internuclear distance. The curves displayed, from top to bottom, correspond to the triplet state, Ψ_T, the quasi-classical state, Ψ_{QC}, the HL state, Ψ_{HL}, and the exact (full CI) curve, Ψ_{exact}.

ionic terms (Ψ_{exact} in Fig. 3). This shows that, in the covalent approximation, all the bonding comes from the K terms. Thus, *the physical phenomenon responsible for the bond is the exchange of spins between the two AOs, that is, the resonance between the two spin arrangements* (see **1**).

Examination of the K term in Eq. [22] shows that it is made of a repulsive exchange integral, which is positive but necessarily small (unlike Coulomb two-electron integrals), and of a negative term, given by the product of the overlap S and an integral that is called the "resonance integral", which is itself proportional to S.

Replacing Ψ_{HL} by Ψ_T in Eq. [24] leads to the energy of the triplet state, Eq. [25].

$$E(\Psi_T) = \frac{\langle(|\,a\overline{b}\,| + |\overline{a}b\,|)|\,H\,|(|\,a\overline{b}\,| + |\overline{a}b\,|)\rangle}{\langle(|\,a\overline{b}\,| + |\overline{a}b\,|)|(|\,a\overline{b}\,| + |\overline{a}b\,|)\rangle} = \frac{Q - K}{1 - S^2} \qquad [25]$$

Recalling that the Q integral is a quasi-constant from R_{eq} to infinite distance, Q remains nearly equal to the energy of the separated fragments and can serve, at any distance, as a reference for the bond energy. It follows from Eqs. [24] and [25] that, if we neglect overlap in the denominator, the triplet state (Ψ_T in Fig. 3) is repulsive by the same quantity ($-K$) as the singlet is bonding ($+K$). Thus, at any distance larger than R_{eq}, the bonding energy is about one-half of the singlet–triplet gap. This property will be used later in applications to reactivity.

Qualitative VB Theory

A VB calculation is just a configuration interaction in a space of AO or FO determinants, which are in general nonorthogonal to each other. It is therefore essential to derive some basic rules for calculating the overlaps and Hamiltonian matrix elements between determinants. The fully general rules have been described in detail elsewhere.[52] Examples will be given here for commonly encountered simple cases.

Overlaps between Determinants

Let us illustrate the procedure with VB determinants of the type Ω and Ω' below,

$$\Omega = N|a\bar{a}b\bar{b}| \quad \Omega' = N'|c\bar{c}d\bar{d}| \qquad [26]$$

where N and N' are normalization factors. Each determinant is made of a diagonal product of spin orbitals followed by a signed sum of all the permutations of this product, which are obtained by transposing the order of the spin orbitals. Denoting the diagonal products of Ω and Ω', by Ψ_d and Ψ'_d, respectively, the expression for Ψ_d reads

$$\Psi_d = a(1)\,\bar{a}(2)\,b(3)\,\bar{b}(4) \quad (1, 2, \ldots \text{ are electron indices}) \qquad [27]$$

and an analogous expression can be written for Ψ'_d.

The overlap between the (unnormalized) determinants $|a\,\bar{a}\,b\,\bar{b}|$ and $|c\,\bar{c}\,d\,\bar{d}|$ is given by Eq. [28]:

$$\langle(|a\,\bar{a}\,b\,\bar{b}|)(|c\,\bar{c}\,d\,\bar{d}|)\rangle = \left\langle \Psi_d \left| \sum_P (-1)^t P(\Psi'_d) \right. \right\rangle \qquad [28]$$

where the operator P represents a *restricted subset of permutations*: The ones made of pairwise transpositions between spin orbitals of the same spin, and t determines the parity, odd or even, and hence also the sign of a given pairwise

transposition P. Note that the identity permutation is included. In the present example, there are four possible such permutations in the product Ψ'_d:

$$\sum_P (-1)^t P(_d') = c(1)\,\bar{c}(2)\,d(3)\,\bar{d}(4) - d(1)\,\bar{c}(2)\,c(3)\,\bar{d}(4)$$
$$- c(1)\,\bar{d}(2)\,d(3)\,\bar{c}(4) + d(1)\,\bar{d}(2)\,c(3)\,\bar{c}(4) \qquad [29]$$

One then integrates Eq. [28] electron by electron, leading to Eq. [30] for the overlap between $|\,a\,\bar{a}\,b\,\bar{b}\,|$ and $|\,c\,\bar{c}\,d\,\bar{d}\,|$:

$$\langle(|\,a\,\bar{a}\,b\,\bar{b}\,|)|(|\,c\,\bar{c}\,d\,\bar{d}\,|)\rangle = S_{ac}^2 S_{bd}^2 - S_{ad}S_{ac}S_{bc}S_{bd}$$
$$- S_{ac}S_{ad}S_{bd}S_{bc} + S_{ad}^2 S_{bc}^2 \qquad [30]$$

where S_{ac}, for example, is a simple overlap between two orbitals a and c.

Generalization to different types of determinants is trivial.[52] As an application, let us obtain the overlap of a VB determinant with itself, and calculate the normalization factor N of the determinant Ω in Eq. [26]:

$$\langle(|\,a\,\bar{a}\,b\,\bar{b}\,|)|(|\,a\,\bar{a}\,b\,\bar{b}\,|)\rangle = 1 - 2S_{ab}^2 + S_{ab}^4 \qquad [31]$$
$$\Omega = (1 - 2S_{ab}^2 + S_{ab}^4)^{-1/2}|a\,\bar{a}\,b\,\bar{b}| \qquad [32]$$

Generally, normalization factors for determinants are larger than unity. The exception is those VB determinants that do not have more than one spin orbital of each spin variety (e.g., the determinants that compose the HL wave function). For these latter determinants the normalization factor is unity (i.e., $N = 1$).

An Effective Hamiltonian

Using the exact Hamiltonian for calculating matrix elements between VB determinants would lead to complicated expressions involving numerous bielectronic integrals, owing to the $1/r_{ij}$ terms. Thus, for practical qualitative or semiquantitative applications, one uses an effective Hamiltonian in which the $1/r_{ij}$ terms are only implicitly taken into account, in an averaged manner. One then defines a Hamiltonian made of a sum of independent monoelectronic Hamiltonians, much like in simple MO theory:

$$H^{\text{eff}} = \sum_i h(i) \qquad [33]$$

where the summation runs over the total number of electrons. Here the operator h has a meaning different from Eq. [20] since it is now an effective

monoelectronic operator that incorporates part of the electron–electron and nuclear–nuclear repulsions. Going back to the four–electron example above, the determinants Ω and Ω' are coupled by the following effective Hamiltonian matrix element:

$$\langle\Omega|H^{\text{eff}}|\Omega'\rangle = \langle\Omega|h(1) + h(2) + h(3) + h(4)|\Omega'\rangle \qquad [34]$$

It is apparent that the above matrix element is composed of a sum of four terms that are calculated independently. The calculation of each of these terms (e.g., the first one) is quite analogous to the calculation of the overlap in Eq. [30], except that the first monoelectronic overlap S in each product is replaced by a monoelectronic Hamiltonian term:

$$\langle(|\,a\,\bar{a}\,b\,\bar{b}\,|)|\,h(1)\,|(|\,c\,\bar{c}\,d\,\bar{d}\,|)\,\rangle = h_{ac}S_{ac}S_{bd}^2 - h_{ad}S_{ac}S_{bc}S_{bd}$$
$$- h_{ac}S_{ad}S_{bd}S_{bc} + h_{ad}S_{ad}S_{bc}^2 \qquad [35a]$$
$$h_{ac} = \langle a|h|c\rangle \qquad [35b]$$

In Eq. [35b], the monoelectronic integral accounts for the interaction between two overlapping orbitals. A diagonal term of the type h_{aa} is interpreted as the energy of the orbital a, and will be noted ε_a in the following equations. By using Eqs. [34] and [35], it is easy to calculate the energy of the determinant $|\,a\,\bar{a}\,b\bar{b}\,|$:

$$E(|a\bar{a}b\bar{b}|) = N^2(2\varepsilon_a + 2\varepsilon_b - 2\varepsilon_a S_{ab}^2 - 2\varepsilon_b S_{ab}^2 - 4h_{ab}S_{ab} + 4h_{ab}S_{ab}^3) \qquad [36]$$

An interesting application of the above rules is the calculation of the energy of a spin-alternant determinant such as **14** in Scheme 5 for butadiene.
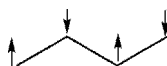
14

Scheme 5

Such a determinant, in which the spins are arranged so that two neighboring orbitals always display opposite spins is referred to as a "quasiclassical" (QC) state and is a generalization of the QC state that we already encountered above for H_2. The rigorous formulation of its energy involves some terms that arise from permutations between orbitals of the same spins, which are necessarily nonneighbors. Neglecting interactions between non-nearest neighbors, all these vanish, so that the energy of the QC state is given by the simple expression below.

$$E|\,a\,\bar{b}\,c\,\bar{d}\,| = \varepsilon_a + \varepsilon_b + \varepsilon_c + \varepsilon_d \qquad [37]$$

Generalizing, the energy of a spin-alternant determinant is always the sum of the energies of its constituent orbitals. In the QC state, the interaction between overlapping orbitals is therefore neither stabilizing nor repulsive. This is a nonbonding state, which can be used for defining a reference state, with zero energy, in the framework of VB calculations of bonding energies or repulsive interactions.

Note that the rules and formulas that are expressed above in the framework of qualitative VB theory are independent of the type of orbitals that are used in the VB determinants: purely localized AOs, fragment orbitals or Coulson–Fischer semilocalized orbitals. Depending on the kind of orbitals that are chosen, the h and S integrals take different values, but the formulas remain the same.

Some Simple Formulas for Elementary Interactions

In qualitative VB theory, it is customary to take the average value of the orbital energies as the origin for various quantities. With this convention, and using some simple algebra,[52] the monoelectronic Hamiltonian between two orbitals becomes β_{ab}, the familiar "reduced resonance integral":

$$\beta_{ab} = h_{ab} - 0.5(h_{aa} + h_{bb})S_{ab} \qquad [38]$$

It is important to note that these β integrals, used in the VB framework are the same as those used in simple MO models such as extended Hückel theory.

Based on the new energy scale, the sum of orbital energies is set to zero, that is:

$$\sum_i \varepsilon_i = 0 \qquad [39]$$

In addition, since the energy of the QC determinant is given by the sum of orbital energies, its energy then becomes zero:

$$E(|\,a\,\overline{b}\,c\,\overline{d}\,|) = 0 \qquad [40]$$

The Two-Electron Bond

By application of the qualitative VB theory, Eq. [41] expresses the HL-bond energy of two electrons in atomic orbitals a and b, which belong to the atomic centers A and B. The binding energy D_e is defined relative to the quasiclassical state $|a\overline{b}|$ or to the energy of the separate atoms, which are equal within the approximation scheme.

$$D_e(A-B) = 2\beta S/(1 + S^2) \qquad [41]$$

Here, β is the reduced resonance integral that we have just defined and S is the overlap between orbitals a and b. Note that if instead of using purely localized AOs for a and b, we use semilocalized Coulson–Fischer orbitals, Eq. [41] will not be the simple HL-bond energy but would represent *the bonding energy of the real A–B bond* that includes its optimized covalent and ionic components. In this case, the origins of the energy would still correspond to the QC determinant with the localized orbitals. Unless otherwise specified, we will always use qualitative VB theory with this latter convention.

Repulsive Interactions

By using the above definitions, one gets the following expression for the repulsive energy of the triplet state:

$$\Delta E_T(A \uparrow\uparrow B) = -2\beta S/(1 - S^2) \qquad [42]$$

The triplet repulsion arises due to the Pauli exclusion rule and is often referred to as a Pauli repulsion.

For a situation where we have four electrons on the two centers, VB theory predicts a doubling of the Pauli repulsion, and the following expression is obtained in complete analogy to qualitative MO theory:

$$\Delta E(A{:}\,{:}B) = -4\beta S/(1 - S^2) \qquad [43]$$

One can, in fact, simply generalize the rules for Pauli repulsion. Thus, the electronic repulsion in an interacting system is equal to the quantity:

$$\Delta E_{\text{rep}} = -2n\beta S/(1 - S^2) \qquad [44]$$

n being the number of electron pairs with identical spins.

Now, consider VB structures with three electrons on two centers, $(A{:}\,{}^{\bullet}B)$ and $(A^{\bullet}\,{:}B)$. The interaction energy of each one of these structures by itself is repulsive and following Eq. [42] will be given by the Pauli repulsion term in Eq. [45]:

$$\Delta E((A{:}\,{}^{\bullet}B) \quad \text{and} \quad (A^{\bullet}\,{:}B)) = -2\beta S/(1 - S^2) \qquad [45]$$

Mixing Rules for VB Structures

Whenever a wave function is written as a normalized resonance hybrid between two VB structures of equivalent energies (e.g, as in Eq. [46], the energy of the hybrid is given by the normalized averaged self-energies of the constituent resonance structures and the interaction matrix element, H_{12},

between the structures in Eq. [47].

$$\Psi = N[\Phi_1 + \Phi_2]$$
$$\text{where} \quad N = 1/[2(1 + S_{12})]^{1/2} \tag{46}$$
$$E(\Psi) = 2N^2 E_{av} + 2N^2 H_{12}$$
$$\text{where} \quad H_{12} = \langle\Phi_1|\mathbf{H}|\Phi_2\rangle \quad \text{and} \quad E_{av} = [(E_1 + E_2)/2] \tag{47}$$

Such a mixed state is stabilized relative to the energy of each individual VB structure, by a quantity that is called the "resonance energy" (*RE*):

$$\text{RE} = [H_{12} - E_{av}S_{12}]/(1 + S_{12}) \quad S_{12} = \langle\Phi_1|\Phi_2\rangle \tag{48}$$

Equation [48] expresses the RE in the case where the two limiting structures Φ_1 and Φ_2 have equal or nearly equal energies, which is the most favorable situation for maximum stabilization. However, if the energies E_1 and E_2 are different, then according to the rules of perturbation theory, the stabilization will still be significant, albeit than in the degenerate case.

   A typical situation where the VB wave function is written as a resonance hybrid is odd-electron bonding (one-electron or three-electron bonds). For example, a one-electron bond A•B is a situation where only one electron is shared by two centers A and B (Eq. [49]), while three electrons are distributed over the two centers in a three-electron bond A∴B (Eq. [50]):

$$\text{A•B} = \text{A}^{+}\,{}^{\bullet}\text{B} \leftrightarrow \text{A}^{\bullet\,+}\text{B} \tag{49}$$
$$\text{A}∴\text{B} = \text{A}^{\bullet}\text{:B} \leftrightarrow \text{A:}^{\bullet}\text{B} \tag{50}$$

Simple algebra shows that the overlap between the two VB structures is equal to S (the $\langle a|b\rangle$ orbital overlap)[a] and that resonance energy follows Eq. [51]:

$$\text{RE} = \beta/(1 + S) = D_e(\text{A}^{+}\,{}^{\bullet}\text{B} \leftrightarrow \text{A}^{\bullet\,+}\text{B}) \tag{51}$$

Equation [51] also gives the bonding energy of a one-electron bond. Combining Eqs. [45] and [51], we get the bonding energy of the three-electron bond, Eq. [52]:

$$D_e(\text{A}^{\bullet}\text{:B} \leftrightarrow \text{A:}^{\bullet}\text{B}) = -2\beta S/(1 - S^2) + \beta/(1 + S)$$
$$= \beta(1 - 3S)/(1 - S^2) \tag{52}$$

---

[a] Writing ϕ_1 and ϕ_2 so that their positive combination is the resonance-stabilized one.

These equations for odd-electron bonding energies are good for cases where the forms are degenerate or nearly so. In cases where the two structures are not identical in energy, one should use the perturbation theoretic expression.[52]

For more complex situations, general guidelines for derivation of matrix elements between polyelectronic determinants are given in Appendix A.2. Alternatively, one could follow the protocol given in the original literature.[52,143]

Nonbonding Interactions in VB Theory

Some situations are encountered where one orbital bears an unpaired electron in the vicinity of a bond, such as **15** in Scheme 6:

$$A\uparrow \quad B\bullet\!\!-\!\!\bullet C$$

15

Scheme 6

Since A•B•—•C displays a singlet coupling between orbitals b and c, Eq. [53] gives its wave function:

$$A\bullet B\bullet\!\!-\!\!\bullet C = N(|a\,b\,\bar{c}| - |a\,\bar{b}\,c|) \qquad [53]$$

in which it is apparent that the first determinant involves a triplet repulsion with respect to the electrons in a and b while the second one is a spin-alternant determinant. The energy of this state, relative to a situation where A and BC are separated, is therefore:

$$E(A\bullet B\bullet\!\!-\!\!\bullet C) - E(A) - E(B\bullet\!\!-\!\!\bullet C) = -\beta S/(1 - S^2) \qquad [54]$$

which means that bringing an unpaired electron into the vicinity of a covalent bond results in half of the full triplet repulsion. This property will be used below when we discuss VB correlation diagrams for radical reactions. The

$$A\bullet\!\!-\!\!\bullet B \quad C\bullet\!\!-\!\!\bullet D$$

16

Scheme 7

repulsion is the same if we bring two covalent bonds, A•—•B and C•—•D, close to each other, as in **16** (Scheme 7):

$$E(A\bullet\!\!-\!\!\bullet B \cdots C\bullet\!\!-\!\!\bullet D) - E(A\bullet\!\!-\!\!\bullet B) - E(C\bullet\!\!-\!\!\bullet D) = -\beta S/(1 - S^2) \qquad [55]$$

Equation [55] can be used to calculate the total π energy of one canonical structure of a polyene, for example, structure **17** of butadiene (Scheme 8).
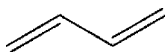
17

Scheme 8

Since there are two covalent bonds and one nonbonded repulsion in this VB structure, its energy is expressed simply as follows:

$$\Psi(\mathbf{17}) = 4\beta S/(1 + S^2) - \beta S/(1 - S^2) \tag{56}$$

As an application, let us compare the energies of two isomers of hexatriene. The linear s-trans conformation can be described as a resonance between the canonical structure **18** and "long bond" structures **19–21** (Scheme 9)
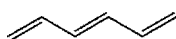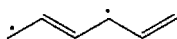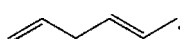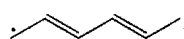
18   **19**   **20**   **21**
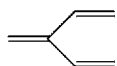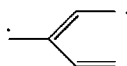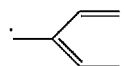
22   **23**   **24**

Scheme 9

where one short bond is replaced by a long bond. On the other hand, the branched isomer is made only of structures **22–24**, since it lacks an analogous structure to **21**.

It is apparent that the canonical structures **18** and **22** have the same electronic energies (three bonds, two nonbonded repulsions), and that structures **19–21**, **23**, and **24** are also degenerate (two bonds, three nonbonded repulsions). Furthermore, if one omits structure **21**, the matrix elements between the remaining long-bond structures and the canonical ones are all the same. Thus, elimination of structure **21** will make both isomers isoenergetic. If, however, we take structure **21** into account, it will mix and increase, however, slightly, the RE of the linear polyene that becomes thermodynamically more stable than the branched one. This subtle prediction, which is in agreement with experiment, will be demonstrated again below in the framework of Heisenberg Hamiltonians.

Table 1 Elementary Interaction Energies in the Qualitative MO and VB Models

Type of Interaction	Stabilization (MO Model)	Stabilization (VB Model)
1-Electron	$\beta/(1+S)$	$\beta/(1+S)$
2-Electron	$2\beta/(1+S)$	$2\beta S/(1+S^2)$
3-Electron	$\beta(1-3S)/(1-S^2)$	$\beta(1-3S)/(1-S^2)$
4-Electron	$-4\beta S/(1-S^2)$	$-4\beta S/(1-S^2)$
Triplet repulsion	$-2\beta S/(1-S^2)$	$-2\beta S/(1-S^2)$
3-Electron repulsion		$-2\beta S/(1-S^2)$

Comparison with Qualitative MO Theory

Some (but not all) of the elementary interaction energies that are discussed above also have qualitative MO expressions, which may or may not match the VB expressions. In qualitative MO theory, the interaction between two overlapping AOs leads to a pair of bonding and antibonding MOs, the former being stabilized by the quantity $\beta/(1+S)$ and the latter destabilized by $-\beta/(1-S)$ relative to the nonbonding level. The stabilization–destabilization of the interacting system relative to the separate fragments is then calculated by summing up the occupancy-weighted energies of the MOs. A comparison of the qualitative VB and MO approaches is given in Table 1, where the energetics of the elementary interactions are calculated with both methods. It is apparent that both qualitative theories give identical expressions for the odd-electron bonds, the four-electron repulsion, and the triplet repulsion. This is not surprising if one notes that the MO and VB wave functions for these four types of interaction are identical. On the other hand, the expressions for the MO and VB two-electron-bonding energies are different; the difference is related to the fact, discussed above, that MO and VB wave functions are themselves different in this case. Therefore, we suggest a rule that may be useful if one is more familiar with MO theory than VB: *Whenever the VB and MO wave functions of an electronic state are equivalent, the VB energy can be estimated using qualitative MO theory.*

INSIGHTS OF QUALITATIVE VB THEORY

This section demonstrates how the simple rules of the above VB approach can be utilized to treat a variety of problems. Initially, we treat a series of examples, which were mentioned in the introduction as "failures" of VB theory, and show that properly done VB theory leads to the right result for the right reason. Subsequently, we proceed with a relatively simple problem in chemical bonding of one-electron versus two-electron bonds and demonstrate that VB theory can make surprising predictions that stand the

test of experiment. Finally, we show how VB theory can lead to a general model for chemical reactivity, the VB diagram. Since these subtopics cover a wide range of chemical problems we cannot obviously treat them in-depth, and wherever possible we refer the reader to more extensive reviews.

Are the "Failures" of VB Theory Real?

As mentioned in the introduction, VB theory has been accused of a few "failures" that are occasionally used to dismiss the theory, and have caused it to have an unwarranted reputation. The next few subsections use the simple VB guidelines drawn above to demonstrate that VB theory is free of these "failures".

Dioxygen

One of the major "failures" that has been associated with VB theory concerns the ground state of the dioxygen molecule, O_2. It is true that a naive application of hybridization followed by perfect pairing (simple Lewis pairing) would predict a $^1\Delta_g$ ground state, that is, the diamagnetic doubly bonded molecule O=O. This is likely the origin of the notion that VB theory makes a flawed prediction that contradicts experiment (see, e.g., references [50] and [51]). However, this conclusion is not valid, since in the early 1970s Goddard et al.[107] performed GVB calculations and demonstrated that VB theory predicts a triplet $^3\Sigma_g^-$ ground state. This same outcome was reported in papers by McWeeny[144] and Harcourt.[145] In fact, any VB calculation, at whatever imagined level, would lead to the same result, so the myth of "failure" is definitely baseless.

Goddard et al.[107] and subsequently the present two authors[53] also provided a simple VB explanation for the choice of the ground state. Let us reiterate this explanation based on our qualitative VB theory, outlined above.

Apart from one σ bond and one σ lone pair on each oxygen atom, the dioxygen molecule has six π electrons to be distributed in the two π planes, say π_x and π_y. The question is What is the most favorable mode of distribution? Is it **25** in which three electrons are placed in each π plane, or perhaps is it **26** where two electrons are allocated to one plane and four to the other (Scheme 10)? Obviously, **25** is a diradical structure displaying one three-electron bond

| 25 | 25' | 26 | 26' |
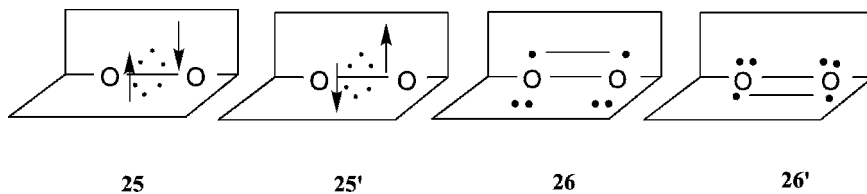
Scheme 10

in each of π planes, whereas **26** exhibits a singlet π bond, in one plane, and a four-electron repulsion, in the other. A naive application that neglects the repulsive three-electron and four-electron interactions would predict that structure **26** is preferred, leading to the above-mentioned legendary failure of VB theory, namely, that VB predicts the ground state of O_2 to be the singlet closed-shell structure, O=O. Inspection of the repulsive interactions shows that they are of the same order of magnitude or even larger than the bonding interactions, that is, the neglect of these repulsion is unjustified. The right answer is immediately apparent, if we carry out the VB calculation correctly, including the repulsion and bonding interactions for structures **25** and **26**. The resulting expressions and the respective energy difference, which are shown in Eqs. [57–59], demonstrate clearly that the diradical structure **25** is more stable than the doubly bonded Lewis structures **26**.

$$E(\mathbf{25}) = 2\beta(1 - 3S)/(1 - S^2) \qquad [57]$$

$$E(\mathbf{26}) = 2\beta S/(1 + S^2) - 4\beta S/(1 - S^2) \qquad [58]$$

$$E(\mathbf{26}) - E(\mathbf{25}) = -2\beta(1 - S)^2/(1 - S^4) > 0 \qquad [59]$$

Thus far we have not considered the set of Slater determinants **25′** and **26′**, which are symmetry-equivalent to **25** and **26** by inversion of the π_x and π_y planes. The interactions between the two sets of determinants yield two pairs of resonant–antiresonant combinations that constitute the final low-lying states of dioxygen, as represented in Figure 4. Of course, our effective VB theory was chosen to disregard the bielectronic terms and, therefore, the theory, as
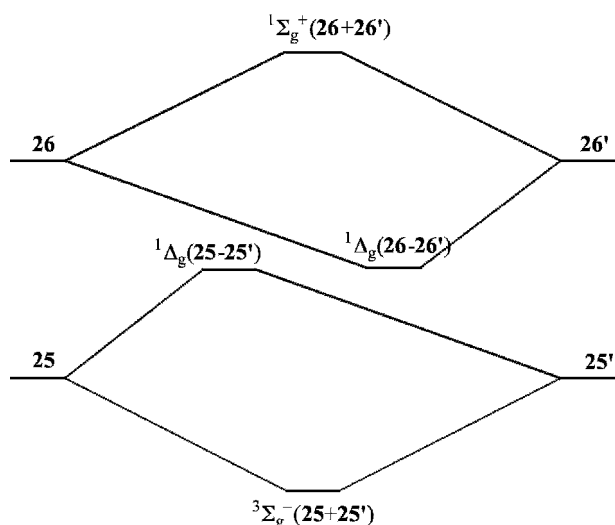
Figure 4 Formation of the symmetry adapted states of O_2 from the biradical (**25**, **25′**) and perfectly-paired (**26**, **26′**) structures.

such, will not tell us what the lowest spin state in the O_2 diradical is. This, however, is a simple matter, because further considerations can be made by appealing to Hund's rule, which is precisely what qualitative MO theory must do in order to predict the triplet nature of the O_2 ground state. Accordingly, the in-phase and out-of-phase combinations of the diradical determinants **25** and **25′** lead to triplet ($^3\Sigma_g^-$) and singlet ($^1\Delta_g$) states, respectively, the former being the lowest state by virtue of favorable exchange energy.

Similarly, **26** and **26′** yield a resonant $^1\Delta_g$ combination and an antiresonant $^1\Sigma_g^+$ one. Thus, it is seen that simple qualitative VB considerations not only predict the ground state of O_2 to be a triplet, but also yield a correct energy ordering for the remaining low-lying excited states.

The Valence Ionization Spectrum of CH₄

As discussed in the introduction, the development of PES showed that the spectra could be simply interpreted if one assumed that electrons occupy delocalized molecular orbitals.[47,48] By contrast, VB theory, which uses localized bond orbitals (LBOs), seems completely useless for interpretation of PES. Moreover, since VB theory describes equivalent electron pairs that occupy LBOs, the PES results seem to be in disagreement with this theory. An iconic example of this "failure" of VB theory is the PES of methane that displays two different ionization peaks. These peaks correspond to the a_1 and t_2 MOs, but not to the four equivalent C—H LBOs in Pauling's hybridization theory.

Let us now examine the problem carefully in terms of LBOs to demonstrate that VB gives the right result for the right reason. A physically correct representation of the CH_4^+ cation would be a linear combination of the four forms such that the wave function does not distinguish the four LBOs that are related by symmetry. The corresponding VB picture, more specifically an FO–VB picture, is illustrated in Figure 5, which enumerates the VB structures and their respective determinants. Each VB structure involves a localized one-electron bond situation, while the other bonds are described by doubly occupied LBOs. To make life easier, we can use LBOs that derive from a unitary transformation of the canonical MOs. As such, these LBOs would be orthogonal to each other and one can calculate the Hamiltonian matrix element between two such VB structures by simply setting all overlaps to zero in the VB expressions, or by using the equivalent rules of qualitative MO theory. Thus, to calculate the Φ_1–Φ_2 interaction matrix element, one first puts the orbitals of both determinants in maximal correspondence, by means of a transposition in Φ_2. The resulting two transformed determinants differ by only one spin orbital, $c \neq d$, so that their matrix element is simply β. Going back to the original Φ_1 and Φ_2 determinants, it appears that their matrix element is negatively signed (Eq. [60]),

$$\langle \Phi_1 | H^{\text{eff}} | \Phi_2 \rangle = \langle (| \, a \, \overline{a} \, b \, \overline{b} \, c \, \overline{c} \, d \, |) | \, H^{\text{eff}} \, | (| \, d \, \overline{d} \, a \, \overline{a} \, b \, \overline{b} \, c \, |) \rangle$$

$$= -\langle (| \, a \, \overline{a} \, b \, \overline{b} \, c \, \overline{c} \, d \, |) | \, H^{\text{eff}} \, | (| \, a \, \overline{a} \, b \, \overline{b} \, c \, \overline{d} \, d \, |) \rangle = -\beta \qquad [60]$$

Φ_1 Φ_2 Φ_3 Φ_4

$|\,\overline{a}a\overline{b}b\overline{c}cd\,|$ $|\,\overline{d}d\overline{a}a\overline{b}bc\,|$ $|\,\overline{c}c\overline{d}d\overline{a}ab\,|$ $|\,\overline{b}b\overline{c}c\overline{d}da\,|$
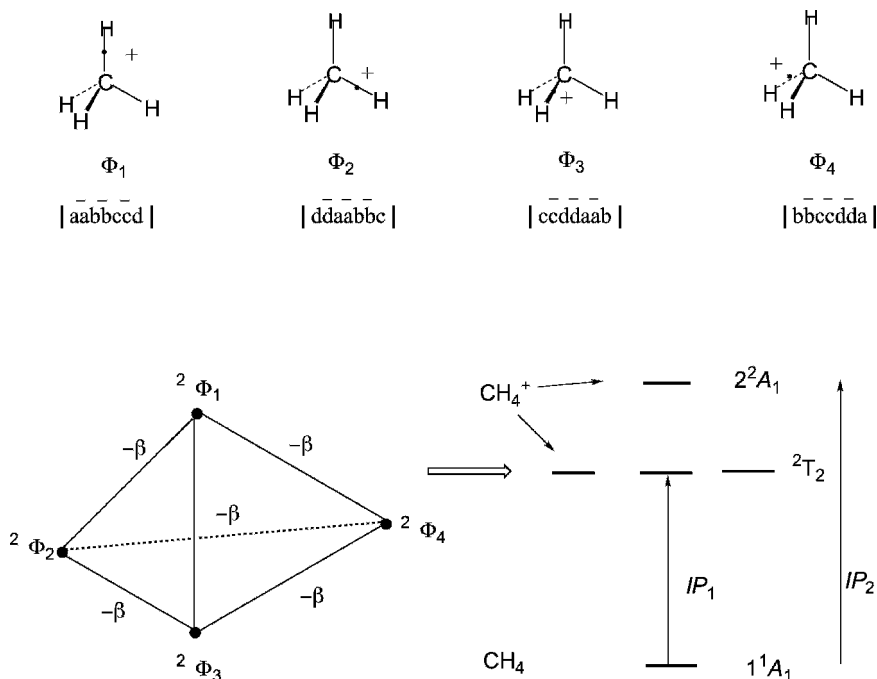
Figure 5 Generation of the $^2T_2$ and 2^2A_1 states of CH_4^+, by VB mixing of the four localized structures. The matrix elements between the structures, shown graphically, leads to the three-below-one splitting of the states, and to the observations of two ionization potential peaks in the PES spectrum (adapted from Ref. 61 with permission of Helvetica Chemica Acta).

and this can be generalized to any pair of Φ_i–Φ_j VB structure in Figure 5.

$$\langle \Phi_i | H^{\text{eff}} | \Phi_j \rangle = -\beta \qquad [61]$$

There remains to diagonalize the Hamiltonian matrix in the space of the four configurations, Φ_1–Φ_4, to get the four states of CH_4^+. This can be done by diagonalizing a matrix of Hückel type, with the only difference being that the β matrix elements have a negative sign, as shown below in Scheme 11.

$$\begin{vmatrix} -E & -\beta & -\beta & -\beta \\ -\beta & -E & -\beta & -\beta \\ -\beta & -\beta & -E & -\beta \\ -\beta & -\beta & -\beta & -E \end{vmatrix} = 0$$

Scheme 11

The diagonalization can be done using a Hückel program; however, the result can be found even without any calculation (e.g, by use of symmetry projection operators of the T_d point group). Diagonalization of the above Hückel matrix, with negatively signed β leads to the final states of CH_4^+, shown alongside the interaction graph in Figure 5. These cationic states exhibit a three-below-one splitting (i.e., a low-lying triply degenerate $^2T_2$ state and above it a $^2A_1$ state). The importance of the sign of the matrix element can be appreciated by diagonalizing the above Hückel matrix using a positively signed β. Doing that would have reversed the state ordering to one-below-three, which is of course incorrect. Thus, simple VB theory correctly predicts that methane will have two ionization peaks, one (IP$_1$) at lower energy corresponding to transition to the degenerate $^2T_2$ state and one (IP$_2$) at a higher energy corresponding to transition to the $^2A_1$ state. The facility of making this prediction and its agreement with experiment show once more that, here, too, the "failure" of VB theory is due more to a myth that caught on due to the naivety of the initial argument than to any true failure of VB.

Aromaticity–Antiaromaticity

As discussed in the introduction, simple resonance theory completely fails to predict the fundamental differences between $C_5H_5^+$ and $C_5H_5^-$, $C_3H_3^+$, and $C_3H_3^-$, $C_7H_7^+$, and $C_7H_7^-$, and so on. Hence, a decisive defeat was dealt to VB theory when, during the 1950–1960s, organic chemists were finally able to synthesize these transient molecules and establish their stability patterns (which followed Hückel rules) with no guide or insight coming from resonance theory. We shall now demonstrate (which has been known for quite a while[52,146,147]) that the simple VB theory outlined above is capable of deriving the celebrated $4n + 2/4n$ dichotomy for these ions.

As an example, we compare the singlet and triplet states of the cyclopropenium molecular ions, $C_3H_3^+$ and $C_3H_3^-$, shown in Figures 6 and 7. The VB configurations needed to generate the singlet and triplet states of the equilateral triangle $C_3H_3^+$ are shown in Figure 6. It is seen that the structures can be generated from one another by shifting single electrons from a singly occupied p_π orbital to a vacant one. By using the guidelines for VB matrix elements (see Appendix A.2), we deduce that the leading matrix element between any pair of structures with singlet spins is $+\beta$, while for any pair with triplet spin the matrix element is $-\beta$. The corresponding configurations of $C_3H_3^-$ are shown in Figure 7. In this case, the signs of the matrix elements are inverted compared with the case of the cyclopropenium cation, and are $-\beta$ for any pair of singlet VB structures, and $+\beta$ for any pair of triplet structures.

If we symbolize the VB configurations by heavy dots we can present these resonance interactions graphically, as shown in the mid-parts of Figures 6 and 7. These interaction graphs are all triangles and have the topology of corresponding Hückel and Möbius AO interactions.[148] Of course, one could diagonalize the corresponding Hückel–Möbius matrices and obtain energy levels

Figure 6 The VB structures for singlet and triplet states of $C_3H_3^+$, along with the graphical representation of their interaction matrix elements (adapted from Ref. 61 with permission of Helvetica Chemica Acta). The spread of the states is easily predicted from the circle mnemonic used in simple Hückel theory. The expressions for the VB structures are deduced from each other by circular permutations: $^1\Phi_1 = |a\bar{b}| - |\bar{a}b|$, $^1\Phi_2 = |b\bar{c}| - |\bar{b}c|$, $^1\Phi_3 = |c\bar{a}| - |\bar{c}a|$, $^3\Phi_1 = |ab|$, $^3\Phi_1 = |bc|$, $^3\Phi_1 = |ca|$.

and wave functions, but a shortcut based on the well-known mnemonic of Frost and Musulin[149] exists. A triangle is inscribed within a circle having a radius $2|\beta|$, and the energy levels are obtained from the points where the vertices of the triangle touch the circle. Using this mnemonic for the VB mixing shows that the ground state of $C_3H_3^+$ is a singlet state, while the triplet state is higher lying and doubly degenerate. By contrast, the ground state of $C_3H_3^-$ is a triplet state, while the singlet state is higher lying, doubly degenerate, and

Figure 7 The VB structures for singlet and triplet states of $C_3H_3^-$, along with the graphical representation of their interaction matrix elements (adapted from Ref. 61 with permission of Helvetica Chemica Acta). The spread of the states is easily predicted from the circle mnemonic used in simple Hückel theory. The expressions for the VB structures are deduced from each other by circular permutations: $^1\Phi_1 = |ab\,c\bar{c}| - |\bar{a}\,bc\bar{c}|$, $^1\Phi_2 = |bc\,a\bar{a}| - |\bar{b}\,c\,a\,\bar{a}|$, $^1\Phi_3 = |ca\,b\bar{b}| - |\bar{c}\,a\,bb|$, $^3\Phi_1 = |ab\,c\bar{c}|$, $^3\Phi_1 = |bc\,a\bar{a}|$, $^3\Phi_1 = |ca\,b\bar{b}|$.

hence Jahn-Teller unstable. Thus, $C_3H_3^+$ is aromatic, while $C_3H_3^-$ is antiaromatic.[52]

In a similar manner, the VB states for $C_5H_5^+$ and $C_5H_5^-$ can be constructed. Restricting the treatment to the lowest energy structures, there remain five structures for each spin state, and the sign of the matrix elements will be inverted compared to the $C_3H_3^{-,+}$ cases. The cation will have $-\beta$ matrix

elements for the singlet configurations and $+\beta$ for the triplets, while the anion will have the opposite signs. The VB-mnemonic shows that $C_5H_5^-$ possesses a singlet ground state, and by contrast, $C_5H_5^+$ has a triplet ground state, whereas its singlet state is higher in energy and Jahn–Teller unstable. Thus, in the cyclo-pentadienyl ions, the cation is antiaromatic while the anion is aromatic.

Moving next to the $C_7H_7^{+,-}$ species, the sign patterns of the matrix element will invert again and agree with those in the $C_3H_3^{+,-}$ case. As such, the VB-mnemonic will lead to similar conclusions, that is, that the cation is aromatic, while the anion is antiaromatic with a triplet ground state. Thus, the sign patterns of the β-matrix element, and hence also the ground state's stability obey the $4n/4n + 2$ dichotomy.

Clearly, a rather simple VB theory is all that is required to reproduce the rules of aromaticity and antiaromaticity of the molecular ions, and to provide the correct relative energy levels of the corresponding singlet and triplet states. This VB treatment is virtually as simple as HMO theory itself, with the exception of the need to know the sign of the VB matrix element. But, with some practice, this can be learned.

Another highly cited "failure" of VB theory concerns the treatments of antiaromatic molecules such as CBD and COT versus aromatic ones like benzene. The argument goes as follows: Since benzene, CBD, and COT can all be expressed as resonance hybrids of their respective Kekulé structures, they should have similar properties, and since they do not, this must mean that VB theory fails. As we have already stressed, this is a failure of resonance theory that simply enumerates resonance structures, but not of VB theory. Indeed, at the ab initio level, Voter and Goddard[58] demonstrated that GVB calculations, predict correctly the properties of CBD. Subsequently, Gerratt and co-workers[150,151] showed that spin-coupled VB theory correctly predicts the geometries and ground states of CBD and COT. Recently, in 2001, the present authors and their co-workers used VB theory to demonstrate[57] that (a) the vertical *RE* of benzene is larger than that of CBD and COT, and (b) the standard Dewar resonance energy (DRE) of benzene is 21 kcal/mol, while that for CBD is negative, in perfect accord with experiment. Thus, properly done ab initio VB theory indeed succeeds with CBD, COT, or with any other antiaromatic species. A detailed analysis of these results for benzene CBD and COT, has been given elsewhere[55,152] but is beyond the scope of this chapter.

Can VB Theory Bring New Insight into Chemical Bonding?

The idea that a one-electron bond might be stronger than a two-electron bond between the same atoms sounds unnatural in simple-MO theory. How could two bonding electrons stabilize a molecular interaction less than a single one? If we take a common interatomic distance for the two kinds of bonds, the one-electron bonding energy should be half the two-electron bonding energy

according to the qualitative MO formulas in Table 1. Relaxing the bond length should disfavor the one-electron bond even more than the two-electron one, since the latter is shorter and enjoys larger overlap between the fragments' orbitals.

The simple VB model makes a very different prediction. By using VB formulas, an overlap-dependent expression is found for the ratio of one-electron to two-electron bonding energies (Table 1 and Eq. [62]):

$$\frac{D_e(1-\mathrm{e})}{D_e(2-\mathrm{e})} = \frac{1+S^2}{2S(1+S)} \qquad [62]$$

According to Eq. [62], the one-electron bond is weaker than the two-electron bond in the case of strong overlap (typically the H_2^+/H_2 case), but the reverse is true if the overlap S is smaller than a critical value of 0.414. There are many chemical species that possess smaller overlap than this critical value (e.g., alkali dimers and other weak binders). By contrast, strong binders like H, C, and so on, usually maintain larger overlaps, $S \geq 0.5$. The qualitative prediction based on Eq. [62], compares favorably with experimental and computational data. Indeed the binding energy of the two-electron bond in H_2 (4.75 eV) is somewhat less than twice that of the one-electron bond in H_2^+ (2.78 eV). In contrast, comparing Li_2^+ and Li_2 leads to the intriguing experimental result that the binding energy for Li_2^+ (1.29 eV) is *larger* than that for Li_2 (1.09 eV), which is in agreement with the VB model but at variance with qualitative MO theory.

What is the reason for the discrepancy of the MO and VB approaches? As we have seen, the qualitative expression for the odd-electron bonding energies is the same in both theories. However, the two-electron bonding energies are different. Assuming that the β integral is proportional to the overlap S, the two-electron bonding energy is a linear function of S in the MO model, but a quadratic function of S in the VB model. It follows that, for large overlaps, the VB and MO models more or less agree with each other, while they qualitatively differ for weak overlaps. In this latter case, the VB model predicts a larger one-electron versus two-electron ratio of bonding energies than the MO model. Note that the reasoning can be extended to three-electron bonds as well: for weakly overlapping binders, the VB model predicts that three-electron bonds might approach the strength of the corresponding two-electron bonds. In comparison, application of simple MO theory would have predicted that any three-electron bond energy should always be less than one-half of the corresponding two-electron bond energy, for any overlap. In agreement with the VB prediction, the three-electron bond in F_2^-, in which the two interacting orbitals have a typically weak overlap (~ 0.10), has a binding energy of 1.31 eV, not much smaller than the two-electron bonding energy of F_2 which is no larger than 1.66 eV.

Insight into bonding is not limited to this example. In fact, VB theory gives rise to new bonding paradigms that are discussed in the literature but are not reviewed here for lack of space. One such paradigm is called "charge-shift bonding" and concerns two-electron bonds that are neither covalent nor ionic but whose bonding energy is dominated by the covalent–ionic resonance interaction; for example, F—F and O—O are charge-shift bonds.[153–155] Another paradigm is the "ferromagnetic-bonding" that occurs in high-spin clusters (e.g., $^{n+1}Li_n$) that are devoid of electron pairs.[156,157]

VB Diagrams for Chemical Reactivity

One advantage of representing reactions in terms of VB configurations is the unique and unified insight that it brings to reactivity problems. The center-piece of the VB diagram model is the VB correlation diagram that traces the energy of the VB configurations along the reaction coordinate. The subsequent configuration mixing reveals the cause of the barrier, the nature of the transition state, and the reasons for occurrence of intermediates. Furthermore, the diagram allows qualitative and semiquantitative predictions to be made about a variety of reactivity problems, ranging from barrier heights, stereo- and regio-selectivities, and mechanistic alternatives. Since its derivation, via the projection of MO-based wave functions along the reaction coordinate,[81] the VB diagram model has been applied qualitatively[53,83–85,158] as well as quantitatively by direct computation of the VB diagram;[159–168] as such this is a qualitative model with an isomorphic quantitative analogue.

The straightforward representation of the VB diagram focuses on the "active bonds", those that are being broken or made during the reaction. Of course, it is the localized nature of the electron pairs in the VB representation that makes this focusing possible. The entire gamut of reactivity phenomena requires merely two generic diagrams, which are depicted schematically in Figure 8, and that enable a systematic view of reactivity. The first is a diagram of two interacting states, called a VB state correlation diagram (VBSCD), which describes the formation of a barrier in a single chemical step due to avoided crossing or resonance mixing of the VB states that describe reactants and products. The second is a three-curve diagram (or generally a many-curve diagram), called a VB configuration-mixing diagram (VBCMD), which describes a stepwise mechanism derived from the avoided crossing and VB mixing of the three curves or more. The ideas of curve crossing and avoided crossing were put to use in the early days of VB theory by London, Eyring, Polanyi, and Evans, who pioneered the implementation of VB computation as a means of generating potential energy surfaces and locating transition states. In this respect, the VB diagrams (VBSCD and VBCMD) are developments of these early ideas into a versatile system of thought that allows prediction of a variety of reactivity patterns from properties of the reactants and products.
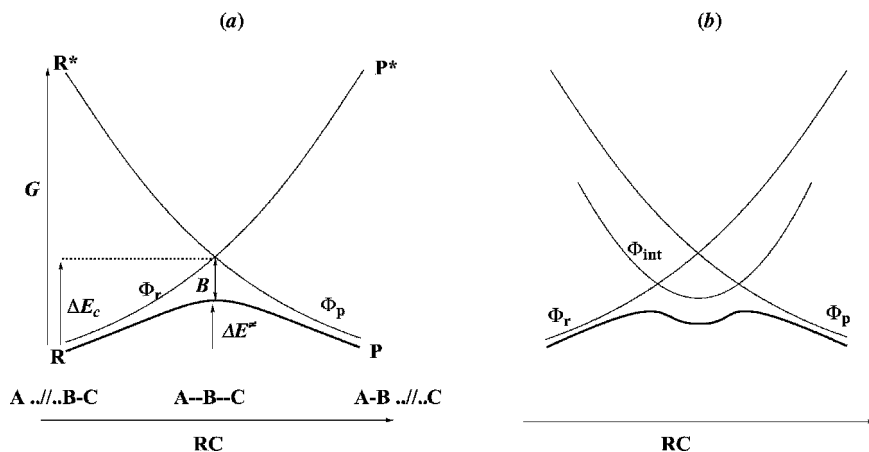
Figure 8 The VB diagrams for conceptualizing chemical reactivity: (*a*) VBSCD showing the mechanism of barrier formation by avoided crossing of two curves of reactant and product type state curves. (*b*) VBCMD showing the formation of a reaction intermediate. The final adiabatic states are drawn in bold curves.

A review of both kinds of VB diagrams has recently appeared,[85] and we refer the reader to this review paper for comprehensive information. Here we will concentrate on diagrams of the first type, VBSCD, and give a brief account of their practical use.

The VBSCDs apply to the general category of reactions that can be described as the interplay of two major VB structures, that of the reactants (A/B—C in Fig. 8*a*) and that of the products (A—B/C). The diagram displays the ground state energy profile of the reacting system (bold curve), as well as the energy profile of each VB structure as a function of the reaction coordinate (thin curves). Thus, starting from the reactant's geometry on the left, the VB structure that represents the reactant's electronic state, R, has the lowest energy and merges with the supersystem's ground state. Then, as one deforms the supersystem towards the products' geometry, the latter VB structure gradually rises in energy and finally reaches an excited state P^* that represents the VB structure of the reactants in the products' geometry. A similar diabatic curve can be traced from P, the VB structure of the products in its optimal geometry, to R^*, the same VB structure in the reactants' geometry. Consequently, the two curves cross somewhere in the middle of the diagram. The crossing is of course avoided in the adiabatic ground state, owing to the resonance energy B that results from the mixing of the two VB structures. The barrier is thus interpreted as arising from avoided crossing between two diabatic curves, which represent the energy profiles of the VB structures of the reactants and products.

The VBSCD is a handy tool for making predictions by relating the magnitudes of barriers to the properties of reactants. Thus, the barrier $\Delta E^{\neq}$ of a

reaction can be expressed as a function of some fundamental parameters of the diagrams. The first of these parameters is the vertical energy gap G (Fig. 8a) that separates the ground state of the reactant, R, from the excited state R^*. This parameter can take different expressions, depending on which reaction is considered, but is always related to simple and easily accessible energy quantities of the reactants. Another important factor is the height of the crossing point, ΔE_c, of the diabatic curves in the diagram, relative to the energy of the reactants. For predictive purposes, this quantity can, in turn, be expressed as a fraction f, smaller than unity, of the gap G (Eq. [63]).

$$\Delta E_c = f\, G \qquad\qquad [63]$$

This parameter is associated with the curvature of the diabatic curves, large upward curvatures meaning large values of f, and vice versa for small upward curvature. The curvature depends on the descent of R^* and P^* toward the crossing point and on the relative pull of the ground states, R and P, so that f incorporates various repulsive and attractive interactions of the individual curves along the reaction coordinate. The last parameter is the resonance energy B arising from the mixing of the two VB structures in the geometry of the crossing point. The barrier $\Delta E^{\neq}$ can be given a rigorous expression as a function of the three physical quantities f, G, and B as in Eq. [64]:

$$\Delta E^{\neq} = f\, G - B \qquad\qquad [64]$$

A similar expression can be given for the barrier of the reverse reaction as a function of the product's gap and its corresponding f factor. One then distinguishes between the reactant's and product's gaps, G_r and G_p, and their corresponding f factors f_r and f_p. A unified expression for the barrier as a function of the two promotion gaps and the endo- or exothermicity of the reaction can be derived by making some simplifying approximations.[85,169,170] One such simplified expression has been derived recently[168] and is given in Eq. [65].

$$\Delta E^{\neq} = f_0 G_0 + 0.5\Delta E_{rp} - B \qquad f_0 = 0.5(f_r + f_p) \quad G_0 = 0.5(G_r + G_p) \quad [65]$$

Here, the first term is an intrinsic factor that is determined by the averaged f and G quantities, the second term gives the effect of the reaction thermodynamics, and the third term is the resonance energy of the transition state, due to the avoided crossing.

Taken together the barrier expressions describe the interplay of three effects. The intrinsic factor $f_0 G_0$ describes the energy cost due to unpairing of bonding electrons in order to make new bonds, the ΔE_{rp} factor accounts for the classical rate-equilibrium effect, while B involves information about the preferred stereochemistry of the reaction. Figure 9 outlines pictorially
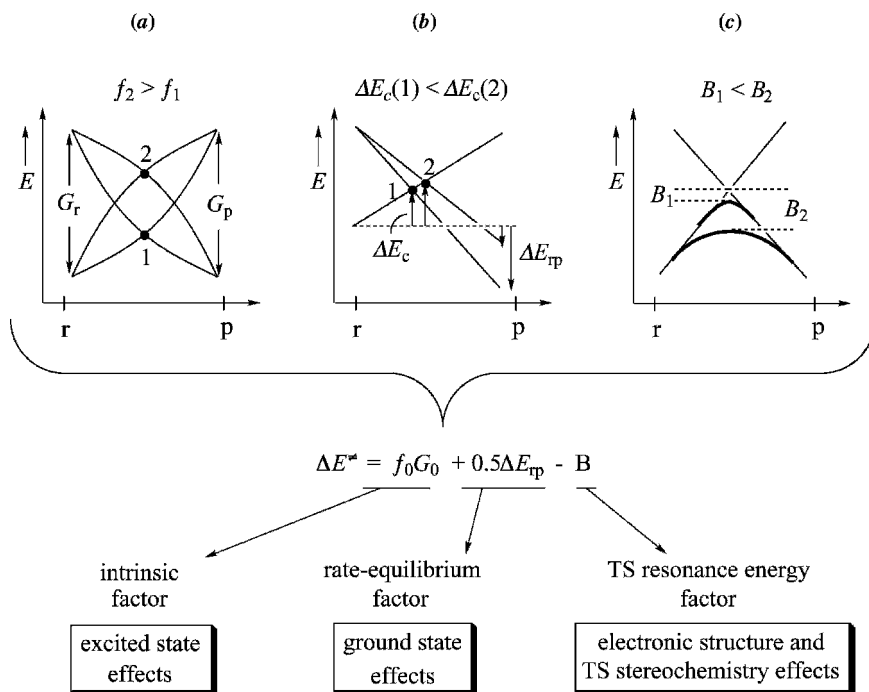
Figure 9 Illustration of the factors that control the variation of the barrier height in the VBSCD.

the impact of the three factors on the barrier. As such, the VB diagram constitutes in principle a unified and general structure–reactivity model.

A quantitative application of the diagram requires calculations of either ΔE_c and B or of f, G, and B. The energy gap factor, G, is straightforward to obtain for any kind of process. The height of the crossing point incorporates effects of bond deformations (bond stretching, angular changes, etc.) in the reactants and nonbonded repulsions between them at the geometry corresponding to the crossing point of the lowest energy on the seam of crossing between the two state curves (Fig. 8a). This, in turn, can be computed by means of ab initio calculations (e.g., straightforwardly by use of a VB method [159,166–168] or with any MO-based method), by determining the energy of the reactant wave function at zero iteration (see Appendix A.3) or by constrained optimization of block-localized wave functions.[171] Alternatively, the height of the crossing point can be computed by molecular mechanical means.[172–174] Except for VB theory that calculates B explicitly, in all other methods this quantity is obtained as the difference between the energy of the transition state and the computed height of the crossing point. In a few cases, it is possible to use analytical formulas to derive expressions for the

parameters f and B.[53,85,167] Thus, in principle, the VBSCD is computable at any desired accuracy.[142]

The purpose of this section is to teach an effective way for using the diagrams in a qualitative manner. The simplest way starts with the G parameter, which is the origin of the barrier, since it serves as a promotion energy needed to unpair the bonds of the reactants and pair the electrons in the mode required by the products. In certain families of related reactions both the curvatures of the diabatic curves (parameter f) and the avoided crossing resonance energy (parameter B) can be assumed to be nearly constant, while in other reaction series f and B vary in the same manner as G. In such cases, the parameter G is the crucial quantity that governs the reaction barriers in the series: the larger the gap G, the larger the barrier. Let us proceed with a few applications of this type.

Radical Exchange Reactions

Figure 10 describes the VB correlation diagram for a reaction that involves cleavage of a bond A—Y by a radical $X^{\bullet}$ (X, A, Y = any atom or molecular fragment):

$$X^{\bullet} + A{-}Y \rightarrow X{-}A + Y^{\bullet} \qquad [66]$$

Since R^{*} is just the VB image of the product in the geometry of the reactants, this excited state displays a covalent bond coupling between the infinitely
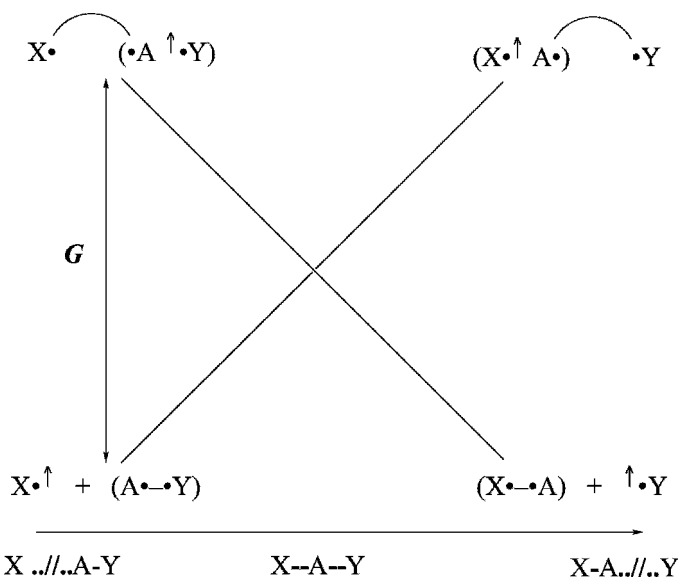

Figure 10 The state correlation in the VBSCD that describes a radical exchange reaction. Avoided crossing as in Figure 8*a* will generate the final adiabatic profile.

separated fragments X and A, and an uncoupled fragment Y$^{\bullet}$ in the vicinity of A. The VB wave function of such a state reads (dropping normalization factors):

$$\psi(R^*) = |\,x\,\bar{a}\,y\,| - |\,\bar{x}\,a\,y\,| \qquad [67]$$

where x, a, and y are, respectively, the active orbitals of the fragments X, A, Y. By using the rules of qualitative VB theory (Eqs. [40] and [42] where S^2 is neglected), the energy of R^* relative to the separated X, A, Y fragments becomes $-\beta_{ay}S_{ay}$, while the energy of R is just the bonding energy of the A—Y fragment (i.e., $2\beta_{ay}S_{ay}$). It follows that the energy gap G for any radical exchange reaction of the type in Eq. [66] is $-3\beta_{ay}S_{ay}$, which is just three quarters of the singlet–triplet gap ΔE_{ST} of the A—Y bond, namely,

$$G \approx 0.75\,\Delta E_{ST}(A-Y) \qquad [68]$$

The state R^* in Eq. [67] keeps strictly the wave function of the product P, and is hence a quasi-spectroscopic state that has a finite overlap with R. If one orthogonalizes the pair of states R and R^*, by for example, a Graham–Schmidt procedure, the excited state becomes a pure spectroscopic state in which the A—Y is in a triplet state and is coupled to X$^{\bullet}$ to yield a doublet state. In such an event, one could simply use, instead of Eq. [68], the gap G' in Eq. [69] that is simply the singlet–triplet energy gap of the A—Y bond:

$$G' = \Delta E_{ST}(A-Y) \qquad [69]$$

Each formulation of the state R^* has its own advantages,[175] but what is essential for the moment is that both use a gap that is either the singlet–triplet excitation of the bond that is broken during the reaction, or the same quantity scaled by approximately a constant 0.75. As mentioned above, a useful way of understanding this gap is as a promotion energy that is required in order to enable the A—Y bond to be broken before it can be replaced by another bond, X—A.

As an application, let us consider a typical class of radical exchange reactions, the hydrogen abstractions from alkanes. Eq. [70] describes the identity process of hydrogen abstraction by an alkyl radical:

$$R^{\bullet} + H-R \rightarrow R-H + R^{\bullet} \qquad [70]$$

Identity reactions proceed without a thermodynamic driving force, and project therefore the role of promotion energy as the origin of the barrier.

The barriers for a series of radicals have been computed by Yamataka and Nagase,[176] and were found to increase as the R—H bond energy D

increases; the barrier is the largest for $R = CH_3$ and the smallest for $R = C(CH_3)_3$. This trend has been interpreted by Pross et al.[177] using the VBSCD model. The promotion gap G that is the origin of the barrier (Eq. [68]) involves the singlet–triplet excitation of the R—H bond. Now, according to Eqs. [41] and [42], this singlet–triplet gap is proportional to the bonding energy of the R—H bond, that is, $\Delta E_{ST} \approx 2D$. Therefore, the correlation of the barrier with the bond strength is equivalent to a correlation with the singlet–triplet promotion energy (Eq. [68]), a correlation that reflects the electronic reorganization that is required during the reaction. In fact, the barriers for the entire series calculated by Pross et al.[177] can be fitted very well to the barrier equation, as follows:

$$\Delta E^{\neq} = 0.3481G - 50\,\text{kcal/mol} \quad G = 2D_{RH} \qquad [71]$$

which indicates that this is a reaction family with constant $f = 0.3481$ and $B = 50$ kcal/mol.

Recently, ab initio VB computations demonstrated that the ΔE_{ST} quantity[167] is the factor that organizes the trends for the barriers for the hydrogen exchange identity reaction, $R^{\bullet} + RH \rightarrow RH + {}^{\bullet}R$, when R varies down the column of the periodic table, that is, $R = CH_3$, SiH_3, GeH_3, and PbH_3. Thus, in this series, the barriers decrease down the column since the ΔE_{ST} quantity decreases.

Similar reaction series abound.[53,85] Thus, in a series of Woodward–Hoffmann forbidden $2 + 2$ dimerizations, the promotion gap is proportional to the sum of the ΔE_{ST} ($\pi\pi^*$) quantities of the two reactants. Consequently, the barrier decreases from 42.2 kcal/mol for the dimerization of ethylene, where $\Sigma\Delta E_{ST}$ ($\pi\pi^*$) is large (~200 kcal/mol) down to <10 kcal/mol for the dimerization of disilene for which $\Sigma\Delta E_{ST}(\pi\pi^*)$ is small (~80 kcal/mol). A similar trend was noted for Woodward–Hoffmann allowed reactions ($4 + 2$ or $2 + 2 + 2$), where the barrier jumps from 22 kcal/mol for the Diels–Alder reaction where $\Sigma\Delta E_{ST}(\pi\pi^*)$ is small (~173 kcal/mol) to 62 kcal/mol for the trimerization of acetylene where $\Sigma\Delta E_{ST}(\pi\pi^*)$ is very large (~297 kcal/mol).

Reactions between Nucleophiles and Electrophiles

Figure 11 illustrates the formation of the VB correlation diagram for a reaction between a nucleophile and an electrophile, Eq. [72]:

$$X^- + A{-}Y \rightarrow X{-}A + Y^- \qquad [72]$$
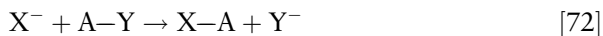
Equation [72] represents a typical S_N2 reaction where the nucleophile, X^-, shifts an electron to the A—Y electrophile, forms a new X—A bond, while the leaving group Y departs with the negative charge.

Let us now examine the nature of the R^* excited state for this process. Geometrically, A and Y are close together (as in the ground state R) and
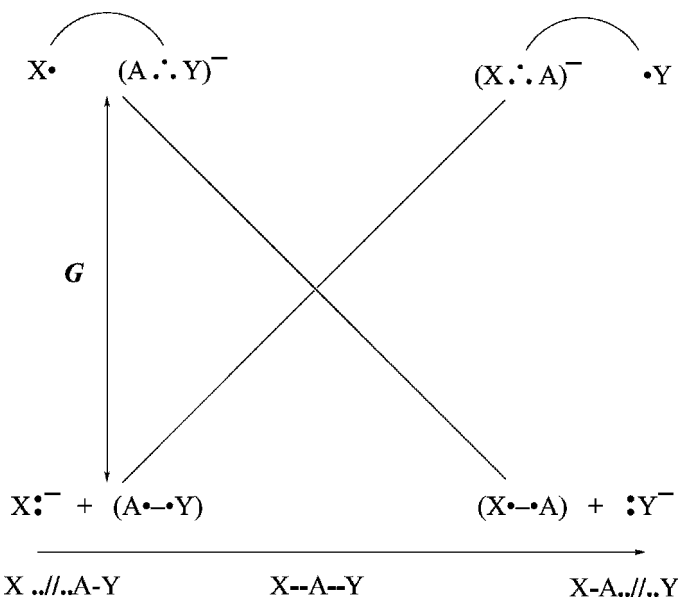
Figure 11 The state correlation in the VBSCD that describes a nucleophilic substitution reaction. Avoided crossing as in Figure 8*a* will generate the final adiabatic profile.

separated from X by a long distance. The X fragment, which is neutral in the product P, must remain neutral in R^*, and therefore carries a single active electron. As a consequence, the negative charge is located on the A—Y complex, so that the R^* state is the result of a charge transfer from the nucleophile to the electrophile, and can be depicted as $X^{\bullet}/(A \therefore Y)^-$. It follows that the promotion from R to R^* is made of two terms: An electron detachment from the nucleophile (e.g., $X\colon^-$) and an electron attachment to the electrophile (e.g, A—Y). The promotion energy G is therefore the difference between the vertical ionization potential of the nucleophile, $I^*_{X\colon}$, and the vertical electron affinity of the electrophile, A^*_{A-Y}, given by Eq. [73],

$$G = I^*_{X\colon} - A^*_{A-Y} \qquad [73]$$

where the asterisk denotes a vertical quantity with respect to molecular as well as solvent configurations.[105,106] Thus, the mechanism of a nucleophilic substitution may be viewed as an electron transfer from the nucleophile to the electrophile, and a coupling of the supplementary electron of the electrophile to the remaining electron of the nucleophile.

A whole monograph and many reviews were dedicated to discussion of S_N2 reactivity based on the VBSCD model, and the interested reader may consult these.[85,169,170,178] One important feature that emerges from these
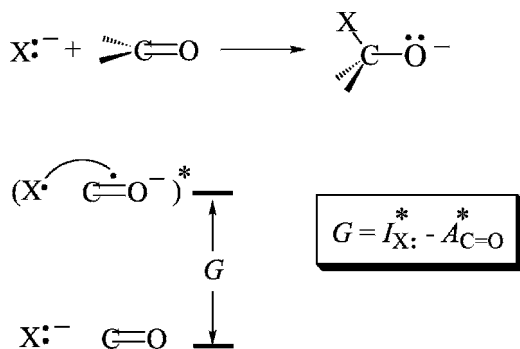
Figure 12 The ground and vertical charge-transfer states in the VBSCD that describes a nucleophilic attack on a carbonyl group.

treatments is the insight into variations of f. Thus, whether or not the single electrons in the R^* state are easily accessible to couple to a bond determines the size of the f factor; the easier the bond coupling along the reaction coordinate, the smaller the f and vice versa. For example, in delocalized nucleophiles (acetate, phenyl thiolate, etc.), the active electron is not 100% located on the atom that is going to be eventually linked to the fragment A in the reaction in Eq. [72]. So the diabatic curve will slowly descend from R^* to P and one may expect a large f factor. On the other hand, localized nucleophiles will correspond to smaller f factors. Of course, the same distinction can be made between localized and delocalized electrophiles, leading to the same prediction regarding the magnitude of f.

In general, all reactions between closed-shell electrophiles and nucleophiles subscribe to the same diagram type[85] with R^* and P^* states, which are vertical charge-transfer states that involve an electron transfer from the nucleophile to the electrophile, while coupling the single electron on the oxidized nucleophile to that on the reduced electrophile to form a bond pair. An example is the nucleophilic cleavage of an ester where the rate-determining step is known[179,180] to involve the formation of a tetrahedral intermediate, as depicted in Figure 12.

The promotion energy for the rate-determining step is, accordingly, the difference between the vertical ionization potential of the nucleophile and the electron attachment energy of the carbonyl group. The latter quantity is a constant for a given ester, and therefore the correlation of barriers with the promotion energy becomes a correlation with the vertical ionization energy of the nucleophiles. Figure 13 shows a structure–reactivity correlation for the nucleophilic cleavage of a specific ester based on the VBSCD analysis of Buncel et al.[181] It is seen that the free energies of activation correlate with the vertical ionization energies of the nucleophile in the reaction solvent. Furthermore, localized and delocalized nucleophiles appear to generate correlation lines of
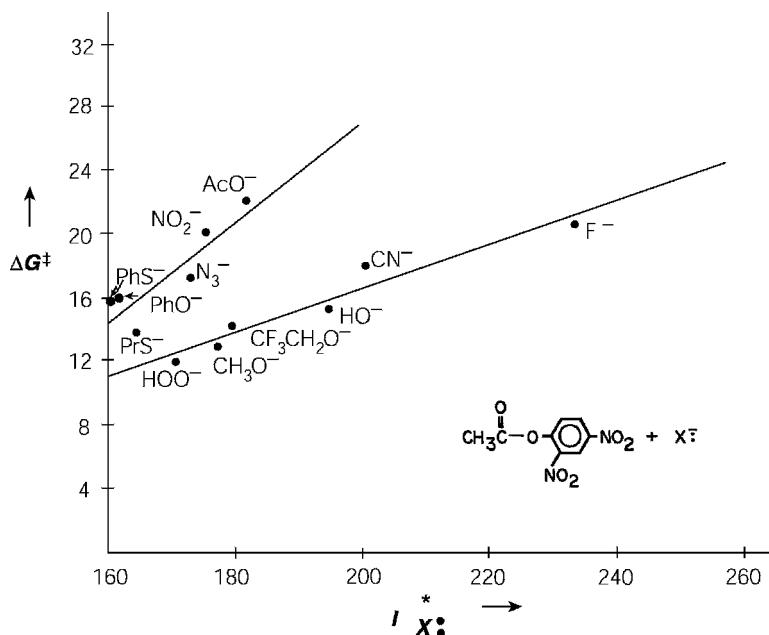
Figure 13 A plot of the free energy of activation for nucleophilic cleavage of an ester vs. the vertical ionization potential of the nucleophile (adapted from Ref. 85).

different slopes. The two correlation lines obtained for the experimental data in Figure 13 are readily understood based on Eq. [64] as corresponding to different f values, where the localized nucleophiles possess the smaller f value and hence a smaller structure–reactivity slope in comparison with the delocalized nucleophiles.

Significance of the f Factor

The f factor defines the intrinsic selectivity of the reaction series to a change in the vertical gap,[85,169] that is,

$$f = \partial(\Delta E^{\neq})/\partial G \qquad [74]$$

In reactions of electrophiles and nucleophiles, we just indicated that f increases as the nucleophile becomes more delocalized. Thus, the series of delocalized nucleophiles, in Figure 13, is more selective to changes (of any kind) that affect the gap, G, compared with the series of localized nucleophiles. This would be general for other processes as well; delocalization of the single electrons in the R^* states of the diagram results in higher f values, and vice versa. Such trends abound in electrophile–nucleophile combinations;

they were analyzed for radical addition to olefins,[182] and are likely to be a general feature of reactivity.

Another factor that raises f is the steric bulk of the substrate or the nucleophile.[169] For example in S_N2 reactions the bulkier the alkyl group in A—Y (Eq. [72]) the larger will be the value of f, and vice versa.[169] As a result, bulkier substrates will exhibit higher sensitivity to changes in the vertical gap. One such variation occurs when the reaction conditions change from gas phase to solution, in which case the promotion gap, $G = I^*_{X^\bullet} - A^*_{A-Y}$, increases by a significant amount. If we now compare two A—Y substrates such as methyl chloride and neopentyl chloride, the latter will possess a larger f value. *The consequence is that the steric effect that is observed in the gas phase will be amplified and become more significant in a solvent.* This exciting finding was recently published by Ren and Brauman.[183]

Making Stereochemical Predictions with the VBSCD Model

Making stereochemical predictions is easy using FO–VB configurations.[52,81,85] To illustrate the manner by which this can be practiced, let us take a simple example with well-known stereochemistry, the nucleophilic substitution reaction, Eq. [72]. The corresponding R^* state is depicted in Figure 14 in its FO–VB formulation, where the nucleophile appears here in its one-electron reduced form $X^\bullet$, with a single electron in ϕ_X, while the substrate has an extra electron in its σ^*_{CY} orbital. The two single electrons are coupled into a $\phi_X - \sigma^*_{CY}$ bond pair.

The R^* state correlates to product, X—C/:Y$^-$, since it contains a $\phi_X - \sigma^*_{CY}$ bond-pair that becomes the X—C bond, and at the same time the occupancy of the σ^*_{CY} orbital causes the cleavage of the C—Y bond to release

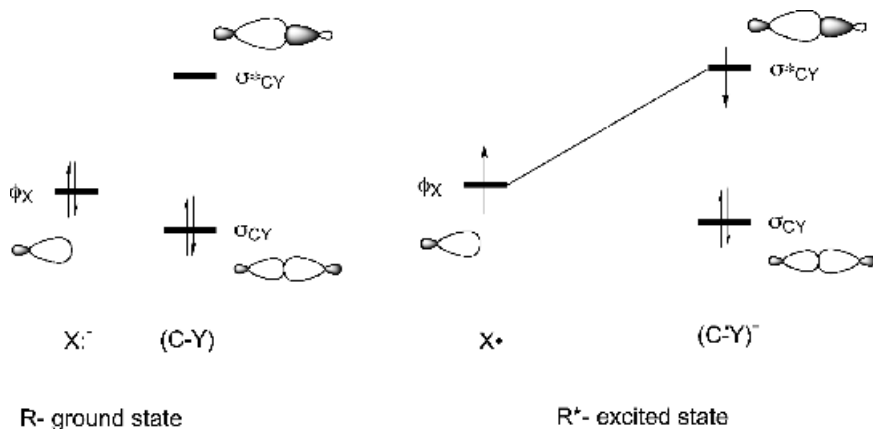R- ground state   R*- excited state

Figure 14 The ground (R) and charge-transfer (R^*) states in the VBSCD of the S_N2 reaction $X^- + C - Y \rightarrow X - C + Y^-$. The R^* state has a bond pair shown by the line connecting the orbitals ϕ_x and σ^*_{cy}.

the: Y^- anion. Furthermore, the R^* state contains information about the stereochemical pathway. Since the bond pair involves a $\phi_X - \sigma^*_{CY}$ overlap, due to the nodal properties of the σ^*_{CY} orbital the bond pair will be optimized when the $X^\bullet$ is coupled to the substrate in a colinear $X-C-Y$ fashion. Thus, the steepest descent of the R^* state, and the lowest crossing point will occur along a backside trajectory of the nucleophile toward the substrate.

If we assume that the charge-transfer state remains the leading configuration of R^* near the crossing point, then the matrix element between R and R^* will dominate the size of the resonance energy B, and will enable making predictions about B. Since these two VB configurations differ by the occupancy of one spin orbital (ϕ_X in R is replaced by σ^*_{CY} in R^*) then following the qualitative rules for matrix elements (see Appendix A.2), the resonance energy of the transition state (TS) will be proportional to the overlap of these orbitals, that is,

$$B \propto \langle \phi_X | \sigma^*_{CY} \rangle \qquad [75]$$

It follows therefore, that in a backside trajectory, we obtain both the lowest crossing point as well as the largest TS resonance energy. Computationally, the back-side barrier is smaller by ~10–20 kcal/mol compared with a frontside attack.[184] Equation [75] constitutes an orbital selection rule for an S_N2 reaction. Working out this rather trivial prediction is nevertheless necessary since it constitutes a prototypical example for deriving orbital selection rules in other reactions, using FO–VB configurations. *Thus, the intrinsic bonding features of R^* provide information about the reaction trajectory, while the $\langle R | R^* \rangle$ overlap provides information about the geometric dependence of the resonance energy of the TS, B.*

By using this approach, it is possible to *derive orbital selection rules* for cases that are ambiguous in qualitative MO theory. For example, for radical cleavage of σ bonds, using the R^* with a triplet $\sigma^1 \sigma^{*1}$ configuration on the substrate leads to prediction that the course of the reaction and the resonance interaction in the transition state will be determined by the product of overlaps between the orbital of the attacking radical, ϕ_R, and the σ and σ^* orbitals of the substrate, namely, $\langle \phi_R | \sigma \rangle \langle \phi_R | \sigma^* \rangle$. This product is optimized once again in a back-side attack, and therefore one can predict that radical cleavage of σ bonds will proceed with inversion of configuration. All known experimental data[185–190] conform to this prediction. Another area where successful predictions have been made involves nucleophilic attacks on radical cations. Here using the corresponding R and R^* states,[191] it was predicted that stereoselectivity and regioselectivity of nucleophilic attack should be controlled by the lowest unoccupied molecular orbital (LUMO) of the radical cation. Both regioselectivity and stereospecificity predictions were verified by experiment[192,193] and computational means.[184] For a more in depth discussion the reader may consult the most recent review of the VBSCD and VBCMD models.[85]

VBSCD: A GENERAL MODEL FOR ELECTRONIC DELOCALIZATION AND ITS COMPARISON WITH THE PSEUDO-JAHN–TELLER MODEL

The valence bond state correlation diagram (VBSCD) serves as a model for understanding the status of electronic delocalization in isoelectronic series. Consider, for example, the following exchange process between monovalent atoms, which exchange a bond while passing through an $X_3^\bullet$ cluster in which three electrons are delocalized over three centers.

$$X^\bullet + X–X \rightarrow [X_3^{\bullet\bullet}] \rightarrow X–X +^\bullet X \qquad [76]$$
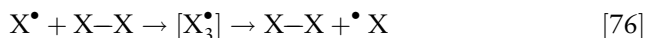
We can imagine a variety of such species (e.g., X = H, F, Cl, Li, Na, Cu), and ask ourselves the following question: When do we expect the $X_3^\bullet$ species to be a transition state for the exchange process, and when will it be a stable cluster, an intermediate en-route to exchange? In fact, the answer to this question comes from the VBSCD model, that describes all these process in a single diagram where G is given by Eq. [68], that is, $G \approx 0.75 \ \Delta E_{ST}(X–X)$. Thus, as shown in Figure 15 a very large triplet promotion energy for X = H (250 kcal/mol) results in an $H_3^\bullet$ transition state, while the small promotion energy for X = Li (32 kcal/mol) results in a stable $Li_3^\bullet$ cluster. The VB computations of Maître et al.[166] in Figure 15 show that, as the promotion gap drops drastically, the avoided crossing state changes from a transition state for $H_3^\bullet$ to a stable cluster for $Li_3^\bullet$. Moreover, this transition from a barrier to an intermedi-
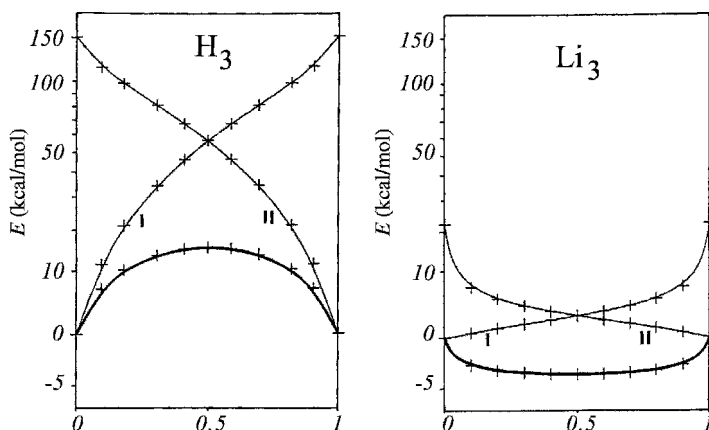
Figure 15 Ab initio computations of VBSCDs for the exchange processes, X•+ X–X → X–X + •X, for X = H and Li (adapted from Ref. 166). The abscissa is a reaction progress coordinate that stretches between zero and one (using the normalized reaction coordinates, $0.5(n_1 - n_2 + 1)$, where n_1 and n_2 are the X–X bond orders in X–X–X).

ate can in fact be predicted quantitatively from the barrier equation, by deriving explicit expressions for G, f, and B.[167]

The spectacular relationship between the nature of the $X_3^\bullet$ species and the promotion energy shows that the VBSCD is in fact a general model of the pseudo-Jahn–Teller effect (PJTE). A qualitative application of PJTE would predict all the $X_3^\bullet$ species to be transition state structures that relax to the distorted $X^\bullet{-}X{-}X$ and $X{-}X{-}^\bullet X$ entities. The VBSCD makes a distinction between strong binders that form transition states and weak binders that form stable intermediate clusters.

The variable nature of the $X_3^\bullet$ species in the isoelectronic series form a general model for electronic delocalization, enabling one to classify the species either as distortive or as stable. By using the isoelectronic analogy, one might naturally ask about the isoelectronic π-species in allyl radical; does it behave by itself like $H_3^\bullet$ or like $Li_3^\bullet$? Moreover, the same transformation displayed for $X_3^\bullet$ in Figure 15 can be shown for X_3^+, X_3^-, X_4, and X_6 species.[57] Likewise one might wonder about the status of the corresponding isoelectronic π components in allyl cation, anion, cyclobutadiene, or benzene. These questions were answered in detail elsewhere and the reader is advised to consult a recent review,[57] while here we deal only with the intriguing question concerning the π-electrons of benzene.

What Is the Driving Force, σ or π, Responsible for the D_{6h} Geometry of Benzene?

The regular hexagonal structure of benzene can be considered as a stable intermediate in a reaction that interchanges two distorted Kekulé-type isomers, each displaying alternating C—C bond lengths as shown in Figure 16. It is well known that the D_{6h} geometry of benzene is stable against a Kekuléan distortion (of b_{2u} symmetry), but one may still wonder which of the two sets of bonds, σ or π, is responsible for this resistance to a b_{2u} distortion. The σ frame, which is just a set of identical single bonds, is by nature symmetrizing and prefers a regular geometry. It is not obvious whether the π electronic component, by itself, is also symmetrizing or on the contrary distortive, with a weak force constant that would be overwhelmed by the symmetrizing driving force of the σ frame. To answer this question, consider in Figure 16 the VBSCD that represents the interchange of Kekulé structures along the b_{2u} reaction coordinate; the middle of the b_{2u} coordinate corresponds to the D_{6h} structure, while its two extremes correspond to the bond-alternated mirror-image Kekulé geometries. Part a of the figure considers π *energies only*. Starting at the left-hand side, Kekulé structure K_1 correlates to the excited state K_2^* in which the π bonds of the initial K_1 structure are elongated, while the repulsive nonbonding interactions between the π bonds are reinforced. The same argument applies if we start from the right-hand side, with structure K_2 and follow it along the b_{2u} coordinate; K_2 will then rise
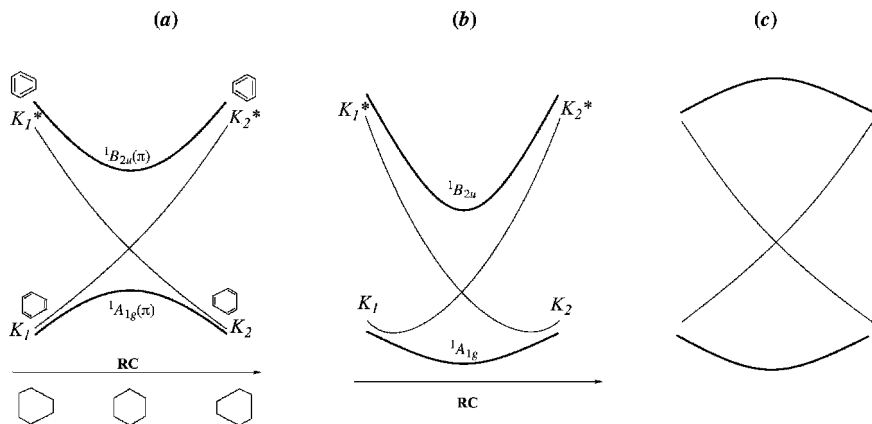
Figure 16 The VBSCDs showing the crossing and avoided crossing of the Kekulé structures of benzene along the bond alternating mode, b_{2u} for: (a) π-only curves, (b) full $\pi + \sigma$ curves, and (c) π-only curves in a putative situation where the avoided crossing leads to a ground state with a π-symmetrizing tendency. In this latter case, the excited state will have a distortive π-state and hence, a low frequency for the b_{2u} mode.

and correlate to K_1^*. To get an estimate for the gap, we can extrapolate the Kekulé geometries to a complete distortion, in which the π bonds of K_1 and K_2 would be completely separated (which in practice is prevented by the σ frame that limits the distortion). At this asymptote, the promotion energy, $K_i \rightarrow K_i^* (i = 1, 2)$, is due to the unpairing of three π bonds in *the ground state*, K_i, and replacing them, in K_i^*, by three nonbonding interactions. As we recall the latter are repulsive triplet interactions. The fact that such a distortion can never be reached is of no concern. What matters is that this constitutes an asymptotic estimate of the energy gap G that correlates the two Kekulé structures, and that eventually determines if their mixing results in a barrier or in a stable situation, in the style of the X_3 problem in Figure 15 above. According to the VB rules, G is given by Eq. [77]:

$$G(K \rightarrow K^*) = 9/4 \Delta_{ST}(C{=}C) \qquad [77]$$

Since the ΔE_{ST} value for an isolated π bond is of the order of 100 kcal/mol, Eq. [77] places the π electronic system in the region of large gaps. Consequently, the π component of benzene is predicted by the VBSCD model to be an *unstable transition state*, as illustrated in Figure 16a. This "π-transition state" prefers a distorted Kekuléan geometry with bond alternation, but is forced by the σ frame, with its strong symmetrizing driving force, to adopt the regular D_{6h} geometry. This proposal, which appeared as a daring prediction at the time, was made by Shaik and Bar on the basis of a qualitative VB diagram and semiempirical calculations.[194] It was later confirmed by rigorous

ab initio calculations, using different techniques of σ–π separations, by the present authors and their co-workers[195–198] and by others.[199–202] It was further linked, by the work of Haas and Zilberg,[203] to experimental data associated with the vibrational frequencies of the excited states of benzene.

The experimental data discussed by Haas and Zilberg,[203] as well as those of pioneering assignments[204–206] show a peculiar phenomenon. This phenomenon is both state specific to the $^1B_{2u}$ excited state, as well as vibrationally mode specific, to the bond-alternating mode, that is, *the Kekulé mode b_{2u}*. Thus, upon excitation from the $^1A_{1g}$ ground state to the $^1B_{2u}$ excited state, with exception of b_{2u} all other vibrational modes behave "normally" and undergo frequency lowering in the excited state, as expected from the decrease in π bonding and disruption of aromaticity following a $\pi \rightarrow \pi^*$ excitation. By contrast, the Kekulé b_{2u} mode, undergoes an upward shift of 257–261 cm^{-1}. As explained below, this phenomenon is predictable from the VBSCD model and constitutes a critical test of π distortivity in the ground state of benzene.

Indeed, the VBSCD model is able to lead to predictions not only on the ground state of an electronic system, but also on some selected excited state. Thus, the mixing of the two Kekulé structures K_1 and K_2 in Figure 16a leads to a pair of resonant and antiresonant states $K_1 \pm K_2$; the $^1A_{1g}$ ground state $K_1 + K_2$ is the resonance-stabilized combination, and the $^1B_{2u}$ excited state $K_1 - K_2$ is the antiresonant mixture (this is the first excited state of benzene[207]). In fact, the VBSCD in Figure 16a predicts that the curvature of the $^1A_{1g}(\pi)$ ground state (restricted to the π electronic system) is negative, whereas by contrast, that of the $^1B_{2u}(\pi)$ state is positive. Of course, when the energy of the σ frame is added as shown in Figure 16b, the net total driving force for the ground state becomes symmetrizing, with a small positive curvature. By comparison, the $^1B_{2u}$ excited state displays now a steeper curve and is much more symmetrizing than the ground state, having more positive curvature. As such, the VBSCD model predicts that an $^1A_{1g} \rightarrow {}^1B_{2u}$ excitation of benzene should result in the reinforcement of the symmetrizing driving force, which will be manifested as a frequency increase of the Kekulean b_{2u} mode. We may consider an alternative scenario, displayed in Figure 16c where now we assume that the π component for the ground state is symmetrizing (positive curvature) as might have been dictated by common wisdom. In such an event, the π component would be distortive in the $^1B_{2u}$ state, and consequently, the excitation would have resulted in the lowering of the b_{2u} frequency. Since this is clearly not the case, the finding of an enhanced b_{2u} frequency in the excited state constitutes an experimental proof of the π distortivity in the ground state of benzene.

In order to show how delicate the balance is between the σ and π opposing tendencies, we recently[57] derived an empirical equation, Eq. [78], for $4n + 2$ annulenes:

$$\Delta E_{\pi+\sigma} = 5.0(2n + 1) - 5.4(2n) \quad \text{kcal/mol} \qquad [78]$$

Here $\Delta E_{\pi+\sigma}$ stands for the total (π and σ) distortion energies, the terms $5.0(2n + 1)$ represent the resisting σ effect, which is 5.0 kcal/mol for an adjacent pair of σ bond, whereas the negative term, $-5.4(2n)$, accounts for the π distortivity. This expression predicts that for $n = 7$, namely, the $C_{30}H_{30}$ annulene, the $\Delta E_{\pi+\sigma}$ becomes negative and the annulene undergoes bond localization. If we increase the π distortivity coefficient a tiny bit, namely, to

$$\Delta E_{\pi+\sigma} = 5.0(2n + 1) - 6.0(2n) \quad \text{kcal/mol} \qquad [79]$$

the equation would now predict that the annulene with $n = 3$, namely, $C_{14}H_{14}$, will undergo bond localization. This extreme sensitivity, which is predicted to manifest in computations and experimental data of annulenes, is a simple outcome of the VBSCD prediction that the π component of these species behaves as a transition state with a propensity toward bond localization.

VBSCD: THE TWIN-STATE CONCEPT AND ITS LINK TO PHOTOCHEMICAL REACTIVITY

Photochemistry is an important field for future applications. The pioneering work of van Der Lugt and Oosterhoff[89] and Michl[91] highlighted the importance of avoided crossing regions as decay channels in photochemistry. Köppel and co-workers[208,209] showed that conical intersections, rather than avoided crossing regions, are the most efficient decay channels, from excited to ground states. Indeed, this role of conical intersections in organic photochemistry has been extensively investigated by Robb and co-workers,[93,96] and conical intersections are calculated today on a routine basis using software such as GAUSSIAN. Bernardi et al.[93] further showed that VB notions can be useful to rationalize the location of conical intersections and their structure.

As was subsequently argued by Shaik and Reddy,[97] the VBSCD is a straightforward model for discussing the relation between thermal and photochemical reactions and between the avoided crossing region and a conical intersection. Thus, the avoided crossing region of the VBSCD leads to the twin-states $\Psi^{\ddagger}$ and Ψ^{*} (Fig. 17); one corresponds to the resonant state of the VB configurations and the other to the antiresonant state.[85] Since the extent of this VB mixing is a function of geometry, there should exist in principle, *a specific distortion mode that converts the avoided crossing region into a conical intersection* where the twin-states $\Psi^{\ddagger}$ and Ψ^{*} become degenerate, and thereby enable the excited reaction complex to decay into the ground-state surface. In this manner, the conical intersection will be anchored at three structures; two of them are the reactant (R) and product (P_1) of the thermal reaction, and the third is the product (P_2) generated by the distortion mode that causes the degeneracy of the twin-states $\Psi^{\ddagger}$ and Ψ^{*}. *The new product would therefore*
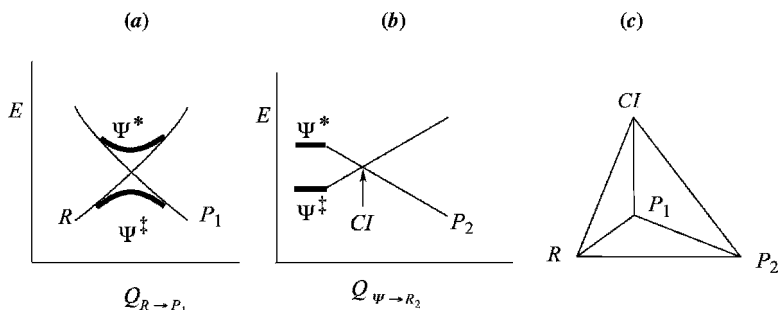
Figure 17 (*a*) The VBSCD showing the twin-states formed by avoided crossing along the reaction coordinate of the thermal reaction leading to product P_1. (*b*) The crossover of the twin-states to generate a conical intersection (CI) along a coordinate that stabilizes the twin excited state, and leading to product P_2. (*c*) The conical intersection will be anchored in three minima (or more): reactants (R), P_1, and P_2.

be characteristic of the distortion mode that is required to convert the avoided crossing region into a conical intersection. Assuming that most of the excited species roll down eventually to the Ψ^* funnel, then P_2 would be a major photoproduct.[a]

A trivial example is the celebrated hydrogen exchange reaction, $H_a - H_b + H_c \rightarrow H_a + H_b - H_c$, where the transition state has a colinear geometry, $H_a - H_b - H_c$. In this geometry, the ground state $\Psi^\ddagger$ is the resonating combination of R and P and the transition state for the thermal reaction, while the twin-excited state Ψ^* is the corresponding antiresonating combination:

$$\Psi^\ddagger = R - P;$$
$$R = |a\overline{b}c| - |\overline{a}bc| \quad P = |ab\overline{c}| - |a\overline{b}c| \tag{80}$$
$$\Psi^* = R + P = |ab\overline{c}| - |\overline{a}bc| \tag{81}$$

where the orbitals a, b, and c belong to H_a, H_b, and H_c, respectively.

It is clear from Eq. [81] that Ψ^* involves a bonding interaction between H_a and H_c and will be lowered by the bending mode that brings H_a and H_c together. Furthermore, the expression for the avoided crossing interaction B (Eq. [82]) shows that this quantity shrinks to zero in an equilateral triangular

$$B = \langle R|H^{\mathrm{eff}}|P\rangle = -2\beta_{ab}S_{ab} - 2\beta_{bc}S_{bc} + 4\beta_{ac}S_{ac} \tag{82}$$

---

[a] If, however, there exist other excited-state funnels near the twin excited state, Ψ^*, other products will be formed, which are characteristic of these other excited states and can be predicted in a similar manner provided one knows the identity of these excited states.

structure where the $H_a - H_c$, $H_a - H_b$, and $H_b - H_c$ interactions are identical. As such, the equilateral triangle defines a conical intersection with a doubly degenerate state, in the crossing point of the VBSCD. This D_{3h} structure will relax to the isosceles triangle with short $H_a - H_c$ distance that will give rise to a "new" product $H_b + H_a - H_c$. The photocyclization of allyl radical to cyclopropyl radical is precisely analogous. The ground state of allyl is the resonating combination of the two Kekulé structures, while the twin-excited state, Ψ^*, is their antiresonating combination with the long bond between the allylic terminals.[52] As such, rotation of the two allylic terminals will lower Ψ^*, raise the ground state, and establish a conical intersection that will channel the photoexcited complex to the cyclopropyl radical, and vice versa.

The photostimulation of S_N2 systems such as $X^- + A\text{—}Y$ (A = Alkyl) was analyzed before, using VBSCD-based rationale, for predicting the location of conical intersections.[97] Here, the transition state for the thermal reaction is the colinear $[X\text{—}A\text{—}Y]^-$ structure, which is the $\Psi^{\neq}(A')$ resonating combination of the two Lewis structures, while the twin-excited state, $\Psi^*(A'')$, is their anti-resonating combination; the symmetry labels refer to C_s symmetry. This latter excited state is readily written as an A'' symmetry-adapted combination of Lewis structures, Eq. [83]:

$$\Psi^* = (|\,x\bar{x}\,a\bar{y}\,| - |\,x\bar{x}\,\bar{a}\,y\,|) - (|\,y\bar{y}\,x\,\bar{a}\,| - |\,y\bar{y}\,\bar{x}\,a\,|) \qquad [83]$$

where the orbitals x, a, and y belong to the fragments X, A, and Y, respectively.

Rearranging Eq. [83] to Eq. [84] reveals a stabilizing three-electron bonding interaction between X and Y, of the type $(X^\bullet \; {:}Y^- \to X{:}^- \; {}^\bullet Y)$.

$$\Psi^* = (|\,\bar{x}\,x\bar{y}\,a\,| + |\,\bar{x}\,y\bar{y}\,a\,|) - (|\,x\bar{x}\,y\bar{a}\,| + |\,x\bar{y}\,y\bar{a}\,|) \qquad [84]$$

As such, the bending mode that brings the X and Y groups together destabilizes the $[X\text{—}A\text{—}Y]^-$ structure and stabilizes the twin-excited state, until they establish a conical intersection that correlates down to $X\,\therefore\,Y^-$ and $R^\bullet$, as shown in Figure 18. This analysis is supported by experimental observation that the irradiation of the I^-/CH_3I cluster at the charge-transfer band leads to I_2^- and $CH_3^\bullet$, while for I^-/CH_3Br such excitation generates IBr^- and $CH_3^\bullet$.[210]

The notion of twin-states of the VBSCD and the phase inversion rule of Longuet–Higgins were utilized by Zilberg and Haas[98] to delineate unified selection rules for conical intersections, and rationalize the outcome of a variety of photochemical reactions.

The presence of excited-state minima above the thermal transition state is a well known phenomenon.[89,91–93] The VBSCD model merely gives this ubiquitous phenomenon a simple mechanism in terms of the avoided crossing of
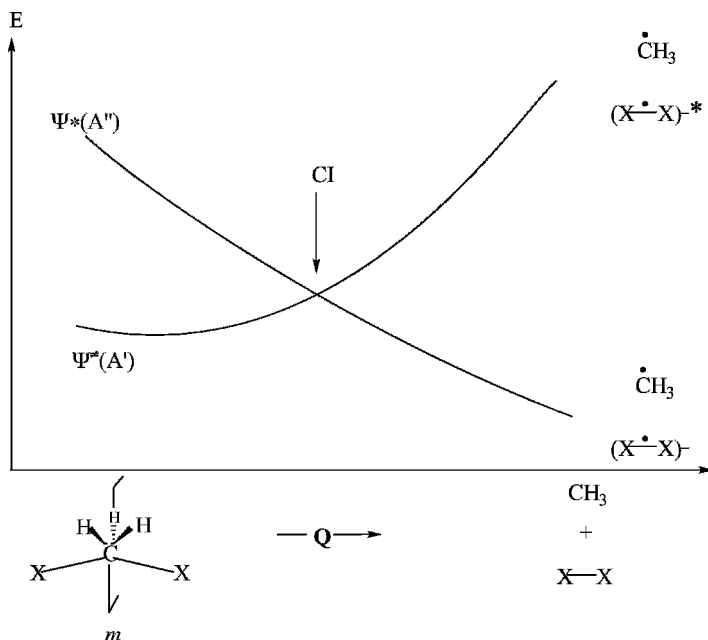
Figure 18 Generation of a conical intersection (*CI*) by crossing of the twin states along the bending distortion mode, in S_N2 systems. Symmetry labels refer to the mirror plane *m*.

VB structures, and hence enables one to make predictions in a systematic manner. Other important applications of the twin states concern the possibility of spectroscopic probing or accessing the twin excited state that lies directly above the transition state of a thermal reaction. Thus, much like the foregoing story of benzene, any chemical reaction will possess a transition state, $\Psi^{\ddagger}$ and a twin excited state, Ψ^*.[81,211] For most cases, albeit not all, the twin excited state should be stable, and hence observable; its geometry will be almost coincident with the thermal transition state and its electronic state symmetry should be identical to the symmetry of the reaction coordinate of the ground-state process,[212] namely,

$$\Gamma(\Psi^*) = \Gamma(Q_{RC}) \qquad [85]$$

In addition, the twin excited state will possess a real and greatly increased frequency of the reaction coordinate mode, by analogy to the benzene story where the b_{2u} mode was enhanced in the $^1b_{2u}$ twin excited state. Thus, since the twin pair has coincident geometry, a spectroscopic characterization of Ψ^* will provide complementary information on the transition state $\Psi_{\ddagger}$ and will enable resolution of the transition state structure.
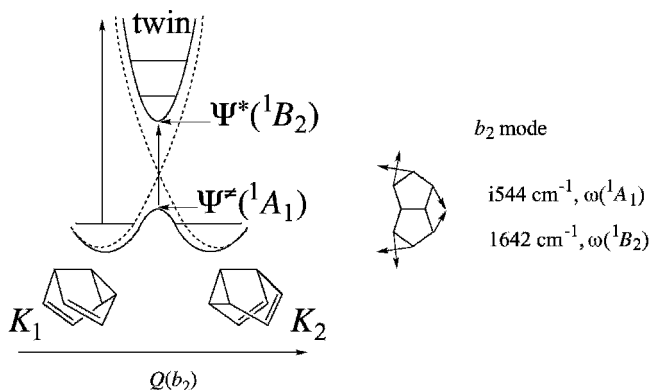
Figure 19 The twin states along the b_2 reaction coordinate for the semibullvalene rearrangement. When the thermal barrier is NOT much higher than the zero-point levels of the two isomers, the transition state ($\Psi^{\neq}$) region becomes available thermally. Absorption in the transition state region is in the visible, leading to thermochromism at elevated temperature.

As a proof of principle, the twin states were characterized for the semi-bullvalene rearrangement[212] and found to possess virtually identical geometries. As shown in Figure 19, the twin excited state possesses B_2 symmetry as the symmetry of the reaction coordinate of the thermal process. And the transition state mode, b_2, which is imaginary for $\Psi^{\neq}(A_1)$ was shown to be real for $\Psi^*(B_2)$.[212] These calculations match the intriguing findings of Quast et al.[213] in the semibullvalene and barbaralene systems. Thus, these authors[213,214] have designed semibullvalene and barbaralene derivatives in which the barrier for the rearrangement could be lowered drastically, to a point where it almost vanishes. Quast[213,214] found that these molecules exhibit thermochromism without having a chromophore; they are colorless at low temperatures but highly colored at 380 K. According to Quast, the thermo-chromism arises due to the low energy transition from the transition state ($\Psi^{\neq}$) to the twin excited state (Ψ^*), Figure 19. Thus, since the thermal barrier is exceptionally low, at elevated temperatures the transition state becomes thermally populated. Since the $\Psi^{\neq}$-Ψ^* gap is small, one observes color due to absorption within the visible region. However, at low temperatures, the molecules reside at the bottom of the reactant–product wells, where the gap between the ground and excited state is large and hence, the absorption is in the ultraviolet (UV) region and the color is lost. To quote Quast, "thermochro-mic … semibullvalene allow the observation of transition states even with one's naked eye".[214] Of course, identifying appropriate systems where the twin excited state is observable is required for the eventual "observation" of the transition states of thermal reactions.

Coherent control[215] is a powerful new chemical method that makes use of the availability of the twin excited state to control the course of chemical reactions by laser excitation. Thus, laser excitation from $\Psi^\ddagger$ to Ψ^*(Fig. 17*a*), using two different and complementary photons causes the decay of Ψ^* to occur in a controlled manner either to the reactant or products. In the case where the reactants and products are two enantiomers, the twin excited state is achiral, and the coherent control approach leads to chiral resolution.

In summary, the twin excited state plays an important role in photo-chemistry as well as in thermal chemistry.

THE SPIN HAMILTONIAN VB THEORY

Quite a different brand of VB theory comes from physics, and is rooted in the phenomenological Hamiltonians that are called magnetic- or spin-Hamiltonians after their first formulation by Heisenberg.[9] Unlike the theory used above, which relies on VB structures that are eigenfunctions of both the S_z and S^2 operators, this theory relies on VB determinants, which are eigenfunctions of only the S_z operator. The following section describes the type of insight that can be gained from this VB approach.

Theory

The spin-Hamiltonian VB theory uses the same approximations as the qualitative theory presented above to calculate the Hamiltonian matrix elements, but with a few simplifications. The theory is restricted to determinants having one electron per AO; this restriction excludes ionic structures or molecules bearing lone pairs. As such, the theory has mainly been applied to conjugated polyenes. Another simplification is the zero-differential overlap approximation, which means that all overlaps are neglected in the formulas.

Apart from these simplifying assumptions, a fundamental difference between qualitative VB theory and spin-Hamiltonian VB theory is that the basic constituent of the latter theory is the AO determinant, without any a priori bias for a given electronic coupling into bond pairs. Instead of an interplay between VB structures, a molecule is viewed then as a collective spin-ordering: The electrons tend to occupy the molecular space (i.e., the various atomic centers) in such a way that *an electron of α spin will be surrounded by as many β spin electrons as possible, and vice versa*. Determinants having this property, called the "most spin-alternated determinants" (MSAD) have the lowest energies (by virtue of the VB rules, in *Qualitative VB Theory*) and play the major role in electronic structure. As a reminder, the reader should recall from our discussion above that the unique spin-alternant determinant, which we called the quasiclassical state, is used as a reference for the interaction energy.

The usefulness of such a magnetic description in chemistry has been demonstrated by Malrieu and his co-workers.[64,65,216] Without any numerical computations, the method can be used to deduce qualitative rules, regarding the spin multiplicity of the ground-states of polyenes (especially for diradicals), the spin distribution in free radicals and triplet states, differences in bond lengths, and relative stabilities of isomers. It can also be used quantitatively, through CI, leading to ground-state equilibrium geometries, rotational barriers, excited-states ordering (for neutral excited states), and so on.

We now briefly describe the principles of the method and simple rules for the construction of the Hamiltonian matrix. For the sake of consistency, rather than the original formulation of Malrieu,[64,65,216] we use here a formulation[52,71–73] that is in harmony with the qualitative VB theory above. The method can be summarized with a few principles:

1. All overlaps are neglected.
2. The energy of a VB determinant Ψ_D is proportional to the number of Pauli repulsions that take place between adjacent AOs having electrons with identical spins:

$$E(\Psi_D) = \sum_{r\uparrow,s\uparrow} g_{rs} \qquad [86]$$

where g_{rs} is a parameter that is quantified either from experimental data, or is ab initio (DFT) calculated as one-half of the singlet–triplet gap of the r–s bond. In terms of the qualitative theory above, g_{rs} is therefore just the key quantity $-2\beta_{rs}S_{rs}$. (We, however, avoid the integral S in the present theory since the overlaps are neglected).
3. The Hamiltonian matrix element between two determinants differing by one spin permutation between orbitals r and s is equal to g_{rs}. Any other off-diagonal matrix elements are set to zero (see Scheme 12).

| $\lvert a\bar{b}c\bar{d}\rvert$	$\lvert a\bar{b}\bar{c}d\rvert$	$\lvert ab\bar{c}\bar{d}\rvert$	$\lvert \bar{a}\bar{b}cd\rvert$	$\lvert a\bar{b}c\bar{d}\rvert$	$\lvert \bar{a}bc\bar{d}\rvert$
0	0	g_{ab}	g_{cd}	0	g_{bc}
	0	g_{cd}	g_{ab}	g_{bc}	0
		g_{bc}	0	0	0
			g_{bc}	0	0
				$g_{ab}+g_{cd}$	0
					$g_{ab}+g_{cd}$

Scheme 12

Diagonalization of this matrix gives the energy of the ground state relative to the nonbonding state (the spin-alternant determinant), and in addition leads to the entire spectrum of the lowest neutral excited states. Note that applying the spin-Hamiltonian model to ethylene leads to a π bonding energy $-g$, which is equivalent to the $2\beta S$ used in the qualitative VB theory above.

Applications

Ground States of Polyenes and Hund's Rule Violations

A simple principle of the spin-Hamiltonian VB theory is that *the lowest state of a molecule will have the multiplicity associated with the S_z value of its MSAD*, that is, it will be a singlet if $n_\alpha = n_\beta$ in the MSAD, a doublet if $n_\alpha = n_\beta + 1$, a triplet if $n_\alpha = n_\beta + 2$, and so on.[217] For example, the MSAD of orthoxylylene **27** and paraxylylene **28** (Scheme 13) both have $S_z = 0$ while that of metaxylylene (**29**) has $S_z = 1$.

27   **28**   **29**
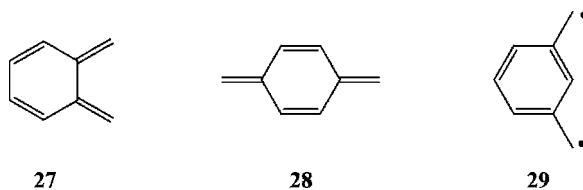
Scheme 13

It follows that ortho- and para-xylylenes will have singlet ground states while metaxylylene has a triplet ground state. The prediction is correct but not particularly surprising, since **27** and **28** can be described by a perfectly paired Kekulé structure while **29** cannot and is therefore a diradical that will be a triplet state based on Hund's rule. More intriguing are the predictions of Hund's rule *violations*. Let us consider, for example, 2,3-dimethylene-butadiene and 1,3-dimethylene-butadiene. These are two polyenes for which it is impossible to draw a Kekulé structure, and which are therefore diradicaloids. Now the MSAD of these two species (**30** and **31** in Scheme 14) have different S_z values, $S_z = 0$ for **30** versus $S_z = 1$ for **31**.


30   **31**
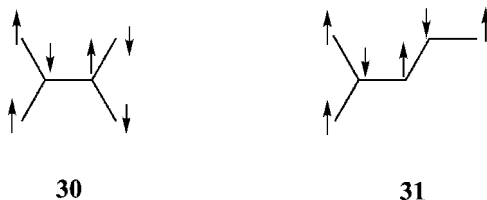
Scheme 14

In this case, the spin-Hamiltonian predicts 2,3-dimethylene-butadiene to be a singlet diradicaloid (in violation of Hund's rule) and 1,3-dimethylene-butadiene to be a triplet, in agreement with experiment. By contrast, monode-terminantal MO calculations predict that all these diradicaloids have triplet ground states. It is only after CI that one gets the correct assignments.[218] Violations of Hund's rule can be explained by the phenomenon of dynamic spin-polarization and predicted to take place when the degenerate singly occupied MOs form a disjointed set.[218,219] In such a case, the advantage of the triplet over the singlet becomes very weak owing to a small exchange integral, and when CI is applied, it preferentially stabilizes the singlet, and reverses the singlet–triplet energy order. Comparison of the spin-polarization argument to the present VB analysis, shows the VB method to be faster, physically intuitive, and independent of any numerical calculation.

Relative Stabilities of Polyenes

Subtle predictions can be made about the relative energies of two isomers having comparable Kekulé structures, such as the linear s-trans conformation and branched conformation of hexatriene, **18** and **22** in Scheme 9 above. For each of these isomers, we shall consider that the total π energy is a perturbation of

32   **33**
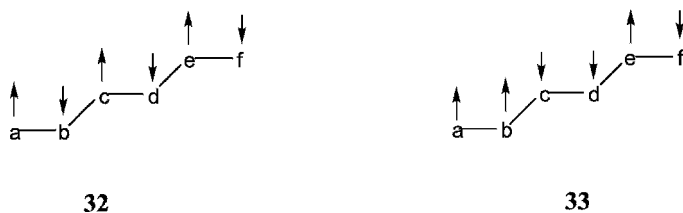
Scheme 15

the energy of the MSAD (e.g., **32** for the linear conformation in Scheme 15) by less ordered determinants. Each of the latter determinants is generated from the MSAD by the inversion of two spins along a given linkage (e.g., **33** vs. **32** in Scheme 15), while keeping the total S_z constant. According to the above rules, the Hamiltonian matrix element between **32** and **33** is the integral g_{bc}, and the energy of **32** relative to **33** is $g_{ab} + g_{cd}$, since the spin reorganization introduces two Pauli repulsions along the *a-b* and *c-d* linkages.

More generally, the number of Pauli repulsions that one introduces, relative to the MSAD, by inverting the spins in a linkage *r-s* is equal to the number of linkages that are adjacent to *r-s*. Thus, assuming that all the *g* integrals are the same for the sake of simplicity, the energy of a determinant Ψ_{rs} generated by spin inversion relative to a MSAD Ψ is given by Eq. [87]:

$$E(\psi_{rs}) - E(\psi) = g \times n_a(rs) \tag{87}$$

where n_a is the number of linkages that are adjacent to *r-s*. We now consider all determinants displaying a spin transposition between two adjacent atoms with respect to the MSAD. The matrix elements between the determinants Ψ_{rs} and Ψ will be the same and all equal to the *g* integral. Hence, the total π energy that arises from a second order perturbation correction (*PT2*) will be given by Eq. [88]:

$$E(PT2) = \sum_{rs} \frac{g^2}{gn_a(rs)} \quad = \quad g\sum_{rs} \frac{1}{n_a(rs)} \qquad [88]$$

where the energy is calculated relative to the MSAD. Therefore, it appears that the energy of a polyene is a simple topological function that is related to the shape of the molecule and to the way the various linkages are connected to each other. Calculating the energies of the two isomers of hexatriene is thus

34   **35**
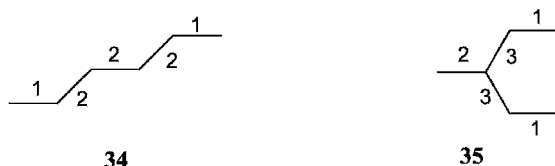
$E(PT2) = -(2/1 + 3/2)g$ $E(PT2) = -(2/1 + 1/2 + 2/3)g$

Scheme 16

a simple matter. In Scheme 16, each linkage in **34** and **35** is labeled by the number of bonds that are adjacent it. From these numbers, the expressions for the total energies of each isomer are immediately calculated (Scheme 16), and clearly show that the linear isomer is more stable than the branched one, in agreement with experimental facts.

AB INITIO VB METHODS

A number of ab initio VB methods have been implemented to calculate VB wave functions and their associated energies and molecular properties. Once the general scheme for writing VB wave functions is established (see *Basic VB Theory* above), an important task is the optimization of the orbitals that are used to construct the AO or FO determinants of the VB structures. Historically, the classical VB method used the atomic orbitals of the free atoms, without any further change. This crude approximation, which is no longer employed, resulted in highly inaccurate energies, since it does not take into account the considerable rearrangements in size and shape that an

AO undergoes when fragments assemble to a molecule. Accordingly, we shall restrict ourselves here to modern VB methods that perform orbital optimization.

Orbital-Optimized Single-Configuration Methods

A great step forward in accuracy and compactness was made when optimized orbitals of Coulson–Fischer (CF) type were employed in VB calculations. As shown above (*Basic VB Theory*), describing a two electron bond as formally covalent singlet coupling between two CF orbitals φ_a and φ_b (Eqs. [6b] and [6c]), which are optimized and free to delocalize over the two centers, is an ingenious way to include both the covalent and ionic components of the bond in an implicit way in a wave function of the Heitler–London type. Thus, the CF representation has the advantage of keeping the well-known picture of perfect pairing while treating the left–right electron correlation associated with any given bond in a variational way.

The CF proposal, generalized to polyatomic molecules, gave rise to the "separated electron pair" theory that was initiated by Hurley et al.[220] and later developed as the GVB method by Goddard and co-workers,[109,221,222] and as the SC method by Gerratt and co-workers.[112–114,223–225] In both these latter methods the valence electrons are described by a single configuration of singly occupied orbitals, and the various spin-coupled structures—generated so as to form a complete and linearly independent set of spin-eigenfunctions—are allowed to mix to generate the final state. In the SC method, both the orbitals and the mixing coefficients are optimized simultaneously, while in the most general form of GVB theory they are optimized sequentially. It is important to note that, while no constraint of any kind is applied to the shapes of the orbitals during the optimization, they are generally obtained in a form that is pretty much localized, as will be exemplified below. Thus, each bond in a polyatomic VB structure is viewed as a pair of singlet-coupled orbitals that are quasi-atomic and display a strong mutual overlap.

The Generalized VB Method

The GVB method is generally used in its restricted perfectly paired form, referred to as GVB–PP, which pairs the atoms as in the most important Lewis structure. The GVB–PP method introduces two simplifications. The first one is the Perfect-Pairing (PP) approximation, by which only one VB structure is generated in the calculation. The wave function may then be expressed in the simple form of Eq. [89], where each term in parentheses is a so-called "geminal" two-electron function, which takes the form of a singlet-coupled GVB pair $(\varphi_{ia}, \varphi_{ib})$ and is associated with one particular bond or lone pair.

$$\psi_{GVB} = |(\varphi_{1a}\overline{\varphi}_{1b} - \overline{\varphi}_{1a}\varphi_{1b})(\varphi_{2a}\overline{\varphi}_{2b} - \overline{\varphi}_{2a}\varphi_{2b})\cdots(\varphi_{na}\overline{\varphi}_{nb} - \overline{\varphi}_{na}\varphi_{nb})| \quad [89]$$

The second simplification, which is introduced for computational convenience, is the *strong orthogonality* constraint, whereby all the orbitals in Eq. [89] are required to be orthogonal to each other unless they are singlet paired, that is,

$$\langle \varphi_{ia} | \varphi_{ib} \rangle \neq 0 \qquad \qquad [90a]$$

$$\langle \varphi_i | \varphi_j \rangle = 0 \text{ otherwise} \qquad \qquad [90b]$$

This strong orthogonality constraint is, of course, a restriction, however, usually not a serious one, since it applies to orbitals that are not expected to overlap significantly. By contrast, the orbitals that are coupled together in a given GVB pair display, of course, a strong overlap.

For further mathematical convenience, each geminal in Eq. [89] can be rewritten, by simple orbital rotation, as an expansion in terms of natural orbitals,

$$| (\varphi_{1a}\overline{\varphi}_{1b} - \overline{\varphi}_{1a}\varphi_{1b}) | = C_i | \phi_i \overline{\phi}_i | + C_i^* | \phi_i^* \overline{\phi_i^*} | \qquad [91]$$

This alternative form of the geminal contains two closed-shell terms. The natural orbitals ϕ_i *and* ϕ_i^*, in Eq. [91], have the shapes of localized bond MOs, respectively bonding and antibonding, and are orthogonal to each other. They are connected to the GVB pairs by the simple transformation below:

$$\varphi_{ia} = \frac{\phi_i + \lambda \phi_i^*}{(1 + \lambda^2)^{1/2}} \qquad \qquad [92a]$$

$$\varphi_{ib} = \frac{\phi_i - \lambda \phi_i^*}{(1 + \lambda^2)^{1/2}} \qquad \qquad [92b]$$

$$\lambda^2 = -\frac{C_i^*}{C_i} \qquad \qquad [92c]$$

The use of natural orbitals, which constitute an orthogonal set, avoids the $N!$ problem, resulting in a great computational advantage over the use of the GVB pairs in the effective equations that have to be solved for self-consistency. A GVB–PP calculation is thus just a special case of a low-dimensional MCSCF calculation, with all the CPU advantages of MO calculations and the additional interpretability of a wave function that is transformed eventually to a VB form.

The perfect-pairing and strong-orthogonality restrictions result in considerable computer time savings and no great loss of accuracy, as long as the computed molecule is made of clearly separated local bonds (e.g., methane).[226] On the other hand, it is clear that these restrictions would be

highly inappropriate for delocalized electronic species like benzene, for which the PP approximation is not meaningful, and all electron-pairing schemes have to be considered to provide a reasonable state wave function.[207,227]

The GVB method takes care of all the left–right correlation in molecules, but does not include the totality of the "nondynamical" electron correlation since the various local ionic situations are constrained to be equal with this method (e.g., two adjacent local ionic forms $+-/-+$ and $+-/+-$ will be found to possess the same weight). Accounting for the full nondynamical correlation, requires a "Complete Active Space" MCSCF calculation (CASSCF,which involves all possible configurations that can be constructed within the space of valence orbitals). Having said that, we nevertheless emphasize that as a rule, the GVB method provides results that are much closer to CASSCF quality than to Hartree–Fock.

As a VB method, GVB ensures correct homolytic dissociation as a bond is broken. However, the calculated dissociation energy is generally too low, due to lack of dynamical electron correlation, although far better than the value computed at the Hartree–Fock level. For example, while Hartree–Fock gives a negative bond dissociation energy of F_2, GVB yields a positive bond energy, but one that is less than one-half of the experimental value.[132] As shown below, better accuracy can be reached by going beyond the one-configuration VB model.

The perfect-pairing GVB wave function is a good starting point for further CI, called "Correlation-Consistent Configuration Interaction" (CCCI). Thus, Carter and Goddard defined a general method employing a relatively small but well-defined CI expansion for calculating accurate bonding energies.[228] In this method, one first generates a restricted CI expansion (RCI) in which each GVB pair is allowed to have all three possible occupancies for two electrons distributed among the orbitals of that bond pair. Then, the CI is extended by including all single and double excitations from each bond pair that undergoes dissociation to all other orbitals. Further, since bond dissociation generally leads to geometric and hybridization changes in the resultant fragments, the change in shape of the orbitals adjacent to the dissociating bond(s) is also taken into account. This is done by adding, from each RCI configuration, all single excitations from the valence space to all orbitals. The GVB–CCCI approach has been successfully applied to single and double bonds and to transition metal complexes.[228]

The Spin-Coupled Method

The spin-coupled method of Gerratt and co-workers[112–114,223–225] differs from the GVB–PP method in that it removes any orthogonality and perfect-pairing restrictions. The method is still of the single-configuration type, but all the modes of spin-pairing are included in the wave functions and the orbitals are allowed to overlap freely with each other. The SC method has often been used to provide firm theoretical support to some basic concepts

like orbital hybridization, or resonance between Kekulé structures, which were qualitative postulates in the early days of VB theory. The chemical picture that emerges from the SC method has the following features: (a) the SC method deals with correlated electrons; (b) no preconceptions or constraints are imposed on the spin-couplings nor on the shapes of the orbitals, which are determined by the variational principle alone; (c) the set of orbitals arising from such calculations is unique. As such, the SC method represents the ultimate level of accuracy compatible with the orbital approximation that describes the molecule as a single configuration with fixed orbital occupancies. Thus, it is clear that the shape of the orbitals and the relative importance of the various spin-couplings determined by this method, should have strong relevance to the nature of chemical bonding.

The methane molecule, as the archetypal system displaying hybridization, has been studied by Cooper et al.[229] in the framework of SC theory. It appears that the spin-coupled description of methane resembles very closely our intuitive view of four localized C–H bonds. The eight spin-coupled orbitals that arise from the variational principle fall into two groups of four. Four of the orbitals are each localized on a hydrogen atom. The other four degenerate orbitals are localized on carbon, and each represents a slightly distorted, approximately sp^3 hybrid pointing toward one of the H atoms. All the hybrid orbitals are identical in shape and mutually related by symmetry operations of the T_d point group. The full spin-coupled wave function, with its 14 different spin-couplings, lies 65 mh below the Hartree–Fock wave function and only 12 mh above the full valence CASSCF wave function with its 1764 spin functions. The perfect-pairing function is the dominant mode of spin-coupling, only 3 mh above the full spin-coupled wave function. It is noted that the strong orthogonality restriction that is often used in GVB theory is an excellent approximation that barely raises the total energy, by < 2 mh.[226] The hybridization picture is of course very general, and allows any type of hybridization beyond the classical sp^3, sp^2 and sp types. For example, according to a GVB calculation by Goddard,[221] the hybrids involved in the O–H bonds of H_2O have more p character than the lone pairs (82 and 59%, respectively, as compared to the 75% expected for sp^3 hybrids), in agreement with the fact that the HOH angle is smaller than the standard tetrahedral angle.

Calculations of SC[230] or GVB[231,232] types have also been able to provide a simple picture for the electronic structure of lithium clusters Li_n ($n = 3$–8). In these cases, once again a single spin-coupling is found to be sufficient, but the optimized orbitals, though being localized, are not atomic but interstitial, that is, localized between two nuclei or more. The rhomboid structure **36** of Li_4, for example, is easily explained by the single spin-coupling displaying two bonds between interstitial orbitals, as illustrated in Scheme 17.

The SC method has also been used to probe the validity of the traditional description of conjugated molecules, and in particular aromatic systems, as sets of resonating Kekulé structures. Taking benzene as an example and using

36
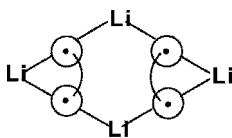
Scheme 17

the σ–π separation, the converged spin-coupled wave function[207] displays two dominant spin functions, which correspond to the traditional Kekulé structures. The orbitals that arise from the calculation are highly localized and have the form of slightly distorted $2p$ AOs perpendicular to the molecular plane. The three remaining spin functions that are necessary to form a complete basis set of neutral VB structures, the so-called Dewar structures, contribute only 20% to the ground state. This one-configuration wave function is considerably lower in energy than the Hartree–Fock level, by 75 mh, and only 7 mh higher than the full valence CI within the π-valence space. The description of benzene as a mixture of limiting Kekulé structures is thus given a firm foundation that proves to be generally valid for other aromatic and antiaromatic systems.

The spin-coupled valence bond (SCVB) theory is an extension of the spin-coupled method, in which further CI is performed after the one-configuration calculation. At the simplest level, the CI includes all the configurations that can possibly be generated by distributing the electrons within the set of the active orbitals that were optimized in the preliminary SC calculation; both covalent and "ionic" type configurations are considered. When applied to the π system of benzene,[207] this level of calculation was found to provide a satisfactory account of the valence states, and showed that the first excited state, $^1B_{2u}$, is made of the antiresonant combination of the two Kekulé structures. A higher level of SCVB theory includes additional excitations, for example, from the orbitals of the σ core, or to orbitals that are virtual in the one-configuration calculation. To preserve the valence bond character of the wave function, the virtual orbitals have to be localized as much as possible. This condition is met in the SCVB method,[223] in which each occupied orbital of the ground configuration is made to correspond to a stack of virtual orbitals localized in the same region of space, by means of an effective operator representing the field created by the remaining occupied orbitals. There remains to perform a simple CI (of nonorthogonal type) among the space of the configurations so generated. By experience, the excited configurations generally bring very little stabilization as far as ground states are concerned. This is easily explained by the fact that the orbitals are optimized precisely so as to concentrate all important physical effects in the reference single configuration. On the other

hand, excited configurations are important for satisfactory state ordering and transition energies.[207]

Orbital-Optimized Multiconfiguration VB Methods

VBSCF

The VBSCF method of van Lenthe and Balint-Kurti[117] is a general method of multiconfiguration self-consistent field (MCSCF) type, which is able to deal with nonorthogonal orbitals. The VBSCF wave function is, in principle, a linear combination of VB structures, in which both orbitals and coefficients are optimized simultaneously. It is therefore a generalization of the above one-configuration methods to the multiconfiguration case, with the interesting advantage that no particular configuration is favored during the course of the orbital optimization. The orbitals can be optimized freely as in GVB or SC methods, but may also be constrained to be localized each on a single atom or fragment. The method has been efficiently implemented[118,119,233,234] by the Utrecht group in the TURTLE program.[120] A program having similar capabilities, XIAMEN 99, has been developed by Wu and co-workers, based on the spin-free formulation of VB theory.[128] Being a multiconfigurational method, the VBSCF theory, in TURTLE and XIAMEN99, is an ideal tool for studying problems that involve resonance energies and avoided crossing situations. Some examples of this usage are discussed below.

The VBSCF method has been used to probe the validity of the resonance model in organic chemistry following some controversies that appeared in the literature, regarding the presence or absence of resonance stabilization, for example, in the peptide bond, carboxylic acids, and enols. The enhanced acidity of carboxylic acids relative to alcohols is traditionally attributed to the stabilization of the carboxylate anion by delocalization of its π electrons via resonance structures **37–39** in Scheme 18.

37   **38**   **39**

Scheme 18

A similar resonating scheme can be applied to the enolate anion. On the other hand, not being a conjugated system, this does not apply to the alkoxide anion. However successful, this traditional view was challenged by several authors[235–238] who advanced the idea that the enhanced acidities originate from the high polaritizabilities of the carbonyl and vinyl groups. To resolve

the controversy, one must answer the key question: how much does π electron delocalization stabilize the carboxylate and enolate anions relative to a reference situation in which the delocalization would be "turned off"? Clearly, a meaningful answer to this question would emerge only when the orbitals in the VB wave function are strictly localized, as in the VBSCF method.

A direct estimate of the stabilization energy due to delocalization is very simple, as illustrated with the following example of the carboxylate anion, in Scheme 18. First, a localized reference state is calculated, in which the geometry and the orbitals are optimized with the unique restriction that the π atomic orbital of one of the oxygens cannot delocalize over the other atoms and remains doubly occupied, as in **37**. Second, the ground state is calculated at the same level of theory, but with electron delocalization being fully allowed. The results of the calculations[239] give a clear-cut answer: In all cases the delocalization of the oxygen π lone pair stabilizes the anion more than the parent acids. These excess values are 23 kcal/mol for carboxylic acids and 21 kcal/mol for enols compared with only 8 kcal/mol for alcohols. It follows that, in accord with the traditional view, π electron delocalization plays an important role in the acidity enhancement of carboxylic acids and enols relative to alcohols. By comparison with the experimental acidities, it was concluded[239] that a lower limit for the contribution of electron delocalization to the total acidity enhancement is 48% for the carboxylic acids and 62% for the enols, values that clearly establish the importance of resonance effects, while leaving some room for nonnegligible inductive effects.

The peptide and thio-peptide bonds have some specific properties like coplanarity, substantial rotational barrier and kinetic stability towards nucleophilic attack or hydrolysis. All these properties are easily rationalized by the
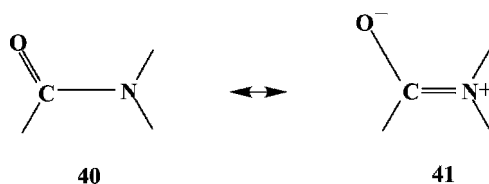
Scheme 19

classical resonance hybrid model, illustrated in Scheme 19 for an amide. According to this resonating picture, the peptide bond is mainly described by **40,** with a significant contribution from the charge-transfer structure **41,** and this resonance contribution is the root cause of both the low basicity of the nitrogen's lone pair and the barrier to rotation around the C—N bond.

As in the preceding case, the simple resonance picture was criticized[240–242] on the basis of electron population analyses using the AIM method,[243] to the extent that (thio)amides were proposed to be viewed as special

cases of amines with a carbonyl substituent.[242] At the heart of the debate[244–247] was the role of the π electron delocalization energy in the barrier to rotation (16 kcal/mol for formamide, 18 kcal/mol for thioformamide[248]) around the C—N bond. To settle the question, the adiabatic energy difference between the localized form **40**, with the π lone pair localized on the nitrogen atom, and the fully delocalized ground state, was calculated[249] for formamide and thioformamide with the VBSCF method,[117] and the same type of calculation was repeated for the 90° rotated conformations. As a result, the contribution of resonance stabilization to the rotational barrier, estimated as that quantity by which electron delocalization stabilizes the planar conformation more than the 90° rotated conformation, was found to be 7.3 and 13.7 kcal/mol, respectively, for formamide and thioamide. While this indicates that other factors do contribute to the rotational barrier, resonance stabilization in amides and thioamides emerges as an important factor, in agreement with the traditional view and the common wisdom that allylic resonance is an important driving force in organic chemistry.

Clearly, therefore, VBSCF constitutes a handy tool for studies of the role of electronic delocalization, in molecules that possess more than one Lewis structure.

VBCI: A Post VBSCF Method that Involves Dynamic Correlation

The VBCI method, recently developed by Wu et al.[138] is a post-VBSCF calculation that uses configuration interaction to supplement the VBSCF energy with dynamic correlation. At the same time, the method preserves the interpretability of the final wave function in terms of a minimal number of VB structures, each having a clear chemical meaning. The VB structures that are used in the VBSCF calculations are referred to as fundamental structures, denoted as Φ_K^0, and the orbitals that appear in the VBSCF calculation are referred to as occupied orbitals. Depending on the problem at hand, the VBSCF calculation may use semidelocalized CF orbitals, or orbitals that are each localized on a single atom or fragment; in the latter case the fundamental structures will explicitly involve the covalent and ionic components of the bonds.

The CI calculation that follows the VBSCF step requires the definition of virtual orbitals. To keep the interpretability of the final wave function, the virtual orbitals are defined, by use of a projector, so as to be localized on the same fragments as the corresponding occupied orbitals. After generating the virtual orbitals, the excited VB structures are created in the following way. Given a fundamental structure Φ_K^0, an excited VB structure Φ_K^i is built-up by replacing occupied orbital(s) φ_i with virtual orbital(s) φ_j^*. By restricting the replacement of virtual orbital φ_j^* to the same fragment as φ_i, the excited structure Φ_K^i retains the same electronic pairing pattern and charge distribution as Φ_K^0. In other words, both Φ_K^0 and Φ_K^i describe the same classical VB structure. Thus, the collection of excited VB structures nascent from a given fundamental VB structure serves to relax the latter and endow it with dynamic correlation.

Several levels of CI can be employed. The starting point always involves single excitations and is referred to as VBCIS. This can be followed by VBCISD, VBCISDT, and so on, where D stands for double excitations and T for triples. The level at which truncation is made will depend on the size of the problem and the desired accuracy. In practice, the VBCISD level has been tested for some dissociation energies and reaction barriers for hydrogen exchange reactions[138,142] and has been shown to match the accuracy of the molecular orbital based coupled cluster CCSD and CCSD(T) methods, while retaining the interpretability of simpler VB methods. In the case of the hydrogen exchange reaction[142] of $H + H_2$, the method gave a barrier of 10 kcal/mol, compatible with the corresponding experimental data (9.6–9.8 kcal/mol). In summary: The VBCI method can be used like the VBSCF method for problems involving resonance and for calculating VBSCDs. The accuracy of VBCI is comparable to CCSD and CCSD(T) methods.

Different Orbitals for Different VB Structures

There are many molecules, in particular some radicals, that are naturally described in terms of two or more resonance structures, and for which the one-configuration approximation is not appropriate. Such molecules are generally subject to the well-known broken-symmetry artifact, whereby a wave function calculated at an insufficient level of theory is of lower symmetry than the nuclear framework, which results in erroneous energetics and discontinuities of the calculated potential surface. The formyloxyl radical (**42** ↔ **43** in Scheme 20) is a typical example, but the problem is very general and includes

42   **43**
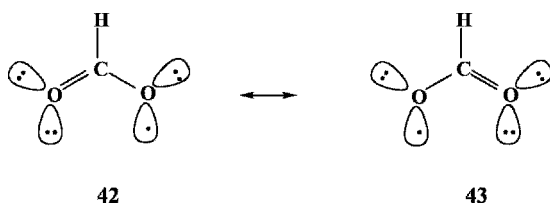
Scheme 20

an enormous variety of open-shell electronic states, as, for example, allyl radicals[250] or radicals of allylic type,[251–256] core-ionized diatoms,[257] $n–\pi^*$ excited molecules containing two equivalent carbonyl groups,[258] n-ionized molecules having equivalent remote lone pairs,[259] and charged clusters.[260–263] The same problem arises in localized versus mixed-valent organometallic species with two metal ions that can have different oxidation states, in doped stacks of aromatic conductors and semiconductors, and in electron-transfer processes between two identical species (e.g., metal ion centers separated by a bridge). Clearly, this is a ubiquitous problem in chemistry.

The problem has been lucidly rationalized by McLean et al.[255] in VB terms. It arises from a competition between two VB-related effects. The first is the familiar resonance effect whereby a mixture of two resonance structures is lower in energy than either one taken separately. The other is the so-called orbital size effect, whereby each VB structure gains stabilization if it can have its particular set of orbitals, which are specifically optimized for that VB structure and not the other. The two effects cannot be taken into account simultaneously in any one-configuration theory, be it of VB or MO type, because it employs a common set of orbitals. In the (frequent) case where the orbital size effect is the important factor, the wave function takes more or less the form of one particular VB structure, thereby resulting in an artefactual symmetry-breaking. In the MO-based framework, the remedy consists of performing MCSCF calculations in a rather large space of configurations.[255] On the other hand, the remedy is very simple in the VB framework, and consists of allowing different orbitals for different VB structures in the course of the orbital optimization, as illustrated in Scheme 21, by **44** and **45** for the formyloxyl radical,

44   **45**
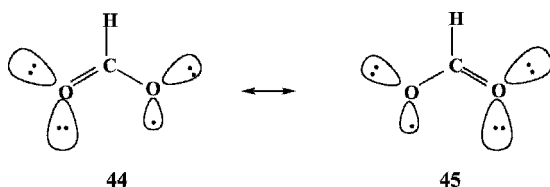
Scheme 21

in which the doubly occupied orbitals are diffuse and hence drawn larger than the more compact singly occupied ones. Note that *all* the orbitals of **44** are different from those of **45**, although the major differences are seen between the two orbitals that are involved in the electron transfer.

In the spirit of the above described method, Jackels and Davidson[252] cured the symmetry-breaking problem in the NO_2 radical by using a symmetry-adapted combination of two symmetry-broken Hartree–Fock wave functions, by means of a 2×2 nonorthogonal CI. The generalized multistructural (GMS) method of Hollauer and Nascimento[264,265] includes both the symmetry broken structures and the symmetry-adapted one in the same calculation, followed by subsequent CI. The symmetry-broken subwave functions are optimized at the GVB level in the R-GVB (Resonating-GVB) method of Voter and Goddard.[257] In all these methods, the subwave functions representing the individual resonance structures are optimized separately, which may lead to an underestimation of the resonance energy since the orbital optimization only takes care of the size effect. To remedy this defect, Voter and Goddard subsequently improved their method by allowing the subwave functions

to be optimized in the presence of each other, leading to the final generalized resonating valence bond method (GRVB).[258]

Breathing Orbitals: A Post VBSCF Method that Involves Dynamic Correlation

The breathing orbital valence bond (BOVB) method[132–137] is a generalization of the principle of "different orbitals for different structures" to the description of the elementary bond, be it of the one-electron, two-electron, or three-electron type. The objective of the method is threefold: (a) yielding accurate bond dissociation energy curves, which is a necessary condition for a meaningful description of the elementary events of a reaction, bond breaking and bond formation; (2) keeping the wave function compact and transparent in terms of structural formulas; (3) being suitable for calculations of diabatic states. In order to achieve these requirements, the method rests on the basic principle that if all relevant structural formulas for a given electronic system are generated, and if their VB description is made optimal by a proper orbital optimization, then a variational combination of the corresponding VB structures would accurately reproduce the energetics of this electronic system throughout a reaction coordinate. Accordingly, the composite VB structures of CF type are abandoned and the wave function takes a classical VB form in which all possible structural formulas (e.g., covalent and ionic) are generated. Then, each structural formula is made to correspond to a single VB structure that displays the appropriate orbital occupancy.

Since the ionic and covalent components of the bonds are explicitly included in the wave function, it is not necessary (and in fact, not useful) to let the orbitals of the VB structures be delocalized. This exclusion permits a better interpretability of the wave function in terms of unambiguous structural formulas, by dealing with VB structures defined with orbitals that are each strictly localized on a single atom or fragment. Within this constraint, the orbitals are optimized with the freedom to be different for different VB structures, so as to minimize the energy of the full multistructure wave function. It is important to note that the different VB structures are not optimized separately but in the presence of each other, so that the orbital optimization not only lowers the energies of each individual VB structure but also maximizes the resonance energy resulting from their mixing. As such, the BOVB wave function is a post-VBSCF method that incorporates dynamic correlation.

The difference between the BOVB and GVB or SC philosophies is best appreciated by comparing their respective descriptions of the two-electron bond. The classical representation for the GVB or SC wave function, obtained after expansion of the CF expression into AO determinants as in Eq. [7], takes the form of a linear combination of covalent and ionic classical VB structures (**46–48**), for which both coefficients and orbitals are optimized. However, there is the penalizing restriction that the same common set of AOs is used for all three structures, as shown in Scheme 22 for the F_2 molecule.
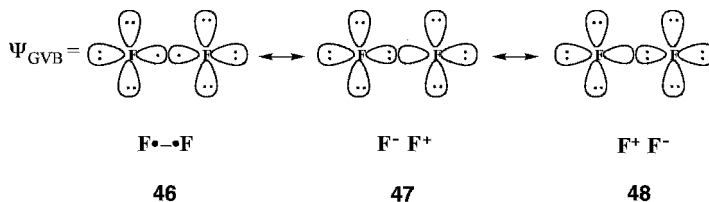
Scheme 22

On the other hand, the BOVB method assumes the three-structure clas-sical form of the wave function right at the outset. Like the GVB or SC meth-ods, it optimizes the coefficients and the orbitals simultaneously, but with the important feature that each VB structure (**49–51**) may now have its specific set of orbitals, different from one structure to the other, as pictorially represented in Scheme 23, for the same F—F bond.
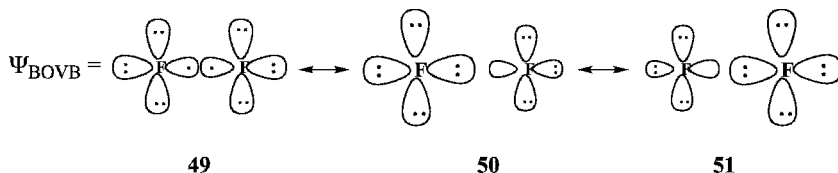
Scheme 23

As a consequence of the BOVB procedure, the active orbitals (those involved in the bond) can use this extra degree of freedom to adapt themselves to their instantaneous occupancies. The spectator orbitals (not involved in the bond) can fit the instantaneous charges of the atoms to which they belong. Thus, all the orbitals follow the charge fluctuation that is inherent to any bond by undergoing instantaneous changes in size and shape, hence the name "breathing orbitals". The same philosophy underlies the description of odd-electron bonds, in terms of two VB structures.

Since the BOVB wave function takes a classical VB form, it is not prac-tical for the VB description of large electronic systems, because a large number of VB structures would have to be generated in such a case. As such, the usual way of applying BOVB is to describe with it only those orbitals and electrons that undergo significant changes in the reaction, like bond breaking or forma-tion, while the remaining orbitals and electrons are described as doubly occu-pied MOs. Thus, even though the spectator electrons reside in doubly occupied MOs, these orbitals too are allowed to optimize freely, but are other-wise left uncorrelated.

The BOVB method has several levels of accuracy. At the most basic level, referred to as L-BOVB, all orbitals are strictly localized on their respective fragments. One way of improving the energetics by allowing more degrees of freedom is to let the inactive orbitals get delocalized. This option, which does not alter the interpretability of the wave function, accounts better for the nonbonding interactions between the fragments and is referred to as D-BOVB. Another improvement can be achieved by incorporating radial electron correlation in the active orbitals of the ionic structures, by allowing the doubly occupied orbitals to split into two singly occupied orbitals that are spin-paired. This option carries the label "S" (for split), leading to the SL-BOVB, and SD-BOVB levels of calculation, the latter being the most accurate.

The BOVB method has been successfully tested for its ability to reproduce dissociation energies and/or dissociation energy curves close to full CI results or other highly accurate calculations performed with the same basis sets. A variety of two-electron and odd-electron bonds, including difficult test cases as F_2, FH, or F_2^-,[133–135] and the H_3M-Cl series (M = C, Si, Ge, Sn, Pb)[137,155,266] were investigated. Owing to its use of strictly localized active orbitals, the method is suitable for calculating clearly defined diabatic states that are supposed to retain the physical features of a given asymptotic state at any point of a reaction coordinate without collapsing to the ground state by virtue of uncontrolled orbital optimization.

It is interesting to interpret the improvement of BOVB with respect to a CASSCF, GVB, or SC calculation of a two-electron bond. These four methods account for all the nondynamic correlation associated with the formation of the bond from separate fragments, but differ in their dynamic correlation content. In a medium-sized basis set, say 6-31+G(d), CASSCF, GVB, or SC account for less than one-half of the bonding energy of F_2, 14–16 kcal/mol.[133] On the other hand, an SD-BOVB calculation yields a bonding energy of 36.2 kcal/mol,[a] versus an experimental value of 38.2 kcal/mol.[137] Where does this difference come from? It appears that the BOVB method brings just what is missing in the CASSCF calculation, that is, dynamical correlation, not all of it but just *that part that is associated to the bond that is being broken or formed*. In other words, the BOVB method takes care of the differential dynamical correlation. In this respect it is approximately equivalent to the VBCI method.

The importance and physical nature of dynamic correlation is even better appreciated in the case of three-electron bonds, a type of bond in which the electron correlation is entirely dynamic, since there is no left–right correlation

---

[a]Note that this bonding energy is overestimated with respect to a full CI calculation for the same basis set, which is estimated as close to 30 kcal/mol. The SD-BOVB systematically overestimates bonding energies relative to full CI and yields values that are intermediate between full CI and experiment, a "fortunate" systematic error that compensates for basis set insufficiency.

associated with odd-electron bonds. As has been noted above, the Hartree–Fock and simple VB functions for three-electron bonds (hence GVB, SC, or VBSCF) are nearly equivalent and yield similar bonding energies. If we take the F_2^- radical anion as an example, it turns out that the Hartree–Fock bonding energy is exceedingly poor, only 4 kcal/mol at the spin-unrestricted Hartree–Fock level (UHF), and even worse at the restricted Hartree–Fock (RHF) level, while the experimental bonding energy is 30.3 kcal/mol. By contrast, the SD-BOVB calculation, which involves only two VB structures (**52**, **53**) with breathing orbitals as in Scheme 24 below, yields an excellent bonding energy of 28.0 kcal/mol.

52 **53**
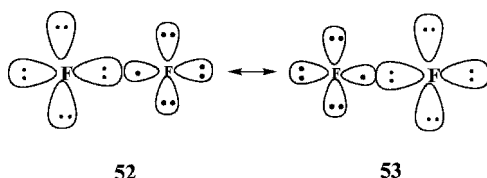
Scheme 24

Looking at **52** and **53** in Scheme 24 allows a clear understanding of the nature of the dynamic correlation effect. Indeed, with respect to a Hartree–Fock or VBSCF calculation, the BOVB wave function brings the additional effect that the orbitals adapt themselves to the net charge of each fragment, for example, being more diffuse when the fragment is negatively charged and less so when the fragment is neutral. This effect, which we have called the "breathing orbital effect" but which is called "size effect" by others, corresponds to the differential dynamic correlation associated with the bond, and is just *the instantaneous adaptation of the orbitals to the dynamic charge fluctuations that transpire in the bond*. This interpretation of dynamic correlation, which is particularly apparent in the three-electron bond, carries over to the two-electron bond (e.g., F_2 above) that also undergoes some charge fluctuation through its ionic components.

The BOVB method has been used for many applications relevant to bonding in organic, inorganic, and organometallic chemistry.[133,134,155,167,168,266–274] Recently, the L-BOVB method was applied to compute the barriers to hydrogen abstraction in the series X• + H—X' → X—H + •X', and gave results comparable with CCSD at the same basis set.[167]

In summary, the VBSCF,[117–120] VBCI,[138] and BOVB[133–137] methods are ideal tools for studying bonding and for generating VBSCDs for chemical reactions. However, while VBSCF will provide a qualitatively correct picture, both VBCI and BOVB methods will give quantitatively good results in addition to a lucid chemical picture.

PROSPECTIVE

The many examples included in this chapter clearly demonstrate that far from being dead, VB theory is a vibrant field of research that produces many new methods and key paradigms of chemical bonding and reactivity. It is hoped that this chapter will serve its intended purpose of teaching some elements of this theory.

This review of VB theory and its applications is by no means exhaustive. The two most important omissions are the applications of this theory to the study of chemical dynamics and to enzymatic chemistry. Ever since the pioneering paper of London on the potential energy surface of H_3,[275] and the paper of Eyring and Polanyi[276] on elementary reactions, most of the surfaces used in the studies of chemical dynamics are based on VB formalisms and thinking, for example, LEPS surfaces, and those generated by application of DIM theory or the BEBO methods.[277,278] This kind of thinking was recently extended to the treatment of large molecules in the molecular mechanics-based VB method, called MCMM.[140,173] The empirical VB (EVB) method, initiated by Warshel and Weiss,[99] has gradually evolved into a general QM(EVB)/MM method[100,101] for the study of enzymatic reactions within their native protein environment. Owing to its lucid insight into chemical reactivity the prospects of this VB-based method are far reaching, and an example is a recent analysis of the role of near-attack-configuration (NAC) in enzymatic catalysis.[279] Elsewhere, in the field of enzymatic reactions, the use of VB ideas led to new paradigms, such as the notion of a chameleon oxidant, for the active species of the enzyme cytochrome P450.[280] Thus, in many respects, VB theory is coming of age, with the development of faster, and more accurate ab initio VB methods,[142] and with generation of new post-Pauling concepts. As these activities flourish further, so will the usage of VB theory spread among practicing chemists.

APPENDIX

A.1 Expansion of MO Determinants in Terms of AO Determinants

Let D_{MO} be a single determinant involving molecular spin orbitals φ_i and φ_j, which can be of α or β spins:

$$D_{\mathrm{MO}} = |\cdots \varphi_i \cdots \varphi_J \cdots| \qquad [\mathrm{A1}]$$

$$\varphi_i = \sum_\mu C_{\mu i}\chi_\mu \qquad [\mathrm{A2}]$$

$$\varphi_j = \sum_\nu C_{\nu j}\,\chi_\nu \qquad [\mathrm{A3}]$$

Replacing φ_i and φ_j in Eq. [A1] by their expansions in terms of AOs, D_{MO} can be expanded into a linear combination of AO-based determinants. The procedure is carried out in the same manner by which one would expand a simple product of orbitals, as long as one remembers that the ordering of the orbitals is important in the AO determinants, and that two determinants that differ by permutation of two of their orbitals are equivalent but of opposite sign. Thus, many AO determinants in Eq. [A4] can be regrouped after permuting their orbitals and changing their signs.

$$|\cdots \varphi_i \cdots \varphi_j \cdots| = \left| \left(\sum_\mu C_{\mu i} \chi_\mu \right) \cdots \left(\sum_\nu C_{\nu j} \chi_\nu \right) \right|$$
$$= \sum_\mu C_{\mu i} \cdots \sum_\nu C_{\nu j} \cdots |\cdots \chi_\mu \cdots \chi_\nu \cdots| \qquad [A4]$$

While this is a trivial matter for small determinants, larger ones require a bit of algebra and a systematic method[74] that is shown below.

Let us consider the determinant D_{MO} below as being composed of two "half-determinants", h^α_{MO} and h^β_{MO}, one regrouping the spin-orbitals of α spins and the other those of β spins.

$$D_{MO} = (h^\alpha_{MO}, h^\beta_{MO}) \qquad [A5]$$

Half-determinants have no physical meaning but are defined here as a convenient mathematical intermediary. Each of these MO-based half-determinants can be expanded into AO-based half-determinants, just as has been done for the determinants in Eq. [A4]. After orbital permutations the AO-based half-determinants that are equivalent are regrouped, and we are left with some AO-based half-determinants h^α_r, each having a unique collection of AOs

$$h^\alpha_{MO} = \sum_r C^\alpha_r h^\alpha_r \qquad [A6]$$

where the label r designates a given set of AOs.

The coefficients of each of these AO half-determinants in the expansion is given by Eq. [A7]:

$$C^\alpha_r = \sum_P (-1)^t P(\cdots \times C_{\mu i} \times \cdots \times C_{\nu j} \cdots) \qquad [A7]$$

where P is a permutation between indices μ and ν and t is the parity of the permutation. By associating two AO half-determinants h^α_r and h^β_s, one gets the full AO-based determinant (h^α_r, h^β_s) whose coefficient in the expansion of

D_{MO} is just the product of the coefficients of its two half-determinants:

$$D_{MO} = \sum_{r,s} C_r^\alpha C_s^\beta (h_r^\alpha, h_s^\beta) \qquad [A8]$$

A.2 Guidelines for VB Mixing

Derivation of matrix elements between polyelectronic VB determinants follows from the discussion in the text, and can be carried out by enumerating all the permutations of the respective diagonal terms, as in Eq. [A9]. Subsequently, one must define the reduced matrix element in Eq. [A10].[52]

$$\langle\Omega|H^{eff}|\Omega'\rangle = \left\langle \Psi_d \left| \sum h(i) \right| \sum (-1)^t P(\Psi_d') \right\rangle \qquad [A9]$$

$$\langle\Omega|H^{eff}|\Omega'\rangle_{reduced} = \langle\Omega|H^{eff}|\Omega'\rangle - 0.5(E(\Omega) + E(\Omega'))\langle\Omega|\Omega'\rangle \qquad [A10]$$

Unfortunately, the retention of overlap leads to many energy and overlap terms that need to be collected and organized, making this procedure quite tedious. A practice that we found useful and productive is to focus on the leading term of the matrix element. In this respect, we show a few qualitative guidelines that were derived in detail in the original paper[52] and discussed elsewhere.[53,84,143] Initially, one has to arrange the two VB determinants with maximum correspondence of their spin–orbitals. Then, one must find the number of spin–orbitals that are different in the two determinants, and apply the following rules.

1. The first and foremost rule is that the entire matrix element between two VB determinants is signed as the corresponding determinant overlap and has the same power in AO overlap. For example, the overlap between the two determinants of an HL bond, $|a\overline{b}|$ and $|\overline{a}b|$, is $-S_{ab}^2$, and hence the matrix element is negatively signed, $-2\beta_{ab}S_{ab}$. Since β_{ab} is proportional to S_{ab}, both the matrix element and the determinant overlap involve AO overlap to the power 2. For the one-electron bond case (Eq. [51]), the overlap between the determinants is $+S_{ab}$ and the matrix element $+\beta_{ab}$, while for the three-electron bond situation (Eq. [52]) the overlap between the determinants $|a\overline{a}b|$ and $|b\overline{b}a|$ is $-S_{ab}$ and the matrix element is likewise $-\beta_{ab}$.

2. When the VB determinants differ by the occupancy of one spin-orbital, say orbital a in one determinant is replaced by b in the other (keeping the ordering of the other orbitals unchanged), the leading term of the matrix element will be proportional to β_{ab}. Both the one- and three-electron bonds are cases that differ by a single electron occupancy and the corresponding matrix elements are indeed $\pm\beta$, with a sign as the corresponding overlap between the determinants.

3. When the VB determinants differ by the occupancy of two spin–orbitals, the leading term of the matrix element will be the sum of the corresponding $\beta_{ij}S_{ij}$ terms with the appropriate sign. An example is the matrix element $-2\beta_{ab}S_{ab}$ between the $|a\overline{b}|$ and $|\overline{a}b|$ determinants, which differ by the occupancy of two spin–orbitals, a and b.

4. The above considerations are the same whether the spin–orbitals are AOs, CF orbitals, or FOs.

A.3 Computing Mono-Determinantal VB Wave Functions with Standard Ab Initio Programs

This technique utilizes a possibility that is offered by most ab initio standard programs to compute the energy of the guess function even if it is made of nonorthogonal orbitals. The technique orthogonalizes the orbitals without changing the Slater determinant, then computes the expectation energy by use of Slater's rules. In the course of the subsequent optimization of the Hartree–Fock orbitals, this expectation value of the energy appears as the energy at iteration zero. If the guess determinant is made of localized bonding orbitals that typify a given VB structure, then the expectation energy of this wave function at iteration zero defines the energy of this VB structure. Practically, the localized bonding orbitals that are used to construct the guess determinant can be determined by any convenient means. For example, a Kekulé structure of benzene will display a set of three two-centered π-bonding MOs that can arise from the Hartree–Fock calculation of an ethylene molecule.[196,281] In a VBSCD calculation, the energy of the crossing point will be the energy of a guess function made of the orbitals of the reactants, but in the geometry of the transition state, without further orbital optimization. The zero-iteration technique has also been used to estimate the energy of spin-alternated determinants (quasi-classical state).[175,198]

ACKNOWLEDGMENTS

REFERENCES

1. *Valence Bond Theory*, D. L. Cooper, Ed., Elsevier, Amsterdam, The Netherlands, 2002.

2. J. W. Servos, *Physical Chemistry from Ostwald to Pauling*, Princeton University Press, Princeton, New Jersey, 1990.

3. S. G. Brush, *Stud. Hist. Phil. Sci.*, **30**, 21 (1999). Dynamics of Theory Change in Chemistry: Part 1. The Benzene Problem 1865–1945.

4. S. G. Brush, *Stud. Hist. Phil. Sci.* **30**, 263 (1999). Dynamics of Theory Change in Chemistry: Part 2. Benzene and Molecular Orbitals, 1945–1980.

5. G. N. Lewis, *J. Am. Chem. Soc.*, **38**, 762 (1916). The Atom and the Molecule.

6. I. Langmuir, *J. Am. Chem. Soc.*, **41**, 868 (1919). The Arrangement of Electrons in Atoms and Molecules.

7. W. Heitler and F. London, *Z. Phys.*, **44**, 455 (1927). Wechselwirkung Neutraler Atome un Homöopolare Bindung nach der Quantenmechanik.

8. For an English translation, see H. Hettema, *Quantum Chemistry Classic Scientific Paper*, World Scientific, Singapore, 2000.

9. W. Heisenberg, *Z. Phys.*, **411**, 38, (1926). Mehrkorperproblem und Resonanz in der Quantenmechanik,

10. F. London *Z. Phys.*, **455**, 46, (1928). On The Quantum Theory of Homo-polar Valence Numbers.

11. L. Pauling, *Proc. Natl. Acad. Sci. U.S.A.*, **14**, 359 (1928). The Shared-Electron Chemical Bond.

12. J. C. Slater, *Phys. Rev.*, **34**, 1293 (1929). The Theory of Complex Spectra.

13. J. C. Slater, *Phys. Rev.*, **38**, 1109 (1931). Molecular Energy Levels and Valence Bonds.

14. G. Rumer, *Gottinger Nachr.*, **27**, 337 (1932). Zum Theorie der Spinvalenz.

15. G. A. Gallup, in *Valence Bond Theory*, D. L. Cooper, Ed., Elsevier, Amsterdam, The Netherlands, 2002, pp. 1–40. A Short History of VB Theory.

16. J. C. Slater, *Phys. Rev.*, **37**, 481 (1931). Directed Valence in Polyatomic Molecules.

17. J. C. Slater, *Phys. Rev.*, **41**, 255 (1931). Note on Molecular Structure.

18. L. Pauling, *J. Am. Chem. Soc.*, **53**, 1367 (1931). The Nature of the Chemical Bond. Application of Results Obtained from the Quantum Mechanics and from a Theory of Magnetic Susceptiblity to the Structure of Molecules.

19. L. Pauling, *J. Am. Chem. Soc.*, **53**, 3225 (1931). The Nature of the Chemical Bond. II. The One-Electron Bond and the Three-Electron Bond.

20. L. Pauling, *The Nature of the Chemical Bond*, Cornell University Press, Ithaca, New York, 1939 (3rd ed., 1960).

21. R. S. Mulliken, *Phys. Rev.*, **32**, 186 (1928). The Assignment of Quantum Numbers for Electrons in Molecules. I.

22. R. S. Mulliken, *Phys. Rev.*, **32**, 761 (1928). The Assignment of Quantum Numbers for Electrons in Molecules. II. Correlation of Atomic and Molecular Electron States.

23. R. S. Mulliken, *Phys. Rev.*, **33**, 730 (1929). The Assignment of Quantum Numbers for Electrons in Molecules. III. Diatomic Hydrides.

24. R. S. Mulliken, *Phys. Rev.*, **41**, 49 (1932). Electronic Structures of Polyatomic Molecules and Valence. II. General Considerations.

25. F. Hund, *Z. Phys.*, **73**, 1 (1931). Zur Frage der Chemischen Bindung.

26. F. Hund, *Z. Phys.*, **51**, 759 (1928). Zur Deutung der Molekelspektren. IV.

27. J. E. Lennard-Jones, *Trans. Faraday Soc.*, **25**, 668 (1929). The Electronic Structure of some Diatomic Molecules.

28. J. A. Berson, *Chemical Creativity. Ideas from the Work of Woodward, Hückel, Meerwein, and Others*, Wiley-VCH, NewYork, 1999.

29. E. Hückel, *Z. Phys.*, **60**, 423 (1930). Zur Quantentheorie der Doppelbindung.

30. E. Hückel, *Z. Phys.*, **70**, 204 (1931). Quantentheoretische Beitrag zum Benzolproblem. I. Dies Elektronenkonfiguration des Benzols und verwandter Verbindungen.

31. E. Hückel, *Z. Phys.*, **76**, 628 (1932). Quantentheoretische Beitrag zum Problem der Aromatischen Ungesättigten Verbindungen. III.

32. L. Pauling and G. W. Wheland, *J. Chem. Phys.*, **1**, 362 (1933). The Nature of the Chemical Bond. V. The Quantum-Mechanical Calculation of the Resonance Energy of Benzene and Naphthalene and the Hydrocarbon Free Radicals.

33. G. W. Wheland, *Resonance in Organic Chemistry*, Wiley, New York, 1955, pp. 4, 39, 148.

34. J. H. van Vleck and A. Sherman, *Rev. Mod. Phys.*, **7**, 167 (1935). The Quantum Theory of Valence.

35. P. Laszlo and R. Hoffmann, *Angew. Chem. Int. Ed.*, **39**, 123 (2000). Ferrocene: Ironclad History or Roshomon Tale?

36. G. W. Wheland, *Proc. R. Soc. London*, **A159**, 397 (1938). The Electronic Structure of Some Polyenes and Aromatic Molecules. V—A Comparison of Molecular Orbital and Valence Bond Methods.

37. G. W. Wheland, *J. Chem. Phys.*, **2**, 474 (1934). The Quantum Mechanics of Unsaturated and Aromatic Molecules: A Comparison of Two Methods of Treatment.

38. D. P. Craig, *J. Chem. Soc.*, 3175 (1951). Cyclobutadiene and Some Other Pseudoaromatic Compounds.

39. D. P. Craig, *Proc. R. Soc. London*, **A200**, 498 (1950). Electronic Levels in Simple Conjugated Systems. I. Configuration Interaction in Cyclobutadiene.

40. C. A. Coulson, *Proc. R. Soc. London*, **A207**, 63 (1951). Critical Survey of the Method of Ionic-Homopolar Resonance.

41. M. J. S. Dewar, *Electronic Theory of Organic Chemistry*, Clarendon Press, Oxford, 1949, pp. 15–17.

42. C. A. Coulson, *Valence*, Oxford University Press, London, 1952.

43. J. R. Platt, *Science*, **154**, 745 (1966). Nobel Laureate in Chemistry: Robert S. Mulliken.

44. K. Fukui, T. Yonezawa, and H. Shingu, *J. Chem. Phys.*, **20**, 722 (1952). A Molecular Orbital Theory of Reactivity in Aromatic Hydrocarbons.

45. R. B. Woodward and R. Hoffmann, *The Conservation of Orbital Symmetry*, Verlag Chemie, Weinheim, 1971.

46. M. G. Evans, *Trans. Faraday Soc.*, **35**, 824 (1939). The Activation Energies in Reactions Involving Conjugated Systems.

47. E. Heilbronner and H. Bock, *The HMO Model and its Applications*, Wiley, New York, 1976.

48. E. Honegger and E. Heilbronner, in *Theoretical Models of Chemical Bonding*, Z. B. Maksic, Ed., Springer-Verlag, Berlin- Heidelberg, 1991, Vol. 3, pp. 100–151. The Equivalent Orbital Model and the Interpretation of PE Spectra.

49. S. Wolfe and Z. Shi, *Isr. J. Chem.*, **40**, 343 (2000). The S–C–O (O–C–S) Edward-Lemieux Effect is Controlled by *p*-Orbital on Oxygen. Evidence from Electron Momentum Spectroscopy, Photoelectron Spectroscopy, X-Ray Crystallography, and Density Functional Theory.

50. P. Atkins and L. Jones, *Chemical Principles. The Quest for Insight,* W. H. Freeman and Co., New York, 1999, pp. xxiii and 121–122.

51. L. Jones and P. Atkins, *Chemistry Molecules, Matter and Change*, W. H. Freeman and Co., New York, 2000, pp. 400–401.

52. S. Shaik, in *New Theoretical Concepts for Understanding Organic Reactions*, J. Bertran and I. G. Csizmadia, Eds., NATO ASI Series, **C267**, Kluwer Academic Publ., 1989, pp. 165–217. A Qualitative Valence Bond Model for Organic Reactions.

53. S. Shaik and P. C. Hiberty, *Adv. Quant. Chem.*, **26**, 100 (1995). Valence Bond Mixing and Curve Crossing Diagrams in Chemical Reactivity and Bonding.

54. P. C. Hiberty, *J. Mol. Struct. (THEOCHEM)*, **398**, 35 (1997). Thinking and Computing Valence Bond in Organic Chemistry.

55. A. Shurki, F. Dijkstra, P. C. Hiberty, and S. Shaik, *J. Phys. Org. Chem.*, **16**, 731 (2003). Aromaticity and Antiaromaticity: What Role Do Ionic Configurations Play in Delocalization and Induction of Magnetic Properties?

56. W. Heitler and G. Pöschl, *Nature (London)*, **133**, 833 (1934). Ground State of C_2 and O_2 and the Theory of Valency.

57. S. Shaik, A. Shurki, D. Danovich, and P. C. Hiberty, *Chem. Rev.*, **101**, 1501 (2001). A Different Story of π-Delocalization—The Distortivity of the π-Electrons and Its Chemical Manifestations.

58. A. F. Voter and W. A. Goddard, III, *J. Am. Chem. Soc.*, **108**, 2830 (1986). The Generalized Resonating Valence Bond Description of Cyclobutadiene.

59. J. H. van Vleck, *J. Chem. Phys.*, **3**, 803 (1935). The Group Relation Between the Mulliken and Slater–Pauling Theories.

60. H. Zuilhof, J. P. Dinnocenzo, A. C. Reddy, and S. Shaik, *J. Phys. Chem.*, **100**, 15774 (1996). A Comparative Study of Ethane and Propane Cation Radicals by B3LYP Density Functional and High-Level Ab Initio Methods.

61. S. Shaik and P. C. Hiberty, *Helv. Chem. Acta*, **86**, 1063 (2003). Myth and Reality in the Attitude Toward Valence-Bond (VB) Theory: Are Its 'Failures' Real?"

62. D. J. Klein, in *Valence Bond Theory*, D. L. Cooper, Ed., Elsevier, Amsterdam, The Netherlands, 2002, pp. 447–502. Resonating Valence Bond Theories for Carbon π-Networks and Classical/Quantum Connections.

63. T. G. Schmalz, in *Valence Bond Theory*, D. L. Cooper, Ed., Elsevier, Amsterdam, The Netherlands, 2002, pp. 535–564. A Valence Bond View of Fullerenes.

64. J. P. Malrieu, in *Theoretical Models of Chemical Bonding*, Z. B. Maksic, Ed., Springer-Verlag, Berlin-Heidelberg, 1990, Vol. 1, pp. 108–136. The Magnetic Description of Conjugated Hydrocarbons.

65. J. P. Malrieu and D. Maynau, *J. Am. Chem. Soc.*, **104**, 3021 (1984). A Valence Bond Effective Hamiltonian for Neutral States of π-Systems. 1. Methods.

66. Y. Jiang and S. Li, in *Valence Bond Theory*, D. L. Cooper, Ed., Elsevier, The Netherlands, Amsterdam, 2002, 565–602. Valence Bond Calculations and Theoretical Applications to Medium-Sized Conjugated Hydrocarbons.

67. F. A. Matsen, *Acc. Chem. Res.*, **11**, 387 (1978). Correlation of Molecular Orbital and Valence Bond States in π Systems.

68. M. A. Fox and F. A. Matsen, *J. Chem. Educ.*, **62**, 477 (1985). Electronic Structure in π-Systems. Part II. The Unification of Hückel and Valence Bond Theories.

69. M. A. Fox and F. A. Matsen, *J. Chem. Educ.*, **62**, 551 (1985). Electronic Structure in π-Systems. Part III. Application in Spectroscopy and Chemical Reactivity.

70. S. Ramasesha and Z. G. Soos, in *Valence Bond Theory*, D. L. Cooper, Ed., Elsevier, Amsterdam, The Netherlands, 2002, pp. 635–697. Valence Bond Theory of Quantum Cell Models.

71. W. Wu, S. J. Zhong, and S. Shaik, *Chem. Phys. Lett.*, **292**, 7 (1998). VBDFT(s): A Hückel-Type Semi-empirical Valence Bond Method Scaled to Density Functional Energies. Applications to Linear Polyene.

72. W. Wu, D. Danovich, A. Shurki, and S. Shaik, *J. Phys. Chem., A* **104**, 8744 (2000). Using Valence Bond Theory to Understand Electronic Excited States. Applications to the Hidden Excited State (2^1A_g) of Polyenes.

73. W. Wu, Y. Luo, L. Song, and S. Shaik, *Phys. Chem. Chem. Phys.*, **3**, 5459 (2001). VBDFT(s): A Semiempirical Valence Bond Method: Application to Linear Polyenes Containing Oxygen and Nitrogen Heteroatoms.

74. P. C. Hiberty and C. Leforestier, *J. Am. Chem. Soc.*, **100**, 2012 (1978). Expansion of Molecular Orbital Wave Functions into Valence Bond Wave Functions. A Simplified Procedure.

75. T. Thorsteinsson, D. L. Cooper, J. Gerratt, and M. Raimondi, *Molecular Engineering*, **7**, 67 (1997). A New Approach to Valence Bond Calculations CASVB.

76. Thorsteinsson, D. L. Cooper, J. Gerratt, P. Kardakov, and M. Raimondi, *Theor. Chim. Acta (Berl.)*, **93**, 343 (1996). Modern Valence Bond Representation of CASSCF Wave Functions.

77. H. Nakano, K. Sorakubo, K. Nakayama, and H. Hirao, in *Valence Bond Theory*, D. L. Cooper, Ed. Elsevier, The Netherlands, Amsterdam, 2002, pp. 55–77. Complete Active Space Valence Bond (CASVB) Method and its Application in Chemical Reactions.

78. K. Hirao, H. Nakano, and K. Nakayama, *J. Chem. Phys.*, **107**, 9966 (1997). A Complete Active Space Valence Bond Method with Nonorthogonal Orbitals.

79. N. D. Epiotis, J. R. Larson, and H. L. Eaton, *Lecture Notes Chem.*, **29**, 1 (1982). Unified Valence Bond Theory of Electronic Structure.

80. N. D. Epiotis, *Deciphering the Chemical Bond. Bonding Across the Periodic Table*, VCH, New York, 1996, pp. 1-933.

81. S. S. Shaik, *J. Am. Chem. Soc.*, **103**, 3692 (1981). What Happens to Molecules As They React? A Valence Bond Approach to Reactivity.

82. A. Pross and S. S. Shaik, *Acc. Chem. Res.*, **16**, 363 (1983). A Qualitative Valence Bond Approach to Chemical Reactivity.

83. A. Pross, *Theoretical and Physical Principles of Organic Reactivity*, J. Wiley, New York, 1995, pp. 83–124; 235–290.

84. S. Shaik and P. C. Hiberty, in *Theoretical Models of Chemical Bonding*, Z.B. Maksic, Ed., Springer-Verlag, Berlin-Heidelberg, 1991, Vol. 4, pp. 269–322. Curve Crossing Diagrams as General Models for Chemical Structure and Reactivity.

85. S. Shaik and A. Shurki, *Angew. Chem. Int. Ed. Engl.*, **38**, 586 (1999). Valence Bond Diagrams and Chemical Reactivity.

86. J. W. Linnett, *The Electronic Structure of Molecules. A New Approach,* Methuen & Co Ltd, London, 1964, pp. 1–162.

87. R. D. Harcourt, *Lecture Notes Chem.*, **30**, 1 (1982). Qualitative Valence-Bond Descriptions of Electron-Rich Molecules: Pauling "3-Electron Bonds" and "Increased-Valence" Theory.

88. R. D. Harcourt, in *Valence Bond Theory*, D. L. Cooper, Ed., Elsevier, Amsterdam, The Netherlands, 2002, pp. 349–378. Valence Bond Structures for Some Molecules with Four Singly-Occupied Active-Space Orbitals: Electronic Structures, Reaction Mechanisms, Metallic Orbitals.

89. A. Th. Van der Lugt and L. J. Oosterhoff, *J. Am. Chem. Soc.*, **91**, 6042 (1969). Symmetry Control and Photoinduced Reactions.

90. J. J. C. Mulder and L. J. Oosterhoff, *Chem. Commun.*, 305 (1970). Permutation Symmetry Control in Concerted Reactions.

91. J. Michl, *Topics Curr. Chem.*, **46**, 1 (1974). Physical Basis of Qualitative MO Arguments in Organic Photochemistry.

92. W.Gerhartz, R. D. Poshusta, and J. Michl, *J. Am. Chem. Soc.*, **99**, 4263 (1977). Potential Energy Hypersurfaces for H$_4$. 2. "Triply Right" (C_{2v}) Tetrahedral Geometries. A Possible Relation to Photochemical "Cross Bonding" Processes.

93. F. Bernardi, M. Olivucci, and M. Robb, *Isr. J. Chem.*, **33**, 265 (1993). Modeling Photochemical Reactivity of Organic Systems. A New Challenge to Quantum Computational Chemistry.

94. M. Olivucci, I. N. Ragazos, F. Bernardi, and M. A. Robb, *J. Am. Chem. Soc.*, **115**, 3710 (1993). A Conical Intersection Mechanism for the Photochemistry of Butadiene. A MC-SCF Study.

95. M. Olivucci, F. Bernardi, P. Celani, I. Ragazos, and M. A. Robb, *J. Am. Chem. Soc.*, **116**, 1077 (1994). Excited-State Cis-Trans Isomerization of *cis*-Hexatriene. A CAS–SCF Computational Study.

96. M. A. Robb, M. Garavelli, M. Olivucci, and F. Bernardi, in *Reviews in Computational Chemistry*, K. B. Lipkowitz and D. B. Boyd, Eds., Vol. 15, pp. 87–146, (2000). A Computational Strategy for Organic Photochemistry.

97. S. Shaik and A. C. Reddy, *J. Chem. Soc. Faraday Trans.*, **90**, 1631 (1994). Transition States, Avoided Crossing States and Valence Bond Mixing: Fundamental Reactivity Paradigms.

98. S. Zilberg and Y. Haas, *Chem. Eur. J.*, **5**, 1755 (1999). Molecular Photochemistry: A General Method for Localizing Conical Intersections Using the Phase-Change Rule.

99. A. Warshel and R. M. Weiss, *J. Am. Chem. Soc.*, **102**, 6218 (1980). Empirical Valence Bond Approach for Comparing Reactions in Solutions and in Enzymes.

100. A. Warshel and S. T. Russell, *Quart. Rev. Biophys.*, **17**, 282 (1984). Calculations of Electrostatic Interactions in Biological Systems and in Solutions.

101. A. Warshel, *J. Phys. Chem.*, **83**, 1640 (1979). Calculations of Chemical Processes in Solutions.

102. H. J. Kim and J. T. Hynes, *J. Am. Chem. Soc.*, **114**, 10508 (1992). A Theoretical Model for S_N1 Ionic Dissociation in Solution. 1. Activation Free Energies and Transition-State Structure.

103. J. R. Mathias, R. Bianco, and J. T. Hynes, *J. Mol. Liq.*, **61**, 81 (1994). On the Activation Free Energy of the $Cl^- + CH_3Cl$ S_N2 Reaction in Solution.

104. J. I. Timoneda and J. T. Hynes, *J. Phys. Chem.*, **95**, 10431 (1991). Nonequilibrium Free Energy Surfaces for Hydrogen-bonded Proton Transfer Compexes in Solution.

105. S. Shaik, *J. Am. Chem. Soc.*, **106**, 1227 (1984). Solvent Effect on Reaction Barriers. The S_N2 Reactions. 1. Application to the Identity Exchange.

106. S. Shaik, *J. Org. Chem.*, **52**, 1563 (1987). Nucleophilic Reactivity and Vertical Ionization Potentials in Cation–Anion Recombinations.

107. W. A. Goddard, III, T. H. Dunning, Jr., W. J. Hunt, and P. J. Hay, *Acc. Chem. Res.*, **6**, 368 (1973). Generalized Valence Bond Description of Bonding in Low-Lying States of Molecules.

108. W. A. Goddard, III, *Phys. Rev.*, **157**, 81 (1967). Improved Quantum Theory of Many-Electron Systems. II. The Basic Method.

109. W. A. Goddard, III, and L. B. Harding, *Annu. Rev. Phys. Chem.*, **29**, 363 (1978). The Description of Chemical Bonding from Ab-Initio Calculations.

110. W. A. Goddard, III, *Int. J. Quant. Chem.*, **IIIS**, 593 (1970). The Symmetric Group and the Spin Generalized SCF Method.

111. C. A. Coulson and I. Fischer, *Philos. Mag.*, **40**, 386 (1949). Notes on the Molecular Orbital Treatment of the Hydrogen Molecule.

112. D. L. Cooper, J. Gerratt, and M. Raimondi, *Chem. Rev.*, **91**, 929 (1981). Application of Spin-Coupled Valence Bond Theory.

113. D. L. Cooper, J. P. Gerratt, and M. Raimondi, *Adv. Chem. Phys.*, **69**, 319 (1987). Modern Valence Bond Theory.

114. M. Sironi, M. Raimondi, R. Martinazzo, and F. A. Gianturco, in *Valence Bond Theory*, D. L. Cooper, Ed., Elsevier, Amsterdam, The Netherlands, 2002, pp. 261–277. Recent Developments of the SCVB Method.

115. G. G. Balint-Kurti and M. Karplus, *J. Chem. Phys.*, **50**, 478 (1969). Multistructure Valence-Bond and Atoms-in-Molecules Calculations for LiF, F_2, and F_2^-.

116. J. H. van Lenthe and G. G. Balint-Kurti, *Chem. Phys. Lett.*, **76**, 138 (1980). The Valence-Bond SCF (VB SCF) Method. Synopsis of Theory and Test Calculations of the OH Potential Energy Curve.

117. J. H. van Lenthe and G. G. Balint-Kurti, *J. Chem. Phys.*, **78**, 5699 (1983). The Valence-Bond Self-Consistent Field Method (VB–SCF): Theory and Test Calculations.

118. J. Verbeek and J. H. van Lenthe, *J. Mol. Struct. (THEOCHEM)*, **229**, 115 (1991). On the Evaluation of Nonorthogonal Matrix Elements.

119. J. Verbeek and J. H. van Lenthe, *Int. J. Quant. Chem.*, XL, 201(1991). The Generalized Slater–Condon Rules.

120. J. Verbeek, J. H. Langenberg, C. P. Byrman, F. Dijkstra, and J. H. van Lenthe, *TURTLE: An Ab Initio VB/VBSCF Program (1998–2000)*.

121. J. H. van Lenthe, F. Dijkstra, and W. A. Havenith, in *Valence Bond Theory*, D. L. Cooper, Ed., Elsevier, Amsterdam, The Netherlands, 2002, pp. 79–116. TURTLE—A Gradient VBSCF Program Theory and Studies of Aromaticity.

122. F. A. Matsen, *Adv. Quant. Chem.*, **1**, 60 (1964). Spin-Free Quantum Chemistry.

123. F. A. Matsen, *J. Phys. Chem.*, **68**, 3282 (1964). Spin-Free Quantum Chemistry. II. Three-Electron Systems.

124. R. McWeeny, *Int. J. Quant. Chem.*, **XXXIV**, 23 (1988). A Spin Free Form of Valence Bond Theory.

125. Q. Zhang, and L. Xiangzhu, *J. Mol. Struct. (THEOCHEM),* **198**, 413 (1989). Bonded Tableau Method for Many Electron Systems.

126. X. Li and Q. Zhang, *Int. J. Quant. Chem.*, **XXXVI**, 599 (1989). Bonded Tableau Unitary Group Approach to the Many-Electron Correlation Problem.

127. W. Wu, Y. Mo, Z. Cao, and Q. Zhang, in *Valence Bond Theory*, D. L. Cooper, Ed., Elsevier, Amsterdam, The Netherlands, 2002, pp. 143–186. A Spin Free Approach for Valence Bond Theory and Its Application.

128. W. Wu, L. Song, Y. Mo, and Q. Zhang, *XIAMEN-99– An Ab Initio Spin-free Valence Bond Program*, Xiamen University, Xiamen, China, 1999.

129. J. Li and R. McWeeny, *VB2000: An Ab Initio Valence Bond Program Based on Product Function Method and the Algebrant Algorithm. 2000.*

130. G. A. Gallup, R. L. Vance, J. R. Collins, and J. M. Norbeck, *Adv. Quant. Chem.*, **16**, 229 (1982). Practical Valence Bond Calculations.

131. G. A. Gallup, The CRUNCH Suite of Atomic and Molecular Structure Programs, 2001. ggallup@phy-ggallup.unl.edu.

132. P. C. Hiberty, J. P. Flament, and E. Noizet, *Chem. Phys. Lett.*, **189**, 259 (1992). Compact and Accurate Valence Bond Functions with Different Orbitals for Different Configurations: Application to the Two-Configuration Description of F_2.

133. P. C. Hiberty, S. Humbel, C. P. Byrman, and J. H. van Lenthe, *J. Chem. Phys.*, **101**, 5969 (1994). Compact Valence Bond Functions with Breathing Orbitals: Application to the Bond Dissociation Energies of F_2 and FH.

134. P. C. Hiberty, S. Humbel, and P. Archirel, *J. Phys. Chem.*, **98**, 11697 (1994). Nature of the Differential Electron Correlation in Three-Electron Bond Dissociation. Efficiency of a Simple Two-Configuration Valence Bond Method with Breathing Orbitals.

135. P. C. Hiberty, in *Modern Electronic Structure Theory and Applications in Organic Chemistry*, E. R. Davidson, Ed., World Scientific, River Edge, NJ, 1997, pp. 289–367. The Breathing Orbital Valence Bond Method.

136. P. C. Hiberty and S. Shaik, in *Valence Bond Theory*, D. L. Cooper, Ed., Elsevier, Amsterdam, The Netherlands, 2002, pp. 187–226. Breathing-Orbital Valence Bond—A Valence Bond Method Incorporating Static and Dynamic Electron Correlation Effects.

137. P. C. Hiberty and S. Shaik, *Theor. Chem. Acc.*, **108**, 255 (2002). BOVB—A Modern Valence Bond Method That Includes Dynamic Correlation.

138. W. Wu, L. Song, Z. Cao, Q. Zhang, and S. Shaik, *J. Phys. Chem. A*, **106**, 2721 (2002). Valence Bond Configuration Interaction. A Practical Valence Bond Method Incorporating Dynamic Correlation.

139. J. J. W. McDouall, in *Valence Bond Theory*, D. L. Cooper, Ed., Elsevier, Amsterdam, The Netherlands, 2002, pp. 227–260. The Biorthogonal Valence Bond Method.

140. T. Albu, J. C. Corchado, and D. G. Truhlar, *J. Phys. Chem. A*, **105**, 8465 (2001). Molecular Mechanics for Chemical Reactions: A Standard Strategy for Using Multiconfiguration Molecular Mechanics for Variational Transition State Theory with Optimized Multidimensional Tunneling.

141. T. K. Firman and C. R. Landis, *J. Am. Chem. Soc.*, **123**, 1178 (2001). Valence Bond Concepts Applied to Molecular Mechanics Description of Molecular Shapes. 4. Transition Metals with π-bonds.

142. L. Song, W. Wu, P. C. Hiberty, and S. Shaik, *Chem. Eur. J.*, **9**, 4540 (2003). An Accurate Barrier for the Hydrogen Exchange Reaction. Is This Theory Coming of Age?

143. S. S. Shaik, E. Duzy, and A. Bartuv, *J. Phys. Chem.*, **94**, 6574 (1990). The Quantum Mechanical Resonance Energy of Transition States: An Indicator of Transition State Geometry and Electronic Structure.

144. R. McWeeny, *J. Mol. Struct. (THEOCHEM)*, **229**, 29 (1991). On the Nature of the Oxygen Double Bond.

145. R. D. Harcourt, *J. Phys. Chem.*, **96**, 7616 (1992). Valence Bond Studies of Oxygen and Superoxides: A Note on One-electron and Two-electron Transfer Resonances.

146. H. Fischer and J. N. Murrell, *Theor. Chim. Acta (Berl.)*, **1**, 463 (1963). The Interpretation of the Stability of Aromatic Hydrocarbon Ions by Valence Bond Theory.

147. N. D. Epiotis, *Nouv. J. Chim.*, **8**, 421 (1984). How to "Think" at the Level of MO—CI Theory Using Hückel MO Information!

148. E. Heilbronner, *Tetrahedron Lett.*, 1923 (1964). Hückel Molecular Orbitals of Möbius-Type Conformation of Annulenes.

149. A. A. Frost and B. Musulin, *J. Chem. Phys.*, **21**, 572 (1953). A Mnemonic Device for Molecular Orbital Energies.

150. S. C. Wright, D. L. Cooper, J. Gerratt, and M. Raimondi, *J. Phys. Chem.*, **96**, 7943 (1992). Spin-coupled Description of Cyclobutadiene and 2,4-Dimethylenecyclobutane-1,3-diyls: Antipairs.

151. P. B. Karadakov, J. Gerratt, D. L. Cooper, and M. Raimondi, *J. Phys. Chem.*, **99**, 10186 (1995). The Electronic Structure of Cyclooctatetraene and the Modern Valence Bond Understanding of Antiaromaticity.

152. A. Shurki, *VB Theory as a Tool for Understanding Structure and Reactivity in Chemistry*, Ph.D. Dissertation, 1999, Hebrew University, Israel.

153. G. Sini, P. Maître, P. C. Hiberty, and S. S. Shaik. *J. Mol. Struct. (THEOCHEM)*, **229**, 163 (1991). Covalent, Ionic and Resonating Single Bonds.

154. S. Shaik, P. Maître, G. Sini, and P. C. Hiberty, *J. Am. Chem. Soc.*, **114**, 7861 (1992). The Charge-Shift Bonding Concept. Electron Pair Bonds with Very Large Resonance Energies.

155. A. Shurki, P. C. Hiberty, and S. Shaik, *J. Am. Chem. Soc.*, **121**, 822 (1999). Charge-Shift Bonding in Group IVB Halides: A Valence Bond Study of MH_3—Cl (M = C, Si, Ge, Sn, Pb) Molecules.

156. S. P. de Visser, D. Danovich, W. Wu, and S. Shaik, *J. Phys. Chem. A*, **106**, 4961 (2002). Ferromagnetic Bonds: Properties of "No-pair" Bonded High-Spin Lithium Clusters; $^{N+1}Li_N$ (N = 2–12).

157. D. Danovich and S. Shaik, *J. Am. Chem. Soc.*, **121**, 3165 (1999). No-Pair Bonding in the High-Spin $^3\Sigma_u^+$ State of Li_2. A Valence Bond Study of its Origins.

158. A. Pross, *Acc. Chem. Res.*, **18**, 212 (1985). The Single Electron Shift as a Fundamental Process in Organic Chemistry: The Relationship Between Polar and Electron-transfer Pathways.

159. G. Sini, S. S. Shaik, J.-M. Lefour, G. Ohanessian, and P. C. Hiberty, *J. Phys. Chem.*, **93**, 5661 (1989). Quantitative Valence Bond Computation of a Curve Crossing Diagram for a Model S_N2 Reaction, $H^- + CH_3H' \rightarrow HCH_3 + H'^-$.

160. G. Sini, S. Shaik, and P. C. Hiberty, *J. Chem. Soc. Perkin Trans.*, 2, 1019 (1992). Quantitative Valence Bond Computations of Curve Crossing Diagrams for a Gas Phase Reaction, $F^- + CH_3F \rightarrow FCH_3 + F^-$.

161. J. Mestres and P. C. Hiberty, *New J. Chem.*, **20**, 1213 (1996). Quantitative Valence Bond Computations of Curve Crossing Diagrams for a Hydride Transfer Model Reaction: $CH_4 + CH_3^+ \rightarrow CH_3^+ + CH_4$.

162. G. Sini, G. Ohanessian, P. C. Hiberty, and S. S. Shaik, *J. Am. Chem. Soc.*, **112**, 1407 (1990). Why is SiH_5^- a Stable Intermediate While CH_5^- is a Transition State ? A Quantitative Curve Crossing Valence Bond Study.

163. G. Sini and P. C. Hiberty, *J. Chem. Soc. Chem. Commun.*, 772 (1989). The Origin of the Different Bonding Features in SiH_5^- and CH_5^-; A Valence Bond Curve Crossing Model.

164. P. Maître, F. Volatron, P. C. Hiberty, and S. S. Shaik, *Inorg. Chem.*, **29**, 3047 (1990). Hypercoordination in SiH_5^- and SiH_5. An Electron-count Dependence.

165. P. R. Benneyworth, G. G. Balint-Kurti, M. J. Davis, and I. H. Williams, *J. Phys. Chem.*, **96**, 4346 (1992). Ab initio Valence Bond Study of the Origin of Barriers to Hydrogen Exchange Reactions: Application of the Valence Bond Self-Consistent-Field Method to the $F + HF \rightarrow FH + F$ Reaction.

166. P. Maître, P. C. Hiberty, G. Ohanessian, and S. S. Shaik, *J. Phys. Chem.*, **94**, 4089 (1990). Quantitative Computations of Curve Crossing Diagrams for Model Atom Exchange Reaction.

167. S. Shaik, W. Wu, K. Dong, L. Song, and P. C. Hiberty, *J. Phys. Chem. A*, **105**, 8226 (2001). Identity Hydrogen Abstraction Reactions, $X + H-X' \rightarrow X-H + X'(X = X' = CH_3, SiH_3, GeH_3, SnH_3, PbH_3)$: A Valence Bond Modeling.

168. L. Song, W. Wu, K. Dong, P. C. Hiberty, and S. Shaik, *J. Phys. Chem. A*, **106**, 11361 (2002). Valence Bond Modeling of Barriers in the Nonidentity Hydrogen Abstraction Reactions, $X' \bullet + H-X \rightarrow X'-H + X \bullet (X' \neq X - CH_3, SiH_3, GeH_3, SnH_3, PbH_3)$.

169. S. S. Shaik, *Prog. Phys. Org. Chem.*, **15**, 197 (1985). The Collage of S_N2 Reactivity Patterns: A State Correlation Diagram Model.

170. S. S. Shaik, H. B. Schlegel, and S. Wolfe, *Theoretical Aspects of Physical Organic Chemistry*, Wiley-Interscience, New York, 1992.

171. Y. Mo and S. D. Peyerimhoff, *J. Chem. Phys.*, **109**, 1687 (1998). Theoretical Analysis of Electronic Delocalization.

172. F. Jensen and P.-O. Norrby, *Theor. Chim. Acc.* **109**, 1 (2003). Transition States from Empirical Force Fields.

173. Y. Kim, J. C. Corchado, J. Villa, J. Xing, and D. G. Truhlar, *J. Chem. Phys.*, **112**, 2718 (2000). Multiconfiguration Molecular Mechanics Algorithm for Potential Energy Surfaces of Chemical Reactions.

174. F. Jensen, *Introduction to Computational Chemistry*, Wiley, New York, 1999, pp. 48–49.

175. R. Méreau, M. T. Rayez, J. C. Rayez, and P. C. Hiberty, *Phys. Chem. Chem. Phys.*, **3**, 3650 (2001). Alkoxy Radical Decomposition Explained by a Valence Bond Model.

176. H. Yamataka and S. Nagase, *J. Org. Chem.*, **53**, 3232 (1988). Ab Initio Calculations of Hydrogen Transfers. A Computational Test of Variations in the Transition State Structure and the Coefficient of Rate-Equilibrium Correlation.

177. A. Pross, H. Yamataka, and S. Nagase, *J. Phys. Org. Chem.*, **4**, 135 (1991). Reactivity in Radical Abstraction Reactions: Application of the Curve Crossing Model.

178. S. Shaik, *Acta Chem. Scand.*, **44**, 205 (1990). S_N2 Reactivity and its Relation to Electron Transfer Concepts.

179. I. M. Kovach, J. P. Elrod, and R. L. Schowen, *J. Am. Chem. Soc.*, **102**, 7530 (1980). Reaction Progress at the Transition State for Nucleophilic Attack on Esters.

180. D. G. Oakenfull, T. Riley, and V. Gold, *J. Chem. Soc. Chem. Commun.*, 385, (1966). Nucleophilic and General Base Catalysis by Acetate Ion in the Hydrolysis of Aryl Acetates: Substituent Effects, Solvent Isotope Effects, and Entropies of Activation.

181. E. Buncel, S. S. Shaik, I.-H. Um, and S. Wolfe, *J. Am. Chem. Soc.*, **110**, 1275 (1988). A Theoretical Treatment of Nucleophilic Reactivity in Additions to Carbonyl Compounds. Role of the Vertical Ionization Energy.

182. S. S. Shaik and E. Canadell, *J. Am. Chem. Soc.*, **112**, 1446 (1990). Regioselectivity of Radical Attacks on Substituted Olefins. Application of the State-Correlation-Diagram (SCD) Model.

183. J. H. Ren and J. I. Brauman, *Science*, **295**, 5563 (2002). Steric Effects and Solvent Effects in Ionic Reactions.

184. S. Shaik, A. C. Reddy, A. Ioffe, J. P. Dinnocenzo, D. Danovich, and J. K. Cho, *J. Am. Chem. Soc.*, **117**, 3205 (1995). Reactivity Paradigms. Transition State Structures, Mechanisms of Barrier Formation, and Stereospecificity of Nucleophilic Substitutions on σ-Cation Radicals.

185. J. H. Incremona and C. J. Upton, *J. Am. Chem. Soc.*, **94**, 301 (1972). Bimolecular Homolytic Substitution with Inversion. Stereochemical Investigation of an SH_2 Reaction.

186. C. J. Upton and J. H. Incremona, *J. Org. Chem.*, **41**, 523 (1976). Bimolecular Homolytic Substitution at Carbon. Stereochemical Investigation.

187. B. B. Jarvis, *J. Org. Chem.*, **35**, 924 (1970). Free Radical Additions to Dibenzotricyclo[3.3.0.02,8]-3,6-octadiene.

188. G. G. Maynes and D. E. Appliquist, *J. Am. Chem. Soc.*, **95**, 856 (1973). Stereochemistry of Free Radical Ring Cleavage of *cis*-1,2,3-Trimethylcyclopropane by Bromine.

189. K. J. Shea and P. S. Skell, *J. Am. Chem. Soc.*, **95**, 6728 (1973). Photobromination of Alkylcyclopropanes. Stereochemistry of Homolytic Substitution at a Saturated Carbon Atom.

190. M. L. Poutsma, *J. Am. Chem. Soc.*, **87**, 4293 (1965). Chlorination Studies of Unsaturated Materials in Nonpolar Media. V. Norbornene and Nortricyclene.

191. S. S. Shaik and J. P. Dinnocenzo, *J. Org. Chem.*, **55**, 3434 (1990). Nucleophilic Cleavages of One-electron σ Bonds are Predicted to Proceed with Stereoinversion.

192. J. P. Dinnocenzo, W. P. Todd, T. R. Simpson, and I. R. Gould, *J. Am. Chem. Soc.*, **112**, 2462 (1990). Nucleophilic Cleavage of One-electron σ Bonds. Stereochemistry and Cleavage Rates.

193. L. Eberson, R. Gonzalez-Luque, M. Merchan, F. Radner, B. O. Roos, and S. Shaik, *J. Chem. Soc. Perkin Trans. 2*, 463 (1997). Radical Cations of Non-Alternant Systems as Probes of the Shaik-Pross VB Configuration Mixing Model.

194. S. Shaik and R. Bar, *Nouv. J. Chim.*, **8**, 411 (1984). How Important is Resonance in Organic Species?

195. P. C. Hiberty, S. S. Shaik, J. M. Lefour, and G. Ohanessian, *J. Org. Chem.*, **50**, 4657 (1985). The Delocalized π-system of Benzene is not a Stable Electronic System.

196. S. S. Shaik, P. C. Hiberty, J.-M. Lefour, and G. Ohanessian, *J. Am. Chem. Soc.*, **109**, 363 (1987). Is Delocalization a Driving Force in Chemistry? Benzene, Allyl Radical, Cyclobutadiene and Their Isoelectronic Species.

197. S. S. Shaik, P. C. Hiberty, G. Ohanessian, and J.-M. Lefour, *J. Phys. Chem.*, **92**, 5086 (1988). When Does Electronic Delocalization Become a Driving Force of Chemical Bonding?

198. P. C. Hiberty, D. Danovich, A. Shurki, and S. Shaik, *J. Am. Chem. Soc.*, **117**, 7760 (1995). Why Does Benzene Possess a D_{6h} Symmetry? A Theoretical Approach Based on the π-Quasiclassical State for Probing π-Bonding Energies.

199. K. Jug and A. M. Koster, *J. Am. Chem. Soc.*, **112**, 6772 (1990). Influence of σ and π Electrons on Aromaticity.

200. A. Gobbi, Y. Yamaguchi, Y. Frenking, and H. F. Schaefer III, *Chem. Phys. Lett.*, **244**, 27 (1995). The Role of σ and π Stabilization in Benzene, Allyl Cation and Allyl Anion. A Canonical Orbital Energy Derivative Study.

201. R. Janoschek, *J. Mol. Struct. (THEOCHEM)*, **229**, 197 (1991). Has the Benzene Molecule an Extra Stability?

202. M.-C. Ou and S.-Y. Chu, *J. Phys. Chem.*, **98**, 1087 (1994). The π-Electron Stabilization in Benzocyclobutenes.

203. Y. Haas and S. Zilberg, *J. Am. Chem. Soc.*, **1995**, *117*, 5387. The v_{14} (b_{2u}) Mode of Benzene in S_0 and S_1 and the Distortive Nature of the π Electron System: Theory and Experiment.

204. L. Wunsch, H. J. Neusser, and E. W. Schlag, *Chem. Phys. Lett.*, **31**, 433 (1975). Two Photon Excitation Spectrum of Benzene and Benzene-d_6 in the Gas Phase: Assignment of Inducing Modes by Hot Band Analysis.

205. L. Wunsch, F. Metz, H. J. Neusser, and E. W. Schlag, *J. Chem. Phys.*, **66**, 386 (1977). Two-Photon Spectroscopy in the Gas Phase: Assignments of Molecular Transitions in Benzene.

206. D. M. Friedrich and W. M. McClain, *Chem. Phys. Lett.*, **32**, 541 (1975). Polarization and Assignment of the Two-Photon Excitation Spectrum of Benzene Vapor.

207. E. C. da Silva, J. Gerratt, D. L. Cooper, and M. Raimondi, *J. Chem. Phys.*, **101**, 3866 (1994). Study of the Electronic States of the Benzene Molecule Using Spin-Coupled Valence Bond Theory.

208. U. Manthe and H. Köppel, *J. Chem. Phys.*, **93**, 1658 (1990). Dynamics on Potential Energy Surfaces with a Conical Intersection: Adiabatic, Intermediate, and Diabatic Behavior.

209. H. Köppel, W. Domcke, and L. S. Cederbaum, *Adv. Chem. Phys.*, **57**, 59 (1984). Multimode Molecular Dynamics Beyond the Born–Oppenheimer Approximation.

210. D. M. Cyr, G. A. Bishea, M. G. Scranton, and M. A. Johnson, *J. Chem. Phys.*, **97**, 5911 (1992). Observation of Charge-transfer Excited States in the $I^-\cdot CH_3I$, $I^-\cdot CH_3Br$, and $I^-\cdot CH_2Br_2$ S_N2 Reaction Intermediates Using Photofragmentation and Photoelectron Spectroscopies.

211. I. B. Bersuker, *Nouv. J. Chim.*, **4**, 139 (1980). Are Activated Complexes of Chemical Reactions Experimentally Observable Ones?

212. S. Zilberg, Y. Haas, D. Danovich, and S. Shaik, *Angew. Chem. Int. Ed. Engl.*, **37**, 1394 (1998). The Twin-Excited State as a Probe for the Transition State in Concerted Unimolecular Reactions. The Semibullvalene Rearrangement.

213. H. Quast, K. Knoll, E.-M. Peters, K. Peters, and H. G. von Schnering, *Chem. Ber.*, **126**, 1047 (1993). 2,4,6,8-Tetraphenylbarbaralan—Ein Orangeroter, Thermochromer Kohlenwasserstoff ohne Chromophor.

214. H. Quast and M. Seefelder, *Angew. Chem. Int. Ed. Engl.*, **38**, 1064 (1999). The Equilibrium Between Localized and Delocalized States of Thermochromic Semibullvalenes and Barbaralanes—Direct Observation of Transition States of Degenerate Cope Rearrangements.

215. M. Shapiro and P. Brumer, *Adv. At. Mol. Opt. Phys.*, **42**, 287 (2000). Coherent Control of Atomic, Molecular and Electronic Processes.

216. M. Said, D. Maynau, J. P. Malrieu, and M. A. Garcia-Bach, *J. Am. Chem. Soc.*, **106**, 571 (1984). A Nonempirical Heisenberg Hamiltonian for the Study of Conjugated Hydrocarbons. Ground-state Conformational Studies.

217. A. O. Ovchinnikov, *Theor. Chim. Acta (Berl.)*, **47**, 297 (1978). Multiplicity of the Ground State of Large Alternant Organic Molecules with Conjugated Bonds.

218. W. T. Borden, H. Iwamura, and J. A. Berson, *Acc. Chem. Res.*, **27**, 109 (1994). Violations of Hund's Rule in Non-Kekulé Hydrocarbons: Theoretical Predictions and Experimental Verifications.

219. W. T. Borden, in *Encyclopedia of Computational Chemistry*, P. v. R. Schleyer, N. L. Allinger, T. Clark, J. Gasteiger, P. A. Kollman, H. F. Schaefer, III, and P. R. Schreiner, Eds., Wiley, Chichester, 1998, Vol. 1, p. 708.

220. A. C. Hurley, J. Lennard-Jones, and J. A. Pople, *Proc. R. Soc. London*, **A220**, 446 (1953). The Molecular Orbital Theory of Chemical Valency. XVI. A Theory of Paired-Electrons in Polyatomic Molecules.

221. W. J. Hunt, P. J. Hay, and W. A. Goddard, III, *J. Chem. Phys.*, **57**, 738 (1972). Self-Consistent Procedures for Generalized Valence Bond Wave Functions.

222. F. B. Bobrowicz and W. A. Goddard, III, in *Methods of Electronic Structure Theory*, H. F. Schaefer, III, Ed., Plenum Press, New York, 1977, pp. 79–127.

223. D. L. Cooper, J. Gerratt, and M. Raimondi, *Int. Rev. Phys. Chem.*, **7**, 59 (1988). Spin-Coupled Valence Bond Theory.

224. D. L. Cooper, J. Gerratt, and M. Raimondi, in *Valence Bond Theory and Chemical Structure*, D. J. Klein and N. Trinajstic, Eds., Elsevier, 1990, p. 287.

225. D. L. Cooper, J. Gerratt, and M. Raimondi, in *Advances in the Theory of Benzenoid Hydrocarbons*, *Top. Current Chem.* I. Gutman and S. J. Cyvin (Eds.), **153**, 41 (1990).

226. P. C. Hiberty and D. L. Cooper, *J. Mol. Struct. (THEOCHEM),* **169**, 437 (1988). Valence Bond Calculations of the Degree of Covalency in a C—X Bond. Application to CH_4 and CH_3Li.

227. D. L. Cooper, J. Gerratt, and M. Raimondi, *Nature London*, **323**, 699 (1986). The Electronic Structure of the Benzene Molecule.

228. E. A. Carter and W. A. Goddard, III, *J. Chem. Phys.*, **88**, 3132 (1988). Correlation-consistent Configuration Interaction: Accurate Bond Dissociation Energies from Simple Wave Functions. Application to H_3, BH, H_2O, C_2H_6 and O_2.

229. F. Penotti, J. Gerratt, D. L. Cooper, and M. Raimondi, *J. Mol. Struct. (THEOCHEM),* **169**, 421 (1988). The Ab Initio Spin-Coupled Description of Methane: Hybridization Without Preconceptions.

230. E. Tornaghi, D. L. Cooper, J. Gerratt, M. Raimondi, and M. Sironi, *J. Mol. Struct. (THEOCHEM)*, **259**, 383 (1992). The Spin-Coupled Description of Lithium Clusters: Part I. Optimal Geometrical Arrangements and Body-Centred Cubic Fragments.

231. M. H. McAadon and W. A. Goddard, III, *Phys. Rev. Lett.*, **55**, 2563 (1985). New Concepts of Metallic Bonding Based on Valence-Bond Ideas.

232. M. H. McAadon and W. A. Goddard, III, *J. Phys. Chem.*, **91**, 2607 (1987). Generalized Valence Bond Studies of Metallic Bonding: Naked Clusters and Applications to Bulk Metals.

233. J. Verbeek, Ph. D. Dissertation, University of Utrecht, 1990.

234. J. Verbeek, J. H. van Lenthe, and P. Pulay, *Mol. Phys.*, **73**, 1159 (1991). Convergence and Efficiency of the Valence Bond Self-Consistent Field Method.

235. M. R. F. Siggel and T. D. Thomas, *J. Am. Chem. Soc.*, **108**, 4360 (1986). Why are Organic Acids Stronger Than Organic Alcohols?

236. T. D. Thomas, T. X. Carroll, and M. R. F. Siggel, *J. Org. Chem.*, **53**, 1812 (1988). Isodesmic Reaction Energies and the Relative Acidities of Carboxylic Acids and Alcohols.

237. T. D. Thomas, M. R. F. Siggel, and A. Streitwieser, Jr., *J. Mol. Struct. (THEOCHEM),* **165**, 309 (1988). Resonance Delocalization in the Anion Is Not the Major Factor Responsible for the Higher Acidity of Carboxylic Acids Relative to Alcohols.

238. M. R. F. Siggel, A. Streitwieser, Jr., and T. D. Thomas, *J. Am. Chem. Soc.*, **110**, 8022 (1988). The Role of Resonance and Inductive Effects in the Acidity of Carboxylic Acids.

239. P. C. Hiberty and C. P. Byrman, *J. Am. Chem. Soc.*, **117**, 9875 (1995). The Role of Delocalization in the Enhanced Acidity of Carboxylic Acids and Enols Relative to Alcohols.

240. K. B. Wiberg and K. E. Laidig, *J. Am. Chem. Soc.*, **109**, 5935 (1987). Barrier to Rotation Adjacent to Double Bonds. 3. The Carbon–Oxygen Barrier in Formic Acid, Methyl Formate, Acetic Acid, and Methyl Acetate. The Origin of Ester and Amide Resonance.

241. K. B. Wiberg and C. L. Breneman, *J. Am. Chem. Soc.,* **114**, 831 (1992). Resonance Interactions in Acyclic Systems. 3. Formamide Internal Rotation Revisited. Charge and Energy Redistribution Along the C—N Bond Rotational Pathway.

242. K. E. Laidig and L. M. Cameron, *J. Am. Chem. Soc.*, **118**, 1737 (1996). Barrier to Rotation in Thioformamide. Implications for Amide Resonance.

243. R. F. W. Bader, *Atoms in Molecules*: *A Quantum Theory*, Oxford University Press, Oxford, **1990**.

244. C. L. Perrin, *J. Am. Chem. Soc.*, **113**, 2865 (1991). Atomic Size Dependence of Bader Electron Populations: Significance for Questions of Resonance Stabilization.

245. S. Yamada, *Angew. Chem. Int. Ed. Engl.,* **34**, 1113 (1995). Relationship Between C(O)—N Twist Angles and ^{17}O NMR Chemical Shifts in a Series of Twisted Amides.

246. S. Yamada, *J. Org. Chem.*, **61**, 941 (1996). Effects of C(O)—N Bond Rotation on the ^{13}C, ^{15}N and ^{17}O NMR Chemical Shifts and Infrared Carbonyl Absorption in a Series of Twisted Amides.

247. A. J. Bennet, V. Somayaji, R. S. Brown, and B. D. Santarsiero, *J. Am. Chem. Soc.*, **113**, 7563 (1991). The Influence of Altered Amidic Resonance on the Infrared and Carbon-13 and

Nitrogen-15 NMR Spectroscopic Characteristics and Barriers to Rotation about the N—C(O) Bond in Some Anilides and Toluamides.

248. K. B. Wiberg and P. R. Rablen, *J. Am. Chem. Soc.*, **117**, 2201 (1995). Why Does Thiofomamide Have a Larger Rotational Barrier Than Formamide?

249. D. Lauvergnat and P. C. Hiberty, *J. Am. Chem. Soc.*, **119**, 9478 (1997). Role of Conjugation in the Stabilities and Rotational Barriers of Formamide and Thioformamide. An ab initio Valence Bond Study.

250. J. Paldus and A. Veillard, *Mol. Phys.*, **35**, 445 (1978) and references therein. Doublet Stability of Ab Initio SCF Solutions for the Allyl Radical.

251. D. Feller, E. Huyser, W. T. Borden, and E. R. Davidson, *J. Am. Chem. Soc.*, **105**, 1459 (1983). MCSCF/CI Investigation of the Low-lying Potential Energy Surfaces of the Formyloxyl Radical, HCO_2.

252. C. F. Jackels and E. R. Davidson, *J. Chem. Phys.*, **64**, 2908 (1976). The Two Lowest Energy $^2A'$ States of NO_2.

253. D. Feller, W. T. Borden, and E. R. Davidson, *J. Am. Chem. Soc.*, **106**, 2513 (1984). Allylic Resonance—When is it Unimportant?

254. D. Feller, E. R. Davidson, and W. T. Borden, *J. Am. Chem. Soc.*, **105**, 334 (1983). When is Allylic Resonance Unimportant?

255. A. D. McLean, B. H. Lengsfield III, J. Pacansky, and Y. Ellinger, *J. Chem. Phys.*, **83**, 3567 (1985). Symmetry Breaking in Molecular Calculations and the Reliable Prediction of Equilibrium Geometries. The Formyloxyl Radical as an Example.

256. A. Rauk, D. Yu, and D. A. Armstrong, *J. Am. Chem. Soc.*, **116**, 8222 (1994). Carbonyl Free Radicals. Formyloxyl (HCOO) and Acetoxyl (CH_3OO) Revisited.

257. A. F. Voter and W. A. Goddard, III, *Chem. Phys.*, **57**, 253 (1981). A Method for Describing Resonance Between Generalized Valence Bond Wave Functions.

258. A. F. Voter and W. A. Goddard, III, *J. Chem. Phys.*, **75**, 3638 (1981). The Generalized Resonating Valence Bond Method: Barrier Heights in the $HF + D$ and $HCl + D$ Exchange Reactions.

259. W. R. Wadt and W. A. Goddard, III, *J. Am. Chem. Soc.*, **97**, 2034 (1975). Electronic Structure of Pyrazine. Valence Bond Model for Lone Pair Interactions.

260. M. Amarouche, G. Durand, and J. P. Malrieu, *J. Chem. Phys.*, **88**, 1010 (1988). Structure and Stability of Xe_n^+ Clusters.

261. M. Rosi and C. W. Bauschlicher, Jr., *Chem. Phys. Lett.*, **159**, 349 (1989). Ultrafast Shock Induced Uniaxial Strain in a Liquid.

262. F. Tarentelli, L. S. Cederbaum, and P. Campos, *J. Chem. Phys.*, **91**, 7039 (1989). Symmetry Breaking and Symmetry Restoring in Ions of Loosely Bound Systems.

263. O. K. Kabbaj, M. B. Lepetit, and J. P. Malrieu, *Chem. Phys. Lett.*, **172**, 483 (1990). Inclusion of Dynamical Polarization Effects is Sufficient to Obtain Reliable Energies and Structures of He_n^+ Clusters.

264. E. Hollauer and M. A. C. Nascimento, *Chem. Phys. Lett.*, **184**, 470 (1991). A Generalized Multi-Structural Wave Function. The He_2^+ Molecule as an Example.

265. E. Hollauer and M. A. C. Nascimento, *J. Chem. Phys.*, **99**, 1207 (1993). A Generalized Multi-Structural Wave Function.

266. D. Lauvergnat, P. C. Hiberty, D. Danovich, and S. Shaik, *J. Phys. Chem.*, **100**, 5715 (1996). A Comparison of C—Cl and Si—Cl Bonds. A Valence Bond Study.

267. J. H. Langenberg and P. J. A. Rutink, *Theor. Chim. Acta (Berl.)*, **85**, 285 (1993). Optimization of Both Resonance Structures of the Glyoxal Radical Cation by Means of the Valence Bond Self-Consistent Field Method.

268. H. Basch, J. L. Wolk, and S. Hoz, *J. Phys. Chem. A*, **101**, 4996 (1997). Valence Bond Study of the SiH_3—F Bond.

269. D. Lauvergnat and P. C. Hiberty, *J. Mol. Struct. (THEOCHEM),* **338**, 283 (1995). The Non-linear Tendencies in Homonuclear X—X Bonds (X = Li to F) and the Lone-Pair Bond Weakening Effect. An Ab Initio Theoretical Analysis.

270. S. Humbel, I. Demachy, and P. C. Hiberty, *Chem. Phys. Lett.,* **247**, 126 (1995). $HO \therefore OH^-$: A Model for Stable Three-Electron-Bonded Peroxide Radical Anions.

271. D. Lauvergnat, P. Maître, P. C. Hiberty, and F. Volatron, *J. Phys. Chem.,* **100**, 6463 (1996). A Valence Bond Analysis of the Lone Pair Bond Weakening Effect for the X—H Bonds in the Series $XH_n = CH_4$, NH_3, OH_2, FH.

272. J. M. Galbraith, E. Blank, S. Shaik, and P. C. Hiberty, *Chem. Eur. J.,* **6**, 2425 (2000). π-Bonding in Second and Third Row Molecules: Testing the Strength of Linus's Blanket.

273. J. M. Galbraith, A. Shurki, and S. Shaik, *J. Phys. Chem. A,* **104**, 1262 (2000). A Valence Bond Study of the Bonding in First Row Transition Metal Hydride Cations: What Energetic Role Does Covalency Play?

274. B. Braïda, L. Thogersen, W. Wu, and P. C. Hiberty, *J. Am. Chem. Soc.,* **124**, 11781 (2002). Stability, Metastability and Unstability of Three-Electron-Bonded Radical Anions. A Model ab initio Study.

275. F. London, *Z. Elekrochem.,* **35**, 552 (1929). Quantenmechanic Deutung des Vorgangs der Aktivierierung.

276. H. Eyring and M. Polanyi, *Z. Phys. Chem.,* **B12**, 279 (1931). On Simple Gas Phase Reactions.

277. J. N. Murrell, S. Carter, S. C. Farantos, P. Huxley, and A. J. C. Varandas, *Molecular Potential Energy Functions,* Wiley, New York, 1984.

278. D. G. Truhlar and R. E. Wyatt, *Adv. Chem. Phys.,* **36**, 141 (1977). $H + H_2$: Potential-Energy Surfaces and Elastic and Inelastic Scattering.

279. A. Shurki, M. Strajbl, J. Villa, and A. Warshel, *J. Am. Chem. Soc.,* **124**, 4097 (2002). How Much Do Enzymes Really Gain by Restraining Their Reacting Fragments?

280. S. P. de Visser and S. Shaik, *Angew. Chem. Int. Ed. Engl.,* **41**, 1947 (2002). Hydrogen Bonding Modulates the Selectivity of Enzymatic Oxidation by P450: A Chameleon Oxidant Behavior by Compound I.

281. H. Kollmar, *J. Am. Chem. Soc.,* **101**, 4832 (1979). Direct Calculation of Resonance Energies of Conjugated Hydrocarbons with ab initio MO Methods.

CHAPTER 2

Modeling of Spin-Forbidden Reactions

Nikita Matsunaga[*] and Shiro Koseki[†]

[*]*Department of Chemistry and Biochemistry, Long Island University, 1 University Plaza, Brooklyn, New York 11201*
[†]*Department of Material Sciences, College of Integrated Arts and Sciences, Osaka Prefecture University, 1-1 Gakuen-cho, Sakai 599-8531, Japan*

OVERVIEW OF REACTIONS REQUIRING TWO STATES

During a chemical transformation, some bonds are broken, and new bonds are formed. Chemists think of such a reaction as proceeding from reactant molecules colliding with each other giving rise to transition states. Subsequently, the transition states fall apart, and the molecular complexes become products on a single potential energy surface of a given state. This view is the so-called adiabatic approximation to the Born–Oppenheimer approximation.[1a] There are many chemical transformations, however, where one must include two or more potential energy surfaces in the model to correctly view the reactions in question. Examples include internal conversion of the excited state and intersystem crossing in photochemical reactions. These and related transformations are more ubiquitous than we generally believe they are.

Let us loosely define processes requiring two or more potential energy surfaces as electronically nonadiabatic processes.[1] More specific well-known examples of electronically nonadiabatic processes include the cis–trans photo-isomerization induced upon absorption of a photon by the rhodopsin molecule
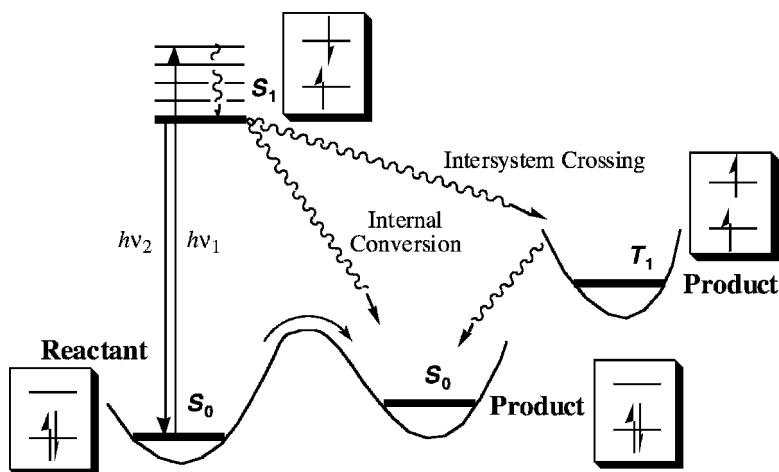
Figure 1 Schematics of decay processes of excited states.

in rod cells, and the Jahn–Teller distortion found in highly symmetric molecules possessing degenerate molecular orbitals.

In the case of photochemistry, electronically nonadiabatic processes can be viewed schematically as depicted in the Jablonski-like diagram (Fig. 1). The adiabatic reaction path is given by the curved arrow; there exists a transition state at the height of the barrier between the reactant and product. The reactant molecule, in the S_0 (or singlet ground) state, can absorb a photon with energy equal to $h\nu_1$, represented by the straight arrow, and the molecule becomes an excited state, S_1, by preserving the total spin angular momentum. Because the Franck–Condon region of the S_1 state is not in general a stationary state, the molecule in the S_1 state starts to follow its decay path (the zigzag arrow indicates nuclear motion taking place). There are several ways in which the S_1 state decays. One decay path may involve radiative decay where the ground vibrational level of the S_1 state emits a photon with energy $h\nu_2$ (fluorescence), returning the molecule to the S_0 state.

For nonradiative decay, one can consider a variety of ways to dissipate the excess energy. The internal conversion process involves the decay of an excited state having the same spin multiplicity as that of the lower energy electronic state. In order to go to the lower energy state from the excited state the molecule must access points on the two surfaces that come close to each other (so-called avoided crossings), or actually touch each other at a conical intersection (also known as a funnel state). Another possible nonradiative decay path is one where the S_1 state can access the triplet state, T_1, via a crossing point between the singlet and triplet potential energy surfaces. Under these conditions, intersystem crossing is accompanied by a change of spin multiplicity. The product distribution may not always be statistical or determined by

thermodynamics alone for these different decay paths. The details of both the potential energy surfaces and the dynamics of molecular motion are important contributing factors in determining product distribution. To model processes such as internal conversion or intersystem crossing one must acquire knowledge of, at least, the potential energy surfaces of reactant and product states and the coupling between the two states in question.

For treating either internal conversion or a spin-forbidden reaction, one can view the coupling of the two surfaces to be the off-diagonal elements of the $n \times n$ general Hamiltonian matrix, where n is the number of states included in a given problem. Equation [1] shows this matrix for a two state problem ($n = 2$).

$$\begin{pmatrix} H_{11} - E_1 & H_{12} \\ H_{21} & H_{22} - E_2 \end{pmatrix} \qquad [1]$$

The diagonal elements are the potential energy of the two states considered, and the coupling potentials between the two electronic states are given by H_{12}, and H_{21}. These off-diagonal elements vary in form; in the case of the internal conversion process the coupling is given by derivative coupling or a nonadiabatic coupling matrix element,[1b] $H_{12} = \langle \Psi_1 | \partial \Psi_2 / \partial R \rangle$ where R is the nuclear coordinate. For intersystem crossing, spin–orbit (SO) coupling, gives the mechanism for two states to couple and corresponds to $H_{12} = H^{SO}$. Although the origin of the two interstate couplings is different, one can view them both as being off-diagonal elements of the general Hamiltonian.[2]

Spin-Forbidden Reaction, Intersystem Crossing

Spin-forbidden reactions are ubiquitous. For example, transition metal catalysis is often spin-forbidden because of the degeneracy (or near degeneracy) of d orbitals of the metal giving rise to a number of possible spin states.[3] Hence, a metal-containing enzyme can undergo spin-forbidden transitions. Biological molecules containing transition metal ions can undergo intersystem crossing depending on the ligand field, and therefore, the spin-forbidden path can become important.[4] The latter example in particular has not been explored very much. Except for the fact that these biological molecules are large, the procedures discussed below are applicable.

Intersystem crossing occurs when the product spin multiplicity differs from the reactant spin multiplicity. Because the spin angular momentum is not conserved in such a reaction, it is referred to as a spin-forbidden reaction.

Figure 2 shows a schematic representation of spin-allowed and spin-forbidden reactions. The total spin of the reaction is conserved in the spin-allowed path ($S_0 \rightarrow S_0$ or product 1 channel, which is the usual reaction path). This reaction path can be represented as a minimum energy (or valley) path connecting reactant and product. In between there exists a stationary point, that is, a point where the gradient of the potential energy with
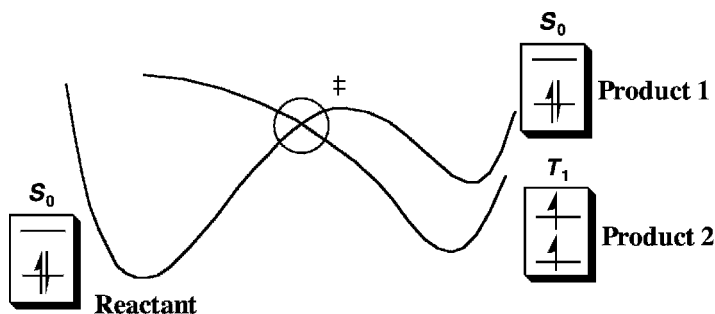
Figure 2 Schematics of spin-forbidden reaction.

respect to nuclear coordinates vanishes, $\partial V/\partial R = 0$. This is called a transition state, denoted in Figure 2 as ‡. The transition state is further characterized by the curvature of the potential energy surface in the vicinity of the transition state forming a saddle point (one dimension having negative curvature and the rest being positive, determined by the second derivatives of the potential energy with respect to all nuclear coordinates). Methods like the intrinsic reaction coordinate (IRC), are available for following the minimum energy path from transition state to reactant or product.[2] The spin-forbidden path on the other hand must be accompanied by a "spin flip", in this case to become a triplet product ($S_0 \rightarrow T_1$ or product 2 channel). In the case of spin-forbidden reactions, there is no transition state as defined in the single surface case. The two surfaces of different multiplicity can cross at an arbitrary geometry, since there is no coupling between the two surfaces in the nonrelativistic theory. The crossing point (in a circle shown in Fig. 2) between the singlet and triplet states gives, in effect, the location on the potential energy surfaces where a spin flip can occur. The crossing point is the point on the two potential energy surfaces where the singlet and triplet states share the same energy and geometry.

   The crossing points between two surfaces of a polyatomic molecule in the case of a spin-forbidden reaction can form a surface of crossing points, with dimension $N^{int} - 1$, where N^{int} is the number of internal coordinates, and the crossing of the potential energy surface is therefore described as a hypersurface. In principle, one can compute two potential energy surfaces of interest to reveal the location of the crossing points (or seam, or surface). To characterize the point of intersection that is most meaningful, one should locate the minimum energy crossing point (MEXP).[5] The MEXP is defined as the surface crossing point of lowest energy. If the system's dynamics (classical or quantal) is of interest, one needs to calculate all relevant points of the two potential energy surfaces without specifically characterizing the MEXP.

   The two surfaces that cross at the minimum energy crossing point must have a mechanism that couple the two. In the standard nonrelativistic electronic structure theory, there is no mechanism for interaction between the two

potential energy surfaces of different spin multiplicity. The spin–orbit coupling gives the mechanism for coupling two potential energy surfaces in spin-forbidden reactions. That coupling of spin must be derived from the relativity theory, or at least, reduction from the theory. Some of the methods and procedures that account for such coupling are discussed below, are well established, and some are incorporated in standard electronic structure theory programs.

SPIN–ORBIT COUPLING AS A MECHANISM FOR SPIN-FORBIDDEN REACTION

General Considerations

A current flowing through a closed loop of wire in a magnetic field, such as in an electric motor, generates torque due to the familiar right-hand rule of electromagnetism. The potential energy can be calculated by integrating the torque over all rotation angles; one must do work against the rotation. Therefore, one obtains the potential energy after integration,

$$V = -\vec{\mu}_s \cdot \mathbf{B}_n \qquad [2]$$

Similarly, in an atom, one can view the electron as orbiting around the nucleus, classically. Since both are charged, the motion creates electric current. The current created by the nucleus induces a magnetic field and since an electron possesses an intrinsic magnetic spin moment (m_S quantum number, $\pm\frac{1}{2}$ or α and β electrons), the magnetic field induced by the nucleus can be coupled to the electron spin, producing an energy difference between α and β electrons in analogy to the classical electric motor. The energy difference, or splitting, described in such atoms is called the fine-structure splitting, or zero-field splitting. In the case of atoms, the coupling between orbital angular momentum, $\ell(\ell = r \times p)$, and spin angular momentum, s, gives the spin–orbit coupling.

$$V = \ell \cdot s \qquad [3]$$

The coupling between the magnetic moment of the electron and its orbital motion gives rise to spin–orbit coupling. One may then express the Hamiltonian for spin–orbit coupling in a many-electron system as

$$H^{SO} = \sum_i \xi(\mathbf{r}_i)\ell_i \cdot s_i \qquad [4]$$

Table 1 Magnitude of Spin–Orbit Coupling for Atoms[a]

Atoms (term order)	Spin–Orbit[b] (cm^{-1})	Atoms (term order)	Spin–Orbit (cm^{-1})	Atoms (term order)	Spin–Orbit (cm^{-1})
C	16,43	F	404		
$(^3P_0 - {}^3P_1 - {}^3P_2)$	(15, 44)	$(^2P_{3/2} - {}^2P_{1/2})$	(411)		
Si	77, 223	Cl	881	Cu	2,043
$(^3P_0 - {}^3P_1 - {}^3P_2)$	(72, 213)	$(^2P_{3/2} - {}^2P_{1/2})$	(877)	$(^2D_{5/2} - {}^2D_{3/2})$	(2,064)
Ge	557, 1,410	Br	3685	Ag	4,472
$(^3P_0 - {}^3P_1 - {}^3P_2)$	(457, 1,421)	$(^2P_{3/2} - {}^2P_{1/2})$	(3,464)	$(^2D_{5/2} - {}^2D_{3/2})$	(4,481)
Sn	1,692, 3,428	I	7603	Au	12,274
$(^3P_0 - {}^3P_1 - {}^3P_2)$	(1,149, 2,983)	$(^2P_{3/2} - {}^2P_{1/2})$	(7,404)	$(^2D_{5/2} - {}^2D_{3/2})$	(12,113)
Pb	7,819, 10,651	At	23,850		
$(^3P_0 - {}^3P_1 - {}^3P_2)$	(4,162, 8,156)	$(^2P_{3/2} - {}^2P_{1/2})$			

[a]In units of cm^{-1}.
[b]Two values of the spin–orbit splittings are for $^3P_0 - {}^3P_1$ and $^3P_1 - {}^3P_2$.

where $\xi(\mathbf{r}_i)$ is a prefactor that is proportional to $Z_i/\mathbf{r}_i^3$, where Z_i is the nuclear charge and $\mathbf{r}_i$ is the distance of the ith electron from the nucleus. The phenomenologically derived spin–orbit Hamiltonian can be a very useful tool in understanding spin-forbidden processes.

Atomic Spin–Orbit Coupling

The atomic spin–orbit coupling sets the stage for understanding what happens in the molecular case. As has been reviewed by Pyykkö[6a,b] and others,[6c,d] the spin–orbit coupling has large effects on chemistry, particularly for atoms with large nuclear charge Z. The prefactor, $\xi(\mathbf{r}_i)$, in the spin–orbit Hamiltonian (Eq. [4]) contains the term $Z/\mathbf{r}^3$, and the expectation value of the operator $1/\mathbf{r}^3$ for a hydrogen-like atom is on the order of $Z^3/a_0 n^3$, where a_0 and n are the Bohr radius and principal quantum number, respectively. Therefore, one can expect that the spin–orbit coupling in atoms for a given principal quantum number will grow with Z^4, and that the heavy elements will have relatively large spin–orbit couplings (Table 1).

Table 1 gives examples of the periodic trend of spin–orbit splitting in atoms. In this table, the energetic ordering of levels arising from a given state, as well as the splittings between successive levels, is shown along with the theoretical calculations of Koseki et al.[7–9] For the first two rows of the periodic table, the splitting is relatively small. However, for the third row onward, the splitting of the levels starts to exceed the vibrational spacing in molecules. Note that the splitting in the last row is in the same energetic range as covalent bond energies in molecules!

The small values of the spin–orbit coupling in molecules containing first- and second-row elements does not mean, however, that spin–orbit coupling is unimportant. It will be shown in the next section that intersystem crossing can be efficient even for molecules with small spin–orbit coupling.
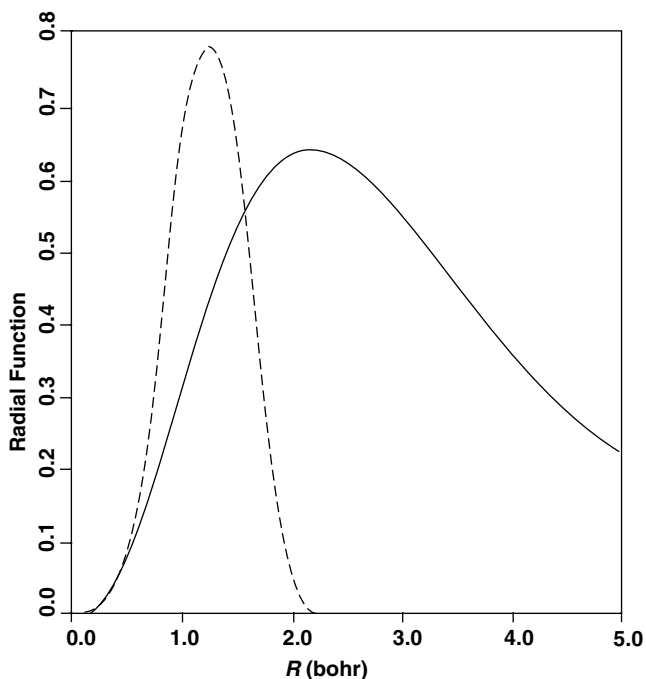
Figure 3 The radial functions of the 3*p* pseudo-orbital of silicon and its spin–orbit integral. The solid line is the 3*p* pseudo-orbital and the dashed line represents spin–orbit integrals. (Reproduced from Ref. 11 with permission.)

The magnitude of spin–orbit coupling can be computed from the spin–orbit integral, $\langle r\psi | H^{SO} | r\psi \rangle$. Figure 3 shows a 3*p* radial pseudo-orbital for silicon with the effective core potential (ECP) approach, in addition to the corresponding 3*p* spin–orbit integral.[11] It clearly shows that the integral originates in the core region in comparison to the maximum of the valence 3*p* pseudo-orbital.

Molecular Spin–Orbit Coupling

Spin–Orbit coupling in molecules can give rise to interesting effects in chemistry. For example, the *g*-factor (or gyromagnetic ratio) of free radicals measured with electron spin resonance (ESR) spectroscopy can deviate from its free-electron value (2.0023) due to spin–orbit coupling.[12] Other examples include chemically induced dynamic nuclear polarization, chemically induced dynamic electron polarization, and stimulated nuclear polarization (the results of such experiments are reviewed in Ref. 13). Spin–orbit coupling has even been attributed to the breakdown of Pauling's electronegativity equation for bond dissociation energies of heavy halide-containing molecules.[14]
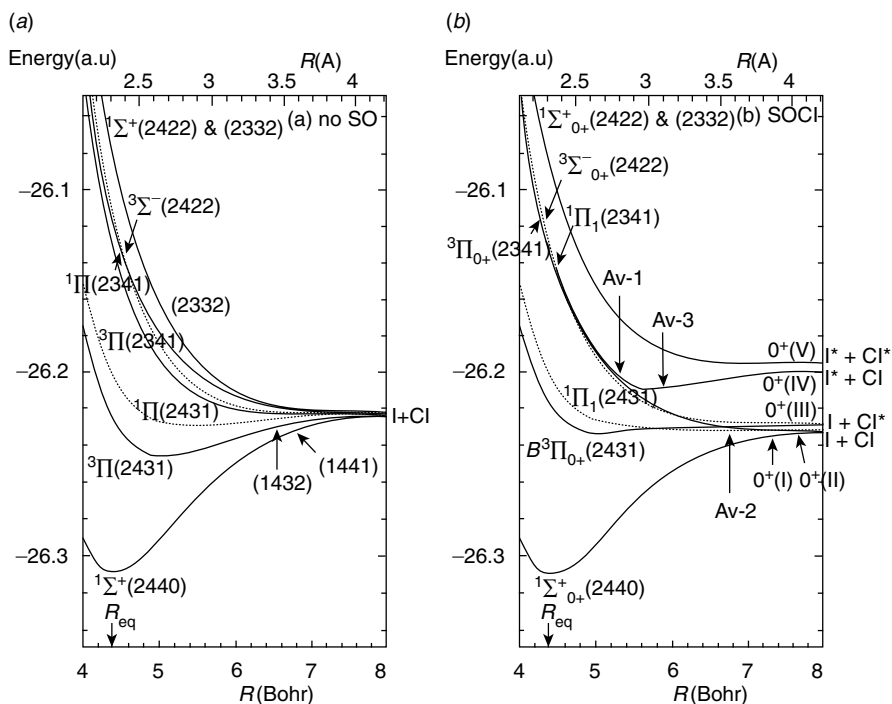
Figure 4 Potential energy curves of ICl. (*a*) Without spin–orbit coupling, and (*b*) with spin–orbit coupling. [Reproduced from Ref. 15 with permission.]

An illustrative example of the effect of spin–orbit coupling in molecules is given by the potential energy curves of ICl.[15] The potential energy curves shown in Figure 4 are the results of second-order[16] configuration interaction (CI) calculations without spin–orbit contributions (Fig. 4*a*) and the results of second-order CI including spin–orbit coupling (Fig. 4*b*). The two figures, even on a qualitative basis, are quite different. At the dissociation asymptote, iodine shows large spin–orbit splitting (7600 cm^{-1} between $^2P_{3/2}$ and $^2P_{1/2}$), in addition to the small but significant splitting of chlorine (880 cm^{-1} between $^2P_{3/2}$ and $^2P_{1/2}$). The ground-state dissociation energy is smaller by $\sim$4200 cm^{-1} in the calculations with the spin orbit coupling (compare Figure 4*a* and Figure 4*b*). At intermediate distances, spin–orbit coupling induces the formation of a metastable minimum on one of the potentials. To compare the experimental spectra of molecules containing relatively heavy elements, it is absolutely essential to include spin–orbit coupling explicitly.

If a molecule possesses relatively high symmetry, a nonzero spin–orbit matrix element can be understood by considering the character table corresponding to the symmetry group to which that molecule belongs. Consider coupling of a C_{2v}-symmetric molecule in its $^1A_1$ and $^3B_1$ states as an example. The molecule is placed on the *X–Z* plane of the Cartesian coordinate with the
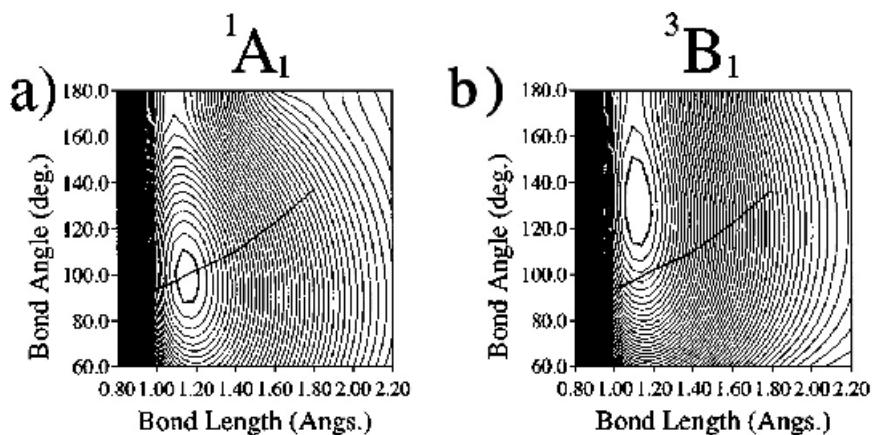
Figure 5 Two-dimensional (bending and symmetric stretch) potential energy surfaces of CH_2. (a) $^1A_1$ state and the line segment represents the crossing seam, and (b) $^3B_1$ state with crossing seam. [Reproduced from Ref. 17 with permission.]

Z axis as the principal axis of rotation. The nonzero matrix elements of the spin–orbit coupling are given by the symmetry of the singlet and triplet states and by the symmetry of the orbital angular momentum operator that transforms as a rotation. Because the spin–orbit coupling is given as $\ell \cdot s$, the matrix elements become $\langle {}^1\psi(A_1)|(\ell_x s_x + \ell_y s_y + \ell_z s_z)|{}^3\psi(B_1)\rangle$. Therefore, the nonzero matrix elements arise only from $\langle \psi(A_1)|\ell_y|\psi(B_1)\rangle \langle {}^1\chi|s_y|{}^3\chi\rangle$, where ℓ_y corresponds to the orbitals perpendicular to the molecular plane and χ corresponds to spin functions. The spin operators s_x and s_y change the spin such that $s_x|\alpha\rangle = \hbar/2|\beta\rangle$, $s_x|\beta\rangle = \hbar/2|\alpha\rangle$, $s_y|\alpha\rangle = i\hbar/2|\beta\rangle$, and $s_y|\beta\rangle = -i\hbar/2|\alpha\rangle$, therefore giving rise to nonzero matrix elements. In contrast, s_z does not; $s_z|\alpha\rangle = -\hbar/2|\alpha\rangle$ and $s_z|\beta\rangle = -\hbar/2|\beta\rangle$, thus giving matrix elements to vanish.

An illustrative example for efficient intersystem crossing, despite the small magnitude of spin–orbit coupling, is given in Figure 5, which shows the potential energy surfaces of $^1A_1$ (first excited state) and $^3B_1$ (ground state) states (a and b in the figure, respectively) of CH_2 for symmetric stretching and bending coordinates.[17] Also shown is the crossing seam between the two potential energy surfaces. It is clear from the figure that the $^3B_1$ state crosses almost at the equilibrium geometry of the singlet state. Figure 6 shows the energies of the crossing seam as a function of the stretching coordinate along with the magnitudes of spin–orbit couplings calculated at the crossing points. The spin–orbit coupling between the two states is small ($<10\ \mathrm{cm}^{-1}$) along the seam (Fig. 6). However, because the two surfaces cross close to the equilibrium structure of the singlet state, and the maximum of the vibrational wave function of the $^1A_1$ state in this coordinate is located close to the minimum energy crossing point, the intersystem crossing from the singlet to the triplet ground state is therefore efficient. In a classical point of view, the
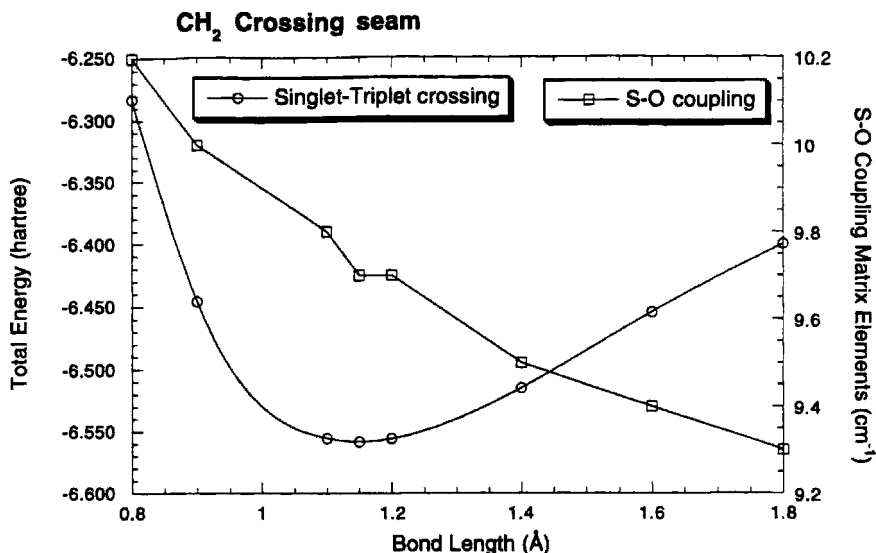
Figure 6 Energetics and magnitude of spin–orbit coupling along the crossing seam in CH_2. Open circles represent crossing points between $^1A_1$ and $^3B_1$ states in their bending and symmetric stretch coordinates. Open squares represent spin–orbit matrix elements calculated with Z^{eff} method (see text). [Reproduced from Ref. 17 with permission.]

region of the potential energy in the vicinity of the minimum of the $^1A_1$ state is accessed by the molecule many times, and even the small crossing probability in one trajectory becomes cumulatively sizable. One must therefore be concerned with spin–orbit coupling as well as the location of crossing points in determining efficiency of intersystem crossing.

CROSSING PROBABILITY

Once the magnitude of the coupling between the two surfaces is determined, one can calculate the probability of crossing from one spin state to another at a given geometry. There are several well-established approximation methods for obtaining the crossing probability. Once obtained, it can then be incorporated into a statistical theory of rate such as the nonadiabatic version of RRKM theory to obtain rate constants for spin-forbidden processes.[18–20] By integrating the microcanonical rate constant over energy, one can obtain thermal rate constants that are directly comparable to the experimental thermal rate constants.

Fermi Golden Rule

From time-dependent perturbation theory, the probability of transition from one state to another can be described by Fermi's golden rule, which

says that the probability is given by the square of the transition matrix element. In the case of a spin-forbidden reaction, the crossing probability is given by the square of the spin–orbit matrix elements, which is expressed as

$$P = \frac{2\pi}{\hbar} \sum_f |\langle \Psi_f | H^{SO} | \Psi_i \rangle \langle \chi_f | \chi_i \rangle|^2 \qquad [5]$$

Here $\langle \chi_f | \chi_i \rangle$ is the Franck–Condon factor that represents the overlap of the vibrational wave functions of the initial and final states. The geometry dependence of the spin–orbit coupling is neglected in this case. Therefore, the contributing factor for spin-forbidden transitions is having not only spin–orbit coupling nonzero and the crossing point energetically accessible, but also ensuring that the vibrational wave functions have nonzero overlap.

Landau–Zener Semiclassical Approximation

In this approximation, the probability of transition is given by Eq. [6]

$$P = e^{-2\gamma} \qquad [6]$$

In this equation, γ is a so-called Massey parameter that is defined as

$$\gamma = \frac{\hbar}{2m} \frac{|\langle \Psi_f | H^{SO} | \Psi_i \rangle|^2}{\Delta g_{fi} v} \qquad [7]$$

where v is the velocity of the particle with mass m passing through the crossing point, and Δg_{fi} is the difference in the gradients of the two potential energy surfaces at the crossing point. Since the Landau–Zener approximation is derived from a semiclassical approximation, the tunneling contribution below the crossing point energy is not included, and it is known[21–23] that the transition probability calculated using the Landau–Zener treatment in this region is underestimated. Above the crossing point energy, the approximation gives good results. Generalization of the Landau–Zener method is reviewed by Nakamura in his monograph.[23]

METHODOLOGIES FOR OBTAINING SPIN–ORBIT MATRIX ELEMENTS

In this section, relativistic quantum mechanics and methods for calculating the spin–orbit matrix elements are presented. Excellent reviews of this material have been published by Almlöf and Gropen[24] and Hess et al.[25] The

basic theory of relativistic quantum mechanics is presented in many texts, such as those in Ref. 26.

Electron Spin in Nonrelativistic Quantum Mechanics

The classic experiments of Stern and Gerlach showed that a beam of silver atoms (later confirmed for hydrogen atoms) in an inhomogeneous magnetic field gave rise to two distinct spots on the photographic plate, instead of a broadened spot as expected from classical mechanics. In addition, the multiplet structure appears in atomic spectra when a weak magnetic field is applied. These results indicate that electrons possess magnetic angular momentum and they are quantized to two distinct states.

The spin angular momentum has homologous properties to the orbital angular momentum, namely,

$$[s_x, s^2] = [s_y, s^2] = [s_z, s^2] = 0 \qquad [8]$$

$$[s_x, s_y] = i\hbar s_z \qquad [9]$$

$$[s_y, s_z] = i\hbar s_x \qquad [10]$$

$$[s_z, s_x] = i\hbar s_y \qquad [11]$$

$$s^2 = s_x^2 + s_y^2 + s_z^2 \qquad [12]$$

To match the two-valuedness of the electron spin and the commuting properties shown above, Pauli introduced spin matrices, σ_i. Each component of spin can then be written in terms of the 2×2 spin matrices,

$$s_x = \frac{1}{2}\hbar\sigma_x \qquad [13]$$

$$s_y = \frac{1}{2}\hbar\sigma_y \qquad [14]$$

$$s_z = \frac{1}{2}\hbar\sigma_z \qquad [15]$$

Then the eigenvalue of the σ_i is +1. Because the spin matrices are 2×2 matrices, the internal state of electrons must be represented by two-column matrices,

$$\psi_P(r, m_s) = \begin{pmatrix} \psi_+(r) \\ \psi_-(r) \end{pmatrix} \qquad [16]$$

where ψ_P is Pauli's spinor (spin orbital). If $m_s = +\frac{1}{2}$, then $\Psi_- = 0$, and if $m_s = -\frac{1}{2}$, then $\Psi_+ = 0$. The Pauli spinor can then be represented as

$$\psi_P(r, m_s) = \psi_+(r)\chi(m_s) + \psi_-(r)\chi(m_s) \qquad [17]$$

where χ is the spin function that depends only on m_s, and

$$\chi\left(+\frac{1}{2}\right) = \begin{pmatrix} 1 \\ 0 \end{pmatrix} \qquad [18]$$

$$\chi\left(-\frac{1}{2}\right) = \begin{pmatrix} 0 \\ 1 \end{pmatrix} \qquad [19]$$

The complex conjugate of the Pauli spinor is given by a two-row matrix,

$$\psi_P^*(r, m_s) = \begin{pmatrix} \psi_+^*(r) & \psi_-^*(r) \end{pmatrix} \qquad [20]$$

Therefore, the spin operators must be 2×2 matrices. When the eigenvalue is either -1 or $+1$ assuming that the quantization is observed in the z direction, it is readily seen that

$$\sigma_z = \begin{pmatrix} 1 & 0 \\ 0 & -1 \end{pmatrix} \qquad [21]$$

Furthermore, consistency in the commutation relations is only achieved by having

$$\sigma_x = \begin{pmatrix} 0 & 1 \\ 1 & 0 \end{pmatrix} \qquad [22]$$

$$\sigma_y = \begin{pmatrix} 0 & i \\ -i & 0 \end{pmatrix} \qquad [23]$$

By using the spin matrices, the two-valuedness of an electron can be incorporated into the Schrödinger equation. For a hydrogen-like atom, one can write the Schrödinger equation in the form,

$$\left[\frac{(\sigma\mathbf{p}) \cdot (\sigma\mathbf{p})}{2m} + V\right]\psi_P = \left[\frac{1}{2m}\begin{pmatrix} p_z & p_x + ip_y \\ p_x - ip_y & -p_z \end{pmatrix}^2 + V\right]\psi_P = E\psi_P \qquad [24]$$

where $\mathbf{p}$ and p_i are the vector and ith component of the scalar form of the momentum operators, respectively, V is the Coulomb potential, and ψ_P is the Pauli spinor comprised of two components. The kinetic energy part of Eq. [24] reduces to the usual $(2m)^{-1}(p_x^2 + p_y^2 + p_z^2)$, except that we have two components corresponding to the electron spin. In nonrelativistic theory, electron spin is incorporated into the Schrödinger equation in this fashion.

Klein–Gordon Equation

According to the special theory of relativity, all physical laws are postulated to be invariant in any inertial frame of reference. Furthermore, the equations of motion must be invariant under a Lorentz transformation,

$$x' = \frac{1}{(1 - v^2/c^2)^{1/2}}(x - vt) \tag{25}$$

$$t' = \frac{1}{(1 - v^2/c^2)^{1/2}}(t - vx/c^2) \tag{26}$$

where x is position, v is velocity, c is the speed of light, and t is time. Primes on the left-hand side indicate a different reference frame from the quantity without the prime. From these equations, it is clear that when a particle is traveling at a small fraction of the speed of light, that is, where the v^2/c^2 term is small, Eqs. [25] and [26] reduce to the classical Galilean transformation equations.

Another requirement in satisfying the special theory of relativity is to have the spatial and temporal variables being treated on the same footing. The differential operators in Lorentz invariant form are $\partial/\partial x$, $\partial/\partial y$, $\partial/\partial z$, and $(1/ic)\partial/\partial t$, giving the magnitude for spatial and temporal dimensions as $x^2 + y^2 + z^2 - c^2t^2$. This means that the order of the differentials for the coordinate and time in the equation of motion must be the same. The time-dependent Schrödinger equation exhibits time derivatives in the first order and coordinate derivatives in the second order; therefore it is not Lorentz invariant.

The classical relativistic energy of a free particle moving in space is given as

$$E = \sqrt{p^2c^2 + m^2c^4} \tag{27}$$

which relates rest mass and the kinetic energy of a particle. By using the relation $E \rightarrow i\hbar\partial/\partial t$ from the Schrödinger correspondence rule, and substituting it into the time-dependent Schrödinger equation, the relativistic quantum mechanical equation of a free particle may be written as

$$-\hbar^2 \frac{\partial^2 \psi(x,t)}{\partial t^2} = [p^2c^2 + m^2c^4]\psi(x,t) \tag{28}$$

This equation is called the Klein–Gordon equation. The Klein–Gordon equation satisfies the order of the differentials to be in the same order for space and time, and thus is Lorentz invariant. This equation, however, does not give rise to a positive definite density due in part to the second-order differential in time. Furthermore, for a fermion system, the Klein–Gordon equation is

not adequate since it contains no properties of spin that can be derived naturally.

Dirac Equation

Dirac was seeking an equation that is analogous to the Schrödinger equation, with a first-order derivative in time, and simultaneously satisfying the Lorentz invariance. He took a bold step: If the relativistic energy, the expression under the radical in the energy expression (Eq. [27]) or in the square bracket (Eq. [28]), is factored into a perfect square such that

$$E^2 = \mathbf{p}^2 c^2 + m^2 c^4 \rightarrow E = (\mathbf{p}c) + mc^2 \tag{29}$$

the Hamiltonian can then be expressed as

$$H_D = c\boldsymbol{\alpha} \cdot \mathbf{p} + \beta mc^2 \tag{30}$$

This is called the Dirac Hamiltonian. To obtain the correct mathematics, Dirac introduced parameters α and β. Then, by expanding out all terms in the four dimensions (originally thought of as spatial and temporal dimensions) the parameters, α and β, must anticommute and their squares must be unity. The choice of α and β must then be that

$$\alpha_1 = \begin{pmatrix} 0 & 0 & 0 & 1 \\ 0 & 0 & 1 & 0 \\ 0 & 1 & 0 & 0 \\ 1 & 0 & 0 & 0 \end{pmatrix} \quad \alpha_2 = \begin{pmatrix} 0 & 0 & 0 & -i \\ 0 & 0 & i & 0 \\ 0 & -i & 0 & 0 \\ i & 0 & 0 & 0 \end{pmatrix} \quad \alpha_3 = \begin{pmatrix} 0 & 0 & 1 & 0 \\ 0 & 0 & 0 & -1 \\ 1 & 0 & 0 & 0 \\ 0 & -1 & 0 & 0 \end{pmatrix} \quad \beta = \begin{pmatrix} 1 & 0 & 0 & 0 \\ 0 & 1 & 0 & 0 \\ 0 & 0 & -1 & 0 \\ 0 & 0 & 0 & -1 \end{pmatrix}$$

$$\tag{31}$$

Then, the time-dependent wave equation is, written as

$$i\hbar \frac{\partial \Psi(x,t)}{\partial t} = (c\boldsymbol{\alpha} \cdot \mathbf{p} + \beta mc^2)\Psi(x,t) \tag{32}$$

Therefore, the four components of the Hamiltonian must give rise to four components to the wave functions. The off-diagonal blocks of α_i above are the corresponding Pauli spin matrices (Eqs. [22], [23], and [21], respectively). Therefore, the four components of the wave function contain electron spin as a natural extension of the Klein–Gordon equation. Given these choices, the time-dependent wave equation for a free particle is rigorously Lorentz invariant. Furthermore, it turns out that the four-component Dirac equation gives rise to positive and negative eigenstates, and the two contain the electronic and positronic solutions, respectively.

For hydrogen and hydrogen-like atoms, the Dirac Hamiltonian must have the form,

$$H_D = c\alpha \cdot \mathbf{p} + \beta mc^2 + V \qquad [33]$$

where V is the interaction potential of an electron with a point nucleus. The relativistic correction to the interaction potential is small (order of $1/c^3$) and is usually ignored. If the potential contains electron–electron Coulombic interactions just as in a many-electron atom, the Hamiltonian is no longer Lorentz invariant; nonetheless, the Coulomb interaction is often used. The rationale for the molecular four-component Dirac calculation using the usual Coulomb interactions is that the magnitude of the Lorentz variance is of relatively small importance. Analogous to the Hartree–Fock method in nonrelativistic theory, the Dirac equation for many-electron systems can be cast into one-particle operators utilizing the antisymmetrized product functions. This type of theory is called Dirac–Fock (or Dirac–Hartree–Fock) theory.[27] More specifically, if a Coulomb potential is used, it is referred to as Dirac–Coulomb theory. In addition to single configuration theory, a multiconfigurational self-cosistent field (MCSCF) variant also exists.[28] Dynamical electron correlation can also be included in the calculations by CI, many-body perturbation theory, and coupled-cluster theory (CCSD).[29d,e]

The Coulomb interaction, however, can be corrected for relativistic constraints with approximate solution good to $1/c^2$. This so-called Breit interaction is given by[30]

$$V_{12}^{\text{Breit}} = \frac{1}{r_{12}} - \frac{1}{2r_{12}}\left[\alpha_1 \cdot \alpha_2 + \frac{(\alpha_1 \cdot \mathbf{r}_{12})(\alpha_1 \cdot \mathbf{r}_{12})}{\mathbf{r}_{12}^2}\right] \qquad [34]$$

where the first and second terms in the brackets on the right-hand side of Eq. [34] are known as the Gaunt interaction and retardation terms, respectively. Depending on the type of electron–electron interaction used in the calculations, the corresponding single configuration theory is called, Dirac–Breit or Dirac–Gaunt theory. Further details on these theories are reviewed in Ref. 29.

The eigenspectrum of the four-component Dirac equation is given by the positive and negative eigenstates centered at the quantity $\pm mc^2$. The positive energy solution is the electron solution, while the negative energy solution is for positrons. The wave functions associated with the Dirac equation contain four components, as mentioned earlier. For the positive energy (electronic) solution, two components are larger than the other two components. The two large components for the positive solution become the small component when solving for positron states. In the nonrelativistic limit, assuming the wave function to be hydrogen-like, the small component, Ψ_S, is shown[31] to be a small fraction of the large component, Ψ_L, by

$$\Psi_S \approx \frac{Z}{2c}\Psi_L \qquad [35]$$

For the solution to the electronic problem, the two components of the Dirac spinors are larger by a factor $Z/2c$, and a natural question to ask is whether there exists a separable solution to describe only electronic solutions. This question is addressed below.

Foldy–Wouthuysen Transformation

As described above, the nonrelativistic Pauli wave function consists of two component spinors. It would be of interest to see if the Dirac equation can be reduced to two-component equations since we are specifically interested in the solution to the electronic problem, particularly given that the small component of the Dirac functions are on the order of $Z/2c$. Furthermore, computational effort is much smaller in two-component solutions than in four-component solutions. The following derivation is due to Greiner.[26a]

Consider first a free particle case. The Dirac equation of a free particle can be written as

$$\begin{pmatrix} mc^2 & c\alpha \cdot \mathbf{p} \\ c\alpha \cdot \mathbf{p} & -mc^2 \end{pmatrix} \begin{pmatrix} \Psi_+ \\ \Psi_- \end{pmatrix} = E \begin{pmatrix} \Psi_+ \\ \Psi_- \end{pmatrix} \qquad [36]$$

where Ψ_+ and Ψ_- represent the wave functions corresponding to large and small components. If a transformation is performed such that the off-diagonal term in the transformed Hamiltonian becomes zero, Eq. [36] separates into large and small components. Foldy and Wouthuysen[32] devised a unitary transformation that results in the block diagonal form of the Dirac equation; therefore one can obtain a solution containing only the electronic components. The unitary operator for such a transformation has the form

$$U = e^{iS} \qquad [37]$$

and,

$$U^\dagger U = e^{-iS} e^{iS} = 1 \qquad [38]$$

For a free electron, if the S operator is chosen to have the following form in momentum space,

$$S = -\left(\frac{i}{2mc}\right) \beta\alpha \cdot \mathbf{p}\,\omega\left(\frac{p}{mc}\right) \qquad [39a]$$

where

$$\omega = \frac{mc}{p}\tan^{-1}\left(\frac{p}{mc}\right) \qquad [39b]$$

the free-particle Dirac Hamiltonian, Eq. [30], can then be shown to give

$$H_\phi = U^\dagger H_D U = e^{2iS}(c\alpha \cdot \mathbf{p} + \beta mc^2) \qquad [40]$$

By expanding e^{2iS} in a Taylor series and collecting the even and odd powers of the expansion terms, one can relate these terms to a trigonometric expansion, such that

$$e^{2iS} = \left(\cos\left(\frac{p}{mc}\omega\right) + \beta \frac{\alpha \cdot \mathbf{p}}{p} \sin\left(\frac{p}{mc}\omega\right) \right) \qquad [41]$$

Then, Eq. [40] can be shown to be exactly

$$H_\phi = \beta E_p \qquad [42]$$

where E_p is the free electron kinetic energy of Eq. [27].

In the presence of a Coulomb potential, there is no exact solution as we found for the free-particle case. By choosing a certain unitary operator, one can systematically reduce the coupling between the large and small components. The Hamiltonian is first decomposed into parts,

$$H = \beta mc^2 + \varepsilon + O \qquad [43]$$

where ε and O are the even and odd operators, and they are in general

$$\varepsilon = eV(r) \qquad [44]$$

$$O = c\alpha\left(p - \frac{e}{c}\mathbf{A}\right) \qquad [45]$$

where $\mathbf{A}$ is the vector potential. The exponential unitary operator, Eq. [37], is used here with the similar choice of S, given by

$$S = -\frac{i}{2mc^2}\beta O \qquad [46]$$

With this choice of the S operator, the unitary transformation is performed, such that

$$H' = U^\dagger H U = \left(1 + \frac{iS}{1!} + \frac{i^2 S^2}{2!} + \cdots\right) H \left(1 - \frac{iS}{1!} + \frac{i^2 S^2}{2!} - \cdots\right) \qquad [47]$$

Here the exponential operator is expanded in a power series. The transformed Hamiltonian can be written in terms of commutators in the usual sense, that is, $[a, b] = ab - ba$ (therefore, $[a, [b, c]] = [a, (bc - cb)] = abc - bca - acb + cba$), as,

$$H' = H + i[S, H] + \frac{i^2}{2}[S, [S, H]] + \frac{i^3}{3!}[S, [S, [S, H]]] + \cdots \qquad [48]$$

By expanding out the commutators up to the order $1/m^3c^6$, one finds

$$i[S, H] = -O + \frac{\beta O^2}{mc^2} + \frac{\beta}{2mc^2}[O, \varepsilon] \tag{49}$$

$$\frac{i^2}{2}[S, [S, H]] = -\frac{1}{2mc^2}\beta O^2 - \frac{1}{2m^2c^4}O^3 - \frac{1}{8m^2c^4}[O, [O, \varepsilon]] \tag{50}$$

$$\frac{i^3}{3!}[S, [S, [S, H]]] = -\frac{1}{6m^2c^4}O^3 - \frac{1}{6m^2c^4}\beta O^4 - \frac{1}{48m^3c^6}\beta[O, [O, [O, \varepsilon]]] \tag{51}$$

$$\frac{i^4}{4!}[S, [S, [S, [S, H]]]] \approx \frac{1}{24m^3c^6}\beta O^4 \tag{52}$$

By substituting the commutators, Eqs. [49]–[52], into Eq. [48] one arrives at

$$H' = \beta mc^2 + \frac{\beta O^2}{2mc^2} - \frac{\beta O^4}{8m^3c^6} + \varepsilon - \frac{[O, [O, \varepsilon]]}{8m^2c^4} + \frac{\beta[O, \varepsilon]}{2mc^2} - \frac{O^3}{3m^2c^4} - \frac{\beta[O, [O, [O, \varepsilon]]]}{48m^3c^6} \tag{53}$$

The next step is to further reduce the terms with odd powers of the O operators, which can be accomplished by another unitary transform using the S' operator,

$$S' = -\frac{i}{2mc^2}\beta O' \tag{54}$$

where O' is the odd powers of the O operators appearing in the transformed Hamiltonian H' (Eq. [53]) neglecting the last term due to large powers of $1/mc^2$, given as

$$O' = \frac{\beta[O, \varepsilon]}{2mc^2} - \frac{O^3}{3m^2c^4} \tag{55}$$

With the choice of S' the, Hamiltonian H' is transformed into H'' as

$$H'' = e^{iS'}H'e^{-iS'} = \beta mc^2 + \varepsilon' + \frac{\beta[O', \varepsilon']}{2mc^2} - \frac{O'^3}{3m^2c^4} \tag{56}$$

where ε' is ε plus the operators of even powers of O in H' (Eq. [53]). The last term containing O'^3 can be neglected because that term contains large powers of $1/mc^2$. Further reduction is achieved by another unitary transformation using

$$S'' = -\frac{i}{2mc^2}\beta O'' \tag{57}$$

where O'' contains the terms with odd powers of O in H'' (Eq. [56]). Then, one finally arrives at

$$H''' = \beta mc^2 + \varepsilon' = \beta mc^2 + \frac{\beta O^2}{2mc^2} - \frac{\beta O^4}{8m^3c^6} + \varepsilon - \frac{[O, [O, \varepsilon]]}{8m^2c^4} \tag{58}$$

The Hamiltonian H''' now contains only even powers of the O operators. When each term of the transformed Hamiltonian H''' is expanded, one obtains the so-called Breit–Pauli Hamiltonian.

For a many-electron system, one starts with the Breit equation, instead of Eq. [33]. The Breit equation includes the relativistic correction terms, Eq. [34], for electron–electron interactions, and is given as

$$\left(E - H_{Di} - \frac{e^2}{r_{ij}}\right)\Psi = -\frac{e^2}{2r_{ij}}\left[\alpha_i \cdot \alpha_j + \frac{(\alpha_i \cdot \mathbf{r}_{ij}) \cdot (\alpha_j \cdot \mathbf{r}_{ij})}{r_{ij}^2}\right]\Psi \qquad [59]$$

Here H_{Di} is the Dirac Hamiltonian for a single particle, given by Eq. [30]. Recall from above that the Coulomb interaction shown is not strictly Lorentz invariant; therefore, Eq. [59] is only approximate. The right-hand side of the equation gives the relativistic interactions between two electrons, and is called the Breit interaction. Here α_i and α_j denote Dirac matrices (Eq. [31]) for electrons i and j. Equation [59] can be cast into equations similar to Eq. [36] for the Foldy–Wouthuysen transformation. After a sequence of unitary transformations on the Hamiltonian (similar to Eqs. [37]–[58]) is applied to reduce the off-diagonal contributions, one obtains the Hamiltonian in terms of commutators, similar to Eq. [58]. When each term of the commutators are expanded explicitly, one arrives at the Breit–Pauli Hamiltonian, H^{BP}, for a many-electron system[33,34]

$$H^{BP} = \sum_{i=1}^{6} H_i^{BP} \qquad [60]$$

$$H_1^{BP} = \frac{e^2\hbar}{2m_e^2 c^2}\left[\sum_{i,a}\frac{Z_a}{r_{ia}^3}(\mathbf{r}_{i,a} \times \mathbf{p}_i) \cdot \mathbf{s}_i - \sum_{i,j\neq i}(\mathbf{r}_{ij} \times \mathbf{p}_i) \cdot (\mathbf{s}_i + 2\mathbf{s}_j)\right] \qquad [61]$$

$$H_2^{BP} = \frac{e^2\hbar}{2m_e^2 c^2}\sum_{i,j\neq i}\frac{|\mathbf{r}_{ij}|^2\mathbf{s}_i \cdot \mathbf{s}_j - 3(\mathbf{r}_{ij} \cdot \mathbf{s}_i)(\mathbf{r}_{ij} \cdot \mathbf{s}_j)}{|\mathbf{r}_{ij}|^5} - \frac{e^2\hbar}{2m_e^2 c^2}\frac{8\pi}{3}\sum_{i,j\neq i}\delta(r_{ij})\mathbf{s}_i \cdot \mathbf{s}_j \qquad [62]$$

$$H_3^{BP} = -\frac{e^2\hbar}{4m_e^2 c^2}\left[\sum_{i,a}\frac{Z_a}{|r_{ia}|^3}\mathbf{r}_{ia} \cdot \mathbf{p}_i - \sum_{i,j\neq i}\frac{1}{|r_{ij}|^3}\mathbf{r}_{ij} \cdot \mathbf{p}_i\right] \qquad [63]$$

$$H_4^{BP} = -\frac{e^2\hbar}{4m_e^2 c^2}\sum_{i,j}\left[\frac{\mathbf{p}_i \cdot \mathbf{p}_j}{|\mathbf{r}_{ij}|} + \frac{[\mathbf{r}_{ij} \cdot (\mathbf{r}_{ij} \cdot \mathbf{p}_j)\mathbf{p}_i]}{|\mathbf{r}_{ij}|^3}\right] \qquad [64]$$

$$H_5^{BP} = -\frac{1}{8m_e^3 c^2}\sum_i p_i^4 \qquad [65]$$

$$H_6^{BP} = \frac{e\hbar}{2m_e^2 c^2}\sum_i[(\mathbf{E}_i \times \mathbf{p}_i) \cdot \mathbf{s}_i] - \frac{ie\hbar}{4m_e^2 c^2}\sum_i(\mathbf{E}_i \cdot \mathbf{p}_i) + \frac{e\hbar}{mc}\sum_i(\mathbf{H}_i \cdot \mathbf{s}_i) \qquad [66]$$

The first term, H_1^{BP}, is the spin–orbit (one electron term) and spin–other-orbit (two electron term) couplings, which are the topic of the following subsection. The second term H_2^{BP} contains the spin–spin coupling term and Fermi contact interaction. Both the H_1^{BP} and H_2^{BP} can lift degeneracy in multiplets. The parameter H_3^{BP} is the Dirac correction term for electron spin and H_4^{BP} is the classical relativistic correction to the interaction between electrons due to retardation of the electromagnetic field produced by an electron. The parameter H_5^{BP} is the so-called mass-velocity effect, due to the variation of electron mass with velocity. Finally, H_6^{BP} is the effect of external electric and magnetic fields.

An alternative formulation[35] that one can use to obtain the Breit–Pauli Hamiltonian is to start with the Breit equation (Eq. [59]). The equation is first transformed by Fourier transformation to momentum space. The terms involving the positive and negative eigenstates into Pauli functions ψ_+ and ψ_- are then written, and only the electronic part of the equations is kept. Then, expanding the energy (in momentum space) in powers of p/mc, and Fourier transforming back to the coordinate space, one finally arrives at a differential equation of the form containing the Breit–Pauli Hamiltonian.

Breit–Pauli Hamiltonian

The most popular way in which nonscalar relativistic effects, such as spin–orbit coupling, are incorporated into molecular calculations, is to use the Breit–Pauli Hamiltonian. This approach is most convenient, because the relativistic effects under consideration can be added to the nonrelativistic Hamiltonian after the zeroth-order wave function is determined. By utilizing perturbation theory, or during the calculation of the electron correlation with procedures, such as MCSCF or CI, spin–orbit coupling matrix elements and associated wave functions can be calculated. Algorithm development utilizing the Breit–Pauli Hamiltonian in terms of perturbation theory have been discussed in detail by Langhoff and Kern,[33] Yarkony,[34] Furlani and King,[36] and Federov and Gordon.[37]

The scalar relativistic corrections of the Breit–Pauli Hamiltonian, H_3^{BP}, H_4^{BP}, and H_5^{BP}, gives rise to atomic properties such as core orbital contraction and *f*-orbital expansion observed in experiment, therefore affecting geometry in molecular calculations. However, the Breit–Pauli operators containing terms with higher powers of r^{-n} give a singularity near the nucleus which is, at least, "more" singular than the *1/r* term of Coulombic interaction. In many applications, however, particularly of molecules containing light elements, the singularity is generally avoided due to truncation of the basis set expansion to a finite set.

Z^{eff} Method

The first approximation method for the Breit–Pauli spin–orbit Hamiltonian is to neglect the contribution from the two-electron terms. Justification

for such an omission is that the two-electron terms are relatively small, at least for lighter elements. To compensate for the small error that is created by neglecting the two-electron term, the effective nuclear charge Z^{eff} is introduced.[38] The spin–orbit Hamiltonian is then given by

$$H^{\text{SO}} = \frac{\alpha^2}{2} \sum_i^{n_e} \sum_A^N \frac{Z_A^{\text{eff}}}{r_{iA}^3} \ell_{iA} \cdot s_i \qquad [67]$$

where α is the fine-structure constant, and Z_A^{eff} is the effective nuclear charge of the atom A. Koseki et al.[7,8,39] examined the magnitude of Z^{eff} for the main group elements systematically. They adjusted the Z^{eff} so that the fine-structure splitting of spectral terms of diatomic hydrides is reproduced by utilizing the MCSCF/SBKJC method. SBKJC uses the effective core potentials and the corresponding basis sets of Stevens et al.[40] The proposed equation for the effective nuclear charge is

$$Z^{\text{eff}} = Z \cdot f_k \qquad [68]$$

where $k = 1$–6, denotes the kth row of the periodic table. The parameters f_k for each row of the periodic table are determined to be

$$
\begin{aligned}
&f_1 = 1 && \text{for H} \\
&f_2 = 0.45 + 0.05m \\
&f_3 = 12 \\
&f_4 = 41 && (f_4 = 11 \text{ for Ga}) \\
&f_5 = 110 && (f_5 = 33 \text{ for In}) \\
&f_6 = 222 && (f_6 = 113 \text{ for Tl})
\end{aligned}
$$

Here m is the number of valence electrons.

The effective nuclear charge for transition metals[7] is determined from the atomic spectral terms[10] because few experimental data on diatomic transition metal hydrides are available (see e.g., Ref. 41). The effective nuclear charges determined for transition elements are given by

$$Z^{\text{eff}} = Z \cdot f_k^{\text{TM}} \qquad [69]$$

where

$$
\begin{aligned}
f_4^{\text{TM}} &= 0.385 + 0.025 && (m - 2) \\
f_5^{\text{TM}} &= 4.680 + 0.060 && (m - 2) \\
f_6^{\text{TM}} &= 13.960 + 0.140 && (m - 2)
\end{aligned}
$$

Here m is the number of electrons occupying the nd and $(n + 1)s$ orbitals in a neutral atom. The value of m can assume a number 1–9. The group 12 (IIB) elements, Zn, Cd, and Hg, have filled d orbitals, so that Z^{eff} values were determined to be in a different category. Even though the $3d$ SBKJC pseudo-orbitals are qualitatively similar to the correct $3d$ atomic orbitals, the $4d$ and $5d$ SBKJC pseudo-orbitals are nodeless and, as a result, large Z^{eff} values are given to the second- and third-row elements. Such large Z^{eff} values lose their physical meaning and are recognized as simply being empirical parameters. A similar approach has been taken by several authors in the past[11,38] for different systems, like carbon and silicon atoms, and used for atom–rare gas collisions.

Effective Core Potential-Based Method

Three key review articles exist that describe the derivation and utilization of the ECP method.[42–44] For a molecular system containing atoms of large Z, an all-electron calculation is a formidable task. Furthermore, for such molecules one must contend with scalar relativistic effects, such as the core-orbital contraction due to mass-velocity and Darwin terms that lead to geometry changes in molecules, in addition to spin–orbit coupling effects. The relativistic effective core potential replaces core electrons by a potential, but implicitly incorporates scalar relativistic effects through a fit of the core potential to the atomic Dirac–Fock results. For general applications, the relativistic effective potential is averaged over two spin states for a given l thereby averaging out the effect of spin–orbit coupling.[45,46]

The relativistic effective potential U^{REP} is the j (total angular momentum) dependent core potential fit to the large component of the Dirac four-component wave functions. The average relativistic effective potential U^{AREP} is the average relativisitic potential of the j states, given as

$$U_\ell^{AREP} = \frac{\ell U_{\ell,\ell-1/2}^{REP} + (\ell + 1)U_{\ell,\ell+1/2}^{REP}}{2\ell + 1} \qquad [70]$$

Because U^{AREP} is constructed from a potential fit to the Dirac four-component wave functions, it contains all relativisitic effects, except for spin–orbit coupling. The spin–orbit coupling operator for the effective core potential is then given as the difference between the relativistic effective potential, U^{REP}, and the averaged relativistic effective potential, U^{AREP},

$$H^{SO} = U^{REP} - U^{AREP} \qquad [71]$$

The spin–orbit operator can be shown to be

$$H^{SO} = \sum_{\ell=1}^{L-1} \Delta U_\ell^{REP}(r) \left[\frac{\ell}{2\ell+1} \sum_{-\ell-1/2}^{\ell+1/2} \left| \ell, \ell + \frac{1}{2}, m \right\rangle \left\langle \ell, \ell + \frac{1}{2}, m \right| - \frac{\ell+1}{2\ell+1} \cdot \right.$$

$$\left. \sum_{-\ell+1/2}^{\ell-1/2} \left| \ell, \ell - \frac{1}{2}, m \right\rangle \left\langle \ell, \ell - \frac{1}{2}, m \right| \right] \qquad [72]$$

where $\Delta U^{REP}(r)$ is given as

$$\Delta U_\ell^{REP}(r) = U_{\ell,\ell+1/2}^{REP} - U_{\ell,\ell-1/2}^{REP} \qquad [73]$$

The spin–orbit operator, Eq. [72], is constructed from the effective core potentials.

    The spin–orbit coupling is incorporated into the calculations at the post-Hartree–Fock level, particularly with CI. This is generally referred to as spin–orbit CI. The core potential and associated basis sets for Li–Kr, including the spin–orbit operator, have been published.[47–50] Implementation of the spin–orbit CI method has been discussed by Pitzer and co-workers.[51–53] It has also been reported that the spin–orbit CI code has been adapted to a parallel computing enviroment.[54]

Model Core Potential-Based Method

    Model core potential (MCP) methods[55] replace core orbitals by a potential just as in ECP. On the other hand, MCP valence orbitals preserve the nodal structure of valence orbitals, unlike ECP valence orbitals. The expectation values of $\langle r^{-3} \rangle$ for the valence orbitals show that the results of MCP are closer to those calculated with all-electron orbitals when comparing MCP, ECP, and the all electron case.[56] Comparisons between MCP and an all electron basis utilizing the full Breit–Pauli spin–orbit Hamiltonian based on multiconfigurational quasidegenerate perturbation theory (MCQDPT) calculations show good agreement between the two methods for hydrides of P, As, and Sb.[57] The MCP based spin–orbit calculation appears to be a promising technique, but systematic studies of many different molecular systems are still needed to assess its characteristics and accuracy.

Douglas–Kroll Transformation

    The singularity that may arise when using the Breit–Pauli Hamiltonian can cause instability in variational calculations and it is desirable that such singularity be avoided formally. Douglas and Kroll[58] showed that the singularity

is eliminated if certain successive unitary transformations are applied to reduce off-diagonal contributions to the Dirac equation, thus separating electronic and positronic solutions, in analogy to the Foldy–Wouthueysen transformation. The first step is to apply the free-particle Foldy–Wouthuysen transformation using a unitary operator of the form,

$$U_0 = A_i(1 + \beta R_i) \tag{74}$$

where

$$A_i = \sqrt{\frac{E_i + mc^2}{2E_i}} \tag{75}$$

$$R_i = \frac{c\alpha \cdot \mathbf{p}}{E_i + mc^2} \tag{76}$$

and E_i is the free-particle relativistic energy (Eq. [27]). The transformed Hamiltonian, H_1, is given as

$$H_1 = U_0^\dagger H_D U_0 = \beta E_i + \varepsilon_1 + O_1 \tag{77}$$

where

$$\varepsilon_1 = A_i(V + R_i V R_i)A_i \tag{78}$$
$$O_1 = \beta A_i[R_i, V]A_i \tag{79}$$

Again, here ε and O are even and odd operators, respectively, as we have seen in the Foldy–Wouthuysen transformation. The next step is to choose other unitary operators and apply them successively such that

$$H^{DK} = \cdots U_4^\dagger U_3^\dagger U_2^\dagger H_1 U_2 U_3 U_4 \cdots \tag{80}$$

where U_n are unitary operators that correspond to the order of the successive operation. The successive unitary transformation expands the Hamiltonian in ascending order in the external potential V such that the odd terms are successively smaller. The form of the unitary operator can be chosen from a number of possible operators, such as

$$U_n = (1 + W_n^2)^{1/2} + W_n \tag{81}$$
$$U_n = e^{W_n} \tag{82}$$

where W_n is an anti-Hermitian operator for the nth successive application. The original transformation utilizes Eq. [81] as the second unitary transformation; however, for the second-order transformation applying either of Eqs. [81] or [82] yields the same Hamiltonian. More recently,[59] it has been shown that Eq. [82] can be used to obtain a higher order transformation, exploiting

the exponential expansion of anti-Hermitian operators cast into commutator forms, as seen above for transforming Eq. [47] into Eq. [48]. Other closely related approaches have been explored by Dyall.[60]

In most current applications of the Douglas–Kroll transformation, the Hamiltonian is truncated at second order in the successive unitary transformation, that is, $H^{DK2} = U_2^\dagger H_1 U_2$, and the resulting Hamiltonian can be written in terms of spin-free and spin-dependent components,

$$H^{DK2} = U_2^\dagger H_1 U_2 = \sum_i (E_i + V_i^{eff}) + \sum_{i \neq j} V_{ij}^{eff} + \sum_i H_i^{SO} + \sum_{i \neq j} H_{ij}^{SO} \quad [83]$$

where the summation terms are one-electron spin-free, two-electron spin-free, one-electron spin–orbit, and two-electron spin–orbit terms, respectively. The effective potentials for spin-free terms are given by

$$V_i^{eff} = A_i[V + R_i V R_i]A_i - \frac{1}{2}\{\{E_i, W_1\}, W_1\} \quad [84]$$

$$V_{ij}^{eff} = A_i A_j \left[\frac{e^2}{r_{ij}} + R_i \frac{e^2}{r_{ij}} R_i + R_j \frac{e^2}{r_{ij}} R_j + R_i R_j \frac{e^2}{r_{ij}} R_i R_j \right] A_i, A_j \quad [85]$$

and where

$$W_1 = A_i(Q_i - Q_i')A_i' \frac{V(\mathbf{p}_i, \mathbf{p}_i')}{E_i - E_i'} \quad [86]$$

Here, Eq. [86] is an integral equation with a kernel, and $V(\mathbf{p}_i, \mathbf{p}_i')$ is the potential energy operator in momentum space. The curly bracket in Eq. [84] denotes the anticommutator, where $\{a, b\} = ab + ba$. Implementation of the spin-free part of the Hamiltonian is generally given only to the one-electron term, Eq. [84], and for electron–electron repulsion[61] is usually ignored. Incorporation of the DK Hamiltonian to existing electronic structure theory code is then relatively straightforward by adding one new type of one-electron integral (all others can be obtained from the existing nonrelativistic code).[62]

The spin-dependent part of Eq. [83] is the one-electron and two-electron spin–orbit operators,

$$H_i^{SO} = e^2 Z_a \frac{A_i}{E_i + mc^2} \sigma_i \left(\frac{\mathbf{r}_{i\alpha}}{r_{i\alpha}^3} \times \mathbf{p}_i \right) \frac{A_i}{E_i + mc^2} \quad [87]$$

$$H_{ij}^{SO} = -e^2 \frac{A_i A_j}{E_i + mc^2} \left(\frac{\mathbf{r}_{ij}}{r_{ij}^3} \times \mathbf{p}_i \right) \cdot (\sigma_i + 2\sigma_j) \frac{A_i A_j}{E_i + mc^2} \quad [88]$$

The spin–orbit operators in the Douglas–Kroll Hamiltonian still contain the $1/r^3$ term; however, that term is offset by the $1/(E_i + mc^2)$ term, where as

$r_i \rightarrow 0$, $p_i \rightarrow \infty$. Therefore, the spin–orbit operators in the Douglas–Kroll Hamiltonian are stable in the variational calculations.

The spin-free Douglas–Kroll Hamiltonian has been implemented in publically available electronic structure codes,[63] and has been utilized for computing properties of molecules containing heavy atoms. Electron correlation can be evaluated once the spin-free DK orbitals are formed, just as in nonrelativistic post-Hartree–Fock methods, with only small modification to the code. For example, coupled cluster theory has been implemented as a post-DK method.[64] Furethermore, the spin-free ab initio model core potential (AIMP),[65] based on the DK3 Hamiltonian, has been developed for the actinide elements by Paulovic et al.[66] On the other hand, the spin-dependent Douglas–Kroll Hamiltonian has been implemented only in a few codes, and therefore the utility of the formalism is currently limited in scope. Hess et al.[25] reviewed their results on transition metal containing diatomics and small polyatomic molecules. Their work is one of only a few studies carried out for DK spin–orbit coupling. Fedorov, Nakajima, and Hirao used the DK3 spin-free Hamiltonian and the one-electron spin–orbit DK Hamiltonian plus the two-electron Breit–Pauli spin–orbit operator to investigate the uranium atom and uranium fluoride.[67]

The treatment of spin–orbit coupling can be incorporated into molecular calculations in the form of atomic mean-field spin–orbit integrals (AMFI).[68] Because the method is a mean-field approach, the original formulation was limited to spin–orbit splitting in a single state. Later, MCSCF methodology in the framework of a restricted active space was used to obtain interstate spin–orbit coupling, thereby enabling examination of coupling between states of different spins.[69]

New transformation formalisms for obtaining two component equations are currently being investigated and being applied to atomic systems.[70] Such studies and others[71] together with implementation of the Douglas–Kroll spin–orbit Hamiltonian, give special importance to this active field of relativistic quantum chemistry.

POTENTIAL ENERGY SURFACES

The potential energy surfaces of two states of different symmetry and spin can cross in $N^{int} - 1$ dimensions, where N^{int} is the number of internal coordinates (one coordinate as a constraint to have the same energy). Therefore, in general, the potential energy crossing forms a hypersurface as described earlier in this chapter. A priori determination of the MEXP on the hypersurface is highly desirable through analytical gradient techniques by analogy to locating a transition state in adiabatic reactions. In what is to follow, minimum energy crossing point location algorithms are discussed.

Minimum Energy Crossing-Point Location

A procedure for locating a minimum energy crossing point between two potential energy surfaces closely follows the geometry optimization techniques available in most modern electronic structure theory codes.[2b] In essence, a stationary point is searched by means of an iterative Newton–Raphson procedure whereby the knowledge of gradients and the Hessian at a current point of evaluation gives a displacement vector to which the next evaluation of the gradient and Hessian is to be carried out. For an adiabatic potential energy surface, the potential energy is expanded in a Taylor series to the linear term; the linear Newton–Raphson equation is then obtained

$$g^I(R)\delta R = -E^I(R) \tag{89}$$

Here, $g^I(R)$ is the gradient evaluated at nuclear coordinate R, and $E^I(R)$ is the Ith state energy. Given the fact that the gradient itself can also be expanded in a Taylor series, one can utilize the recursion to obtain the more familiar quadratic Newton–Raphson equation,

$$Q^I(R)\delta R = -g^I(R) \tag{90}$$

where $Q^I(R)$ is the Hessian and $g^I(R)$ is the gradient evaluated at the current point R. At convergence, the predicted displacement δR meets a preset convergence criterion. Instead of calculating the Hessian at every iteration, various Hessian updating procedures can be used to avoid relatively expensive Hessian calculations.[1a]

Koga and Morokuma[72] treated the MEXP search as a constrained optimization. In their Lagrange multiplier method, the energy of the Ith state, $E^I(R)$, is minimized with a constraint that the energy difference between two states, I and J, becomes zero. The Lagrangian is written as

$$L(R,\lambda) = E^I(R) + \lambda[E^I(R) - E^I(R)] \tag{91}$$

The Lagrangian is expanded in a Taylor series, analogous to Eq. [90] above, and one obtains the Newton–Raphson equation for the Lagrangian,

$$\begin{pmatrix} Q^{IJ}(R,\lambda) & g^{IJ}(R) \\ g^{IJ}(R) & 0 \end{pmatrix} \begin{pmatrix} \delta R \\ \delta \lambda \end{pmatrix} = -\begin{pmatrix} g^I(R) + \lambda g^{IJ}(R) \\ \Delta E^{IJ}(R) \end{pmatrix} \tag{92}$$

where $Q^{IJ}(R)$ is the Hessian of the Lagrangian and is given by

$$Q^{IJ}(R,\lambda) = Q^I(R) - \lambda[Q^I(R) - Q^J(R)] \tag{93}$$

In addition, $g^{IJ}(R)$ is the difference gradient,

$$g^{IJ}(R) = g^I(R) - g^J(R) \qquad [94]$$

and

$$\Delta E^{IJ}(R) = E^I(R) - E^J(R) \qquad [95]$$

Yarkony[73,1b] has extended the Lagrange multiplier method and derived the Newton–Raphson equations. One of the extensions is to give geometry constraints so that a crossing point is located with, for example, a bond length kept constant; this is analogous to the familiar constrained geometry optimization technique in single-surface calculations. Other extensions deal with locating conical intersections and avoided crossing points for two states of the same symmetry and spin (internal conversion process), which require calculations of nonadiabatic coupling matrix elements. The Lagrange multiplier for such a process corresponds to the two states being orthogonal to each other. The Lagrangian, including the orthogonality and geometry constraints, is given by

$$L(R, \lambda, \xi) = E^I(R) + \lambda_1 \Delta E^{IJ}(R) + \lambda_2 H^{IJ}(R) + \sum_{k=1}^{M} \xi_k C_k(R) \qquad [96]$$

The last two terms are the orthogonality and geometry constraints. The Newton–Raphson equations derived from the Lagrangian (Eq. [96]) are given by

$$
\begin{pmatrix}
Q^{IJ}(R, \lambda, \xi) & g^{IJ}(R) & h^{IJ}(R) & k^{IJ}(R) \\
g^{IJ}(R) & 0 & 0 & 0 \\
h^{IJ}(R) & 0 & 0 & 0 \\
k^{IJ}(R) & 0 & 0 & 0
\end{pmatrix}
\begin{pmatrix}
\delta R \\
\delta \lambda_1 \\
\delta \lambda_2 \\
\delta \xi
\end{pmatrix}
$$
$$
= -\begin{pmatrix}
g^I(R) + \lambda_1 g^{IJ}(R) + \lambda_2 h^{IJ}(R) + \sum_i \xi_i k_i(R) \\
\Delta E_{IJ}(R) \\
0 \\
C(R)
\end{pmatrix} \qquad [97]
$$

where $Q^{IJ}(R, \xi, \lambda)$ is the Hessian matrix of the Lagrangian with respect to the variables in parentheses and is similar to Eq. [93], $g^{IJ}(R) = g^I(R) - g^J(R)$, is the difference gradient as before, $h^{IJ}(R)$ is related to the derivative coupling due to the orthogonality condition, and $C(R)$ are the values of the geometry constraint. The $k_i(R) = \partial C_i / \partial R$, and the λ_1, λ_2, and ξ_i are the

Lagrange multipliers corresponding to energy, orthogonality, and geometry constraints, respectively. In the case of spin-forbidden reactions, the terms derived from $\lambda_2 H^{IJ}(R)$ in Eq. [96] should be neglected, and one should use the 3×3 matrix form.

Another closely related approach for locating the MEXP is a direct optimization of the stationary point of the crossing surface. The following effective gradients[3,74] vanish at the MEXP.

$$f_\perp = \Delta E^{IJ}(R) g^{IJ}(R) \tag{98}$$

$$f_\parallel = g^I(R) - \frac{g^{IJ}(R)}{|g^{IJ}(R)|} \left[g^I(R) \cdot \frac{g^{IJ}(R)}{|g^{IJ}(R)|} \right] \tag{99}$$

These components of the effective gradients consist of the gradient component that is perpendicular and parallel to the direction of the $N^{int} - 1$ crossing surface. The term $g^{IJ}(R)/|g^{IJ}(R)|$ is normal to the crossing surface. The Newton–Raphson iterative procedure, Eq. [90], is used to locate the MEXP.

The level of electronic structure theory required to locate the MEXP depends on the problem at hand. If the MEXP is found on the repulsive part of the potential energy surface of one state, the calculated MEXP becomes highly sensitive to the level of theory because a small change in geometry causes the energy to change by large amounts. Hence, the dynamical electron correlation must be incorporated via various methods in searching for the MEXP. Furthermore, it is desirable that the molecular orbitals describing the two states are determined from a set of orbitals that are common to both states under examination. Taking these considerations into account, both the dynamical and nondynamical electron correlation may become important in order to describe the MEXP correctly, in addition to subsequent determination of spin–orbit coupling. In this respect, the second-order CI based on the state averaged-MCSCF wave functions (SA–MCSCF/SOCI method) proposed and utilized by Yarkony[1b] are the best methods available. As seen in the derived Newton–Raphson equations above, analytical gradients are highly desirable for calculating the MEXP. Unfortunately, the gradients of SA–MCSCF are difficult to implement and most of the publicly or commercially available electronic structure theory programs do not have such capability. In addition, the SA–MCSCF/SOCI method is computationally demanding and compromising methods may be needed, particularly when dealing with relatively large molecules.

Harvey et al. proposed a hybrid method for calculating the effective gradients (Eqs. [98] and [99]) by approximating the difference gradients at lower level of theory from the evaluation of the energy term.[75] For the approximation to work, the force fields of the two states calculated at a higher level of theory must be equal to those calculated at a lower level of theory. In cases that Harvey et al. have examined, they have shown that the approximation is reliable.

AVAILABLE PROGRAMS FOR MODELING SPIN-FORBIDDEN REACTIONS

A significant amount of research has been directed toward understanding the basic principles and fundamental concepts associated with spin-forbidden reactions. Some of that body of work has been incorporated into software that is available for public use. Here we list several such programs that may be of use to the readers.

General Atomic and Molecular Electronic Strucutre System (GAMESS)[76]

GAMESS is a multipurpose, multifunction electronic structure code, developed by Gordon and his colleagues at Iowa State University. This package can perform quantum chemical calculations that include single reference Hartree–Fock, MCSCF, CI, many-body perturbation theory (MBPT) methods, and quasidegenerate perturbation theory (QDPT) based on MCSCF functions (MCQDPT). Some of these methods can use an analytical gradient and provide a Hessian so that stationary point evaluation including vibrational frequencies can be computed. Of relevance to spin-forbidden reaction calculations is that GAMESS can perform three different types of Breit–Pauli Hamiltonian derived calculations: (1) The effective nuclear charge approximation, Z^{eff}, using all-electron and SBKJC ECP and its basis sets, (2) full Breit–Pauli with all-electron basis, and (3) full Breit–Pauli with model core potential. In addition, the Newton–Raphson MEXP search algorithm utilizing Eqs. [98] and [99] has also been implemented.

Columbus[77]

Columbus is also a multipurpose multifunction electronic structure code, developed mainly by the Shavitt and Pitzer groups at Ohio State University. The strength of *Columbus* is in multireference calculations, which include MRCI and MRCC approaches. A specialized and modified program, called CIDBG, is capable of performing spin–orbit CI using relativistic ECP. This program has been implemented for massively parallel environments.[55]

In addition to these all-purpose programs, script-driven MEXP search routines have been written by several groups.[75,78] These programs utilize shell scripts to prepare input files and execute electronic structure codes of choice, given a gradient code, regardless of whether it is numerical or analytical gradients that are available. Upon finishing the calculations, these programs extract data from the output file of the electronic structure calculations, and subsequently calculate the displacement vector for the next iteration of the search.

Four-Component Programs

DIRAC[79] is a relativistic quantum chemistry code for solving Dirac–Fock calculations based on a Dirac–Coulomb Hamiltonian. It is capable of

post-Hartree–Fock methods including MP2 and CCSD. Analytical gradients are available for Dirac–Fock and numerical gradients are available for correlated calculations.

MOLFDIR[80] is also a relativistic quantum chemistry code for solving Dirac–Fock theory. Post-Dirac–Fock capability includes CI and CCSD(T) and it is also adaptable to general contraction basis sets. It uses the MPI library for parallel processing.

Other programs that solve the Dirac–Fock equations include *BERTHA*[81] and *REL4D*.[82]

APPLICATIONS TO SPIN-FORBIDDEN REACTIONS

Diatomic Molecules

There have been many calculations performed on diatomic molecules that include spin–orbit coupling. Hess, Marian, and Peyerimhoff have reviewed[25] calculations of transition metal containing diatomic molecules using their Douglas–Kroll spin–orbit operators. A compilation of relativistic ECP-based spin–orbit CI calculations for transition metal containing diatomics is given by Balasubramanian.[83] More recent diatomic molecules that have been studied include BH,[84] N_2^-,[85] HI and DI,[86] TeH and TeLi,[87] HCl$^+$ and HBr$^+$,[88] and IO.[89]

For illustrative purposes, MgBr potential energy curves calculated by Sadygov et al.[90] are presented in Figure 7. This example is not a spin-forbidden reaction; however, it is a dramatic example of the heavy atom effect. In the absorption spectra for the transition $X^2\Sigma^+ \to A^2\Pi$, the vibrational structure for $A^2\Pi_{3/2}$ up to $v = 3$ is observed, while for the lower component $A^2\Pi_{1/2}$ up to $v = 5$ is observed. In addition predissociation starts at lower vibrational levels of $A^2\Pi_{3/2}$ ($v = 1$) and $A^2\Pi_{1/2}$ ($v = 2$) in laser-induced fluorescence experiments. The $A^2\Pi$ state is predominantly ionic in character, Mg$^+$Br$^-$, and consequently the spin–orbit splitting should be relatively small. The authors examined the A state predissociation by obtaining the potential energy curves for the $X^2\Sigma^+$ and the lowest two $^2\Pi$ states (denoted as $1,2\,^2\Pi$), transition dipole moments, nonadiabatic coupling matrix elements between the $1,2\,^2\Pi$ states, and spin–orbit coupling. The electronic structure calculations start with the SA–MCSCF averaging $X^2\Sigma^+$ and $1,2\,^2\Pi$ states, using active orbitals consisting of Mg $3s^2 3p^0$ and Br $4p^5$. The basis set used was triple zeta plus double polarization and a set of diffuse p functions. The SA–MCSCF calculation was followed by second-order CI to obtain potential energy curves of the three states, as well as nonadiabatic coupling matrix elements between the $^2\Pi$ states and full Breit–Pauli spin–orbit coupling.
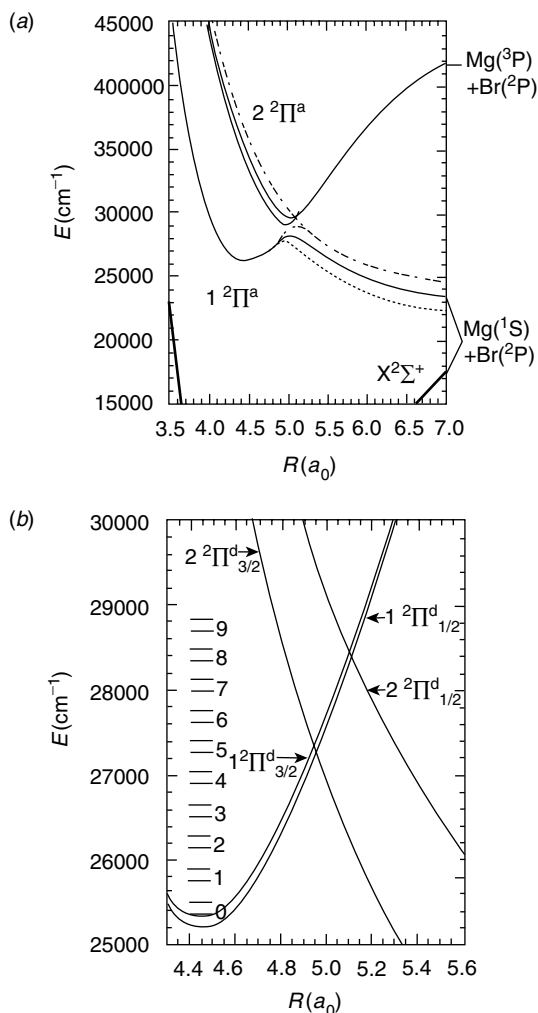
Figure 7 Potential energy curves of low-lying $^2\Pi$ states of MgBr. (*a*) Adiabatic potential energy curves. Solid lines indicate potentials without spin–orbit contribution, and dashed lines are the potentials with spin–orbit coupling. (*b*) Diabatic potential energy curves and energy levels of diabatic $1^2\Pi_{1/2}$ and $1^2\Pi_{3/2}$ states. Calculations are done at the SA-MCSCF/SOCI + full Breit–Pauli level. [Reproduced from Ref. 91 with permission.]

Figure 7*a* shows a part of the calculated adiabatic potential energy curves (solid lines), and the curves with spin–orbit coupling incorporated (dashed lines). The two $^2\Pi$ states show an avoided crossing at an internuclear distance of 5 a_0. It is interesting to see that the $1^2\Pi$ state shows only small spin–orbit splitting until the avoided crossing region, while the spin–orbit coupling

becomes larger at larger internuclear distances, approaching the $^2P_{3/2} -^2 P_{1/2}$ asymptotic limit of Br. The two $^2\Pi$ adiabatic states are transformed into a diabatic basis by unitary transformation so that the interstate coupling in the diabatic basis becomes a local quantity. Also, each potential becomes distinctly one-character; one becomes ionic and another becomes covalent.[91]

Figure 7b shows the diabatic $^2\Pi$ states, labeled with superscript d, along with the $J = \frac{3}{2}$ and $\frac{1}{2}$ states including their vibrational levels for $1^2\Pi^d$. As can be seen, the $1^2\Pi^d$ shows relatively small spin–orbit splitting compared to the $2^2\Pi^d$ state, where the crossing points of two diabatic states are separated by at least three vibrational levels. This is the origin of the difference in the vibrational signature of the predissociation in the A state.

Spin–orbit coupling can be incorporated into nuclear dynamics as off-diagonal elements of the Hamiltonian matrix containing two or more potential energy curves. The wave function in the form of a wavepacket can then be propagated in time by means of the time-dependent Schrödinger equation. For example, Regan et al.[92] studied the photodissociation dynamics of HCl using the potential and spin–orbit coupling calculated by Alexander et al.[93] to examine the effect of internal vibrational excitation in the ground state on photodissociative branching between the $^2P_{3/2}$ and $^2P_{1/2}$ states of Cl atom. They used the Chebychev time evolution operator[94] to solve the time-dependent Schrödinger equation, utilizing an absorbing boundary condition[95] and a fast Fourier transform method.[96] By calculating the branching fraction, the ratio of cross-section of Cl* product to the sum of cross-sections of Cl and Cl* products, the authors were able to correlate experimental and theoretical results qualitatively.

Polyatomic Molecules

Geometries and Energetics of MEXP

The best electronic structure method for obtaining the MEXP and spin–orbit coupling in a consistent manner is to carry out SA–MCSCF calculations followed by second-order CI. By mixing wave functions of the two states of interest, a common set of orbitals can be generated that are mutually orthonormal and simultaneously satisfy possible near degeneracy problems, without resorting to constructing a common set by the corresponding orbitals.[97] The SA–MCSCF method gives a well-behaved starting point for the subsequent electron correlation and spin–orbit coupling calculations. Only a few codes exist[98] for analytical evaluation of CI gradients based on the SA–MCSCF orbitals. Furthermore, the electron correlation using second-order CI can become computationally demanding for larger molecular species with large basis sets and large active space. Computationally, less expensive methods are desirable for computing MEXP and perhaps spin–orbit coupling.

Most methods available to quantum chemists are adaptable for finding the location of the MEXP. For example, consider singlet–triplet intersystem

Table 2 Geometries of Singlet CH_3ON Calculated at Various Level of Theory[a]

Method	R(O–N)	R(O–C)	(N–O–C)	R(C–H)
RHF	1.228	1.440	117.9	1.080
UHF	1.228	1.440	117.9	1.081
RMP2	1.240	1.487	116.7	1.088
UMP2	1.240	1.487	116.7	1.089
RB3LYP	1.224	1.563	117.1	1.088
UB3LYP	1.240	1.532	117.4	1.089
RQCISD	1.246	1.494	116.8	1.090
UQCISD	1.246	1.494	116.8	1.090
BLYP	1.173	1.998	119.2	1.090
BVWN	1.171	2.054	119.9	1.085
GLYP	1.172	1.988	120.1	1.090
PBELYP	1.174	1.978	119.5	1.092
PBEOP	1.173	2.008	119.9	1.092

[a]The 6-311G(d,p) basis set used for all cases.

crossing in methyl-O-nitrene (CH_3ON), suspected to be an important reactive intermediate in the generation of NO from diamine diolate as an antineoplastic agent.[99] Tables 2–4 show the geometries of the singlet, triplet, and the MEXP of CH_3ON, respectively, calculated at various levels of theory and using the 6-311G(d,p) basis set in all cases. The geometry calculated for the singlet and triplet states is what is expected of the given method. The RHF method performs quite well for the singlet-state geometry when compared with the highly correlated method such as QCISD. Several different DFT functionals are also compared in Tables 2–4. While the B3LYP functional performs well for the singlet state, the other functionals appear to be less virtuous. For the triplet state, all methods including all DFT functionals agree relatively well. However, for the MEXP, all HF and DFT methods, except B3LYP, perform poorly compared to the values obtained with the QCISD calculations.

Table 3 Geometries of Triplet CH_3ON Calculated at Various Level of Theory[a]

Method	R(O–N)	R(O–C)	(N–O–C)	R(C–H)
UHF	1.301	1.424	114.8	1.081
ROHF	1.303	1.423	114.7	1.082
UMP2	1.313	1.446	112.9	1.090
UB3LYP	1.311	1.454	114.5	1.090
UQCISD	1.322	1.446	113.1	1.092
BLYP	1.331	1.484	115.2	1.095
BVWN	1.333	1.492	115.5	1.090
GLYP	1.329	1.480	115.4	1.094
PBELYP	1.329	1.482	115.2	1.096
PBEOP	1.331	1.485	115.2	1.096

[a]The 6-311G(d,p) basis set used for all cases.

Table 4 Geometries of the MEXP of CH_3ON Calculated at Various Level of Theory[a]

Method	R(O–N)	R(O–C)	(N–O–C)	R(C–H)
RHF/UHF	1.004	1.600	113.9	1.138
UHF/UHF	1.004	1.600	114.0	1.138
RHF/ROHF	1.057	1.698	115.2	1.094
RMP2/UMP2	1.174	1.656	117.3	1.090
UMP2/UMP2	1.174	1.657	117.2	1.090
RB3LYP/UB3LYP	1.174	1.734	118.4	1.087
UB3LYP/UB3LYP	1.174	1.734	118.3	1.087
RQCISD/UQCISD	1.183	1.714	117.6	1.090
UQCISD/UQCISD	1.183	1.714	117.6	1.090
BLYP	1.226	1.701	118.5	1.092
BVWN	1.230	1.713	118.7	1.087
GLYP	1.220	1.717	118.7	1.091
PBELYP	1.228	1.678	118.2	1.094
PBEOP	1.232	1.680	118.4	1.094

[a]The 6-311G(d,p) basis set used for all cases.

As expected, the restricted versus unrestricted HF wave functions give essentially the same results for the singlet state. The same conclusion can be drawn for the MEXP search *in this particular example*. Overall, optimization of the MEXP geometry must incorporate electron correlation; MP2 methods perform quite well for obtaining geometric parameters for intersystem crossing. Furthermore, the B3LYP functional also performs equally well in MEXP geometry searches. It is interesting to note that the geometry of the MEXP is closer to the singlet state, which is the higher energy state of the two compared.

Table 5 shows the singlet–triplet energy gap and the energies of the MEXP. The calculated energy differences are with respect to the singlet state. The energetics calculated with the HF and DFT, except B3LYP, methods give quite poor results, as shown in Table 5. As with geometry, it is essential to include electron correlation in order to accurately determine the energetics of the MEXP as well as to predict the singlet–triplet energy gap. The MEXP is energetically closer to the singlet state by several kcal/mol at the QCISD level. Again, the MP2 and B3LYP methods perform well in comparison to QCISD. The restricted versus unrestricted wave functions in the HF methods do not give substantially different results for energies, as seen for geometries. This is an important point to stress since the RHF based method, particularly for RHF and RHF-based MP2, should perform poorly as a bond is stretched (RHF eventually converges to the ionic asymptote and perturbation theory breaks down due to near degeneracy). However, for the problem at hand RHF and UHF based wave functions give essentially the same results, because the MEXP is located energetically close to the singlet state, as seen in Table 5. The ground state of CH_3ON is a triplet state, and the MEXP is found close to the first excited state, which is the closed-shell singlet state. Hence, the RHF wave function is reliable for this example.

Table 5 Singlet–Triplet Energy Gap and Energies of the MEXP of CH_3ON^a

Method	ΔE_{S-T}	ΔE_{MEXP}
RHF/UHF	−39.1	80.6
UHF/UHF	−39.1	80.6
RHF/ROHF	−32.9	80.6
RMP2/UMP2	−15.4	4.4
UMP2/UMP2	−15.4	4.4
RB3LYP/UB3LYP	−16.6	−0.8
UB3LYP/UB3LYP	−16.0	1.5
RQCISD/UQCISD	−16.5	3.4
UQCISD/UQCISD	−16.5	3.4
BLYP	−5.4	2.4
BVWN	−3.9	3.3
GLYP	−6.6	2.1
PBELYP	−4.6	2.6
PBEOP	−3.8	3.1

^{a}The methods used for calculations are denoted as "A/B", where A is for the singlet state and B for the triplet state. For the DFT functionals, BLYP to PBEOP (last five rows) only the restricted calculations for the singlet and unrestricted calculations for the triplet states were performed. The calculated energetics is with respect to respective singlet state energies. All calculations were performed with the 6-311G(d,p) basis set.

For larger polyatomic molecules, many more degrees of freedom exist giving rise to flexibility in crossing. In comparing HON and C_6H_5—ON, in which the ground states are the triplet states, $\Delta E_{S-T} = -21.8$ and -17.4 kcal/mol, respectively. The MEXP lies 11.8 and 1.1 kcal/mol higher than the corresponding singlet states at the MP2/6-311G(d,p) level of theory (the zeroth-order functions are RHF for singlet and UHF for triplet). These results indicate that the higher the number of degrees of freedom the closer in energy the MEXP is to the higher energy of the two states in question. Therefore, the effective barrier toward spin-forbidden reaction is lower in larger polyatomic molecules resulting in facile intersystem crossing.

Phenyl Cation

Intersystem crossing in the phenyl cation was examined by Harvey et al.[75] The aforementioned hybrid method utilizing Eqs. [98] and [99] was used to locate the MEXP between singlet and triplet states at various levels of theory with the 6-31G(d) basis set. A comparison was made between HF//HF, B3LYP//HF, B3LYP//B3LYP B3LYP//HF, and CCSD(T)//B3LYP, where the double-slashes delineate the higher level (energy calculation) and lower level (gradient calculation) in the hybrid method. The singlet state of the phenyl cation is the ground state, and the triplet state lies 19 kcal/mol

above the singlet using the CCSD(T)/6-31G(d) energy at the B3LYP/6-31G(d) optimized geometry. By using the CCSD(T)//B3LYP method, the MEXP was found to be only 0.2 kcal/mol above the triplet state. If B3LYP/6-31G(d) is used for the optimization, the singlet–triplet energy gap is 16.4 and the MEXP is 0.3 kcal/mol above the triplet state. The geometry of the MEXP calculated with the correlated systems (including B3LYP) is close to that of the triplet-state geometry. The authors also calculated the spin–orbit coupling matrix elements using the Z^{eff} method and obtained 8 cm^{-1}. Even with the spin–orbit interaction being small, the triplet state should undergo very efficient intersystem crossing due to its closeness to the MEXP geometry.

Norbornene

The triplet state of ethylene assumes a twisted conformation, and has a relatively short lifetime. The triplet state of norbornene also has a short lifetime, even though the twisted configuration cannot be achieved due to its rigid framework.[100] The short lifetime of triplet norbornene has been investigated by Harvey et al.[101] Their calculations were carried out at the unrestricted B3LYP/SV+ d level of theory by varying the dihedral angle around the π bond. The dihedral angle must become 98° for the singlet surface to cross the triplet state, and this point of crossing is 15 kcal/mol above the triplet minimum. From a one-dimensional dihedral coordinate, the anharmonic vibrational Schrödinger equation was solved in order to obtain the Franck–Condon overlap for a golden rule calculation (Eq. [5]). The rest of the vibrational degrees of freedom were treated as unity, being considered as the bath modes. In conjunction with spin–orbit coupling matrix elements calculated by using the method of Koseki et al.,[7,8] Harvey et al.[101] were able to calculate the intersystem crossing rate to be 3.4×10^8 s^{-1}, which corresponds to a 3-ns lifetime. This result underestimates the experimental lifetime of 250 ns. They further calculated the MEXP using Eqs. [98] and [99], and found that a triplet minimum is 67 kcal/mol above the singlet state and that the optimized MEXP with dihedral angles >90° lies 8 kcal/mol above the triplet state. These results were based on utilizing two-electron two-orbital CASSCF/SV + d level of theory. Using their nonadiabatic RRKM theory[20] with an Airy function predicts a crossing rate of 3×10^5 s^{-1}, which corresponds to a 3000-ns lifetime, giving better agreement with the experimental lifetime.

Conjugated Polymers

Poly(phenylenevinylene) has been considered for many different applications due to its importance in nanoscale electronic devices. One such application is the search for efficient light emitting diodes. This property is the result of the electrooptical effect and constitutes an important area of modern research in theory as well as experiment. The efficiency of the nonradiative

decay path, particularly of singlet–triplet intersystem crossing, can lower device efficiency. Beljonne et al.[102] examined the intersystem crossing in oligo(phenylene ethylene) and oligothiophenes with differing polymeric length within a framework of semiempirical INDO/CIS. The spin–orbit coupling was calculated from the one-electron Breit–Paui Hamiltonian using first-order perturbation theory and was used for subsequent calculation of the intersystem crossing rate through the Fermi golden rule. The singlet–triplet energy gaps, $S_0 - T_1$ decreases as the chain becomes longer, as expected from band theory. Hence, intersystem crossing becomes more efficient.

$\mathbf{CH(^2\Pi) + N_2 \rightarrow HCN + N(^4S)}$
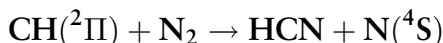
There have been a number of theoretical investigations on the $CH + N_2 \rightarrow HCN + N$ system due, in part, to its importance in the production of NO in the combustion chemistry of hydrocarbons. It is also interesting from the perspective of electronic structure theory because it involves potential energy surfaces of the doublet and quartet states and spin–orbit coupling connecting these states, and because aspects of dynamics by a generalized transition state theory and a nonadiabatic RRKM theory can be used.

Manaa and Yarkony[73b] investigated the stationary points on the relevant part of the potential energy surfaces by using second-order configuration interaction based on SA–MCSCF wave functions. One of the two crossing points found for the study is that of a higher energy, colinear structure where the N atom is coordinated to NCH in $C_{\infty v}$ symmetry. It was suggested that the colinear structure is not involved in the reaction because of its high barrier (50 kcal/mol) with respect to the $HCN + N(^4S)$ asymptote. The lower energy crossing point has an approximately C_{2v} structure with HC bifurcating the two nitrogen atoms. This structure is ~ 7 kcal/mol above the $HCN + N(^4S)$ asymptote. Spin–orbit coupling between doublet and quartet states was calculated at the C_{2v} MEXP, using the full Breit–Pauli Hamiltonian based on SA–MCSCF/CI (second-order) wave functions, and was found to be 11 cm^{-1}. On the basis of their spin–orbit coupling, Manaa and Yarkony also estimated the transition probability from the doublet to the quartet by using the Landau–Zener model. They found the crossing probability to be in the range of 1.5×10^{-3}–5×10^{-4}, which translates to the same order of magnitude obtained for a reasonable Arrhenius A factor. Later, Cui and Morokuma obtained a similar potential energy surface for the reaction, including the two minimum energy crossing points.[103] Based on the points of the potential energy surface calculated by Manaa and Yarkony, Seideman and Walch[104] constructed a two-dimensional surface for doublet and quartet states. Subsequently, Seideman[105] computed the energy-dependent reaction probability by utilizing the discrete variable representation[106] with absorbing boundary conditions (ABC–DVR).[95] The energy-dependent reaction probability was calculated in terms of two unimolecular decay probabilities and of the

doublet–quartet hopping probability evaluated within the golden rule using spin–orbit coupling data based on Manaa and Yarkony. The calculated energy-dependent reaction probability shows resonance features giving rise to several high reaction probability peaks within the energy range examined. Furthermore, the cumulative reaction probability is averaged over the energy distribution to obtain the thermal rate constant. The calculated thermal rate constant shows qualitative agreement with the available experimental rate constant. Cui et al. derived an expression for cumulative reaction probability for the reaction by extension of the united statistical theory, considering the minimum energy crossing point treated as a transition state, and obtained qualitative agreement with experimental results.[107]

Molecular Properties

As mentioned above, the ESR spectrum is affected by the strength of spin–orbit coupling in molecules. The effect of spin–orbit coupling in ESR is represented by the Hamiltonian, $H = \mu_B \, \mathbf{S} g \mathbf{B}$, where μ_B is the Bohr magneton, $\mathbf{S}$ is spin, g is the so-called g-tensor, and $\mathbf{B}$ is the external magnetic field. For a free electron $\mathbf{g} = 2.0023$. The shift in $\mathbf{g}$ due to the molecular environment and to the external magnetic field was calculated by Engström et al.[108] from the product of spin–orbit and orbital Zeeman matrix elements $[\langle \Psi_0 | H^{SO} | \Psi_n \rangle \langle \Psi_n | L | \Psi_0 \rangle] / (E_0 - E_n)$ with perturbation theory. The authors examined the g-tensor of a spin-label nitroxide with two hydrogen-bonded configurations by using ROHF linear response theory and the atomic mean-field approximation for spin–orbit coupling. They showed that much of the spin density is located at the N and O atoms of the nitroxide group and if the hydrogen bond is directly bonded to the nitroxide center, the spin–orbit coupling decreases. Hence, one of the components of the g-tensor decreases in agreement with the experiments. Similar studies of the g-tensor were carried out, where the atomic mean-field approximation was compared with the full Breit–Pauli results on molecules such as CH_3, SiH_3, GeH_3, ClO_2, $ClSO$, SlS_2, benzene cation, benzene anion, and other molecules.[109]

Due to its tremendous usefulness in many subdisciplines of the chemical sciences, calculations of the (NMR) shielding constant[110] have become an important area of research. The NMR shielding constant is given as a sum of four contributions: diamagnetic, paramagnetic, spin-dipolar, and Fermi contact terms. All terms are affected by spin–orbit coupling, but particularly the Fermi contact term becomes important when heavy atoms are involved. Nakatsuji et al.[111] obtained results based on finite perturbation theory using UHF wave functions. Their method was applied to SnX_4, where $X = H$, Cl, Br, and I as well as to $SnBr_{4-n}I_n$ ($n = 1, 2, 3$) showing the importance of the spin–orbit contribution to the shielding constant.[112] The authors further found that the large spin–orbit coupling contribution is due to the Fermi contact term. Similar work utilizing density functional theory with the mean-field

spin–orbit method was done by Malkina et al.[113] who compared the shieldings of CH_3X, where X = F, Cl, Br, and I. Similar DFT work on the secondary isotope shifts in CX_2, where X = O, S, Se, and Te has also been carried out.[114]

Dynamical Aspects

Nakajima and Kato examined[115] the collision induced intersystem crossing in the excited state of the Ar–glyoxal system. By using CASSCF on the relevant part of the potential energy surfaces of the first excited S_1 and T_1 states, the potentials were fitted to analytical functions. The spin–orbit matrix was calculated by using the Breit–Pauli Hamiltonian at each geometry. The quantum mechanical dynamics were carried out by time-propagating the probability amplitude of the vibrational degrees of freedom. The dynamics were carried out in two ways; one was done perturbatively, and the other was done by introducing the level shift as a parameter. From their electronic structure and dynamics calculations, it was shown that the intermolecular spin–orbit coupling is induced by an Ar atom approaching glyoxal. This approach is due to π-interaction. The Ar atom must approach glyoxal from a direction other than its molecular plane because the coplanar approach by Ar gives zero spin–orbit interaction. Also, it was found that the intermolecular spin–orbit coupling increases the transition cross section by >100 times the cross-section obtained by the intramolecular spin–orbit interaction alone.

Another aspect of dynamics was evaluated by Niv, Bargheer, and Gerber who studied the photodissociation dynamics of F_2 in an Ar_{54} cluser.[116] Modeling condensed-phase reaction dynamics is difficult due to many-body interactions. However, a model with an inert medium is a convenient way to examine the role that a medium can play in the condensed phase. Because the system is large and a full quantum mechanical description of the dynamics is computationally prohibitive, the authors used the semiclassical surface hopping method[117] to carry out the dynamics simulations. The states of F_2, corresponding to a gas-phase equivalent, included in the condensed-phase study are two $^1\Sigma_g$, one $^1\Sigma_u$, two $^1\Pi_g$, two $^1\Pi_u$, two $^1\Delta_g$, two $^3\Pi_u$, two $^3\Pi_g$, two $^3\Sigma_u$, one $^3\Sigma_g$, and two $^3\Delta_g$, giving nine singlet and 27 (3 × 9) triplet states. The empirical potential of Aquilanti et al.[118] as well as an ab initio potential calculated at the CCSD(T)/aug-cc-pVTZ level of theory were used for this study. The dissociating F atoms collide with a cage of Ar atoms and transfer most of their kinetic energy, within ∼ 100 fs, causing evaporation of Ar atoms in the outermost layer. The results of their surface hopping trajectory calculations also indicate that substantial recombination occurs ∼ 100 fs after photoexcitation. The F_2 molecule is initally in its $^1\Pi_u$ state, but becomes trapped in its $^3\Pi_u$ state, which oscillates about 4 bohr. They found two types of dissociative processes; one is the direct dissociation and the other involves cage-oscillation first, followed by dissociation. Direct dissociation takes place within 200 fs. In the case of delayed dissociation, an F atom leaves the cage after two oscillations (first

oscillation takes place within 100 fs with smaller amplitude, and the second oscillation takes place within 700 fs). The average of all triplet-state populations is markedly different from the simulated recombination effect for the $^3\Pi_u$ state. This unusually high population of the $^3\Pi_u$ state is due to the fact that the spin–orbit coupling directly couples the initially prepared state ($^1\Pi_u$) to the $^3\Pi_u$ state. Observation of such an effect has been confirmed recently by femtosecond pump–probe experiments.[119] A similar dynamics study has also been carried out by Krylov et al. on Cl atom relaxation in solid Ar.[120]

Daniel et al.[121] examined photodissociation dynamics involving intersystem crossing in HCo(CO)$_4$. They used the Chebychev propagator[94] for solving the time-dependent Schrödinger equation using one- and two-dimensional potential energy surfaces generated by the CASSCF/CI method. They observed that 35% of the product is the singlet primary product occurring within 20 fs. The triplet channels in comparison are relatively slow, but accessible within 50 ps. They concluded that intersystem crossing is on the same time scale as intramolecular vibrational relaxation and it is competitive to indirect dissociation induced by tunneling in this system.

OTHER REACTIONS

An asymmetric nitric oxide dimer N—N—O—O (*a*-N$_2$O$_2$) has been examined as a possible energetic material. The *a*-N$_2$O$_2$ ($^1A'$ ground state) is calculated to be 102 and 62 kcal/mol higher with respect to N$_2$ + O$_2$ and NO + NO asymptotes, respectively.[122] Nguyen et al.,[123] examined a possible spin-forbidden decay path of *a*-N$_2$O$_2$. They used Eq. [92] to obtain the MEXP between $^1A'$ and $^3A''$ states based on the *a*-N$_2$O$_2$ ($^1A'$) → N$_2$O$_2$ ($^3A''$) → N$_2$O ($X^1\Sigma^+$) + O (^3P) reaction. To do this, they used SA–MCSCF/SOCI along with DZP and TZP basis sets, in addition to full Breit–Pauli spin–orbit matrix elements. They found that the intersystem crossing of *a*-N$_2$O$_2$ is efficient, since the MEXP between $^1A'$ and $^3A''$ is only 1–2 kcal/mol above the singlet state and the calculated spin–orbit coupling is relatively large (75 cm^{-1}).

Using a Fourier transform ion cyclotron resonance (FT–ICR) spectrometer, Janaway and Brauman[124] examined the proton-transfer reaction for $^3NO^- + H_2S \rightarrow {}^1HNO + HS^-$. The reaction is exothermic by 12 kcal/mol, and the triplet complex $^3NO^- \cdot H_2S$ and singlet complex $^1NO^- \cdot H_2S$ are 18 and 23 kcal/mol below reactants, respectively. The minimum energy crossing point is located 2 kcal/mol above the triplet complex suggesting that the reaction should be efficient energetically. However, the reaction is not observed experimentally. Interestingly, $^3NO^-$ reacts with relatively high efficiency with (CH$_3$)$_3$CSH, which the authors speculated arises from similar kinetics as for the curve crossing found in H$_2$S. Their RRKM calculations on the

dissociation rate of the triplet complex to reactants show that the rate differs by three orders of magnitude slower for the $(CH_3)_3CSH$, due to denser vibrational manifolds, than for H_2S. Therefore, the $(CH_3)_3CSH$ complex has more chance to undergo a spin-forbidden transition than the H_2S complex has.

In another study, Mebel et al.[125] examined the photodissociation path involving a spin-forbidden channel in methane. Their MRCI and equation of motion (EOM) CCSD calculations, including MEXP, indicated that the photodissociation pathway is likely to proceed via intersystem crossing from $S_1(^1A")$ to repulsive $T_1(^3A')$, instead of the speculated $S_0 \leftarrow S_1$ internal conversion. Similar studies have been done by Hwang and Mebel on spin-forbidden reactions in $N_2O \rightarrow N_2 + O$ (^3P) and $N_2O \rightarrow N_2 + O$ (^1D).[126]

Other reactions of spin-forbidden processes include a study by Manna and Chabalowski[127] on the reaction, NO $(X^2\Pi) + CO$ $(X^1\Sigma^+) \rightarrow N$ $(^4S) + CO_2$ $(X^1\Sigma_g^+)$, using the SA–MCSCF/SOCI approach to locate the MEXP (60 kcal/mol above the reactants). A similar study was carried out[128] on CH_3 $(X^2A_2") + N(^4S) \rightarrow HCN$ $(X^1\Sigma^+) + H_2$ $(X^1\Sigma_g^+)$, where it was found that the MEXP is located below (8 kcal/mol) the reactants. The barrierless transition occurs at the MEXP in 1 out of 208 vibrational periods, as deduced from the Landau–Zener transition probability using a 30 cm^{-1} spin–orbit matrix element.

Finally, Veige et al.[129] examined singlet- and triplet-state energies as well as MEXP for $M(OH)_3$, where M = V, Nb, and Ta, in connection with the deoxygenation process of $(silox)_3WNO$ by $M(OR)_3$. They found $M(OH)_3$ is a triplet ground state for M = V, singlet for M = Ta, and almost isoenergetic for M = Nb. The MEXP, calculated at the B3LYP/SBKJC[40] level, were found to be 1–2 kcal/mol above the higher states of the two examined for $M(OH)_3$.

BIOLOGICAL CHEMISTRY

One area of research that has not been explored very much by the techniques covered in this chapter is biological chemistry. Many enzymes carry out electron-transfer reactions, and can undergo intersystem crossing.[130] Many of the methodologies discussed in this chapter are applicable to biological systems exhibiting spin-forbidden transitions.

Since the ground state of oxygen is a triplet state $(X^3\Sigma g^-)$, it is reasonable to assume that spin-forbidden reactions should take place at some step in a sequence of reactions that leads eventually to a singlet product. Flavin adenine dinucleotide (FAD) is a cofactor in enzymes, and is the redox center for transferring electrons to and from substrates.[131] Molecular oxygen is one of the substrates that FAD-containing enzymes catalyze to produce H_2O_2. Therefore, the overall reaction is spin-forbidden.

A study by Prabhakar et al.,[132] examined the reaction mechanism of the peroxidation process for glucose oxidase by modeling the active site of the enzyme including $FADH_2$ (reduced form of FAD) and a histidine residue responsible for binding and subsequent transfer of hydrogen atom to molecular oxygen. Their calculations involved full geometry optimization, using the B3LYP/DZ(d,p) and B3LYP/6-311+G(2d,2p) levels of theory; unrestricted wave functions were used for the triplet state. The peroxidation process, $O_2 + FADH_2 \rightarrow H_2O_2 + FAD$, was found to occur via electron trasfer from $FADH_2$ forming a triplet radical pair, subsequent intersystem crossing to the singlet state (open-shell singlet radical), where the minimum geometries of the triplet and open-shell singlet are nearly equal. They concluded that intersystem crossing is barrierless. Subsequently, a proton is transferred from the protonated histidine residue to form hydrogen peroxide and the authors found a transition state for such a process, showing the existence of a deuterium isotope effect in the second step, even though no such effect is found experimentally. Instead, an oxygen isotope effect is found experimentally. This leads to the conclusion that the rate-limiting step is the first intersystem crossing reaction step. The spin–orbit matrix element between open-shell singlet and triplet was estimated to be 76.5 cm^{-1} from a model system. In terms of the Fermi golden rule, the authors discussed how the rate of transition depends on the spin–orbit coupling of the system.

CONCLUDING REMARKS

Models related to spin-forbidden reactions are discussed in this chapter. Coupling between two surfaces of different spin and symmetry is given by various levels of approximation for spin–orbit operators from the reduction of relativistic quantum mechanics. Well-established methods such as the Breit–Pauli Hamiltonian exist, but new relativistic methods such as the Douglas–Kroll Hamiltonian and other new transformation schemes are also being investigated and implemented today.

Locating crossing points between the two surfaces gives an effective barrier in spin-forbidden reactions. Particularly important is the MEXP and algorithms to locate it. A wide range of theoretical methods are available for examining different aspects of spin-forbidden reaction dynamics, ranging from Fermi's golden rule to quantum dynamics by solving the time-dependent Schrödinger equation. Currently, applications in the literature are limited to relatively small molecules. Applications to areas such as biological chemistry and transition metal catalysis are not currently explored by these methods; however, many such systems contain aspects of spin-forbidden reactions that need to be investigated computationally to give meaningful explanations of the observed phenomena.

ACKNOWLEDGMENTS

REFERENCES

1. The nonadiabatic coupling matrix element is a consequence of the Born–Oppenheimer approximation, as shown in texts such as: (a) F. Jensen, *Introduction to Computational Chemistry*, Wiley, West Sussex, England, Chapter 3, p. 53. Further details on the nonadiabatic coupling matrix elements can be found in (b) D. R. Yarkony, *Modern Electronic Structure Theory*, D. R. Yarkony, Ed., World Scientific, Singapore, 1995, Part 1, Chapter 11, p. 642. Electronic Structure Aspects of Nonadiabatic Processes in Polyatomic Systems.

2. (a) K. Fukui, *Acc. Chem. Res.,* **14**, 363 (1981). The Path of Chemical Reactions—The ICR Approach. b) H. B. Schlegel, in *Modern Electronic Structure Theory*, D. R. Yarkony, Ed., World Scientific, Singapore, 1995, Part 1, Chapter 8, p. 459. Geometry Optimization on Potential Energy Surfaces.

3. N. Lehnert, R. Y. N. Ho, L. Que, and E. I. Solomon, *J. Am. Chem. Soc.*, **123**, 8271 (2001). Spectroscopic Properties and Electronic Structure of Low-Spin Fe(III)-Alkylperoxo Complexes: Homolytic Cleavage of the O—O Bond.

4. J. N. Harvey, in *Computational Organometallic Chemistry*, Thomas R. Cundari, Ed., Marcel Dekker, New York, 2001, p. 291. Spin-Forbidden Reactions in Transition-Metal Chemistry.

5. S. Kato, R. L. Jaffe, A. Komornicki, and K. Morokuma, *J. Chem. Phys.*, **78**, 4567 (1983). A Theoretical Study on the Mechanism of Electronic to Vibrational Energy Transfer in $Hg(^3P)$ + CO Collisions.

6. (a) P. Pyykkö and J. Desclaux, *Acc. Chem. Res.*, **12**, 276 (1979). Relativity and the Periodic System of Elements. (b) P. Pyykkö, *Chem. Rev.*, **88**, 563 (1988). Relativiestic Effects in Structural Chemistry. (c) K. S. Pitzer, *Acc. Chem. Res.,* **12**, 271 (1979). Relativistic Effects on Chemical Properties. (d) W. Kutzelnigg, *Physica Scripta,* **36**, 416 (1987). The Relativistic Many Body Problem in Molecular Theory.

7. S. Koseki, M. S. Gordon, M. W. Schmidt, and N. Matsunaga, *J. Phys. Chem.,* **99**, 12764 (1995). Main Group Effective Nuclear Charges for Spin–Orbit Calculations.

8. S. Koseki, M. W. Schmidt, and M. S. Gordon, *J. Phys. Chem. A*, **102**, 10430 (1998). Effective Nuclear Charges for the First- Through Third-Row Transition Metal Elements in Spin–Orbit Calculations.

9. S. Koseki, D. G. Fedorov, M. W. Schmidt, and M. S. Gordon, *J. Phys. Chem. A,* **105**, 8262 (2001). Spin–Orbit Splittings in the Third-Row Transition Elements: Comparison of Effective Nuclear Charge and Full Breit–Pauli Calculations.

10. NIST atomic spectra database. http://physics.nist.gov/cgi-bin/AtData/main_asd

11. W. J. Stevens and M. Krauss, *Chem. Phys. Lett.,* **86**, 320 (1982). Ab Initio Effective Spin–Orbit Operators for Use in Atomic and Molecular Structure Calculations. Results for Carbon and Silicon.

12. N. J. Turro, *Modern Molecular Photochemistry*, Chapter 8, University Science Books, Sausalito, California (1991). ESR.

13. I. V. Khudyakov, Y. A. Serebrennikov, and N. J. Turro, *Chem. Rev.*, **93**, 537 (1993). Spin–Orbit Coupling in Free-Radical Reactions: On the Way to Heavy Elements.

14. N. Matsunaga, D. W. Rogers, and A. A. Zavitsas, *J. Org. Chem.,* **68**, 3158 (2003). Pauling's Electronegativity Equation and a New Corollary Accurately Predict Bond Dissociation Enthalpies and Enhance Current Understanding of the Nature of the Chemical Bond.

15. S. Yabushita, *J. Mol. Struct. (THEOCHEM)*, **461–462**, 523 (1999). Potential Energy Curves of ICl and Non-Adiabatic Interactions Studied by the Spin–Orbit CI Method.

16. H. J. Silverstone and O. Sinanoglu, *J. Chem. Phys.*, **44**, 1899 (1966). Many-Electron Theory of Nonclosed-Shell Atoms and Molecules. I. Orbital Wavefunction and Perturbation Theory.

17. N. Matsunaga, S. Koseki, and M. S. Gordon, *J. Chem. Phys.*, **104**, 7988 (1996). Relativistic Potential Energy Surfaces of XH_2 (X = C, Si, Ge, Sn, and Pb) Molecules: Coupling of $^1A_1$ and $^3B_1$ States.

18. J. C. Tully, *J. Chem. Phys.*, **61**, 61 (1974). Collision Complex Model for Spin Forbidden Reactions: Quenching of $O(^1D)$ by N_2.

19. T. Seideman, *J. Chem. Phys.*, **101**, 3662 (1994). Resonances in the $CH + N_2 \rightarrow HCN + N(^4S)$ Reaction: The Dynamics of a Spin-Forbidden Process.

20. (a) J. C. Lorquet and B. Leyh-Nihant, *J. Phys. Chem.*, **92**, 4778 (1988). Nonadiabatic Unimolecular Reactions. 1. A Statistical Formulation for the Rate Constants. (b) F. Remacle, D. Dehareng, and J. C. Lorquet, *J. Phys. Chem.*, **92**, 4784 (1988). Nonadiabatic Unimolecular Reactions. 2. Isotope Effects on the Kinetic Energy Release.

21. M. S. Child, *Molecular Collision Theory*, Dover, Mineola, New York, 1976.

22. C. Zhu, Y. Teranishi, and H. Nakamura, *Adv. Chem. Phys.*, **117**, 127 (2001). Nonadiabatic Transitions Due to Curve Crossings: Complete Solutions of the Landau–Zener–Stueckelberg Problems and Their Applications.

23. H. Nakamura, *Nonadiabatic Transition, Concepts, Basic Theories, and Applications*, World Scientific, Singapore, 2002.

24. J. Almlöf and O. Gropen, in *Reviews in Computational Chemistry*, K. B. Lipkowitz and D. B. Boyd, Eds., VCH Publishers, Weinheim, Germany (1996), pp. 203–244. Relativistic Effects in Chemistry.

25. B. A. Hess, C. M. Marian, and S. D. Peyerimhoff, in *Modern Electronic Structure Theory, Part 1*, D. R. Yarkony, Ed., World Scientific, Singapore, 1995, p. 152. Ab Initio Calculation of Spin–Orbit Effects in Molecules Including Electron Correlation.

26. (a) W. Greiner, *Relativistic Quantum Mechanics, Wave Equations*, Springer-Verlag, Berlin, 1990. (b) A. Messiah, *Quantum Mechanics*, Dover Publications, Inc., Mineola, New York, 1999.

27. See, for example, (a) L. Pisani and E. Clementi, *J. Comput. Chem.*, **15**, 466 (1994). Relativistic Dirac–Fock Calculations for Closed-Shell Molecules. (b) *Relativistic Effects in Heavy-Element Chemistry and Physics*, B. A. Hess, Ed., Wiley, West Sussex, England, 2003.

28. J. P. Desclaux, *Computer Phys. Comm.*, **9**, 31 (1975). A Multiconfiguration Relativistic Dirac–Fock Program.

29. (a) A. J. Sadlej, in *Lecture Notes in Chemistry*, 64, *Lecture Notes in Quantum Chemistry: European Summer School in Quantum Chemistry*, B. O. Roos, Ed., Springer-Verlag, Berlin (1994) p. 203. Methods of Relativistic Quantum Chemistry. (b) J. Sucher, *Phys. Rev. A*, **22**, 348 (1980). Foundations of the Relativistic Theory of Many-Electron Atoms. (c) O. Visser, L. Visscher, P. J. C. Aerts, and W. C. Nieuwpoort, *Theor. Chim. Acta*, **81**, 405 (1992). Relativistic All-Electron Molecular Hartree–Fock–Dirac–(Breit) Calculations on CH_4, SiH_4, GeH_4, SnH_4, PbH_4. (d) E. Eliav and U. Kaldor, *Chem. Phys. Lett.*, **248**, 405 (1996). The Relativistic Four-Component Coupled Cluster Method for Molecules: Spectroscopic Constants of SnH_4. (e) E. Eliav, U. Kaldor, and Y. Ishikawa, *Phys. Rev. A*, **49**, 1724 (1994). Open-Shell Relativistic Coupled-Cluster Method with Dirac–Fock–Breit Wave Functions: Energies of the Gold Atom and Its Cation.

30. G. Breit, *Phys. Rev.*, **34**, 553 (1929). The Effect of Retardation on the Interaction of Two Electrons.

31. K. G. Dyall, *J. Chem. Phys.*, **100**, 2118 (1994). An Exact Separation of the Spin-Free and Spin-Dependent Terms of the Dirac–Coulomb–Breit Hamiltonian.

32. L. L. Foldy and S. A. Wouthuysen, *Phys. Rev.*, **78**, 29 (1950). On the Dirac Theory of Spin $\frac{1}{2}$ Particles and Its Nonrelativistic Limit.

33. S. R. Langhoff and C. W. Kern, in *Modern Theoretical Chemistry*, H. F. Schaefer III, Ed., Vol. 4. Plenum Press, New York, p. 381. Chapter 10. Molecular Fine Structure.

34. D. R. Yarkony, *Int. Rev. Phys. Chem.*, **11**, 195 (1992). Spin-Forbidden Chemistry within the Breit–Pauli Approximation.

35. H. A. Bethe and E. E. Salpeter, *Quantum Mechanics of One- and Two-electron Atoms*, Springer-Verlag, Berlin, 1957, p. 170.

36. (a) T. R. Furlani and H. F. King, *J. Chem. Phys.*, **82**, 5577 (1985). Theory of Spin–Orbit Coupling. Application to Singlet–Triplet Interaction in the Trimethylene Biradical. (b) T. R. Furlani, Ph. D. dissertation, State University of New York, Buffallo, 1984.

37. D. G. Fedorov and M. S. Gordon, *J. Chem. Phys.*, **112**, 5611 (2000). A Study of the Relative Importance of One and Two-Electron Contributions in Spin–Orbit Coupling.

38. W. R. Wadt, *Chem. Phys. Lett.*, **89**, 245 (1982). An Approximate Method to Incorporate Spin–Orbit Effects into Calculations Using Effective Potentials.

39. S. Koseki, M. W. Schmidt, and M. S. Gordon, *J. Phys. Chem.*, **96**, 10768 (1992). MCSCF/6-31G(d,p) Calculations of One-Electron Spin–Orbit Coupling Constants in Diatomic Molecules.

40. (a) W. J. Stevens, H. Basch, and M. Krauss, *J. Chem. Phys.* **81**, 6026 (1984). Compact Effective Potentials and Efficient Shared-Exponent Basis Sets for the First- and Second-Row Atoms. (b) W. J. Stevens, H. Basch, M. Krauss, and P. G. Jasien, *Can. J. Chem*, **70**, 612 (1992). Relativistic Compact Effective Potentials and Efficient, Shared-Exponent Basis Sets for the Third-, Fourth-, and Fifth-Row Atoms. (c) T. R. Cundari and W. J. Stevens, *J. Chem. Phys.*, **98**, 5555 (1993). Effective Core Potential Methods for the Lanthanides.

41. K. P. Huber and G. Herzberg, *Constants of Diatomic Molecules* (data prepared by J.W. Gallagher and R.D. Johnson, III), in *NIST Chemistry WebBook, NIST Standard Reference Database Number 69*, P. J. Linstrom and W. G. Mallard, Eds., March 2003, National Institute of Standards and Technology, Gaithersburg MD, 20899 (http://webbook.nist.gov).

42. T. R. Cundari, M. T. Benson, M. L. Lutz, and S. O. Sommerer, in *Reviews in Computational Chemistry*, Vol. 8, K. B. Lipkowitz and D. B. Boyd, Eds., VCH Publishers, Weinheim, Germany, 1996, p. 145. Effective Core Potential Approaches to the Chemistry of the Heavier Elements.

43. G. Fenking, I. Antes, M. Böhme, S. Dapprich, A. W. Ehlers, V. Jonas, A. Neuhaus, M. Otto, R. Stegmann, A. Veldkamp, and S. F. Vyboishchikov, in *Reviews in Computational Chemistry, Vol. 8*, K. B. Lipkowitz and D. B. Boyd, Eds., VCH Publishers, Weinheim, Germany, 1996, p. 63. Pseudopotential Calculations of Transition Metal Compounds: Scope and Limitations.

44. M. Krauss and W. J. Stevens, *Annu. Rev. Phys. Chem.*, **35**, 357 (1984). Effective Potentials in Molecular Quantum Chemistry.

45. W. C. Ermler, Y. S. Lee, P. A. Christiansen, and K. S. Pitzer, *Chem. Phys. Lett.*, **81**, 70 (1981). Ab Initio Effective Core Potentials Including Relativistic Effects. A Procedure for the Inclusion of Spin–Orbit Coupling.

46. (a) P. A. Christiansen, W. C. Ermler, and K. S. Pitzer, *Annu. Rev. Phys. Chem.*, **36**, 407 (1985). Relativistic Effects in Chemical Systems. (b) W. C. Ermler, R. B. Ross, and P. A. Christiansen, *Adv. Quantum Chem.*, J. R. Sabin and M. C. Zerner, Eds., Academic Press, San Diego, CA, 1988, p.139. Spin–Orbit Coupling and Other Relativistic Effecs in Atoms and Molecules.

47. L. F. Pacios and P. A. Christiansen, *J. Chem. Phys.,* **82**, 2664 (1985). Ab Initio Relativistic Effective Potentials with Spin–Orbit Operators. I. Li through Ar.

48. M. M. Murley, L. F. Pacios, P. A. Christiansen, R. B. Ross, and W. C. Ermler, *J. Chem. Phys.*, **84**, 6840 (1986). Ab Initio Relativistic Effective Potentials with Spin–Orbit Operators. II. K through Kr.

49. L. A. LaJohn, P. A. Christiansen, R. B. Ross, T. Atashroo, and W. C. Ermler, *J. Chem. Phys.*, **87**, 2812 (1987). Ab Initio Relativistic Effective Potential with Spin–Orbit Operators. III. Rb through Xe.

50. R. B. Ross, J. M. Powers, T. Atashroo, W. C. Ermler, L. A. LaJohn, and P. A. Christiansen, *J. Chem. Phys.*, **93**, 6654 (1990). Ab Initio Relativistic Effective Potentials With Spin–Orbit Operators. IV. Cs through Rn.

51. S. Yabushita, Z. Zhang, and R. M. Pitzer, *J. Phys. Chem.*, **103**, 5791 (1999). Spin–Orbit Configuration Interaction Using the Graphical Unitary Group Approach and Relativistic Core Potential and Spin–Orbit Operators.

52. R. M. Pitzer and N. W. Winter, *J. Phys. Chem.*, **92**, 3061 (1988). Electronic Structure Methods for Heavy-Atom Molecules.

53. R. M. Pitzer and N. W. Winter, *Int. J. Quantum Chem.*, **40**, 773 (1991). Spin–Orbit (Core) and Core Potential Integrals.

54. J. L. Tilson, W. C. Ermler, and R. M. Pitzer, *Comput. Phys. Commun.* **128**, 128 (2000). Parallel Spin–Orbit Coupled Configuration Interaction.

55. (a) S. Huzinaga, M. Klobukowski, and Y. Sakai, *J. Phys. Chem.*, **88**, 4880 (1984). Model Potential Method in Molecular Calculations. (b) Y. Sakaki, E. Miyoshi, M. Klobukowski, and S. Huzinaga, *J. Chem. Phys.*, **106**, 8084 (1997). Model Potentials for Main Group Elements Li through Rn.

56. M. Klobukowski, *Chem. Phys. Lett.*, **183**, 417 (1991). Comparison of the Effective-Core-Potential and Model-Potential Methods in the Studies on Spin–Orbit Effects: Zero-Field Splitting of the $X^3\Sigma^-$ State of Pnictogen Hydrides.

57. D. G. Fedorov and M. Klobukowski, *Chem. Phys. Lett.*, **360**, 223 (2002). Spin–Orbit Coupling with Model Core Potentials.

58. M. Douglas and N. M. Kroll, *Ann. Phys.*, **82**, 89 (1974). Quantum Electrodynamical Corrections to the Fine Structure of Helium.

59. (a) T. Nakajima and K. Hirao, *J. Chem. Phys.*, **113**, 7786 (2000). The Higher-Order Douglas–Kroll Transformation. (b) J. Paulovic, T. Nakajima, K. Hirao, and L. Seijo, *J. Chem. Phys.*, **117**, 3597 (2002). Third-Order Douglas–Kroll Ab Initio Model Potential for Actinide Elements.

60. (a) K. G. Dyall, *J. Chem. Phys.*, **100**, 2118 (1994). An Exact Separation of the Spin-Free and Spin-Dependent Terms of the Dirac–Coulomb–Breit Hamiltonian. (b) K. G. Dyall, *J. Chem. Phys.*, **109**, 4201 (1998). Interfacing Relativistic and Nonrelativistic Methods. II. Investigation of a Low-Order Approximation. (c) K. G. Dyall and T. Enevoldsen, *J. Chem. Phys.*, **111**, 10,000 (1999). Interfacing Relativistic and Nonrelativistic Methods. III. Atomic 4-Spinor Expansions and Integral Approximations. (d) K. G. Dyall, *J. Chem. Phys.*, **115**, 9136 (2001). Interfacing Relativistic and Nonrelativistic Methods. IV. One- and Two-Electron Scalar Approximations.

61. (a) R. Samzow, B. A. Hess, and G. Jansen, *J. Chem. Phys.*, **96**, 1227 (1992). The Two-Electron Terms of the No-Pair Hamiltonian. (b) C. Park and J. E. Almlöf, *Chem. Phys. Lett.*, **231**, 269 (1994). Two-Electron Relativistic Effects in Molecules.

62. A. Wolf, M. Reiher, and B. A. Hess, *J. Chem. Phys.*, **117**, 9215 (2002). The Generalized Douglas–Kroll Transformation.

63. W. A. de Jong, R. J. Harrison, and D. A. Dixon, *J. Chem. Phys.*, **114**, 48 (2001). Parallel Douglas–Kroll Energy and Gradients in NWChem: Estimating Scalar Relativistic Effects Using Douglas–Kroll Contracted Basis Sets.

64. B. A. Hess and U. Kaldor, *J. Chem. Phys.*, **112**, 1809 (2000). Relativistic All-Electron Coupled-Cluster Calculations on Au_2 in the Framework of the Douglas–Kroll Transformation.

65. (a) S. Huzinaga, L. Seijo, Z. Barandiaran, and M. Klobukowski, *J. Chem. Phys.*, **86**, 2132 (1987). The Ab Initio Model Potential Method. Main Group Elements. (b) L. Seijo, Z. Barandiaran, and S. Huzinaga, *J. Chem. Phys.*, **91**, 7011 (1989). The Ab Initio Model Potential Method. First Series Transition Metal Elements.

66. J. Paulovic, T. Nakajima, K. Hirao, and L. Seijo, *J. Chem. Phys.*, **117**, 3597 (2002). Third-Order Douglas–Kroll Ab Initio Model Potential for Actinide Elements.

67. D. G. Fedorov, T. Nakajima, and K. Hirao, *J. Chem. Phys.*, **118**, 4970 (2003). An Ab Initio Study of Excited States of U and UF.

68. (a) B. A. Hess, C. M. Marian, U. Wahlgren, and O. Gropen, *Chem. Phys. Lett.*, **251**, 365 (1996). A Mean-Field Spin–Orbit Method Applicable to Correlated Wavefunctions. (b) M. Ilias, V. Kellö, L. Visscher, and B. Schimmelpfennig, *J. Chem. Phys.,* **115**, 9667 (2001). Inclusion of Mean-Field Spin–Orbit Effects Based on All-Electron Two-Component Spinors: Pilot Calculations on Atomic and Molecular Properties.

69. (a) P. Å. Malmqvist, B. O. Roos, and B. Schimmelpfennig, *Chem. Phys. Lett.,* **357**, 230 (2002). The Restricted Active Space (RAS) State Interaction Approach with Spin–Orbit Coupling. (b) F. Rakowitz, C. M. Marian, and B. Schimmelpfennig, *Phys. Chem. Chem. Phys.,* **2**, 2481 (2000). Ground and Excited States of $PtCH_2^+$: Assessment of the No-Pair Douglas–Kroll Ab Initio Model Potential Method.

70. (a) M. Barysz and A. J. Sadlej, *J. Molec. Struct. (THEOCHEM)*, **573**, 181 (2001). Two-Component Methods of Relativistic Quantum Chemistry: from the Douglas–Kroll Approximation to the Exact Two-Component Formalism. (b) M. Barysz, *J. Chem. Phys.*, **114**, 9315 (2001). Systematic Treatment of Relativistic Effects Accurate through Arbitrarily High Order in α^2.

71. E. van Lenthe, E. J. Baerends, and J. G. Snijders, *J. Chem. Phys.*, **105**, 2373 (1996). Construction of the Foldy–Wouthuysen Transformation and Solution of the Dirac Equation Using Large Components Only.

72. N. Koga and K. Morokuma, *Chem. Phys. Lett.* **119**, 371 (1985). Determination of the Lowest Energy Point on the Crossing Seam between Two Potential Surfaces Using the Energy Gradient.

73. (a) D. R. Yarkony, *J. Chem. Phys.*, **92**, 2457 (1990). On the Characterization of Regions of Avoided Crossings Using an Analytic Gradient Based Method. (b) M. R. Manaa and D. R. Yarkony, *J. Chem. Phys.,* **95**, 1808 (1991). On the Mechanism of the Reaction $CH(X^2\Pi) + N_2(X^1\Sigma_g^+) \rightarrow HCN(X^1\Sigma^+) + N(^4S)$. I. A Theoretical Treatment of the Electronic Structure Aspects of the Intersystem Crossing.

74. (a) A. Farazdel and M. Dupuis, *J. Comput. Chem.*, **12**, 276 (1991). On the Determination of the Minimum on the Crossing Seam of Two Potential Energy Surfaces. (b) M. J. Bearpark, M. A. Robb, and H. B. Schlegel, *Chem. Phys. Lett.*, **223**, 269 (1994). A Direct Method for the Location of the Lowest Energy Point on a Potential Surface Crossing.

75. J. N. Harvey, M. Aschi, H. Schwarz, and W. Koch, *Theoret. Chem. Acc.*, **99**, 95 (1998). The Singlet and Triplet States of Phenyl Cation. A Hybrid Approach for Locating Minimum Energy Crossing Points between Noninteracting Potential Energy Surfaces.

76. M. W. Schmidt, K. K. Baldridge, J. A. Boatz, S. T. Elbert, M. S. Gordon, J. H. Jensen, S. Koseki, N. Matsunaga, K. A. Nugyen, S. Su, T. L. Windus, M. Dupuis, and J. A. Montgomery, *J. Comput. Chem.* **14**, 1347 (1993). General Atomic and Molecular Electronic Structure System.

77. Columbus. (a) H. Lischka, R. Shepard, F. B. Brown and I. Shavitt, *Int. J. Quantum Chem., Quantum Chem. Symp.*, **15**, 91 (1981). (b) R. Shepard, I. Shavitt, R. M. Pitzer, D. C. Comeau, M. Pepper, H. Lischka, P. G. Szalay, R. Ahlrichs, F. B. Brown, and J. Zhao, *Int. J. Quantum Chem., Quantum Chem. Symp.*, **22**, 149 (1988). (c) H. Lischka, R. Shepard, R. M. Pitzer, I. Shavitt, M. Dallos, Th. Müller, P. G. Szalay, M. Seth, G. S. Kedziora, S. Yabushita, and Z. Zhang, *Phys. Chem. Chem. Phys.*, **3**, 664 (2001). (d) H. Lischka, R. Shepard, I. Shavitt, R. M. Pitzer, M. Dallos, Th. Müller, P. G. Szalay, F. B. Brown, R. Ahlrichs, H. J. Böhm, A. Chang, D. C. Comeau, R. Gdanitz, H. Dachsel, C. Ehrhardt, M. Ernzerhof, P. Höchtl, S. Irle, G. Kedziora, T. Kovar, V. Parasuk, M. J. M. Pepper, P. Scharf, H. Schiffer, M. Schindler, M. Schüler, M. Seth, E. A. Stahlberg, J.-G. Zhao, S. Yabushita, and Z. Zhang, COLUMBUS, An Ab Initio Electronic Structure Program, release 5.8 (2001); (e) Also, see http://www.itc.univie.ac.at/~ hans/Columbus/columbus.htm

78. K. M. Dunn and K. Morokuma, *J. Phys. Chem.,* **100**, 123 (1996). Ab Initio Study of Photochemical Dissociation of Methylamine.

79. T. Saue, K. Faegri, T. Helgaker, and O. Gropen, *Mol. Phys.*, **91**, 937 (1997). Principles of Direct 4-Component Relativistic SCF: Application to Caesium Auride.

80. L. Visscher, O. Visser, H. Aerts, H. Merenga, and W. C. Nieuwpoort, *Comput. Phys. Commun.*, **81**, 120 (1994). Relativistic Quantum Chemistry: the MOLFDIR Program Package. Also, see http://theochem.chem.rug.nl/∼ broer/Molfdir/Molfdir.html

81. (a) H. M. Quiney, H. Skaane, and I. P. Grant, *Adv. Quantum Chem.*, **32**, 1 (1999). Ab Initio Relativistic Quantum Chemistry: Four Components Good, Two Components Bad! (b) I. P. Grant and H. M. Quiney, *Int. J. Quantum Chem.*, **80**, 283 (2000). Application of Relativistic Theories and Quantum Electrodynamics to Chemical Problems.

82. T. Yanai, T. Nakajima, Y. Ishikawa, and K. Hirao, *J. Chem. Phys.*, **114**, 6526 (2001). A New Computational Scheme for the Dirac–Hartree–Fock Method Employing an Efficient Integral Algorithm.

83. K. Balasubramanian, *Relativistic Effects in Chemistry*, Part A and B, Wiley, New York, 1997.

84. L. A. Pederson and D. R. Yarkony, *Mol. Phys.*, **84**, 611 (1995). On the Spin–Orbit Induced Radiationless Decay of the $b^3\Sigma^-$ State of BH.

85. A. Dreuw and L. S. Cederbaum, *Int. J. Mass Spectrom.*, **188**, 199 (1999). Long-Lived High-Spin States of N_2^-.

86. N. Balakrishnan, A. B. Alekseyev, and R. J. Buenker, *Chem. Phys. Lett.*, **341**, 594 (2001). Ab Initio Quantum Mechanical Investigation of Photodissociation of HI and DI.

87. K. D. Setzer, E. H. Fink, A. B. Alekseyev, H.-P. Liebermann, and R. J. Buenker, *J. Mol. Spectrosc.*, **206**, 181 (2001). Experimental and Theoretical Study of the Electronic States and Spectra of TeH and TeLi.

88. M. V. Korolkov, K.-M. Weitzel, and S. D. Peyerimhoff, *Int. J. Mass Spectrosc.*, **201**, 109 (2000). Spin–Orbit Induced Predissociation Dynamics of HCl^+ and HBr^+ Ions: Temporal and Spectral Representations.

89. S. Roszak, M. Krauss, A. B. Alekseyev, H.-P. Liebermann, and R. J. Buenker, *J. Phys. Chem. A*, **104**, 2999 (2000). Spin–Orbit Configuration Interaction Calculation of the Potential Energy Curves of Iodine Oxide.

90. R. G. Sadygov, J. Rostas, G. Taieb, and D. R. Yarkony, *J. Chem. Phys.*, **106**, 4091 (1997). Resonances in the Predissociation of the $A^2\Pi_\Omega$ State of MgBr.

91. Adiabatic–diabatic transformation is a unitary transformation of two surfaces of the same symmetry and spin. The rotation angle of the transformation is represented by an integral of derivative coupling. See, for example, (a) N. Matsunaga and D. R. Yarkony, *Mol. Phys.*, **93**, 79 (1998). Energies and Derivative Coupling in the Vicinity of a Conical Intersection 3. The 'Most' Diabatic Basis. (b) H.-J. Werner, B. Follmeg, and M. H. Alexander, *J. Chem. Phys.*, **89**, 3139 (1988). Adiabatic and Diabatic Potential Energy Surfaces for Collisions of CN ($X^2\Sigma^+$, $A^2\Pi$) with He.

92. P. M. Regan, D. Ascenzi, A. Brown, G. G. Balint-Kurti, and A. J. Orr-Erwing, *J. Chem. Phys.*, **112**, 10259 (2000). Ultraviolet Photodissociation of HCl in Selected Rovibrational States: Experiment and Theory.

93. M. H. Alexander, B. Pouilly, and T. Duhoo, *J. Chem. Phys.*, **99**, 1752 (1993). Spin–Orbit Branching in the Photofragmentation of HCl.

94. H. Tal-Ezer and R. Kosloff, *J. Chem. Phys.*, **81**, 3967 (1984). An Accurate and Efficient Scheme for Propagating the Time Dependent Schrödinger Equation.

95. (a) C. Leforestier and R. E. Wyatt, *J. Chem. Phys.*, **78**, 2334 (1983). Optical Potential for Laser Induced Dissociation. (b) R. Kosloff and D. Kosloff, *J. Comput. Phys.*, **63**, 363 (1986). Absorbing Boundaries for Wave Propagation Problems.

96. R. Kosloff, in *Dynamics of Molecules and Chemical Reactions*, R. E. Wyatt and J. Z. H. Zhang Eds., Marcel Dekker, Inc., New York (1996) Chapter 5, p. 185. Quantum Molecular Dynamics on Grids.

97. B. H. Lengsfield, J. A. Jafri, D. H. Philips, and C. W. Bauschlicher, *J. Chem. Phys.*, **74**, 6849 (1981). On the Use of Corresponding Orbitals in the Calculation of Nonorthogonal Transition Moments.

98. For example, *Brooklyn* by the Yarkony group and *MESKIT* by the Simon group.

99. K. M. Bushan, H. Xu, P. H. Ruane, R. A. D'Sa, C. M. Pavlos, J. A. Smith, T. C. Celius, and J. P. Toscano, *J. Am. Chem. Soc.*, **124**, 12640 (2002). Controlled Photochemical Release of Nitric Oxide from O^2-Naphthylmethyl- and O^2-Naphthylallyl-Substituted Diazeniumdiolates.

100. M. Filatov, S. Shaik, M. Woeller, S. Gimme, and S. D. Peyerimhoff, *Chem. Phys. Lett.*, **316**, 135 (2000). Locked Alkenes with a Short Triplet-State Lifetime.

101. J. N. Harvey, S. Grimme, M. Woeller, S. D. Peyerimhoff, D. Danovich, and S. Shaik, *Chem. Phys. Lett.*, **332**, 358 (2000). Computational Prediction of the ISC Rate for Triplet Norbornene.

102. D. Beljonne, Z. Shuai, G. Pourtois, and J. L. Bredas, *J. Phys. Chem.*, **105**, 3899 (2001). Spin–Orbit Coupling and Intersystem Crossing in Conjugated Polymers: A Configuration Interaction Description.

103. Q. Cui and K. Morokuma, *Theor. Chem. Acc.*, **102**, 127 (1999). The Spin-Forbidden Reaction $CH(^2\Pi) + N_2 \rightarrow HCN + N(^4S)$ Revisited I. Ab Initio Study of the Potential Energy Surfaces.

104. T. Seideman and S. P. Walch, *J. Chem. Phys.*, **101**, 3656 (1994). Two-Dimensional Potential Energy Surfaces for $CH(X^2\Pi) + N_2(X^1\Sigma_g^+) \rightarrow HCN(X^1\Sigma^+) + N(^4S)$.

105. T. Seideman, *J. Chem. Phys.*, **101**, 3662 (1994). Resonances in the $CH + N \rightarrow HCN + N(^4S)$ Reaction: The Dynamics of a Spin-Forbidden Process.

106. (a) J. C. Light, I. P. Hamilton, and J. V. Lill, *J. Chem. Phys.*, **82**, 1400 (1985). Generalized Discrete Variable Approximation in Quantum Mechanics. (b) Z. Bacic and J. C. Light, *Ann. Rev. Phys. Chem.*, **40**, 469 (1989). Theoretical Methods for Rovibrational States of Floppy Molecules.

107. Q. Cui, K. Morokuma, J. M. Bowman, S. J. Klippenstein, *J. Chem. Phys.*, **100**, 9469 (1999). The Spin-Forbidden Reaction $CH(^2\Pi) + N_2 \rightarrow HCN + N(^4S)$ Revisited. II. Nonadiabatic Transition State Theory and Application.

108. M. Engström, R. Owenius, and O.Vahtras, *Chem. Phys. Lett.*, **338**, 407 (2001). Ab Initio g-Tensor Calculations of Hydrogen Bond Effects on a Nitroxide Spin Label.

109. O. Vahtras, M. Engström, and B. Schimmelpfennig, *Chem. Phys. Lett.*, **351**, 424 (2002). Electric g-Tensor Obtained with The Mean-Field Spin–Orbit Hamiltonian.

110. D. B.Chesnut, in *Reviews in Computational Chemistry*, Vol. 8, K. B. Lipkowitz and D. B. Boyd, Eds., VCH Publishers, Weinheim, Germany 1996, p. 245. The Ab Initio Computation of Nuclear Magnetic Resonance Chemical Shielding.

111. H. Nakatsuji, H. Takashima, and M. Hada, *Chem. Phys. Lett.*, **233**, 95 (1995). Spin–Orbit Effect on the Magnetic Shielding Constant Using the Ab Initio UHF Method.

112. H. Kaneko, M. Hada, T. Nakajima, and H. Nakatsuji, *Chem. Phys. Lett.*, **261**, 1 (1996). Spin–Orbit Effect on the Magnetic Shielding Constant Using the Ab Initio UHF Method: Tin Tetrahalides.

113. O. L. Malkina, B. Schimmelpfennig, M. Kaupp, B. A. Hess, P. Chandra, U. Wahlgren, and V. G. Malkin, *Chem. Phys. Lett.*, **296**, 93 (1998). Spin–Orbit Corrections to NMR Shielding Constant from Density Functional Theory. How Important are the Two-Electron Term?

114. P. Lantto, J. Vaara, A. M. Kantola, V.-V. Telkki, B. Schimmelpfennig, K. Ruud, and J. Jokisaari, *J. Am. Chem. Soc.*, **124**, 2762 (2002). Relativistic Spin–Orbit Coupling Effects on Secondary Isotope Shifts of ^{13}C Nuclear Shielding in CX_2 (X = O, S, Se, Te).

115. T. Nakajima and S. Kato, *J. Phys. Chem. A*, **105**, 10657 (2001). Theoretical Study of the Effect of the Intermolecular Spin–Orbit Interaction in the Collision-Induced Intersystem Crossing of S_1 State Glyoxal by Ar.

116. M. Y. Niv, M. Bargheer, and R. B. Gerber, *J. Chem. Phys.*, **113**, 6660 (2000). Photodissociation and Recombination of F_2 Molecule in Ar_{54} Cluster: Nonadiabatic Molecular Dynamics Simulations.

117. (a) J. C. Tully and R. K. Preston, *J. Chem. Phys.*, **55**, 562 (1971). Trajectory Surface Hopping Approach to Nonadiabatic Molecular Collisions: The Reaction of H^+ with D_2. (b) J. C. Tully, *J. Chem. Phys.*, **93**, 1061 (1990). Molecular Dynamics with Electronic Transitions.

118. V. Aquilanti, E. Luzzatti, F. Pirani, and G. G. Volpi, *J. Chem. Phys.*, **89**, 6165 (1988). Molecular Beam Studies of Weak Interactions for Open-Shell Systems: The Ground and Lowest Excited States of ArF, KrF, and XeF.

119. M. Bargheer, M. Y. Niv, R. B.Gerber, and N. Schwentner, *Phys. Rev. Lett.*, **89**, 10301 (2002). Ultrafast Solvent-Induced Spin-Flip and Nonadiabatic Coupling: ClF in Argon Solids.

120. A. I. Krylov, R. B. Gerber, and R. D. Coalson, *J. Chem. Phys.*, **105**, 4626 (1996). Nonadiabatic Dynamics and Electronic Energy Relaxation of $Cl(^2P)$ Atoms in Solid Ar.

121. (a) C. Daniel, M.-C. Heitz, J. Manz, and C. Ribbing, *J. Chem. Phys.*, **102**, 905 (1995). Spin–Orbit Induced Radiationless Transitions in Organometallics: Quantum Simulation of the $^1E \rightarrow^3 A_1$ Intersystem Crossing Process in $HCo(CO)_4$. (b) M.-C. Heitz, C. Ribbing, and C. Daniel, *J. Chem. Phys.*, **106**, 1421 (1997). Spin–Orbit Induced Radiationless Transition in Organometallics: Quantum Simulation of the Intersystem Crossing Processes in the Photodissociation of $HCo(CO)_4$.

122. H. H. Michels and J. A. Montgomery, *J. Chem. Phys.*, **88**, 7248 (1988). The Electronic Structure and Stability of Asymmetric Dinitrogen Dioxide (a-N_2O_2).

123. K. A. Nguyen, M. S. Gordon, J. A. Montgomery, H. H. Michels, and D. R. Yarkony, *J. Chem. Phys.*, **98**, 3845 (1993). Theoretical Studies of Spin-Forbidden Radiationless Decay in Polyatomic Systems. II. Radiationless Decay of a-N_2O_2.

124. G. A. Janaway and J. I. Brauman, *J. Phys. Chem. A*, **104**, 1795 (2000). Direct Observation of Spin-Forbidden Proton-Transfer Reactions: $^2NO^- + HA \rightarrow {}^1HNO + A^-$.

125. A. M. Mebel, S.-H. Lin, and C.-H. Chang, *J. Chem. Phys.*, **106**, 2612 (1997). Theoretical Study of Vibronic Spectra and Photodissociation Pathways of Methane.

126. D.-Y. Hwang and A. M. Mebel, *Chem. Phys.*, **259**, 89 (2000). Ab Initio Study of the Reaction Mechanism of Singlet and Triplet N_2O and their Intersystem Crossing.

127. M. R. Manaa and C. F. Chabalowski, *Chem. Phys. Lett.,* **300**, 619 (1999). A Theoretical Treatment of the Intersystem Crossing in the Spin-Forbidden Reaction NO $(X^2\Pi)$ + CO $(X^1\Sigma^+) \rightarrow N(^4S) + CO_2 (X^1\Sigma_g^+)$.

128. R. Sadygov and D. R. Yarkony, *J. Chem. Phys.*, **107**, 4994 (1997). Electronic Structure Aspects of the Spin-Forbidden Reaction $CH_3 (X^2A_2'') + N(^4S) \rightarrow HCN (X^1\Sigma^+) + H_2 (X^1\Sigma_g^+)$.

129. (a) A. S. Veige, L. M. Slaughter, P. T. Wolczanski, N. Matsunaga, S. A Decker, and T. R. Cundari, *J. Am. Chem. Soc.*, **123**, 6419 (2001). Deoxygenations of $(silox)_3WNO$ and R_3PO by $(silox)_3M$ (M = V, Ta) and $(silox)_3NbL_n$: Consequences of Electronic Effects. (b) A. S. Veige, L. M. Slaughter, E. B. Lobkovsky, P. T. Wolczanski, N. Matsunaga, S. A. Decker, and T. R. Cundari, *Inorg. Chem.*, **42**, 6204 (2003). Symmetry and Geometry Considerations of Atom Transfer: Deoxygenation of $(silox)_3WNO$ and R_3PO (R = Me, Ph, t-Bu) by $(silox)_3M$ (M = V, NbL (L = PMe_3, 4-picoline), Ta; silox = tBu_3SiO).

130. M. Metz and E. I. Solomon, *J. Am. Chem. Soc.,* **123**, 4938 (2001). Dioxygen Binding to Deoxyhemocyanin: Electronic Structure and Mechanism of the Spin-Forbidden Two-Electron Reduction of O_2.

131. G. L. Zubay, *Biochemistry*, 4th ed., Wm. C. Brown Publishers, Dubuque, Iowa, 1998. p. 244.

132. R. Prabhakar, P. E. M. Siegbahn, B. F. Minaev, and H. Ågren, *J. Phys. Chem. B,* **106**, 3742 (2002). Activation of Triplet Oxygen by Glucose Oxidase: Spin–Orbit Coupling in the Superoxide Ion.

CHAPTER 3

Calculation of the Electronic Spectra of Large Molecules

Stefan Grimme

Theoretische Organische Chemie, Organisch-Chemisches Institut der Universität Münster, Corrensstraße 40, D-48149 Münster, Germany

INTRODUCTION

With the development of more sophisticated quantum chemical methods in recent years, realistic calculations of molecular excited states became increasingly feasible. Electronically excited molecules play important roles in flames, plasmas, the atmosphere, and photochemical synthesis. Large organic molecules that absorb or emit in the visible region of the electromagnetic radiation spectrum are used as dyes or fluorescent markers in biological processes. The photochemistry of living systems, namely photosynthesis and the vision process, are currently under intense investigation. All these phenomena require (at least initially) a detailed consideration of the spectral properties of the excited states involved.

Electronic spectra arise from transitions between electronic states of different quantum numbers induced by electromagnetic radiation with ultraviolet or visible (UV/vis) light. The term ''electronic spectra'' implies the Born–Oppenheimer (BO) picture of molecules where the electronic and nuclear degrees of freedom are separated. Similarly, the description of the spectra in terms of particular electronic states is valid solely in a small region of the

nuclear configuration space, that is, for chemically similar structures. Each excited state has, in all respects, different properties than the ground state, namely, energy, geometry, electron density, dipole moment, and so on. In this sense, we can consider the excited states of one molecule as different types of entities or occurrences of the same Hamiltonian.

Excited states are very important in quantum chemistry. Obviously, they are the basic quantities of interest when electronic spectra are considered. Furthermore, because the excited states form a complete basis of the Hamiltonian, all second-order properties such as polarizabilities (van der Waals forces), NMR chemical shifts, ESR *g*-tensors, or optical rotations of chiral molecules can be calculated quite accurately by sum-over-(excited) state expressions. It should also be clear that any attempt to model photochemical reactions must be preceded by a careful examination of the electronic spectra of the reactants and products in order to deduce the electronic character of the states involved.

The interpretation of electronic spectra is more difficult than those obtained by IR or NMR techniques and also the theoretical–computational requirements are higher. The reason for this is that usually a significant reorganization of the electronic and nuclear coordinates occurs upon excitation and, in addition, the induced changes are often delocalized in nature. Furthermore, even for medium-sized systems, the density of states in small energy regions can be very large, which leads to overlapping spectral features (due to large band widths). These feature are theoretically (and also experimentally) difficult to resolve.

The ability of electronic structure theory to make reliable predictions for excitation energies and transition moments has advanced extraordinarily in recent years. By using time-dependent density functional theory (TDDFT), linear-response (LR) or equation-of-motion (EOM) coupled-cluster (CC), or multireference perturbation theory (MRPT), even relatively large molecules now can be investigated routinely. On the other hand, investigations of excited-state problems are still not as routine as most ground states. Also, reliable "black-box" type methods to simulate a wide variety of electronic spectra are still missing. Although some of the problems may be solved in the near future by more efficient computer algorithms and advanced hardware capabilities, inherent difficulties in the description of excitation processes will remain. It seems obvious that the complexity of the problem requires more human efforts, that is, a careful examination and understanding of the system under consideration, and furthermore a bit more than basic knowledge about the theoretical methods that are used.

This chapter provides a comprehensive overview of the current status of computational chemistry to describe electronic spectra. The focus is predominantly on larger molecular systems under medium-to-low resolution conditions. A quantitative description of the high-resolution spectra of diatomic to four-atom molecules requires special treatments for vibrational and relativistic

fine-structure effects and must also employ highly accurate quantum chemical methods (e.g., multireference configuration interaction, MRCI), which are currently not feasible for larger molecules. The main intention of this presentation is to provide the nonspecialist with an introduction to the field and a review of the key references that may be helpful as a starting point for his or her own investigations.

After a very basic introduction to the problem in which the general types of spectra and excited states are discussed, various theoretical aspects of the simulation of electronic spectra are outlined in the following section. This section includes the important topics of excitation energies and transition moments as well as some consideration of vibrational effects that can now be included routinely even for larger systems. It also includes a comprehensive but condensed presentation of quantum chemical methods that can, and should, be applied to these problems. The last section contains case studies of a variety of problems including UV spectra of organic and transition metal systems, Rydberg spectra, spectra of open-shell systems, and circular dichroism (CD) spectroscopy, which also involves magnetic transition moments. In addition, recent advances in the description of vibrational structure in the electronic spectra of larger molecules are described.

Before continuing, we want to refer the reader to some of the existing reviews and key references about this topic. Many of the general theoretical and technical aspects of quantum chemical methods cannot be considered here. In this respect, the reader is referred to the excellent book of Helgaker et al.[1] The most recent introduction to the problem of electronic spectroscopy is that of Peyerimhoff,[2] where many important older references can also be found. Much older, but still valuable books, are those of Murrel,[3] Jaffe and Orchin,[4] Mataga and Kubota,[5] and Robin.[6] The standard textbooks on photochemistry from Turro,[7] Michl and Bonacic-Koutecky,[8] and Klessinger and Michl[9] also include good introductions to the theoretical description of electronic spectra. More specific reviews, that is, those dealing with a particular theoretical method (such as CASPT2) can be found in the excellent contributions from the Roos group.[10–12] A recent review of electronic excitations in aggregates–oligomers including density matrix based techniques to analyze the states has recently been given by Tretiak and Mukamel.[13] A very good survey of spin–orbit effects on electronic spectra (not considered here), which emphasizes theoretical aspects, has recently been given by Marian[14] (see also Ref. 15).

Types of Electronic Spectra

To perform reliable quantum chemical simulations of electronic spectra, a detailed understanding of the different state and possible transition types is necessary. Figure 1 provides a schematic overview of the processes usually observed for molecules where, for simplicity, the rovibrational fine structure of the electronic levels has been neglected.
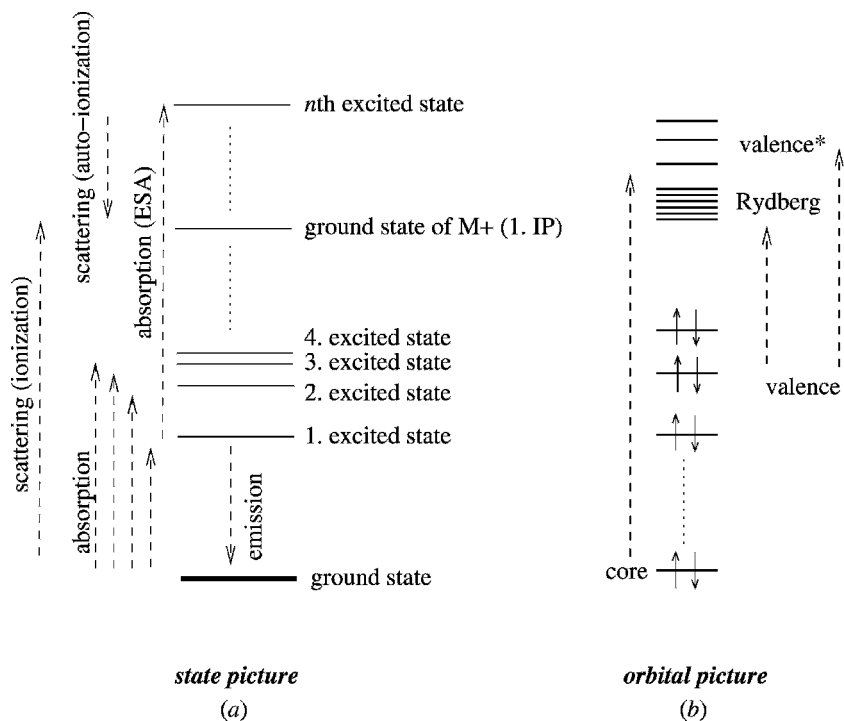
Figure 1 Overview of different state and transition types in a state (*a*) and orbital picture (*b*). Abbreviations: IP (ionization potential), ESA (excited-state absorption).

One of the key points here is that state and orbital pictures should not be interchanged or mixed. Electronic absorption spectra originate from transitions between eigenstates and *not* from those between one-electron wave functions (orbitals). While the state picture is exact, but provides no detailed information about the electronic structures, the orbital picture is approximate. However, it is intuitively understandable and allows for easy classification of electronic spectra. In the orbital picture, a transition between the ground and an excited state is simplified to an excitation between origin (occupied in the ground state) and target (virtual, i.e., usually empty in the ground state) orbitals. More mathematically speaking, one implicitly uses single excitations between the orbitals (even more precisely: singly substituted Slater determinants; the terms "excited" and "substituted" are used synonymously) to express the wave functions of the excited states. Beside the most common valence–valence excitations, valence–Rydberg excitations are important in which the final orbital has relatively large spatial extent resembling atomic functions of higher principal quantum number. Core excitation spectra are an important tool in material science for the assignment of molecular oxidation states [for a very early and the most recent density functional theory (DFT) study on this topic see Refs. 16 and 17].

The dominating importance of single excitations is based on physical reasons. They dominate the most common one-photon processes, since they usually have low excitation energies and involve large transition moments (intensities). This is different for two-photon spectra; for a recent DFT study on this topic, see Ref. 18.

The large number of excitation possibilities, especially in higher lying energy regions, is one of the reasons why absorption spectra simulations are so difficult. Because emission processes are usually observed only from the lowest excited state to the ground state (in rare cases a second excited state must be considered), their theoretical description is much easier. Energetically embedded into the electronic spectrum are ionic states, where at least one electron has been removed from the system. These continuum states and their formation are the topic of scattering theory, which will not be considered here. However, especially for Rydberg spectra, ionized states are important because they represent the asymptotic limit of a Rydberg series with infinite principal quantum number.

The second important issue to consider is the measurement conditions under which the experimental spectra are recorded. This not only has dramatic consequences for the shape of the spectra but also determines which theoretical approaches should be taken. Figure 2 shows different visible absorption
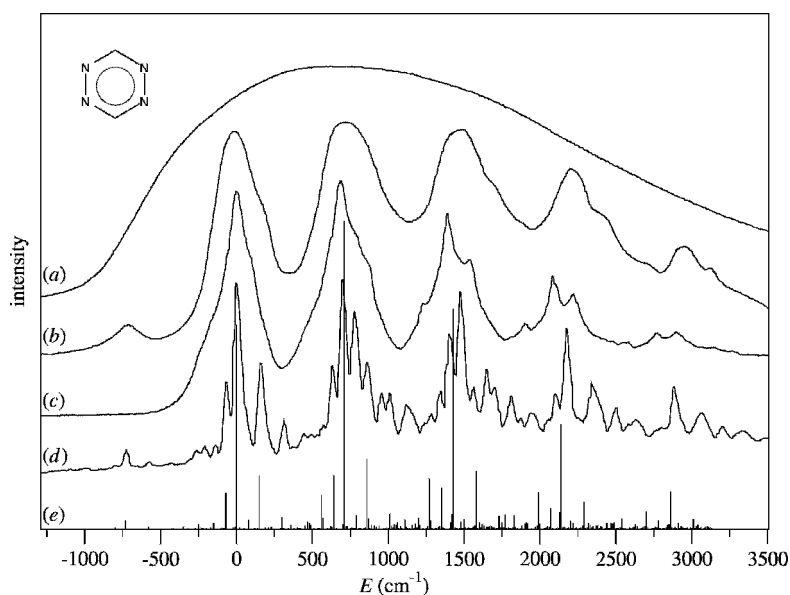
Figure 2 Visible absorption spectra ($n \rightarrow \pi^*$ state, onset at $\sim$550 nm) of tetrazine under different conditions (from top to bottom): (*a*) aqueous solution at room temperature (RT), (*b*) cyclohexane at RT, (*c*), hydrocarbon matrix at 77 K, (*d*) gas phase at RT, and (*e*) TDDFT–B3LYP[20,21] simulation of the vibronic transitions at RT. The 0–0 vibronic transition has been set to zero.

spectra for the $n \rightarrow \pi^*$ band of tetrazine, where the influence of environment and temperature can be seen very clearly (this nice example was first presented by Mason[19]).

Spectrum (*d*) shows a medium-resolved UV spectrum in the gas phase at room temperature for which a huge number of vibronic transitions occurring simultaneously with the change of electronic quantum number are resolved. A detailed understanding of this spectrum including hot-bands (excitations out of vibrationally excited levels of the ground state, excitation energies < 0 in Figure 2) requires a vibrational treatment of both electronic states. Trace (*e*) shows the result of such a simulation (outlined in more detail in later sections) presented as a "stick-spectrum," which is in almost perfect agreement with experiment. Due to solvent–matrix-induced line-broadening, the fine structure is clearly reduced in the spectrum that is recorded in a hydrocarbon matrix at low temperatures. Note the missing hot band, for example, at $-700 \, cm^{-1}$ due to decreasing population of thermally excited vibrational levels in the ground state. With increasing temperature (spectrum *b*), the density of vibrational states increases thereby further broadening the bands. It seems clear that changes of this kind require the inclusion of temperature in the simulations, for example, via population of levels according to a Boltzmann distribution. The spectra (*b*) and (*c*) have been recorded in weakly interacting hydrocarbon solvents that more or less resemble the gas-phase spectrum. Experience shows that such spectra can be safely used in theoretical treatments (which mostly neglect solvent effects) as substitutes for the often missing gas-phase spectra. In most cases, weakly interacting solvents just induce a small red-shift of the entire spectrum due to a higher polarizability (larger stabilization by van der Waals interactions) of the excited states. On the contrary, spectrum (*a*) recorded in water shows complete loss of any vibrational structure due to strong interactions with the solvent (mostly weak $N \cdots H$ bonds). This situation would require the calculation of a number of different water–tetrazine aggregates, including their dynamic behavior, which is currently out of reach for any reliable quantum mechanical treatment.

Types of Excited States

Selection of the theoretical method to be employed in practical simulations is the decisive factor for the overall accuracy of a calculated spectrum. The main problem in computing the various electronic states is to properly account for the electron correlation (EC) effects, which is the difference between a Hartree–Fock (HF) independent particle model and reality. Usually, one distinguishes between dynamic (short-ranged) EC, which is ubiquitous and can be understood as a pure many-particle effect, and static (long-ranged) EC resulting from the energetic near-degeneracy of different electronic configurations. This very important issue is outlined schematically in Figure 3. Note that in the following we deal exclusively with spin-allowed transitions (i.e., no

(*a*)   (*b*)   (*c*)
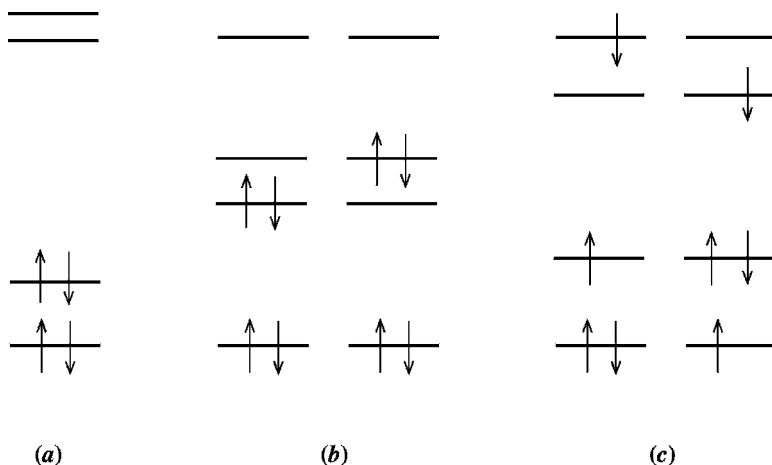
Figure 3 Orbital pictures of electron correlation effects: (*a*) ground state of a closed-shell system with a large highest occupied molecular orbital–lowest unoccupied molecular orbital (HOMO–LUMO) gap showing predominantly dynamic EC. (*b*) Near-degeneracy of two electronic configurations occurring, for example, in biradicals or during homolytic bond cleavage. (*c*) Near-degeneracy of two singly substituted electronic configurations in an excited state.

change of spin-multiplicity between the states) and that mostly even-numbered electron systems with singlet multiplicity will be discussed (exceptions are the phenoxyl radical and the lowest triplet state of naphthalene, both discussed in a later section).

Electronic excitation is usually connected with an unpairing of electrons, which, as a rule of thumb, contributes ~1 eV correlation energy change per pair. Furthermore, even the usual definition of the correlation energy ($E_{corr} = E_{exact} - E_{HF}$) is not unambiguous for excited states because a HF self-consistent field (SCF) description (which is used as "uncorrelated" reference) is rarely possible. Because the degree of sophistication of the theoretical treatment that can be performed is usually limited, it is important to know which main factors influence the magnitude of the electron-correlation contributions.

For that purpose, electronic spectra are first classified according to the character of the states involved. A very basic distinction relies on the electronic structure of the corresponding initial state from which the transition occurs. This initial state is not necessarily the ground state of the system, shown schematically in Figure 4, which includes the three most common possibilities. For a more detailed discussion of this point in the context of restricted and unrestricted TDDFT approaches, see Ref. 22.

Most electronic spectra are measured for closed-shell systems that usually have a large gap between occupied and virtual orbitals. This case is the
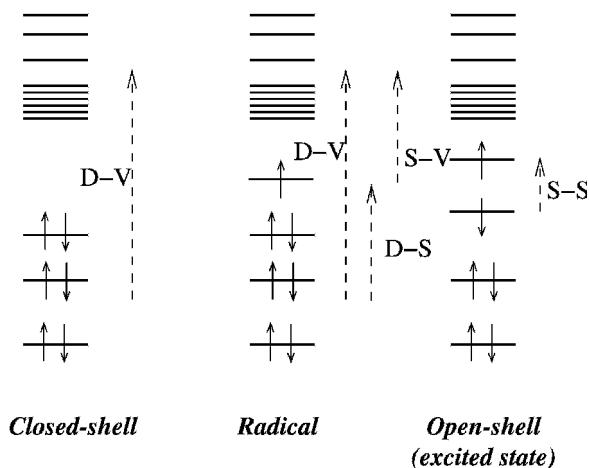
Figure 4 Orbital pictures of the most common initial-state configurations and the different types of single excitations. The open-shell state shown on the right side additionally has the possibility of *S-S* excitations. Abbreviations: doubly occupied MO (D), virtual MO (V), singly occupied MO (S).

simplest because the initial state is then often the ground state of the system (we consider absorption here) and it is, furthermore, usually well described by a single Slater determinant. In these systems, doubly occupied MO to virtual MO (D–V) single excitations (see Figure 4) play the most important role, although important exceptions with low-energy double excitations (e.g., polyenes) are known. It is clear that the number of different excitation types increases for systems that are already open shell in the ground state. For radicals, doubly occupied to singly occupied (D–S) and singly occupied to virtual (S–V) excitations must also be considered and in the case of excited-state absorption, S–S excitations are also possible. While many different theoretical approaches have been developed and extensively tested for the closed-shell situation, the open-shell systems are more complex. For low-spin states especially, only a few methods are, in principle, applicable.

Table 1 contains a state classification in terms of the more chemically–physically motivated language often used in the literature. Note that the entries in the different sections can in fact occur in almost arbitrary combinations, for example a charge-transfer excited state can be single reference dominated by single excitations (a state often occurring lowest in dyes) or one can have a high-spin Rydberg state, and so on. The last column contains theoretical issues that may be applicable in particular cases.

As already mentioned, the accurate account of the electron correlation effects in the different states is the most important precondition to obtain reliable predictions for electronic spectra. Before considering some details of this simulation process, a few words on general aspects of EC in larger systems

Table 1 Overview of Excited-State Types[a]

State Classification	Description	Theoretical Aspects to Consider
Valence	Excitations between (non)bonding–anti-bonding orbitals	Strongly varying amounts of EC
Rydberg	Excitations to virtual orbitals of large spatial extent	Special AO basis sets required asymptotics of potential[b]
Core excited	Excitations out of core orbitals	Special treatments–algorithms to extract high-lying roots
Locally excited	Excitations between spatially close orbitals	
Charge transfer	Excitations between very distant orbitals	Asymptotics of potential[b]
Singly excited	WF are dominated by singly excited determinants	Simple TD approaches sufficient[c]
Multiply excited	WF includes important contributions from doubles, triples, and so on	Multireference approaches necessary
Single reference	WF can be described mainly by one determinant	Mostly dynamic EC
Multi-configurational (multireference)	WF includes many important contributions	Breakdown of MO picture Static EC
Low spin	Spins are mostly paired (e.g., singlet, doublet)	EC larger for low-spin than for high-spin states
High spin	$M_s > M_s$ (min) (e.g., triplet, quartet)	

[a] Abbreviations: WF (wave function), EC (electron correlation), TD (time-dependent), AO (atomic orbital).
[b] Mainly apply to TDDFT, where approximate exchange-correlation potentials are used in the effective Kohn–Sham Hamiltonian.
[c] For example, adiabatic TDDFT or LR(EOM) coupled-cluster singles and doubles.

seem appropriate. Large molecules are close to a crossover region when going from molecular systems to solids, and, from a physicist's point of view would be classified as insulators, semiconductors, or metals. The EC effects in insulators (saturated with σ-bonds only) are mostly local (short-ranged, dynamic) in nature and can thus be described by local wave function or density functional methods. The variations of the EC effects between the different states of insulators are expected to be small or roughly constant so that even simple methods completely lacking EC may be sufficient. However, these simple systems are not very interesting chemically and, thus, most theoretical treatments performed in practice must consider semiconductor- or even metal-like molecules. One characteristic of the states in these systems is the nonlocality of

the EC (or even exchange) effects, where also a separation into static and dynamical EC is no longer appropriate. This nonlocality is difficult to describe theoretically mainly because (a) three or more particle correlations become important and (b) theoretical approximations that rely on "spatial separation" cannot be used. Thus, only correlated wave function approaches that include these effects explicitly will ultimately yield the desired accuracy in these cases. In this context, a strong warning should be noted: For obvious reasons, most developments of new quantum chemical methods for excited states will be tested and "benchmarked" on atoms or small molecules with only a few electrons. The results and conclusions thus obtained are not always transferable to "real" problems (i.e., a method that gives good results for ethene is not necessarily appropriate for porphyrin) mostly because the importance of higher order EC effects increases with the size of the system.

THEORY

Excitation Energies

In the Born-Oppenheimer picture, electronic transitions occur between rovibrational levels of two electronic states n and m. The excitation energy is the energy difference between the two levels yielding the spectral position of the transition

$$\Delta E_{nm,vv',jj'} = E_{m,v',j'} - E_{n,v,j} \qquad [1]$$

where v and j indicate vibrational and rotational quantum numbers, respectively. Because the rotational structure is rarely resolved experimentally for larger molecules, we always assume in the following that $j = j' = 0$ and drop the corresponding index. For the special case that the transition occurs between the two vibrational ground states ($v = v' = 0$), Eq. [1] reduces to

$$\Delta E_{nm}^{0-0} = E_m^{el} - E_n^{el} + E_m^{ZPE} - E_n^{ZPE} \qquad [2]$$

yielding the 0–0 transition energy E^{0-0}, where E^{ZPE} are the vibrational zero-point energies. At low temperatures, the 0–0 transition can usually be identified as the onset of the experimental spectrum. The calculation of this important quantity thus requires the computation of the two electronic-state energies and their vibrational normal modes. Because the calculation of E^{ZPE} is relatively demanding (even in the usually employed harmonic approximation), one often replaces the 0–0 transition energy by the pure electronic part,

$$\Delta E_{nm}^{el} = E_m^{el} - E_n^{el} \qquad [3]$$

This approximation is relatively accurate yielding errors typically < 0.1–0.2 eV. If transitions from the ground state are considered, these errors are systematic because the vibrational frequencies in the excited state are usually smaller than in the ground state and thus, $\Delta E^{\text{el}} > \Delta E^{0-0}$.

So far, all energies discussed for the two states necessarily refer to energy minima, and thus, two separate geometry optimizations of the molecular structures are required. While this is a routine task for most ground states, excited-state geometry optimization is a very difficult problem. First, for most of the more accurate excited-state quantum chemical models, implementations of analytical gradients are still missing. Although numerical derivatives can in principle always be obtained, their calculation is usually too costly and thus they are used only for benchmark purposes on small systems.[23] Second, in higher energy regions, the density of states is usually very large, which leads to many avoided surface crossings. In such situations, geometry optimizations are almost impossible because state flippings often occur and induce a complete breakdown of the most common quasi-Newton optimization algorithms. These are the reasons that even today most investigations rely on the so-called vertical approximation. In this approach, the optimized ground-state geometry is used to calculate all excited-state energies and transition moments. Note that the vertical excitation energy

$$\Delta E'^{\text{el}}_{nm} = E'^{\text{el}}_{m} - E^{\text{el}}_{n} \qquad [4]$$

(where the prime indicates the use of the nonrelaxed ground-state geometry) does not correspond to any observable. Instead, it represents a relatively good approximation (often to within 0.1–0.2 eV) to the intensity maximum of a spectral band. It should be clear that this approach works best for large molecules with small geometry changes between the states and for spectra obtained in solution under low-resolution conditions. Typical values for the difference between vertical and 0–0 excitation energies are given in Table 3.

The ultimate goal of theoretical electronic spectroscopy is to provide reliable and realistic simulations of electronic spectra. For that purpose, one usually needs a relatively high accuracy for the excitation energies. If we consider valence and Rydberg states with ΔE values of < 10 eV, and if we assume typical bandwidths of ~ 0.3–0.5 eV, the errors for ΔE should not exceed 0.2–0.3 eV. Even more important than the accuracy of the absolute values (systematic errors can be corrected by global shifting or scaling as is usually done in IR spectroscopy) is the relative accuracy obtained for the different states of one molecule. A wrong ordering of states can lead especially to misinterpretation of experimental data, an issue that is a particular problem in photochemical studies.

To illustrate the accuracy that can be obtained by modern quantum chemical methods, the results for a benchmark set of molecules is now briefly discussed. An outline of the theoretical background of the applied methods is

Table 2 Comparison of Calculated Vertical Singlet–Singlet Excitation Energies with Experimental Absorption Band Maxima[a]

Molecule	State	Experimental (eV)	TDDFT-B3LYP	CC2	MR-MP2
				Error[b] (eV)	
Anthracene	$1^1B_{3u}(\pi\pi^*, L_a)$	3.3	0.03	0.69	0.39
	$1^1B_{2u}(\pi\pi^*, L_b)$	3.5	0.42	0.43	−0.15
Indole	$2^1A'(\pi\pi^*, L_b)$	4.4	0.52	0.53	−0.15
	$3^1A'(\pi\pi^*, L_a)$	4.8	−0.02	0.47	0.15
Porphyrin	$1^1B_{1u}(\pi\pi^*)$	2.0	0.08	0.32	−0.33
	$1^1B_{2u}(\pi\pi^*)$	2.4	0.05	0.31	−0.07
	$2^1B_{1u}(\pi\pi^*)$	3.1	0.24		−0.03
	$2^1B_{2u}(\pi\pi^*)$	3.3	0.22		−0.02
Indigo	$1^1B_u(\pi\pi^*)$	2.0	0.08	0.36	0.10
Pyridazine	$1^1B_2(n \to \pi^*)$	3.4	0.14	0.47	0.22
Benzocyclo-butendione	$1^1B_2(n \to \pi^*)$	2.8	0.10	0.19	−0.12
	$1^1A_2(n \to \pi^*)$	3.5	0.05	0.33	0.12
Benzaldehyde	$1^1A''(n \to \pi^*)$	3.8	−0.17	0.12	0.18
C$_5$	$\Pi_u(n \to \pi^*)$	2.8	0.56		−0.19
Pyrrole	$1^1A_2(\pi \to 3s)$	5.2	−0.45	−0.06	0.06
	$1^1B_2(\pi \to 3p)$	5.9	−0.36	−0.10	0.10
Si$_2$(CH$_3$)$_6$	$1E_u(\sigma \to 4p)$	6.4	−0.38	−0.68	0.12
Ferrocene	$1^1E_{1g}(d \to d)$	2.8	−0.79		−0.09
Cr(CO)$_6$	$1^1T_{1u}(d \to \pi^*)$	4.4	0.08		0.34
	$2^1T_{1u}(d \to \pi^*)$	5.5	0.50		0.10
P$_4$	1^1T_2	5.6	−0.08	−0.08	−0.22
Na$_4$	1^1B_{3u}	1.8	0.06	0.03	0.05
mean absolute deviation (MAD)			0.24	0.32	0.15

[a]For technical details and references to the experimental data see Ref. 25.
[b]Error $= \Delta E(\text{calc.}) - \Delta E(\text{exp.})$.

given in a later section. Table 2 shows results for vertical singlet–singlet excitation energies obtained with TDDFT (time-dependent density functional theory), CC2 (a simplified coupled-cluster model), and MR-MP2 methods (multireference perturbation theory). The systems tabulated have been chosen to cover a broad range of molecules and states of different character. Further discussions on the accuracy of calculated ΔE values are given below in the sections containing the case studies; another TDDFT benchmark study can be found in Ref. 24.

Inspection of the data clearly shows how difficult it is to meet the accuracy requirements of ∼0.2–0.3 eV even for these lowest-lying states. Although the mean absolute deviation (MAD) for all three methods falls in this range, only the MR-MP2 method achieves a good overall accuracy for the entire range of systems. Both TDDFT and CC2 have some outliers with errors

> 0.5 eV and CC2, especially, completely breaks down for C_5 and the difficult transition metal systems. Note that the three methods tested represent the most accurate approaches that can also be applied to larger systems and that other "cheap" methods (like CIS or semiempirical treatments) often yield quite unreliable results with errors >0.5–1 eV.

As already mentioned, a direct comparison of vertical excitation energies with experimental data is not possible and such results contain uncertainties due to geometry relaxation effects. A more reliable assessment of theoretical methods can be achieved by a comparison of the ΔE^{0-0} values that are presented for the lowest states of some unsaturated molecules in Table 3. The last column of this table indicates the difference between 0–0 and vertical excitation energies.

These data indicate more clearly the problems theoretical methods (TDDFT in this case) have in accounting for the change of electronic structure upon excitation. For the ionic L_a states of the aromatic compounds (using Platts nomenclature derived from the perimeter model, see, Ref. 9 e.g.) and the $1B_u$ state of the polyene, a systematic underestimation of the excitation energies is observed while the opposite is true for the other more covalent states that exhibit stronger multiconfigurational character (for a more detailed discussion of these problems see Refs. 35 and 36).

The effects of geometry relaxation (sixth column) are significant for the smaller and medium-sized systems (0.4–0.6 eV) but diminish with the size of the molecule. For the larger aromatic molecules, differences between $\Delta E^{'el}$ and ΔE^{0-0} of ~ 0.2–0.3 eV are found. Note, however, that the geometry relaxation effects can be more important (up to 1 eV) in the case of larger systems as well when single-bond torsions between conjugated fragments are possible.[37] The differences between the ΔE^{el} and ΔE^{0-0} values (the ZPE contribution) are much smaller (0.12–0.17 eV, 0.03 eV for azulene) and roughly constant for the systems considered.

Transition Moments

Band intensities (transition probabilities) are the second important factor determining the shape of an electronic spectrum. Including the oscillating radiation field as a perturbation to the molecular Hamiltonian and applying time-dependent perturbation theory yields, under some approximations (the most important being that the radiation wavelength is much larger than the size of the molecule and small field strengths), the electronic transition moment (TM) as an expectation value over the initial and final wave functions with the relevant one-electron operator $\hat{O}$,

$$\mathrm{TM} = \left\langle \Psi_m | \hat{O} | \Psi_n \right\rangle \qquad [5]$$

Table 3 Comparison of Calculated [TDDFT-B3LYP/TZV(d,p)] and Experimental 0–0 Excitation Energies (in eV) for the Lowest Singlet States ($\pi\pi^*$) of Unsaturated Systems

Molecule	Transition	ΔE^{0-0}			$\Delta E^{\mathrm{rel}} - \Delta E^{0-0}$	Conditions	Reference
		Calc.	Exp.	Error	Calc.		
Naphthalene	$1B_{2u}, L_a$	3.98	4.44	−0.46	0.42	Gas phase	26
Anthracene	$1B_{2u}, L_a$	2.90	3.43	−0.53	0.33	Gas phase	26
Tetracene	$1B_{2u}, L_a$	2.18	2.77	−0.59	0.29	Argon jet	27
Pentacene	$1B_{2u}, L_a$	1.66	2.12	−0.46	0.33	Hexadecane matrix	28
Pyrene	$1B_{2u}, L_a$	3.43	3.84	−0.41	0.26	Gas phase	26
Azulene	$1B_1$	1.99	1.78	0.21	0.41	Cyclohexane	29
Octatetraene	$1B_u$	3.71	4.41	−0.70	0.34	Argon jet	30
Octatetraene	$2A_g$	4.46	3.59	0.87	0.45	Helium jet	31
Styrene	$2A'$	4.41	4.88	−0.46	0.56	Argon jet	32
Phenol	$2A', L_b$	4.79	4.51	0.28	0.31	Argon jet	33
o-Cyanophenol	$2A', L_b$	4.32	4.21	0.11	0.31	Helium jet	34

A comprehensive discussion of this important derivation can be found in Refs. 38 and 39. The nuclear contributions to the TM leading to vibrational fine structure in the spectra are discussed in the following section. Alternatively, the electronic part of the TM is obtained from the first-order reduced transition density matrix γ as

$$TM = \text{tr}(\mathbf{O}\gamma) \qquad [6]$$

where the matrix $\mathbf{O}$ is the representation of the operator in the basis of orbitals ψ ($O_{ij} = \int \psi_i(r)\hat{O}\psi_j(r)dr$) and γ is the analogous matrix representation of the transition density given by

$$\gamma_{ij} = \int \psi_i(r_1)\gamma(r_1, r_1')\psi_j(r_1')dr_1 dr_1' \qquad [7]$$

with

$$\gamma(r_1, r_1') = N_{\text{el}} \int \Psi_m \Psi_n dr_2 \cdots dr_N \qquad [8]$$

The importance of the concept of transition density matrices is that they allow a straightforward interpretation of excited states[13] either by plotting or by population analyses as usually performed for "normal" ($n = m$) densities.

The leading term in the interaction of radiation with matter is the electric dipole contribution ($\boldsymbol{\mu}$) for which the one-electron operator $\hat{O}$ is given by the position coordinates r_k of the electrons as

$$\hat{O} \equiv \hat{\boldsymbol{\mu}}_L = e \sum_k^{N_{\text{el}}} \hat{\boldsymbol{r}}_k \qquad [9]$$

which is called the "dipole-length" form. Note that $\boldsymbol{\mu}$ are vector quantities (given in bold) including x, y, and z components. The alternative "velocity" formulation uses

$$\hat{O} \equiv \hat{\boldsymbol{\mu}}_V = \frac{-ie}{\Delta E^{\text{el}}} \sum_k^{N_{\text{el}}} \hat{\boldsymbol{\nabla}}_k \qquad [10]$$

For exact wave functions and those that fulfill the hyper-virial theorem by construction [e.g., time-dependent Hartree–Fock (TDHF) or random phase approximation (RPA), TDDFT, see below] both forms are equivalent. Note that all virial theorems are exactly fulfilled only in a complete (i.e., usually infinitely large) AO basis. By a simultaneous computation of the transition dipole moments in the length and velocity forms and subsequent numerical

Table 4 The TDHF Transition Dipole Moments (in Debye) for the $1^1A' \rightarrow 1^1A''$ Transition ($n \rightarrow \pi^*$ excited state) in Acetaldehyde Calculated with Dunning's Correlation Consistent cc-VXZ Basis Sets[a]

Basis Set		μ_V	μ_L
cc-VDZ	$[3s2p/2s]$	0.0701	0.0363
cc-pVDZ	$[3s2p1d/2s1p]$	0.0072	0.0330
cc-pVTZ	$[4s3p2d1f/3s2p1d]$	0.0317	0.0534
aug-cc-pVTZ	$[4s3p2d1f/3s2p1d] + [1s1p1d1f/1s1p1d]$	0.0695	0.0674
cc-pVQZ	$[5s4p3d2f1g/4s3p2d1f]$	0.0513	0.0591
aug-cc-pVQZ	$[5s4p3d2f1g/4s3p2d1f] + [1s1p1d1f1g/1s1p1d1f]$	0.0675	0.0670

[a]See Refs. 40 and 41.

comparison, the above mentioned time dependent (TD) methods allow some estimate of basis set completeness for the corresponding transition. Table 4 provides a numerical comparison of the two transition dipole moments for the weakly allowed $n \rightarrow \pi^*$ transition in acetaldehyde calculated with different AO basis sets.

It can be seen that if a certain degree of basis set saturation is reached (cc-pVTZ, third row), the two values start to converge to the same value (~ 0.067), which is almost reached at the aug-cc-pVTZ level. Note the strong effect of "diffuse" functions (denoted as aug) for this property (compare rows three/four and five/six) and also the relatively large fluctuations for the velocity form that are caused by the more complicated structure of the differential operator in Eq. [10]. In addition, there is a lot of numerical evidence that for other systems the length form is more stable yielding, with small AO basis sets, results closer to the basis set limit (see, e.g., Ref. 42). Note too that the presented example is quite challenging due to the "almost" symmetry forbidden character of the transition and that both the fluctuations for the V-form are smaller and the agreement between L- and V-forms is better for dipole allowed transitions.

The (dimensionless) oscillator strength for an electronic transition is given by

$$f_{nm} = \frac{2}{3} \Delta E_{nm} |\mathbf{\mu}_{nm}|^2 \qquad [11]$$

where ΔE and the length of the transition dipole vector are expressed in atomic units. Theoretically, $f = 1$ corresponds to the transition probability of a harmonically moving electron bound to a proton (an early model of the hydrogen atom). Experimentally, one obtains f by integrating the area under the absorption band between energies $\bar{\nu}_1$ and $\bar{\nu}_2$ (in wavenumbers)

$$f = 4.3 \times 10^{-9} \int_{\bar{\nu}_1}^{\bar{\nu}_2} \varepsilon(\bar{\nu}) d\bar{\nu} \qquad [12]$$

where ε is the decadic molar extinction coefficient given in L/(mol cm). Although in experimental investigations a nonlinear energy scale $\lambda = hc/E$ (wavelengths) is usually used, it is strongly recommended that one transform all data (experimental and theoretical) first to linear eV or cm^{-1} units. Inversion of Eq. [12] allows one to deduce $\varepsilon(\bar{v})$ from calculated oscillator strengths. For the band form of the individual transitions (also called "shape-function"), Gaussian functions have been successfully employed, which accounts for vibrational (and solvent, if present) induced broadening. To simulate entire spectra, the contributions from all transitions are added according to

$$\varepsilon(E) = \frac{2.87 \times 10^4}{\sqrt{\sigma}} \sum_i f_i e^{[-(E-\Delta E_i)/2\sigma]^2} \qquad [13]$$

where σ is the full width of the band at $1/e$ height (for most UV bands $\sigma = 0.4$ eV is appropriate) and ΔE_i (in eV) and f_i are the excitation energies and oscillator strengths for transition i, respectively. Figure 5 schematically shows a typical outcome for the simulation of a conventional UV spectrum. The vertical lines indicate the position and oscillator strength of the individual transitions (right f axis), while the dashed curve is the overall result from Eq. [13]. Very weak or forbidden transition should be indicated by special symbols.
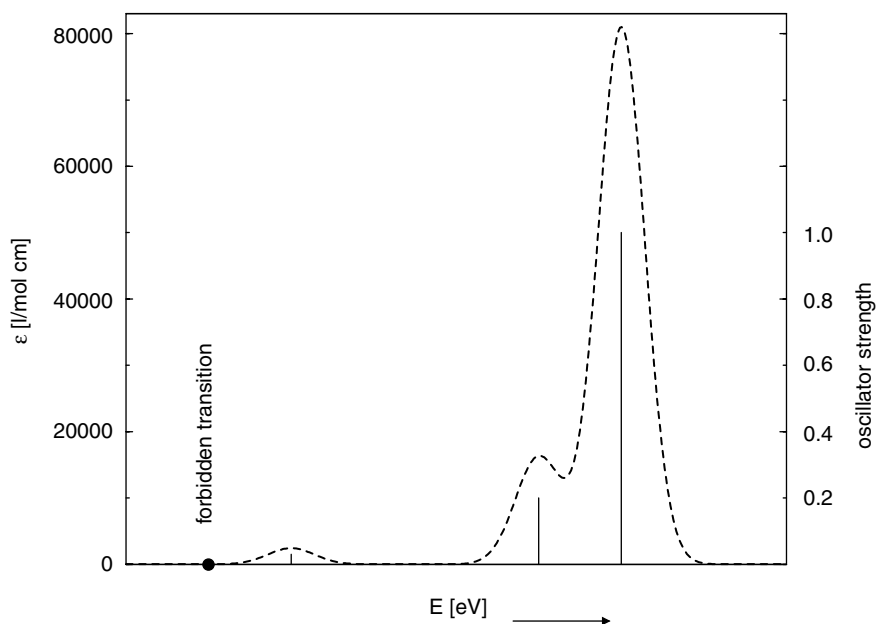
Figure 5 Example of the graphical presentation of a simulated (vertical) UV spectrum.
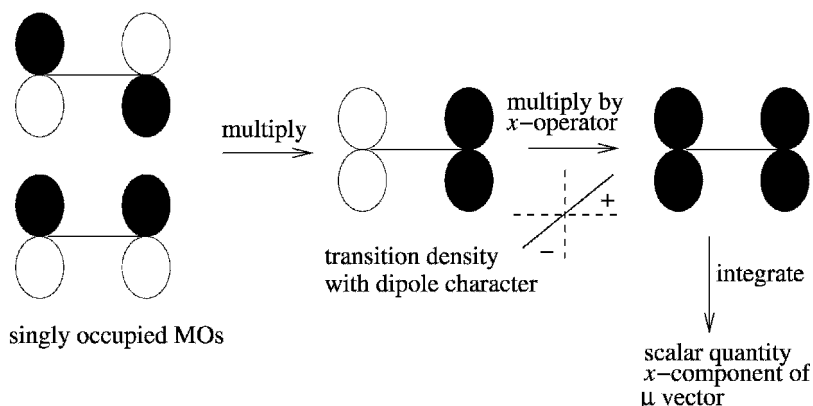
Figure 6 Schematic description for the process of generating the electric transition dipole moment for the $\pi \rightarrow \pi^*$ excitation of ethene. Transparent (black) areas correspond to a positive (negative) phase.

For an electric dipole allowed transition, the radiation field must create or destroy a node in the corresponding transition density. A simple example is an atomic $s \rightarrow p$ excitation, where the transition density is simply given by the product $s \times p$, which yields a scalar quantity when multiplied by r and integrated over space. In other words, the transition density must have a dipolar structure, where "probability" is shifted from positive-to-negative (and vice versa) regions. The mathematical process of generating the electric dipole transition moments is schematically outlined for the example of the $\pi \rightarrow \pi^*$ transition of ethene in Figure 6.

If the transition density simultaneously has some rotational character, the magnetic component of the radiation field becomes important. For noncircularly polarized light, that is, in conventional UV spectroscopy, the magnetic component of the radiation field can be neglected in the time-dependent perturbation because it enters with a factor ν_{el}^{av}/c; the average electron velocity is much smaller than the speed of light. The effect of the magnetic component in circularly polarized light is observed experimentally in electronic circular dichroism (CD) spectroscopy of chiral molecules.[43] As a conventional absorption, it is a first-order, linear effect but depends on the combined interaction of a molecule with the electric and magnetic components of the radiation field.

The main quantity in CD is the rotatory strength R, which is completely analogous to the oscillator strength in UV spectroscopy and is given by the scalar product[44,45]

$$R_{nm} = Im\langle\Psi_n|\hat{\boldsymbol{\mu}}|\Psi_m\rangle \times \langle\Psi_n|\hat{\boldsymbol{m}}|\Psi_m\rangle$$
$$= |\boldsymbol{\mu}_{nm}| \cdot |\boldsymbol{m}_{nm}| \cdot \cos(\boldsymbol{\mu}_{nm}, \boldsymbol{m}_{nm}) \qquad [14]$$

where $\hat{\boldsymbol{m}}$ is the magnetic dipole operator (angular momentum)

$$\hat{\boldsymbol{m}} = \frac{\hbar e}{2mci} \sum_k^{N_{\text{el}}} \hat{\boldsymbol{r}}_k \times \hat{\boldsymbol{\nabla}}_k \qquad [15]$$

In oriented media (which will not be considered here), additional dipole–quadrupole terms contribute to the CD. The rotatory strength is zero by symmetry if the molecule possesses at least one improper S_n axis as symmetry element (this causes either μ or m to be zero or an orthogonal arrangement of the two vectors, see Eq. [14]). Also, in complete analogy to UV spectra, R can be obtained from Eq. [12] with ε replaced by the difference of extinction coefficients for left- and right-circularly polarized light ($\Delta\varepsilon = \varepsilon_L - \varepsilon_R$).

The main perspective of CD spectroscopy is its potential to determine the absolute configurations of chiral substances that is of particular importance for compounds with biological or pharmacological relevance, for example. Furthermore, unlike optical spectra, the CD bands can be positive or negative, and for this reason carry more information and sometimes allow one to resolve close-lying or hidden electronic transitions. More details about theoretical CD spectroscopy can be found in Refs. 43 and 46–48. In Ref. 49 the CD spectra of a benchmark set of molecules have been investigated with the most recent quantum chemical methods. Some representative examples are discussed in a later section of this chapter. Recent advances in the theoretical description of magnetically induced CD, which in addition employs a static magnetic field, can be found in Ref. 50.

Vibrational Structure

In general, the intensity I of a transition between the two states Ψ_m and Ψ_n is proportional to the square of the transition dipole moment

$$\boldsymbol{\mu}_{n,m} = \langle \Psi_n | \hat{\boldsymbol{\mu}} | \Psi_m \rangle \qquad [16]$$

with the dipole operator

$$\hat{\boldsymbol{\mu}} = -e \sum_i \hat{\boldsymbol{r}}_i + e \sum_s Z_s \hat{\boldsymbol{R}}_s = \hat{\boldsymbol{\mu}}_e + \hat{\boldsymbol{\mu}}_N \qquad [17]$$

where $\hat{\boldsymbol{r}}_i$ and $\hat{\boldsymbol{R}}_s$ denote the electron and nuclear coordinates, respectively, and Z_s represents the nuclear charges.

For the description of a vibronic transition both electronic and nuclear coordinates must be taken into account. In the adiabatic BO approximation, the complete wave function can be separated into the product

$$\Psi(\boldsymbol{r}, \boldsymbol{R}) = \Psi_\varepsilon(\boldsymbol{r}; \boldsymbol{R})\Psi_N(\boldsymbol{R}) \qquad [18]$$

where $\Psi_\varepsilon(\boldsymbol{r}; \boldsymbol{R})$ and $\Psi_N(\boldsymbol{R})$ denote the electronic and nuclear wave functions, respectively (for a good review about treatments beyond the BO approximation see Ref. 51).

After the separation of translational, rotational, and vibrational modes of nuclear motion

$$\Psi_N(\boldsymbol{R}) = \Psi_t(\boldsymbol{R}_t)\Psi_r(\boldsymbol{R}_r)\Psi_v(\boldsymbol{R}_v) \qquad [19]$$

the vibrational modes can be represented within the harmonic approximation as a product of eigenfunctions of the harmonic oscillator $v_i(Q_i)$

$$\Psi_v(\boldsymbol{R}_v) = v(\boldsymbol{Q}) = v_1(Q_1)v_2(Q_2)\cdots v_N(Q_N) \qquad [20]$$

where Q_i denote the vibrational normal coordinates. For the transition dipole moment $\boldsymbol{\mu}_{\varepsilon'v',\varepsilon v}$ of a vibronic transition $\varepsilon v \to \varepsilon'v'$ with quantum numbers ε and ε' for the electronic and v and v' for the vibrational parts of the initial and final state, respectively, these expressions give[39]

$$\boldsymbol{\mu}_{\varepsilon'v',\varepsilon v} = \langle v'(\boldsymbol{Q}')|\boldsymbol{\mu}_{\varepsilon',\varepsilon}(\boldsymbol{Q})|v(\boldsymbol{Q})\rangle \qquad [21]$$

where $v(\boldsymbol{Q})$ and $v'(\boldsymbol{Q}')$ are the vibrational functions, $\boldsymbol{Q}$ and $\boldsymbol{Q}'$ are the normal modes of the initial and final states, respectively, and $\boldsymbol{\mu}_{\varepsilon',\varepsilon}(\boldsymbol{Q})$ denotes the electronic transition dipole moment as a function of the initial state normal modes. Because for the transition dipole moment in general no analytical expression is available, it is expanded in a Taylor series around the initial state minimum geometry $\boldsymbol{Q}_0$.

$$\boldsymbol{\mu}_{\varepsilon',\varepsilon}(\boldsymbol{Q}) \approx \boldsymbol{\mu}_{\varepsilon',\varepsilon}(\boldsymbol{Q}_0) + \sum_i \frac{\partial\boldsymbol{\mu}_{\varepsilon',\varepsilon'}}{\partial Q_i}(Q_i - Q_{i,0}) + \cdots \qquad [22]$$

Truncation of the expansion after the first term yields the Franck–Condon (FC) approximation for the transition dipole moment

$$\boldsymbol{\mu}_{\varepsilon'v',\varepsilon v} = \boldsymbol{\mu}_{\varepsilon',\varepsilon}(\boldsymbol{Q}_0)\langle v'(\boldsymbol{Q}')|v(\boldsymbol{Q})\rangle \qquad [23]$$

In the FC picture, the transition occurs from the vibrational ground state of the initial electronic state to the vibrational excited state of the electronically excited state (considered in the following absorption), which most resembles the first one.[52–54] This is shown schematically in Figure 7 for two excited states that (with respect to the ground state) are shifted differently along one vibrational normal coordinate Q.

A description of electric dipole forbidden transitions, where $\boldsymbol{\mu}_{\varepsilon',\varepsilon}(\boldsymbol{Q}_0) = 0$ is not possible in terms of the FC approximation, because vibronically induced
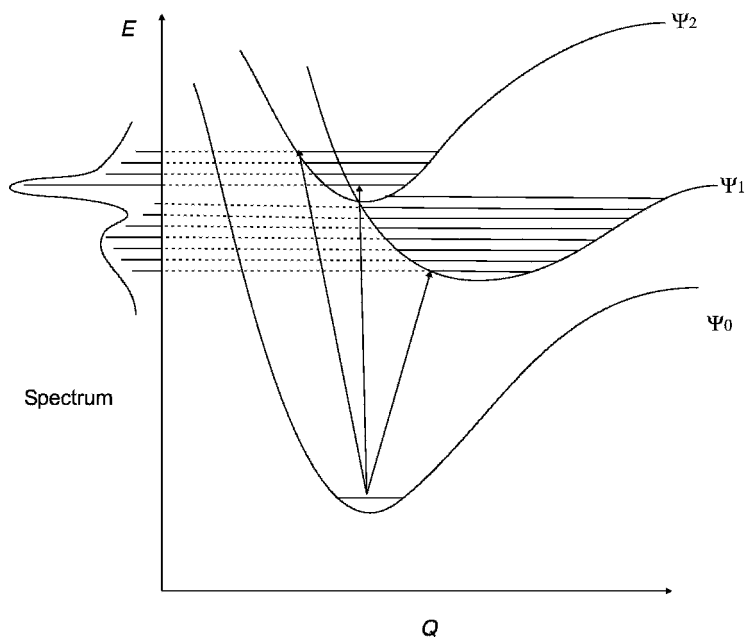
Figure 7 Schematic description of the FC principle for two excited states with dominating 0–0 transition (Ψ_2, almost parallel potential surfaces) and a broad intensity distribution (Ψ_1, shifted minimum), respectively. The nonzero intensities for 0–1, 0–2, … vibrational transitions to Ψ_2 result entirely from the different shapes of the surfaces, while the intensity distribution for the other transition originates mainly from the shifted minimum.

transition moments are neglected. Truncation of the Taylor expansion (Eq. [22]) after the second term yields the Franck–Condon–Herzberg–Teller (FC–HT) approximation for the transition dipole moment

$$\boldsymbol{\mu}_{\varepsilon'v',\varepsilon v} = \boldsymbol{\mu}_{\varepsilon',\varepsilon}(\boldsymbol{Q}_0)\langle v'(\boldsymbol{Q}')|v(\boldsymbol{Q})\rangle + \sum_i \frac{\partial \boldsymbol{\mu}_{\varepsilon',\varepsilon}}{\partial Q_i}\langle v'(\boldsymbol{Q}')|(Q_i - Q_{i,0})|v(\boldsymbol{Q})\rangle \quad [24]$$

This description accounts for transition dipole moments induced by displacements along the normal modes during the electronic transition, that is, a simultaneous excitation of vibrational modes. This approximation is also denoted as double-harmonic. For electric dipole forbidden transitions, the first term in Eq. [24] vanishes and the resulting expression is denoted as the Herzberg-Teller (HT) approximation.

$$\boldsymbol{\mu}_{\varepsilon'v',\varepsilon v} = \sum_i \frac{\partial \boldsymbol{\mu}_{\varepsilon',\varepsilon'}}{\partial Q_i}\langle v'(\boldsymbol{Q}')|(Q_i - Q_{i,0})|v(\boldsymbol{Q})\rangle \quad [25]$$

A physical explanation for the influence on the transition dipole moment of vibrational excitations that occur simultaneously to the electronic transition is that displacements along the normal modes result in a perturbation of the electron–nuclear interaction. Thereby a mixing of the excited-state electronic wave function with other excited-state wave functions occurs that leads to a mixing of the corresponding transition dipole moments[39,55] ("intensity borrowing" from dipole-allowed transitions). Because this process depends critically on the energy separation between the target and the mixing states, a good overall description of the electronic spectrum is necessary to obtain reliable HT transition moments.

For molecules with more than one internal degree of freedom the normal modes of the ground and excited state are not in general identical (Duschinsky effect). Thus, for the calculation of the multidimensional integrals in Eqs. [23]–[25] it is necessary to describe the excited-state normal modes on the basis of the ground state taking into account the different minimum geometries. This is achieved by the following linear transformation (Duschinsky-transformation)[56]

$$Q' = JQ + K \qquad [26]$$

with $K = L'^T M^{1/2} \Delta R$ and the Duschinsky-matrix $J = L'^T L$, where L and L' denote the normal modes in mass-weighted Cartesian coordinates of the ground and excited state, respectively, ΔR the difference of the minimum geometries and M the diagonal matrix of the atomic masses. This relationship is exact for normal modes that—in the common symmetry group of ground and excited states—do not span the same symmetry species as one of the rotations. For normal modes having the same symmetry as one of the rotations, so-called "axis switching effects" occur.[57,58] Nevertheless the Duschinsky-transformation has been proven to be a good approximation.

With the use of a recursive algorithm,[59] the resulting integrals $\langle v'(JQ + K)|v(Q)\rangle$ are reduced to the integral over the vibrational ground state from which the $\langle v'(JQ + K)|Q_i|v(Q)\rangle$ terms can be derived as well.[60] A further technical issue concerns the calculation of the normal modes and frequencies of the ground and excited states. In all vibronic structure treatments we employ a numerical approach, where the second derivatives of the energy and the derivatives of the transition moments are calculated by finite differences from analytical gradients and the transition moments, respectively. This is done very efficiently in parallel using an extended version of the program SNF 2.2.1.[61,62] For the calculation of the FC and HT integrals and all required level combinations in a user-specified energy interval, the HOTFCHT 1.2[60] program is used.

Quantum Chemical Methods

General

Before continuing with an overview of existing quantum chemical approaches for computing the excited states of large molecules, it seems appropriate to first define a "wish list" of the properties these methods should provide. Generally desired properties that also apply to ground states (e.g., size-consistency, weak AO basis set dependence, systematic improvability, etc.) are not included in this list.

1. Applicability: The method should be able to treat arbitrary types of excited states (see Table 1, first column), especially highly excited ones, and those occurring in photochemical applications. Spectral simulations sometimes require the simultaneous description of 10–100 states.
2. Accuracy: Errors for excitation energies should be < 0.1–0.2 eV, transition moments should be accurate to within 20–30% and the sign (direction) of the moment should be correct.
3. Properties: All standard one-electron properties and transition moments as well as analytical nuclear gradients for geometry optimization should be available. The method should allow interpretation of the results within simple (e.g., MO) models.
4. Human effort: The method should be of "black-box" character including as few technical parameters as possible.
5. Computational: Memory and CPU requirements should not be significantly larger than for the corresponding ground-state calculation.

Unfortunately, none of the methods currently in use simultaneously fulfill all these requirements. The user's choice is thus determined by a consideration of the assets and drawbacks of a particular method which, in relation to the type of electronic spectra/states, may change from one problem to the other. Figure 8 provides the reader with a comprehensive overview of existing quantum chemical methods for excited states.

One of the basic problems to consider in advance concerns the multireference character of the ground state and the importance of multiply excited configurations in the excited states. The choice depicted in Figure 8 distinguishes between single-reference CI or TD approaches on the left and multireference treatments on the right (MR-CC and quantum Monte Carlo treatments also shown on the right side are currently under intense development and included only for completeness). Both groups of methods have their own advantages and disadvantages. The MR methods are general in a sense that once a zeroth-order [reference, $\Psi^{(0)}$] wave function has been built up, any type of excited state can be treated. The price to pay, however, is that the choice of $\Psi^{(0)}$ is not unique and furthermore requires a lot of human effort. In contrast, the starting point for the TD approaches is the electronic ground state, where the excitation energies (transition moments) are obtained as poles

Single-reference ground state and
excited states dominated by singles?

"black-box"   "general"   "non routine"

Yes   No

Single–Reference   Multi–Reference   Quantum Monte Carlo

MR–Coupled Cluster
(various variants)

Type of Reference
– **CAS(SCF)**
– **RAS(SCF)**
– Individually selected conf.

MR–SD space

contraction   selection

variational   full   perturbative
– MRCI   – **MR–MP2 (CASPT2, CASMP2)**
– MRCI+Dav.   – MR–MP3

time–dependent   variational

variational   +perturbative corrections
– **CIS**   – **CIS(D)**
– CISD   – CIS–MP2
– CISDT...

Hamiltonian/ground state?

correlated   uncorrelated
– TDCC (EOM-CC)   – **TDHF**
CC2,CC3,...
– **TDDFT**
– **TDsemiempirical**

Figure 8 An overview of quantum chemical methods for excited states. Bold-italic entries indicate methods that are currently applicable to large molecules. Important abbreviations used: CI (configuration Interaction), TD (time-dependent), CC (coupled-cluster), HF (Hartree–Fock), CAS (complete active space), RAS (restricted active space), MP (Møller–Plesset perturbation theory), S (singles excitation), SD (singles and doubles excitation), MR (multireference). Geometry optimizations of excited states for larger molecules are now possible with CIS, CASSCF, CC2, and TDDFT methods.

(residuals) of the response of the ground state to a time-dependent perturbation (electric field).

The basic theoretical background of the most widely used methods will be outlined in the following sections including the most important working equations and technical issues that must be considered in large-scale applications.

CI Methods

Although the application of configuration interaction (CI) methods to excited-state problems has decreased in recent years, they should be considered here first because the formalism is easy to understand and if properly developed, are also most general in application. A recent comprehensive review can be found in Ref. 63.

All CI methods are variational, that is, the electronic Schrödinger equation

$$\hat{H}|\Psi_n^{CI}\rangle = E_n^{CI}|\Psi_n^{CI}\rangle \tag{27}$$

is solved for state n with the following ansatz for the wave function

$$|\Psi_n^{CI}\rangle = (\hat{T}_1 + \hat{T}_2 + \hat{T}_3 + \cdots)|\Psi^{(0)}\rangle \tag{28}$$

where $\Psi^{(0)}$ is a so-called reference wave function and $\hat{T}_k$ are the single (one-electron, $k = 1$), double (two-electron, $k = 2$) and triple (three-electron, $k = 3$) excitation (replacement) operators, respectively. By acting onto $\Psi^{(0)}$ these operators generate complete sets of (excited) determinants by substitutions of occupied orbitals $i, j, k, \ldots$ in the determinants of $\Psi^{(0)}$ with virtual orbitals $b, c, d, \ldots$. Note that in general, open-shell determinants are not eigenfunctions of the $\hat{S}^2$ operator (they cannot be classified according to multiplicity as, e.g., singlet, doublet, triplet, ...). Actual treatments are often based on so-called configuration-state functions (CSF), which are represented by appropriate linear combinations of several determinants with the same M_s value (the term ''configuration'', which is often used to characterize the spatial distribution of the electrons in the different orbitals, is merely used linguistically but cannot be employed in actual computations).

The most important contributions from singles and doubles excitation are given, for example, by

$$\hat{T}_1 = \sum_{ib} t_i^b a_i a_b^\dagger \tag{29}$$

$$\hat{T}_2 = \frac{1}{4}\sum_{ibjc} t_{ij}^{bc} a_i a_b^\dagger a_j a_c^\dagger \tag{30}$$

where t represent the unknown amplitudes (CI coefficients) and a and $a^\dagger$ are the annihilation and creation operators, respectively. If $\Psi^{(0)}$ is taken as a single determinant (usually the HF ground state), this leads to single-reference CI methods. Depending on the level of truncation of the excitation operator in Eq. [28], one obtains CIS (includes only $\hat{T}_1$), CISD ($\hat{T}_1 + \hat{T}_2$), CISDT, and so on, models. Of these, only CIS is widely used to calculate electronic spectra:

- The computational cost for CIS is similar to that of the ground-state HF calculation and can also be performed directly in the AO basis thus minimizing hard-disk I/O. The accuracy of CIS for excited states is roughly that of HF for the ground state, that is, dynamic electron correlation effects are neglected (for ground and excited states).
- The CISD provides an unbalanced description for the excited states relative to the ground state, because for a closed-shell ground state, the most important double excitations (which mainly account for EC) are included. On the contrary, an excited state, which is already singly excited with respect to the ground state, requires at least the inclusion of triple excitations (triples are related to the singles as the doubles are to the HF state). Thus, CISD grossly overestimates the excitation energies.[64] Note that this does not hold for LR–CCSD, which accounts for higher excitations by the exponential of the excitation operator. Compared to CIS, all other CI schemes are not size-consistent (i.e., the calculated excitation energy for two noninteracting fragments is not exactly the same as for separate calculations on the individual monomers).

There are two major routes to improve the CI methods. The first is by including size-consistent corrections for dynamical EC leading to the CIS(D) and CIS-MP2 methods[65] (which are closely related to the coupled-cluster methods described in a later section). The second is by improving the reference wave functions, which leads to multireference CI (MRCI) methods, that, however, remain size-inconsistent.

In the MRCI approach, one tries to reach a balanced description by setting up a zeroth-order wave function $\Psi_n^{(0)}$ for each state of interest that includes the most important electronic configurations (static EC). For one particular state, then,

$$|\Psi_{\mathrm{MR}}^{(0)}\rangle = \sum_{a}^{\mathrm{references}} c_a^{(0)}|\Phi_a^{(0)}\rangle \qquad [31]$$

where $\Phi_a^{(0)}$ represent electronic configurations (determinants) with variationally determined coefficients $c_a^{(0)}$. A wide variety of different choices for $\Psi_{\mathrm{MR}}^{(0)}$ are currently in use, including full-CI within a selected set of orbitals (CAS), excitation restricted CI within a selected set of orbitals (RAS), or even individually (iteratively) selected configurations.

Application of this ansatz together with the truncation to single and double excitations as before (Eq. [28]) now includes all important contributions in a balanced manner. Hence, for a singly excited state, important parts of the triple excitations are included. The MR(SD)CI (the SD term is usually discarded in the abbreviation) method is very accurate for small- and medium-sized systems when the remaining size-consistency errors are corrected empirically, for example, via the Davidson scheme. Unfortunately, it is computationally very demanding to have an N_{el}^6 scaling behavior with system size and a very large prefactor. It can be routinely applied only to systems with $\sim$20–40 electrons (for benchmark or calibration purposes). For a more efficient approach that empirically combines DFT and MRCI methods, and that can be applied also to large systems see Ref. 66, applications in electronic spectroscopy can be found in Refs. 67–71.

Perturbation Methods

One way to retain the generality of the MR ansatz while reducing the computational costs is to use perturbation theory (PT). Perturbation theory has the important property of being size-consistent if properly formulated and implemented.[72] The starting point is again a reference wave function $\Psi_n^{(0)}$ for a particular electronic state n that includes the most important contributions to the wave function. By construction, $\Psi_n^{(0)}$ satisfies the eigenequation

$$\hat{H}_0|\Psi_n^{(0)}\rangle = E_n^{(0)}|\Psi_n^{(0)}\rangle \qquad [32]$$

where $\hat{H}_0$ is the zeroth-order Hamiltonian. In MP partitioning, $\hat{H}_0$ is defined via the perturbation V, which is

$$\lambda\hat{V} = \hat{H} - \hat{H}_0 = \sum_i^{N_{el}} \sum_{j>i}^{N_{el}} 1/\hat{r}_{ij} - \left\langle \hat{V}_{ee} \right\rangle_{average} \qquad [33]$$

the difference between the true and the mean-field (HF) electron–electron repulsion. In the MP schemes, $\hat{H}_0$ is represented as a sum of general Fock operators that are state-dependent. As usual in perturbation theory, the energy and wave function are expanded in a Taylor series for λ that then leads to a (decoupled) system of linear equations for each perturbation order. For large systems, one usually truncates at second-order (for an approximate fourth-order treatment see Ref. 73) which leads to methods that scale as N_{el}^5 with the system size. The second-order energy correction $E^{(2)}$ is

$$E^{(2)} = -\sum_a t_a^{(1)} \langle \Phi_a^{(1)}|\hat{H}|\Psi_n^{(0)}\rangle \qquad [34]$$

where $\Phi_a^{(1)}$ is an element (CSF) of the first-order corrected wave function with amplitude $t_a^{(1)}$ that is obtained by solving the linear equations

$$\sum_a t_a^{(1)} \langle \Phi_b^{(1)} | \hat{H}_0 - E_n^{(0)} | \Phi_a^{(1)} \rangle = -\langle \Phi_b^{(1)} | \hat{H} | \Psi_n^{(0)} \rangle \qquad [35]$$

In general, $\Psi^{(1)} = \sum_a t_a^{(1)} \Phi_a^{(1)}$ contains all single and double excitations from the reference that directly interacts through the true operator $\hat{H}$ [the various variants of MRPT differ in how the annihilation and creation operators act on $\Psi^{(0)}$].

A key point here is that in contrast to the MRCI case, the very large interaction matrix contains only elements between CSF and the simple one-electron operator $\hat{H}_0$ (the costly interactions with $\hat{H}$ appear only on the right side of Eq. [35] with the reference). This not only decreases the scaling behavior from N_{el}^6 (CI) to N_{el}^5 (PT), but also reduces the computational effort considerably because the one-electron matrix elements are very easy to evaluate. Apart from technical details for the solution of Eq. [35] (which especially holds for CASPT2, which uses a density matrix approach[74]), the different implementations of multireference perturbation theory (CASPT2,[74–76] CASMP2,[77] MR-MP2[78]) differ mainly by the choice of the reference wave function. Both CASPT2 and CASMP2 are based on complete-active-space wave functions as references that consist of a full CI treatment within an active space of orbitals–electrons and state-optimized orbitals while the MR-MP2 variant can employ arbitrary CI references and orbital sets. To be applicable for large molecules, careful consideration of technical details and implementation is necessary: There are at least two approaches[76,78] that have demonstrated good accuracy at reduced computational costs.

Within the "ab initio world", CASPT2 became the de facto standard by chemists for the calculation of electronic spectra. Its first success was the accurate description of the electronic spectrum of benzene,[75] which at that time was a challenging goal for quantum chemistry. Since then, hundreds of applications of CASPT2 in electronic spectroscopy appeared that are described in existing reviews[10–12] (for the most recent application see Ref. [79]). The most severe drawback of CASPT2 is the full CI reference wave function on which it is based. Without symmetry, active spaces of 12 electrons in 12 orbitals in the preceeding CASSCF treament are the current limit that is often not enough for large unsaturated systems.

TDHF and TDDFT

It is an understatement to say that DFT[80,81] has strongly influenced the evolution of quantum chemistry during the past 10–15 years. In the last 5 years, this statement also holds true for the treatment of excited states and, since then, time-dependent Kohn–Sham (KS) DFT (TDDFT)[82,83] has

become a routine tool to simulate electronic spectra. Both TDDFT and TDHF methods can be derived along similar lines as outlined briefly below.

We consider an N-electron system that is initially at time $t = t_0$ in its ground state $|\Psi_0\rangle$. At times $t > t_0$ a time-dependent perturbation $\lambda\hat{U}(t)$ is applied. For our purposes, the most important perturbation is the electric dipole part ($\boldsymbol{\mu}$) of a monochromatic radiation field given by

$$\hat{U}(t) = -\boldsymbol{\mu}Ee^{-i\omega t} \qquad [36]$$

that oscillates with frequency ω and has a (constant) field strength E. The linear response (LR) [index (1)] of an observable $O(t)$ is defined as the first variation of the expectation value with respect to the scalar variable λ

$$O^{(1)}(t) = \delta\langle\Psi(t)|\hat{O}(t)|\Psi(t)\rangle = \frac{d}{d\lambda}\langle\Psi(t)|\hat{O}(t)|\Psi(t)\rangle|_{\lambda=0} \qquad [37]$$

where $\Psi(t)$ is the time-dependent (ground-state) wave function. Graphically, we can imagine that $\Psi(t)$ can be represented by the complete set of all excited eigenstates (including Ψ_0) of the Hamiltonian and, thus, one can derive information about the desired excited states by considering the time evolution of $\Psi(t)$. More precisely, at certain frequencies ω electronic transitions are stimulated and the first-order response of the ground state must diverge. For these values of ω, the first-order response equations are exactly satisfied even if $\boldsymbol{\mu}E$ is zero, since these are intrinsic molecular properties corresponding to free oscillations. In other words, solving the TD equations for some Hamiltonian with a particular ansatz for the ground-state wave function is equivalent to finding the poles of the frequency-dependent polarizability $\alpha(\omega)$ (see Figure 9) that is given by the sum-over-states formula

$$\alpha(\omega) = \sum_{n}^{\text{all excited states}} \frac{f_{0n}}{\omega_n^2 - \omega^2} \qquad [38]$$

The transition moment can be obtained as the residue given by

$$\langle\Psi_0|\boldsymbol{\mu}|\Psi_n\rangle = \lim_{\omega\to\omega_n}(\omega - \omega_n)\alpha(\omega) \qquad [39]$$

Both the DFT and HF methods use an effective, one-particle (mean-field) Fock operator F. In general, it can be written as a functional of the first-order density matrix γ (see Eq. [8] with $m = n = 0$) as

$$F[\gamma](t) = b[\gamma](t) + v_H[\gamma](t) - v_{xc}[\gamma](t) + \lambda U(t) \qquad [40]$$
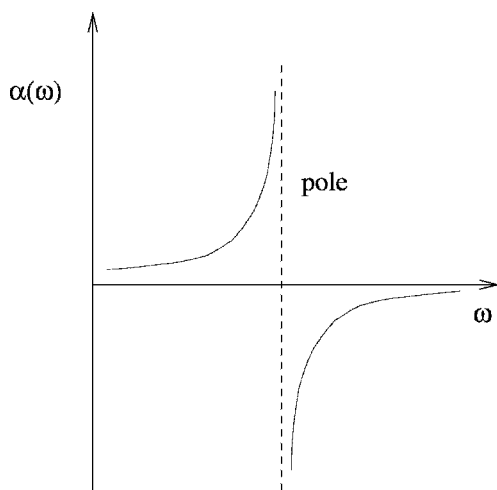
Figure 9 Frequency dependence of the electric dipole polarizability $\alpha(\omega)$. The position of the dashed line corresponds to the system's excitation energy.

where h is the one-electron part of the Hamiltonian, the index H indicates the e–e Coulomb (Hartree) part and v_{xc} is a general (non-local, HF + local, DFT) exchange-correlation potential. In analogy to Eq. [37], the linear response of the mean-field (KS or HF) density matrix is

$$\gamma^{(1)}(t) = \frac{d}{d\lambda}\gamma(t)|_{\lambda=0} \qquad [41]$$

By a Fourier transformation to the frequency domain, one obtains after expansion in the complete set of KS or HF one-particle eigenstates the following expression:

$$\gamma^{(1)}(\omega) = \sum_i \sum_a \left(\frac{u_{ai}(\omega)}{\omega - (\varepsilon_a - \varepsilon_i)}|i\rangle\langle a| \right) - \left(\frac{u_{ai}^*(\omega)}{\omega + (\varepsilon_a - \varepsilon_i)}|a\rangle\langle i| \right) \qquad [42]$$

where i and a are occupied and virtual orbitals, respectively, ε are their energies and u_{ai} are the matrix elements of the perturbation in the basis of the orbitals. Combining Eqs. [40] and [42] leads, after some algebraic manipulations, to a non-Hermitian eigenvalue problem that has to be solved for $\omega = \Delta E$. It is of the form

$$\begin{pmatrix} A & B \\ B & A \end{pmatrix}\begin{pmatrix} X \\ Y \end{pmatrix} = \Delta E \begin{pmatrix} 1 & 0 \\ 0 & -1 \end{pmatrix}\begin{pmatrix} X \\ Y \end{pmatrix} \qquad [43]$$

where **X** and **Y** are the solution vectors of the single particle-hole (excitations, $|i\rangle\langle a|$) and hole-particle (deexcitation, $|a\rangle\langle i|$) amplitudes, respectively, and **A**, **B** are related to Hamiltonian matrices between the single (de)excitations that are made from one-particle eigenvalues and Coulomb and exchange integrals over the MOs.[84,85] If formulated in the AO basis, Eq. [43] can be solved efficiently with computational effort similar to that of the preceeding ground-state SCF calculation. If the matrix **B** is set to zero, Eq. [43] reduces to a normal eigenvalue problem including only single excitations (**Y** = 0, CIS). For DFT variants of CIS, see Refs. 86 and 87. An important advantage of TDHF(DFT) over CIS is that the former methods satisfy, in a complete AO basis, certain sum-rules, for example, $\sum_i^\infty f_i = N_{el}$.

The actual form of the mean-field applied to the ground state (HF or Kohn–Sham DFT) determines the explicit expressions for the matrix elements. In a general notation including TDHF as well as TDDFT, they read

$$A_{ia\sigma,jb\tau} = \delta_{\sigma\tau}\delta_{ij}\delta_{ab}(\varepsilon_{a\sigma} - \varepsilon_{i\tau}) \qquad [44]$$
$$+ (i_\sigma a_\sigma|j_\tau b_\tau) - \delta_{\sigma\tau}c_{HF}(i_\sigma j_\sigma|a_\tau b_\tau)$$
$$+ (1 - c_{HF})(i_\sigma a_\sigma|f_{\sigma\tau}|j_\tau b_\tau)$$

$$B_{ia\sigma,jb\tau} = (i_\sigma a_\sigma|b_\tau j_\tau) - \delta_{\sigma\tau}c_{HF}(i_\sigma b_\sigma|a_\tau j_\tau) \qquad [45]$$
$$+ (1 - c_{HF})(i_\sigma a_\sigma|f_{\sigma\tau}|b_\tau j_\tau)$$

where i,j are used for ground-state occupied orbitals, a,b for virtual orbitals, and σ and τ are the spin variables. The parameter c_{HF} is the coefficient of the "exact" HF exchange (EEX) part in hybrid functionals. Thus, similar to the ground state, there is a continuous change from TDHF to TDDFT when hybrid functionals with a variable amount of HF exchange contribution are considered. A lot of numerical evidence indicates that this also holds for calculated properties of ground and excited states.

The last terms in these equations, which are of DFT origin, are defined as

$$(i_\sigma a_\sigma|f_{\sigma\tau}|j_\tau b_\tau) = \int\int i(r_1)a(r_1)f_{\sigma\tau}^{xc}(r_1,r_2)j(r_2)b(r_2)dr_1dr_2 \qquad [46]$$

In the so-called adiabatic approximation, the time-dependent exchange-correlation kernel f^{xc} is derived from the time-independent ground-state functional,

$$f_{\sigma\tau}^{xc}(r_1,r_2) = \frac{\delta^2 E_{xc}}{\delta\rho_\sigma(r_1)\delta\rho_\tau(r_2)} \qquad [47]$$

This approximation should work best for $\omega \to 0$, that is for energetically low-lying excited states.

The magnitude of the excitation energies is determined mainly by the diagonal part of the matrix **A**. For the closed-shell case, one obtains as a

zeroth-order approximation for the excitation energy of a state represented by a single substitution between MOs i and b

$$\Delta E = \varepsilon_b - \varepsilon_i - c_{\mathrm{HF}}(ii|bb) - (1 - c_{\mathrm{HF}})(ii|f|bb) + 2(ib|ib) \qquad [48]$$

Although this is often quantitatively a drastic approximation (due to the neglect of configuration mixing), a closer inspection of Eq. [48] gives some insight into the factors that determine excitation energies. In the HF case ($c_{\mathrm{HF}} = 1$), the difference of orbital energies is a very crude approximation because the Coulomb integral $(ii|bb)$ represents a significant correction, that is, lowering of the excitation energy [the exchange integrals $(ib|ib)$ are usually one order of magnitude smaller]. This is different in DFT, where the $\Delta\varepsilon$ term is much smaller and where the Coulomb interaction is replaced by a response integral containing the (local) exchange-correlation kernel. This locality of the DF leads to severe problems when the excitation is connected with a spatial separation of the hole–particle as for Rydberg or charge-transfer states. For a very early attempt to correct this in the DFT/SCI(CIS) methods, see Ref. 86. Consider, for example, a charge-transfer excitation from donor orbital i to the acceptor orbital b [where $(ib|ib) \approx 0$]. One obtains

$$\Delta E = \mathrm{IP} + \mathrm{EA} - c_{\mathrm{HF}}(ii|bb) - (1 - c_{\mathrm{HF}})(ii|f|bb) \qquad [49]$$

where we have approximated the ionization potential IP by ε_i and the electron affinity EA by ε_b. The interaction between the separated charges must be described by the Coulomb law, that is, $c_{\mathrm{HF}}(ii|bb) + (1 - c_{\mathrm{HF}})(ii|f|bb) \propto 1/R$, where R is the distance between the hole–particle. Because $c_{\mathrm{HF}} = 0$ for pure DF and $(ii|f|bb)$ falls off exponentially, the $1/R$ fall-off condition is not fulfilled. This analysis shows that the inclusion of nonlocal HF exchange $c_{\mathrm{HF}} > 0$ in a local (pure) density functional is essential to describe charge-and-spin-separating situations.

Coupled-Cluster Methods

The basic idea of most coupled-cluster (CC) approaches for excited states is the same as for the TDHF/DFT methods: Excitation energies are obtained as the poles (where, e.g., the frequency-dependent polarizability goes to infinity) of the ground-state response with respect to a time-dependent perturbation. The important difference is that the ground state is not described by a single HF/KS determinant but (similar to the CI ansatz) by many singly, doubly, and so on, substituted configurations. The important size-consistency property is included in the CC methods by using the exponential of the excitation operator

$$|\Psi_{\mathrm{CC}}\rangle = e^{\hat{T}}|\Psi^{(0)}\rangle \qquad [50]$$

By choosing $|\Psi^{(0)}\rangle \neq \Psi_{HF}$, one arrives at MR–CC methods that are currently an active field of research, but that are not applied routinely except for benchmark systems. Similar to the CI method, truncation of the excitation operator then leads to a hierarchy of methods termed CCS (which is equivalent to CIS for energies), CCSD, CCSDT, and so on.

Applying the time-dependent perturbation is straigthforward and leads to LR–CC methods. The nonlinear systems of equations include the "normal" T_1 and T_2 (for CCSD) operators–amplitudes and additionally single and double excitation (time-dependent) response amplitudes (for details the reader is referred to Refs. 1, 64, 88, 89 and references cited therein). An alternative approach, that, although conceptually different yields exactly the same excitation energies, is the equation-of-motion coupled cluster (EOM–CC) method [90]. The EOM–CC equations also contain the CC wave function $|\Psi_{CC}\rangle$ (Eq. [50]) and a second (state-dependent) excitation operator $\hat{R}_n$ including single, double, ... excitations (usually $\hat{R}$ is truncated in the same manner as $\hat{T}$). The EOM equations read as

$$[\hat{H}', \hat{R}_n]|\Psi_{CC}\rangle = \omega\hat{R}_n\Psi_{CC} \qquad [51]$$

where $\hat{H}' = \hat{H} - E_{HF}$.

One characteristic of all LR/EOM–CC methods is that a non-Hermitian eigenvalue problem finally has to be solved (which cannot be reduced to a standard eigenvalue problem as Eq. [43]) yielding "left" and "right" sets of solutions, and therefore also two sets of transition moments.

A "break through" for the application of the CC methods to excited states of large systems has recently been obtained by Christiansen et al.[91] These authors introduced a simplified LR–CCSD method termed CC2, where the doubles excitation operator is taken from second-order perturbation theory ($\hat{Q}_2$). The CC2 ground-state wave function can be written as

$$|\Psi_{CC2}\rangle = e^{\hat{T}_1+\hat{Q}_2}|\Psi^{(0)}\rangle \qquad [52]$$

and thus only the singles amplitudes remain as free parameters while the doubles contributions $\hat{Q}_2$ are taken from a MP2 treatment, that is, from

$$q_{ij}^{ab} \approx \frac{\langle ia|jb\rangle}{(\varepsilon_a + \varepsilon_b - \varepsilon_i - \varepsilon_j)} \qquad [53]$$

which reduces the scaling behavior from $\mathcal{O}(\mathcal{N}_{el}^6)$ to $\mathcal{O}(\mathcal{N}_{el}^5)$. In general, CC2 excitation energies are only slightly inferior to those from full CCSD. A further reduction of the computational costs in CC2[92] has been obtained by using the resolution-of-the-identity (RI) approximation for the two-electron integrals. The very efficient RI method is also used here in MR-MP2 and MRCI

methods as described before [66, 78]. The error for the excitation energies introduced by the RI approach is ~0.01–0.03 eV, which is clearly insignificant compared to other sources of error like basis set truncation error that is of the order of 0.1–0.2 eV with standard cc-pVTZ basis sets. An analytical gradient for RI-CC2 has also been reported recently,[93] which routinely allows for geometry optimizations of medium-sized molecules. This recent advance includes a significant fraction of dynamical electron correlation (as opposed to CIS and CASSCF that have hitherto been frequently used for that purpose).

Recommendations

Here, we provide a summary of the quantum chemical methods that can, and should be applied to the calculation of electronic spectra of large systems:

1. Hartree–Fock based methods (TDHF and CIS): Good energetic results from these methods cannot be obtained; the errors for excitation energies often exceed 0.5 eV. For low-spin states, ΔE is often too large so scaling factors of ~0.7–0.8 are in use while the ΔE values for high-spin states are usually underestimated. Contrary to statements in the literature,[94] the results are often even qualitatively wrong (false state ordering). The Rydberg states, for which they appear to perform reasonably well, are not really important for large systems. Because excited-state geometries are relatively insensitive to correlation effects, these methods may be used (after careful calibration) for that purpose but even this is difficult because the predicted order of states is often wrong. Both TDHF and CIS methods have a tendency (as does HF for ground states) to break symmetry, and consequently they often yield geometries that are too distorted. They are to be preferred over TDDFT if the asymptotic behavior of the potential (see below) is of crucial importance. They are sometimes applicable if only relative trends in a series of very similar molecules are of interest.

2. Coupled-cluster methods: For systems with well-behaved ground states, and, if the excited states are reasonably described by single excitations, low-order coupled cluster methods (CC2[91] or LR/EOM-CCSD[64, 90]) can provide good accuracy (errors < 0.3 eV). Especially when used together with efficient integral approximations (RI-CC2[92]) computations can be performed for fairly large molecules. For more complicated excited states or when the ground state is already strongly correlated, the inclusion of $\hat{T}_3$ is mandatory, which limits the applicability to small molecules.

3 Perturbation methods: In general, second-order multireference PT methods can be recommended for excited-state problems. They usually show very good accuracy (errors < 0.2 eV, excitation energies are systematically underestimated) and they can be applied to a wide variety of states and problems. However, MRPT methods are not "black-box" and careful checks of the technical details like the size of reference space, choice of orbitals, and so on, must be done. These methods require a lot of user

experience, as well as detailed insight into the system. For many states in the high-energy regions, the reference wave functions become prohibitively large, and, the second-order treatment often breaks down. The most serious disadvantage is that the results are very sensitive to the so-called "intruder states", which have low zeroth-order energies but are only weakly interacting with the reference state.

4. Density functional methods: The TDDFT approaches employing hybrid functionals such as B3LYP[20,21] or BHLYP[95] are always the method of choice for providing a first overview about the electronic spectrum of a particular molecule. The errors for ΔE are much smaller than with TDHF/ CIS and usually within 0.3–0.4 eV of experiment (often ΔE is underestimated). For larger transition metal compounds, TDDFT is the only method that is routinely applicable. The same holds for spectra, where on the order of a hundred different states must be considered. With common (asymptotically incorrect) functionals, larger errors are obtained for Rydberg[85,96] (see the following section) and charge-transfer states[97–99] or for states with strong contributions from ionic valence-bond structures.[35] A calibration on ab initio or experimental data and a check of the functional dependence of the results is strongly recommended.

5. Basis sets: The basis set requirements in excited-state applications are not very different than those for the corresponding ground state if only low-lying valence states are considered, and thus, properly polarized valence-triple-ζ (or even double-ζ) sets are often good enough (i.e., they provide ΔE to within 0.1 eV). Because the valence excited states of medium-sized systems can sometimes include diffuse components, a check of, for example, the $\langle r^2 \rangle$ expectation values (see the following section) is recommended and depending on its value, diffuse basis functions must be added (for an example, see a later section). For low-lying Rydberg states, additional atom-centered diffuse sets of single-ζ quality ([$1s1p1d$]/[$1s1p$] for main group compounds) are sufficient.

6. Semiempirical approaches represent an alternative quantum chemical method especially for very large systems or when only main group compounds without complicated electronic structure are involved. As for the ground states, however, they are gradually being displaced by the more accurate and robust DFT methods. Of the many semiempirical approaches, the all-valence methods with orthogonalization corrections[100,101] and the simplest Pariser–Parr–Pople (PPP) type methods for very large π-systems can be recommended (for a recent application to a 600 atom system, see Ref. 102). One area of application is the prediction of excited-state geometries where MNDO/CI approaches seem to be quite successful.[103,104] For excitation energies, however, standard MNDO, AM1, or PM3 Hamiltonians employing small CI expansions show large systematic as well as unpredictable (random) errors. Careful calibration is thus mandatory with all semiempirical methods.

CASE STUDIES

Vertical Absorption Spectra

Acetone

In this section, some general aspects of the computation of Rydberg spectra are discussed (for reviews on this topic, see Ref. 6 and Ref. 105; for a recent theoretical study on very high-lying Rydberg states (which will not be considered here), see Ref. 106). Although Rydberg states are ubiquitous, they are of lesser importance in the spectra of large molecules that are dominated by valence states. The reason to begin this section with this topic is twofold: First, Rydberg states are mostly of relatively simple structure, being dominated by a few (mostly one) single excitations and are thus easy to understand intuitively in a MO picture. Second, the excitation process is accompanied with a spatial separation of the electrons that is typical also for some valence states. This leads to problems with most density functionals as already discussed in an earlier section.

The transitions to Rydberg states generally have low intensities because of the large spatial extension of the final orbital (small overlap with the origin orbital yields weak transition densities) and consequently they are often hidden under more intense valence bands. As an example, here we therefore have to investigate a small molecule where the valence transitions are spectrally separated. Saturated ketones show only two valence states, namely, the $n \to \pi^*$ state at ~4 eV and a very high-lying $\pi \to \pi^*$ state so that a number of Rydberg transitions can be observed in the 6–9-eV range. Acetone, the simplest aliphatic ketone, is probably the best experimentally studied molecule of this group of important organic systems. Of the few theoretical studies that exist, we mention here only the most recent CASPT2 work of Merchan et al.,[107] where key references to the experimental data and older theoretical work can also be found.

Figure 10 shows the two orbitals that are involved in the first $n \to 3s$ Rydberg transition of acetone. The very different spatial extensions are clearly visible and especially in the outer regions of the 3s MO its almost spherical character can be seen.

The distinction between Rydberg and valence states is not that clear in larger molecules. A good indicator for the state character can be obtained from the $\langle r^2 \rangle$ expectation value (a measure of spatial extension) difference for state n with respect to the ground state. This is given by

$$\Delta \langle r^2 \rangle = \langle \Psi_n | \hat{r}^2 | \Psi_n \rangle - \langle \Psi_0 | \hat{r}^2 | \Psi_0 \rangle \qquad [54]$$

where

$$\hat{r}^2 = \hat{x}^2 + \hat{y}^2 + \hat{z}^2 \qquad [55]$$

(*a*)   (*b*)
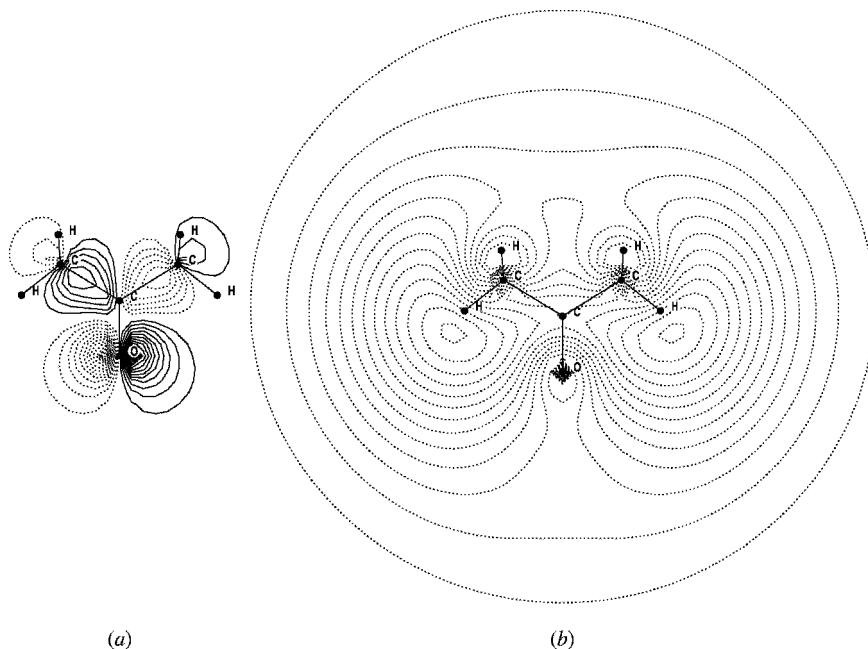
Figure 10 Contour plots of the lone-pair MO (*a*) and 3*s* Rydberg MO (*b*) for acetone in the O—CCC plane. Because of the too high potential for the virtual orbitals in ground-state HF treatments, the calculations refer to a ROHF/d-aug-cc-pVDZ treatment for the $^2B_2$ cation ground state.

is the trace of the Cartesian electric quadrupole operator. For molecules com-posed of second-row atoms, the $\Delta\langle r^2\rangle$ values are usually in the range 30–50 (3*s*), 50–100 (3*p*), and > 100 a_0^2 for 3*d* states, respectively, while they are usually $< 10\,a_0^2$ for pure valence states.

The "diffuseness" of Rydberg states leads to complications with some quantum chemical approaches. When using MRCI or MRPT2 methods it is absolutely necessary to use virtual orbitals that are optimized in the presence of the correct potential of $N_{el} - 1$ electrons. The (closed-shell) HF potential for the virtual orbitals includes the (nuclear charge) shielding of all N_{el} electrons and thus the Rydberg part of the spectrum is too diffuse, which leads to arti-ficial configuration mixing in the CI procedures (to a lesser extent, however, this also holds for some valence states, especially for medium-sized systems). Experience shows that individually optimized orbitals are not necessary, but instead, ROHF orbitals of, for example, the lowest cation state, can be employed.

The problems of most density functionals with Rydberg states are also related to the electronic potential far away from the nuclei. It is well known that the local density approximation (LDA) exchange potential $v_X^{LDA} \propto \rho(r)^{1/3}$
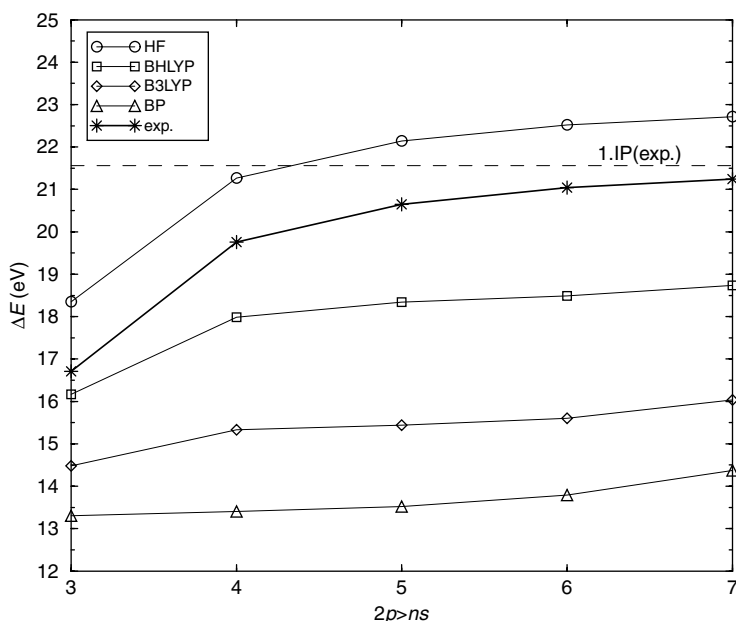
Figure 11 Excitation energies for the singlet $2p \rightarrow ns(n = 3\text{–}7)$ Rydberg series of the neon atom ($[6s4p] + 8s$ AO basis).

decays asymptotically exponentially with r [as the density $\rho(r)$ itself] instead of with $1/r + \text{const}$. This behavior, which can also be explained by the artificial electron self-interaction, leads to (a) too small electron binding, that is, too low Rydberg excitation energies and to (b) a too fast approach of the asymptotic (ionized) limit. Figure 11 shows the ΔE values for the $2p \rightarrow ns$ ($n = 3\text{–}7$, n indicates the principal quantum number) Rydberg series of the neon atom as calculated with TDHF and various TDDFT methods.

It is seen that while the TDHF results are just shifted with respect to the experimental data, the shape of the ΔE versus n curves is qualitatively wrong with the TDDFT methods. With a pure DF completely lacking "exact" HF exchange (e.g., BP86[108, 109]) there is not only a large underestimation of the ΔE values, but furthermore almost no dependence on n up to $n = 6$ and after that even a strong energy increase is clearly visible. As expected, the situation is gradually improved by "exact" exchange mixing (from 20% in B3LYP to 50% in BHLYP[95]) and only the latter functional can be recommended for the computation of Rydberg spectra. The construction of a DF with the correct asymptotic behavior is currently an active field of research (for details and possible solutions to the problem see Refs. 96, 110, 111 and references cited therein).

This behavior of the DF is also observed in molecular applications. Vertical singlet excitation energies from CASPT2[107], TDDFT-B3LYP, and

Table 5. Calculated and Experimental Excitation Energies (in eV) and Other Properties of the Vertical Singlet Excited States of Acetone

| State | ΔE | | | | f^L | $\Delta\langle r^2 \rangle$ |
	B3LYP	CASPT2[a]	MRCI	Exp.[a]		
$1B_2(n \rightarrow 3s)$	5.71	6.58	6.51	6.35	0.037	46.2
$2A_2(n \rightarrow 3p_x)$	6.61	7.34	7.41	7.36		75.7
$2A_1(n \rightarrow 3p_y)$	6.50	7.26	7.44	7.41	0.006	90.7
$2B_2(n \rightarrow 3p_z)$	6.66	7.48	7.49	7.45	0.002	85.6
$3A_1(n \rightarrow 3d_{yz})$	7.12	7.91	8.14	7.80	0.047	123.0
$3B_2(n \rightarrow 3d_{x^2-y^2})$	6.93	8.04	7.92	8.09	0.048	109.7
$3A_2(n \rightarrow 3d_{xz})$	7.24	8.09	8.17			118.0
$4B_2(n \rightarrow 3d_{z^2})$	7.18	8.18	8.21		0.004	133.3
$1B_1(n \rightarrow 3d_{xy})$	7.17	8.20	8.25	8.17	0.002	131.1

[a]Ref. 107.

MRCI computations (d-aug-cc-pVDZ AO basis, B3LYP/TZV(d,p) ground-state geometry) are compared with experimental data in Table 5. A graphical comparison with an experimental gas-phase absorption spectrum is shown in Figure 12.

The underestimation of the ΔE values with TDDFT increases from ~0.65 eV for the $n \rightarrow 3s$ transition to >1 eV for the $n \rightarrow 3d$ states. The
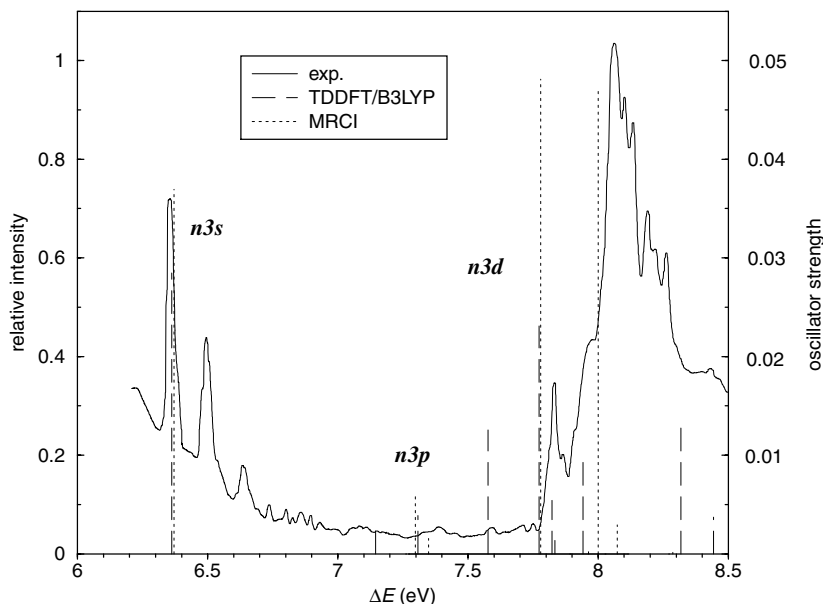
Figure 12 Comparison of the experimental UV spectrum of acetone[112] with calculated vertical transitions. The theoretical ΔE values are shifted by -0.15 (MRCI) and 0.65 eV (TDDFT), respectively.

ab initio methods CASPT2 and MRCI uniformly provide a very accurate description of the spectrum with errors of ~0.1–0.2 eV, which is on the order of the expected geometry relaxation effects. The largest error is found for the most core-penetrating $3s$ state. Significant differences between CASPT2 and MRCI results are obtained for the order of the $3p_x$ and $3p_y$ states, where MRCI seems to be better. According to the MRCI results, the assignment of the $3d_{yz}$ and $3d_{x^2-y^2}$ has to be interchanged. As can be seen from Figure 12, the relative oscillator strengths compare quite well with the experimental intensities keeping in mind that geometry changes in the excited states are quite significant for acetone (cf. the potential curves in Ref. 107).

Organic Dyes

Compounds that absorb in the range 380–720 nm are perceived as being colored, and, if the absorbance is strong they can be used as colorants.[113] Due to their industrial importance, there is continued interest in the theoretical prediction of the spectral properties of such compounds. While the computation of the lowest-lying (visible) bands in dyes is relatively straightforward due to the simple electronic structure of the corresponding excited states (mostly HOMO–LUMO single excitations), the higher-lying transitions are rarely considered. It is to be noted, however, that most $\pi \rightarrow \pi^*$ excited states (even the simple HOMO–LUMO excited ones) have large dynamic EC contributions (mainly due to $\sigma - \pi$ correlation), which must be considered in accurate work.

In this section, we consider, as examples, the UV spectra of two organic dyes: thioindigo and coumarin 102. We will use TDDFT, which today is the most successful and widely used method to calculate the electronic spectra of such compounds. Thioindigo belongs to the group of the indigoid dyes with one of the oldest known organic dyes, indigo, as a parent system. Thioindigo, in which both NH groups are replaced by sulfur, is a useful red vat dye and some of its halogenated derivatives are used as pigments.[113] Compounds based on the coumarin ring system give rise to one of the most extensively investigated and commercially important groups of organic fluorescent materials that are very well characterized for their use as laser dyes.[114] For other theoretical (DFT) work on coumarins, see Refs. 115–117.

The geometry optimizations for the ground-state structures of the investigated dyes as well as all TDDFT computations were carried out with the B3LYP functional and employed a TZV(d,p) AO basis set. The optimized ground-state structure of thioindigo has C_{2h} symmetry; coumarin is already nonplanar in the ground state due to slight pyramidalization of the NR_2 group. A comparison between the experimental and calculated spectra of thioindigo and coumarin 102 is given in Figures 13 and 14, respectively. Note that in contrast to most of the other spectra presented in this work no energy shift has been applied meaning that the uncorrected TDDFT excitation energies already match the experimental (solution) data very closely.
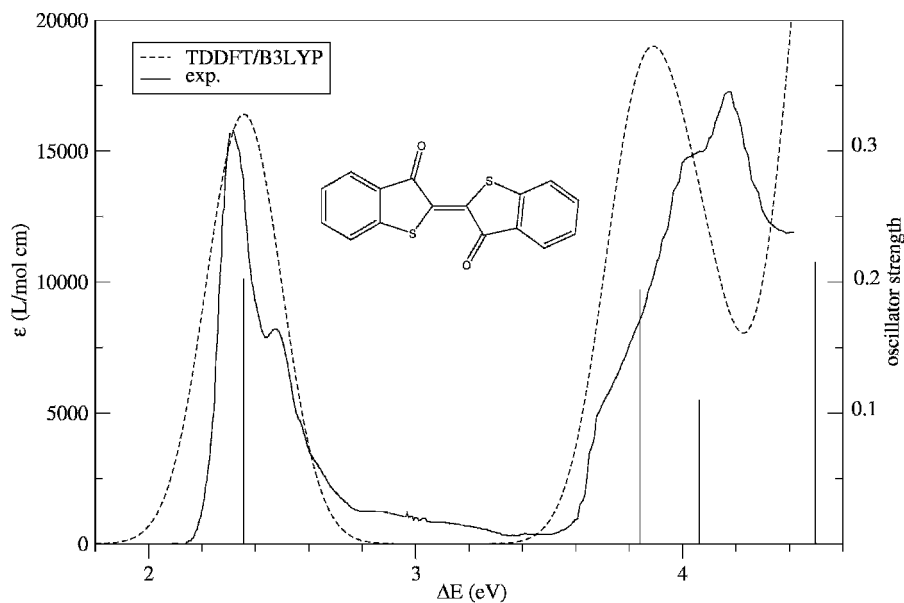
Figure 13 Comparison of experimental and computed [B3LYP/TZV(d,p)] UV spectra of thioindigo.
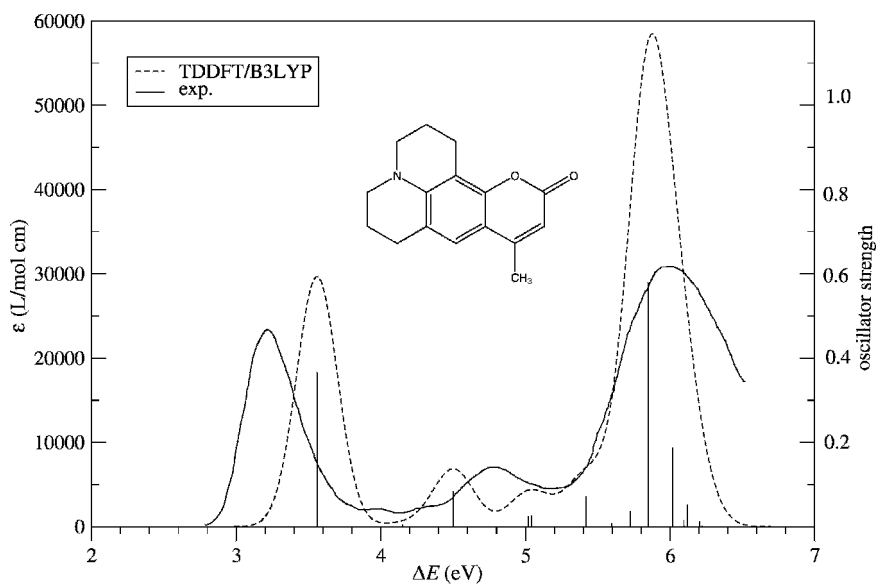
Figure 14 Comparison of experimental and computed [B3LYP/TZV(d,p)] UV spectra of coumarin 102.

The visible and near-UV spectrum of thioindigo measured in benzene show two major bands with maxima at ~2.3 and 4.2 eV,[118] respectively. The calculated lowest excitation energy and oscillator strengths, which are arguably of most interest to the dye chemist, are in excellent agreement with the experimental values. The lowest lying 1^1B_u state computed at 2.36 eV is of $\pi \rightarrow \pi^*$ character and results mainly from the HOMO $\rightarrow$ LUMO excitation. Despite this simple electronic structure, the (dynamical) EC contributions are large as can be seen by comparison with the TDHF excitation energy (3.77 eV), which is in error by > 1.4 eV. The second feature observed in the UV spectrum of thioindigo is a relatively broad absorption including two shoulders at 3.7 and 4.1 eV. Our calculations show that in this energy region there are two ^1B_u transitions close in energy: The 2^1B_u computed at 3.84 eV and the 3^1B_u at 4.06 eV. Both states have purely $\pi \rightarrow \pi^*$ character and result mainly from HOMO-3→LUMO and HOMO-6→LUMO excitations, respectively. The almost perfect agreement between the experimental and calculated spectral data demonstrates that TDDFT provides a very reliable description of higher-lying valence states.

The experimental absorption spectrum of coumarin 102 obtained in ethanol solution exhibits two intense absorption bands at 3.2 and 5.9 eV and one band with a lower intensity located at ~4.8 eV.[114] As for thioindigo, the lowest-lying state is of $\pi \rightarrow \pi^*$ type and mainly results from the HOMO $\rightarrow$ LUMO excitation. The third state calculated at 4.50 eV with small intensity ($f = 0.085$) is due to the two nearly degenerate configurations HOMO-1→LUMO and HOMO $\rightarrow$ LUMO + 1 and assigned to the band located in the experimental spectrum at 4.8 eV. The third band in the spectrum of coumarin 102 is relatively broad with a maximum ~5.9 eV. According to the TDDFT calculations, this band is composed mainly of two transitions to the 10A and 11A states calculated at 5.85 and 6.02 eV, respectively. In this case, we observe some overestimation of the calculated intensities that may be caused by solvent effects. Note, however, that TDDFT errors of ~50% for oscillator strengths, especially for higher-lying transitions, are not unusual and that the neglected vibronic effects (FC factors much smaller than unity) may also contribute to this error.

Transition Metal Complexes

Describing the electronic structure of transition metal compounds remains a challenging goal in quantum chemistry in general. The importance of static correlation effects arising from near degeneracy within the metal d-shells causes difficulties in ab initio single-reference treatments (in TDDFT there is some implicit account of static EC). Additionally, the low quality of the Hartree–Fock orbitals for transition metal compounds complicates the application of approaches lacking appropriate orbital relaxation effects. The TDDFT method is currently the only one that can be applied routinely to these systems, especially when large compounds without any symmetry
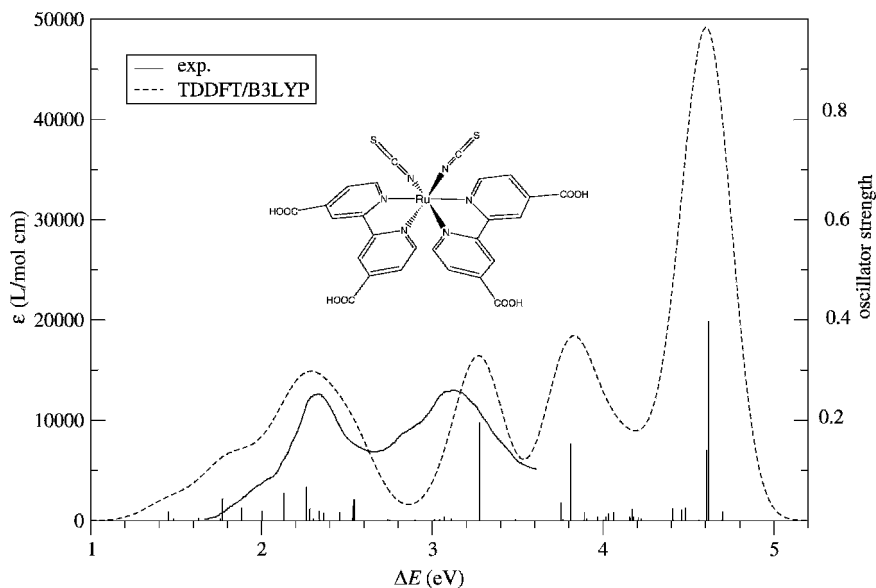
Figure 15 Comparison of experimental and computed [B3LYP/SV(d)] UV spectra of the bipyridine–ruthenium complex. The theoretical ΔE values are blue-shifted by 0.5 eV.

are considered (for CASPT2 investigations of the spectra of small TM compounds, see Ref. 11). Although in some cases semiempirical methods like INDO seem to be applicable[119] the DFT methods are more robust and even with nontrivial basis sets the calculation times are small enough to allow routine applications on "real" systems. For other applications of the TDDFT method to TM systems, see, for example, Ref. 120 and for a recent photochemical TDDFT study, see Ref. 121.

As an example, we present in this section a TDDFT study of the optical absorption spectrum of [Ru(4,4'-COOH-2,2'-bpy)$_2$(NCS)$_2$] (bpy = 2,2'-bipyridine) (see inset in Figure 15), a widely used charge-transfer sensitizer in nanocrystalline TiO_2 solar cells. In the calculations, we considered the neutral system where the four carboxylic groups are protonated to represent a realistic model of the complex under the experimental conditions[122] (water solutions at pH < 1.5). The geometry optimization of the complex results in a pseudo-octahedral structure with C_2 symmetry and a cis arrangement of the thiocyanite ligands. This optimization was carried out with the DFT-BP86[108,109] method employing SV(d) basis sets,[123] a quasirelativistic effective core potential (ECP) with 28 core electrons[124] and a [5s5p3d] AO basis set[123] for ruthenium. The excited-state calculations were carried out using the B3LYP functional. The calculated and the experimental absorption spectra are compared in Figure 15.

The experimental spectrum exhibits two bands in the visible and near-UV region centered at 2.3 and 3.1 eV,[125] respectively. The overall band shapes and their relative and absolute intensities are well described by the TDDFT approach and even the shoulder at ~1.9 eV is predicted correctly. The under-estimation of the calculated excitation energies by ~0.5 eV may on the one hand be attributed to inabilities of the chosen density functional but on the other hand certainly includes solvation effects that have been studied in Ref. 126 in the framework of continuum models. The neglected effects of spin–orbit coupling may be on the order of 0.1–0.2 eV, which seems to be significantly smaller than the differences obtained with various density functionals. As can be seen by the vertical lines included in Figure 15, which indicate the position and f values of the individual transitions, the density of electronic transitions even in the low-energy range is quite high. For the first two bands, ~25 electronic states have to be considered, which increases to ~60 in the range up to 5 eV. The TDDFT method is the only one that is currently applicable in such situations.

The character of the electronic transitions is usually analyzed in terms of the contributing single excitations. Although this is sometimes problematic due to extensive orbital and configuration mixing, the analysis is straightforward in our particular example. The first absorption band has strong multi-configurational character and involves excitations from the highest occupied to the lowest unoccupied π^* molecular orbitals. The many orbitals close to the HOMO are mainly of ruthenium d-orbital character with significant amplitudes on the isothiocyanate ligands. The second and the third absorption band involve excitations from a second set of metal d orbitals, to the lowest unoccupied π^* molecular orbitals, which can be characterized as metal–ligand charge-transfer (MLCT) bands. The fourth band at ~4.6 eV is very intense and can easily be assigned to intraligand $(\pi \rightarrow \pi^*)$ excitations.

Open-Shell Systems: The Phenoxyl Radical
Due to its crucial role in combustion chemistry and biology, the phenoxyl radical has been the subject of intense experimental and theoretical studies for many years (for recent work, see Ref. 127 and references cited therein). For these reasons we present it here as an example of UV spectroscopy of (neutral) radicals (for the application of DFT to the spectra of aromatic radical cations, see, e.g., Ref. 128 and for results of MRCI computations, see Ref. 129). The phenoxyl radical is well known as a difficult case for electronic structure methods because it requires a sophisticated treatment of electron correlation similar to closed-shell aromatic hydrocarbons.

In agreement with previous DFT studies,[127] we found a $^2B_1$ ground state (assuming C_{2v} symmetry with yz being the molecular plane) corresponding to a singly occupied orbital (SOMO) of π type. The lowest excited state corresponds to a $n \rightarrow \pi$(D-S) transition of B_2 symmetry, which is dipole-forbidden. A weak band observed experimentally at ~1.1 eV (1120 nm) supports this
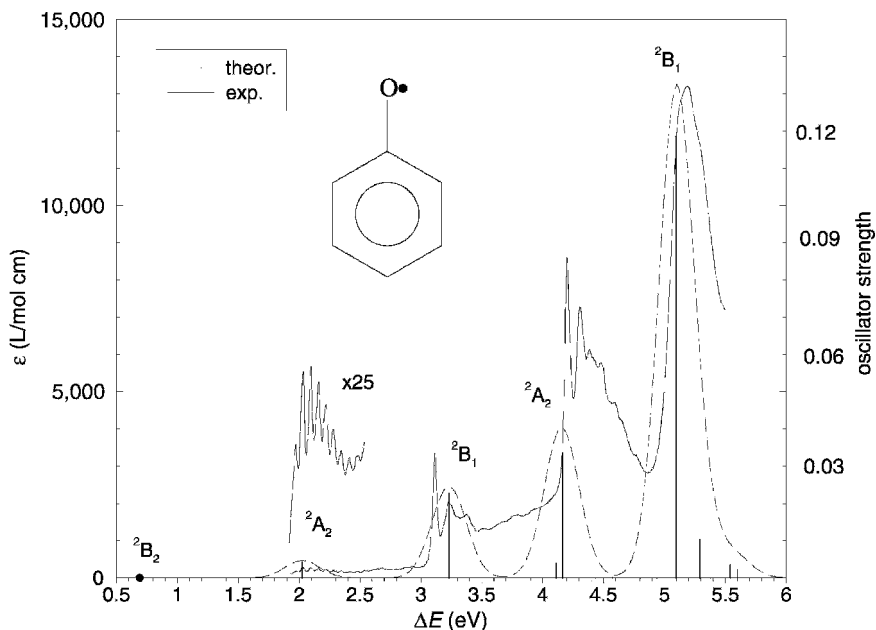
Figure 16 Comparison of the computed [UTDDFT-B3LYP/TZV(d,p)] and experimental[127] UV spectra of the phenoxyl radical. The theoretical ΔE values are shifted by -0.35 eV.

prediction. The calculated vertical excitation energy of 1.04 eV is in almost perfect agreement with the experimental value. For the $\pi\pi^*$ states of A_2 and B_1 symmetry the TDDFT-B3LYP/TZV(d,p) calculation yields energies slightly too high and thus a uniform red-shift of 0.35 eV has been applied in the simulation shown in Figure 16.

    As can been seen from the comparison of the theoretical and experimental spectra, the unrestricted (U)TDDFT method provides a uniformly good description of the allowed transitions and the absolute and relative intensities are predicted quite accurately. The overestimation of all excitation energies seems to be due at least partially to the unrestricted treatment as indicated by a study using a recently developed restricted open-shell TDDFT[22] approach. Except for the 1^2A_2 state discussed below, the 0–0 transitions are most intense indicating only slight geometry changes compared to the ground state.

    Figure 17 shows the vibrationally resolved spectrum obtained for the transition to the second lowest excited 1^2A_2 state. The theoretical treatment has been performed in the Franck–Condon approximation. The results are generally in very good agreement with the experimental data. The prominent progression with a spacing of $\sim$500 cm^{-1} results from a totally symmetric (in-plane) CC stretching–bending mode. The relatively high intensities of the
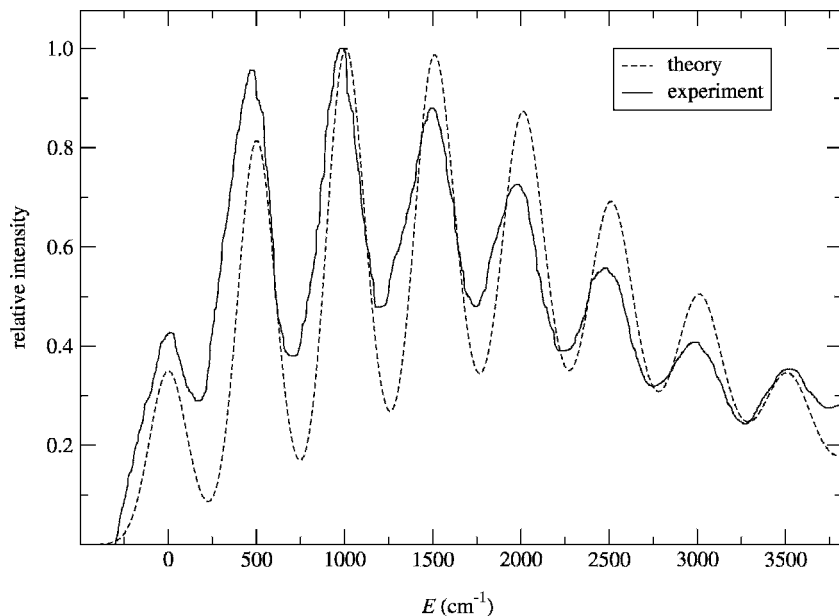
Figure 17 Comparison of the computed [UTDDFT-B3LYP/TZV(d,p)] and experimental[127] UV band of the 1^2A_2 state of the phenoxyl radical. The 0–0 transition energy is set to zero.

0–1, 0–2, and 0–3 vibrational transitions can be explained by the geometries of the phenoxyl radical in the ground and excited states and the nature of the normal modes. The X^2B_1 ground state has a partially chinoid structure with short C—O (1.25 Å) and C2–C3/C5–C6 (1.37 Å) bond lengths. The C—C bonds elongate in the 1^2A_2 state to ∼1.43 Å, thus matching almost exactly the geometric changes induced by the above mentioned stretching–bending mode. This example clearly shows how a vibrational analysis can reveal structural details of the corresponding states. Further examples of this type will be discussed in a later section.

Open–Shell Systems: Excited-State Absorption of Naphthalene

Excited-state absorption (ESA) is a type of electronic spectroscopy for which only a few theoretical studies have been performed (for a recent study on the singlet–singlet ESA spectrum of azulene, see Ref. 130 and for some benchmark calculations on small molecules, see Ref. 131). From the experimental point of view ESA is a very important topic in photophysical (kinetic) investigations of energy, electron or hydrogen-transfer processes. Although in principle all excited states of a molecule show a distinct electronic absorption spectrum, only the ESA spectra of the lowest excited state in each multiplicity (i.e., S_1 or T_1) are usually accessible experimentally. Because of the short
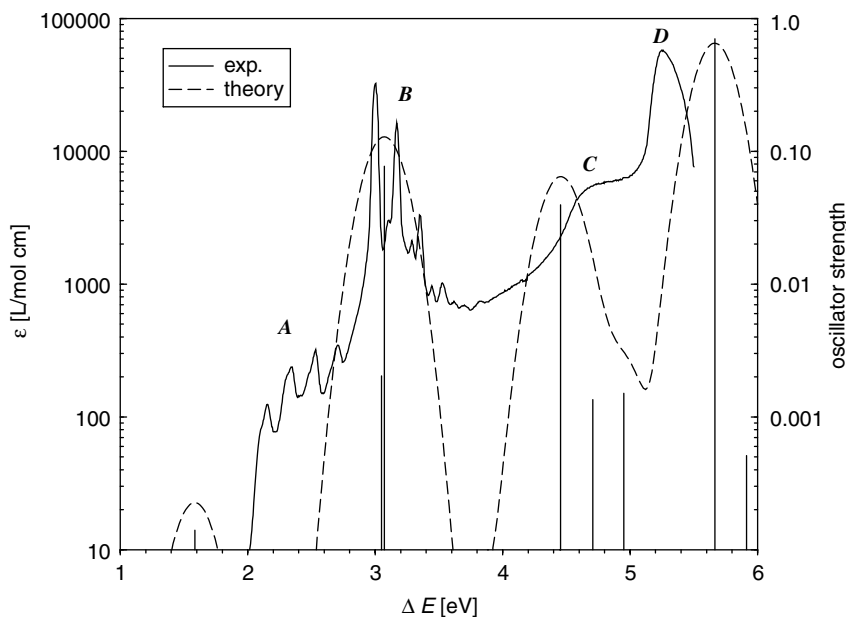
Figure 18 Comparison of the computed (UTDDFT-B3LYP/cc-pVDZ) and experimental[132] triplet–triplet absorption spectra of naphthalene. Note the logarithmic intensity scale.

lifetime (low concentration) of excited molecules, special experimental (laser)-techniques are employed in ESA spectroscopy. Furthermore, background absorption by molecules in the ground state or by photoproducts need to be accounted for by taking difference spectra. Similar to the case of radicals, ESA spectra usually start in the visible and, sometimes, bands are observed even in the IR region (>1000 nm).

The naphthalene molecule, which is used as an example here, has a lowest triplet state of B_{2u} symmetry and $\pi \rightarrow \pi^*$ (L_a) character. The dipole allowed transitions that are polarized in the plane of the molecule thus belong to transitions to A_g and B_{1g} excited states. The results of the unrestricted TDDFT-B3LYP treatment are shown in comparison with the experimental spectrum in Figure 18.

The assignments of the most intense bands seen in the experimental spectrum (bands B-D) agree with those from previous semiempirical PPP-type calculations[132] and will not be discussed here. Substantial disagreement between the theoretical and experimental data is observed only for the band A assigned to the $1^3 A_g$ state that is calculated too high by $\sim$0.5 eV. The transition to the $1^3 B_{1g}$ state (band B) is described almost perfectly while the

predicted excitation energies for band C and D show the typical TDDFT errors on the order of ± 0.2–0.4 eV. Note, however, that the relative description for the different states is worse compared to the phenoxyl radical where a global shift of all excitation energies yields a satisfactory agreement with experiment. This is because of the more complicated electronic structure of the naphthalene T_1 state (two vs. one open shell for the phenoxyl radical), which seems not to be described well enough by the simple TDDFT treatment. Furthermore, due to technical limitations it is currently not possible to check the degree of spin-contamination of the excited states ($\langle \hat{S}^2 \rangle$ expectation value). Conclusive answers about the applicability of TDDFT in this area of spectroscopy requires more detailed work on other systems.

Circular Dichroism

2,3-(S,S)-Dithiadecalin

The nature of the chromophore of a molecule has a major influence on the corresponding CD spectroscopic properties. If the chromophore itself is chiral, it is denoted as being "inherently chiral", whereas the term "inherently achiral" is used for locally achiral chromophores that are disturbed by their chiral surrounding (for a more detailed classification, see Ref. 133). The strength of the Cotton effect (rotatory strengths) provided by molecules containing an inherently chiral chromophore usually exceeds what is found for a molecule containing an inherently achiral chromophore by an order of magnitude.

The dithiadecalin (DTD) molecule (see inset in Figure 19) is characterized by the local chiral disulfide chromophore. Its first two transitions are expected to be of valence character and can be understood as single excitations out of the lone-pair orbitals at the sulfur atoms into the corresponding $\sigma(SS)^*$ orbital. However, the $\Delta \langle r^2 \rangle$ values of the transitions indicate significantly more diffuse character than expected for pure valence excited states.

To account for this fact, the TDDFT-B3LYP calculations of the spectra have been carried out with a TZV(2df) basis set augmented with diffuse functions at the sulfur atoms as well as at the neighboring carbon atoms and a TZV(d,p) basis set for the remaining atoms. The B3LYP/TZV(d,p) ground-state geometry has been used for these calculations. The theoretical spectrum has been blue shifted by 0.39 eV to match the experimental band A.

The experimental spectra of DTD[134] have been recorded in hexane. Keeping in mind the above described diffuse character of all excited states in DTD, an unbalanced theoretical description of states with stronger Rydberg character is to be expected when gas-phase data are compared with those from the condensed phase (Pauli-repulsion between the Rydberg state and solvent molecule wave functions). Figure 19, however, shows an almost perfect match between the theoretical gas-phase and experimental CD spectrum in the entire energy range. Even band C, which is theoretically predicted to have almost
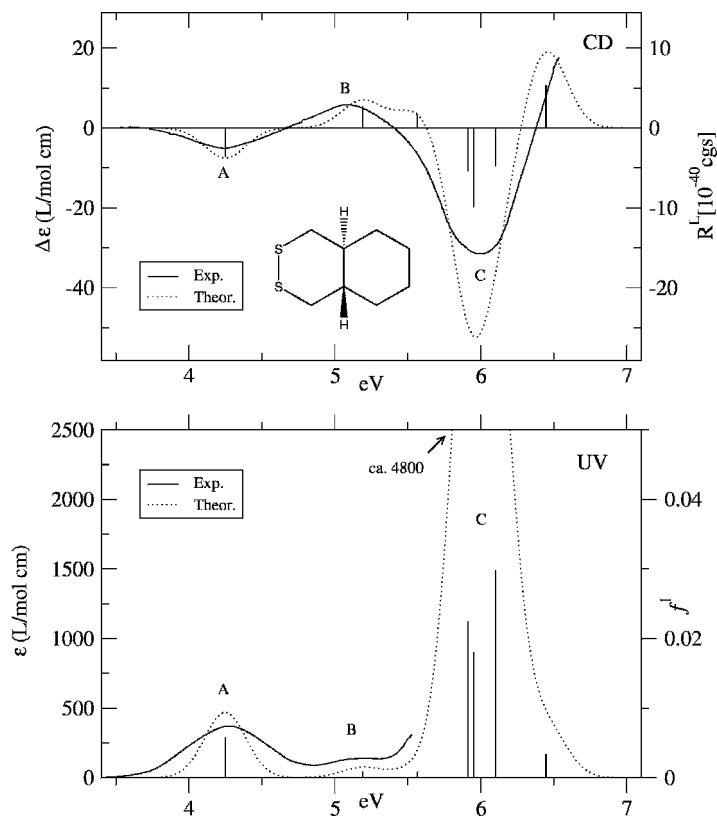
Figure 19 Comparison of the experimental and computed [TDDFT-B3LYP/aug-TZV(2df)] UV and CD spectra for 2,3-(S,S)-dithiadecalin. The theoretical spectra have been blue-shifted by 0.39 eV.

exclusively Rydberg contributions, is described very well. It is pointed out here that the prevailing opinion that the excitation energies of Rydberg states are generally blue-shifted when going from the gas to the condensed phase[6] has been questioned recently for some molecules.[135] It should also be mentioned here that theoretical methods to describe the solvent effects on excited electronic states beyond simple electrostatics (i.e., continuum models) are in fact not yet developed.

The comparison with the UV spectrum shows an important advantage of CD over conventional UV spectroscopy for chiral molecules. Because the CD is a signed quantity, the band B is considerably better separated in the CD spectrum. If the bands would lie even closer to each other such that they could no longer be resolved by UV spectroscopy, CD spectroscopy would still yield two well-separated bands since the corresponding Cotton effects are oppositely signed.

(M)-[6]Helicene

Hexahelicene is one of the most widely studied molecules in theoretical CD spectroscopy (see, e.g., Refs. 47 and 136 and references cited therein). The system is rather large [120 valence electrons, 590 basis functions with a TZV(d,p) AO basis] and ~15–20 excited states are necessary to describe the experimental spectrum entirely. This example is presented here to show that correlated ab initio treatments are also applicable for such cases. The simplified coupled-cluster model CC2 together with the RI approximation is used and compared to the standard TDDFT-B3LYP approach.

The experimental CD spectrum (see Figure 20) consists of two very intense CD bands with opposite sign at 5.1 eV (240 nm, F) and 3.8 eV (320 nm, C). Shoulders (B, D, and E), and a very weak band (A) can, however, be clearly identified. With the exception of the region of band D, which is predicted with the wrong CD sign in both calculations, the theoretical data are in good agreement with the experimental spectrum; that is to say, all bands have a clear correspondence to calculated states. The theoretical excitation energies from CC2 have been red-shifted by 0.22 eV, which is on the order
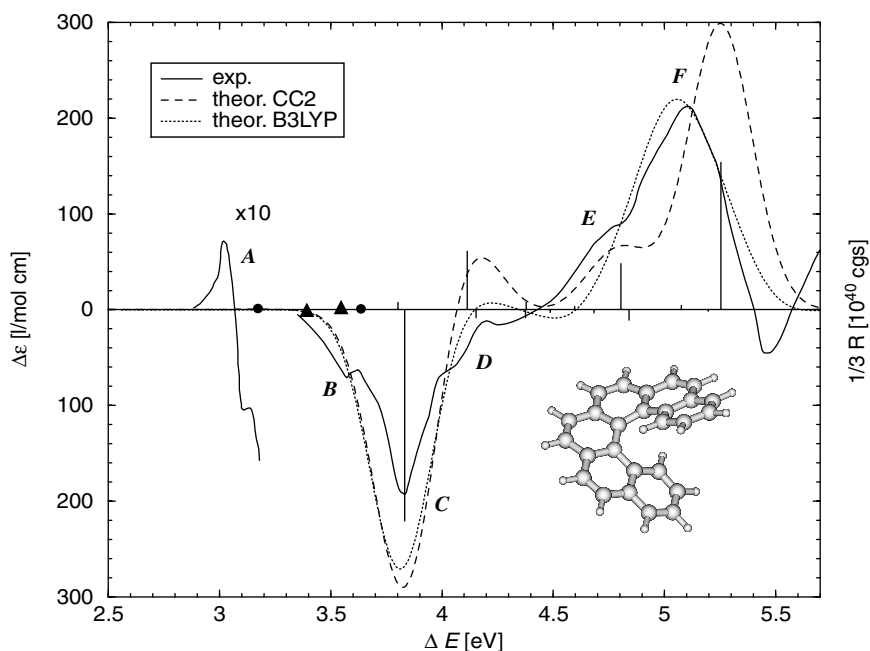
Figure 20 Comparison of the experimental and computed [TZV(d,p) AO basis, B3LYP optimized geometry] CD spectrafor *(M)*-[6]helicene. The theoretical spectra have been shifted by 0.20 (B3LYP) and −0.22 eV (CC2), respectively. The filled circles/triangles indicate the two lowest states with small intensity obtained by CC2/TDDFT-B3LYP. The vertical lines correspond to results from the CC2 method.

of the expected solvent effect. Further enlarging of the AO basis would bring the CC2 data in even closer agreement with experiment (estimated effect of ∼0.1–0.2 eV). The TDDFT-B3LYP error is of opposite sign where the excitation energies are underestimated by ∼0.2 eV. The CC2 results are furthermore superior to those from TDDFT with respect to the splitting between the lowest L_b (band A) and L_a (band B) states. The larger error for the high-energy band F may be explained by some deficiencies of the TZV(d,p) AO basis set used, which lacks diffuse components as well as requisite higher angular momentum functions that are more important for explicitly correlated treatments than in DFT.

The computed intensities are also in reasonable agreement with experiment. The small R value for the L_b transition [-0.8×10^{-40} cgs (CC2) vs. -1.6×10^{-40} cgs (exp.)[137]] is predicted correctly with CC2 but has the wrong sign with TDDFT. However, this and the following L_a transition (band B) gain intensity by vibronic coupling with the close-lying intense B_b state and thus, results from vertical treatments should be taken cautiously.

When judging the accuracy of CC2 with respect to the TDDFT method, one should also consider the necessary computation times. While the TDDFT calculation was completed in ∼15 hours (on a PIII/1.4-GHz machine), the CC2 treatment took >11 days, which corresponds to a timing ratio of ∼18. As mentioned before, the best strategy is thus to first calibrate the chosen density functional(s) by comparison with ab initio approaches on smaller (but structurally similar) molecules (in our example, e.g., [3]- or [4]helicene) and finally to perform the calculation on the large target system using only the cheaper TDDFT method.

(2S)-Tricarbonyl-η⁴-pentadi-2,4-enal-iron

As mentioned in a previous section, the description of the electronic spectra of transition metal compounds in low-oxidation states is relatively complicated. When applying DFT-based methods, it is recommended that one carefully investigate the influence of the selected density functional. This is of particular importance here because there are currently no ab initio methods on which the TDDFT approaches can be calibrated. As an example we present a study of the CD spectrum of (2S)-tricarbonyl-η⁴-pentadi-2,4-enal-iron (ITP, for details, see Ref. 49). The molecule contains two achiral chromophores [pent-2,4-die-nal and the $Fe(CO)_3$ fragment] which, attached to each other, form the chiral system. The spectroscopic activity of ITP in the near-UV originates mainly from $3d(\text{metal}) \rightarrow \pi^*$ excitations. As a result of the similar energies of several electronic configurations, extensive mixing is observed including various $n \rightarrow \pi^*$ states. Hence, it is understandable that the electronic nature of the excited states in ITP is described very differently depending on which method is applied. Furthermore, the energetic ordering and character of the MOs differs substantially between Hartree–Fock based and DFT approaches as well as between different DFT functionals. A reasonable direct comparison of the
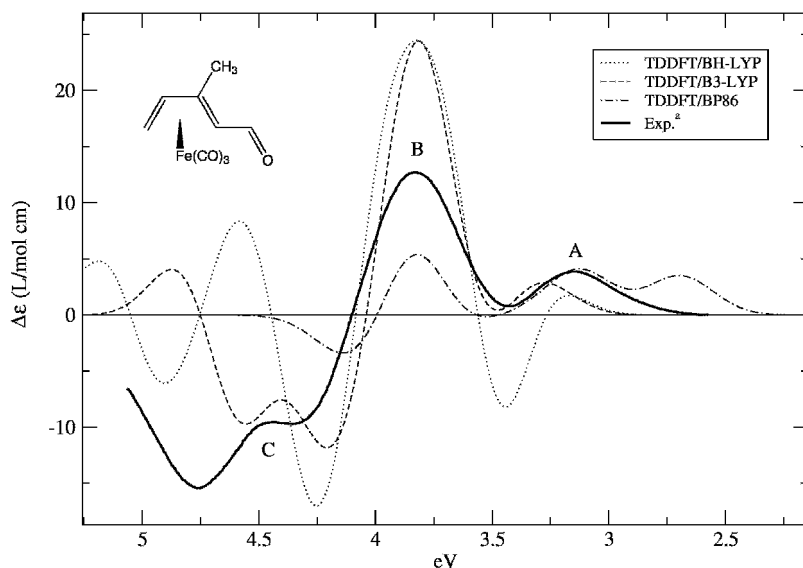
Figure 21 Comparison of the experimental and computed CD spectra for the *(2S)*-tricabonyl-η^4-pentadi-2,4-enal-iron complex. The theoretical excitation energies have been shifted by -0.31 (BHLYP), 0.02 (B3LYP), and 0.21 eV (BP), respectively (positive values refer to a blue-shift). The simulations include the contributions from the 15 lowest excited states.

results with the help of an MO based classification of the excited states is therefore not possible so, only the simulated spectra without any transition assignment are presented here. Figure 21 shows a comparison of experimental and theoretical data [SV(*d*) basis set for C, H, O and a [5*s*3*p*2*d*] set for Fe].

Inspection of Figure 21 shows relatively good agreement of the TDDFT-B3LYP spectrum with its experimental counterpart. The simulation with the BHLYP functional yields wrong signs for parts of bands A and C while the BP data seem to have little "overlap" with experiment. Strong dependencies of the results on the chosen density functional are not uncommon for more complicated systems. This type of dependency is the most severe drawback of the TDDFT method. In the original publication concerning this planar-chiral system,[49] conformational effects (cis vs. trans orientation of the carbonyl group) were investigated. The conformational preference seems to be resolvable by comparison of experiment with theory.

Vibrational Structure

The shape and width of an absorption band in the visible region of the spectrum determines our color impression and is thus of fundamental importance in the area of dye chemistry. Theoretical simulations of the vibronic structure

of absorption bands allow us to evaluate the accuracy of the methods for find-
ing the minimum energy geometries and vibrational frequencies. Systematic
studies of the vibrational structures of the absorption bands for large mole-
cules have not been performed to date. A few investigations have been under-
taken using semiempirical[138] or CIS[139] methods that however, did not give
fully satisfactory results. For the first time, we will show here that reliable pre-
dictions can be obtained in the framework of TDDFT. This has become
possible due to the recently developed analytical TDDFT excited-state
gradient.[140] In fact, it will be shown that the excited-state geometries and
vibrational frequencies from (TD)DFT are much more accurate than the
corresponding excitation energies (see also Ref. 141).

Anthracene

As a first example, let us consider the vibronic structure of the first
absorption band in the UV spectrum of anthracene. In agreement with experi-
ment, the TDDFT calculation gives an S_1 state with B_{2u} symmetry and a ver-
tical excitation energy of 3.23 eV [ΔE^{0-0}(exp.) = 3.43 eV]. This band can be
described by a HOMO $\rightarrow$ LUMO excitation and in the Platt nomenclature
(perimeter model) it is denoted as the L_a state. Both states were optimized
at the (TD)DFT-B3LYP/TZV(d,p) level in D_{2h} symmetry.

A comparison of the spectrum simulation with a low-resolution gas-
phase absorption spectrum[26] is shown in Figure 22. This type of spectrum is
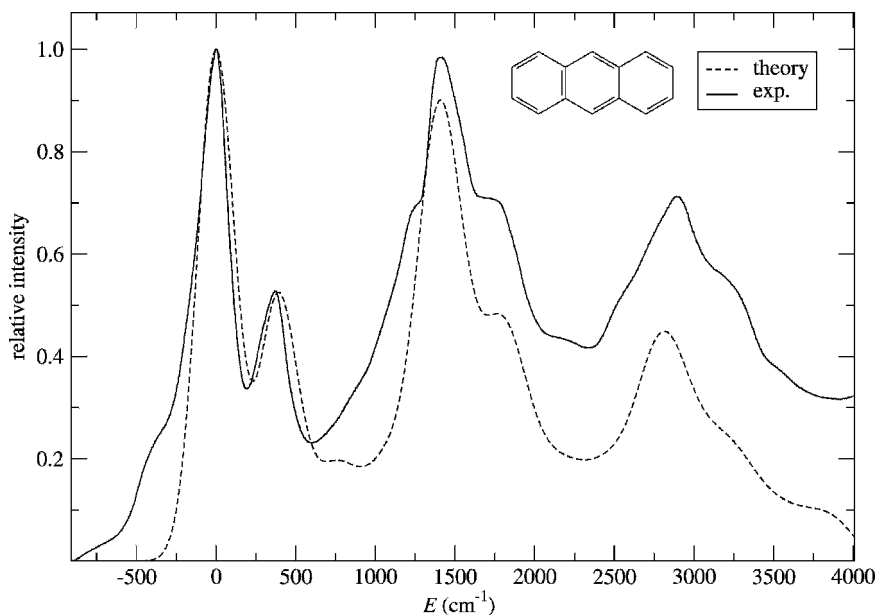
Figure 22 Comparison of the computed [TDDFT-B3LYP/TZV(d,p)] and experimen-
tal[26] UV spectra for the ^1L_a state of anthracene. The 0–0 transition energy is set to zero.

typical for large systems (normal UV spectra), and has therefore been chosen for discussion here. The theoretical intensities were obtained within the FC approximation at 0 K and the individual transitions were broadened by Gaussian shape functions using a half-width of $\sigma = 165 \, \text{cm}^{-1}$.

The computed spectrum shows a good agreement with its experimental counterpart over the entire energy range. This indicates that the geometry and frequency–normal mode changes between the two states are much better described by DFT than are the excitation energies (the DFT error for ΔE^{0-0} is -0.59 eV). The weak shoulders (hot-bands) located $\sim$300–750 cm^{-1} below the 0–0 transition cannot be described by the present calculation. Although the description of hot-bands is straightforward in principle (by thermal population of vibrational ground-state levels), the current implementation of the recursive integral algorithm leads to unacceptably long computation times in such cases. As expected, the FC approximation seems to be very good for a dipole-allowed transition as considered here. The gradual increase of the experimental intensity relative to the calculated one in Figure 22 may arise from a nonhorizontal baseline in the measured spectrum. Furthermore, the second, less intense transition to the S_2 state (L_b) hidden under the L_a band may also contribute to this intensity mismatch. All vibronic transitions with a high intensity correspond to excitations of totally symmetric normal modes with a maximum excitation of two quanta in a single vibration.

Octatetracene

Polyenes represent a class of widely studied molecules. Their ability to undergo photochemical isomerizations is exploited by Nature to transduce radiative energy into chemical energy and thus, these systems perform vital functions in many biochemical processes. *All-trans* octatetraene is used here as a model system to assess the ability of DFT methods to predict the important spectroscopy of this and related systems.

A weak first absorption is found experimentally ($\Delta E^{0-0} = 3.59$ eV) corresponding to the electric dipole-forbidden $1A_g \rightarrow 2A_g$ transition. The second (intense) band results from the allowed $1A_g \rightarrow 1B_u$ transition ($\Delta E^{0-0} = 4.41$ eV). This situation is challenging for any theoretical method because the character of both states is very different (single-configurational, ionic $1B_u$ state vs. multiconfigurational, covalent $2A_g$ state with significant contributions from double excitations).

All calculations were performed at the (TD)DFT-B3LYP/TZV(d,p) level employing C_{2h} symmetry. In contrast to the experimental data, the TDDFT calculation yields an S_1 state with B_u symmetry ($\Delta E^{\text{rel}} = 4.05$ eV) and the $2A_g$ state as the second one ($\Delta E^{\text{rel}} = 4.89$ eV). This error can be traced to the systematic underestimation of excitation energies for ionic states with TDDFT-B3LYP.[35] Because of the adiabatic approximation used in the TDDFT treatments, the $2A_g$ state is described solely by a mixing of HOMO $\rightarrow$ LUMO + 1 and HOMO-1$\rightarrow$LUMO single excitations. It lacks

the important HOMO–LUMO double excitation that has ∼30% weight in MR-MP2 wave functions. Thus we show here how such deficiencies of the theoretical treatment transfer to the description of the geometries and vibrational frequencies, and finally to the simulated vibronic structure.

A comparison of computed (FC approximation, broadened by Lorentzian functions with a half-width of $\sigma = 20\,cm^{-1}$) and experimental gas-phase spectra[30] for the $1B_u$ state is shown in Figure 23. Compared to the previous example, the theoretical description using B3LYP is worse. An obvious deviation from experiment is the relatively strong progression of the nontotally symmetric normal mode with a frequency of $143\,cm^{-1}$. This indicates an overestimation of the frequency change for this mode upon electronic excitation. Because ionic $\pi \rightarrow \pi^*$ states benefit from the inclusion of "exact" HF exchange,[25] the calculation was repeated with the BHLYP functional (EEX = 50%). As can be seen from Figure 23, this significantly improves the description of the vibronic structure that is now in acceptable agreement with experiment over the entire energy range. Test calculations using TDHF (EEX = 100%) yield results that deviate more strongly from experiment (not shown) indicating that there is some (state-dependent!) optimum of exchange mixing in the density functionals.
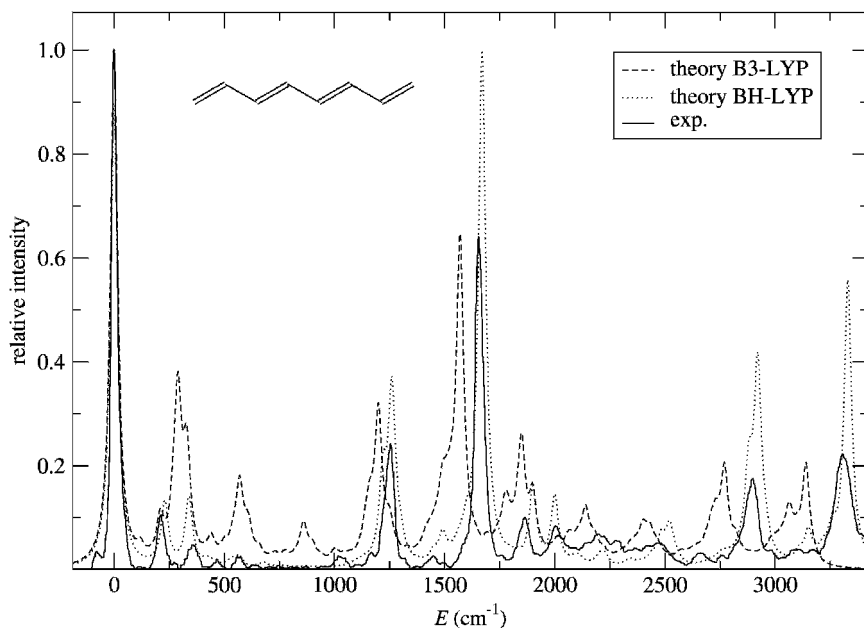
Figure 23 Comparison of the computed [TDDFT/TZV(d,p)] and experimental[30] spectra for the ^1B_u state of octatetrene. The 0–0 transition energy is set to zero.
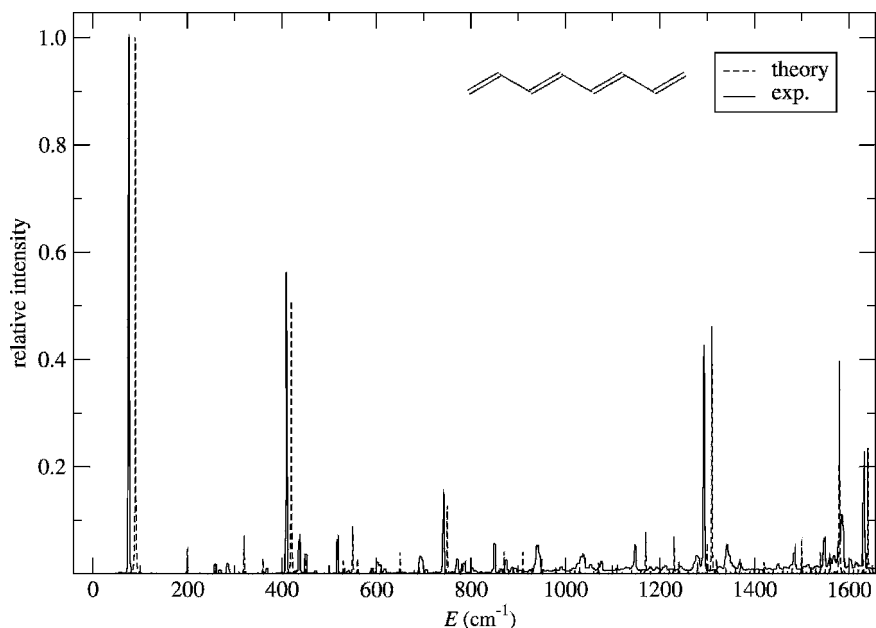
Figure 24 Comparison of the computed [TDDFT-B3LYP/TZV(d,p)] and experimental[31] spectra for the $2A_g$ state of octatetraene. The 0–0 transition energy is set to zero.

The dipole forbidden $1A_g \rightarrow 2A_g$ transition must be treated at the Herzberg–Teller level (see earlier section) including the derivatives of the electronic transition dipole moment. These results are shown in Figure 24 in comparison with the experimental jet spectrum.[31] The computed intensities were broadened with Lorentzian functions using a half-width of $\sigma = 0.5\,cm^{-1}$.

Somewhat surprisingly, the calculated spectrum shows an almost perfect agreement with the experiment. This seems to indicate that either the density functional implicitly accounts for the missing double excitation (see also Ref. 142) or that its influence on the shape of the excited-state potential energy surface is small or similar to that of the HOMO $\rightarrow$ LUMO + 1 and HOMO$-$1 $\rightarrow$ LUMO excitations. Based upon the intensity inducing b_u mode with a frequency of $94\,cm^{-1}$, which leads to mixing of the S_1 and S_2 states, several excitations of totally symmetric modes with low quantum numbers are observable.

Formaldehyde

The harmonic approximation is essential for computing the vibrational structure of electronic bands for large molecules. For more "floppy" (low-energy) nuclear motions (like torsions and bendings), it is inadequate. Here, we present an example of how the harmonic treatment of such motions effects the shape of the calculated spectra. The electric dipole forbidden $n \rightarrow \pi^*$
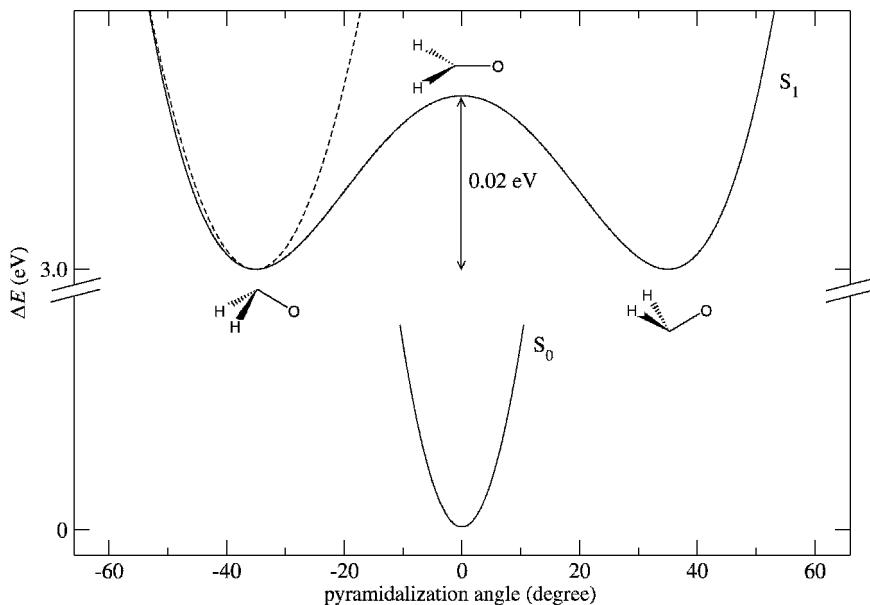
Figure 25 Ground and first excited-state potential energy curves [TDDFT-B3LYP/TZV(d,p)] along the pyramidalization coordinate of formaldehyde. For comparison, the dashed line shows the harmonic potential.

transition of formaldehyde is used to illustrate this issue (for other TDDFT treatments of the excited-state surfaces of this molecule, see Ref. 143).

The geometry of the ground state was optimized at the DFT-B3LYP(TZV(d,p) level in C_{2v} symmetry. The TDDFT calculation yields an S_1 state with A_2 symmetry and a vertical excitation energy of 3.99 eV ($\Delta E^{0-0} = 3.56$ eV, exp. 3.51 eV[144]), which can be described by the HOMO (lone-pair) $\rightarrow$ LUMO (π^*) single excitation. The geometry optimization of the S_1 state was carried out in C_s symmetry. In agreement with experimental data, we obtain a nonplanar minimum for the excited state with a pyramidalization angle of 34.9° (experimentally 33.6°[145]), which lies only 0.02 eV (experimentally 0.044 eV[145]) below a planar transition state for inversion (see Figure 25). Based on a Herzberg–Teller treatment, a simulation of the vibronic structure was performed and the obtained intensities were broadened with Lorentzian functions with a half-width of $\sigma = 50$ cm^{-1}.

A comparison of the calculated and experimental gas-phase spectra[144] (see Figure 26) clearly shows the limits of a harmonic treatment. Although the overall shape of the spectrum is reproduced quite well including the dominant C—O stretch progression, the inversion doubling of most peaks due to the double-minimum potential is obviously missing. Because such situations can
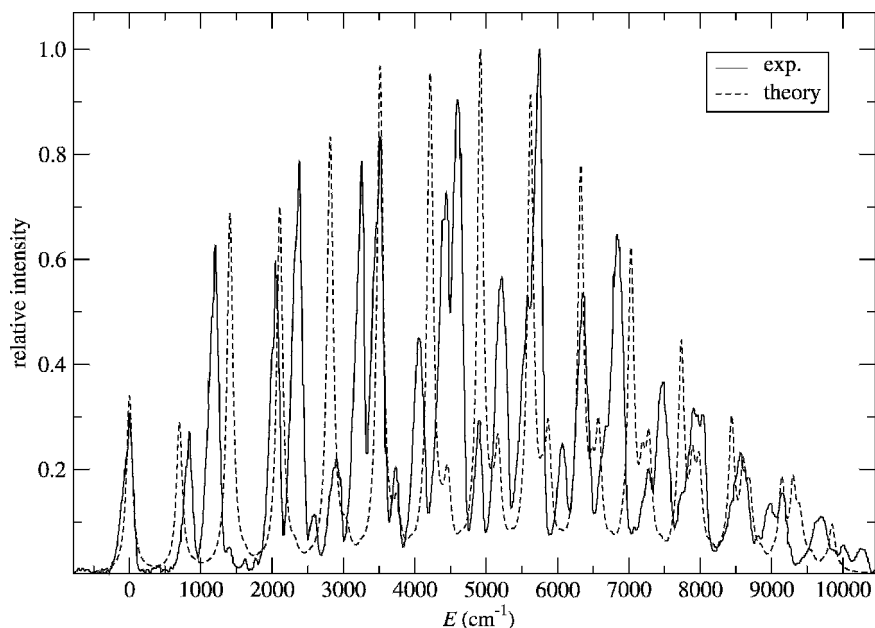
Figure 26 Comparison of computed [TDDFT-B3LYP/TZV(d,p)] and experimental[144] absorption spectra of formaldehyde. The 0–0 transition energy is set to zero.

also be found in larger systems (although the consequences for the shape of the spectra are expected to be of lesser importance) these limits of the currently feasible theoretical treatments must be kept in mind.

SUMMARY AND OUTLOOK

In this chapter, we have attempted to demonstrate that present-day quantum chemical electronic structure methods can provide an effective tool for predicting and interpreting electronic spectra of large molecules. This includes the calculation of vertical and 0–0 excitation energies, relative and absolute intensities, as well as details of vibrational features of absorption bands. A wide range of structurally different molecules and transitions between states of various characteristics have been successfully considered. This fact in turn strongly indicates that electronically excited states can be satisfactorily described by some of the above mentioned theoretical methods. The development of density functional based methods in particular has opened new areas of application that 10 years ago would have been "unthinkable". Progress has also emerged in pure ab initio (wave function) approaches in

recent years. These systematically improvable methods are still necessary to calibrate and test the density functionals or even other more approximate techniques. Because of the complexity of most excited-state problems, combined approaches using very different theoretical methods from all areas of quantum chemistry are strongly recommended because a multifaced approach will increase the overall reliability of the predictions. On the other hand, there is still a long way to go to improve existing theories and challenging problems remain to be solved. Beside the constant necessity to increase accuracy and applicability, the two issues of solvent effects on electronic spectra and the development of treatments for large and flexible systems are relevant topics for future researchers.

ACKNOWLEDGMENTS

REFERENCES

1. T. Helgaker, P. Jørgensen, and J. Olsen, *Molecular Electronic-Structure Theory*, Wiley, New York, 2000.

2. S. D. Peyerimhoff, in *Encyclopedia of Computational Chemistry*, Wiley, New York, 1998, pp. 2646–2664. Spectroscopy: Computational Methods.

3. J. N. Murrel, *The Theory of the Electronic Spectra of Organic Molecules*, Methuen, London, 1963.

4. H. H. Jaffe and M. Orchin, *Theory and Applications of Ultraviolet Spectroscopy*, Wiley, New York, 1962.

5. N. Mataga and A. Kubota, *Molecular Interactions and Electronic Spectra*, Marcel Dekker, Inc., New York, 1970.

6. M. B. Robin, *Higher Excited States of Polyatomic Molecules*, Vol. 1–2, Academic Press, New York, 1975.

7. N. J. Turro, *Modern Molecular Photochemistry*, Benjamin Cummings, Menlo Park, CA, 1978.

8. J. Michl and V. Bonacic-Koutecky, *Electronic Aspects of Organic Photochemistry*, Wiley, New York, 1990.

9. M. Klessinger and J. Michl, *Excited States and Photochemistry of Organic Molecules*, VCH, New York, 1995.

10. B. O. Roos, M. Fülscher, P.-A. Malmqvist, M. Merchan, and L. Serrano-Andres, in *Quantum Mechanical Electronic Structure Calculations with Chemical Accuracy*, S. R. Langhoff, Ed., Kluwer Academic Publishers, Dordrecht, 1995, pp. 357–438. Theoretical Studies of Electronic Spectra of Organic Molecules.

11. B. O. Roos, K. Andersson, M. P. Fülscher, P.-K. Malmqvist, L. Serrano-Andres, K. Pierloot, and M. Merchan, *Adv. Chem. Phys.*, **18**, 219 (1996). Multiconfigurational Perturbation Theory: Applications in Electronic Spectroscopy.

12. M. Merchan, L. Serrano-Andres, M. P. Fülscher, and B. O. Roos, in *Recent Advances in Multireference Methods*, K. Hirao, Ed., World Scientific, Singapore, 1999, pp. 161–195. Multiconfigurational Perturbation Theory Applied to Excited States of Organic Compounds.

13. S. Tretiak and S. Mukamel, *Chem. Rev.*, **102**, 3171 (2002). Density Matrix Analysis and Simulation of Electronic Excitations in Conjugated and Aggregated Molecules.

14. C. Marian, in *Reviews in Computational Chemistry*, K. B. Lipkowitz and D. B. Boyd, Eds., Vol. 17, Wiley-VCH, New York, 2001, pp. 99–204. Spin–Orbit Coupling in Molecules.

15. B. A. Heß, C. M. Marian, and S. D. Peyerimhoff, in *Modern Electronic Structure Theory*, D. R. Yarkony, Ed., World Scientific, Singapore, 1995, pp. 152–278. Ab Initio Calculation of Spin–Orbit Effects in Molecules Including Electron Correlation.

16. C. Engemann, G. Köhring, A. Pantelouris, J. Hormes, S. Grimme, S. D. Peyerimhoff, J. Clade, F. Frick, and M. Jansen, *Chem. Phys.*, **221**, 189 (1997). Experimental and Theoretical Investigations of the X-Ray Absorption Near Edge Spectra (XANES) of P_4O_6 and P_4O_6X (X = O, S, Se).

17. M. Stener, G. Fronzoni, and M. de Simone, *Chem. Phys. Lett.*, **373**, 115 (2003). Time-Dependent Density Functional Theory of Core Electron Excitations.

18. P. Salek, O. Vahtras, J. Guo, Y. Luo, T. Helgaker, and H. Ågren, *Chem. Phys. Lett.*, **374**, 446 (2003). Calculations of Two-Photon Absorption Cross Sections by Means of Density-Functional Theory.

19. S. F. Mason, *J. Chem. Soc.*, 1263 (1959). The Electronic Spectra of N-Heteroaromatic Systems: Part 4. The Vibrational Structure of the $n \rightarrow \pi^*$ Band of sym-Tetrazine.

20. A. D. Becke, *J. Chem. Phys.*, **98**, 5648 (1993). Density-Functional Thermochemistry. III. The Role of Exact Exchange.

21. P. J. Stevens, F. J. Devlin, C. F. Chabalowski, and M. J. Frisch, *J. Phys. Chem.*, **98**, 11623 (1994). Ab Initio Calculation of Vibrational Absorption and Circular Dichroism Spectra using Density Functional Force Fields.

22. Z. Rinkevicius, I. Tunell, P. Salek, O. Vahtras, and H. Ågren, *J. Chem. Phys.*, **119**, 34 (2003). Restricted Density Functional Theory of Linear Time-Dependent Properties in Open-Shell Molecules.

23. C. S. Page and M. Olivucci, *J. Comput. Chem.*, **24**, 298 (2003). Ground and Excited State CASPT2 Geometry Optimizations of Small Organic Molecules.

24. J. Fabian, L. A. Diaz, G. Seifert, and T. Niehaus, *J. Mol. Struct.*, **594**, 41 (2002). Calculation of Excitation Energies of Organic Chromophores: A Critical Evaluation.

25. M. Parac and S. Grimme, *J. Phys. Chem. A*, **106**, 6844 (2002). Comparison of Multireference Møller–Plesset Theory and Time-Dependent Methods for the Calculation of Vertical Excitation Energies of Molecules.

26. J. Ferguson, L. W. Reeves, and W. G. Schneider, *Can. J. Chem.*, **35**, 1117 (1957). Vapor Absorption Spectra and Oscillator Strengths of Naphthalene, Anthracene and Pyrene.

27. A. Amirav, U. Even, and J. Jortner, *J. Chem. Phys.*, **75**, 3770 (1981). Energetics and Intramolecular Dynamics of the Isolated Ultracold Tetracene Molecule in its First Singlet State.

28. M. Banasiewicz, I. Deperasińska, and B. Kozankiewicz, *J. Phys. Chem. A*, **107**, 662 (2003). Spectroscopic Characteristics of Pentacene in Shpol'skii Matrixes.

29. Y. Lou, J. Chang, J. Jörgensen, and D. M. Lemal, *J. Am. Chem. Soc.*, **124**, 15302 (2002). Octachloroazulene.

30. D. G. Leopold, V. Vaida, and M. F. Granville, *J. Chem. Phys.*, **81**, 4210 (1984). Direct Absorption Spectroscopy of Jet-Cooled Polyenes. I. The $1^1B_u^+ \leftarrow 1^1A_g^-$ Transition of *trans,trans*-1,3,5,7-Octatetraene.

31. H. Petek, A. J. Bell, Y. S. Choi, K. Yoshihara, B. A. Tounge, and R. L. Christensen, *J. Chem. Phys.*, **98**, 3777 (1993). The 2^1A_g State of trans,trans-1,3,5,7-octatetraene in Free Jet Expansions.

32. D. G. Leopold, R. J. Hemley, V. Vaida, and J. L. Roebber, *J. Chem. Phys.*, **75**, 4758 (1981). Direct Absorption Spectra of Higher Excited States of Jet-Cooled Monosubstituted Benzenes: Phenylacetylene, Styrene, Benzaldehyde and Acetophenone.

33. O. Dopfer, Ph.D. Dissertation, Technische Universität, München, 1994.

34. P. Imhof and K. Kleinermanns, *J. Phys. Chem. A*, **105**, 8922 (2001). Dispersed Fluorescence Spectra and Ab Initio Calculations of *o*-Cyanophenol.

35. S. Grimme and M. Parac, *Chem. Phys. Chem.*, **4**, 292 (2003). Substantial Errors from Time-Dependent Density Functional Theory for the Calculation of Excited States of Large π-Systems.

36. M. Parac and S. Grimme, *Chem. Phys.*, **292**, 11 (2003). A TDDFT Study of the Lowest Excitation Eenergies of Polycyclic Aromatic Hydrocarbons.

37. S. Tirapattur, M. Belletete, M. Leclerc, and G. Durocher, *J. Mol. Struct.*, **625**, 141 (2003). Study of Excited State Properties of Oligofluorenes by the Singles Configuration Interaction (CIS) Theoretical Approach.

38. H. Eyring, J. Walter, and G. E. Kimball, *Quantum Chemistry*, Wiley, New York, 1949.

39. P. W. Atkins and R. S. Friedman, *Molecular Quantum Mechanics*, Oxford University Press, Oxford, 1997.

40. T. H. Dunning, Jr., *J. Chem. Phys.*, **90**, 1007 (1989). Gaussian Basis Sets for Use in Correlated Molecular Calculations. I. The Atoms Boron Through Neon and Hydrogen.

41. R. A. Kendall, T. H. Dunning, Jr., and R. J. Harrison, *J. Chem. Phys.*, **96**, 6796 (1992). Electron Affinities of the First-Row Atoms Revisited. Systematic Basis Sets and Wave Functions.

42. C. W. Bauschlicher, Jr., and S. R. Langhoff, *Theor. Chim. Acta*, **79**, 93 (1991). Computation of Electronic Transition Moments: the Length versus the Velocity Representation.

43. K. Nakanishi, N. Berova, and R. Woody, Eds., *Circular Dichroism*, VCH, Weinheim, 1994.

44. E. Charney, *The Molecular Basis of Optical Activity*, Wiley, New York, 1979.

45. J. A. Schellman, *Chem. Rev.*, **75**, 323 (1975). Circular Dichroism and Optical Rotation.

46. G. H. Wagniere, *Linear and Nonlinear Optical Properties of Molecules*, VCH, Weinheim, 1993.

47. S. Grimme, A. Sobanski, J. Harren, and F. Vögtle, *Eur. J. Org. Chem.*, 1491 (1998). Structure–Chiroptic Relations of Planar Chiral and Helical Molecules.

48. D. A. Lightner and J. E. Gurst, *Organic Conformational Analysis and Stereochemistry from Circular Dichroism Spectroscopy*, Wiley-VCH, New York, 2000.

49. C. Diedrich and S. Grimme, *J. Phys. Chem. A*, **107**, 2524 (2003). Systematic Investigation of Modern Quantum Chemical Methods to Predict Electronic Circular Dichroism Spectra.

50. S. Coriani, P. Jørgensen, A. Rizzo, K. Ruud, and J. Olsen, *Chem. Phys. Lett.*, **300**, 61 (1999). Ab Initio Determinations of Magnetic Circular Dichroism.

51. I. Özkan and L. Goodman, *Chem. Rev.*, **79**, 275 (1979). Coupling of Electronic and Vibrational Motions in Molecules.

52. J. Franck, *Trans. Faraday Soc.*, **21**, 536 (1925). Elementary Processes of Photochemical Reactions.

53. E. U. Condon, *Phys. Rev.*, **28**, 1182 (1926). A Theory of Intensity Distribution in Band Systems.

54. E. U. Condon, *Phys. Rev.*, **32**, 858 (1928). Nuclear Motions Associated with Electron Transitions in Diatomic Molecules.

55. G. Herzberg and E. Teller, *Z. Phys. Chem. B*, **21**, 410 (1933). Schwingungsstruktur der Elektronenübergänge bei Mehratomigen Molekülen.

56. F. Duschinsky, *Acta Physiochem. URSS*, **7**, 551 (1937). Zur Deutung der Elektronenspekren Mehratomiger Moleküle.

57. G. M. Sando and K. G. Spears, *J. Phys. Chem.*, **105**, 5326 (2001). Ab Initio Calculation of the Duschinsky mixing of Vibration and Nonlinear Effects.

58. I. Özkan, *J. Mol. Spectrosc.*, **139**, 147 (1990). Franck–Condon Principle for Polyatomic Molecules: Axis-Switching Effects and Transformation of Normal Coordinates.

59. E. V. Doktorov, I. A. Malkin, and V. I. Man'ko, *J. Mol. Spectrosc.*, **64**, 302 (1977). Dynamical Symmetry of Vibronic Transitions in Polyatomic Molecules and the Franck–Condon Principle.

60. R. Berger, C. Fischer, and M. Klessinger, *J. Phys. Chem. A*, **102**, 7157 (1998). Calculation of the Vibronic Fine Structure in Electronic Spectra at Higher Temperatures. 1. Benzene and Pyrene.

61. J. Neugebauer, M. Reiher, C. Kind, and B. A. Heß, *J. Comput. Chem.*, **23**, 895 (2002). Quantum Chemical Calculation of Vibrational Spectra of Large Molecules—Raman and IR Spectra for Buckminsterfullerene.

62. C. Kind, M. Reiher, J. Neugebauer, and B. A. Heß. SNF Version 2.2.1, Universität, Erlangen, 2003.

63. C. D. Sherrill and H. F. Schaefer, III, *Adv. Quant. Chem.*, **34**, 143 (1999). The Configuration Interaction Method: Advances in Highly Correlated Approaches.

64. R. J. Rico and M. Head-Gordon, *Chem. Phys. Lett.*, **213**, 224 (1993). Single-Reference Theories of Molecular Excited States with Single and Double Substitutions.

65. M. Head-Gordon, R. J. Rico, M. Oumi, and T. J. Lee, *Chem. Phys. Lett.*, **219**, 21 (1994). A Doubles Correction to Electronic Excited States from Configuration Interaction in the Space of Single Substitutions.

66. S. Grimme and M. Waletzke, *J. Chem. Phys.*, **111**, 5645 (1999). A Combination of Kohn-Sham Density Functional Theory and Multi-Reference Configuration Interaction Methods.

67. A. B. J. Parusel and S. Grimme, *J. Porphyrins Phthalocyanines*, **5**, 225 (2001). DFT/MRCI Calculations on the Excited States of Porphyrin, Hydroporphyrins, Tetrazaporphyrins, and Metalloporphyrins.

68. J. Tatchen, M. Waletzke, C. M. Marian, and S. Grimme, *Chem. Phys.*, **264**, 245 (2001). The Photophysics of Pyranthione: A Theoretical Investigation Focussing on Spin-Forbidden Transitions.

69. M. Kleinschmidt, J. Tatchen, and C. M. Marian, *J. Comput. Chem.*, **23**, 824 (2002). Spin–Orbit Coupling of DFT/MRCI Wavefunctions: Method, Test Calculations, and Applications to Thiophene.

70. C. M. Marian, F. Schneider, M. Kleinschmidt, and J. Tatchen, *Eur. Phys. J. (D)*, **20**, 357 (2002). Electronic Excitation and Singlet–Triplet Coupling in Uracil Tautomers and Uracil–Water Complexes, a Quantum Chemical Investigation.

71. M. Kleinschmidt Tatchen, C. M. Marian, M. Parac, and S. Grimme, *Z. Phys. Chem.*, **217**, 205 (2003). Quantum Chemical Investigation of Spin-Forbidden Transitions in Dithiosuccinimide.

72. H. J. J. Van Dam, J. H. Van Lenthe, and P. J. A. Ruttink, *Int. J. Quant. Chem.*, **72**, 5498 (1999). Exact Size Consistency of Multireference Møller–Plesset Perturbation Theory.

73. S. Grimme, M. Parac, and M. Waletzke, *Chem. Phys. Lett.*, **334**, 99 (2001). On the Importance of Third and Fourth-Order Corrections in Multi-Reference Møller–Plesset Theory.

74. B. O. Roos and K. Andersson, in *Modern Electronic Structure Theory*, D. R. Yarkony, Ed., World Scientific, Singapore, 1995, pp. 55–109. *Multiconfigurational Second-Order Perturbation Theory.*

75. B. O. Roos, K. Andersson, and M. P. Fülscher, *Chem. Phys. Lett.*, **192**, 5 (1992). Towards an Accurate Molecular Orbital Theory for Excited States: The Benzene Molecule.

76. P. Celani and H.-J. Werner, *J. Chem. Phys.*, **112**, 5546 (2000). Multireference Perturbation Theory for Large Restricted and Selective Active Space Reference Wave Functions.

77. J. J. W. McDoull, K. Peasley, and M. A. Robb, *Chem. Phys. Lett.*, **148**, 183 (1988). A Simple MCSCF Perturbation Theory: Orthogonal Valence Bond Møller–Plesset 2 (OVB MP2).

78. S. Grimme and M. Waletzke, *Phys. Chem. Chem. Phys.*, **2**, 2075 (2000). Multi-Reference Møller–Plesset Theory: Computational Strategies for Large Molecules.

79. L.-M. Frutos, O. Castano, and M. Merchan, *J. Phys. Chem. A.*, **107**, 5472 (2003). Theoretical Determination of the Singlet–Singlet and Singlet–Triplet Electronic Spectra, Lowest Ionization Potentials, and Electron Affinity of Cyclooctatetraene.

80. R. G. Parr and W. Yang, *Density-Functional Theory of Atoms and Molecules*, Oxford University Press, Oxford, 1989.

81. W. Koch and M. C. Holthausen, *A Chemist's Guide to Density Functional Theory*, Wiley-VCH, Weinheim, 2000.

82. E. K. U. Gross, J. F. Dobson, and M. Petersilka, *Top. Curr. Chem.*, **181**, 81 (1996). Density Functional Theory.

83. M. E. Casida, in *Recent Advances in Density Functional Methods*, Vol. 1, D. P. Chong, Ed., World Scientific, Singapore, 1995, pp. 155–213. Time-Dependent Density Functional Response Theory for Molecules.

84. H. Weiss, R. Ahlrichs, and M. Häser, *J. Chem. Phys.*, **99**, 1262 (1993). A Direct Algorithm for Self-Consistent Field Linear Response Theory and Application to C_{60}: Excitation Energies, Oscillator Strengths and Frequency-Dependent Polarizabilities.

85. R. Bauernschmitt and R. Ahlrichs, *Chem. Phys. Lett*, **256**, 454 (1996). Treatment of Electronic Excitations within the Adiabatic Approximation of Time Dependent Density Functional Theory.

86. S. Grimme, *Chem. Phys. Lett.*, **259**, 128 (1996). Density Functional Calculations with Configuration Interaction for the Excited States of Molecules.

87. S. Hirata and M. Head-Gordon, *Chem. Phys. Lett.*, **314**, 291 (1999). Time-Dependent Density Functional Theory within the Tamm–Dancoff Approximation.

88. H. Koch and P. Jørgensen, *J. Chem. Phys.*, **93**, 3333 (1990). Coupled Cluster Response Functions.

89. H. Koch, H. J. A. Jensen, P. Jørgensen, and T. Helgaker, *J. Chem. Phys.*, **93**, 3345 (1990). Excitation Energies from the Coupled Cluster Singles and Doubles Linear Response Function (CCSDLR). Applications to Be, CH^+, CO, and H_2O.

90. D. C. Comeau and R. J. Bartlett, *Chem. Phys. Lett.*, **207**, 414 (1993). The Equation-of-Motion Coupled-Cluster Method. Applications to Open- and Closed-Shell References States.

91. O. Christiansen, H. Koch, and P. Jørgensen, *Chem. Phys. Lett.*, **243**, 409 (1995). The Second-Order Approximate Coupled Cluster Singles and Doubles Model CC2.

92. C. Hättig and F. Weigend, *J. Chem. Phys.*, **113**, 5154 (2000). CC2 Excitation Energy Calculations on Large Molecules using the Resolution of the Identity Approximation.

93. A. Köhn and C. Hättig, *J. Chem. Phys.*, **119**, 5021 (2003). Analytical Gradients for Excited States in the Coupled-Cluster Model CC2 Employing the Resolution-of-the-Identity Approximation.

94. J. B. Forseman and E. Frisch, *Exploring Chemistry with Electronic Structure Methods*, Gaussian, Inc., Pittsburgh, 1996.

95. A. D. Becke, *J. Chem. Phys.*, **98**, 1372 (1993). A New Mixing of Hartree–Fock and Local Density Functional Theories.

96. D. J. Tozer and N. C. Handy, *J. Chem. Phys.*, **109**, 10180 (1998). Improving Virtual Kohn–Sham Orbitals and Eigenvalues: Application to Excitation Energies and Static Polarizabilities.

97. A. Dreuw, J. L. Weismann, and M. Head-Gordon, *J. Chem. Phys.*, **119**, 2943 (2003). Long-Range Charge-Transfer Excited States in Time-Dependent Density Functional Theory Require Non-local Exchange.

98. M.-S. Liao, Y. Lu, and S. Scheiner, *J. Comput. Chem.*, **24**, 623 (2003). Performance Assessment of Density-Functional Methods for Study of Charge-Transfer Complexes.

99. A. S. Zyubin and A. M. Mebel, *J. Comput. Chem.*, **24**, 692 (2003). Performance of Time-Dependent Density Functional and Green Functions Methods for Calculation of Excitation Energies in Radicals and for Rydberg Electronic States.

100. J. Spanget-Larsen, *Theor. Chem. Acc.*, **98**, 137 (1997). The Alternant Hydrocarbon Pairing Theorem and All-Valence Electrons Theory. An Approximate LCAO Theory for the Electronic Absorption and MCD Spectra of Conjugated Organic Compounds, Part 2.

101. W. Weber and W. Thiel, *Theor. Chem. Acc.*, **103**, 495 (2000). Orthogonalization Corrections for Semiempirical Methods.

102. F. Vögtle, A. Hünten, E. Vodel, and S. Grimme, *Angew. Chem. Int. Ed. Engl.*, **40**, 2468 (2001). Novel Amide-Based Molecular Knots: Complete Enantiomeric Separation, Chiroptical Properties and Absolute Configuration.

103. M. Klessinger, T. Pötter, and C. van Wüllen, *Theoret. Chim. Acta*, **80**, 1 (1991). Semiempirical Valence-Electron Calculations of Excited State Geometries and Vibrational Frequencies.

104. A. Koslowski, M. E. Beck, and W. Thiel, *J. Comput. Chem.*, **24**, 714 (2003). Implementation of a General Multireference Configuration Interaction Procedure with Analytic Gradients in a Semiempirical Context using the Graphical Unitary Group Approach.

105. C. Sandorfy, Ed., *The Role of Rydberg States in Spectroscopy and Reactivity*, Kluwer Academic Publishers, Dordrecht, 1999.

106. A. S. Zyubin and A. M. Mebel, *J. Chem. Phys.*, **119**, 6581 (2003). Accurate Prediction of Excitation Energies to High-Lying Rydberg Electronic States: Rydberg States of Acetylene as a Case Study.

107. M. Merchan, B. O. Roos, R. McDiarmid, and X. Xing, *J. Chem. Phys.*, **104**, 1791 (1996). A Combined Theoretical and Experimental Determination of the Electronic Spectrum of Acetone.

108. A. D. Becke, *Phys. Rev. A*, **38**, 3098 (1988). Density-Functional Exchange-Energy Approximation with Correct Asymptotic Behaviour.

109. J. P. Perdew, *Phys. Rev. B*, **33**, 8822 (1986). Density-Functional Approximation for the Correlation-Energy of the Inhomogenous Electron Gas.

110. F. D. Sala and A. Görling, *J. Chem. Phys.*, **116**, 5374 (2002). The Asymptotic Region of the Kohn–Sham Exchange Potential in Molecules.

111. F. D. Sala and A. Görling, *Int. J. Quan. Chem.*, **91**, 131 (2003). Excitation Energies of Molecules by Time-Dependent Density Functional Theory Based on Effective Exact Exchange Kohn–Sham Potentials.

112. P. Brint and L. O'Toole, *J. Chem. Soc. Faraday Trans.*, **87**, 2891 (1991). Multiphoton Ionisation Spectroscopy of the $3s(2+2,1)$ and $4s(3+1)$ Rydberg States of Acetone: Evidence for a Molecular Valence State at 153 nm.

113. R. M. Christie, *Colour Chemistry*, The Royal Society of Chemistry, Cambridge, UK, 2001.

114. U. Brackmann, *Lambdachrome Laser Dyes*, Lambda Physik AG, Göttingen, 2000.

115. A. Mühlpfordt, R. Schanz, N. Ernsting, V. Farztdinov, and S. Grimme, *Phys. Chem. Chem. Phys.*, **14**, 3209 (1999). Coumarin 153 in the Gas Phase: Optical Spectra and Quantum Chemical Calculations.

116. R. J. Cave and E. W. Castner, *J. Phys. Chem. A*, **106**, 12117 (2002). Time-Dependent Density Functional Theory Investigation of the Ground and Excited States of Coumarins 102, 152, 153, and 343.

117. R. J. Cave, K. Burke, and E. W. Castner, *J. Phys. Chem. A*, **106**, 9294 (2002). Theoretical Investigation of the Ground and Excited States of Coumarin 151 and Coumarin 120.

118. G. Haucke and R. Paetzold, *Photophysikalische Chemie Indigoider Farbstoffe*, Deutsche Akademie der Naturforscher Lepoldina, Halle (Saale), 1978.

119. M. C. Zerner, in *Reviews in Computational Chemistry*, K. B. Lipkowitz and D. B. Boyd, Eds., Vol. 2, Wiley-VCH, New York, 1991, pp. 313–365. Semiempirical Molecular Orbital Methods.

120. S. Záliš, I. R. Farrell, and A. Vlček, Jr., *J. Am. Chem. Soc.*, **125**, 4580 (2003). The Involvement of Metal-to-CO Charge Transfer and Ligand-Field Excited States in the Spectroscopy and Photochemistry of Mixed-Ligand Metal Carbonyls. A Theoretical and Spectroscopic Study of [W(CO)$_4$(1,2-ethylenediamine)] and [W(CO)$_4$(N,N-bis-alkyl-1,4-diazabutadiene)].

121. T. P. M. Goumans, A. W. Ehlers, M. C. van Hemert, A. Rosa, E.-J. Baerends, and K. Lammertsma, *J. Am. Chem. Soc.*, **125**, 3558 (2003). Photodissociation of the Phosphine-Substituted Transition Metal Carbonyl Complexes Cr(CO)$_5$L and Fe(CO)$_4$L: A Theoretical Study.

122. M. K. Nazeeruddin, S. M. Zakeeruddin, R. Humpry-Basker, M. Jirousek, P. Liska, N. Vlachopoulos, V. Shklover, C.-H. Fisher, and M. Grätzel, *Inorg. Chem.*, **38**, 6298 (1999). Acid–Base Equilibria of (2,2′-Bipyridyl-4,4′-dicarboxylic acid)ruthenium(II) Complexes and the Effect of Protonation on Charge-Transfer Sensitization of Nanocrystalline Titania.

123. A. Schäfer, H. Horn, and R. Ahlrichs, *J. Chem. Phys.*, **97**, 2571 (1992). Fully Optimized Contracted Gaussian Basis Sets for Atoms Li to Kr.

124. D. Andrae, U. Häussermann, M. Dolg, H. Stoll, and H. Preuss, *Theor. Chim. Acta*, **77**, 123 (1990). Energy-Adjusted Ab Initio Pseudopotentials for the Second and Third Row Transition Elements.

125. J. E. Monat, J. H. Rodriguez, and J. K. McCusker, *J. Phys. Chem. A*, **106**, 7399 (2002). Ground- and Excited-State Electronic Structures of the Solar Cell Sensitizer bis(4,4′-dicarboxylato-2,2′-bipyridine)bis(isothiocyanato)ruthenium(II).

126. S. Fantacci, F. D. Angelis, and A. Selloni, *J. Am. Chem. Soc.*, **125**, 4381 (2003). Absorption Spectrum and Solvatochromism of the [Ru(4,4′-COOH-2,2′-bpy)2(NCS)2] Molecular Dye by Time Dependent Density Functional Theory.

127. J. G. Radziszewski, M. Gil, A. Gorski, J. Spanget-Larsen, J. Waluk, and B. J. Mroz, *J. Chem. Phys.*, **115**, 9733 (2001). Electronic States of the Phenoxyl Radical.

128. S. Hirata, M. Head-Gordon, J. Szczepanski, and M. Vala, *J. Phys. Chem. A*, **107**, 4940 (2003). Time-Dependent Density Functional Study of the Electronic Excited States of Polycyclic Aromatic Hydrocarbon Radical Ions.

129. C. Niederalt, S. Grimme, and S. D. Peyerimhoff, *Chem. Phys. Lett.*, **245**, 455 (1995). Ab Initio Theoretical Study of the Electronic Absorption Spectra of Polycyclic Aromatic Hydrocarbon Radical Cations of Naphthalene, Anthracene and Phenanthrene.

130. P. Foggi, F. V. R. Neuwahl, L. Moroni, and P. R. Salvi, *J. Phys. Chem. A*, **107**, 1689 (2003). $S_1 \rightarrow S_n$ and $S_2 \rightarrow S_n$ Absorption of Azulene: Femtosecond Transient Spectra and Excited State Calculations.

131. P. Cronstrand, O. Christiansen, P. Norman, and H. Ågren, *Phys. Chem. Chem. Phys.*, **2**, 5357 (2000). Theoretical Calculations of Excited State Absorption.

132. Y. H. Meyer, R. Astier, and J. M. Leclercq, *J. Chem. Phys.*, **56**, 801 (1972). Triplet–Triplet Spectroscopy of Polyacenes.

133. G. Snatzke, *Angew. Chem.*, **91**, 380 (1979). Circulardichroismus und Absolute Konfiguration: Anwendung der Qualitativen MO-Theorie auf die Chiroptischen Phänomene.

134. L. A. Neubert and M. Carmack, *J. Am. Chem. Soc.*, **96**, 943 (1974). Circular Dichroism of Disulfides with Dihedral Angles of 0, 30 and 60 deg. in the 400–185 nm Spectral Region.

135. V. O. Saik and S. Lipsky, *J. Phys. Chem. A*, **105**, 10107 (2001). Absorption Spectra of Some Liquids in the VUV.

136. F. Furche, R. Ahlrichs, C. Wachsmann, E. Weber, A. Sobanski, F. Vögtle, and S. Grimme, *J. Am. Chem. Soc.*, **122**, 1717 (2000). Circular Dichroism of Helicenes Investigated by Time-Dependent Density Functional Theory.

137. W. S. Brickell, A. Brown, C. M. Kemp, and S. F. Mason, *J. Chem. Soc (A)*., 756 (1971). π Electron Absorption and Circular Dichroism Spectra of [6]- and [7]-Helicene.

138. D. Gruner, A. Nguyen, and P. Brumer, *J. Chem. Phys.*, **101**, 10366 (1994). Theoretical Study of the S_1–S_0 Spectroscopy of Anthracene.

139. P. R. Callis, J. T. Vivian, and L. S. Slater, *Chem. Phys. Lett.*, **244**, 53 (1995). Ab Initio Calculations of Vibronic Spectra for Indole.

140. F. Furche and R. Ahlrichs, *J. Chem. Phys.*, **117**, 7433 (2002). Adiabatic Time-Dependent Density Functional Methods for Excited State Properties.

141. M. Odelius, D. Laikov, and J. Hutter, *J. Mol. Struct.*, **630**, 163 (2003). Excited State Geometries within Time-Dependent and Restricted Open-Shell Density Functional Theories.

142. S. Hirata and M. Head-Gordon, *Chem. Phys. Lett.*, **302**, 375 (1999). Time-Dependent Density Functional Theory for Radicals. An Improved Description of Excited States with Substantial Double Excitation Character.

143. M. E. Casida, K. C. Casida, and D. R. Salahub, *Int. J. Quant. Chem.*, **70**, 933 (1998). Excited-State Potential Energy Curves From Time-Dependent Density-Functional Theory: A Cross Section of Formaldehydes $^1A_1$ Manifold.

144. J. D. Rogers, *J. Phys. Chem.*, **94**, 4011 (1990). Ultraviolet Absorption Cross Sections and Atmospheric Photodissociation Rate Contant of Formaldehyde.

145. D. C. Moule and A. D. Walsh, *Chem. Rev.*, **75**, 67 (1975). Ultraviolet Spectra and Excited States of Formaldehyde.

146. R. Ahlrichs, M. Bär, H.–P. Baron, R. Bauernschmitt, S. Böcker, M. Ehrig, K. Eichkorn, S. Elliott, F. Furche, F. Haase, M. Häser, H. Horn, C. Huber, U. Huniar, M. Kattannek, C. Kölmel, M. Kollwitz, K. May, C. Ochsenfeld, H. Öhm, A. Schäfer, U. Schneider, O. Treutler, M. von Arnim, F. Weigend, P. Weis, and H. Weiss. TURBOMOLE (Ver. 5.6), Universität Karlsruhe, 2003.

CHAPTER 4

Simulating Chemical Waves and Patterns

Raymond Kapral

Chemical Physics Theory Group, Department of Chemistry, University of Toronto, Toronto, Ontario M5S 3H6, Canada

INTRODUCTION

When chemically reacting systems are forced to lie far from equilibrium they form a remarkable variety of chemical patterns. Living systems are open to the environment and the displacement from equilibrium arises from chemical or other energy supplied to the system by the surroundings. Sustained chemical patterns can be observed in the laboratory in continuously fed unstirred reactors (CFUR),[1] where feeds of chemicals are supplied to the chemical reactor to maintain it far from equilibrium. A favorite laboratory system that has been studied often is the Belousov–Zhabotinsky (BZ) reaction,[2–4] the catalytic oxidation of citric or malonic acid by bromate ion in an acidic solution. When such a reaction is carried out in a open gel reactor, one sees waves of oxidation pass through the system that often take the forms of spirals as shown in Figure 1(*a*).[5] The wavelength of the pattern is on the order of millimeters and the rotation period of the spiral wave is on a time scale of seconds. Even more complex chemical patterns can be seen in such open reactors; for example, Figure 1(*b*) shows the formation of a labyrinthine pattern in the iodine–ferrocyanide–sulfite chemical reaction in a gel reactor.[6] This chapter discusses how one can model the formation and evolution of such chemical patterns using computer simulation. Related phenomena of temporal patterns such as oscillations and chaos were reviewed in an earlier volume.[7]
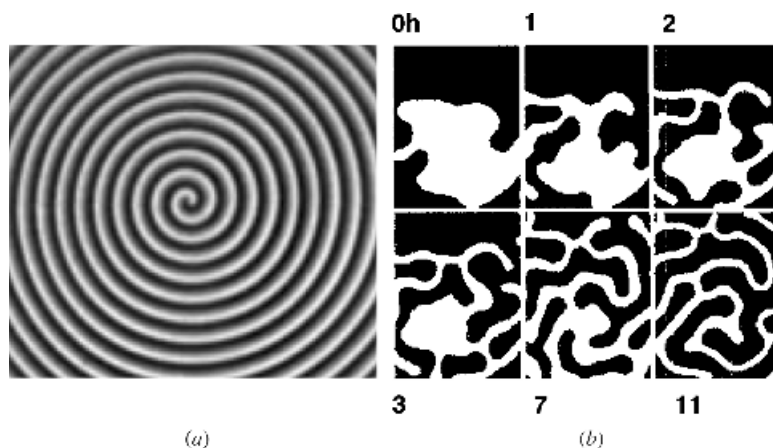
Figure 1 (a) A spiral wave formed in a thin gel layer of the Belousov–Zhabotinsky reaction (from Belmonte and Flesselles, Ref. 5. (b) Formation of a labyrinthine pattern in the bistable region of the iodine–ferrocyanide–sulfite chemical reaction in a gel reactor (from Lee and Swinney, Ref. 6).

Reacting systems can be viewed and modeled on different space and time scales, ranging from the microscopic to the macroscopic. Microscopic models are the domain of classical molecular dynamics or even quantum mechanics. For large, open, spatially distributed systems of the sort discussed above, these fundamental descriptions cannot provide a basis for practical simulation methods. In a macroscopic system, the number of molecules is so large that it is impossible to contemplate the direct solution of Newton's or Schrödinger's equations of motion. Furthermore, while elementary processes corresponding to reactive events typically occur on femtosecond time scales and angstrom length scales, the scales of interest for chemical patterns are usually much larger.

The choice of theoretical tools used to analyze the behavior of these systems depends on the scales on which one wishes to model the dynamics and the questions being asked. If the phenomena of interest are truly macroscopic, for example, the chemical waves in the BZ reaction, then an appropriate level of description is through reaction–diffusion equations. This macroscopic description focuses on chemical concentrations in small (but still macroscopic) system volumes and considers how these local concentrations change as a result of reaction and diffusion. In such an approach, one bypasses the molecular level of description completely and focuses directly on phenomena occurring on macroscopic scales.

If the phenomena of interest occur on shorter mesoscopic length and time scales, say tens to hundreds of nanometers and pico- to microseconds, then a mesoscopic description in terms of Markov processes or Markov chain

models is appropriate. These descriptions model the dynamics as a stochastic process based on the reaction and diffusion mechanisms. Although the stochastic dynamics coarse grains over molecular scales, it incorporates the effects of fluctuations that reaction–diffusion models miss. When building such models it is important to establish a link between the mesoscopic and macroscopic descriptions.

In contrast to these basic approaches at the macroscopic and mesoscopic levels, one can consider a class of models that does not rely on a knowledge of the detailed rate law or reaction mechanism but instead abstract certain generic features of the behavior. These simplified models often provide insight into the system's dynamics and isolate the minimal features needed to rationalize complex phenomena. Cellular automata (CA)[8] and coupled map lattices (CML) are two examples of such abstract models that we shall discuss.[9] In the following sections, we discuss each of these models, give some of the background that led to their formulation, and provide an introduction to how they are constructed. The presentation will focus on a few examples instead of providing an exhaustive overview.

REACTION–DIFFUSION SYSTEMS

Suppose we have an open system with n chemical species, labeled by an index α, which diffuse and undergo chemical reactions. If the chemical and diffusion processes occur on space and time scales that are long compared to microscopic scales, a local equilibrium description is appropriate. In a local equilibrium description, one imagines that the system is partitioned into cells centered at positions $\mathbf{r}$ that contain many molecules and across which gradients in concentrations are negligible. In each cell, we can determine the local chemical concentration $c_\alpha(\mathbf{r}, t)$ of species α at time t. Within each cell, chemical reactions occur and the rate of change of species α due to reactions is called $R_\alpha(c_1(\mathbf{r}, t), \ldots, c_n(\mathbf{r}, t))$. The concentration in cell $\mathbf{r}$ can also change by diffusion of a species from one cell to another. Thus, the changes in the local chemical concentrations are described by reaction–diffusion equations

$$\frac{\partial c_\alpha(\mathbf{r}, t)}{\partial t} = R_\alpha + D_\alpha \nabla^2 c_\alpha(\mathbf{r}, t) \qquad [1]$$

where D_α is the diffusion coefficient of species α. The combination of nonlinear kinetics with positive or negative feedback arising from autocatalytic steps in the reaction mechanism, flows of reagents into and out of the system to maintain it in far-from-equilibrium states and diffusion, with possibly different diffusion coefficients for different species, endow this equation and the physical systems it represents with interesting behavior that has fascinated chemists and researchers in other disciplines.
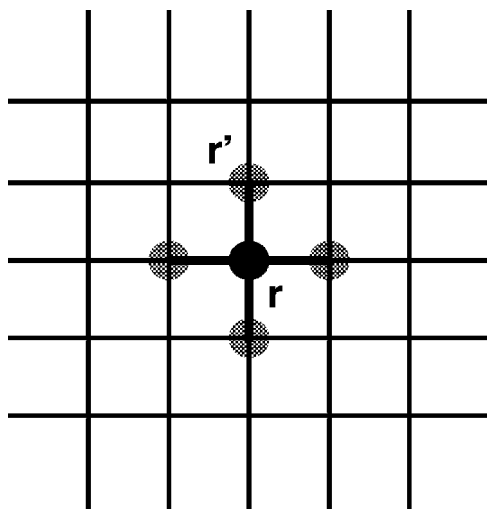
Figure 2 An example of a regular spatial grid used in the simulation of the reaction–diffusion equation. The grid spacing is Δx. The heavy lines connecting grid points show the coupling used in the evaluation of the diffusion term.

In order to model pattern formation in chemical systems at the macroscopic level, we must be able to solve the reaction–diffusion equation [1]. The simplest numerical method that one can use to solve this equation is an Euler scheme, where space is divided into a regular grid of points with separation Δx. In Figure 2, we show such a grid for a two-dimensional system. Each grid point is labeled by $\mathbf{r} = (i, j)$. Time is also divided into small segments Δt.

For simplicity, suppose we consider a single chemical species X with local concentration $c_X(\mathbf{r}, t)$. (We may suppose that other chemical species participating in the reaction are pool species whose concentrations are either in large excess or are held fixed by flows of reagents into and out of the system.) If we approximate the time and space derivatives in Eq. [1] by finite differences we obtain,

$$c_X(\mathbf{r}, t + \Delta t) = c_X(\mathbf{r}, t) + \Delta t R_X(c_X(\mathbf{r}, t)) + \frac{D_X \Delta t}{(\Delta x)^2} \sum_{\mathbf{r}' \in \mathcal{N}(\mathbf{r})} \left(c_X(\mathbf{r}', t) - c_X(\mathbf{r}, t) \right)$$

[2]

where $\mathbf{r}'$ runs over the neighbors of site $\mathbf{r}$ and $\mathcal{N}(\mathbf{r})$ stands for the number of cells (i.e., sites) that are neighbors to the cell $\mathbf{r}$ (see Figure 2). As long as Δx and Δt are sufficiently small and satisfy the stability condition $D\Delta t/(\Delta x)^2 < 1/2d$, where d is the dimension of the system, this scheme will yield a faithful solution to the reaction–diffusion equation. The grid points need not lie on a cubic lattice and the size of the neighborhood used to

compute the spatial derivatives can be enlarged to insure that the chemical patterns do not depend on the underlying grid used in the simulations. If the reaction kinetics has very disparate time scales or the spatial variations of the concentrations are very pronounced, the differential equations are called *stiff* and such a simple explicit scheme may not be efficient. In this case, more complicated implicit partial differential equation solvers or other integration schemes may be used to obtain the solutions of the reaction–diffusion equation.[10–15] The simulation of two often-studied models will illustrate some of the chemical patterns that reaction–diffusion equations can display.

The Schlögl model[16] has the reaction mechanism,

$$(i) \quad A \underset{k_{-1}}{\overset{k_1}{\rightleftharpoons}} X \qquad (ii) \quad B + 2X \underset{k_{-2}}{\overset{k_2}{\rightleftharpoons}} 3X \qquad [3]$$
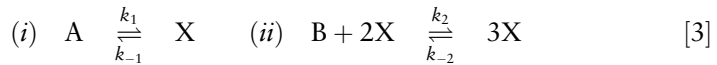
We suppose that the A and B species are pool species, that is, their concentrations are very large. If the concentrations of these species are taken to be constant, only the concentration of species X can change. Following mass action kinetics, the reaction rates corresponding to the two steps in the mechanism (Eq. [3]) are

$$R_X^{(i)}(c_X) = k_1 c_a - k_{-1} c_X$$
$$R_X^{(ii)}(c_X) = k_2 c_b c_X^2 - k_{-2} c_X^3 \qquad [4]$$

where c_a and c_b are the constant concentrations of species A and B, respectively. Consequently, the overall reaction rate for species X is $R_X = R_X^{(i)} + R_X^{(ii)} = k_1 c_a - k_{-1} c_X + k_2 c_b c_X^2 - k_{-2} c_X^3$.

If the system is homogeneous in space, there are no concentration gradients and the reaction–diffusion equation [1] reduces to the chemical rate law,

$$\frac{dc_X(t)}{dt} = k_1 c_a - k_{-1} c_X + k_2 c_b c_X^2 - k_{-2} c_X^3 \qquad [5]$$

whose steady-state concentrations c_X^* (i.e., those for which $dc_X/dt = 0$) are given by the solutions of the cubic equation, $k_1 c_a - k_{-1} c_X^* + k_2 c_b c_X^{*2} - k_{-2} c_X^{*3} = 0$. Depending on the choice of kinetic parameters, the Schlögl model possesses either a single stable steady state or bistable steady states. A sketch of the steady-state solutions are shown in Figure 3. A rate law of this type is applicable to the iodate–arsenous acid system where experimental studies of wave propagation have been carried out.[17]

Suppose the initial concentration of X in the system fluctuates slightly in space around the value c_0^* so that $c_X(\mathbf{r}, 0) = c_0^* + \delta c_X(\mathbf{r})$, where $\delta c_X(\mathbf{r})$ is a small perturbation. If c_0^* corresponds to the unstable state and we solve the
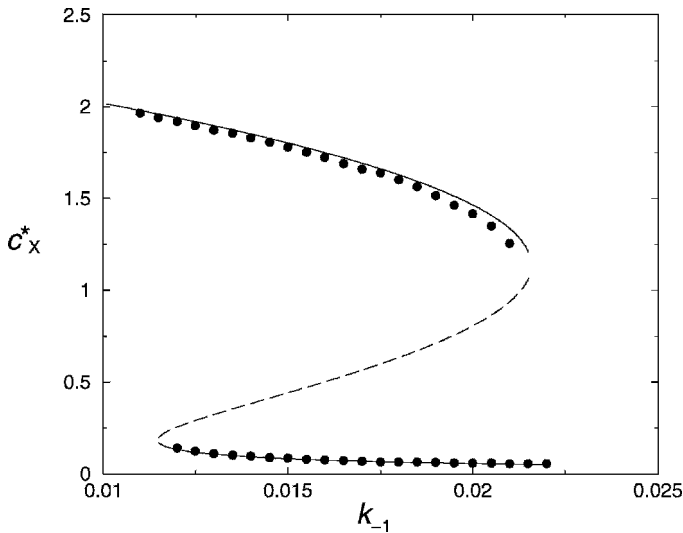
Figure 3 Steady states of the Schlögl model. The steady-state concentration c_X^* is plotted versus the rate constant k_{-1}. The solid (dashed) lines denote stable (unstable) steady states. Parameters are $k_1 c_a = 0.001$, $k_2 c_b = 0.0356$, and $k_{-2} = 0.0153$. The filled circles are the results of a mesocopic Markov chain simulation of the Schlögl reaction dynamics.

reaction–diffusion equation for the Schlögl model in two dimensions using the Euler scheme in Eq. [2] subject to this initial condition, we obtain the results shown in Figure 4. The system quickly evolves from the unstable state and forms domains of the two stable states separated by chemical fronts where
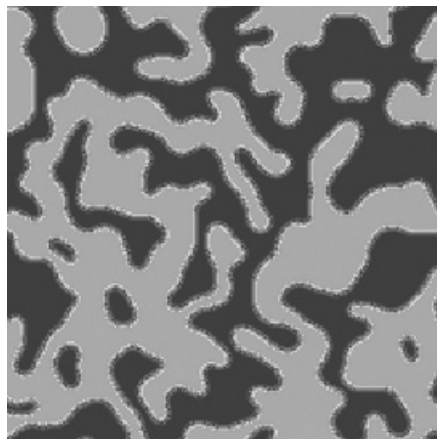
Figure 4 Formation of domains of the two stable states in the Schlögl model color coded in gray shades.

the concentration changes rapidly from one stable state to the other. This segregation into two phases is akin to what one sees when a binary solution is rapidly cooled to the two-phase region of the phase diagram and two immiscible liquids form; however, because the chemical reaction can change the concentration, the pattern will continue to coarsen until a single phase exists in the finite system. Behavior of this type is common in many physical systems and is described by Model A of critical phenomena.[18] Bistable systems with competing interactions can form more complex patterns like the labyrinthine patterns shown in Figure 1(b); such patterns will be discussed later in this chapter.

A second example of a reaction–diffusion equation is the FitzHugh–Nagumo (FHN) model for two chemical concentrations u and v:

$$\frac{\partial u}{\partial t} = -u^3 + u - v + D_u \nabla^2 u$$
$$\frac{\partial v}{\partial t} = \epsilon(u - \alpha v + \beta) + D_v \nabla^2 v \qquad [6]$$

In this model, ϵ is the ratio of the time scales associated with the reactive dynamics of the two variables u and v, while D_u and D_v are their diffusion coefficients. The parameters α and β characterize the local reactive dynamics. The FHN model[19,20] was originally constructed as a simple scheme for describing electrochemical wave propagation in excitable nerve or cardiac tissue. The variable u corresponds to the potential while v represents ion currents in the nerve tissue. It has since been used extensively as a generic model that describes so-called "excitable" behavior of chemically reacting systems. In fact, as we shall show later in this chapter, it is possible to write a chemical reaction scheme whose rate law is of FHN form.[21]

Excitable media are some of the most commonly observed reaction-diffusion systems in Nature. An excitable system has a stable steady state that responds to perturbations in a characteristic way: Small perturbations return quickly to the steady state, while larger perturbations that exceed a certain threshold value make a long excursion in concentration phase space before the system returns to the stable state. In many physical systems, this behavior is captured by the dynamics of two concentration fields, a fast activator variable (the u variable with cubic nullcline in the FHN model) and a slow inhibitor variable (the v variable in the FHN model with linear nullcline).[22] A nullcline is a curve corresponding to zero time derivatives for the variables in the system. Figure 5(a) shows the $\dot{u} = 0 = -u^3 + u - v$ and $\dot{v} = 0 = v - au + b$ nullclines of this system along with trajectories corresponding to sub- and superthreshold excitations. The trajectory arising from the subthreshold perturbation quickly relaxes back to the stable fixed point. Three stages can be identified in the trajectory resulting from the superthreshold perturbation: an excited stage where the phase point quickly evolves far from the fixed point, a refractory stage where the system relaxes back to the
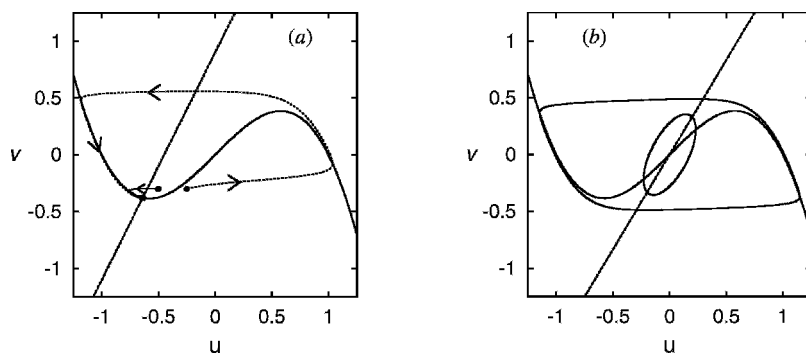
Figure 5 Cubic ($\dot{u} = 0$) and linear ($\dot{v} = 0$) nullclines for the FHN equations: (*a*) displays the excitable dynamics showing trajectories resulting from sub- and super-threshold excitations; (*b*) displays oscillatory dynamics showing two limit cycle orbits; small inner limit cycle close to Hopf point; large outer limit cycle far from Hopf point. See Ref. 7 for the definition of Hopf points.

stable state and is not susceptible to additional perturbation, and the resting state where the system again resides at the stable fixed point.

An excitable medium is a diffusively coupled array of such local excitable elements described by a reaction–diffusion equation. Imagine a local super-threshold perturbation applied to the system in the homogeneous resting state. Due to diffusive coupling, the perturbation will excite neighboring regions of the medium. The originally perturbed region will first relax to the refractory state where it is no longer susceptible to perturbation, and finally back to the stable steady state. Consequently, a circular wave of excitation with a refractory tail will propagate outward from the perturbation through the medium. If an excitable wave is broken (e.g., by an obstacle or inhomogeneity in the medium), since the front velocity is smaller at the tip than the rest of the wave front, free ends of wave fronts will curl, leading to the formation of spiral waves in the system. Examples of a ring of excitation and a spiral wave in the FitzHugh excitable medium are shown in Figure 6.

Excitable waves are seen in many chemical and biological systems. The often-studied BZ reaction was one of the first systems in which such waves were observed.[4,23] Chemical waves of this type have been studied extensively in the catalytic oxidation of CO on Pt.[24] In biological contexts, waves of this type occur in the aggregation stage of the slime mould dictyostelium discoideum where the chemical signaling is through periodic waves of cyclic adenosine monophosphate (cAMP); also, the Ca^{2+} waves in systems like *xenopus laevis* oocytes and pancreatic β cells fall into this category.[25] Electrochemical waves in cardiac and nerve tissue have this origin and the appearance and/or breakup of spiral wave patterns in excitable media are believed to be responsible for various types of arrhythmias in the heart.[26]

(a)   *(b)*
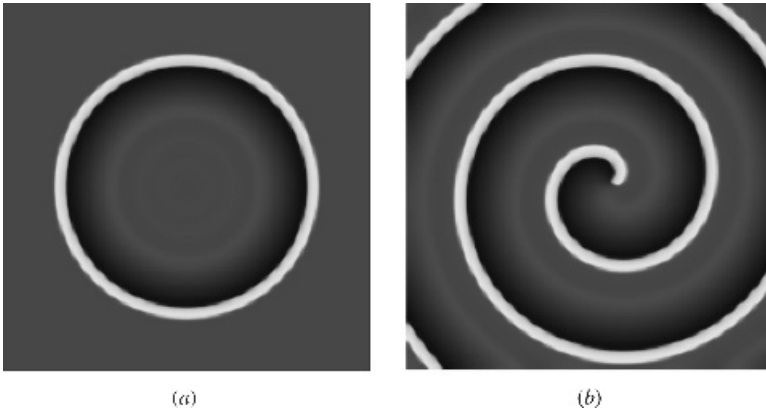
Figure 6 A ring of excitation (*a*) and a spiral wave (*b*) calculated from the excitable FHN medium, Eq. [6].

In addition to excitability, the FHN model can also possess oscillatory solutions. Figure 5(*a*) shows the configuration of the nullclines for a different choice of parameters. Now the system has an unstable fixed point or steady state and the stable attracting state is a limit cycle oscillation shown as the closed loop surrounding the unstable fixed point in the (*uv*)-plane of the figure. Chemical patterns such as spiral waves can form in oscillatory as well as excitable systems[27] and we shall have occasion to discuss some aspects of patterns in oscillatory media below.

CELLULAR AUTOMATA

The chemically reacting systems we have been considering are relatively simple—at least our models for them have been so. However, most of the pattern forming reacting media studied in the laboratory have very complex mechanisms whose full nature is still a matter of debate, even for the extensively studied BZ reaction.[28] The situation becomes very complicated indeed if one turns to living systems where the basic underlying mechanisms involve very complex networks of reactions. One question one might pose is, are there certain basic underlying principles or mechanisms that complex systems exploit to achieve a particular kind of behavior? Or, stated another way, are there simple rules that underlie the dynamics of complex systems?

Cellular automata were constructed by Von Neumann and Ulam as simple models of self-reproducing systems that mimic living systems.[29] The Von Neumann cellular automaton is not so simple and comprises a fairly complex set of rules that specifies how the system evolves in time. Codd devised a much simpler rule that achieves self-reproduction.[30,31] Wiener and Rosenbluth

constructed the forerunner of a cellular automaton to model the behavior of excitable cardiac tissue.[32] The use of cellular automata to model condensed phases was discussed in an earlier chapter in this series.[8] We shall show below that variants of the Wiener–Rosenbluth model can be used more generally to model chemical wave propagation in excitable chemical systems.

Before showing how this can be done, we must first define more precisely what a cellular automaton (CA) is. A CA model for a system is constructed as follows: The dynamical evolution is imagined to take place on a set of cells. Each cell is defined by a finite set of values of a dynamical variable $\mathscr{S} = \{s_k : k = 1, \ldots, n\}$. The values of the s_k in a cell change at discrete time instants according to a rule $\mathscr{R}$ that depends on the value of s_k in the cell as well as that of its neighbors. Even very simple rules, $\mathscr{R}$, can produce complicated dynamics.[33] In fact, CA rules that are Turing machines, that is, are capable of universal computation, can be devised.

As a simple example of a CA rule, suppose the cells are arranged in a line and the cell variable takes the values 0 or 1, $s \in (0, 1)$. Let $s(i)$ be the value of s in cell i. Next, we need a rule $\mathscr{R}$ that tells us how the $s(i)$ change with time. Suppose the rule depends on the value of $s(i, t)$, that is, the cell value at time t, and the values of its nearest neighbors at the sites $i + 1$ and $i - 1$. Because the cell can take only the values 0 and 1, we can enumerate all eight possibilities of $(s(i - 1)s(i)s(i + 1))$: (000), (001), (010), (011), (100), (101), (110), and (111). If we interpret these strings of zeros and ones as binary numbers, they correspond to the decimal numbers 0–7. The CA rule specifies how the central cell value $s(i, t)$ changes as a result of the values of the neighboring cells: $(s(i - 1, t)s(i, t)s(i + 1, t)) \rightarrow s(i, t + 1)$. An example is Rule 90:

$$(000) \rightarrow 0 \quad (001) \rightarrow 1 \quad (010) \rightarrow 0 \quad (011) \rightarrow 1$$
$$(100) \rightarrow 1 \quad (101) \rightarrow 0 \quad (110) \rightarrow 1 \quad (111) \rightarrow 0 \tag{7}$$

If the final values of $s(i)$ are written in reverse order one obtains 01011010, which has the decimal value 90, hence the name of the rule. If one starts with a single one in a row of zeros on a line, one finds the result in Figure 7. This calculation shows that a very simple CA rule can produce very complicated spatio-temporal dynamics.

Returning to our theme of pattern formation in reaction-diffusion systems, we show how a simple CA model of an excitable system can be constructed.[34,35] The main characteristics of an excitable medium, as discussed above, are the presence of a stable steady or resting state and the peculiar form of the evolution back to the resting state after a disturbance. In particular, we saw that if the perturbation exceeded a critical value the system became excited to values of the concentration far from the resting state and then slowly relaxed back to the resting state. During this relaxation, the system was refractory and not susceptible to further perturbation. Consequently,
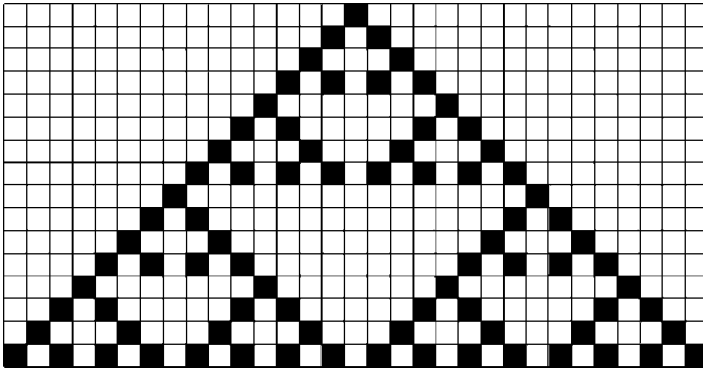
Figure 7 Time evolution given by Rule 90. The abcissa is the cell label while the ordinate is discrete time, with time increasing from top to bottom. The color coding is such that 0 is white and 1 is black.

we can identify three major states of the system: the resting state Q, the excited state E, and the refractory state R. To construct a CA model for an excitable system, we suppose that the cells in the CA model can take values in the set $\mathscr{S} = \{Q, E, R\}$. We arrange the cells on a regular lattice in space, say in two dimensions, as shown in Figure 2 for the discretization of the reaction–diffusion equation. Now all we need is a rule $\mathscr{R}$ that changes the state of the cells and mimics the excitable dynamics.

First, consider a cell in isolation from its neighboring cells. If it is in the resting state Q, it will remain there since this is the stable steady state of the system. If it is excited, that is, in the state E, it will first become refractory, and then finally return to the resting state. Thus, it will undergo the series of changes $E \rightarrow R \rightarrow Q$.

Of course, cells are not isolated but communicate with their neighbors mimicking the diffusion of chemicals in the real system. We can take this coupling effect into account by having the state of a cell labeled by $\mathbf{r}$, its discrete position on the lattice, change as a result of the values in neighboring cells located at sites $\mathbf{r}'$. In particular, we suppose that if the cell at $\mathbf{r}$ is in its resting state Q and any one of the neighboring cells is excited; that is, in the state E, then in the next step the cell will become excited. If we let $s(\mathbf{r}, t)$ be the state of the cell $\mathbf{r}$ at time t, then the rule $\mathscr{R}$ for an excitable medium may be written compactly as

$$s(\mathbf{r}, t+1) = \begin{cases} E & \text{if } s(\mathbf{r}, t) = Q \quad \text{and} \quad s(\mathbf{r}', t) = E \\ R & \text{if } s(\mathbf{r}, t) = E \\ Q & \text{if } s(\mathbf{r}, t) = R \text{ or } s(\mathbf{r}, t) = Q \quad \text{and} \quad s(\mathbf{r}', t) \in \{Q, R\} \end{cases} \qquad [8]$$

By using this rule, it is possible to construct the evolution of simple initial conditions with just a pencil and graph paper. For example, if all the cells in
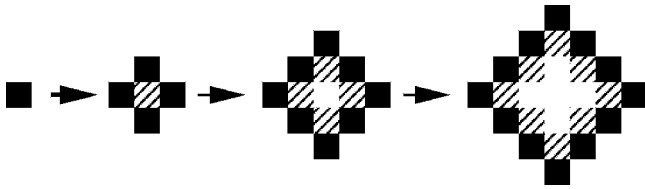
Figure 8 A ring of excitation produced by the excitable medium CA rule. Color coding: Q white, E black, R shaded.

the system are in the resting Q state except for a single cell in the center that is excited and in state E, then, according to the rule this central cell will excite its neighbors to the state E, while it will evolve to the refractory state R. In subsequent time steps, the excited cells will continue to excite neighboring cells that are in the resting state Q, but will not excite cells in the refractory state R, since this state is not susceptible to perturbations. Thus a ring of excitation will grow from the single excited cell as shown in Figure 8. The analogy with the growing ring of excitation in the partial differential equation (PDE) simulation of the FHN model in Figure 6 is evident.

Spiral waves are also easily generated by this CA rule. To produce such chemical waves in the system, we start with an initial condition consisting of a row of cells in the excited state E, adjacent to a row of cells in the refractory state R. All other cells in the system are in the resting state Q. The cells in the center of the row simply advance forward on each time step as the excited cells excite their neighbors; backward excitation is prevented by the row of refractory cells. However, more interesting behavior occurs at the end of the row. Because an additional cell may be excited at the end of the row in the first time step, the excitation will "curl" around the refractory states at subsequent time steps leading to a pair of spiral waves as shown in Figure 9. Once again the similarity to the spiral wave in Figure 6 for the FHN model is evident.
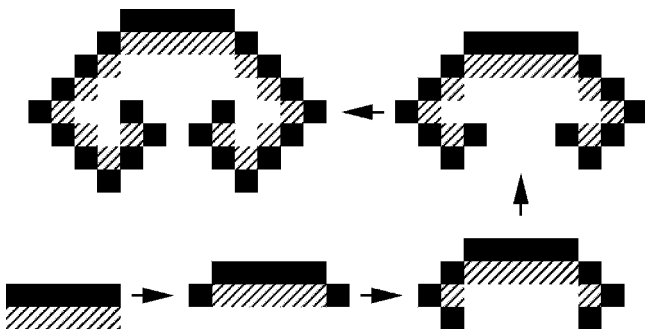
Figure 9 A spiral wave produced by the excitable medium CA rule.

This example illustrates both the power and drawbacks of simple cellular automaton modeling of reaction–diffusion media. The CA rule abstracts the essential features responsible for the different types of wave propagation seen in excitable media and provides considerable insight into how and why such chemical patterns form. However, if one wants to examine the chemical patterns in excitable media in more detail, the artifacts arising from the simplicity of the CA rule are an obstacle to such investigations. For example, one obvious difference between the ring of excitation and spiral patterns in the CA model and those in the PDE simulation of the FHN model is that the CA patterns have sharp corners. The shapes of the waves are also determined by the nature of the lattice on which the CA cells are placed and the nature of the neighborhood used in the CA rule. For example, if nearest plus next-nearest neighbors (called a Moore neighborhood) are used to update the cell values, one obtains a square-shaped ring instead of a diamond-shaped ring. Since the curvature of the wave fronts determines many aspects of their propagation properties, a quantitative description of wave propagation is not possible using this CA model.

It is also interesting to examine the nature of the center or core of the spiral wave in the CA model. By looking at the evolution of the CA spiral wave in Figure 9 one can see that there is a configuration of four cells (shown in Figure 10) that cycles and repeats itself every four time steps. This cycling configuration is responsible for the generation of the spiral wave and does not move: The spiral is pinned to the initial location of this core configuration of cells. In experimental observations of spiral waves of excitable chemical media and PDE simulations, depending on the system parameters, the spiral core is not stationary and may undergo complicated meandering motion.[36–39] This behavior is not captured by the simple CA model.

One can now envisage several ways to try to remedy these deficiencies and there have been numerous generalizations of the simple excitable CA rule discussed above.[40,41] These generalizations typically increase the size of the state space of a cell, including several excited and refractory states.
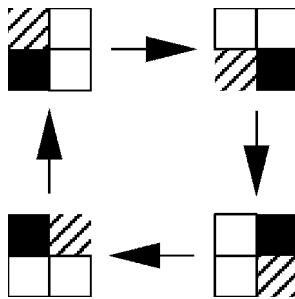
Figure 10 Cycling configuration of cells at the center or core of a CA spiral wave.

Furthermore, the size and nature of the neighborhood can be changed. If the CA rules are made sufficiently elaborate many of the artifacts of the waves can be removed. However, the price one pays is the lack of simplicity and physical insight and increased computational cost. Direct simulation of PDE models is a simple task on current computers, precluding the use of such elaborate CA models.

However, in addition to the physical insight into the nature of excitable wave propagation that CA models provide, they are a powerful tool for analyzing general aspects of complex dynamics. Thus, their utility far surpasses the fact that they are simple models for reaction–diffusion systems. Because very simple rules can yield very complicated dynamical behavior, these models have been investigated extensively in the mathematical and physical literature.[42,43] They provide insight into the basic conditions needed to obtain complex behavior and provide a means of classifying this behavior. The fact that simple CA rules can lead to universal computation or self-replication provides keys to a deeper understanding of Nature.

COUPLED MAP LATTICES

In the preceding two sections, we discussed patterns in chemically reacting media using PDE reaction–diffusion models, where space, time, and chemical concentrations were continuous variables, and cellular automata, where space, time, and the state of a cell were discrete. We now turn our attention to coupled map lattices (CML),[44,45] another type of model that has been used to gain insight into the behavior of systems displaced far from equilibrium. The structure of a CML model of a system has similarities both to discretizations of reaction–diffusion equations and to cellular automata. To build a CML model of a system, space is partitioned into a grid of points on which the dynamical variables (chemical concentrations in our case) are evaluated. A rule or map is associated with each lattice site that specifies how the variables change after a single time step. The rule differs from that used in a CA model since the variables in the cells can take continuous values, not discrete values as in a CA rule, and the map function specifies how these continuous variables change in one time step. The coupled map lattice is constructed by coupling such maps together so that the new value of the variable at the site is determined by the local map plus its coupling to the maps at neighboring sites. Thus, we see that in a CML both space and time are discrete while the dynamical variable at a site takes on continuous values.

We may again use the grid in Figure 2 to show how the maps may be coupled to form CML. As in our earlier discussions the sites of the lattice are labeled by discrete values $\mathbf{r}$. At each site we have a map that is a function $f(c(\mathbf{r}, t))$ that takes the variable $c(\mathbf{r}, t)$ at site $\mathbf{r}$ at time t into its

value at time $t + 1$: $c(\mathbf{r}, t + 1) = f(c(\mathbf{r}, t))$. The coupled map model may then be written as

$$c(\mathbf{r}, t + 1) = f(c(\mathbf{r}, t)) + \gamma \sum_{\mathbf{r}' \in \mathcal{N}(\mathbf{r})} (g(c(\mathbf{r}', t)) - g(c(\mathbf{r}, t))) \qquad [9]$$

where the notation is the same as in earlier sections. Here γ gauges the strength of the coupling of the map at site $\mathbf{r}$ to maps at neighboring sites $\mathbf{r}'$, and g is a function that specifies the nature of the coupling.

At this point it is useful to make comparisons to the Euler solution of the reaction–diffusion equation. If we measure time in units of Δt so that $t/\Delta t \to t$, we can write Eq. [2] (dropping the subscript X) as,

$$c(\mathbf{r}, t + 1) = f(c(\mathbf{r}, t)) + \gamma \sum_{\mathbf{r}' \in \mathcal{N}(\mathbf{r})} \left(c(\mathbf{r}', t) - c(\mathbf{r}, t) \right) \qquad [10]$$

where $f(c) = c + \Delta t R(c)$, $g(c) = c$, and $\gamma = [D_X \Delta t / (\Delta x)^2]$. We mentioned earlier that the Euler solution will be useful only if the stability criterion $\gamma = [D_X \Delta t / (\Delta x)^2] < 1/2d$ is satisfied. (The stability criterion depends on the specific form of the CML model.) Thus, we see that the Euler discretization of the reaction–diffusion equation is a CML model for its evolution. It is often more convenient to write the CML model in a forward difference form where we take $g = f$ so that

$$c(\mathbf{r}, t + 1) = f(c(\mathbf{r}, t)) + \gamma \sum_{\mathbf{r}' \in \mathcal{N}(\mathbf{r})} \left(f(c(\mathbf{r}', t)) - f(c(\mathbf{r}, t)) \right) \qquad [11]$$

which is termed the CML with pure diffusive coupling.[46]

If this were the only context in which CML models were used, their utility would be severely limited. For values γ beyond the stability limit, the Euler method fails and one obtains solutions that fail to represent the solutions of the reaction–diffusion equation. However, it is precisely the rich pattern formation observed in CML models beyond the stability limit that has attracted researchers to study these models in great detail. Coupled map models show spatiotemporal intermittency, chaos, clustering, and a wide range of pattern formation processes.[47] Many of these complicated phenomena can be studied in detail using CML models because of their simplicity and, if there are generic aspects to the phenomena, for example, certain scaling properties, then these could be carried over to real systems in other parameter regimes. The CML models have been used to study chemical pattern formation in bistable, excitable, and oscillatory media.[48]

One example will serve to illustrate the use of CML models in this more general context. Suppose we consider the BZ reaction, not in the excitable regime as earlier, but in the oscillatory regime. Certain versions of the BZ
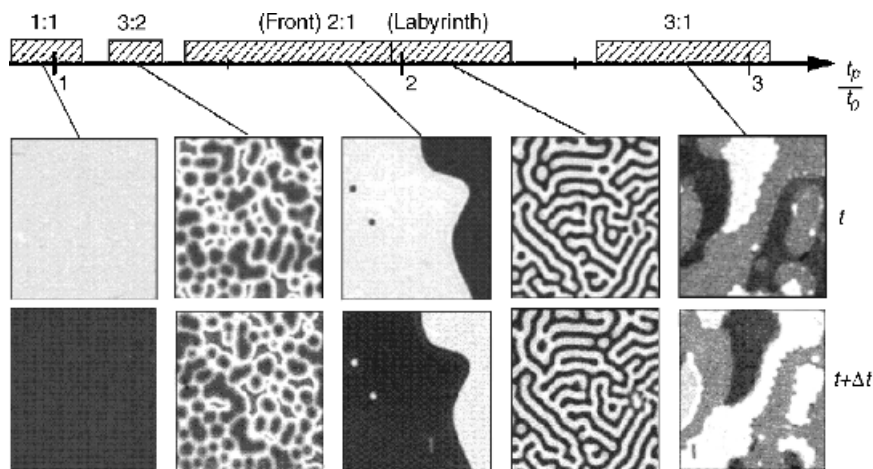
Figure 11 Resonantly forced patterns in the oscillatory light-sensitive BZ medium (from Ref. 49).

reaction are light sensitive. If the BZ reaction is carried out in a CFUR and subjected to periodic illumination, the external periodic forcing of the oscillatory medium can give rise to a new class of chemical patterns.[49,50] If the period of the forcing by the illumination is close to a multiple of the natural period of the oscillation, the system can become locked or entrained to some multiple of the driving period. An example of the experimental results for such a periodically forced oscillatory reaction–diffusion system is shown in Figure 11. The figure shows that the system can lock to different multiples of the driving frequency of the light (labeled 1:1, 1:2, 1:3, etc., in the figure) and that the system forms patches where the chemical concentrations are similar, separated by fronts where the phase of the oscillation jumps by some multiple of π. For example, in the right-most panel we have 3:1 mode locking. Here we see three different types of patches coded by white, gray, and black. If we observe one patch, at time intervals corresponding to the external forcing period, it will cycle according to white $\rightarrow$ black $\rightarrow$ gray $\rightarrow$ white. If we compare the upper and lower panels of the figure, we can see such a change of colors of the homogeneous patches. We can associate a phase $n2\pi/3$, $n = 1, 2, \ldots$ with each color. Thus, we see that the periodic forcing has turned the continuous oscillation into an oscillation with discrete phases in this representation: The periodic forcing has broken the time translation symmetry of the system.

What has all of this to do with coupled map lattices? Suppose we take a CML model where the local map at a site leads to cycling among three states: a period-3 map. An example is

$$f(z) = \begin{cases} bz & \text{for} \quad 0 \leq z \leq 1/b \\ a & \text{for} \quad 1/b < z \leq 1 \end{cases} \qquad [12]$$
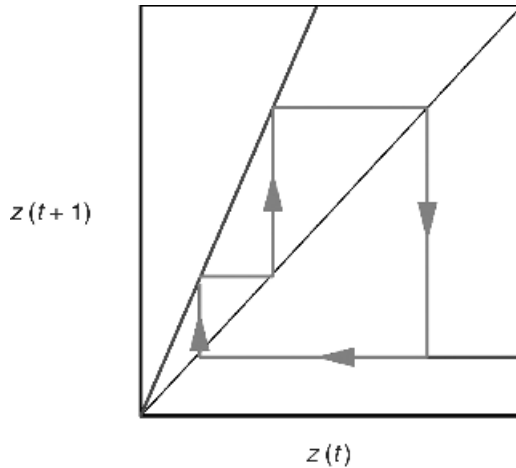
Figure 12 The piece-wise linear map for parameters that support a stable period-3 orbit. The period-3 orbit is shown graphically.

The map $f(z)$ possesses the period-3 solution $A = a \to B = ab \to C = ab^2 \to A = a$ (see Figure 12 for a graphical representation). The local map has the same discrete period-3 behavior as the local dynamics of the resonantly forced system. The discrete time dynamics of the map breaks the time translation symmetry of the system just like the resonant forcing of the local chemical dynamics. We can now make a CML model of the resonantly forced 3:1 reaction–diffusion system by coupling an array of such period-3 maps:

$$z(\mathbf{r}, t+1) = f(z(\mathbf{r}, t)) + \gamma \sum_{\mathbf{r}' \in \mathcal{N}(\mathbf{r})} \Big(f(z(\mathbf{r}', t)) - f(z(\mathbf{r}, t)) \Big) \qquad [13]$$

with the notation as used earlier. The CML model is simple to simulate on a computer. If we start with three patches of the three different values of the period-3 orbit, we obtain the result shown in Figure 13. This figure should be compared with the last panel of Figure 11, where similar coexistence between periodic homogeneous phases, is seen. As in the resonantly forced chemical systems, the colors of the homogeneous patches in the pattern shown in Figure 13 cycle among themselves.

This CML model does not attempt to account for the detailed features of the chemistry of the resonantly forced BZ reaction; instead, like CA models, it focuses on the generic element needed to observe the pattern (in this case the broken time translation symmetry produced by the external forcing). The CML model may then be used to explore the possible types of patterns that may arise in systems with this characteristic feature. In this way, we can gain insight into how such patterns form and even discover new types of possible behavior.
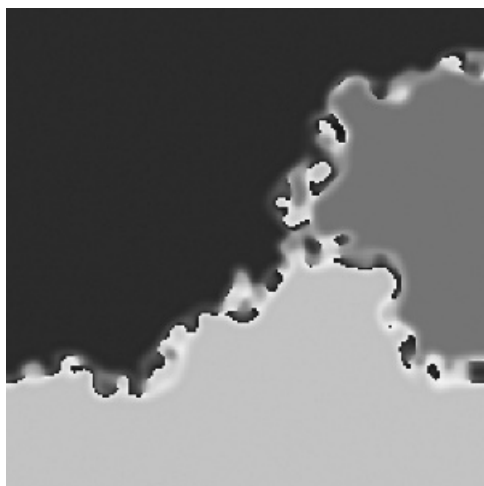
Figure 13 Pattern formation in the period-3 CML. Coexisting patches of three homogeneous phases separated by sharp, rough fronts, where z jumps between values of the homogeneous phases.

The use of a CML in this context can be illustrated by the following example: Prepare an initial condition for the CML, where the left half of the system is in one of the three period-3 states, say A (light gray), and the right half is in state B (black). As in Figure 13, an interface will develop between these two phases where the value of z changes rapidly. The interface will slowly move to the right and we have a traveling "chemical" front. If we now change the map or coupling parameters we can find a situation where the interface becomes very complicated (chemical turbulence) and the interfacial zone grows and actually consumes the homogeneous phases. This is shown in Figure 14. The interfacial zone separating the two homogeneous
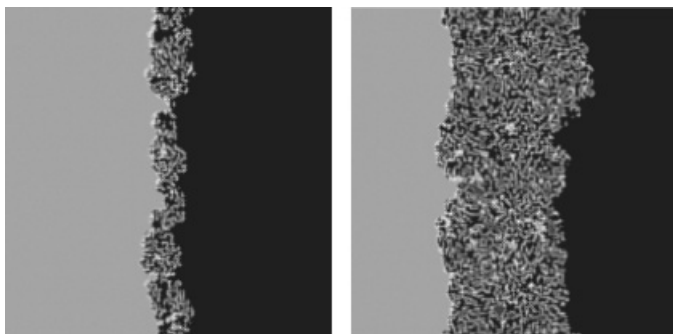
Figure 14 Exploding front in the period-3 CML system. Time increases from the left to the right panel. The turbulent interfacial zone separating the two homogeneous phases grows.

Figure 15 Exploding front in a 3:1 resonantly forced oscillatory reaction–diffusion system. Time increases from panel *a* to panel *b*.

phases grows with time and if the simulation were continued the chaotic phase would fill the entire system resulting in a complicated state termed spatio-temporal turbulence. For other parameter values, the turbulent zone is confined between the two stable phases. Thus, the system exhibits a type of nonequilibrium phase transition between a complex, but confined, interfacial zone and a turbulent phase that consumes the homogeneous phases.[51,52]

Is this behavior a peculiar feature of the CML model or is it real? Figure 15 shows the results of a simulation of a 3:1 resonantly forced oscillatory reaction–diffusion system for a specific choice of parameters.[53,54] As in the CML model, a chemical front separates two of the three homogeneous phases. This front is turbulent and grows to fill the entire system. This suggests that the phenomenon is real and may be found in resonantly forced chemical systems.

MESOSCOPIC MODELS

The models for chemically reacting media discussed above described the evolution of the system on macroscopic scales. In some instances, especially when one considers applications of nonlinear chemical dynamics to biological systems or materials on nanoscales, a mesoscopic description will be more appropriate or even essential. In this section, we show how one can construct mesoscopic models for reaction–diffusion systems and how these more fundamental descriptions relate to the macroscopic models considered previously.

In order to construct mesoscopic models, we again begin by partitioning the system into cells located at the nodes of a regular lattice, but now the cells are assumed to contain some small number of molecules. We cannot use a continuum description of the dynamics in a cell as we did for the reaction–diffusion equation. Instead, we describe the reactions and motions of molecules using stochastic rules that mimic the dynamics of these processes on mesoscales. The stochastic element arises because we do not take into account the detailed motions of all solvent species or the dynamics on microscopic scales. Nevertheless, because the number of molecules in a cell may be small, we must account for the fact that this number can change by random reactive events and random motions of molecules that take them into and out of a
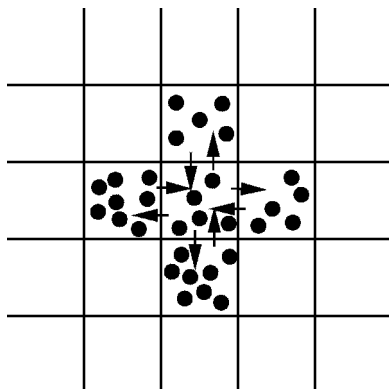
Figure 16 Cell structure used in the construction of mesoscopic models. The number of particles in the cells can change by stochastic reaction rules and by random motion into and out of the cell volumes (shown schematically by arrows).

given cell. A schematic picture of the cell structure for a mesoscopic model is shown in Figure 16. The nodes or cells of the regular lattice with N sites are labeled by $\mathbf{r}^N = (\mathbf{r}_1, \mathbf{r}_2, \ldots, \mathbf{r}_N)$. A site $\mathbf{r}_i$ has $n_X(\mathbf{r}_i)$ molecules of species X. We are interested in the probability $P(\mathbf{n}_X^N, t)$ that the set of N nodes have $\mathbf{n}_X^N = (n_X(\mathbf{r}_1), n_X(\mathbf{r}_2), \ldots, n_X(\mathbf{r}_N))$ molecules of species X at time t.

The equation that governs the time evolution of this probability distribution is taken to be the Markov process model,[55,56]

$$\frac{\partial P(\mathbf{n}_X^N, t)}{\partial t} = \sum_{\mathbf{n}_X'^N} W\left(\mathbf{n}_X^N | \mathbf{n}_X'^N\right) P\left(\mathbf{n}_X'^N, t\right) \qquad [14]$$

where the transition probability matrix $\mathbf{W}$ specifies how $P(\mathbf{n}_X{}^N, t)$ changes because of diffusion of particles from cell to cell and reactions within the cells. Alternatively, we can model the dynamics by Markov chain models[57]

$$P(\mathbf{n}_X^N, t+1) = \sum_{\mathbf{n}_X'^N} \tilde{\mathbf{W}}\left(\mathbf{n}_X^N | \mathbf{n}_X'^N\right) P\left(\mathbf{n}_X'^N, t\right) \qquad [15]$$

where the time is discrete as in CA or CML models.

Random-walk models for diffusion on the lattice can be implemented in various ways. Typically, particles randomly hop between a node $\mathbf{r}$ and its neighbors $\mathbf{r}' \in \mathcal{N}(\mathbf{r})$. If there are no restrictions on the number of particles at a node, the stationary distribution for this diffusive stochastic process is Poissonian,[55]

$$P(n_X; c_X) = \frac{c_X^{n_X}}{n_X!} e^{-c_X} \qquad [16]$$

where c_X is the average density of species X on the lattice. Diffusion may also be modeled by a random walk with exclusion. This may be accomplished in many ways. (For a review of reactive lattice-gas automata, see Ref. 58). Suppose a maximum number of m particles of species X is allowed at a node; then, for example, particles may be assigned to channels corresponding to the links of the lattice. The channel configuration may be randomized and particles propagated synchronously and deterministically to neighboring lattice nodes. This leads to a binomial distribution

$$P(n_X; c_X) = \binom{m}{n_X} \left(\frac{c_X}{m}\right)^{n_X} \left(1 - \frac{c_X}{m}\right)^{m-n_X} \qquad [17]$$

if small correlations arising from exclusion are neglected.

As a simple illustration of how reactions may be treated stochastically on mesoscopic scales, we show how one may construct a mesoscopic Markov process model for the Schlögl reaction (Eq. [3]). As before, we assume that species A and B in the Schlögl mechanism are pool species and their concentrations do not change in time: Their effect is incorporated into the rate constants of the reaction. A Markov model of the reactions is a birth–death process, where chemical species are "born" in some reactions (X is born in the reactions (1) A → X and (3) 2X + B → 3X) and "dies" in others (X dies in the reactions (2) X → A and (4) 3X → 2X + B). Suppose there are n_X molecules of species X in a cell. Then the probability that a reaction X → A occurs and changes the number of molecules in the cell from n_X to $n'_X = n_X - 1$ is just

$$X \overset{k_{-1}}{\to} A \qquad p_2(n_X|n_X - 1) = k_{-1}n_X \qquad [18]$$

Similarly, for the other reactions, we have

$$A \overset{k_1}{\to} X \qquad p_1(n_X|n_X + 1) = k_1 n_A \qquad [19]$$

$$2X + B \overset{k_2}{\to} 3X \qquad p_3(n_X|n_X + 1) = k_2 n_X(n_X - 1)n_B \qquad [20]$$

$$3X \overset{k_{-2}}{\to} 2X + B \qquad p_4(n_X|n_X - 1) = k_{-2}n_X(n_X - 1)(n_X - 2) \qquad [21]$$

Given these reaction probabilities, we can write the rate of change of the probability that there are n_X molecules of species X in the cell at time t, $P(n_X, t)$, as

$$\frac{dP(n_X, t)}{dt} = \left(k_1 n_A + k_2(n_X - 1)(n_X - 2)n_B\right) P(n_X - 1, t)$$

$$+ \left(k_{-1}(n_X + 1) + k_{-2}(n_X + 1)n_X(n_X - 1)\right) P(n_X + 1, t)$$

$$- \left(k_1 n_A + k_{-1}n_X + k_2 n_X(n_X - 1)n_B\right.$$

$$\left. + k_{-2}n_X(n_X - 1)(n_X - 2)\right) P(n_X, t) \qquad [22]$$

The average concentration of species X at time t is given by $c_X(t) = \sum_{n_X} n_X P(n_X, t)$. If diffusion is sufficiently rapid to maintain the system in local equilibrium so that the distribution of molecules in the cells is Poissonian, characterized by the instantaneous value of the chemical concentration, we may replace $P(n_X, t)$ in Eq. [22] by $P(n_x; c_x(t))$ and compute the time rate of change of the average value of the concentration of species X as

$$
\begin{aligned}
\frac{dc_X(t)}{dt} = \sum_{n_X=0}^{\infty} n_X \Bigg[& \Big(k_1 n_A + k_2(n_X - 1)(n_X - 2)n_B \Big) P(n_X - 1; c_X(t)) \\
& + \Big(k_{-1}(n_X + 1) + k_{-2}(n_X + 1)n_X(n_X - 1) \Big) P(n_X + 1; c_X(t)) \\
& - \Big(k_1 n_A + k_{-1} n_X + k_2 n_X(n_X - 1)n_B + k_{-2} n_X(n_X - 1)(n_X - 2) \Big) \Bigg] \\
& \times P(n_X; c_X(t)) = k_1 a - k_{-1} c_X + k_2 b c_X^2 - k_{-2} c_X^3
\end{aligned}
\tag{23}
$$

Thus, we find the macroscopic chemical rate law for the Schlögl model. Mesoscopic simulations of the Schlögl model have been carried out using a Markov chain model.[59] Figure 3 shows the results for the steady-state concentrations derived from such a mesoscopic simulation along with the deterministic steady-state concentrations discussed earlier. The stochastic model yields results that are close to those of the mass action rate law. However, in the vicinities of points where the deterministic stable and unstable fixed points meet, so that one of the stable states loses its stability, fluctuations play an important role.

Stochastic models are also able to capture complicated pattern formation seen in chemically reacting media and can be used to study the effects of fluctuations on chemical patterns and wave propagation. The mesoscopic dynamics of the FHN model illustrates this point. In order to formulate a microscopically based stochastic model for this system, it is first necessary to provide a mechanism whose mass action law is the FHN kinetic equation. Some features of the FHN kinetics seem to preclude such a mechanistic description; for example, the production of u is inhibited by a term linear in v, a contribution not usually encountered in mass action kinetics. However, if each local region of space is assumed to be able to accommodate only a maximum number m of each chemical species, then such a mechanism may be written.[21] We assume that the chemical reactions depend on the local number of molecules of the species as well as the number of vacancies corresponding to each species, in analogy with the dependence of some surface reactions on the number of vacant surface sites or biochemical reactions involving complexes of allosteric enzymes that depend on the number of vacant active sites.

The reaction mechanism consists of the cubic autocatalytic steps involving species A and its corresponding vacancy species A^*,

$$2A + A^* \xrightarrow{k_1} 3A$$

$$2A^* + A \xrightarrow{k_1^*} 3A^*$$

[24]

This part of the mechanism is responsible for the bistability of the system but, in the absence of other coupling, will simply give rise to stable states corresponding to full occupancy or complete vacancy at a site. A second species B involved in bimolecular reactions with A is needed to account for both the linear and cubic parts of the FHN model. The cyclic reaction steps,

$$A^* + B \xrightarrow{k_2} A + B$$

$$k_3^* \uparrow \qquad \downarrow k_3$$

$$A^* + B^* \xleftarrow{k_2^*} A + B^*$$

[25]
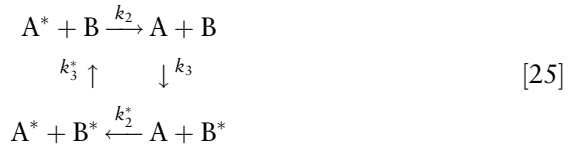
produce this effect. Assuming mass action kinetics, we may write the chemical rate law that follows from this mechanism as

$$\frac{dc_a}{dt} = \{k_1 c_a - k_1^*(1 - c_a)\}c_a(1 - c_a) + k_2(1 - c_a)c_b - k_2^* c_a(1 - c_b)$$

$$\frac{dc_b}{dt} = k_3^*(1 - c_a)(1 - c_b) - k_3 c_a c_b$$

[26]

where c_a and c_b are the average concentrations of A and B at a site (fractional occupancies). While this rate law does not seem to correspond to FHN kinetics, for $k_2^* = k_2$ and $k_3^* = k_3$, these equations can be converted to FHN form by making the linear change of variables, $c_a = au + a_0$ and $c_b = bv + b_0$ where

$$a^2 = \frac{1}{3}\left(\frac{k_1 + 2k_1^*}{k_1 + k_1^*}\right)^2 - \frac{k_2 + k_1^*}{k_1 + k_1^*} \qquad a_0 = \frac{1}{3}\frac{k_1 + 2k_1^*}{k_1 + k_1^*}$$

$$b = -\frac{k_1 + k_1^*}{k_2}c_a^3 \qquad b_0 = a_0 \frac{c_b}{c_a}\left\{1 - \left(\frac{a_0}{c_a}\right)^2\right\}$$

[27]

and use of the scaled time variable $\tau = t/\tau_s$ with $\tau_s^{-1} = (k_1 + k_1^*)a^2$. The parameters in Eq. [6] are related to the rate constants by

$$\alpha = -\frac{c_b}{c_a} \qquad \beta = \frac{1 - a_0 - b_0}{c_a} \qquad \epsilon = \frac{k_3}{k_2}\left(\frac{c_a}{c_b}\right)^2$$

[28]
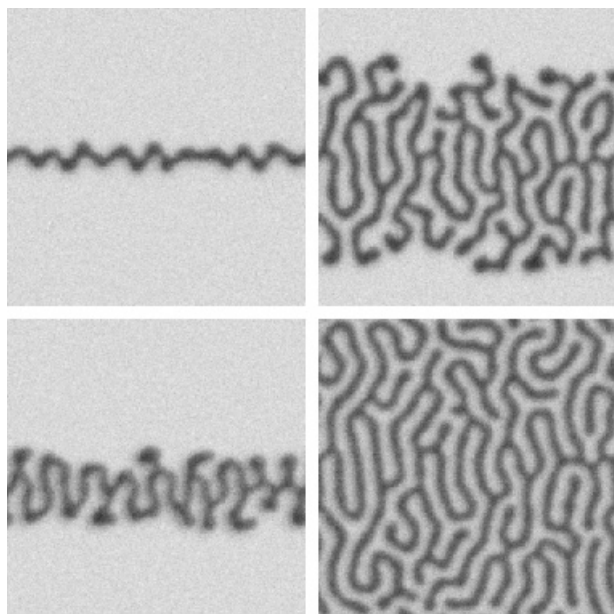
Figure 17 Formation of a labyrinthine pattern in a Markov chain model of the FHN system.

Once a mechanism for a reaction is given, we may use the birth–death kinetic rules to write a stochastic mesoscopic model for the reaction and diffusion processes. Figure 17 presents the results of a simulation of the FHN mechanism using a Markov chain model that shows the formation of a chemical labyrinthine pattern in a region where the FHN model has two stable steady states.[21] This complicated pattern arises from the nonlinear kinetics in the FHN mechanism and the long-range coupling between spatial points in the system because of rapid diffusion of species B relative to that of species A. This causes two chemical fronts to repel each other when they are sufficiently close. Consequently, the domains of the two stable phases in the labyrinthine pattern seen in the last panel of this figure will not "coarsen" like the domains of the two stable phases of the Schlögl model shown in Figure 4. Labyrinthine patterns of this type have been observed experimentally in reaction–diffusion systems with two stable steady states (see Figure 1b).[60] Stochastic models of this kind can be used to investigate the influence of fluctuations on patterns, especially on patterns that exist on small nanoscales as a result of competing interactions.[61]

SUMMARY

This brief introduction to the modeling and simulation of chemical patterns focused only on the basic elements of several schemes. Chemically reacting media displaced far from equilibrium are complicated systems. Not only are the underlying reaction mechanisms complex, but the spatial patterns are diverse and arise through many different mechanisms that have their basis in the competition between nonlinear chemical kinetics and diffusion.[62] Most commonly observed chemical patterns occur on macroscopic length scales and evolve on macroscopic time scales. Consequently, they can be modeled by reaction–diffusion equations. We discussed the solution of such equations using simple Euler discretizations of space and time. While this simple method suffices in many instances, if the kinetics occurs on a range of widely different time scales or the spatial gradients of chemical concentrations are steep due to sharp chemical fronts, the more elaborate integration schemes mentioned above must be used.

Often even complex patterns have their origin in simple general features of the dynamics that are independent of the specific details of the chemical mechanism. Excitable media are an example where the existence of a stable resting or steady state with a characteristic response to perturbations is responsible for many features of the chemical wave propagation seen in such systems. Cellular automaton models specify the dynamics of the system through a simple set of rules. Although CA models are usually abstractions of any real system, they show that even very simple rules are capable of producing very complicated dynamics. Not only can one construct simple CA rules that reproduce the gross features of chemical waves in excitable media as discussed above, but the exploration of these models in a more general context can show what kinds of behavior excitable or oscillatory media can display.

Coupled map lattices are one step closer to the macroscopic description of reaction–diffusion equations since the cell variables are continuous like macroscopic concentration fields. The map that specifies how the cell variables change with time can be varied smoothly by parameter changes. This is in contrast to CA, where the rule specification is often difficult to relate to parameters in the physical system. Like CA models, CML models find their most widespread use in showing what types of behavior are possible in systems driven far from equilibrium and providing a computationally efficient way to quantify generic properties of pattern dynamics. Thus, their strength does not lie in the description of a specific system but rather in exploring pattern dynamics in a general context. Phenomena discovered in this way can then be sought in experiment or models designed to mimic the behavior of a specific system.

Ultimately, we would like to understand the origin of patterns on a microscopic level. Not only are there fundamental issues to be understood,

but the physical situation itself may demand such a more detailed level of description. The mesoscopic models discussed in the last part of this chapter provide one route to describe the system on more microscopic scales. While these models do not provide a full microscopic description of the dynamics (this is the role of molecular dynamics simulation methods), they do incorporate molecular fluctuations that are absent in the macroscopic models. Fundamental questions, such as the validity of macroscopic rate laws for systems with deterministic chaos, can be explored by using such models.[63,64] The description of the biochemistry inside the cell likely demands such mesoscopic models since the chemistry is complex, cell volumes are small, and the number of chemical species in important reactions is too small to validate a description in terms of mass action kinetics.[65] Such approaches will likely see significant development in the future as our ability to probe chemical dynamics on small scales increases.

REFERENCES

1. W. Y. Tam, W. Horsthemke, Z. Noszticzius, and H. L. Swinney, *J. Chem. Phys.*, **88**, 3395 (1988). Sustained Spiral Waves in a Continuously Fed Unstirred Chemical Reactor.

2. B. P. Belousov, in *Sbornik Referatov po Radiatsionni Meditsine Moscow*, Medgiz, Moscow, 1958. A Periodic Reaction and Its Mechanism.

3. A. M. Zhabotinsky, *Biofizika*, **9**, 306 (1964). Periodic Processes of the Oxidation of Malonic Acid in Solution.

4. A. N. Zaikin and A. M. Zhabotinsky, *Nature (London)*, **225**, 535 (1970). Concentration Wave Propagation in Two-Dimensional Liquid-Phase Self-Oscillating System.

5. A. L. Belmonte, O. Y. Qi, and J.-M. Flesselles, *J. Phys. II France*, **7**, 1425 (1997). Experimental Survey of Spiral Dynamics in the Belousov Zhabotinsky Reaction.

6. K. J. Lee and H. L. Swinney, *Phys. Rev. E*, **51**, 1899 (1995). Pattern Formation by Interacting Chemical Fronts.

7. R. Larter and K. Showalter, in *Reviews in Computational Chemistry*, K. B. Lipkowitz and D. B. Boyd, Eds., VCH Publishers, New York, 1997, Vol. 10, pp. 177–270. Computational Studies in Nonlinear Dynamics.

8. L. B. Kier, C.-K. Chang, and P. G. Seybold, in *Reviews in Computational Chemistry*, K. B. Lipkowitz and D. B. Boyd, Eds., Wiley-VCH, New York, 1997, Vol. 17, pp. 205–254. Cellular Automata Models of Aqueous Solution Systems.

9. R. Kapral, *J. Math. Chem.*, **6**, 113 (1991). Discrete Models for Chemically Reacting Systems.

10. G. Rousseau and R. Kapral, *Chaos*, **10**, 812 (2000). Asynchronous Algorithm for Integration of Reaction–Diffusion Equations for Inhomogeneous Excitable Media.

11. D. Barkley, *Physica D*, **49**, 61 (1991). A Model for Fast Computer Simulation of Spiral Waves in Excitable Media.

12. E. M. Cherry, H. S. Greenside, and C. S. Henriquez, *Phys. Rev. Lett.*, **84**, 1343 (2000). A Space–Time Adaptive Method for Simulating Complex Cardiac Dynamics.

13. F. Fenton and A. Karma, *Chaos*, **8**, 20 (1998). Vortex Dynamics in Three-Dimensional Continuous Myocardium with Fiber Rotation: Filament Instability and Fribrillation.

14. M. Dowle, R. M. Mantel, and D. Barkley, *Int. J. Bifurcat. Chaos*, **7**, 2529 (1997). Fast Simulations of Waves in Three-Dimensional Excitable Media.

15. W. L. Quan, S. J. Evans and H. M. Hastings, *IEEE Trans. Biomed. Eng.*, **45**, 372 (1998). Efficient Integration of a Realistic Two-Dimensional Cardiac Tissue Model by Domain Decomposition.

16. F. Schlögl, *Z. Phys.*, **253**, 147 (1972). Chemical Reaction Models for Nonequilibrium Phase Transitions.

17. A. Hanna, A. Saul, and K. Showalter, *J. Am. Chem. Soc.*, **104**, 3838 (1982). Detailed Studies of Propagating Fronts in the Iodate Oxidation of Arsenous Acid.

18. P. C. Hohenberg and B. I. Halperin, *Rev. Mod. Phys.*, **49**, 435 (1977). Theory of Dynamical Critical Phenomena.

19. R. FitzHugh, *Biophys. J.*, **1**, 445 (1961). Impulses and Physiological States in Theoretical Models of Nerve Membrane.

20. J. S. Nagumo, S. Arimoto, and Y. Yoshikawa, *Proc. IRE*, **50**, 2061 (1962). Active Pulse Transmission Line Simulating Nerve Axon.

21. A. Malevanets and R. Kapral, *Phys. Rev. E*, **55**, 5657 (1997). Microscopic Model for FitzHugh-Nagumo Dynamics.

22. P. Fife, in *Non-Equilibrium Dynamics in Chemical Systems*, C. Vidal and A. Pacault, Eds., Springer-Verlag, Berlin, 1984, pp. 76–88. Propagator-Controller Systems and Chemical Patterns.

23. A. T. Winfree, *Science*, **175**, 634 (1972). Spiral Waves of Chemical Activity.

24. G. Ertl, *Adv. Catal.*, **37**, 213 (1990). Oscillatory Catalytic Reactions at Single Crystal Surfaces.

25. A. Goldbeter, *Biochemical Oscillations and Cellular Rhythms*, Cambridge University Press, Cambridge, 1996.

26. A. T. Winfree, *When Time Breaks Down: Three Dimensional Dynamics of Electrochemical Waves and Cardiac Arrythmias*, Princeton University Press, Princeton, 1987.

27. Y. Kuramoto, *Chemical Oscillations, Waves and Turbulence*, Springer-Verlag, Berlin, 1980.

28. R. J. Field and M. Burger, Eds., *Oscillations and Travelling Waves in Chemical Systems*, Wiley, New York, 1985.

29. J. Von Neumann, in *Theory of Self-Reproducing Automata*, A. W. Burks, Ed., University of Illinois, Urbana, IL, 1966.

30. E. F. Codd, *Cellular Automata*, Academic Press, New York, 1986.

31. C. G. Langton, *Physica D*, **10**, 135(1984). Self-Reproduction in Cellular Automata.

32. N. Wiener and A. Rosenblueth, *Arch. Inst. Cardiol. Mexico*, **16**, 205 (1946). The Mathematical Formulation of the Problem of Conduction of Impulses in a Network of Connected Excitable Elements, Specifically in Cardiac Muscle.

33. S. Wolfram, Ed., *Theory and Applications of Cellular Automata*, World Scientific, Singapore, 1986.

34. J. M. Greenberg, B. D. Hassard, and S. P. Hastings, *Bull. Am. Math. Soc.*, **84**, 1296 (1978). Pattern Formation and Periodic Structures in Systems Modeled by Reaction–Diffusion Equations.

35. J. M. Greenberg and S. P. Hastings, *SIAM J. Appl. Math.*, **34**, 515 (1978). Spatial Patterns for Discrete Models of Diffusion in Excitable Media.

36. A. T. Winfree, in *Chemical Waves and Patterns*, R. Kapral and K. Showalter, Eds., Kluwer, Dordrecht, 1995. pp. 3–55. Lingering Mysteries about Organizing Centers in the Belousov–Zhabotinsky Medium and Its Oregonator Model.

37. T. Plesser, S. C. Müller, and B. Hess, *J. Phys. Chem.*, **94**, 7501 (1990). Spiral Wave Dynamics as a Function of Proton Concentration in the Ferroin-Catalyzed Belousov-Zhabotinskii Reaction.

38. G. S. Skinner and H. L. Swinney, *Physica D*, **48**, 1 (1991). Periodic to Quasiperiodic Transition of Chemical Spiral Rotation.

39. D. Barkley, *Phys. Rev. Lett.*, **72**, 1264 (1994). Euclidean Symmetry and the Dynamics of Rotating Spiral Waves.

40. M. Markus and B. Hess, *Nature (London)*, **347**, 56 (1990). Isotropic Cellular Automaton for Modeling Excitable Media.

41. M. Gerhardt, H. Schuster, and J. J. Tyson, *Science*, **247**, 1563 (1990). A Cellular Automaton Model of Excitable Media Including Curvature and Dispersion.

42. D. Griffeath, *Notices Am. Math. Soc.*, **35**, 1472 (1988). Cyclic Random Competition: A Case History in Experimental Mathematics.

43. R. Fisch, J. Gravner, and D. Griffeath, *Ann. Appl. Probability*, **3**, 935 (1993). Metastability in the Greenberg–Hastings Model.

44. I. Waller and R. Kapral, *Phys. Rev. A*, **30**, 2047 (1984). Spatial and Temporal Structure in Systems of Coupled Nonlinear Oscillators.

45. K. Kaneko, *Prog. Theor. Phys.*, **72**, 480 (1984). Period-Doubling of Kink-Antikink Patterns, Quasiperiodicity in Antiferro-Like Structures and Spatial Intermittency in Coupled Logistic Lattice—Towards a Prelude of a Field-Theory of Chaos.

46. S. Kuznetsov, in *Theory and Applications of Coupled Map Lattices*, K. Kaneko, Ed., Wiley, New York, 1993, pp. 51–94. Renormalization Group, Universality and Scaling in Dynamics of Coupled Map Lattices.

47. K. Kaneko, Ed., *Theory and Applications of Coupled Map Lattices*, Wiley, New York, 1993.

48. R. Kapral, in *Theory and Applications of Coupled Map Lattices*, K. Kaneko, Ed., Wiley, New York, 1993, pp. 135–168. Chemical Waves and Coupled Map Lattices.

49. V. Petrov, Q. Ouyang, and H. L. Swinney, *Nature (London)*, **388**, 655 (1997). Resonant Pattern Formation in a Chemical System.

50. A. L. Lin, V. Petrov, H. L. Swinney, A. Ardelea, and G. F. Carey, in *Pattern Formation in Continous and Coupled Systems*, M. Golubitsky, D. Luss, and S. H. Strogatz, Eds., Springer, New York, 1999, pp. 193–201. Resonant Pattern Formation in a Spatially Extended Chemical System.

51. R. Kapral, R. Livi, G.-L. Oppo, and A. Politi, *Phys. Rev. E*, **49**, 2009 (1994). Dynamics of Complex Interfaces.

52. R. Kapral, R. Livi, and A. Politi, *Phys. Rev. Lett.*, **79**, 112 (1997). Critical Behavior of Complex Interfaces.

53. C. J. Hemming and R. Kapral, *Faraday Discuss.*, **120**, 371 (2001). Turbulent Fronts in Resonantly-Forced Oscillatory Systems.

54. C. J. Hemming and R. Kapral, *Physica D*, **168**, 10 (2002). Front Explosion in a Resonantly-Forced Complex Ginzburg-Landau System.

55. C. W. Gardiner, *Handbook of Stochastic Processes*, Springer-Verlag, New York, 1985.

56. G. Nicolis, *Introduction to Nonlinear Science*, Cambridge University Press, Cambridge, 1995.

57. R. Kapral, in *Stochastic Dynamics*, L. Schimansky-Geier and T. Pöschel, Eds., Springer-Verlag, New York, 1997, pp. 294–305. Markov Chain Models for Spatially-Distributed Reacting Systems.

58. J. P. Boon, D. Dab, R. Kapral, and A. Lawniczak, *Phys. Repts.*, **273**, 55 (1996). Reactive Lattice-Gas Automata.

59. D. Gruner, R. Kapral, and A. Lawniczak, *J. Chem. Phys.*, **99**, 3938 (1993). Nucleation, Domain Growth and Fluctuations in a Bistable Chemical System.

60. K. J. Lee, W. D. McCormack, Q. Ouyang, and H. L. Swinney, *Science*, **261**, 192 (1993). Pattern Formation by Interacting Chemical Fronts.

61. M. Hildebrand, A. S. Mikhailov, and G. Ertl, *Phys. Rev. Lett.*, **81**, 2602 (1998). Travelling Nanoscale Structures in Reactive Adsorbates with Attractive Lateral Interactions.

62. R. Kapral and K. Showalter, Eds., *Chemical Waves and Patterns*, Kluwer, Dordrecht, The Netherlands, 1995.

63. X.-G. Wu and R. Kapral, *Phys. Rev. Lett.*, **70**, 1940 (1993). Internal Fluctuations and Deterministic Chemical Chaos.

64. P. Geysermans and G. Nicolis, *J. Chem. Phys.*, **99**, 8964 (1994). Fluctuations and Chemical Chaos in a Well-Stirred Reactor: A Master Equation Analysis.

65. A. S. Mikhailov and B. Hess, *Biophys. Chem.*, **58**, 365 (1996). Transition from Molecular Chaos to Coherent Spiking of Enzymatic Reactions in Small Volumes.

CHAPTER 5

Fuzzy Soft-Computing Methods and Their Applications in Chemistry

Costel Sârbu and Horia F. Pop

Departments of Chemistry and Computer Science, Babeş-Bolyai University, Cluj-Napoca, Romania

INTRODUCTION

Historically, the general point of view in research until recently was that everything could be computed with an arbitrary precision, provided one has (a) enough and sufficiently precise data, and (b) sufficient computing power. But this is not always the case: sometimes, the necessary data are simply not available; often the models themselves are approximations of the real world, or reality does not behave exactly as the model would suggest.

As a consequence, in many real situations: (a) precision is sometimes artificial (it is not necessary to measure room temperature to 0.0001 degree); (b) precision is usually expensive (high-precision measurement devices are expensive); (c) precision and complete information are not always needed to make proper decisions.

The high degree of complexity of typical real problems implies that the final method used to solve a problem is more often a combination of several methods, such as soft computing techniques (namely, fuzzy logic, genetic algorithms, and neural networks) with more classic ones (such as algebraic, analytical, numerical, and stochastic methods).

In addition to fuzzy logic, we will concentrate on the Self-Organizing Map (SOM) algorithm,[1] since it has properties that make it both a data visualization and a clustering technique. We present this method in relation to other

data analysis approaches (projection methods and clustering methods).[2,3] The most important work on this subject has been carried out by the Neural Network Research Center, at the Helsinki University of Technology.[2,3]

In this context, we give here the following definition of Soft Computing (SC), that has been suggested by its founder, Professor Lotfi A. Zadeh.[4]

"Soft computing differs from conventional (hard) computing in that, unlike hard computing, it is tolerant of imprecision, uncertainty, and partial truth. In effect, the role model for soft computing is the human mind. The guiding principle of soft computing is: Exploit the tolerance for imprecision, uncertainty, and partial truth to achieve tractability, robustness, and low-solution cost. The basic ideas underlying soft computing in its current incarnation have links to many earlier influences, among them my 1965 paper on fuzzy sets; the 1973 paper on the analysis of complex systems and decision processes; and the 1979 report (1981 paper) on possibility theory and soft data analysis. The inclusion of neural network theory in soft computing came at a later point. At this juncture, the principal constituents of soft computing (SC) are fuzzy logic (FL), neural network theory (NN), and probabilistic reasoning (PR), with the latter subsuming belief networks, genetic algorithms, chaos theory, and parts of learning theory. What is important to note is that SC is not a melange of FL, NN, and PR. Rather, it is a partnership in which each of the partners contributes a distinct methodology for addressing problems in its domain. In this perspective, the principal contributions of FL, NN, and PR are complementary rather than competitive".

METHODS FOR EXPLORATORY DATA ANALYSIS

Some methods for illustrating structures, that is, multivariate relations between data items in high-dimensional data sets will be described. We will only consider methods that regard the input as metric vectors, and that may be used without any assumptions about the distribution of data. We also assume that limited information is available about the data set (i.e., class labels).

While we will present methods that produce a cluster substructure of the data, we need to emphasize that, sometimes, variable selection and data preprocessing may also be important.

The following questions are important when discussing a method for large, high-dimensional data sets: What kind of structure does the method extract from the data set? How does it illustrate the structure? Does it reduce dimensionality of data? Does it reduce the number of data points?

Visualization of High-Dimensional Data

The simplest method for visualizing a data set is to plot profiles, that is, two-dimensional (2D) graphs in which the dimensions are enumerated on the

x axis, with the corresponding values on y. An alternative, also widely used, is to plot 2D representations of pairs of two original dimensions. There are also methods that produce different curves based on the data points values, for example, the components of data vectors are used as coefficients of orthogonal sinusoids, which are then added together. The most important drawback of such methods is that they do not reduce the amount of data, and thus it cannot be used effectively with large, high-dimensional data sets. However, they can be used for illustrating data summaries.

Clustering Methods

The goal of clustering is to reduce the amount of data by grouping data in classes so that similar items are grouped together and any two items from different classes are less similar than any two items from the same class. Clustering methods can be categorized as one of two types: hierarchical and partitional clustering.

The hierarchical clustering methods are either agglomerative (i.e., the methods successively merge small clusters into larger ones), or divisive (i.e., the methods successively split large clusters into smaller ones). The methods differ in the rule used for merging or splitting clusters, the possibility to use variate metrics, and so on.

Partitional clustering methods attempt to directly decompose a data set into a fixed number of disjoint clusters. The methods attempt to minimize a criterion function, typically based on minimizing the dissimilarity inside classes, while maximizing the dissimilarity between different classes.

Because of its relationship to SOM, we will describe in greater detail the K-means clustering algorithm. The criterion function is the total squared distance of the data items to their nearest cluster centroids,

$$E_K = \sum_k |x_k - m_{c(x_k)}|^2 \tag{1}$$

where $c(x_k)$ is the index of the centroid closest to data item x_k.

There are two algorithms for computing the optimal set of classes. The off-line original version, which requires access to all input vectors, follows:

1. Initialize the set of centroids, m_i, $i = 1, \ldots, K$.
2. Assign each data item to the nearest class.
3. Recompute the class centroids.
4. If the difference between the new value of the criterion function E and its old value is small enough, then **stop**; otherwise, go to Step 2.

The on-line variation of this algorithm, which needs only one input vector at a time, follows:

1. Initialize the set of centroids, m_i, $i = 1, \ldots, K$.
2. Choose a randomly chosen data item.

3. Assign this data item to the nearest class.
4. Recompute the selected class centroid.
5. If the difference between the new value of the criterion function E and its old value is small enough, then **stop**; otherwise go to Step 2.

The K-means clustering algorithm has a few problems, which have been discussed in Reference 5. One problem is the selection of different geometrical prototypes, and the use of suitable dissimilarity functions for them. While variations of this algorithm are available that use line prototypes, or convex combinations between points and lines, it may also be the case that different clusters of the data set have different shapes, and we need a mechanism to determine the optimal prototype for each cluster. Another important problem is the *a priori* choice of the number K of classes. While validity functionals exist that may be used to determine the number of clusters that produce the best results, this approach has two main problems: first, the need to apply the algorithm for a whole range of possible values of K may, thus, miss the optimal value; and, second, the functionals implicitly depend on the number K. A method is needed to produce the optimal number of classes. A solution is to use a hierarchical approach in which, at each node of the binary tree a variation of the K-means algorithm is used to split a class into two subclasses. The decision about whether to split a class or not is based on a polarization index. Another problem relates to the possibility of clustering algorithms based on crisp sets to identify isolated points and bridges between classes, and to deal with overlapping classes. These problems are naturally solved by using clustering algorithms based on fuzzy sets theory.

An approach based on clustering methods has the problem that the cluster prototype is as high dimensional as the original data set, and additional visualization methods are needed to visualize the data. While this is generally not a problem, it becomes important when the data set is large and highly dimensional, as is the case with text mining problems.

Projection Methods

The main feature of clustering algorithms is that they reduce the amount of data cases by grouping them into classes. The projection methods described below can be used for reducing the data dimensionality. The goal of these techniques is to represent the data set in a lower-dimensional space in such a way that certain properties of the data set are preserved as much as possible.

Linear Projection Methods

The most widely used algorithm in this class is the principal component analysis (PCA) algorithm. It can be used to display the data as a linear projection on a subspace of the original data space that best preserves the variance in the data. The algorithm computes the principal components, which are the

orthogonal axes that show the maximal spread of the data, and considers the data set as represented using coordinate axes given by the principal components. The most relevant principal components, based on the data variance, are selected and the data are projected onto the space represented by those orthogonal components.

Nonlinear Projection Methods

Alternate projection methods aim to reduce the data dimensionality by optimizing the representation in the lower-dimension space so that the distances between points in the projected space are as similar as possible to the distances between the corresponding points in the original space. We will describe here a class of methods known as multidimensional scaling (MDS).[6,7] The aim of these methods is to project data from a pseudo-metric space (i.e., one characterized by a dissimilarity measure) onto a metric space. Such methods are especially useful for preprocessing non-metric data in order to use algorithms valid only for metric input.

The first MDS method is the metric MDS, characterized by minimizing the squared error cost function:

$$E_M = \sum_{k \neq l} (d(k,l) - d'(k,l))^2 \qquad [2]$$

where, for the original items x_k and x_l, $d(k,l)$ is their dissimilarity,[6–12] and $d'(k,l)$ is the distance between the corresponding vectors from the projected metric space. If the components of the data vectors are expressed on an ordinal scale, a perfect reproduction of the Euclidean distances may not be the best goal. In such a situation, only the rank order of the distances between the vectors is meaningful. The error function is defined as

$$E_N = \frac{\sum_{k \neq l} (f(d(k,l)) - d'(k,l))^2}{\sum_{k \neq l} (d'(k,l))^2} \qquad [3]$$

where f is a monotonically increasing function that acts on the original distances and always maps the distances to such values that best preserve the rank order.

Another nonlinear mapping method, the Sammon's mapping, is closely related to the metric MDS. The only difference is that the errors in distance preservation are normalized with the distance in the original space. Thus, preservation of small distances is emphasized. The error function is defined as

$$E_S = \sum_{k \neq l} \frac{(d(k,l) - d'(k,l))^2}{d(k,l)} \qquad [4]$$

ARTIFICIAL NEURAL NETWORKS

A neural network is an interconnected assembly of simple processing elements, called units or nodes, whose functionality is loosely based on the animal neuron. The processing ability of the network is stored in the interunit connection strengths, called weights, obtained by a process of adaptation to, or learning from, a set of training patterns.[13,14] In the following sections, we will present the simplest neural network, the perceptron of Rosenblatt. We will continue with some of the most widely used types of neural networks: the multilayer network with feedforward and backpropagation of errors, the associative memories, and the self-organizing maps. We will end with a discussion of other types of neural networks.

Perceptron

The perceptron of Rosenblatt is represented in Figure 1. The signals $x_1, \ldots, x_s$ appear as its input. Each input signal x_i is weighted by the corresponding weight w_i, and all these weighted inputs are then summed to calculate the activation value, which is then passed as the argument of an activation function f, to determine the neuron's output value:[13]

$$o = f(w^T x + w_{s+1}) = f\left(\sum_j w_j x_j + w_{s+1}\right)$$ [5]

The learning problem is to find the weights vector $w \in \mathbf{R}^{s+1}$ such that the computed output of the unit, $o^k \in \mathbf{R}$, is as close as possible, if not equal, to the desired output, $y^k \in \mathbf{R}$, for all the available input vectors x^k. The activation
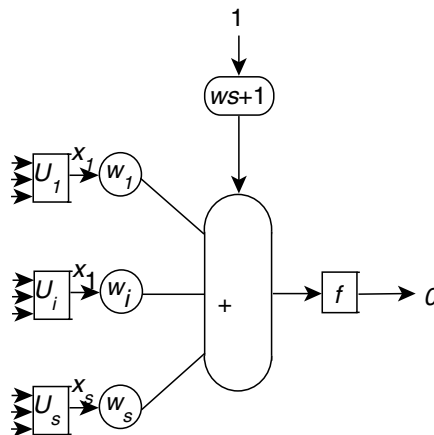
Figure 1 The perceptron of Rosenblatt.

function *f* may have different forms. In the perceptron of Rosenblatt case, *f* is defined as

$$f(x) = \begin{cases} 1 & \text{if } x > 0 \\ 0 & \text{otherwise} \end{cases} \tag{6}$$

Other variations of the perceptron use an identical activation function, that is, $f(x) = x$. The mathematical interpretation of the original perceptron is the problem of linear separability of two classes. The original condition of linear separability is to find a weight vector w such that $w^T x^k > 0$ for all points x^k in one class, and $w^T x^k > 0$ for all points x^k in the other class. With a suitable linear transformation, the separability condition becomes $w^T x^k < 0$ for all the points x^k correctly classified, and $w^T x^k < 0$ otherwise. This means that in the case of the Rosenblatt perceptron, the desired output value y^k is always 1. The training procedure is the following:

1. Arbitrarily initialize the weights vector w.
2. Feed a test input vector x^k to the neuron.
   a. If the output value o^k and the desired value y^k match, do nothing.
   b. If they do not match, then change the values of the weights vector in some way, in order to improve the behavior of the neuron.
3. Repeat Step 2 for all the test vectors available, until no improvement is done for all the test vectors, or until a certain maximal number of iterations has been reached.

The correction realized at Step 2(b) is determined from the error minimization condition, and is called the perceptron learning rule:

$$w := w + c \cdot (y^k - o^k) \cdot x^k \tag{7}$$

Throughout this chapter, the notation $w :=$ denotes the process of evaluation of the given expression and assignment of the produced value to the variable w.

The original perceptron of Rosenblatt works with the desired output values $y^k = 1$, the computed output values $o^k \in \{0, 1\}$, and the activation function as defined above. Even if this algorithm has been proven to converge in a limited number of steps if a separation hyperplane does exist, this particular set of parameters is not the most suitable. First, the separation hyperplane produced is not the best one, but, instead, it is very near one of the classes. Second, this algorithm does not work when a separation hyperplane does not exist. The generalizations of this algorithm allow a different choice of desired values and activation function, and aim to solve both problems. Another feature is the way the test in Step 2 (a) is done. In most cases, it is carried out as described above, that is, a single test, for the current input vector, is made for each iteration. These algorithms are called on-line learning

algorithms, because they only need one input vector at a time. However, in some cases, it is necessary to do complete tests over all the input vectors, not just the current one. These algorithms are called off-line learning algorithms, because they need to have access to all the input vectors. An interesting improvement comes with the Gallant Pocket Algorithm. While this algorithm uses the original version of the perceptron, it may also be applied to other situations. The main feature is that the best weights determined up to a certain point are memorized in a pocket. Thus, in the case where we are unable to produce an optimal weights vector, we still have available the best weights vector determined during the calculation.

Multilayer Nets: Backpropagation

In order to make the system more powerful, and extend its use to more complex learning applications, we need to make it more complex. For example, the perceptron scheme defined above may be used for classifying n linearily separable classes of vectors, with $n > 2$, or with classifying two linearly nonseparable classes. The structure obtained is a neural network with a layer of input nodes and a layer of output nodes. It is called the generalized perceptron of Rumelhart, and is represented in Figure 2.[15,16]

The learning problem is to find the weights vectors w^i such that the vector of the computed outputs of all units, o^k, is as close as possible, if not equal, to the vector of the desired output of all units, y^k, for all the available input vectors x^k. The system works in a manner similar to the simple perceptron
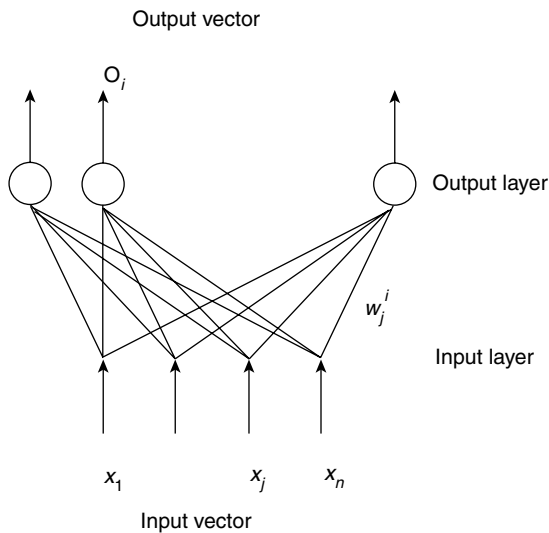
Figure 2 A single-layer network.

described above. One input vector is passed to the net at each iteration. By using the weights and the activation function, which in this case is also linear, the output values of all the nodes are computed. These values are then compared with the desired values for these nodes. For all the nodes that show a mismatch between the computed and the desired values, we need to change the weights to improve the behavior of the system. The correction rule used in this case is determined by minimizing the error function. But, as opposed to the perceptron where the minimization was done on the output values, in this case the minimization is done on the activation values. The correction rule used here is called the delta rule:

$$w^i := w^i + c \cdot (y_i^k - o_i^k) \cdot x^k \qquad [8]$$

where y_i^k and o_i^k are the desired output value and computed output value corresponding to the ith output unit. Again, the input vector is x^k, and w^i is the weights vector of the ith output node.

The rule described above may be further generalized so that it may be applied to the training of a more complex type of network, which contains so-called hidden layers of neurons. Here we have a multilayer net with backpropagation, so-called because of the way the error is propagated backward from the output layer to the input layer. This network is presented in Figure 3. We use the following notations: For an input vector x, x^i is the value
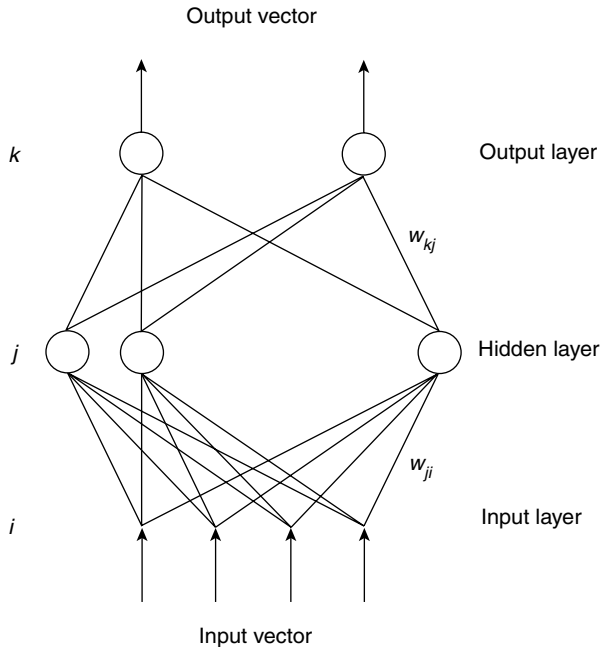
Figure 3 Multilayer neural network with feedforward and error backpropagation.

given at the ith input unit, w_{ji} is the weight of the connection from the ith input unit to the jth hidden unit, w_{kj} is the weight of the connection from the jth hidden unit to the kth output unit, f_j is the activation function of the jth hidden unit, net_j is the activation value of the jth hidden unit, $o_j = f_j(\text{net}_j)$ is the computed output value of the jth hidden unit, and f_k, net_k, and o_k have a similar meaning for the kth unit of the output layer. Finally, y_k is the desired output value for the kth unit of the output layer.

The generalized delta rule for the kth output unit is given by

$$w_{kj} := w_{kj} + c\delta_k o_j \qquad [9]$$

where

$$\delta_k := (y_k - o_k)f'_k(\text{net}_k) \qquad [10]$$

Similarly, the same rule for the jth hidden unit is given by

$$w_{ji} := w_{ji} + c\delta_j x_i \qquad [11]$$

where

$$\delta_j := \left(\sum_k \delta_k w_{kj} \right) f'_j(\text{net}_k) \qquad [12]$$

Note that the δ values on an internal node may be computed based on the δ values of the superior nodes, which is the theoretical reason for evaluating in the first place the errors of the output layer, and later propagating these errors backward to the input layer.

A typical activation function is the sigmoidal function, that is, $f(x) = 1/(1 + e^{-x})$. In this case, $f'(x) = f(x) \cdot (1 - f(x))$, and we have

$$\delta_k := (y_k - o_k)o_k(1 - o_k) \qquad [13]$$

and

$$\delta_j := \left(\sum_j \delta_k w_{kj} \right) o_j(1 - o_j) \qquad [14]$$

The learning algorithm of this network is the following:

1. Present the pattern to the input layer.
2. Let the hidden units evaluate their output using the pattern.
3. Let the output units evaluate their output using the result in Step 2.
4. Calculate the δ_k values for the nodes of the output layer.

5. Train each output node using the generalized delta rule and the δ_k values from Step 4.
6. Calculate the δ_j values for the nodes of the hidden layer.
7. Train each hidden node using the generalized delta rule and the δ_j values from Step 6.

Steps 1–3 are known as the forward pass, while Steps 4–8 are known as the backward pass.

Associative Memories: Hopfield Net

The Hopfield neural network is a simple artificial network, able to store certain memories so that the full pattern can be recovered if the network is presented with only partial information. Furthermore, there is a degree of stability in the system—if just a few connections between nodes (neurons) are severed, the recalled memory is not too badly corrupted—the network can respond with a "best guess".[13] The nodes in the network are vast simplifications of real neurons—they can exist only in one of two possible "states"—firing or not firing. Every node x_i is connected to every other node x_j with some strength w_{ij}, such that $w_{ij} = w_{ji}$ and $w_{ii} = 0$. At any instant of time, a node will change its state (i.e., start or stop firing) depending on the inputs it receives from the other nodes. The values of these neurons are thus binary, meaning that $x_i \in \{0, 1\}$. If the system is initialized with any general pattern of firing and nonfiring nodes, then this pattern will generally change with time. To see this, think of starting the network with just one firing node. This will send a signal to all the other nodes via its connections so that a short time later some of these other nodes will fire. These new firing nodes will then excite others after another short time interval and a whole cascade of different firing patterns will occur. One might imagine that the firing pattern of the network would change in a complicated, perhaps random, way with time. The important property of the Hopfield network that renders it useful for simulating memory recall is the following: One is guaranteed that the pattern will settle down after a long enough time to some fixed pattern. Certain nodes will always be "on" and others always "off". Furthermore, it is possible to arrange that these stable firing patterns of the network correspond to the desired memories we wish to store. The total input of a certain neuron i, H_i, comes from the external input I_i and from other neurons. Thus,

$$H_i := \sum_{j \neq i} w_{ij} x_j + I_i \qquad [15]$$

When the outputs of the neurons are updated, the output value of neuron i is

$$x_i := \begin{cases} 0 & \text{if } H_i < U_i \\ 1 & \text{if } H_i > U_i \end{cases} \qquad [16]$$

where U_i is the threshold value of the neuron i. We need to update the weights w_{ij} so that the system is able to memorize a set of energy-stable states x^s, $s = 1, 2, \ldots$. The produced algorithm is the following:

A. *Memorization.* To memorize the set of binary vectors x^s, $s = 1, 2, \ldots$, set

$$w_{ij} = \sum_s (2x_i^s - 1)(2x_j^s - 1)$$

$$w_{ii} = 0$$

[17]

B. *Recognition.*
  1. For the input vector x', evaluate

$$H_i' = \sum_j w_{ij}(2x_j' - 1)$$

[18]

  2. Update x'

$$x_i = \begin{cases} 0 & \text{if } H_i' < U_i \\ 1 & \text{if } H_i' > U_i \end{cases}$$

[19]

  3. If $\Delta x_i' = 0$, $\forall i$, then **stop**, otherwise, continue from Step 2.

Note that it has theoretically been proven that a Hopfield network with n nodes may accurately recognize a maximum of $n/(2 \log n)$ patterns. This gives 11 patterns for a network with 100 nodes.

Self-Organizing Map

The SOM is an artificial neural network used to visualize and interpret large high-dimensional data sets. Typical applications are visualization of process states or financial results by representing the central dependencies within the data on the map.[1,2] The SOM is a method that can be used both to reduce the amount of data by clustering, and to project the data nonlinearly onto a lower-dimensional display. The map consists of a regular grid of processing units, the "neurons". A model of some multidimensional observation, eventually a vector consisting of features, is associated with each unit. The map attempts to represent all the available observations with optimal accuracy using a restricted set of models. At the same time, the models become ordered on the grid so that similar models are close to each other and dissimilar models are far from each other. Fitting of the model vectors (also called reference vectors) is usually carried out by a sequential regression process, where $t = 1, 2, \ldots$, is the step index. For each sample $x(t)$, first the winner index c (best match) is identified by the condition

$$|x(t) - m_c(t)| \leq |x(t) - m_i(t)| \quad \text{for all } i$$

[20]

After that, all model vectors or a subset of them that belong to nodes centered around node $c = c(x)$ are updated as

$$m_i(t + 1) = m_i(t) + h_{ci}(t)(x(t) - m_i(t)) \qquad [21]$$

Here, h_{ci} is the neighborhood function, a decreasing function of the distance between the ith and cth nodes on the map grid. The regression is usually iterated over the available samples. In practice, the neighborhood area is chosen to be wide in the beginning of the learning process, and both its width and height will decrease during learning.

Properties

Ordered Display
As the data items are mapped to those units on the map that have the closest reference vectors, nearby units will have similar data items mapped on them. This property requires that the map be regarded as an ordered display, which facilitates the understanding of the structures in the data set. This map display may also be used as an ordered groundwork, on which the original data variables, as well as other information related to the data cases, may be displayed.

Cluster Visualization
The ordered display might be used for showing the clustering density in different regions of the data space. The density of the reference vectors of an organized map will reflect the density of the input samples. The cluster display may be constructed as follows: the distance between each pair of neighboring reference vectors is scaled so that it fits between a given minimum and maximum value. Each scaled distance value determines the gray level of the point being situated in the middle of the segment line determined by the corresponding map units. The gray level of the points corresponding to the map units themselves are set to the average of some of the nearest distance values. After these values have been set up, they may be smoothed and then visualized.

Missing Data
An interesting feature of the SOM is its ability to deal with missing data. Some of the components of the data vectors may not be available for all data items, or may not be applicable or defined. The simplest solution when dealing with such incomplete components would be to discard the incomplete variables or incomplete data items completely, but in this way we will lose useful information. In the case of the SOM, the problem of missing data may be treated as follows: When choosing the winning unit, the input vector can be compared with the reference vectors m_i using only those components that are

available in x. When the reference vectors are then adapted, only the components that are available in x will be modified. This approach produces better results than by discarding data from the data set.

Outliers

The outliers are data items situated very far from the main body of data. This may be due to measurement errors, typographical errors, or may simply be correct data that is strikingly different from the rest. In the case of the maps generated by the SOM, each outlier affects only one map unit and its neighborhood, while the rest of the map is available for the rest of the analysis. Furthermore, the outliers can be detected in the map due to the much lower density of the space near them.

Mathematical Characterization

Rigorous mathematical proof of the SOM algorithm is very difficult in general. In the case of a discrete data set and a fixed neighborhood function, the error function of the system may be defined as

$$E = \sum_k \sum_i h_{ci}|x_k - m_i|^2 \qquad [22]$$

where the index c depends on the data item x_k and the reference vectors m_i. The learning rule of the SOM corresponds to a gradient descent step in minimizing the sample function

$$E_1 = \sum_i h_{ci}|x(t) - m_i|^2 \qquad [23]$$

obtained by a random selection of a sample $x(t)$ at iteration t. The cost function of the SOM closely resembles the objective function of the K-means clustering algorithm: In the SOM, the distance of each input to all the reference vectors is taken into account, weighted by the neighborhood kernel h, while in the K-means algorithm, only the distance to the closest centroid is used. The cost function of the SOM can be decomposed to two terms as follows:

$$E = \sum_k |x_k - n_c|^2 + \sum_i \sum_j h_{ij}N_i|n_i - m_j|^2 \qquad [24]$$

where N_i is the number of the data items closest to the reference vector m_i, and n_i is the weighting center of the same data items, with the assumption that $\sum_j h_{ij} = 1$ for all values of i. The first term in the relation above is the objective function of the K-means clustering algorithm. However, here the clusters are not defined in terms of their centroids n_i, but in terms of the reference vectors

m_i. With respect to the second term, note that n_i and m_i will generally be close to each other, since n_i is the centroid of the cluster defined by m_i.

Relation between SOM and MDS

When computing the index of the closest unit to the input vector, the Euclidean distance was used. This is not a restriction, as one may use any type of distance. If there is only a dissimilarity (i.e., pseudo-metric) available, we need to create a space where a distance can be defined that preserves as much as possible the original dissimilarities. The techniques used for that purpose are the MDS methods described in a previous section. Since different data analysis methods display different properties of the data set, the most useful approach is to use several methods together. A possible combination is to first reduce the amount of data either by clustering or by the SOM, and then to display the reference vectors with some distance-preserving projection method, to gain additional insight.

Multiple Views of the SOM

The SOM is a model that emphasizes particular aspects of biological neural nets, especially those ordered "maps" found experimentally in the cortex. The SOM captures some of the fundamental processing principles of the brain. *The SOM is a model of unsupervised machine learning* and also an adaptive knowledge representation scheme. *The SOM is a tool for statistical analysis and visualization*. The SOM is both a projection method that maps high-dimensional data space into low-dimensional space, and a clustering method in which similar data samples tend to be mapped to nearby neurons.

There exist a number of variants of the SOM in which the adaptation rules are different, various distance measures may be used, and the structure of the map interconnections is variable. *The SOM is a tool for the development of complex applications*. The SOM is widely used as a data mining and visualization method for complex data sets. Applications areas include image processing, speech recognition, process control, economical analysis, and diagnostics in industry and medicine.[1–3] Searching the best-matching unit is usually the computationally heaviest operation in the SOM. A way to deal with this is to build a hierarchy of SOMs, teaching the SOM on each level before proceeding to the next layer. Most SOM applications use numerical data. Statistical features of natural text can also be regarded as numerical features that facilitate applications of SOM in apparently nonnumerical contexts.

Other Architectures

The field of artificial neural networks is very large. A large number of different neural networks architectures have been developed.[17] Recurrent

networks deserve a special mention here. They allow participating nodes to simultaneously receive and transmit signals; in this way, no distinction is made between input and output nodes. Some of the nodes, the visible nodes, allow an interface with the environment. As in the feedforward network, there are also hidden nodes, which do not allow such interaction. Another variation among neural networks is related to the way the weights are updated. In an extreme case, all the weights are changed at once. At the other extreme, the weights are updated sequentially, one neuron at a time. These are particular examples of a more general case in which the weights of the neurons are updated periodically with a certain probability, and on an individual basis.

EVOLUTIONARY ALGORITHMS

Evolutionary Algorithms are search and optimization procedures that have their origin and inspiration in the biological world: The theory of evolution, based on the idea of survival of the fittest in a dynamic environment.[18] Evolutionary algorithms are based on the learning process within a population of individuals, each of which represents a point in the solution search space of a certain problem. The population is arbitrarily initialized, and it evolves toward better regions of the search space by means of randomized processes of selection (which favors the reproduction of better individuals), recombination (which allows the mixing of parental information when passing it to the descendants), and mutation (which allows some random innovation to be introduced into the population, in order to prevent premature convergence to local optima). Considering the aim of the search, the problem offers a fitness value of the search points, as an indication of their closeness to the solution. Each evolutionary step is called a generation. A pseudo-code of the generic evolutionary algorithm (EA) is the following:

```
// start with an initial time
t : = 0
// initialize a random population of individuals
initpopulation P(t)
// evaluate fitness of individuals in initial population
evaluate P(t)
// test for termination criterion (time, fitness, etc.)
while not done do
// increase the time counter
t : = t + 1
// select subpopulation for reproduction
P' : = selectparents P(t)
```

// recombine the genes of selected parents

recombine $P'(t)$

// perturb the mated population

mutate $P'(t)$

// evaluate its new fitness

evaluate $P'(t)$

// select the survivors based on the fitness

$P : = $ select $P, P'(t)$

   end while

end EA

Evolutionary algorithms, as simulations of genetic processes, are not random searches for a solution of a problem. Evolutionary algorithms use stochastic processes, but the result is distinctly nonrandom. The most widely used types of evolutionary algorithms, which have developed independently, are genetic algorithms, evolution strategies, and evolutionary programming, which will be discussed in the following sections. As we will see, they differ in the way the individuals are represented, in what genetic operators they use, and in how they are defined.

GENETIC ALGORITHMS

The genetic algorithm (GA) model of computation, as created by Holland in 1975, and referred to as the canonical GA, has some distinct particularities.[19] These include representation, fitness function, and others, which will now be discussed.

Canonical GA

Representation

Canonical GA considers the individuals in the population to be fixed length arrays of bits. Simple bit manipulation operations allow the implementation of genetic operators. In order to apply the canonical GA to optimization problems, the bit string is logically divided into segments. Each segment is then interpreted as the binary code of the corresponding optimization variable. There are many segment decoding functions, the simplest one being the simple binary representation of integer values that, if necessary, are combined with a scaling from a certain real interval to a suitable integer interval.

Fitness Function

Different fitness functions are obtained based on the original objective function, on the individual decoding function (produced by combining the

segment decoding functions), and on a scaling function aimed at generating positive fitness values, higher for better individuals.

Selection

Selection of the next generation of parents is made with respect to the probability distribution based on fitness values. The fitness values for each individual are computed. Based on the relative fitness of an individual to the total fitness of the population, the probabilities of selection of individuals are computed. Then, the cumulative probability for each individual is computed as the sum of probabilities of selection of individuals with a smaller index. The new generation is selected based on generating random numbers in the range [0,1] and on matching them to the cumulative probabilities. Obviously, some individuals will be selected more than once, but this is the intended behavior: The best individuals get more copies, the average stays fixed, and the worst die off.

Recombination

This quantity is an operator working entirely on bit representations and completely ignoring the logical segments representing the optimized variables. Based on the probability given by the crossover rate, p_c, a number of parents is randomly selected. From this set of parents, pairs of parents are also randomly selected. Suppose that two parent individuals, $u = (u_1, u_2, \ldots, u_l)$ and $v = (v_1, v_2, \ldots, v_l)$ have thus been selected for the crossover. There are more crossover operators to be applied here. The one-point crossover operator selects at random a crossing point, and generates two offspring from the two parents: $u' = (u_1, \ldots, u_i, v_{i+1}, \ldots, v_l)$ and $v' = (v_1, \ldots, v_i, u_{i+1}, \ldots, u_l)$. These offspring will replace the parents in the population. This may be generalized to the m-point crossover by using more than one breakpoint. Another option is the uniform crossover, which uses a randomly generated mask for deciding, for each bit, whether to exchange information between parents or not.

Mutation

This operator works on the bit string level, and is considered a background operator. It inverts single bits of individuals with a very small probability p_m, ~ 0.001. The practical implementation of this probability may be done via generating a random real number in the interval [0,1]. If the number is smaller than the given probability, the mutation operation is realized on a bit, also randomly generated.

Evolution Strategies

The first Evolution Strategy (ES) was developed in 1964 at the Technical University of Berlin, as an experimental optimization technique. This variant,

called $(1 + 1) - ES$, works on the basis of two individuals only, one parent and one descendant per generation, created by mutation. Some generalizations of this technique are $(\mu, 1) - ES$ where $\mu \geq 1$ individuals are recombined to form an offspring, which then replaces the worst individual from the population. Others include $(\mu, \lambda) - ES$ and $(\mu + \lambda) - ES$.[20,21]

Representation
Search points are *n*-dimensional vectors in the real Euclidean space. Each individual may include additional strategy parameters, as follows: *n* variances $c_{ii} = \sigma_i^2$, $n \cdot (n - 1)/2$ covariances c_{ij}, of the normal distribution. Often, only variances are used, and sometimes there is a single common variance for all *n* variables. These strategy parameters determine the mutability of variables.

Fitness Evaluation
The fitness value is identical to the objective function value as defined by the problem.

Recombination
Recombination is done not only for variables, but also for strategy parameters. It may be realized in the usual manner, by randomly selecting two parents to recombine, or it may be realized in a global manner, in which the parents are separately selected for each variable or parameter. A few recombination rules are the following: (a) without recombination (select the first parent); (b) discrete recombination (select one of the parents randomly); (c) intermediate recombination (select a random point on the segment between the two parents). Empirically, the best results are obtained with discrete recombination of variables and intermediate recombination of parameters.

Mutation
The mutation operator produces a mutated individual by first mutating the standard deviations σ_i, and then mutating the variable according to the new probability density function.

Selection
In ES, selection is completely deterministic. However, there are differences from version to version. The parameter $(\mu, \lambda) - ES$ selects the best μ individuals out of the set of λ offspring individuals, while $(\mu + \lambda) - ES$ selects the best μ individuals out of the union of μ parent individuals and λ offspring individuals. Investigations show a preference toward the use of $(\mu \lambda) - ES$, with a ratio of $\mu/\lambda \approx 1/7$ considered as optimal.

Evolutionary Programming

Evolutionary programming (EP), created by Lawrence J. Fogel in 1960, is a stochastic optimization strategy similar to genetic algorithms and evolution

strategies, but places the emphasis on the link between parent and offspring, instead of emulating specific genetic operators.[22] Combinatorial and real-valued function optimization problems having many locally optimal solutions are well suited for this technique.

Representation
Initially, the variables are vectors from a bounded subspace of $\mathbf{R}^n$. Afterwards, the search domain is extended to the whole space. The Meta-evolutionary programming approach also incorporates strategy parameters (standard deviations) in this representation.

Fitness Evaluation
The fitness values are obtained from objective function values by scaling to positive values and possibly by imposing a random alteration.

Recombination
No recombination operator combining features of different individuals is used with EP. In EP, individuals are viewed as species, and distinct species do not recombine.

Mutation
Each individual is replicated into a new population. Each offspring is mutated according to a distribution of mutation types, from minor to extreme. The severity of mutations is often reduced as the global optimum is approached.

Selection
The new population is selected via a stochastic q-tournament selection. For each individual from $P(t) \cup P'(t)$, q individuals are randomly selected from the same set, and compared to the original individual, determining its score. The individuals with the highest score form the new population. There is no limitation in the number of offspring produced by an individual. Also, there is no limitation in keeping the population size constant.

FUZZY SETS AND FUZZY LOGIC

The mathematics of Fuzzy Set Theory was originated by L. A. Zadeh in 1965.[4] It deals with the uncertainty and fuzziness arising from interrelated humanistic types of phenomena such as subjectivity, thinking, reasoning, cognition, and perception. This approach provides a way to translate a linguistic model of the human thinking process into a mathematical framework for developing the computer algorithms for computerized decision-making processes.[4,23–27] On the other hand, a fuzzy set is a generalized set to which objects can belong with various degrees (grades) of memberships over the

interval [0,1]. Fuzzy systems are processes that are too complex to be modeled by using conventional mathematical methods. In general, fuzziness describes objects or processes that are not amenable to precise definition or precise measurement. Thus, fuzzy processes can be defined as processes that are vaguely defined and have some uncertainty in their description. The data arising from fuzzy systems are in general, soft, with no precise boundaries. From this point of view, fuzzy set theory is not only a theory dealing with ambiguity, it is also a theory of fuzzy reasoning.[23]

The interpretation of Fuzzy Logic (FL) is twofold. In a narrow sense, FL is a logical system that may be viewed as an extension and a generalization of classical logic. In a wider sense, FL is almost synonymous with the theory of fuzzy sets, encompassing the "strict" FL. The fundamental basis of FL is that any field and any theory may be fuzzified by replacing the concept of a crisp set with the concept of fuzzy set. Thus theoretic fields such as fuzzy arithmetic, fuzzy topology, fuzzy graph theory, fuzzy probability theory, "strict" fuzzy logic, and many others have appeared. Similarly, applied fields that have suffered generalizations are fuzzy neural network theory, fuzzy pattern recognition, fuzzy mathematical programming, and so on. What is gained through fuzzification is greater generality, higher expressivity, an enhanced ability to model real-world problems, and a methodology for exploiting the tolerance for imprecision.

Fuzzy Sets

Fuzzy sets were introduced as generalizations of the classical crisp sets, in order to represent and manipulate imprecise data. However, not all the properties valid for operations on crisp sets are valid for fuzzy sets, and the inability to deal with this may result in improper use of fuzzy sets.[4,14,23–27] The basic concepts are defined below:

Fuzzy Set
Let X be a nonempty crisp set. The fuzzy set A in X is characterized by its membership function, $A : X \rightarrow [0, 1]$, where $A(x)$ is interpreted as the membership degree of element $x \in X$ in the fuzzy set A.

Universal Fuzzy Set
The universal fuzzy set in X, denoted by X, is defined by $X(x) = 1$ for all $x \in X$.

Empty Fuzzy Set
The empty fuzzy set in X, denoted $\emptyset$, is defined by $\emptyset(x) = 0$ for all $x \in X$.

Equality
The fuzzy sets A and B in X are said to be equal, and denoted $A = B$, if $A(x) = B(x)$ for all $x \in X$.

Fuzzy Subset

The fuzzy set A in X is a subset of the fuzzy set B in X, denoted $A \subseteq B$, if $A(x) \leq B(x)$ for all $x \in X$.

Complement

The complement of a fuzzy set A in X, denoted $\overline{A}$, is defined by $\overline{A}(x) = 1 - A(x)$ for all $x \in X$.

Intersection

The intersection of fuzzy sets A and B in X, denoted $A \cap B$ is the fuzzy set defined as $(A \cap B)(x) = T(A(x), B(x))$ for all $x \in X$, where T is a triangular norm (i.e., commutative, associative, nondecreasing in each argument, and $T(a, 1) = a$ for all $a \in [0, 1]$).

Union

The union of fuzzy sets A and B in X, denoted $A \cup B$, is the fuzzy set defined as $(A \cup B)(x) = S(A(x), B(x))$, for all $x \in X$, where S is a triangular conorm (i.e., commutative, associative, nondecreasing in each argument, and $S(a, 0) = a$ for all $a \in [0, 1]$).

In what follows, some of the properties of crisp sets will be analyzed from the point of view of applicability with fuzzy sets. We have listed these properties in Table 1 along with examples of two widely used t-norms and t-conorms:

$$\text{Standard} \quad T_S(a, b) = \min\{a, b\} \quad \text{and} \quad S_S(a, b) = \max\{a, b\}$$
$$\text{Lukasiewicz} \quad T_L(a, b) = \max\{a + b - 1, 0\} \quad \text{and} \quad S_L(a, b) = \min\{a + b, 1\}$$

1. Property 1 in Table 1 is satisfied only by the standard t-norm and t-conorm.
2. Property 4 in Table 1 is satisfied by any t-norm and t-conorm.
3. Any t-norm and t-conorm, defined on nondegenerate fuzzy sets, that satisfy properties 2, do not satisfy property (3).
4. For any t-norm and t-conorm that posses the properties 2 and 3, the fuzzy sets have only crisp values, that is, they reduce to crisp sets.

Table 1 The Properties of Crisp Sets from the Point of View of Applicability with Fuzzy Sets

Property	Crisp Sets	T_s and S_S	T_L and S_L
(1) Idempotence laws	Valid	Valid	Invalid
(2) $A \cap \overline{A} = \emptyset$ and $A \cup \overline{A} = X$	Valid	Invalid	Valid
(3) Distributivity laws	Valid	Valid	Invalid
(4) De Morgan laws	Valid	Valid	Valid

The properties shown in Table 1 use the standard definition suitable for use in "strict" FL, and the Lukasiewicz definition suitable for use in fuzzy clustering.

Fuzzy Logic

The basic assumption upon which two-valued logic is based, that every proposition is either true or false, has been questioned since Aristotle. For example, propositions about future events are neither actually true, nor actually false, but potentially either. Consequently, their truth-value is undetermined, at least prior to the event. Propositions whose truth-value is problematic are not limited to future events. For example, propositions that imply physical or chemical measurements depend on the limitations of measurement.[23–27] While several types of multivalued logic have been proposed, here we will discuss the infinite-valued logic, whose truth-values are represented by all the real numbers in the interval [0,1]. This is also called standard Lukasiewicz logic L_1. The primitives of this logic are defined as

$$\bar{a} = 1 - a$$
$$a \wedge b = \min(a, b)$$
$$a \vee b = \max(a, b) \qquad [25]$$
$$a \Rightarrow b = \min(1, 1 + b - a)$$
$$a \Leftrightarrow b = 1 - |a - b|$$

It can be verified that the relations above reduce to their usual counterparts when applied to binary logic. The standard Lukasiewicz logic L_1 is isomorphic to fuzzy set theory based on the standard fuzzy operations in the same way the two-valued logic is isomorphic to the crisp set theory. The membership degree $A(x)$ for $x \in X$ may be interpreted as the truth value of the proposition "x is a member of the set A". The reciprocal is also valid.

Fuzzy Propositions

There are four types of fuzzy propositions. Unconditional and unqualified propositions are of the form

$$\text{p} : \text{V is } F \qquad [26]$$

where V is a variable that takes values from a universe V of values, and F is a fuzzy set on V that represents a fuzzy predicate (e.g., tall, large, high). The degree of truth of this proposition is defined as $T(p) = F(v)$, for each given particular value v of variable V. Unconditional and qualified propositions are of the form

$$\text{p} : \text{V is } F \text{ is } S \qquad [27]$$

where S is a fuzzy truth qualifier (e.g., fairly true, very false, etc.). The degree of truth of this proposition is defined as $T(p) = S(F(v))$, for each given particular value v of variable V. Conditional and unqualified propositions are of the form

$$p : \text{If X is } A \text{ then Y is } B \qquad [28]$$

where X and Y are variables with values in X, Y and A and B are fuzzy sets on X, Y. This proposition may be viewed as $\langle X, Y \rangle$ is R, where R is a fuzzy set on $X \times Y$. The degree of truth of this proposition is defined as $T(p) = R(x, y) = \mathcal{J}(A(x), B(y))$, for each given particular values x, y of variables $\mathcal{X}$, $\mathcal{Y}$. The parameter $\mathcal{J}$ denotes the fuzzy implication operation. Conditional and qualified propositions are of the form

$$p : \text{If } \mathcal{X} \text{ is } A, \text{ then } \mathcal{Y} \text{ is } B \text{ is } S \qquad [29]$$

Its truth-value is determined in a way similar to the cases above.

Fuzzy Quantifiers

Fuzzy quantifiers are fuzzy numbers that take part in fuzzy propositions. They are of the following two kinds. Absolute quantifiers are defined on **R** (~ 10, >100, *at least* ~ 5) and may be used in two forms of propositions:

$$p : \text{There are } Q \, i\text{'s in } I \text{ such that } \mathcal{V}(i) \text{ is } F$$
$$q : \text{There are } Q i\text{'s in } I \text{ such that } \mathcal{V}_1(i) \text{ is } F_1 \text{ and } \mathcal{V}_2(i) \text{ is } F_2 \qquad [30]$$

where $\mathcal{V}$, $\mathcal{V}_1$, $\mathcal{V}_2$ are variables that take values from sets V, V_1, V_2, I is a set of individuals, Q is a fuzzy number on **R**, and F, F_1, F_2 are fuzzy sets on V, V_1, V_2. The truth-value of these sentences is defined as

$$T(p) = Q\left(\sum_{i \, in \, I} F(\mathcal{V}(i)) \right) T(q) = Q\left(\sum_{i \, in \, I} \min(F_1(\mathcal{V}_1(i)), F_2(\mathcal{V}_2(i))) \right) \qquad [31]$$

The latter case assumes the standard intersection of two fuzzy sets. Relative quantifiers are defined on $[0, 1]$ (almost all, about half, most) and may be used in propositions of the form:

$$p : \text{Among } i\text{'s in } I \text{such that } \mathcal{V}_1(i) \text{ is } F_1 \text{ there are } Q \, i\text{'s in } I \text{ such that } \mathcal{V}_2(i) \text{ is } F_2$$

where Q is a fuzzy number on $[0, 1]$. The truth-value of this sentence is defined assuming the standard intersection of two fuzzy sets.

Linguistic Hedges

These are linguistic terms that modify other linguistic terms, for example, very, more or less, fairly, extremely. They may be used to modify fuzzy predicates, fuzzy truth-values, and fuzzy probabilities. The fuzzy set that defines the hedge is called a modifier.

$$T(p) = Q\left(\frac{\sum_{i \in I} \min(F_1(\text{cal}) V_1(i)), F_2(\text{cal} V_2(i)))}{\sum_{i \in I} F_1(\text{cal} V_1(i))}\right) \qquad [32]$$

The modifier is simply applied over the fuzzy set associated with the predicate, value, or probability it modifies. For example, the proposition "x is young [is true]" may be modified by the hedge *very* in the following ways:

- "x is very young is true"
- "x is young is very true"
- "x is very young is very true"

Inference from Fuzzy Propositions

The inference rules of crisp logic have been generalized in the framework of fuzzy logic in order to facilitate approximate reasoning. Separate generalizations have been made for dealing with conditional fuzzy propositions (generalized modus ponens, generalized modus tolens, generalized hypothetical syllogism), conditional and qualified propositions and quantified propositions.

Fuzzy Clustering

As is well known, Cluster Analysis involves the classification of objects into categories. Since most categories have vague boundaries, and may even overlap, the necessity of introducing fuzzy sets is obvious. A discussion of Fuzzy Clustering must refer to the following issues:[5,28–37]

Data Representation

Input data is obtained from measurements on the objects that are to be recognized. Each object is represented as a vector of measured values $x = (x_1, x_2, \ldots, x_s)$, where x_i is a particular characteristic of the object.

Feature Extraction

Due to the large number of characteristics, there is a need to extract the most relevant characteristics from the input data, so that the amount of information lost is minimal, and the classification realized with the projected data set is relevant with respect to the original data. In order to achieve this feature extraction, different statistical techniques, as well as the fuzzy clustering algorithms outlined here, may be used.

Cluster Shape

Pattern recognition techniques based on fuzzy objective function minimization use objective functions particular to different cluster shapes. Ways to approach the problem of correctly identifying the cluster's shape are the use of adaptive distances in a second run to change the shapes of the produced clusters so that all are unit spheres, and adaptive algorithms that dynamically change the local metrics during the iterative procedure in the original run, without the need of a second run.

Cluster Validity

Another problem with such algorithms is that of determining the optimal number of classes that correspond to the cluster substructure of the data set. There are two approaches: The use of validity functionals, which is a postfactum method, and the use of hierarchical algorithms, which produce not only the optimal number of classes (based on the needed granularity), but also a binary hierarchy that shows the existing relationships between the classes.

Defuzzification of Final Fuzzy Partition

Since humans need crisp partitions for their analysis, such procedures should be able to produce, together with the final fuzzy partition, a crisp version thereof. A number of techniques exist, which differ in their ability to produce a nondegenerate crisp partition (i.e., a crisp partition with all the member crisp sets nonempty), and in their ability to produce the crisp partition closest to the original fuzzy partition.

Method

The method is based on defining a dissimilarity function between the data set and the prototypes (not necessarily vectors in the same space) of the fuzzy classes. A fuzzy objective function is defined based on this dissimilarity function. In order to minimize the fuzzy objective function, a two-step iterative procedure is used: for certain prototypes, the optimal fuzzy partition is determined. Conversely, for a certain fuzzy partition, the optimal prototypes are determined. This procedure continually decreases the value of the objective function.

Fuzzy Regression

Let us consider a data set $X = \{x^1, \ldots, x^p\}$ from $\mathbf{R}^s$. Let us suppose that the set X does not have a clear clustering structure or that the clustering structure corresponds to a single fuzzy set. Let it be assumed that this fuzzy set, denoted by A, may be characterized by a linear prototype, denoted by $L = (v; u)$, where v is the center of the class and u, with $\|u\| = 1$, is its main direction. We raise the problem of finding the most suitable fuzzy set for the given data set. We propose to do this ourselves by minimizing a criterion

function similar to those presented in References 28–39. Let us consider the scalar product in $\mathbf{R}^s$ given by

$$\langle x, y \rangle = x^T My \qquad \text{for every } x, y \in \mathbf{R}^s \qquad [33]$$

where M is a symmetrical, positive definite square matrix of size s. If M is the unit matrix, then the scalar product is the usual one, $\langle x, y \rangle = x^T y$. We will use the unit matrix for all the computations in our examples. Furthermore, let us consider the norm in $\mathbf{R}^s$ induced by the scalar product,

$$||x|| = \langle x, x \rangle^{1/2} \qquad \text{for every } x \in \mathbf{R}^s \qquad [34]$$

and the distance d in $\mathbf{R}^s$ induced by this norm,

$$d(x, y) = ||x - y|| \qquad \text{for every } \quad x, y, \in \mathbf{R}^s \qquad [35]$$

In order to obtain the criterion function, a fuzzy partition $\{A, \overline{A}\}$ must be determined. The fuzzy set A is characterized by the prototype L. With respect to complementary fuzzy set, $\overline{A}$, we will consider that the dissimilarity between its hypothetical prototype and the points x^j is constant and equal to $\alpha/1 - \alpha$, where α is a constant from $[0; 1]$, with a role to be seen later. Denote the dissimilarity between the point x^j and the prototype L by

$$D(x^j; L) = d^2(x^j; L) \qquad [36]$$

where

$$d(x^j, L) = (||x^j - v||^2 - \langle x^j - v, u \rangle^2)^{1/2} \qquad [37]$$

is the distance from the point x^j to the line $L = (v; u)$ in the space $\mathbf{R}^s$. The inadequacy between the fuzzy set A and its prototype L will be

$$I(A, L) = \sum_{j=1}^{p} (A(x^j))^2 D(x^j, L) \qquad [38]$$

and the inadequacy between the complementary fuzzy set A and its hypothetical prototype will be

$$\sum_{j=1}^{p} (\overline{A}(x^j))^2 \frac{\alpha}{1 - \alpha} \qquad [39]$$

Thus, the criterion function $J : F(X) \times \mathbf{R}^d \to \mathbf{R}^+$ becomes

$$J(A, L; \alpha) = \sum_{j=1}^{p} (A(x^j))^2 D(x^j, L) + \sum_{j=1}^{p} (\overline{A}(x^j))^2 \frac{\alpha}{1 - \alpha} \qquad [40]$$

where $\alpha \in [0, 1]$ is a fixed constant. With respect to the minimization of the criterion function J, the following two results are valid. Consider the fuzzy set A of X. The prototype $L = (v; u)$ that minimizes the function $J(A; \cdot)$ is given by

$$v = \frac{\sum_{j=1}^{p} (A(x^j))^2 x^j}{\sum_{j=1}^{p} (A(x^j))^2} \qquad [41]$$

and u is the eigenvector corresponding to the maximal eigenvalue of the matrix

$$S = M \sum_{j=1}^{p} (A(x^j))^2 (x^j - v)(x^j - v)^T M \qquad [42]$$

where M is the matrix from the scalar product definition. Similarly, consider a certain prototype L. The fuzzy set A that minimizes the function $J(; \cdot L)$ is given by

$$A(x^j) = \frac{\frac{\alpha}{1-\alpha}}{\frac{\alpha}{1-\alpha} + d^2(x^j, L)} \qquad [43]$$

The optimal fuzzy set will be determined using an iterative method, where J is successively minimized with respect to A and L. The proposed algorithm will be called Fuzzy Regression:

S1. Choose the constant $\alpha \in [0, 1]$. Initialize $A(x) = 1$, for every $x \in X$, and $l = 0$. Let $A^{(l)}$ be the fuzzy set A determined at the lth iteration.
S2. Compute the prototype $L = (v; u)$ of the fuzzy set $A^{(l)}$ using the relations given above.
S3. Determine the new fuzzy set $A^{(l+1)}$ using the relation given above.
S4. If the fuzzy sets $A^{(l+1)}$ and $A^{(l)}$ are closed enough, that is, if $||A^{(l+1)} - A^{(l)}|| \leq \varepsilon$, where ε has a predefined value, then stop, else increase l by 1 and go to step S2.

Our results show that a good value of ε with respect to the similarity of $A^{(l)}$ and $A^{(l+1)}$ is $\varepsilon = 10^{-5}$.

In practice, in order to avoid the dependency of the memberships on the scale, instead of using the distance d, we will use the normalized distance d_r given by

$$d_r(x^i, L) = \frac{d(x^i, L)}{\max_{x \in X} d(x^i, L)} \qquad [44]$$

The relation used to determine the memberships becomes, thus,

$$A(x^i) = \frac{\frac{\alpha}{1-\alpha}}{\frac{\alpha}{1-\alpha} + d_r^2(x^i, L)} \qquad [45]$$

The Fuzzy Regression algorithm modified by using this membership rule will be named the Modified Fuzzy Regression algorithm. In what follows, the properties of the fuzzy set obtained via the algorithm presented above will be studied. Let X be a given data set and let A be the fuzzy set and L its prototype as they were determined by the Modified Fuzzy Regression algorithm. The following relations are valid (notations are defined above):

1. $A(x) = 1 \Leftrightarrow d(x; L) = 0$
2. $A(x) = \alpha \Leftrightarrow d_r(x; L) = 1$
3. $A(x) \in [\alpha, 1]$ for every $x \in X$
4. $\alpha = 0 \Leftrightarrow A(x) = 0$ for every $x \in X$ [46]
5. $\alpha = 1 \Leftrightarrow A(x) = 1$ for every $x \in X$
6. $A(x^i) < A(x^j) \Leftrightarrow d(x^i; L) < d(x^i; L)$
7. $A(x^i) = A(x^j) \Leftrightarrow d(x^i; L) = d(x^j; L)$

The algorithm presented here converges toward a local minimum. Normally, the results of algorithms of this type are influenced by the initial partition considered.[24] When the initial fuzzy set considered is X, the obtained optimal fuzzy set is the one situated in the vicinity of X; this makes the algorithm even more attractive. The role of the constant α is to affect the polarization of the partition $\{A; \overline{A}\}$. Also, it is now clear why α was chosen to be in $(0, 1)$ and the values 0 and 1 were avoided. By using the relative dissimilarities D_r, this method is independent of the linear transformations of the space. Keeping in mind properties 1–7 and the remarks above, the fuzzy set A determined here may be called the fuzzy set associated with the classical set X and the membership threshold α. We may build a theory to determine the fuzzy set A represented by a point prototype, or by any geometrical prototype using the thory presented above. As seen above, the (Modified) Fuzzy Regression algorithm produces the fuzzy set associated with the classical set X and the membership threshold α, together with its linear representation.

FUZZY PRINCIPAL COMPONENT ANALYSIS (FPCA)

Fuzzy PCA (Optimizing the First Component)

For the data collected on p variables for n cases, PCA performs analyses in the n-dimensional space defined by p variables and p-dimensional space defined by n cases. In PCA, straight lines are sought that best fit the clouds of points in the vector spaces (of variables and cases), according to the least-squares criterion. This, in turn, yields the principal components (factors) that result in the maximum sums of squares for the orthogonal projections. Consequently, a lower-dimensional vector subspace is recovered that best represents the original vector space. Although the first factor is extracted so as to capture the variance to the maximum extent, it can seldom capture the variance in its entirety. What remains should, therefore, be recovered by another (second) factor, a third, and so on. However, the number of factors thus extracted will never exceed the number of original variables.

Fuzzy clustering is an important tool for identifying the structure in data. According to the choice of prototypes and the definition of the distance measure, different fuzzy clustering algorithms are obtained. If the prototype of a cluster is a point—the cluster center—it will produce spherical clusters; if the prototype is a line, it will produce tubular clusters, and so on. Also, elements with a high degree of membership in the ith cluster (i.e., close to the cluster's center) will contribute significantly to this weighted average, while elements with a low degree of membership (far from the center) will contribute almost nothing. In what follows, we briefly review the Fuzzy (first component) PCA algorithm proposed in Reference 40. We wish to determine the particular membership degrees $A(x)$ such that the first principal component is best fitted along the points of the data set X. The algorithm is a natural extension of the Fuzzy Regression Algorithm.

Algorithm FuzzyPCAFirst()

1. Determine the optimal value of α by calling DetermineBestAlpha().
2. Call DetermineFuzzyMembership(α) with the value of α computed above, and determine the optimal value of the fuzzy membership degrees.
3. Using the fuzzy membership degrees determined above, compute the fuzzy covariance matrix C, and compute its eigenvalues and eigenvectors; these are the fuzzy principal components and the corresponding scatter values.

Recall that α is the membership degree corresponding to the farthest outlier of the data set. In the algorithm above, the fuzzy covariance matrix is determined as

$$C_{ij} = \frac{\sum_{k=1}^{n} A(x^k)^m (x_i^k - \bar{x}_i)(x_j^k - \bar{x}_j)}{\sum_{k=1}^{n} A(x^k)^m} \quad i, j = 1, \ldots, p \qquad [47]$$

where $\overline{x_i}$ is the arithmetic mean of the *i*th variable, $m > 1$ is the fuzziness index. The settings above mean that the fuzzy set *A* is characterized by the linear prototype PC1 produced considering the fuzzy covariance matrix *C*. The procedure DETERMINEFUZZYMEMBERSHIPS determines the optimal fuzzy membership degrees and the optimal prototype line associated with the data set and corresponding to the value of α. Procedure DETERMINEBESTALPHA works through a loop between 0 and 1, with a certain step, and selects the value of α that maximizes the criterion function used by the procedure DETERMINEFUZZYMEMBERSHIPS. In this way, the procedure insures the determination of the optimal value of α in terms of producing a better fitted first principal component along the data set.

Fuzzy PCA (Nonorthogonal Procedure)

Encouraged by the good results obtained with the Fuzzy (first component) PCA,[40] we decided to extend the fuzzy approach one step more. A Fuzzy PCA algorithm was written that would extend the fuzzy clustering scheme with computing each particular principal component, not just the first one. The main idea behind the first algorithm in this series rests with the relation

$$M = \lambda_1 e^1 e^{1T} + \lambda_2 e^2 e^{2T} + \cdots + \lambda_p e^p e^{pT} \qquad [48]$$

where *T* denotes the transposing operation, *M* is the matrix whose eigenvectors and eigenvalues are to be determined, λ_i is the *i*th eigenvalue and e^i is the corresponding eigenvector. If λ_1 is the largest eigenvalue of the matrix *M*, and e^1 is its corresponding eigenvector, then the second largest eigenvalue λ_2 and its corresponding eigenvector e^2 are computed as the largest eigenvalue and its corresponding eigenvector of the matrix $M - \lambda_1 e^1 e^{1T}$. This procedure continues until all eigenvalues and eigenvectors are computed. In this way, we are able to reduce the problem of computing the second largest fuzzy principal component to the problem of computing the largest fuzzy principal component of a different matrix. The FUZZYNONORTHOGONALPCA Algorithm is the following:

Algorithm FUZZYNONORTHOGONALPCA():

1. Determine the optimal value of α by calling DETERMINEBESTALPHA().
2. Call DETERMINEFUZZYMEMBERSHIP(α) with the value of α computed above, and determine the optimal value of the fuzzy membership degrees.
3. Using the fuzzy membership degrees determined above, compute the fuzzy covariance matrix *C*.
4. Initialize the value of *i* to *p*, and the matrix C_{dif} to zero.
5. Call DETERMINEFUZZYMEMBERSHIPMODIFIED(α, C_{dif}) with the value of α computed above, and determine the optimal value of the fuzzy membership degrees.

6. Using the fuzzy membership degrees determined above, compute the fuzzy covariance matrix C.
7. Compute the eigenvalues and eigenvectors of matrix C; the largest eigenvalue, and its corresponding eigenvector e are the ith largest fuzzy principal component and its corresponding scatter value.
8. Update the matrix C_{dif} by adding the value λee^T using the eigenvalue and eigenvector from the preceding step.
9. Decrease the value of i by 1. If $i > 0$, go to Step 5 and continue from there. Otherwise, stop the algorithm.

The procedure DETERMINEFUZZYMEMBERSHIPMODIFIED(α, C_{dif}) is a modified version of DETERMINEFUZZYMEMBERSHIPS, and determines the optimal fuzzy membership degrees and the optimal prototype line associated with the data set and corresponding to the value of α and with the diminishing matrix C_{dif}. The quantity in C_{dif} is the exact quantity that should be subtracted from the original covariance matrix C in order to determine the subsequent eigenvector and eigenvalue. But, because in this case the fuzzy covariance matrix depends on fuzzy membership degrees corresponding to a different fuzzy set for each principal component, this subtraction will have to be repeated each time during the process of determining the line prototypes.

Fuzzy PCA (Orthogonal)

The main issue with the Fuzzy PCA algorithm described in the preceding section is that the computed eigenvectors, while being unit vectors, are not mutually orthogonal. The next algorithm is designed to change this. Let us denote $\lambda_1, \ldots, \lambda_p$, and $e^1, \ldots, e^p$ the eigenvalues and the eigenvectors, respectively, that will finally be produced by our suggested algorithm. The first fuzzy principal component is computed as with the FUZZYPCAFIRST algorithm, that is, by finding the optimal fuzzy membership degrees and the optimal linear prototype for the data set. Let us denote $\lambda'_1, \ldots, \lambda'_p$ and $e'_1, \ldots, e'^p$ the eigenvalues and eigenvectors, respectively, produced in this way. Therefore, we will have

$$\lambda_1 = \lambda'_1 \qquad\qquad [49a]$$

and

$$e^1 = e'^1 \qquad\qquad [49b]$$

The major novelty of this algorithm is in the way the other fuzzy principal components are computed. The original data set is projected onto the hyperplane orthogonal to the first fuzzy principal component, that is, determined by all the other principal components, as determined by the Fuzzy First Component PCA algorithm. Practically, this may be done by computing the scores

and removing the first item from the data vectors. Therefore, we first compute the scores:

$$x'^{j^T} = x^{j^T} \cdot (e'^1, \ldots, e'^p) \qquad [50]$$

and then remove the first component of x'^j, thus producing a subset X' of $\mathbf{R}^{p-1}$:

$$X' = \{(x'_2, \ldots, x'_p | \exists j : x'^j = (x'^1, x'^2, \ldots, x'^p)\} \qquad [51]$$

This produces a data set in a Euclidean space of dimension $p-1$, where p is the size of the original data set. Denote $\lambda''_1, \ldots, \lambda''_{p-1}$ and $e''^1, \ldots, e''^{p-1}$ the eigenvalues and eigenvectors, respectively, produced in this way. The first fuzzy principal component of this projected data set, after being rewritten in terms of the original space, is orthogonal on the first fuzzy principal component, as computed originally. In order to account for the fuzziness in the fuzzy data sets, when rewriting the components in terms of the original space, the eigenvalues computed in the $p-1$ sized space will be multiplied by the fuzzy set fuzziness index f_A, given by

$$f_A = \frac{1}{n} \sum_{i=1}^{n} A(x^j)^m \qquad [52]$$

Thus

$$\lambda_2 = \lambda''_1 \cdot f_A \qquad [53]$$

and

$$e^{2T} = (0, e''^1)^T \cdot (e'^1, \ldots, e'^p)^T \qquad [54]$$

where $(0; e''^1)$ denotes a vector having 0 for the first component, and the components of the vector e''^1 for the other components. In order to determine the third fuzzy principal component we will reason in the same way, but here we start with the projected data set and project it onto the hyperplane orthogonal to the first two fuzzy principal components. This twice-projected data set will be in a Euclidean space of dimension $p-2$. Let us suppose that, after proper transformations have been made at the superior level, these newly produced eigenvectors and eigenvalues (now in the $\mathbf{R}^{p-1}$ space) and still denoted by $\lambda''_1, \ldots, \lambda''_{p-1}$ and by $e''^1, \ldots, e''^{p-1}$. These notations will replace the already computed values.

Now we need only a final transformation: to revert these eigenvectors and eigenvalues to the original space. We use relations similar to those used for computing the initial projection, but in reverse. The FUZZYORTHOGONAL-PCA Algorithm is the following:

Algorithm FuzzyOrthogonalPCA():

1. If $p \leq 2$, call FuzzyPCAFirst(), otherwise continue.
2. Determine the optimal value of α by calling DetermineBestAlpha().
3. Call DetermineFuzzyMembership(α) with the value of α computed above, and determine the optimal value of the fuzzy membership degrees.
4. Using the fuzzy membership degrees determined above, compute the fuzzy covariance matrix C.
5. Compute the eigenvalues and eigenvectors of matrix C; the largest eigenvalue, and its corresponding eigenvector e are the current fuzzy principal component and its corresponding scatter value.
6. Compute the scores of the data set and remove the first component of each data item.
7. Recursively call FuzzyOrthogonalPCA() on this reduced data set; after returning, the values $\lambda''_1, \ldots, \lambda''_{p-1}$ and the corresponding eigenvectors $e''^1, \ldots, e''^{p-1}$ will be known, but will be computed in the projected space.
8. Revert to the original data space and rewrite the eigenvalues and their corresponding eigenvectors in terms of the original data space.

FUZZY EXPERT SYSTEMS (FUZZY CONTROLLERS)

A Fuzzy Expert System is an expert system that uses a collection of fuzzy membership functions and fuzzy rules, instead of Boolean logic, to make decisions from data.[41,42] The rules are of the form:

$$\text{If } x \text{ is } low \text{ and } y \text{ is } high \text{ then } z \text{ is } medium \qquad [55]$$

where x and y are input variables, z is an output variable and low, high, medium are called linguistic labels and have associated fuzzy membership functions. The antecedent of the rule describes to what extent the rule applies, and the conclusion of the rule assigns a membership function to each output variable. A Fuzzy Controller is a special type of fuzzy expert system whose purpose is to influence the behavior of a system by changing its inputs according to a set of rules that describe how the system operates. The general inference process proceeds in the following steps:

Linguistic Labels
After identifying the relevant input and output variables of the system, and the range of their values, we need to select meaningful linguistic labels for each variable and associate them with appropriate fuzzy sets. The most commonly employed linguistic labels are approximately zero (AZ), positive small (PS), positive medium (PM), positive large (PL), negative small (NS), negative medium (NM), negative large (NL). The fuzzy sets associated with

these linguistic variables are generally fuzzy numbers, but, when needed, different fuzzy sets may be used.

Fuzzy Inference Rules

The knowledge to be used by the system is formulated in terms of fuzzy inference rules. There are two distinct ways in which these fuzzy rules can be determined: (a) by using the experience of human operators; and (b) by obtaining them from empirical data found through suitable learning, for example, using neural networks. As stated before, the canonical form of the fuzzy inference rules is

$$\text{If } e_1 = A \text{ and } e_2 = B \text{ then } v = C \qquad [56]$$

where A, B, and C are fuzzy membership functions associated with some of the available linguistic labels.

Fuzzification

For each fuzzy inference rule, the fuzzy sets associated with each input variable are applied to their actual values, to determine the degree of truth for each rule premise. The degree of truth for a rule premise, sometimes denoted by α, is computed as $\alpha = T_1(A(e_1), B(e_2))$, where T_1 is a *t*-norm. If α for a certain rule is nonzero, then the rule is said to fire.

Inference

The fuzzy set associated with the output variable is computed as

$$\text{rule}(z) = T_2(\alpha, C(z)) = T_2(T_1(A(e_1), B(e_2)), C(z)) \qquad [57]$$

where T_2 is a *t*-norm, not necessarily the same as T_1. Two *t*-norms generally used in this case are *min* and *product*.

Composition

All the fuzzy sets associated by different rules to the same variable are combined together to form a single fuzzy set for each output variable. This is realised by using a *t*-conorm, that is, by an abuse of notation,

$$\text{fuzzy}(z) = S(\text{rule}_1(z), \text{rule}_2(z), \ldots) \qquad [58]$$

where S is the chosen *t*-conorm. Two *t*-conorms generally used in this case are **max** and **sum**. The latter is not really a *t*-conorm, and it produces fuzzy memberships >1. Thus, it may only be used when followed by an appropriate defuzzification method.

Defuzzification

Sometimes, the fuzzy sets associated with the output variables offer sufficient information, but often we need to provide a crisp value for each output variable given a set of values for the input variables. There are more defuzzification methods that may be used here, and we stress that they are completely different from the defuzzification methods used in fuzzy clustering.

- *Center of gravity*. The defuzzified value of a fuzzy set C is its fuzzy centroid.
- *First of maxima*. The defuzzified value of a fuzzy set C is its smallest element having the highest membership degree.
- *Middle of maxima*. The defuzzified value of a fuzzy set C is the mean of all elements having the highest membership degree.
- *Max criterion*. The defuzzified value of a fuzzy set C is an arbitrary element having the highest membership degree.
- *Height defuzzification*. The elements with membership degrees lower than a certain threshold are completely discarded, and the Center-of-gravity method is applied to the remainder of the fuzzy set.

HYBRID SYSTEMS

The component techniques of soft computing are not competitive, but complementary. Much research has been done to study the ways this complementarity can be exploited. Each of the components has features to offer a potential partnership. Systems that have such a partnership are called "hybrid systems". Fuzzy logic uses the concept of computing with words, it deals with imprecision and information granularity and is an important tool for approximate reasoning. Neural networks learn and adapt. Genetic algorithms make use of a systemized random search and are an important tool for optimization. These three may be combined in different ways, as described below.

Combinations of Fuzzy Systems and Neural Networks

Many types of combinations between fuzzy systems and neural networks have been proposed and studied. In what follows, we use the definitions and classification proposed by Detlef Nauck, from the Department of Computer Science, Technical University of Braunschweig, Germany.[43–46] A "neuro-fuzzy" or "neural fuzzy" system is a combination of neural networks and fuzzy systems in such a way that neural networks are used to determine parameters of fuzzy systems. The main intention of a neuro-fuzzy approach is to create or improve a fuzzy system by means of neural network methods. The system should always be interpretable in terms of fuzzy if-then rules. A "fuzzy

neural network'' is a neural network that uses fuzzy methods to learn faster or to perform better. The main intention is the improvement of the neural network.

Fuzzy Neural Networks

Fuzzy methods are also used to enhance the learning capabilities or performance of a neural network. This can be done by using fuzzy rules to change the learning rate, or by creating a network that works with fuzzy inputs.

Concurrent Neuro-Fuzzy Models

A neural network and a fuzzy system may work together on the same task, but without influencing each other, that is, neither system is used to determine parameters of the other. Usually, the neural network preprocesses the inputs or postprocesses the outputs of the fuzzy system.

Cooperative Neuro-Fuzzy Models

A neural network may also be used to determine the parameters of a fuzzy system. After the learning phase, the fuzzy systems work without the neural network. Cooperative models use the following approaches: (a) learn fuzzy sets off-line; (b) learn fuzzy rules off-line; (c) learn fuzzy sets on-line; (d) learn rule weights.

Hybrid Neuro-Fuzzy Models

A neural network and a fuzzy system may be combined into one homogenous architecture. The system may be interpreted as a special neural network with fuzzy parameters, or as a fuzzy system implemented in a parallel distributed form.

Fuzzy Genetic Algorithms

There are a few approaches in which fuzzy set theory and evolutionary algorithms become highly interactive partners. They mostly concern the following alternatives.[47,48]

Fuzzy Encoding and Fuzzy Set Operations in Genetic Algoritms

There are two different issues involved here. The first concerns the encoding of each variable that comes as a part of the optimization problem, using fuzzy logic. Excepting the case of variable encoding using real numbers, encoding supposes the transformation of a numerical value into a certain string of symbols, from a finite and small alphabet. Instead of using a small number of symbols, we use fuzzy sets (linguistic labels) such as NL, NM, NS, Z (Zero), PS, PM, and PL, which can also be of a different granularity. Of course, any result obtained during the GA search needs to be decoded. The fuzzy decoding mechanism is related to the particular fuzzy encoding

applied previously. The second issue concerns the use of fuzzy set operations (*t*-norms, *t*-conorms, averaging operators, and compensation operators) for developing recombination operators. Also, fuzzy meta-rules are used in the selection of crossover and mutation rates, based on previous experience, and with the help of a series of fuzzy if-then rules, for example, on the population size and the generation time. For example, if population is small and generation is short, then the crossover rate is medium and the mutation rate is large.

Evolutionary Computing in Development of Fuzzy Models

The optimization abilities of genetic algorithms are used to develop the best set of rules to be used by a fuzzy inference engine. Another approach relates to fuzzy or hard clustering problems based on objective function minimization. These problems are regarded as GA search problems (i.e., the problem needs to be specifically encoded and genetic operators have to be devised), and the optimal fuzzy partition is determined by using a GA search. Moreover, such techniques may also be used in the pipeline, with the best partition prototypes produced by the GA search used as the initial configuration for the fuzzy clustering procedure.

Neuro-Genetic Systems

The performance of neural networks (NN) can be enhanced by the use of genetic algorithms. There are two different approaches.[49,50]

Use of GA to Improve the Behavior of NN

This approach includes the use of GA in order to (a) generate the weights of a neural network; (b) generate the architecture of a neural network; and (c) generate both the weights and architecture of a neural network.

Use of NN to Improve the Behavior of GA

This approach defines the evaluation function of the genetic algorithm as a neural network. The genetic operators are used to train the parameters of the neural network. The evaluation function is the forward stage of the neural network, while the genetic parameters are improved in the back-propagation stage of the neural network.

FUZZY CHARACTERIZATION AND CLASSIFICATION OF THE CHEMICAL ELEMENTS AND THEIR PROPERTIES

It may seem that the problem of classification of the chemical elements has already been solved by the development of the periodic table of elements

and that the single item remaining to be solved is to find a certain, adequate and suggestive as possible graphic representation.[51–55] In fact, the groups of the periodic table do not always explain the whole wealth of relations between the properties of the elements and of their compounds. Sometimes unexpected similarities exist between remote elements in the periodic system.

It is, of course, true that most properties of the elements are determined by the outer-electron configurations of their atoms. These configurations are, of course, the basis for the arrangement of elements in the periodic table. However, this effect of the valence electrons is often quite indirect. Along with properties of single atoms, properties exist that are collectively determined, for example, by the lattice structure.

Therefore, we may raise the problem of whether the classical structure of the periodic system is really fully concordant with all the physical and chemical properties of the elements.[32,33,53,54] In what follows, we try to repeat the early procedure of Mendeleev, whose classification was not founded on electron configuration but on observable data concerning physico-chemical properties of the elements. The basic idea of our procedure is that the properties of elements are gradual by nature. Therefore, we must acknowledge that they should be grouped in classes with no clearly cut boundaries. Hence, each element should belong mainly to a single class, but this does not mean that it could not also belong with different small membership degrees to all the other classes.

If we admit that the membership degrees to a group have a gradual character, we may obtain a more accurate classification of the elements, able to account for some irregularities of the standard classification. It also could suggest the occurrence of some new relationships between the elements.

This classification must use primary physical and chemical properties of the elements. Their selection is rather difficult since they have to be expressed numerically and have to be known for all the investigated elements. The method applied for the classification uses fuzzy set theory in order to obtain a clustering of the set of chemical elements. This method is hierarchical and does not suppose a preliminary knowledge with respect to the number of classes in the data set, nor does it suppose a certain structure for the classes. Both the number of classes and their mutual relationships will be detected by the classification algorithm used.

In order to identify which properties (variables) are responsible for the observed similarities and dissimilarities between the chemical elements, we also applied a very interesting algorithm, namely, fuzzy hierarchical cross-classification (FHiCC). The technique produces not only a fuzzy partitioning of the chemical elements but also a fuzzy partitioning of the physical and chemical properties considered. Moreover, the fuzzy hierarchical characteristics clustering (FHiChC) and fuzzy horizontal characteristics clustering (FHoChC) procedures showed very high similarities between the chemical and structural

properties of elements and also between the structural and some of the physical properties.

HIERARCHICAL FUZZY CLASSIFICATION OF CHEMICAL ELEMENTS BASED ON TEN PHYSICAL PROPERTIES

In order to use the methods presented above to classify the chemical elements, the problem we are first faced with is to decide the characteristics this classification is built upon. We started with 10 physical properties: relative atomic mass, A (**1**), density, ρ (**2**), melting point, T_f (**3**), boiling point, T_b (**4**), Pauling electronegativity, χ (**5**), enthalpy of vaporization, ΔH_v (**6**) and fusion, ΔH_f (**7**), specific heat capacity, C_s (**8**), first ionization energy, E_i (**9**), and covalent radius, r (**10**).

These values are known for 84 elements.

The classification hierarchy produced by using the 10 physical properties mentioned above without scaling (nonnormalization) of data is presented in Figure 4. The first partition separates, roughly speaking, the elements of the main groups of the periodic system (class 1) from those of the secondary groups (class 2). To class 1 belong the metals of group 12 (IIB) (Zn, Cd, Hg) and also Ag; all these elements have the d subshell completed and are in this way analogous to those in the main groups. Also, class 1 includes four lanthanides (Sm, Eu, Tm, Yb), all of which have the $5d$ subshell vacant. The $4f$ subshell is complete for Yb and half-complete ($4f^7$) for Eu, that is, these elements have relatively stable subshell configurations. The elements Tm and Sm have one electron fewer than these configurations ($4f^{13}$, $4f^6$). On the other hand, class 2 also contains six elements of the main groups (Be, B, Al, C, Si, Ge). On the whole, the first class contains elements with lower densities and melting and boiling points (smaller fusion and vaporization enthalpies).

The next step for class 1 differentiates mainly between metals (class 1.1) and nonmetals (class 1.2), although the latter class includes the alkali metals K, Rb, and Cs and the group 12 (IIB) metals Cd and Hg. The elements of class 1.2 have lower densities, melting and boiling points and, as a rule, high ionization energies and electronegativities. The dominant features here are, however, the melting and boiling points, and this accounts for the presence of some very electropositive (K, Rb, Cs) or heavy (Hg) elements. However, the metals of this class (1.2), together with the solid nonmetals at room temperature (P, S, Se, I), are separated as a class (1.2.1) from the typical gaseous nonmetals at room temperature (class 1.2.2).

The last subdivision distinguishes a class (1.2.1.1) containing the alkali metals (membership degrees—MDs—of ~ 0.60) and Se and Cd. The last one has a smaller MD (0.43), only a little more than its MD for the class 1.1.2.

Figure 4 The classification of the elements produced with 10 nonnormalized physical characteristics (from Ref. 32).

289

Class 1.1.2 includes, among others, Zn, which has a MD of 0.22 for the class 1.2.1. The elements of the class 1.2.1.1 are similar mostly with respect to their boiling points ($\sim$ 700–750°C), while the elements of class 1.2.1.2 have lower T_b. Class 1.2.1.2 includes solid nonmetals (P, S, I) and Hg, elements with very similar ionization energies (240–250 kcal/mol). Nonmembers of this class, As and Br, have MDs of 0.15–0.16 for it. It is interesting that grouped together here are mercury and sulfur, elements that the alchemists thought to be at the source of all matter.

From class 1.2.2 are first separated chlorine, bromine, and xenon (class 1.2.2.1); among them, Cl and Br have similar MDs (0.79, 0.75), much higher than Xe (0.59). The last is similar to them mostly with respect to its ionization energy. The other elements having much lower densities, T_f and T_b, are grouped into two classes: one includes lighter noble gases, having the highest ionization energies, He and Ne (1.2.2.2.2), the other contains the middle noble gases (Ar, Kr) along with hydrogen and the gaseous elements of period 2 (N, O, F). These elements (class 1.2.2.2.1) have extremely low melting and boiling points and high ionization energies. To some extent, xenon also belongs to this class (MD of 0.25).

By dividing class 1.1, a quite large class (1.1.2) is obtained. This class contains somewhat lighter elements, with lower boiling points (under 1600°C): Li, Na [group 1 (IA)], all the elements of group 2 (IIA) of the periodic table (except beryllium), Tl from group 3 (IIIB), As, Sb, Bi from group 15 (VA), Te [group 16 (VIA)], Zn [group 12(IIB)], and Eu and Yb (the lanthanides with relatively stable configurations of the f-subshell, f^7 and f^{14}). From outside this class, some elements that have significant MDs for it are Cd, Pb, Tm, Se, Rb, and Cs.

The other class (1.1.1) includes elements from group 13 (IIIA) (Ga, In), group 14 (IVA) (Sn, Pb), silver, and the lanthanides Sm and Tm. It is a rather heterogeneous class, its elements having quite different properties and relatively small MDs, from 0.54 (Ga) to 0.26 (Tm). Also, related to this class are Ba, Bi, and Mn.

Now, passing to class 2, the lighter elements of the first and second series of transition metals (class 2.1) are separated from the heavier ones, with higher melting and boiling points (class 2.2). Class 2.1 contains, besides all the transition metals of period 4, also most of those of period 5, lanthanum, and the majority of lanthanides, Th, U, and all the main group elements of class 2, except C. Class 2.2 includes transition metals of the period 5 and 6 as well as carbon.

To continue, class 2.1 is separated from the set of elements with high boiling points (3300–4000°C) (class 2.1.2). From outside this class a few elements have substantial MDs to it: La (0.42), Ce (0.38), B (0.29), Cr (0.27), Pt (0.26), Fe, Rh, and Pr (0.22$\cdots$0.24). The elements of class 2.1.1 are further subdivided into two classes that are rather less differentiated: the first one (class 2.1.1.1) contains Cu, Au, and La, and the early lanthanides (Ce, Pr,

Nd) as well as Al and Ge from the main group of the periodic table. The element Gd has a MD for this class (0.41) almost as high as to its own class (2.1.1.2): Be and Ag also have quite large MDs (nearly 0.20). Class 2.1.1.2 contains Be, B, and Si, some transition metals of the first series, Y, and the heavier lanthanides. From outside this class, significant MDs occur for Cu, Ag, Al, Tm, and Sm.

From class 2.2 is separated a class (2.2.2) that includes the elements with the highest T_f and T_b and very high densities (excepting carbon). The presence of carbon together with molybdenum reminds us that molybdenite (MoS_2) was considered for a long time to be graphite. The elements Pd and Th also have MDs for this class of ~ 0.15. The other class (2.2.1) is divided into two classes, their differences being again mainly the melting and boiling points; the more refractory metals (Ru, Hf, Ir) belong to the class 2.2.1.1 (Mo and C also have MDs of ~ 0.15), while Rh and Pt form the class 2.2.1.2 (Pd and Th have MDs for this class of ~ 0.14–0.16).

It is easy to notice that the criteria of melting and boiling points are those that dominate this classification. However, it appears that chemical properties are quite significant, as well.

In order to ensure a more uniform participation of various characteristics, we may use normalization (autoscaling) of the data. The classification based on the same 10 characteristics but normalized—a procedure that prevents certain properties, expressed by larger numerical values, to prevail– yields just four classes.

The final classification hierarchy including the membership degrees of the elements to the fuzzy sets of the final fuzzy partition is presented in Table 2.

The first separation is, as a matter of fact, the same as the one above. Only Be, Mn, and Al are moved into the class of main group elements, while Ag, Sm, and Tm are passed to the class of transition elements.

Thus, the separation of main group elements and transition metals is more distinct here. Together with the main group elements are left Zn, Cd, and Hg (with complete d subshells), Mn (d^5 configuration), and Eu and Yb (without electrons in the $5d$ subshell and stable configurations of the $4f$ subshell). On the other hand, with the transition metals remain only C, Si, Ge, and B.

The elements from the main groups are divided next, as in the former classification, into metals (to which xenon joins also) and nonmetals, that is, again a more distinct separation than that without normalization. Finally, the transition elements are divided into two classes: First, the more dense elements from the period 5 (Nb–Pd) and 6 (Hf–Au), together with Th and U, as well as the nonmetallic refractory elements from the main groups (B, C, Si); and, second, the early transition elements and the lanthanides, together with Ge. In this way, the classification is more like that given by chemical intuition but less detailed; we may say that by normalization a loss of information arises.

Table 2 Membership Degrees to the Classes of the Final Partition Produced with 10 Normalized Physical Properties

Element	1.1	1.2	2.1	2.2	Element	1.1	1.2	2.1	2.2
H	0.25	0.31	0.23	0.20	Tc	0.07	0.04	0.08	0.81
He	0.26	0.37	0.22	0.16	Ru	0.12	0.07	0.08	0.73
Li	0.40	0.32	0.19	0.09	Rh	0.09	0.05	0.05	0.80
Be	0.30	0.30	0.25	0.16	Pd	0.08	0.04	0.26	0.61
B	0.22	0.19	0.27	0.32	Ag	0.30	0.07	0.52	0.11
C	0.20	0.18	0.22	0.40	Cd	0.65	0.19	0.12	0.03
N	0.14	0.58	0.17	0.11	In	0.58	0.10	0.26	0.06
O	0.16	0.54	0.18	0.13	Sn	0.52	0.09	0.32	0.06
F	0.18	0.47	0.19	0.15	Sb	0.43	0.14	0.34	0.09
Ne	0.25	0.40	0.21	0.14	Te	0.46	0.27	0.20	0.07
Na	0.51	0.25	0.18	0.06	I	0.28	0.53	0.13	0.06
Mg	0.57	0.27	0.12	0.04	Xe	0.40	0.32	0.20	0.09
Al	0.46	0.20	0.25	0.09	Cs	0.40	0.19	0.29	0.12
Si	0.24	0.20	0.28	0.29	Ba	0.44	0.11	0.35	0.09
P	0.06	0.79	0.10	0.05	La	0.26	0.06	0.56	0.12
S	0.08	0.74	0.12	0.06	Ce	0.28	0.07	0.54	0.12
Cl	0.11	0.64	0.15	0.09	Pr	0.29	0.06	0.57	0.09
Ar	0.29	0.42	0.19	0.10	Nd	0.29	0.05	0.59	0.07
K	0.45	0.21	0.25	0.09	Sm	0.39	0.06	0.49	0.06
Ca	0.54	0.14	0.25	0.07	Eu	0.44	0.09	0.39	0.08
Sc	0.29	0.09	0.48	0.15	Gd	0.16	0.03	0.71	0.10
Ti	0.18	0.07	0.48	0.27	Tb	0.14	0.03	0.74	0.09
V	0.14	0.06	0.40	0.40	Dy	0.16	0.04	0.70	0.11
Cr	0.21	0.09	0.47	0.24	Ho	0.14	0.03	0.71	0.12
Mn	0.38	0.13	0.38	0.12	Er	0.13	0.03	0.69	0.14
Fe	0.17	0.08	0.45	0.30	Tm	0.20	0.05	0.61	0.14
Co	0.15	0.07	0.44	0.34	Yb	0.46	0.08	0.39	0.07
Ni	0.15	0.07	0.44	0.34	Lu	0.10	0.03	0.55	0.31
Cu	0.27	0.11	0.43	0.18	Hf	0.12	0.06	0.19	0.62
Zn	0.58	0.38	0.04	0.01	Ta	0.15	0.09	0.17	0.59
Ga	0.61	0.17	0.17	0.05	W	0.16	0.11	0.18	0.55
Ge	0.22	0.13	0.36	0.29	Re	0.16	0.11	0.17	0.56
As	0.32	0.31	0.24	0.13	Os	0.16	0.11	0.17	0.55
Se	0.15	0.72	0.09	0.04	Ir	0.16	0.11	0.17	0.56
Br	0.11	0.68	0.13	0.07	Pt	0.15	0.10	0.19	0.56
Kr	0.33	0.39	0.18	0.09	Au	0.19	0.12	0.31	0.38
Rb	0.44	0.19	0.27	0.10	Ag	0.37	0.27	0.25	0.12
Sr	0.50	0.12	0.30	0.08	Tl	0.38	0.15	0.35	0.12
Y	0.22	0.05	0.62	0.11	Pb	0.37	0.15	0.36	0.12
Zr	0.10	0.04	0.51	0.35	Bi	0.37	0.15	0.36	0.12
Nb	0.10	0.05	0.20	0.66	Th	0.14	0.06	0.36	0.44
Mo	0.12	0.07	0.12	0.69	U	0.18	0.09	0.33	0.40

HIERARCHICAL FUZZY CLASSIFICATION OF CHEMICAL ELEMENTS BASED ON TEN PHYSICAL, CHEMICAL, AND STRUCTURAL PROPERTIES

In order to pass beyond the limits of this "physical" classification of elements, we tried to base the classification on some chemical properties and features of electronic structure. We have thus kept only five physical properties density, ρ (**1**), melting point, T_f (**2**), boiling point, T_b (**3**), ionization energy, E_i (**4**), covalent radius, r (**5**), and, in exchange, five other chemical characteristics were added: two indices to describe the electron configuration, two others to describe the oxidation states, and the formation free energy for chlorides. For the characterization of electron configuration, and oxidation states we used values having the same number of digits. For the electron configuration, the first index, *conf* (**6**), is built as follows: The first digit gives the number of electrons in the last (outermost) shell ($1 \cdots 8$), the next two digits give the number of electrons in the next to last shell ($0 \cdots 18$), and the final two decimal digits give the number of electrons in the second to last shells ($0 \cdots 32$). For example, for chromium this index is 113.08. The second index, *spdf* (**7**), of electron configuration has as its first digit the number of electron shells in the atom ($1 \cdots 7$), the next two digits give the number of d electrons in the next to last shell ($1 \cdots 10$), and the two decimal digits give the number of f electrons in the second to last shell ($1 \cdots 14$). For example, for Cr this index is 405.00 and for Gd is 601.07.

The index for positive oxidation states, *os*+ (**8**) contains the digits that show these states, in order of their importance, the most usual one being the most significant digit. Similarly, in order to describe the negative oxidation states, *os*− (**9**), a negative number, was used, whose digits represent the oxidation states in decreasing order of their importance.

In order to characterize the chemical reactivity of an element, the formation free energy (ΔF_{Cl}) of its chloride (**10**) was taken into account. The values were computed for the standard ambient temperature and pressure (298 K, 1 bar) in kilocalories per mole of Cl.

The classification hierarchy produced by using the 10 properties discussed above is shown in Figure 5.

It is interesting to see that the first separation into two classes is the same as that for the classification based on the 10 physical properties: class 1 contains, as a whole, elements of the main groups of the periodic system and class 2 elements of the secondary groups and most of the lanthanides. Silver is situated just at the boundary of the two classes (membership degree, MD, of 0.50 to class 1). The lanthanides with $4f^6$ and $4f^{13}$ configurations (Sm, Tm) also have small MDs for class 1 (0.63 and 0.57). Other elements having MDs of < 0.7 for this class are Sn and Ga. On the other hand, the MD of Al for class 2 is small (0.53). The element Mn also comes near class 1 (MD of 0.44), due to

Block 1

```
            H He
Li            N  O  F  Ne
Na Mg              P  S  Cl Ar
K  Ca    Zn Ga    As Se Br Kr
Rb Sr Ag Cd In Sn Sb Te I  Xe
Cs Ba    Hg Tl Pb Bi
Sm Eu Tm Yb
```

Block 2

```
Be                          B  C
                               Al Si
Sc Ti V  Cr Mn Fe Co Ni Cu  Ge
Y  Zr Nb Mo Tc Ru Rh Pd
La Hf Ta W  Re Os Ir  Pt Au
Ce Pr Nd Gd Tb Dy Ho Er Lu  Th U
```

Block 11

```
Li
Na Mg
Ca    Zn Ga  As
Sr Ag In Sn Sb Te
Ba    Tl Pb Bi
Sm Eu Tm Yb
```

Block 12

```
H He
N O F Ne
P S Cl Ar
K       Se Br Kr
Rb Cd      I Xe
Cs Hg
```

Block 21

```
Be                       B
                            Al Si
Sc Ti V Cr Mn Fe Co Ni Cu Ge
Y Zr Nb  Tc       Pd
La             Au
Ce Pr Nd Gd Tb Dy Ho Er Lu Th U
```

Block 22

```
C
          Mo  Ru Rh
Hf Ta W Re  Os  Ir Pt
```

Block 111

```
Li
Na Mg
Zn As
Cd Sb Te
Tl
```

Block 112

```
Ca    Ga
Sr Ag In Sn
Ba       Pb
Bi
Sm Eu Tm Yb
```

Block 121

```
P S
K
Rb
I
Cs Hg
```

Block 122

```
H He
N O F Ne
Cl Ar
Br Kr
Xe
```

Block 211

```
Be
Sc Cr Mn Fe Co Ni
Y
La
Ce Pr Nd Gd Tb Dy Ho Er
```

Block 212

```
Ti V
Zr Nb Tc Pd
```

Block 221

```
Ru Rh
Ir
Pt
Hf
```

Block 222

```
C
Mo    W
Ta
Re Os
```

Block 2111

```
Al
Cu Ge
Au La
Ce Pr Nd
Gd
```

Block 2112

```
Si
Sc Cr Mn Fe Co Ni
Y
Tb Dy Ho Er
```

Block 2121

```
Ti
Lu
U
```

Block 2122

```
V
Zr Nb Tc
Pd Th
```

Block 2211

```
Ru
Ir
Hf
```

Block 2212

```
Rh
Pt
```

Block 1221

```
H He
N Cl
```

Block 1222

```
O F Ne
Ar
Br Kr
Xe
```

Figure 5 The classification of the elements produced with nonnormalized physical, chemical and structural characteristics (from Ref. 32).

its relatively stable electron configuration $4s^2 3d.^5$ As an average, the elements of class 1 have lower densities and clearly lower melting and boiling points, more electrons in the outermost shell (the elements in class 2 generally have two such electrons), an average of four shells, against five in class 2, lower positive oxidation states and a greater trend to negative oxidation states. The next division of class 1 is again mostly the same as for the 10 physical properties classification (class 1.1, metals; class 1.2, nonmetals plus K, Rb, Cs, and Hg). The single difference is the position of cadmium in class 1.1 (with zinc) and not in the class 1.2 (with mercury).

The alkali metals as well as selenium lie near the boundary between the classes. As an average, class 1.2 contains lighter elements having high ionization energies, more electrons in the last shell, a stronger trend toward negative oxidation states, and a smaller affinity for chlorine. In class 1.1, but near the boundary of class 1.2, are situated As, Cd, and Na.

Class 1.2 is further divided in the same way as for the 10 physical properties classification. Class 1.2.2 includes gaseous elements, with low densities, high ionization energies, smaller atomic radii, more electrons in the outermost shell, and weaker trends to positive oxidation states and to combinination with chlorine. Chlorine itself is situated near the boundary of the class 1.2.1. The MD for this class is mainly determined by the physical properties. Typical elements for this class are S and Se. The elements Cl, As, and Na also have significant MDs for this class.

While class 1.2.1 is not further divided here, class 1.2.2 is split up in a different manner than the classification based on physical properties: on the one hand, H, He, N, and Cl (1.2.2.1) and, on the other hand, the noble gases from Ne to Xe, F, Br, and O (class 1.2.2.2). The former class generally contains lighter elements, with lower melting and boiling points (except for Cl, which is placed near the boundary of the class), with less electrons in the outermost shell and a marked trend for combinations of positive oxidation states (the elements in class 1.2.2.2 have almost no positive states). From class 1.2.2.2, oxygen is the nearest to class 1.2.2.1. The separation between the two classes is not a clear one, except for the noble gases from Ne to Xe.

Class 1.1 is divided as for the 10 physical characteristics classification, with the difference that Ca, Sr, Ba, Bi, Eu, and Yb join with Ga, In, Sn, Pb, Ag, Sm, and Tm. Therefore, class 1.1.1 includes only main-group elements and some elements of group 12 (IIB) (Zn, Cd). The elements Bi, Sb, and Sr lie near the boundary of the two classes. Significant MDs for class 1.1.1 also exist for the other elements of group 1 (IA) (K, Rb) and group 2 (IIA) (Ca, Sr) as well as for As, Os, Se, Yb, Eu, In, Ga, and Sn. The elements Tl, Al, Mn, Li, Cu, As, Ge, and Mg belong to some extent to class 1.1.2.

Class 2 is also divided as in the previous classification. In class 2.2, the reactivity of the elements toward chlorine is a little below average. Among the elements of class 2, Pt and Rh are close to the boundary of class 2.1, while Nb, Pd, and Th of this latter class also have significant MDs for this class.

The next separation of class 2.2 does not bring anything new regarding the "physical" classification. The elements of class 2.2.2 show positive oxidation states higher on average than those of the elements of class 2.2.1. Near the border of the two classes lie C and Ir, followed by Mo and Hf.

The last division of class 2.2.1 is also identical to that obtained by the "physical" classification. The elements of class 2.2.1.1 (Ru, Hf, and Ir) have a higher affinity toward chlorine than those of class 2.2.1.2 (Rh and Pt). To the former class are related to some extent Mo and C and to the latter Pd, Th, and Nb.

The division of class 2.1 is again the same as before. The elements of class 2.1.2 are heavier, have higher melting and boiling points, and also have slightly higher positive oxidation states. Unlike in the previous classification, three elements from this class (Ti, Lu, and U) are separated (class 2.1.2.1) from the other six (Zr, V, Nb, Tc, Pd, and Th), on the basis of lower melting and boiling points, lower ionization energies, greater affinities with chlorine and positive oxidation states (with an average of four against five for the other class). Actually, U on one side and Pd on the other are near the boundary between the classes, while Nb, Th, and Tc are also attracted to a certain extent to class 2.1.2.1. Other elements, as well, have significant MDs for this class: La, Ce, Pr, Cr, and Fe, while elements that belong somewhat to class 2.1.2.2 are Pt, Ti, Lu, Cr, La, Ce, and Rh.

Class 2.1.1 divides as in the previous classification, with the single exception of Gd, which joins class 2.1.1.1 (together with Ce, Pr, and Nd). The two classes are only a little differentiated as far as properties are concerned. Both Cu and Mn are situated at the border of the two classes, but there are many other elements having significant MDs for both classes. For example, Si, Tb, Fe, Cr, Dy, Sn, Er, and Sm belong in some measure to class 2.1.1.1 and Gd, Ge, Ag, Tm, Al, and Sm to belong class 2.1.1.2.

The classification hierarchy produced by using the same 10 properties, only normalized, is presented in Figure 6. The first class includes all the non-metals as well as Be, Sb (with a MD of 0.57), and Ge; these three elements and the nonmetals B, C, Si, As, Te, and Xe add to those of the "physical" classification. From the other elements, near the boundary of the two classes are Zn (MD of 0.50) and Al (MD of 0.47).

Class 2, with the metals, is roughly speaking, further divided, into main group elements (class 2.2) and transition metals (2.1). Aluminum is missing, from class 2.2, but is quite near the border of the class. This set is also in the other classification of elements of group 12 (IIB) (Zn, Cd, and Hg), which is reasonable from the point of view of electron configuration, as well as elements of group 3 (IIIB) (Sc, Y, La), the lanthanides, and thorium.

Uranium is situated in the other class, but near the border. Actually, the elements of group 3 (IIIB) are chemically similar to the alkaline earth metals, and so are their compounds. It is also interesting that Zr is included in this class (even if near the border). Indeed, its behavior shows some analogies to

```
 1    H He                              Li                          2
      Be B C N O F Ne                  Na Mg                                    Al
               Si P  S Cl Ar                K  Ca  Sc Ti V Cr Mn Fe Co Ni Cu Zn Ga
               Ge As Se Br Kr               Rb  Sr  Y Zr Nb Mo Tc Ru Rh Pd  Ag Cd  In Sn
                    Sb Te I  Xe             Cs  Ba  La Hf Ta W  Re Os Ir Pt  Au Hg Tl Pb Bi
                                            Ce Pr Nd Sm Eu Gd Tb Dy Ho Er Tm Yb Lu Th U

                                    21               Al           Li               22
                           Ti V Cr  Mn Fe Co Ni Cu        Na Mg
                           Nb Mo Tc  Ru Rh Pd Ag           K  Ca Sc      Zn Ga
                           Hf Ta W  Re Os Ir Pt  Au        Rb Sr  Y Zr Cd In Sn
                                                           Cs Ba La      Hg Tl  Pb Bi
                                                           Ce----Lu Th U
```

Figure 6 The classification of the elements produced with normalized physical, chemical, and structural characteristics (from Ref. 32).

those of the main group elements. The compound ZrO_2 forms solid solutions with CaO (used as a solid electrolyte), Zr shows some similarities to Be, and so on. The other *d*-block elements and U form the class 2.1. Consequently, the introduction of chemical properties has little influence upon classification, as their effect was indirectly contained within the physical properties taken into account at the beginning.

FUZZY HIERARCHICAL CROSS-CLASSIFICATION OF CHEMICAL ELEMENTS BASED ON TEN PHYSICAL PROPERTIES

The classification hierarchy produced in this way for the 84 chemical elements using characteristics (the 10 physical properties) without data normalization is presented in Figure 7. The first partitioning of elements in classes 1 and 2 is exactly the same as in the analogous classification (Figure 4), and so are the partitioning of the second level, into classes 1.1, 1.2 and 2.1, 2.2. What is new is the partitioning of characteristics. Class 1 contains eight of the physical properties, while class 2, which includes mostly elements in the secondary groups of the periodic, table, is characterized mainly by the melting and boiling point. Their next division is into lighter transition metals (class 2.1) and heavier ones (class 2.2), and is associated with the separation by the melting point, for the former class, and the boiling point, for the latter. There are no more subsequent divisions of the classes 2.1 and 2.2, while the analogous classification above produced five clusters here.

The characteristic associated with class 1.1, comprised mostly of main group metals, is the ionization energy, but the boiling point and the atomic mass also have rather important MDs. Unlike the analogous classification above, the cross-clustering does not further divide this class, the only larger division being for class 1.2. Classes 1.2.1 and 1.2.2 are again the same as

Figure 7 The classification of the elements and characteristics produced with 10 nonnormalized physical properties (from Ref. 33).

above. The elements of class 1.2.1, metals and nonmetals that are solid at room temperature, have as their main characteristic the atomic mass, but the boiling point also carries some weight. This class is not further divided, but neither are the typical gaseous nonmetals of the class 1.2.2. As in Figure 1, Cl, Br, and Xe are distinctly grouped (class 1.2.2.1), and their characteristic is the vaporization enthalpy, while from class 1.2.2.2 the lighter

noble gases He and Ne (class 1.2.2.2.1) are separated from the other elements. These last two classes are each subject to a further division. One new class (1.2.2.2.1.1) includes N, O, and H. Their MDs to the class to which they belong (class 1.2.2.2.1.2) are much smaller than that of Ar; their characteristic is the electronegativity. On the other hand, He and Ne are each separated to a different class. For helium, the characteristic is the fusion enthalpy and the specific heat capacity, while for neon, it is the covalent radius, and to some extent the specific heat capacity and fusion enthalpy.

The hierarchical cross-clustering using the same 10 physical properties, but with data normalization, gave a very similar partition as that obtained with the 10 normalized physical characteristics. Also, the membership degrees of the elements in the fuzzy sets of the fuzzy partition were similar.

The main-group elements of class 1 are classified by the following properties: atomic mass, density, melting and boiling points, vaporization, and fusion enthalpy. The other properties: electronegativity, specific heat capacity, ionization energy, and covalent radius belong to class 2, the transitional metals. In the final cluster 1.1, containing mostly the main-group metals, we find the properties density, atomic mass, and, with a much smaller MD, the fusion enthalpy and the melting and boiling points. An important MD of this class is the fusion enthalpy. As for class 2.1 (including the transition elements of period 4 and some of period 5, in addition to the lanthanides), class 2.1's characteristics are the electronegativity, ionization energy, and specific heat capacity, all three having approximately the same MD. The last class (class 2.2) containing the transition metals from periods 6 and 5, Th, U, together with B, C, and Si, have as their only characteristic the covalent radius. The MDs over 0.10 to this class also include the atomic mass and specific heat capacity.

The classification hierarchy produced with the use of 10 physical, chemical, and structural characteristics is presented in Figure 8.

The first partitioning in classes 1 and 2 is the same as in the nonnormalized classification on the basis of 10 physical, chemical, and structural characteristics, except for aluminum, which is classified with the main group elements; Tm and Cu are near the boundary between classes. All the characteristics, except the boiling point, are assigned to this class; only the melting point has a lower MD, being at the limit of the class.

The next partitioning of class 1 exhibits, only small differences from the previous one; Na passes to class 1.2, with the other alkaline metals, and Cd also moves to class 1.2, while Al belongs to class 1.1. The element Tm is at the boundary between these classes. The characteristics attributed to class 1.1 are the density, the covalent radius, the chloride formation free energy, and the index of negative oxidation states. The melting point is included in class 1.2, but near the classes boundary.

The division of class 1.1 is different from that of the classification in Figure 3. Lithium, the second group elements (Mg–Ba), those of group 13 (IIIA)

1

```
                   H  He
                   N  O  F  Ne
Li                 Al    P  S  Cl Ar
Na Mg   Al   Zn Ga      As Se Br Kr
K  Ca   Zn Ga   Cd In Sn Sb Te I Xe
Rb Sr Ag   Cd In Sn Sb Te I Xe
Cs Ba   Hg Tl Pb Bi
        Sm Eu Tm Yb
        1 2 4 5 6 7 8 9 10
```

2

```
Be              2          B C
                Si
Sc Ti V Cr Mn Fe Co Ni Cu   Ge
Y Zr Nb Mo Tc Ru Rh Pd
La Hf Ta W Re Os Ir Pt Au
Ce Pr Nd Gd Tb Dy Ho Er Lu Th U
                3
```

11

```
      Li      11
Mg    Al      As
Ca    Zn Ga   Sn Sb Te
Sr Ag In      Pb Bi
Ba    Tl      Sm Eu Tm Yb
Sm Eu Tm Yb
      1 5 9 10
```

12

```
      12           H He
                   N O F Ne
          Na       P S Cl Ar
          K        Se Br Kr
          Rb Cd    I  Xe
          Cs Hg
          2 4 6 7 8
```

112

```
112
As
Sn Sb Te
Pb Bi
Sm Eu Tm Yb
9 10
```

121   **122**

```
121   H                122   N  Ne
      He
Na    O F                    P S Cl Ar
K                            Se Br Kr
Rb Cd                        I  Xe
Cs Hg
2 4 7 8                       6
```

1211   **1212**

```
1211  H        1212  O F
      He
Na
K              4 7
Rb Cd
Cs Hg
2 8
```

Figure 8 The classification of the elements and characteristics produced with 10 nonnormalized physical, chemical, and structural properties (from Ref. 33).

(Al–Tl), and Ag and Zn, are included in class 1.1.1, while in class 1.1.2 we find elements of groups 14 (IVA), 15 (VA), and 16 (VIA), together with the four lanthanides (Sm, Eu, Tm, Yb). The separation is rather clear-cut. Elements with significant MDs to class 1.1.1 include Cd, Cu, Na, Pb, and K and to class 1.1.2 are Se, Mn, Ge, and Si. The characteristics of class 1.1.1 are the density and covalent radius; smaller MDs are found for the ionization energy and the negative oxidation states.

The chloride formation free energy and the index of negative oxidation states belong to class 1.1.2. The division of class 1.2 is also different from the previous: H, He, O, and F pass from class 1.2.2 to class 1.2.1, joining the alkaline metals (Na–Cs), Cd, and Hg, while in exchange P, S, Se, and I pass from class 1.2.1 to class 1.2.2, joining Cl, Br, and the noble gases Ne–Kr. Other elements with important MDs to this last class are Hg, As, Cd, Te, and F. The characteristic of this class is the electron configuration index for the outer shell; another important MD is also obtained for the index for s, p, d, and f subshells.

Class 1.2.1 is divided by the separation of the most electronegative elements (O and F), forming class 1.2.1.1; Ne, Ar, and Hg also have significant MDs for this class. Their characteristics are the ionization energy and the number of s, p, d, and f electrons in the outer shells, both with relatively small MDs. Among the metals of class 1.2.1.1, Cd and Hg are at the border between the two classes.

This class also has important MDs for Li and Zn. Here we find two characteristics: the index of positive oxidation states and the melting point (but with a much smaller MD). Unlike the classification in Figure 6, class 2 is not divided further; Tm, Sm, Al, Ag, Sn, and Sb are also related to this class. The characteristic here is the boiling point, but the melting point also has an MD of 0.49. In this case, the normalized cross-classification leads to a more profound division that is quite different from the previous ones. The classification hierarchy produced is represented in Figure 9. The first partitioning brings together in class 1 the main group elements: H, He; groups 1, 2, and 13 of the periodic table (entirely); some elements of groups 14 (IVA)–17 (VIIA), and the noble gases (except for Xe). Both Zn and Cd are joined, to these as usual, but also Cu and Ag [group 11 (IB)] and Ni, as well as the three lanthanides (Sm, Eu, and Yb, i.e., without Tm) are also included. Their characteristics are density, melting and boiling points, the s, p, d, and f configuration, and the oxidation states (positive and negative). Class 2 includes most of the d- and f-block elements, but also some p-block elements (from the groups 14 (IVA)–18 (VIIIA)). Near the border of the two classes lie Co, Se, Y, and Tl. The characteristics here are ionization energy, covalent radius, the first index of electron configuration, and the chloride formation free energy.

Furthermore, similar to other classifications, are the typical nonmetals and noble gases He–Kr (class 1.2), which are separated from class 1, on the one hand, and the metals together with some refractory nonmetals (B, C, Si)

Figure 9 — classification table

1
H He
B C N O F Ne
Li Be
Na Mg   Al Si   P S   Ar
K Ca Sc Ni Cu Zn Ga Ge As Se Br Kr
Rb Sr   Ag Cd In
Cs Ba   Tl
Sm Eu Yb
1 2 3 7 8 9

2
Cl
Se
Ti V Cr Mn Fe Co
Y Zr Nb Mo Tc Ru Rh Pd   Sn Sb Te I Xe
La Hf Ta W Re Os Ir Pt Au Hg Pb Bi
Ce Pr Nd Gd Tb Dy Ho Er Tm Lu
Th U
4 5 6 10

11
Li Be   B C
Na Mg   Al Si
K Ca Sc Ni Cu Zn Ga Ge As
Rb Sr   Ag Cd In
Cs Ba   Tl
Sm Eu Tm
1 8

12
H He
N O F Ne
P S   Ar
Br Kr
2 3 7 9

21
Ti V Cr Mn Fe Co
Y Zr   Pd
La
Ce Pr Nd Gd Tb Dy Ho Er Tm
4 6

22
Nb Mo Tc Ru Rh
Hf Ta W Re Os Ir Pt Au
Lu Th U
5 10

111 C
Sc Ni Cu
Sr   Ag In
Ba   Tl
Sm Eu Yb
1

112
Li Be   B
Na Mg   Al Si
K Ca Zn Ga Ge As
Rb Cd
Cs
8

121
N
P S
237

122
H He
O F Ne
Ar
Br Kr
9

211
Cl
Se
Sb Te I Xe
Hg Pb Bi
4

212
Ti V Cr Mn Fe Co
Y Zr   Pd Sn
La
Ce Pr Nd Gd Tb Dy Ho Er Tm
6

221
Nb
Hf Ta
Lu Th U
5

222
Mo Tc Ru Rh
W Re Os Ir Pt Au
10

1211
N
2

1212
P S
37

Figure 9 The classification of the elements and characteristics produced with 10 normalized physical, chemical, and structural properties (from Ref. 33).

on the other hand, which are class 1.1. In class 1.1 the characteristics are density and positive oxidation states. From the partitioning of this latter class results a class (class 1.1.2) that includes the alkaline metals (Li–Cs), the first three elements of groups 2 (IIA) and 13 (IIIA), Si, Ge, As, as well as Zn and Cd; in other words, exclusively main-group elements and elements of group 12 (IIB). Their characteristic is the positive oxidation state index. The other class (class 1.1.1) contains not only some elements of the main groups (Sr, Ba, In, Tl, and C) but also Sc, Ni, Cu, and Ag, and the three lanthanides, with density as their characteristic. Other elements with significant MDs to class 1.1.1 are B, Co, Cs, Y, Fe, Cd, Ca, Ga, La, Ti, Pr, and Nd and to class 1.1.2 are C, Sr, Se, and S. The last four are main group elements.

The nonmetals, class 1.2, are more profoundly divided. Thus N, P, and S are categorized separately (class 1.2.1) so that nitrogen is then classified alone as a class (class 1.2.1.1), having the melting point as its characteristic. To the former class, O and P are also related, with small MDs. For the latter class (class 1.2.1.1) of P and S (the only solid nonmetals among those of class 1.2), some external elements with significant MDs are As, Br, Se, and S, and all solid nonmetals (except for the liquid bromine). Their characteristics are the boiling point and the configuration index for s, p, d, and f electrons in the outer shells. Class 1.2.2 contains gaseous nonmetals from groups 16 (VIA)–18 (VIIIA) and also H and Br; smaller MDs to this class also exist for N, Li, Na, Si, and Xe. Here the characteristic that discriminates is the negative oxidation state index.

All the p-block elements are grouped in class 2.1 from class 2 (from the main groups 14 (IVA)–18 (VIIIA)), the d-block elements of period 4 (Ti–Co), and some with lower melting and boiling points from the next periods as well as the early lanthanides that are left (except for Lu). The properties included here are the energy of ionization and the first index of electronic configuration. The remaining class 2.2 elements are the heavy d-block elements of periods 5 and 6: Nb–Rh and Hf–Au together with Lu, Th, and U. Lutetium lies, near the boundary between the two classes. Here the properties are the covalent radius and the chloride formation free energy.

The elements of the main groups (except for Sn, which lies at the border of the two classes) with Hg (class 2.1.1) and the transition metals (class 2.1.2) are separated from class 2.1. Elements from the outside with high MDs for class 2.1.1 are Sn, Kr, and C and for class 2.1.2 are Ti, Ni, Lu, Pb, Sm, Hg, Eu, Ag, In, Nb, Yb, and Rh. The characteristics belonging there are the ionization energy (class 2.1.1) and the index of occupation of the outer electronic shell (class 2.1.2).

Class 2.2 is divided into two very distinct groups. The first one (class 2.2.1) comprises Nb, Hf, Ta, Lu, Th, and U; related to them in some measure are several lanthanides (Er, Gd, Dy, Ho, Nd, Tm, Ce, and Pr) as well as V, Cr, and Zr. Their characteristic is the covalent radius. The heavy d-block elements from periods 5 and 6: Mo to Rh and W to Au are included in class 2.2.2.

Elements with significant MDs to this class are Pd and Zr. The characteristic of this class is the chloride formation free energy.

It is interesting to remark that, by their form with successive ramifications, these classifications remind us of the "genealogical table" of elements proposed by Thierry William Preyer (1841–1897), who conceived a system, based on a genetical theory of elemental origin.[55] However, the resemblance is purely formal.

FUZZY HIERARCHICAL CHARACTERISTICS CLUSTERING

In order to develop the classifications presented in this section, we will apply the fuzzy divisive hierarchical clustering (FDHiC) procedure described in the theoretical section[32,33] to different characteristic sets considered here. The hierarchical procedure obtained in this way is called fuzzy hierarchical characteristics clustering (FHiChC).

The characteristics clustering with 10 physical properties for the 84 elements gave essentially the same results as before, even if the succession of the splitting was changed a little. The membership degrees of the characteristics to the clusters of the final partition, with data normalization, are given in Table 3. To cluster 1, of atomic mass (A), the density (ρ) also has a significant membership degree (MD = 0.25). For the other properties and clusters, the MDs are near 1 and 0. A similar clustering procedure applied to the 10 physical, structural, and chemical characteristics gave similar results. The classification hierarchy produced with nonnormalized data and the membership degrees of the characteristics to the clusters of the final fuzzy partition are shown in Table 4.

In the different steps of the clustering process the melting point (**2**), the boiling point (**3**), and the density (**1**) are successively separated. The two other physical properties (ionization energy and covalent radius) and all the

Table 3 Membership Degrees of the 10 Physical Properties to the Clusters of the Final Fuzzy Partition, with Data Normalization

Property		1	2.1	2.2.1	2.2.2
A	(1)	**0.99**	0.00	0.00	0.00
ρ	(2)	0.25	**0.75**	0.00	0.00
T_f	(3)	0.01	0.02	**0.97**	0.00
T_b	(4)	0.01	0.00	0.00	**0.99**
χ	(5)	0.01	0.00	0.00	**0.99**
ΔH_v	(6)	0.01	0.00	0.00	**0.99**
ΔH_f	(7)	0.01	0.00	0.00	**0.99**
C_s	(8)	0.01	0.00	0.00	**0.99**
E_i	(9)	0.01	0.00	0.00	**0.99**
r	(10)	0.01	0.00	0.00	**0.99**

Table 4 Membership Degrees of the 10 Physical, Chemical, and Structural Properties of the Clusters of the Final Fuzzy Partition, without and with Data Normalization

Property		Without Data Normalization				With Data Normalization			
		1.1	1.2.1	1.2.2	2	1	2.1	2.2.1	2.2.2
ρ	(1)	0.22	**0.78**	0.00	0.00	**0.99**	0.00	0.00	0.00
T_f	(2)	0.00	0.00	0.00	**1.00**	0.28	**0.72**	0.00	0.00
T_b	(3)	**1.00**	0.00	0.00	0.00	0.02	0.04	**0.94**	0.00
E_i	(4)	0.00	0.00	**1.00**	0.00	0.00	0.00	0.00	**1.00**
r	(5)	0.00	0.00	**1.00**	0.00	0.00	0.00	0.00	**1.00**
conf	(6)	0.00	0.00	**1.00**	0.00	0.00	0.00	0.00	**1.00**
spdf	(7)	0.00	0.00	**1.00**	0.00	0.00	0.00	0.00	**1.00**
os+	(8)	0.00	0.00	**1.00**	0.00	0.00	0.00	0.00	**1.00**
os−	(9)	0.00	0.00	**1.00**	0.00	0.00	0.00	0.00	**1.00**
ΔF_{Cl}	(10)	0.00	0.00	**1.00**	0.00	0.00	0.00	0.00	**1.00**

structural and chemical characteristics remain unsplit. Once again, with the exception of the density, only extreme MDs are obtained, The density is classified with a MD of 0.22 to the class 1.1 of the boiling point.

The data normalization does not change the overall pattern of the clustering. The classification hierarchy differs only by the order of successive separations of the characteristics, the first now being the density (**1**), then the melting point (**2**), and the boiling point (**3**) and without any splitting for the other seven characteristics to the final clusters. As is also apparent from Table 4, most characteristics have values near unity and zero, except for the melting point, with an MD of 0.28 to the class 1 (of the density).

FUZZY HORIZONTAL CHARACTERISTICS CLUSTERING

In order to develop the classification presented in this section, we applied the well-known Fuzzy n-Means (FNM) algorithm.[56] The classification procedure obtained in this way is called fuzzy horizontal characteristics clustering (FHoChC).

The characteristic clustering for the 10 physical properties, without data normalization and with a predefined number of five classes, distribute the characteristics in three clusters only; the other two remain empty. Cluster 1 contains the atomic mass (**1**), with an MD of 0.33; this characteristic appears with equal MDs (0.33) to the two empty clusters, 3 and 4. In cluster 2, we find the density (MD = 1), while cluster 5 includes all the remaining eight physical properties, without any separation. All the MDs, except those for atomic mass, are either 1 or 0.

Let us remark that, even though five fuzzy classes were designed, the clustering actually produced only three: cluster 2, cluster 5, and another

cluster that was equally divided into clusters 1, 3, and 4. These last three fuzzy clusters are identical, and they were produced simply because we asked for a number of classes that correspond to the cluster substructure of the data set considered. In practical terms, we should consider only clusters 2 and 5 and the union of clusters 1, 3, and 4. The same procedure, but with data normalization, produces only one empty class (class 5), with all the properties being distributed over four classes: In class 1 we find the atomic mass; in class 2 the density, and in class 3 the melting point, each of these properties having MDs equal to 1 for their own classes and 0 for the rest. Class 4 contains all the seven other physical properties together, each of them with an MD = 0.5; these properties also have MDs = 0.5 for class 5, the vacant one.

The results are very much the same for the 10 physical, structural, and chemical characteristics, without data normalization. For the five predefined number of classes, one remains vacant; the MDs of all the characteristics for this class are zero. From the other four classes, again three contain one characteristic each, while the last includes the rest of the seven properties. All the MDs are 1 or 0. The three properties separated are, again, the density (class 1), the melting point (class 2), and the boiling point (class 3).

The same treatment, but with a predefined number of four classes, gives the same results, except for the missing empty class. This suggests another way in which a number of classes higher than the natural number of classes that corresponds to the cluster substructure of the considered data set is found. In the preceding case, three fuzzy classes were absolutely identical, indicating that they were artificially split. In this case the clustering process actually produced four fuzzy classes, the fifth one having MDs = 0 for all the properties, being produced only to comply with the prerequisite of five classes that was above the natural number of four classes.

It is obvious from the discussions so far that on a chemical as well as a physical basis the same partitions are almost invariably found. These essentially agree with the traditional chemical classifications, although the details may differ. By using this approach, we retain the separation into main group elements (*s*- and *p*-block elements), transition metals (*d*- and *f*-block elements), and so on. Some elements may pass from one group to another, depending on the type of classification, but the general framework remains unchanged from the traditional one. On the other hand, classification details such as the membership degrees to various classes and the distances between elements point out some less trivial similarity relationships between the elements. These might be suggestive of some new ideas with possible applications in different fields. Moreover, the fuzzy cross-classification procedure allows for qualitative and quantitative identification of the properties (physical, chemical, and structural) responsible for observed similarities and dissimilarities between chemical elements. In addition, the fuzzy hierarchical characteristics clustering (FHiChC) and fuzzy horizontal characteristics clustering (FHoChC) procedures revealed a high similarity between chemical and structural proper-

ties and also between the latter and some physical properties. The fact that the discriminant and independent physical properties include relative mass, density, and melting point illustrates that the results obtained in this way refer especially to the elementary substances and less to the elements as atom types. On the contrary, the classical periodic system of chemical elements considers first the properties (e.g., valence) of the chemical elements. Electronegativity, ionization energy, or covalent radius is mainly determined by electron configuration. As a result they are grouped in the same cluster.

CHARACTERIZATION AND CLASSIFICATION OF LANTHANIDES AND THEIR PROPERTIES BY PCA AND FPCA

In the history of chemistry, one can hardly find a more intricate field than the discovery and classification of the rare earths elements. Their unusual similarity of properties, as well as their scarcity (which prevented the exact determination of their properties) raised considerable difficulties. It is even probable that the development of the periodic table would have been significantly delayed were these elements already known in the middle of the nineteenth century. It has been affirmed[57] that "the group of rare earths forms a little periodic system of their own, where all the relations of the main system are reproduced on a small scale".

After failing to classify the rare earths as homologues of other elements, the solution was to group the lanthanides together in a separate series.[58] The atomic model of Bohr made it possible to settle the number of lanthanides at 14, but attempts to find relations within the group of rare earths never ceased. The chapter on lanthanides in van Spronsen's book[59] gives a rather historically complete account, so only some of these relationships will be discussed here.

An early classification of the rare earths (the oxides of lanthanides) in relation to their separation from ores, was in the ceritic earths (the oxides from lanthanum to samarium) and yttric earths (from europium to lutetium, but also scandium and yttrium). A further refinement of analytical methods made it possible to split the yttric earths into terbic (europium, gadolinium, terbium), erbic (dysprosium, holmium, erbium, thulium), and ytterbic (ytterbium and lutetium) earths, along with yttrium oxide and scandium oxide.

In the "arena" system of J. D. Clark,[60] shown below, some of the lanthanides are correlated with other groups of elements:

IIIb	IVb	Vb	VIb	VIIb							Ia	IIa
Y	Zr	Nb	Mo	Tc							Rb	Sr
La	Ce	Pr	Nd	Pm	Sm	Eu	Gd	Tb	Dy	Ho	Er	Tm	Yb
				Lu								

while seven lanthanides remain without analogues.

Scheele[61] suggested that lanthanides could be classed, as could actinides, in new kinds of groups, c, as follows: Ic: thulium [as a homologue of rubidium (Ia) and silver (Ib)]; IIc: ytterbium; IIIc: lutetium; IVc: cerium, praseodymium, neodymium (as homologues of zirconium); Vc: promethium; VIc: samarium; VIIc: europium; VIIIc: gadolinium, terbium, dysprosium, holmium, erbium (as homologues of ruthenium, rhodium, and palladium).

Ternstrom[62] built upon this idea and divided lanthanides into two rows after gadolinium, and distributed them in c-groups as shown:

Sc

		Y La	Ce	Pr	Nd	Pm	Sm	Eu	Gd
			Tb	Dy	Ho	Er	Tm	Yb	Lu
Group	B3		C4	C5		C6		C2	C3

Another aspect, still under discussion, is the identity of the element that should be considered the homologue of yttrium in group 3. This role is usually assigned to lanthanum, with the series of lanthanides going from cerium to lutetium. However, there are also reasons to put lutetium in group 3, as the homologue of yttrium, and thus begin the series of lanthanides with lanthanum.[63]

Since the problem of a rational classification for the rare earth elements, based on their properties, cannot be considered resolved, there would be a real challenge to use the methods of multidimensional analysis to establish some correlations between these elements and group them in distinct classes, and at the same time find correlations among the properties used to characterize them. We have applied PCA and Cluster Analysis to the study of 84 chemical elements (including the lanthanides, except promethium), characterized by 10 physical properties or 10 physical, chemical, and structural characteristics.[52,53] The lanthanides cluster separately from other elements. Only europium and ytterbium (the lanthanides with relatively stable electronic configurations, f^7 and f^{14}, respectively) appear as being close to the elements of the main groups of the periodic table. Also, a certain analogy between these lanthanides and calcium and lead could be observed. Quite similar results were found in a fuzzy classification of chemical elements.[32,33] As a consequence, the processing and rational interpretation of the registered data concerning the lanthanides appeared to be better performed using new chemometric methods.[6–12]

Properties of Lanthanides Considered in This Study

We compared fuzzy principal component analysis (FPCA) to classical PCA methods to characterize lanthanum, the 14 lanthanides, and the other

group 3 elements—scandium and yttrium, with the idea of clarifying the relations of Sc and Y with the lanthanides. The characteristics selected as a basis for the classification were almost exclusively physical properties. Properties were selected for which the values were known for all (or nearly all) the elements under consideration. The data were taken from different tables or textbooks.[64,65] Since the values given in various sources often differ significantly, we tried to select the most probable values to make up a consistent data set. A special case is that of promethium; data for this element are sometimes scarce and uncertain. For some properties, there are no reliable experimental data in the literature, but the values are obtained by interpolation from those of the neighboring elements.

The 18 selected properties were atomic mass (*A*), density (*d*), atomic radius (*r*), first (I1), second (I2) and third (I3) ionization energy, Pauling electronegativity (*X*), melting point (MP), boiling point (BP), enthalpy of fusion (HF), vaporization (HV), atomization (HA), standard entropy (*S*), specific heat capacity (SHC), surface tension (ST) at the melting point, electrical resistivity (ER), heat conductivity (HC), and the formation free energy of the chloride $LnCl_3$ per mol of Cl (FFE)—as a characteristic of chemical reactivity.

The electron configurations of the elements studied and of their tripositive ions are the following:

Sc	(Z = 21) [Ar] $3d^1 4s^2$	Sc^{3+} [Ar]
Y	(Z = 39) [Kr] $4d^1 5s^2$	Y^{3+} [Kr]
La	(Z = 57) [Xe] $5d^1 6s^2$	La^{3+} [Xe]
Ce	(Z = 58) [Xe] $4f^2 5d^0 6s^2$	Ce^{3+} [Xe]$4f^1$
Pr	(Z = 59) [Xe] $4f^3 5d^0 6s^2$	Pr^{3+} [Xe]$4f^2$
Nd	(Z = 60) [Xe] $4f^4 5d^0 6s^2$	Nd^{3+} [Xe]$4f^3$
Pm	(Z = 61) [Xe] $4f^5 5d^0 6s^2$	Pm^{3+} [Xe]$4f^4$
Sm	(Z = 62) [Xe] $4f^6 5d^0 6s^2$	Sm^{3+} [Xe]$4f^5$
Eu	(Z = 63) [Xe] $4f^7 5d^0 6s^2$	Ce^{3+} [Xe]$4f^6$
Gd	(Z = 64) [Xe] $4f^7 5d^1 6s^2$	Gd^{3+} [Xe]$4f^7$
Tb	(Z = 65) [Xe] $4f^9 5d^0 6s^2$	Tb^{3+} [Xe]$4f^8$
Dy	(Z = 66) [Xe] $4f^{10} 5d^0 6s^2$	Dy^{3+} [Xe]$4f^9$
Ho	(Z = 67) [Xe] $4f^{11} 5d^0 6s^2$	Ce^{3+} [Xe]$4f^{10}$
Er	(Z = 68) [Xe] $4f^{12} 5d^0 6s^2$	Er^{3+} [Xe]$4f^{11}$
Tm	(Z = 69) [Xe] $4f^{13} 5d^0 6s^2$	Tm^{3+} [Xe]$4f^{12}$
Yb	(Z = 70) [Xe] $4f^{14} 5d^0 6s^2$	Yb^{3+} [Xe]$4f^{13}$
Lu	(Z = 71) [Xe] $4f^{14} 5d^1 6s^2$	Lu^{3+} [Xe]$4f^{14}$

Therefore, Eu and Yb have relatively stable electron configurations; for the ions, Gd^{3+} and Lu^{3+} should be the most stable, as well as Ce^{4+}, Tb^{4+}, Eu^{2+}, Yb^{2+}. The elements La, Gd, and Lu have configurations analogous to those of Sc and Y.

Table 5 Eigenvalue and Proportion Corresponding to the First Six Principal Components for Classical PCA and FPCA

	PCA			FPCA		
Component	Eigenvalue	Prop. (%)	Cumulative Proportion	Eigenvalue	Prop. (%)	Cumulative Proportion
1	6.1583	**34.21**	34.21	4.7552	**93.41**	93.41
2	4.9328	**27.40**	61.62	0.1576	**3.09**	96.51
3	3.2797	**18.22**	79.84	0.0631	**1.24**	97.75
4	1.5518	**8.62**	88.46	0.0602	**1.18**	98.93
5	0.8119	**4.51**	92.97	0.0171	**0.34**	99.27
6	0.4362	**2.42**	95.36	0.0113	**0.22**	99.49

Classical PCA

In the case of classical PCA, the first principal component explains only 34.21% of the total variance and the second one 27.40%; a two component model, for example, thus accounts for only 61.62% of the total variance; see Table 5.

The first eigenvector obtained by PCA indicates that the contribution to the first principal component is quite similar for some of the properties considered. However, the greatest contribution is realized by the ST (0.379), the next highest is the HA (0.317), r (-0.309), HV (0.298), S (-0.289) BP (0.271), Cs (0.271), and MP (0.269); the smallest contribution was realized by ER (-0.014), FFE (-0.035), and d (-0.095). The second component describes the remaining variance after the first component is removed from the data.

In this case, the highest contribution to PC2 is realized by $I3$ (-0.363), X (-0.338), FFE (-0.334), $I1$ (-0.304), and $I2$ (-0.292). It is interesting to note that, HF (-0.275), HV (0.277), and HA (0.256) are very similar but the value of HF is negative (negative correlation). The lowest contribution to PC2 is given by A (0.010), d (-0.046), r (0.059) and ST (0.066). The most correlated properties with the third principal component appear to be d (0.508), A (0.389), HF (0.314), Cs (-0.306). These statements are well supported by a two dimensional (2D) (i.e., PC1 vs. PC2) representation of the loadings in Figure 10.

In addition, by reducing the number of features from 18 original properties (manifest variables) to three principal components (latent variables), the information preserved is enough to permit a primary examination of the elements according to their origin in a 2D- or 3D-plot, respectively. When these plots of the elements were drawn in the plane described by the first two eigenvectors and in the space defined by the first three principal components, respectively, interesting results were found (see Figure 11).
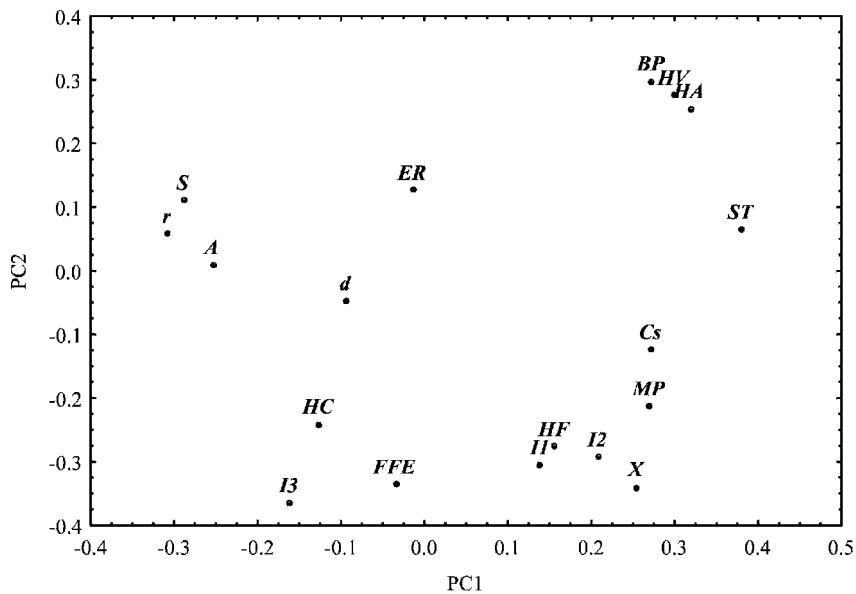
Figure 10 PCA loadings plot for the 18 selected properties (PC1-PC2).
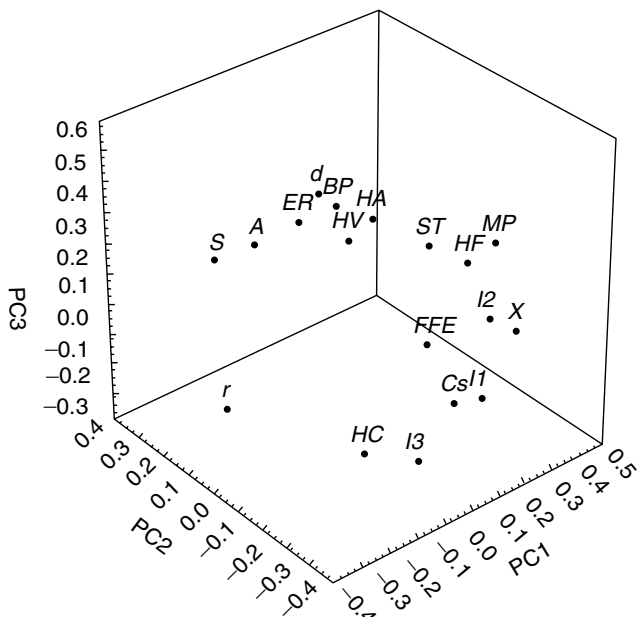
Figure 11 PCA loadings plot for the 18 selected properties (PC1-PC2-PC3).
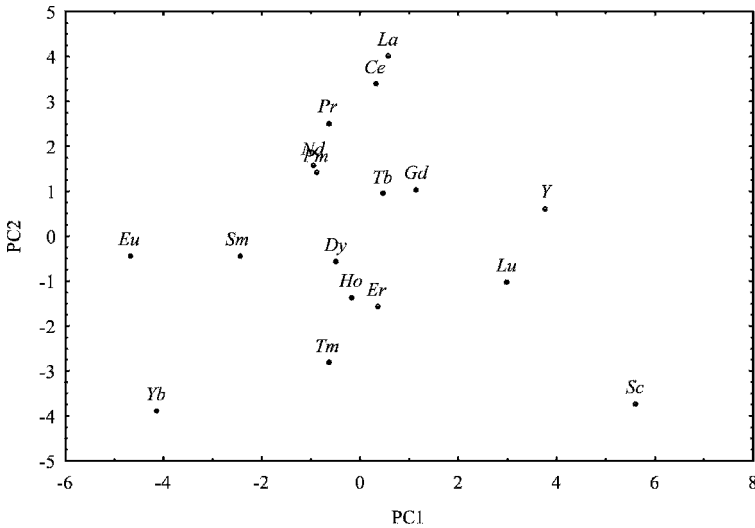
Figure 12 PCA scores plot for the lanthanides including La, Sc, and Y (PC1-PC2).

From the plot of the 17 elements on the plane described by PC1 and PC2 (Figure 12), as well as in the space defined by the first three eigenvectors (Figure 13), we see that the first separation groups together the "light" lanthanides (La, Ce, Pr, Nd, Pm, Sm, Eu) and Yb. In Figure 12, for example, they are situated in the upper half of the diagram, with the elements from La to Eu placed
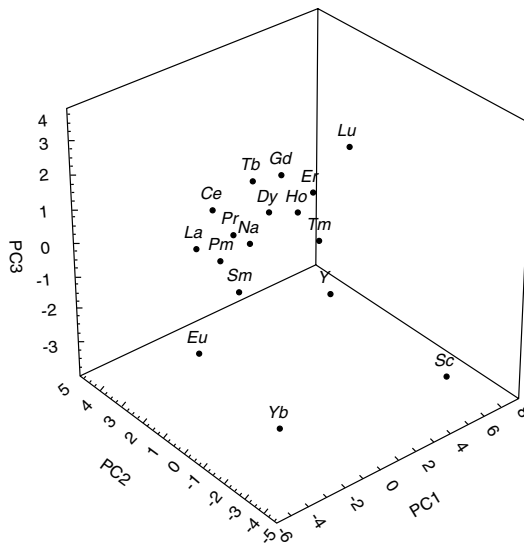
Figure 13 PCA scores plot for the lanthanides including La, Sc, and Y (PC1-PC2-PC3).

in the first quadrant and Yb in the second (Sm and Eu are on the boundary line between the quadrants). Ytterbium is added to the lighter lanthanides due to its similarity to europium. In the electron configurations of these elements, the $4f$ level is less than one-half full, except for Eu (half-complete level, f^7) and Yb (complete level, f^{14}), the two elements with relatively stable configurations. The second group is that of the "heavier" lanthanides, situated in the lower half of the graph (Figure 12), with Gd and Tb in the fourth quadrant and Dy, Ho, Er, Tm in the third, together with Lu—placed at a higher distance from the other. The cluster of "light lanthanides" is further divided into one cluster including the first five elements (from La to Pm) and another containing the elements with relatively stable electron configurations (Yb, Eu) and Sm, which has one electron fewer than such a configuration.

From the "heavier lanthanides", "the similarity chart" (2D plot) and "the similarity space" (3D plot) differentiate the pair Gd–Tb from the cluster Dy, Ho, Er, Tm, and from Lu.

The outlier position of lutetium among the lanthanides (unlike La, which is much closer to its neighbors) assigns it as a homologue of Y in the third group of the periodic table. The other two outliers (Yb and Eu) are the elements with relatively stable electron configuration and many of their properties deviate from the regularities observed for the other lanthanides.

As a matter of fact, multidimensional and fuzzy analysis of the chemical elements[32,33] suggested some analogies of Eu and Yb with main group elements. As for Lu and La, they have an electron configuration with one electron in the d subshell with the f subshell empty (La) or completely occupied (Lu), unlike the other lanthanides.

Fuzzy PCA

Results obtained from the same initial data set (17 elements and 18 properties) using the fuzzy PCA algorithm described above are also shown in Table 5. The results obtained by applying FPCA are quite different from the PCA results. The first component explains 93.41% of the total variance and the second one only 3.09%: A two component model thus accounts for 96.51% of the total variance (as compared to 61.62% for PCA) and a three component model accounts for 97.75% (as compared to 79.84% for PCA), for the fuzzy PCA method (see Table 5). Hence, the FPCA-derived components account for significantly more of the variance than their classical PCA counterparts. The column corresponding to the first fuzzy eigenvector obtained in this case indicates that the contribution to the first component is also very different. The greatest contribution is realized by the HF (0.558), the next highest by the MP (0.373), then *I1* (0.360), *X* (0.339), and *I2* (0.297). A less significant contribution is obtained from the majority of the characteristics as is, for example, HC (-0.039), *S* (0.046), ST (-0.055), and SHC (-0.051). With respect to the second principal component, the highest contribution in this
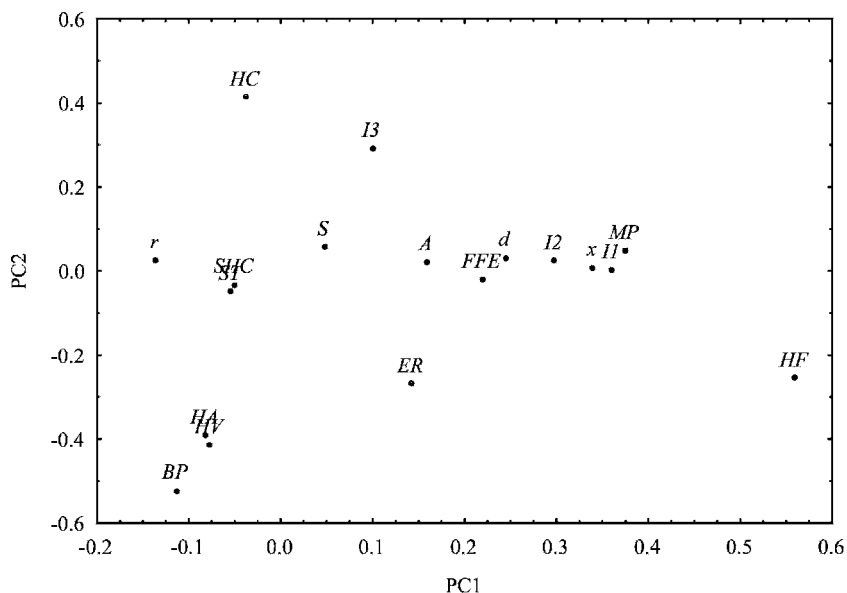
Figure 14 FPCA loadings plot for the 18 selected properties (PC1-PC2).

case is realized by the BP (-0.520), HC (0.415), HV (-0.412), HA (-0.389), I3 (0.294), and ER (-0.267). The third component appears to be well correlated with ER (0.730), HF (-0.354), HA (0.250). These statements are also very well confirmed by the 2D representation of loadings and 2D and 3D representation of fuzzy factor scores, shown in Figures 14 and 15, and better support the similarity between lanthanides and the correlations between their properties, respectively.

Examining all the pairs of variables for relationships between them, we find, indeed, some rather strong correlations, as may also be the case for their correlation coefficients, r. Nevertheless, these relations should be considered with caution, particularly when generalizing to other elements. As a matter of fact, lanthanides are a rather peculiar group of elements; their properties are very similar, that is, the variation of a given property in the series of these elements is rather limited and inferences to all the elements are doubtful. Keeping this in mind, we may, however, discuss the closest correlations (similarities) found here.

The highest correlation coefficient (0.98) is for enthalpy of vaporization and standard enthalpy of atomization. For metals, the latter one is actually the standard sublimation enthalpy and is given, according to Hess' law, by the sum of the standard enthalpies of fusion and vaporization. The enthalpies of vaporization are those at the boiling temperature and, therefore, lower than the standard ones. Other very close correlations are those between the boiling
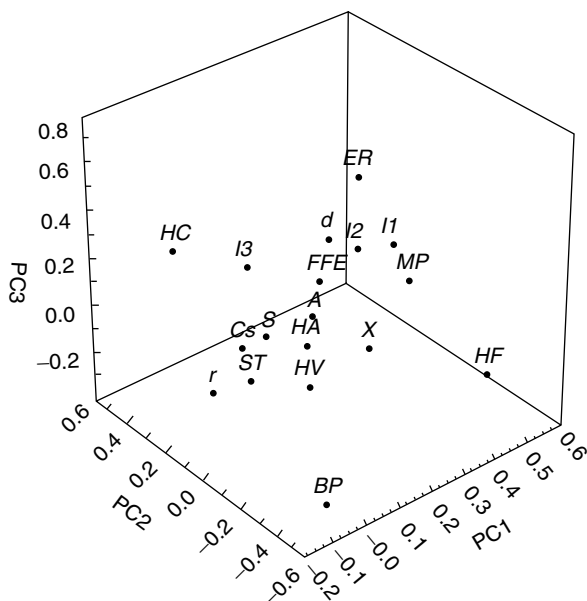
Figure 15 FPCA loadings plot for the 18 selected properties (PC1-PC2-PC3).

point and the enthalpy of atomization (0.96) or the enthalpy of vaporization (0.93). This is in agreement with the well-known rule of Pictet and Trouton, which states that the ratio of the enthalpy of vaporization at the boiling point to the boiling temperature is a constant. For 93 chemical elements, a linear relation with a correlation coefficient of 0.96 was also obtained.[32]

A significant correlation, but with a negative correlation coefficient (−0.93), appears between the specific heat capacity and the atomic mass. For lanthanides, as for most metals, the rule of Dulong and Petit is applicable (inverse proportionality between the two quantities).

The correlation between the enthalpy of fusion and the melting point is looser ($r = 0.87$), but better for the ensemble of chemical elements; for 95 elements, $r = 0.775$.

The negative correlations between the third ionization energy and the enthalpy of vaporization ($r = -0.87$), the enthalpy of atomization ($r = -0.83$), or the boiling point ($r = -0.84$) seem rather fortuitous. The correlation of density and atomic mass ($r = 0.86$) is particular to lanthanides; the density increases with the atomic number (with some exceptions: Eu, Yb), while the atomic volume is nearly constant (actually it decreases slightly, due the contraction of lanthanides). On the other hand, the correlations of surface tension with the enthalpy of atomization ($r = 0.84$), the boiling temperature ($r = 0.78$), and the enthalpy of vaporization ($r = 0.77$) are well-known general relations. Surface tension represents the free energy necessary
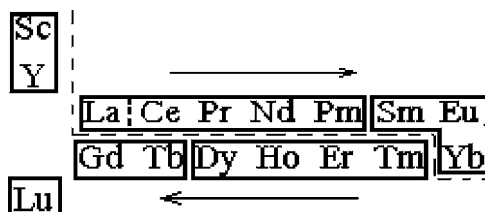
Figure 16 The "periodic system" of lanthanides.

for the creation of a new interface, and is therefore related to the energy spent in the splitting of bonds, the same entity that is implied in vaporization or atomization.

The variables selected as a basis for this classification were mainly physical properties, with only the formation free energy of the chlorides as a chemical property; no structural features, (electron configuration) or chemical properties (the oxidation state), were introduced. Nevertheless, the resultant classification discriminates between groups of lanthanides with different structural and chemical characters. Elements with oxidation state +2 are grouped together, and so are elements with oxidation state +4. Elements with similar peculiarities of electron configuration are also put in the same cluster.

Based on this analysis and on the electron configuration, one may propose a "periodic system" of the lanthanides (Figure 16). Setting lutetium as the homologue of yttrium, the series of lanthanides begins with lanthanum and ends with ytterbium. It is broken into two rows, after europium, so that elements with electron configurations up to f^7 are placed in the first row and those with the f subshell more than half-full are in the second. There is always a difference of 7 f-electrons between the homologous elements in the two rows. For this reason, these elements have the same number of additional electrons as compared with the relative stable configurations $[Xe]6s^2$ (first row) and $[Xe]4f^76s^2$ (second row) or the same number of electrons less than the relative stable configurations $[Xe]4f^76s^2$ (first row) and $[Xe]4f^{14}6s^2$ (second row).

A broken line separates the two classes of "light" lanthanides, including Yb and the "heavier" lanthanides, together with Sc and Y. The clusters are framed by solid borders. Going along the series of lanthanides in the direction of the arrows we find all the clusters given by the fuzzy PCA analysis.

In comparison with the traditional splitting of the lanthanide series,[59] the main difference is the placement of Gd in the second row. While the ions Gd^{3+} and Lu^{3+} have the most stable configurations ($[Xe]4f^7$ and $[Xe]4f^{14}$, respectively). Among the neutral atoms, the most stable configurations are those of Eu; $[Xe]4f^76s^2$ and Yb $[Xe]4f^{14}6s.^2$ Therefore, these two elements should play the part of the "noble gases" in the system of lanthanides, and not Gd and Lu.

On the other hand, the electron configuration of gadolinium $[Xe]4f^7 5d^1 6s^2$ makes this element the natural homologue of lanthanum $[Xe]5d^1 6s.^2$

Compared with the c-groups of Scheele,[61] we find that his IVc-group contains the elements of the same cluster (Ce, Pr, Nd) and in his VIIIc-group we find the elements of two neighboring clusters: Gd and Tb, and Dy, Ho, and Er.

Obviously, the chemical intuition of the chemists who attempted to classify the lanthanides led them to groupings similar in many respects to those found by the methods of multidimensional analysis.

Miscellaneous Applications of FPCA

Fuzzy Principal Component Analysis was also performed on the structural features concerned with the interaction of carbon–hydrogen bonds and molybdenum–oxo bonds. In addition to all possible atom–atom distances and the angles subtended thereof, several additional metrics were defined and tabulated.[66] These include the distance R_{bp}, and the angles α, β, and γ, as well as the dihedral MOCH, Scheme 1. Interactions between metal–oxo and carbon–hydrogen bonds are of importance with respect to microbial and industrial oxidation,[67,68] and for these reasons molybdenum was the focus of this research.
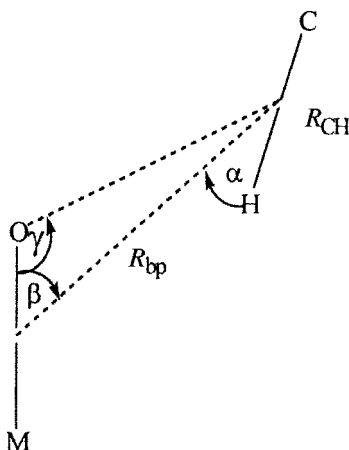
Scheme 1

The results obtained from the initial dataset (71 complexes $\times$ 14 characteristics)—covariance matrix—were presented in Ref. 40. The results obtained and the correlation data confirm that the structural features concerning interaction of C–H and Mo=O bonds are related to each other and so could be reduced. Considering, for example, a two component model, FPCA accounts for 97.20% of the total variance, and the first two PCA components account

for only 69.75%. It would take five-to-six classical principal components to account for the same total variance as two fuzzy principal components. The latter is, of course, much more desirable and makes for a significantly easier dataset analysis. Additionally, PCA showed only a partial separation of the molybdenum–oxo complexes onto the plane described by the first two principal components, whereas a much sharper differentiation of the metric variables along the diagonal is observed when FPCA is used.

FUZZY MODELING OF ENVIRONMENTAL, SAR AND QSAR DATA

Different fuzzy clustering algorithms mentioned above were successfully applied to the study of several German and Romanian natural mineral waters using data obtained from samples collected from different sampling sites covering, for example, a large percentage of the Romanian natural mineral waters. The characteristic clustering technique produces fuzzy partitions of the mineral water properties involved and thus is a useful tool for studying (dis)similarities between different ions (i.e., speciation). The cross-classification algorithm provided not only a fuzzy partition of the mineral waters analyzed, but also a fuzzy partition of the characteristics considered. In this way, it is possible to identify which ions and other physico-chemical features are responsible for the similarities or differences observed between different groups of mineral waters.[69]

Various classification procedures—hierarchical and non-hierarchical crisp and fuzzy clustering, cross-classification fuzzy clustering, and PCA (varimax rotation)—combined with receptor modeling were applied to a data set consisting of wet deposition loads of major ions from five sampling sites in Central Austria collected over a period of 10 years (1984–1993). The data classification with respect to the sampling sites as objects has shown that a distinct separation between the northern Alpine rim and the inner Alpine region is achieved. This indicates the role of geographical disposition of the sampling sites.[70]

In a similar way, fuzzy cluster analysis and fuzzy recognition were successfully used to model a large set of data from the Min River (China).[71] The fuzzy analysis was employed as: A graphical tool to compare ecosystems with respect to their pollution;[72] to identify individual aerosol particles containing Cr, Pb, and Zn above the North Sea;[73] at a rural site in Central Europe during winter;[74] to the characterisation of particulate matter from the Kara Sea using electron probe X-ray micro analysis;[75] to study the correlation between element concentrations in basal till and the uppermost layers of mineral soil at forest sites in Finland[76] or heavy metals in urban soil;[77] to the qualitative identification of trace elements in clinker;[78] for the prediction of petrophysical rock parameters;[79] to process on-line data streaming from five monitoring stations in Chile for forecasting SO_2 levels;[80] to data processing in

on-line laser mass spectrometry of inorganic, organic, or biological airborne particles;[81] and, finally, also for evaluation of PCDD/F emissions during solid-waste combustion.[82]

Fuzzy classification algorithms of the toxicity test systems based on the first 10 MEIC (international multicenter evaluation of in vitro cytotoxicity tests) chemicals allowed an objective interpretation of their similarities and differences. It was very interesting to observe the classification of toxicological test systems on humans, considering their membership degrees. Some of them appeared closer to the test on rats and mice, and others seem to be very specific. The Fuzzy Hierarchical Cross-Classification Algorithm (FHCsC) allowed the qualitative and quantitative identification of the characteristics (chemical compounds) responsible for the observed similarities and dissimilarities between the toxicity test systems. In addition, the Fuzzy Hierarchical Characteristics Clustering (FHiCC) and Fuzzy Horizontal Characteristics Clustering (FHoCC) procedures revealed a high similarity between some MEIC chemicals (amitriptyline, digoxin, ethylene glycol, methanol, ethanol and isopropyl alcohol) and a large difference among others (paracetamol, acetylsalicilic acid, ferrous sulfate and diazepam). This result suggested the highly redundant character of similar chemicals in the diagnosis of toxicological test systems. The results obtained clearly underline the efficiency of the fuzzy clustering algorithms for the comparison of different end points and the selection of a battery of in vitro toxicity tests that allow the estimation of the possible harmful effects of chemicals in vivo.[83]

Lack of certainty is a problem often found in ecological modeling, which is a result of the large amount of variables to be considered. Consequently, many authors have suggested that applying fuzzy methods might be helpful for the interpretation of ecological data because the classification of chemicals in terms of chemical groups or specific and baseline toxicity is rather vague. In the majority of papers dedicated to classifying existing chemicals according to their phytotoxicity[84–86] and other ecotoxicological properties,[87,88] the fuzzy clustering primary procedure used was based on the well-known Fuzzy c-Means algorithm.[56]

SPECTRAL LIBRARY SEARCH AND SPECTRA INTERPRETATION

It is becoming a common practice for modern instruments to be supplied with some form of data library of reference spectra that can be used to identify unknown sample compounds. Most databases of this type consist of a list of the positions and intensities of the peaks contained within the spectra. Once conversion of a sample spectrum has been carried out, its peak list can be matched against each entry in the library to find that which approximates it most closely.

Blaffert applied, for the first time, fuzzy sets for the identification of components in IR spectra of mixtures using peak positions and intensities.[89] The method was implemented in a computer program that was capable of resolving multicomponent samples in infrared (IR) spectroscopy as well as X-ray powder diffractometry. The use of fuzzy set theory did not solve any problems caused by experimental errors, but supports the integration of chemical and physical knowledge into computerized interpretation of spectra in an illustrative manner.[90] The algorithm described above, using IR spectra, has been extended by considering the full spectral information, namely, peak position, intensity, and width.[91–93]

Spectroscopic and chromatographic methods are used to characterize multicomponent samples with respect to chemical components and their concentrations. Apart from the need to report accurate component concentrations, the analyses are frequently applied to ensure the quality of a final product (e.g., by comparing the metal pattern of a steel sample with that of a certified standard) or to classify a complex sample by means of its chromatographic profile used as a "fingerprint". The required data processing schemes are essentially methods of pattern recognition based on supervised learning techniques. However, the commonly used methods are not very suitable for solving these kinds of problems because, at best, only a gross description of the class shape is possible. To overcome these limitations Otto and Bandemer, two of the most active chemists in the field of fuzzy set applications in analytical chemistry, have successfully applied fuzzy set theory to quality control of pharmaceutical products based on monitoring their ultraviolet (UV) spectra and for classifying samples by means of their chromatographic patterns.[94–97]

The determination of double-bond positions in straight-chain alkenyl compounds is a provocative analytical problem when the amount of material available is very small. In view of the frequent occurrence of functionalized alkenes in the chemical structure of female sex pheromones of nocturnal moths, rapid analytical procedures have been developed by fuzzy similarity analysis of GC/MS and ^{13}C NMR data.[98,99] A more sophisticated methodology for protein 2D NMR assignment based upon protein spin coupling graph theory analysis, fuzzy graph pattern recognition, and tree searching[100] and a comparison of depth profiles in SIMS by a fuzzy method[101] has been also reported.

FUZZY CALIBRATION OF ANALYTICAL METHODS AND FUZZY ROBUST ESTIMATION OF LOCATION AND SPREAD

Quantitative determinations involving instrumentation are often accomplished by establishing a calibration function. Calibration must be accomplished before any measurements are made on a chemical system. Calibration

of an instrument for chemical quantification requires that the relationship between the response of the instrument and the concentration be expressed mathematically. Several techniques for expressing this relationship are known.[27–29,101–106] The most common model is a linear regression, usually a first-degree polynomial, although second- and high-degree polynomials have been used.[6–12]

The ordinary linear least-squares regression is based on the assumption of an independent and normal error distribution with uniform variance (homoscedastic). In addition, linear regression based on ordinary least-squares presumes that errors in signal are much higher than those in concentration [error (Y) $\gg$ error (X)]; it is also very sensitive to extreme data points, which may result in biased values of the regression parameters, slope, and intercept.

Some authors suggested that, in the absence of a good analytical model, the use of fuzzy regression could be one of the best approaches to the treatment of calibration data.[107–111] The characteristics of performance of the Fuzzy 1-Lines algorithm described above were very well illustrated in a comparison study of a multitude of regression algorithms for analytical applications,[34–36] and also as a possibility of developing a fuzzy robust estimator of mean (central location) and dispersion.[112] Let us consider as an illustrative example the data discussed by Davies[113] using a modified Huber algorithm to reduce the effect of outliers on central location. The data are presented in Table 6, and the computed results using eight different estimators of central location are presented in Table 7. These are arithmetic mean, median, 5% trimmed mean, Huber (weighting constant 1.339), Hampel (weighting constants 1.700, 3.400, 8.500), Tukey (weighting constant 1.340), and Fuzzy mean ($\alpha = 0.1$), respectively.

Case 1 refers to 50 normally distributed observations with a mean of 10.00 and S.D. of 1. They were created using a pseudo-random number

Table 6 Relevant Data Sets Concerning Robust Methods Comparison Studies

Case 1:	9.08, 9.29, 9.32, 10.57, 10.72, 11.05, 10.36, 10.78, 10.33, 11.42, 10.43, 9.82, 10.41, 10.93, 9.40, 8.94, 8.35, 9.14, 9.92, 8.66, 8.45, 10.35, 10.19, 9.47, 9.24, 11.55, 11.12, 10.16, 9.43, 9.87, 10.63, 10.28, 11.34, 9.07, 9.43, 9.39, 9.68, 11.98, 9.90, 10.08, 10.04, 9.67, 9.13, 8.92, 9.50, 9.71, 10.74, 11.13, 9.82, 11.09
Case 2:	9.08, 9.29, 9.32, 10.57, 10.72, 11.05, 10.36, 10.78, 10.33, 11.42, 10.43, 9.82, 10.41, 10.93, 9.40, 8.94, 8.35, 9.14, 9.92, 8.66, 8.45, 10.35, 10.19, 9.47, 9.24, 11.55, 11.12, 10.16, 9.43, 9.87, 10.63, 10.28, 11.34, 9.07, 9.43, 9.39, 9.68, 11.98, 9.90, 10.08, 10.04, 15.67, 15.13, 14.92, 15.50, 15.71, 16.74, 17.13, 15.82, 17.09
Case 3:	9.08, 9.29, 9.32, 10.57, 10.72, 11.05, 10.36, 10.78, 10.33, 11.42, 10.43, 9.82, 10.41, 10.93, 9.40, 8.94, 8.35, 9.14, 9.92, 8.66, 8.45, 10.35, 10.19, 9.47, 9.24, 11.55, 11.12, 10.16, 9.43, 9.87, 10.63, 10.28, 11.34, 9.07, 9.43, 9.39, 15.68, 17.98, 15.90, 16.08, 16.04, 15.67, 15.13, 14.92, 15.50, 15.71, 16.74, 17.13, 15.82, 17.09

Table 7 Estimated Values of Central Location
Obtained by Analytical Methods

Statistical parameter	Case 1	Case 2	Case 3
Mean	10.006	11.086	11.686
Median	9.910	10.305	10.420
5% Trimmed mean	9.998	10.901	11.545
Huber (1.339)	9.950	10.314	10.585
Hampel (1.7,3.4, 8.5)	9.980	10.149	10.418
Tukey (4.685)	9.948	10.008	9.969
Andrews (1.43)	9.948	10.009	9.975
Fuzzy mean	9.828	10.035	10.074

generator. In this case, a 5% trimmed mean algorithm seems to produces the best result, with Tukey, Andrews, and Huber estimators giving practically the same result. The fuzzy mean is closer to the median and, interestingly, in this situation it is the lowest value.

Case 2, also shown in Table 6, uses the data of case 1, but this time generates outliers by adding the number 6 to the last nine observations. We obtained the results depicted in Table 7. This time the best results are obtained by using the Tukey, Andrews, and fuzzy algorithms, which appear to be the most resistant to outliers. All the rest of the robust procedures are strongly influenced by the presence of outliers. The last case in Table 6 (case 3) refers to data obtained from case 1 by adding 6 to the last 15 observations. Again (see Table 7), the fuzzy, Andrews, and Tukey methods seem to be the best. To summarize, the performance of the Fuzzy 1-Means algorithm has been shown to exceed that of a conventional ordinary mean estimator and equals or exceeds that of the most known M-estimators. This algorithm appears to satisfy very well all the statistical performance criteria: robustness, resistance, and efficiency. Also, the fuzzy mean estimate is practically independent of the value of α (the membership degree of the furthest outlier). The method is simple and intuitive and easy to apply. In addition, one can include other advantages of fuzzy set theory (e.g., the membership degree of each value) as a possibility of developing a fuzzy estimator of dispersion or for other statistical purposes. However, at this moment, one problem remains: How to determine which robust estimator is the best or the most suitable in any situation.

APPLICATION OF FUZZY NEURAL NETWORKS SYSTEMS IN CHEMISTRY

The artificial neural networks, mentioned above, represent a multitude of parallel structures consisting of nonlinear processing units connected by

links of different weights. Because of their good ability to approximate functional dependencies between descriptive parameters and responses of a complex system, ANNs are widely employed for solving recognition problems and quantitative relationships. If we suppose an infinite or large-enough data set, a simple ANN model can provide a satisfactory degree of generalization. However, in real situations one usually deals with restricted sets of training samples. Once trained, neural networks are quick and have a tolerance to incomplete or noisy data, which makes them useful in real-world environments.

Within the field of chemistry, various applications have already been published. Jansson[114] and Zupan and Gasteiger[115] published an overview of an MLP (multilayer perceptron), that is trained by back-propagation of errors, and other types of neural networks. However, the basic source in this field continues to be the well-known book of Zupan and Gasteiger.[116] In analytical chemistry, neural networks have been applied to pattern recognition, modeling, and prediction, for example, in multicomponent analysis or process control, to classification, clustering and pattern association.[117–122]

It is abundantly clear that fuzzy logic is better able to represent human knowledge in a form of rules while ANNs are better able to learn from examples. As a consequence of their complementary properties, then, extensive efforts are being made to combine fuzzy theory and neutral networks to profit from the advantages of each while trying to bypass the disadvantages of the isolated techniques.[123–125]

A fuzzy neural network blends elements of fuzzy and neural network computations into a single connectionist architecture. In general terms, two different types of neural-fuzzy hybrids have emerged: one that uses neural networks to derive the parameters of a fuzzy system, and another that provides an implementation of a fuzzy system within one neural network architecture. A neural fuzzy system is a fuzzy system that uses a learning algorithm derived from or inspired by neural network theory to determine its parameters (fuzzy sets and fuzzy rules) by processing data samples. Neural-fuzzy systems can be used to derive solutions involving the neural network's advantages of model-free learning, good generalization, and powerful nonlinear mapping capabilities. The primary strength obtained from the fuzzy logic component is a system that can both be initialized by the existing semantic knowledge, and have structured information (knowledge) extracted from it in an interpretable format. Thus, the "black-box" difficulty, which is widely regarded as a principle weakness of neural networks, can be lessened. A series of steps exist to implement a basic neural fuzzy system: (1) convert real-valued data into a fuzzified representation; (2) train the fuzzified information with a neural network; and then (3) defuzzify the result to produce real values of the desired output. After the system is trained to satisfaction, fuzzy rules can be extracted from the trained neural network.

A fuzzy multivariate rule-building expert system (FuRES) has been devised that also functions as a minimal neural network.[126] This system builds

from training sets of data that use feature transformation in their antecedents. The rules are constructed using the ID3 algorithm with a fuzzy expression of classification entropy. The rules are optimal with respect to fuzziness and can accommodate overlapped and underlapped clusters of data. Otto[127] applied fuzzy associative memory (FAM) developed by Kosko[128] for the interpretation of UV spectra and Harrington and Wabuyele[129] devised a fuzzy optimal associative memory (FOAM) for background correction of near-IR spectra. The FOAM technique uses enhanced optimal associative memory (OAM) and a fuzzy function for encoding the spectra.

Agapito et al.[130] applied fuzzy logic to an array of semiconductor gas sensors to analyze different atmospheres for the different gases and Otto et al.[131] developed a scheme based on the principles of fuzzy logic that makes use of various pieces of information available either from spectroscopic knowledge or from the particular spectrum that requires evaluation. A fuzzy expert system has also been successfully developed for the automated qualitative and semiquantitative interpretation of X-ray diffraction spectra,[132] automation of matrix-assisted laser desorption–ionization mass spectrometry (MALDI),[133] and for polymer analysis.[134]

Very efficient and promising applications of fuzzy expert systems were also discussed concerning, for example, the optimization of glutamic acid production,[135] control of penicillin concentration in a fed-batch bioreactor,[136,137] and, last but not the least, a fuzzy logic approach to analyzing gene expression data.[138] Finally, two different soft computing techniques (a competitive learning neural network and an integrated neural network-fuzzy logic-genetic algorithm approach) were employed in the analysis of a database subset obtained from the Cambridge Structural Database.[139]

APPLICATIONS OF FUZZY SETS THEORY AND FUZZY LOGIC IN THEORETICAL CHEMISTRY

In our opinion, all major theoretical aspects including some practical applications of fuzzy theory in the field of Theoretical Chemistry are very well illustrated in the book edited by Rouvray.[140] The nine contributors to this book, research chemists and mathematicians, explain the foundations of fuzzy logic and its growing importance in the physical sciences, describe molecular sizes and shapes, define chemical concepts such as chirality and the role of quantum chemical species and systems, and outline the engineering of molecular species, including drug design. More recently, an excellent exploration of the role of fuzzy methods in chemistry providing theoretical background as well as descriptions of practical applications in all the significant areas of chemistry was also published in the *Encyclopedia of Computational Chemistry* by Ehrentreich.[141]

CONCLUSIONS AND REMARKS

Soft computing has become an important computational paradigm due to many factors. On the one hand, it is tolerant of imprecision, uncertainty, and partial truth, properties that do not generally hold for hard computing techniques. On the other hand, soft computing is formed by a set of theories (fuzzy logic, neural networks, evolutionary algorithms) that, even if quite distinct from each other, with different aims and methods, can be combined to generate hybrid approaches, which are more powerful than their individual counterparts. Being a theory that deals with imprecision, uncertainty, and partial truth, soft computing is suitable to model problems from a large number of fields. In this chapter, we presented an introduction to different soft computing methods, and reviewed the applications of soft computing (with a focus on fuzzy methods) in chemistry and related fields. We hope that this work will prove to be useful in research efforts directed toward integrating soft computing methodologies with chemistry and chemical engineering issues and problems.

REFERENCES

1. T. Kohonen, *Self-Organizing Maps*, Second Extended Edition, Springer Series in Information Sciences, Vol. 30, Springer-Verlag, Berlin/Heidelberg, New York, 1995, 1997.

2. S. Kaski, *Data Exploration Using Self-Organizing Maps*, Ph.D. Dissertation, Neural Networks Research Center, Helsinki University of Technology, 1997.

3. T. Honkela, *Self Organizing Maps in Natural Language Processing*, Ph.D. Dissertation, Neural Networks Research Center, Helsinki University of Technology, 1997.

4. L. A. Zadeh, *Inform. Control.*, **8**, 338 (1965). Fuzzy Sets.

5. H. F. Pop, *Intelligent Systems in Classification Problems*, Ph.D. Dissertation, Babeş-Bolyai University, Cluj-Napoca, Romania, 1995.

6. M. Meloun, M. Militky, and M. Forina, *Chemometrics for Analytical Chemistry*, Vol. I: *PC-aided Statistical Data Analysis*, Ellis Horwood, Chichester, 1992.

7. D. L. Massart, B. G. M. Vandeginste, S. N. Deming, Y. Michotte, and L. Kaufman, *Chemometrics: A Textbook*, Elsevier, Amsterdam, The Netherlands, 1988.

8. D. L. Massart and L. Kaufman, *The Interpretation of Analytical Chemical Data by the Use of Cluster Analysis*, Wiley, New York, 1983.

9. P. E. T. Auf der Heyde, *J. Chem. Educ.*, **67**, 461 (1990). Analyzing Chemical Data in More Than Two Dimensions.

10. P. S. Shenkin and D. Q. McDonald, *J. Comput. Chem.*, **15**, 899 (1994). Cluster Analysis of Molecular Conformations.

11. J. Einax, H. W. Zwanziger, and S. Geiß, *Chemometrics in Environmental Analysis*, Wiley, Chichester, 1997.

12. M. Otto, *Chemometrics: Statistics and Computer Application in Analytical Chemistry*, Wiley-VCH, Weinheim, 1998.

13. Y-H. Pao, *Adaptive Pattern Recognition and Neural Networks*, Addison-Wesley Publishing Company, 1989.

14. R. Fullèr, *Introduction to Neuro-Fuzzy Systems*, Advances in Soft Computing Series, Springer-Verlag, Berlin/Heidelberg, 1999.

15. C. D. G. Jondarr, *Backpropagation Family Album*, Department of Computing, Macquarie University, Australia, Technical Report C/TR96-05, 1996.

16. D. R. Tveter, *Backpropagator's Review*, http://www.dontveter.com

17. K. Gurney, *An Introduction to Neural Networks*, UCL Press, London, 1996.

18. Z. Michalewicz, *Genetic Algorithms + Data Structures = Evolution Programs*, Third, Revised and Extended Version, Springer-Verlag, Berlin 1996.

19. M. Tomassini, *A Survey of Genetic Algorithms*, Volume III of Annual Reviews of Computational Physics, World Scientific, Singapore, 1995.

20. T. Bäck and H. P. Schwefel, in *Genetic Algorithms in Engineering and Computer Science*, J. Pèriaux and G. Winter, Eds., Wiley, New York, 1995. Evolution Strategies I: Variants and their Computational Implementation.

21. H. P. Schwefel and Thomas Bäck, in *Genetic Algorithms in Engineering and Computer Science*, J. Pèriaux and G. Winter, Eds., Wiley, 1995. Evolution Strategies II: Theoretical Aspects.

22. T. Bäck, G. Rudolph, and H. P. Schwefel, in *Proceedings of the Second Annual Conference on Evolutionary Programming, Evolutionary Programming Society*, D. F. Fogel and W. Atmar, Eds., San Diego, CA, 1993, pp. 11–22, Evolutionary Programming and Evolution Strategies: Similarities and Differences.

23. G. J. Klir and B. Yuan, *Fuzzy Sets and Fuzzy Logic*, Prentice-Hall, New Jersey, 1995.

24. J. C. Bezdek, *Pattern Recognition with Fuzzy Objective Function Algorithms*, Plenum Press, New York, 1987.

25. R. Lowen, *Fuzzy Set Theory*, Kluwer Academic Publishers, Amsterdam, 1995.

26. H. J. Zimmermann, *Fuzzy Set Theory-and Its Applications*, Kluwer Academic Publishers, Dordrecht, The Netherlands, 1996.

27. K. Tanaka, *An Introduction to Fuzzy Logic for Practical Applications*, Springer-Verlag, New York, 1997.

28. C. Sârbu, D. Dumitrescu, and H. F. Pop, *Rev. Chim.(Bucharest)*, **44**, 450 (1993). Application of Fuzzy Sets Theory in Thin Layer Chromatography.

29. D. Dumitrescu, C. Sârbu, and H. F. Pop, *Anal. Lett.*, **27**, 1031 (1994). A Fuzzy Divisive Hierarchical Clustering Algorithm for the Optimal Choice of Set of Solvent Systems.

30. H. F. Pop, D. Dumitrescu, and C. Sârbu, *Anal. Chim. Acta*, **310**, 269 (1995). A Study of Roman Pottery (terra sigillata) Using Hierarchical Fuzzy Clustering.

31. D. Dumitrescu, H. F. Pop, and C. Sârbu, *J. Chem. Inf. Comput. Sci.*, **35**, 851 (1995). Fuzzy Hierarchical Cross-Classification of Greek Muds.

32. H. F. Pop, C. Sârbu, O. Horowitz, and D. Dumitrescu, *J. Chem. Inf. Comput. Sci.*, **36**, 465 (1996). A Fuzzy Classification of the Chemical Elements.

33. C. Sârbu, O. Horowitz, and H. F. Pop, *J. Chem. Inf. Comput. Sci.*, **36**, 1098 (1996). A Fuzzy Cross-Classification of Chemical Elements, Based on Their Physical, Chemical and Structural Features.

34. H. F. Pop and C. Sârbu, *Anal. Chem.*, **68**, 771 (1996). A New Fuzzy Regression Algorithm.

35. C. Sârbu and H. F. Pop, *Rev. Chim.(Bucharest)*, **48**, 732 (1997). Fuzzy Regression.1. Heteroscedasticity.

36. H. F. Pop and C. Sârbu, *Rev. Chim.(Bucharest)*, **48**, 888 (1997). Fuzzy Regression. 2. Outliers.

37. H. F. Pop and C. Sârbu, *J. Chem. Inf. Comput. Sci.*, **37**, 510 (1997). The Fuzzy Hierarchical Cross-Classification Algorithm. Improvements and Comparative Study.

38. J. C. Bezdek, C. Coray, R. Gunderson, and J. Wantson, *SIAM J. Appl. Math.*, **40**, 339 (1981). Detection and Characterisation of Cluster Substructure: I. Linear Structure: Fuzzy C-lines.

39. J. C. Bezdek, C. Coray, R. Gunderson, and J. Wantson, *SIAM J. Appl. Math.*, **40**, 358 (1981). Detection and Characterization of Cluster Substructure: II. Linear Structure: Fuzzy C-Varieties and Convex Combinations Thereof.

40. T. R. Cundari, C. Sârbu, and H. F. Pop, *J. Chem. Inf. Comput. Sci.*, **42**, 1363 (2002). Robust Fuzzy Principal Component Analysis (FPCA). A Comparative Study Concerning Interaction of Carbon–Hydrogen Bonds with Molybdenum–Oxo Bonds.

41. D. Driankov, H. Hellendoorn, and M. Reinfrank, *An Introduction to Fuzzy Control*, Springer-Verlag, New York, 1993.

42. W. Siler, *Building Fuzzy Expert Systems*, Birmingham, Alabama, http://users.aol.com/wsiler/

43. W. Pedrycz, *Fuzzy Sets and Syst.*, **56**, 1 (1993). Fuzzy Neural Networks and Neurocomputing.

44. D. Nauck, *Proceedings of the Third European Congress on Intelligent Techniques and Soft-Computing (EUFIT '95)*, Aachen (August 28–31, 1995), pp. 1159–1164. Beyond Neuro-Fuzzy: Perspectives and Directions.

45. T. Feuring and W. M. Lippe, *Fuzzy Sets Syst.*, **102**, 227 (1999). The Fuzzy Neural Network Approximation Lemma.

46. T. Bernd, M. Kleutges, and A. Kroll, *Neural Computing Appl.*, **8**, 151 (1999). Nonlinear Black Box Modelling–Fuzzy Networks Versus Neural Networks.

47. W. Pedrycz, *Soft Comput.*, **2**, 61 (1998). Fuzzy Evolutionary Computing.

48. L.O. Hall, B. Ozyurt, and J.C. Bezdek, *IEEE Trans. Evo. Comput.*, **3**, 103 (1999). Clustering with a Genetically Optimized Approach.

49. A. Blanco, M. Delgado, and M.C. Pegalajar, *Int. J. Approx. Reason.*, **23**, 67 (2000). A Genetic Algorithm to Obtain the Optimal Recurrent Neural Network.

50. R. Östermark, *Soft Comput.*, **3**, 206 (1999). A Neuro-Genetic Algorithm for Heteroscedastic Time-Series Processes Empirical Tests on Global Asset Returns.

51. E. G. Mazurs, *Types of Graphic Representations of The Periodic System Of Chemical Elements*, La Grange, IL, 1959.

52. J. W. von Spronsen, *The Periodic System of Chemical Elements. A History of the First Hundred Years*, Elsevier, Amsterdam, The Netherlands, 1959.

53. O. Horowitz, C. Sârbu, and H. F. Pop, *Rev. Chim.(Bucharest)*, **51**, 17 (2000). Pattern Recognition Applied to Chemical Elements.

54. O. Horowitz, C. Sârbu, and H. F. Pop, *Rationale Classification of Chemical Elements*, Dacia Printing House, Cluj-Napoca, Romania, 2000.

55. W. Preyer, *Berliner Deut. Pharm. Ges.*, **2**, 144 (1893). Das Genetische System der Chemischen Elementen.

56. J. C. Bezdek, R. Ehrlich, and W. Full, *Comput. Geosci.*, **10**, 191 (1984). FCM: The Fuzzy c-Means Clustering Algorithm.

57. R. J. Mayer, *Naturwissenschaften*, **2**, 781 (1914). Positions of the Rare Earth Elements in the Periodic System.

58. H. Bassett, *Chem. News*, **65**, 3, 19 (1892). A Tabular Expression of the Periodic Relations of the Elements.

59. J. W. van Spronsen, *The Periodic System of Chemical Elements*, Elsevier, Amsterdam, The Netherlands, 1969.

60. J. D. Clark, *J. Chem. Educ.*, **10**, 675 (1933). A New Periodic Chart.

61. F. Scheele, *Z. Naturforschung*, **4a**, 137 (1949). The Position of the Lanthanides and Actinides in the Periodic Table.

62. T. Ternstrom, *J. Chem. Educ.*, **41**, 190 (1964). A Periodic Table.

63. W. B. Jensen, *J. Chem. Educ.*, **59**, 634 (1982). The Positions of Lanthanum (Actinium) and Lutetium (Lawrencium) in the Periodic Table.

64. B. Earl and D. Wilford, *Chemistry Data Book*, Blackie, London, 1991.

65. D. R. Lide, Ed., *CRC Handbook of Chemistry and Physics*, 71st ed., CRC Press, Boca Raton, FL, 1990.

66. F. H. Allen and O. Kennard, *Chem. Design Autom. News*, **8**, 31 (1993). 3D Search and Research using the Cambridge Structural Database.

67. W. A. Nugent and J. M. Mayer, *Metal-Ligand Multiple Bonds*, Wiley, New York, 1988.

68. J. M. Mayer, *Acc. Chem. Res.*, **31**, 441 (1998). Hydrogen Atom Abstraction by Metal–Oxo Complexes: Understanding the Analogy with Organic Radical Reactions.

69. C. Sârbu and H. W. Zwanziger, *Anal. Lett.*, **34**, 1541 (2001). Fuzzy Classification and Comparison of Some Romanian and German Mineral Waters.

70. V. Simeonov, H. Puxbaum, S. Tsakovski, C. Sârbu, and M. Kalina, *Environmetrics*, **10**, 137 (1999). Classification and Receptor Modeling of Wet Precipitation Data from Central Austria (1984–1993).

71. G. N. Chen, *Anal. Chim. Acta*, **271**, 115 (1993). Assessment of Environmental Water with Fuzzy Cluster Analysis and Fuzzy Recognition.

72. S. Pudenz, R. Brüggemann, B. Luther, A. Kaune, and K. Kreimes, *Chemosphere*, **40**, 1373 (2000). An Algebraic/Graphical Tool to Compare Ecosystems with Respect to their Pollution V: Cluster Analysis and Hasse Diagrams.

73. H. van Malderen, S. Hoornaert, and R. van Grieken, *Environ. Sci. Technol.*, **30**, 489 (1996). Identification of Individual Aerosol Particles Containing Cr, Pb, and Zn Above the North Sea.

74. A. Held, K. P. Hinz, A. Trimborn, B. Spengler, and O. Klemm, *Aerosol Sci.*, **33**, 581 (2002). Chemical Classes of Atmospheric Aerosol Particles at a Rural Site in Central Europe During Winter.

75. W. Jambers, A. Smekens, R. van Grieken, V. Shevchenko, and V. Gordeev, *Colloids and Surfaces A: Physicochem. Eng. Aspects*, **120**, 61 (1997). Characterisation of Particulate Matter from the Kara Sea Using Electron Probe X-ray Micro Analysis.

76. A. M. Lahdenperä, P. Tamminen, and T. Tarvainen, *Appl. Geochem.*, **16**, 123 (2001). Relationships Between Geochemistry of Basal Till and Chemistry of Surface Soil at Forested Sites in Finland.

77. J. A. Markus and A. B. McBratney, *Aust. J. Soil Res.*, **34**, 453 (1996). An Urban Soil Study: Heavy Metals in Glebe, Australia.

78. F. D. Tamás, J. Abonyi, J. Borszéki, and P. Halmos, *Cem. Conc. Res.*, **32**, 1325 (2002). Trace Elements in Clinker II. Qualitative Identification by Fuzzy Clustering.

79. J. Finol, Y. K. Guo, and X. D. Jing, *J. Petrol. Sci. Eng.*, **29**, 97 (2001). A Rule Based Fuzzy Model for the Prediction of Petrophysical Rock Parameters.

80. J. R. Pérez-Correra, M. V. Letelier, A. Cipriano, H. Jorquera, O. Encalada, and I. Solar, in *Air Pollution VI*, C. A. Brebbia, C. F. Ratto, and H. Power, Eds., WIT Press, Southampton, UK, 1998, pp. 257–266. Forecasting High SO_2 Concentration Levels with Fuzzy Clustering Techniques.

81. K. P. Hinz, M. Greweling, F. Drews, and B. Spengler, *J. Am. Soc. Mass Spectrom.*, **10**, 648 (1999). Data Processing in On-Line Laser Mass Spectrometry of Inorganic, Organic, or Biological Airborne Particles.

82. P. Samaras, A. Kungolos, T. Karakasidis, D. Georgiou, and K. Perakis, *J. Environ. Sci. Health, A*, **36**, 153 (2001). Statistical Evaluation of PCDD/F Emission Data During Solid Waste Combustion by Fuzzy Clustering Techniques.

83. C. Sârbu and H. F. Pop, *Chemosphere*, **40**, 513 (2000). Fuzzy Classification of the First 10 MEIC.

84. D. Melcher and M. Matthies, *Ecol. Model.*, **85**, 41 (1996). Application of Fuzzy Clustering to Data Dealing with Phytotoxicity.

85. M. Friederichs, O. Fränzle, and A. Salski, *Ecol. Model.*, **85**, 27 (1996). Fuzzy Clustering of Existing Chemicals According to Their Ecotoxicological Properties.

86. J. C. Frisvad, *Chem. Intell. Lab. Syst.*, **14**, 253 (1992). Chemometrics and Chemotaxonomy: A Comparison of Multivariate Statistical Methods for the Evaluation of Binary Fungal Secondary Metabolite Data.

87. A. Linusson, S. Wold, and B. Nordén, *Chem. Intell. Lab. Syst.*, **44**, 213 (1998). Fuzzy Clustering of 627 Alcohols, Guided by a Strategy for Cluster Analysis of Chemical Compounds for Combinatorial Chemistry.

88. F. Ros, K. Audouze, M. Pintore, and J. R. Chrétien, *SAR and QSAR Environ. Res.*, **11**, 281 (2000). Hybrid Systems for Virtual Screening: Interest of Fuzzy Clustering Applied to Olfaction.

89. T. Blaffert, *Anal. Chim. Acta*, **161**, 135 (1984). Computer-Assisted Multicomponent Spectral Analysis with Fuzzy Data Sets.

90. A. R. Goss and M. J. Adams, *Anal. Proceedings, Anal. Commun.*, **31**, 23 (1994). Spectral Retrieval by Fuzzy Matching.

91. F. Ehrentreich, *Fresenius J. Anal. Chem.*, **357**, 527 (1997). Representation of Extended Infrared Spectrum-Structure-Correlations Based on Fuzzy Theory.

92. F. Ehrentreich, *Fresenius J. Anal. Chem.*, **359**, 56 (1997). Derivation of Substructures from Infrared Band Shapes by Fuzzy Logic and Partial Cross Correlation Functions.

93. S. Kokot, S. Carswell, and D. L. Massart, *Appl. Spectrosc.*, **46**, 1393 (1992). Application of DRIFT Spectroscopy for Comparison of Dye Mixtures Extracted from Small Textile Samples.

94. M. Otto and H. Bandemer, *Anal. Chim. Acta*, **184**, 21 (1986). Pattern Recognition Based on Fuzzy Observations for Spectroscopic Quality Control and Chromatographic Fingerprinting.

95. M. Otto and H. Bandemer, *Anal. Chim. Acta*, **191**, 193 (1986). A Fuzzy Method for Component Identification and Mixture Evaluation in the Ultraviolet Spectral Range.

96. M. Otto, W. Wegscheider, and E. P. Lankmayr, *Anal. Chem.*, **60**, 517 (1988). A Fuzzy Approach to Peak Tracking in Chromatographic Separations.

97. U. Hörchner and M. Otto, *Fresenius J. Anal. Chem.*, **344**, 217 (1992). Identification of UV/VIS-Spectra Based on a Fuzzy Function.

98. Y. Gu, C. Hirano, and M. Horiike, *Rapid Commun. Mass Spectrom.*, **5**, 622 (1991). Fuzzy Classificational Analysis of Continuously Scanned Mass Spectra of Binary Mixtures of Positionally Isomeric Tetradecenols.

99. Y. Gu, *Fresenius J. Anal. Chem.*, **354**, 241 (1996). Identification of the Configuration of Sex Pheromones with a Conjugated Double Bond by Fuzzy Similarity Analysis of Chemical Shifts of Olefinic Carbons.

100. J. Xu, S. K. Straus, and B. C. Sanctuary, *J. Chem. Inf. Comput. Sci.*, **33**, 668 (1993). Automation of Protein 2D Proton NMR Assignment by Means of Fuzzy Mathematics and Graph Theory.

101. M. Otto, G. Stingeder, K. Piplits, M. Grasserbauer, and M. Heinrich, *Mikrochim. Acta*, **106**, 163 (1992). Comparison of Depth Profiles in SIMS by a Fuzzy Method.

102. C. Sârbu, *Anal. Lett.* **28**, 2077 (1995). A Comparative Study of Regression Concerning Weighted Least Squares Methods.

103. C. Sârbu and G. Cîmpan, *J. Planar Chromatogr.*, **9**, 126 (1996). Determination of Some 1,4-Benzodiazepines by Quantitative TLC. A Comparative Study Concerning Ladder of Power.

104. C. Sârbu, *Croat. Chem. Acta*, **70**, 795 (1997). A New Median-Based Regression Method.

105. H. W. Zwanziger and C. Sârbu, *Anal. Chem.*, **70**, 1277 (1998). Validation of Analytical Methods Using Regression Procedure.

106. S. I. Pop, V. Pop, S. Cobzac, and C. Sârbu, *J. Chem. Inf. Comput. Sci.*, **40**, 91 (2000). Use of Weighted Least–Squares Splines for Calibration in Analytical Chemistry.

107. H. Tanaka, S. Uejima, and K. Asai, *IEEE Trans. Syst. Man and Cybernetics*, **SMC-12**, 903 (1982). Linear Regression Analysis with Fuzzy Model.

108. H. Otto and H. Bandemer, *Chem. Intell. Lab. Syst.*, **1**, 71 (1986). Calibration with Imprecise Signals and Concentrations Based on Fuzzy Theory.

109. Y. Hu, J. Smeyers-Verbeke, and D. L. Massart, *Chem. Intell. Lab. Syst.*, **8**, 143 (1990). An Algorithm for Fuzzy Linear Calibration.

110. Y. Hu, J. Smeyers-Verbeke and D. L. Massart, *Chem. Intell. Lab. Syst.*, **9**, 31 (1990). Outliers Detection in Calibration.

111. T. Shimosaka, T. Kitamori, A. Harata, and T. Sawada, *Anal. Sci.*, **7**, 1389 (1991). Fuzzy Treatement of Analytical Data for Colorimetry.

112. C. Sârbu and H. F. Pop, *Talanta*, **40**, 513 (2001). Fuzzy Robust Estimation of Central Location.

113. P. L. Davies, *Fresenius J. Anal. Chem.*, **331**, 513 (1988). Statistical Evaluation of Inter-laboratory Tests.

114. P. A. Jansson, *Anal. Chem.*, **63**, 357A (1991). Neural Networks: An Overview.

115. J. Zupan and J. Gasteiger, *Anal. Chim. Acta*, **248**, 1 (1991). Neural Networks: A New Method for Solving Chemical Problems or Just a Passing Phase?

116. J. Zupan and J. Gasteiger, *Neural Networks for Chemists*, VCH, Weinheim, 1993.

117. M. Otto, T. George, C. Schierle, and W. Wegscheider, *Pure Appl. Chem.*, **64**, 497 (1992). Fuzzy Logic and Neural Networks—Applications to Analytical Chemistry.

118. P. J. Gemperline, J. R. Long, and V. G. Gregoriou, *Anal. Chem.*, **63**, 2313 (1991). Nonlinear Multivariate Calibration Using Principal Components Regression and Artificial Neural Networks.

119. J. R. Long, H. T. Mayfield, and M. V. Henley, *Anal. Chem.*, **63**, 1256 (1991). Pattern Recognition of Jet Fuel Chromatographic Data by Artificial Networks with Back-Propagation of Error.

120. D. N. Rassokhin, V. S. Lobanov, and D. K. Agrafiotios, *J. Comput. Chem.*, **22**, 373 (2001). Nonlinear Mapping of Massive Data Sets by Fuzzy Clustering and Neural Networks.

121. H. Sundgren, I. Lundström, and H. Vollmer, *Sensors and Actuators*, **6**, 225 (1984). Chemical Sensor Arrays and Abductive Networks.

122. H. Sundgren, F. Winquist, I. Lukkart, and I. Lundström, *Meas. Sci. Technol.*, **2**, 464 (1991). Artificial Neural Networks and Gas Sensor Arrays: Quantification of Individual Components in a Gas Mixture.

123. P. B. Harrington, *Chem. Intell. Lab. Syst.*, **18**, 157 (1993). Minimal Neural Networks: Concerted Optimization of Multiple Decision Planes.

124. P. B. Harrington, *Chem. Intell. Lab. Syst.*, **19**, 143 (1993). Minimal Neural Networks: Differentiation of Classification Entropy.

125. P. B. Harrington and B. W. Pack, *Anal. Chim. Acta*, **277**, 189 (1993). FLIN: Fuzzy Linear Interpolating Network.

126. P. B. Harrington, *J. Chemom.*, **5**, 467 (1991). Fuzzy Multivariate Rule-Building Expert Systems: Minimal Neural Networks.

127. M. Otto, *Anal. Chem.*, **62**, 797A (1990). Fuzzy Sets: Applications to Analytical Chemistry.

128. B. Kosko, *Neural Networks and Fuzzy Systems*, Prentice-Hall, Englewood Cliffs, NJ, 1992.

129. B. W. Wabuyele and P. B. Harrington, *Appl. Spectrosc.*, **50**, 35 (1996). Fuzzy Optimal Associative Memory for Background Prediction of Near-Infrared Spectra.

130. J. A. Agapito, L. Agapito, M. Schneider, R. Garcia Rosa, and T. Pedro, *Sensors and Actuators B*, **15–16**, 105 (1993). Fuzzy Logic Applied to Gas Sensors.

131. R. Neuböck, W. Wegscheider, and M. Otto, *Microchem. J.*, **45**, 343 (1992). Automated Qualitative Analysis by Inductively Coupled Plasma Atomic Emission Spectrometry Based on a Fuzzy Reasoning Scheme.

132. B. Adler, P. Schütze, and J. Will, *Anal. Chim. Acta*, **271**, 287 (1993). Expert System for Interpretation of x-Ray Diffraction Spectra.

133. O. L. Jensen, P. Mortensen, O. Vorm, and M. Mann, *Anal. Chem.*, **69**, 1706 (1997). Automation of Matrix-Assisted Laser Desorption/Ionization Mass Spectrometry Using Fuzzy Logic Feedback Control.

134. D. J. Ramsbottom and M. J. Adams, *Chem. Intell. Lab. Syst.*, **19**, 53 (1993). Uncertainty within a Commercial Expert System Shell for Polymer Analysis.

135. M. Kishimoto, M. Moo-Young, and P. Allsop, *Bioprocess Eng.*, **6**, 163 (1991). A Fuzzy Expert System for the Optimization of Glutamic Acid Production.

136. V. G. Nyttle and M. Chidambaram, *Bioprocess Eng.*, **9**, 115 (1993). Fuzzy Logic Control of a Fed-Batch Fermentor.

137. M. Ronen, Y. Shabtai, and H. Guterman, *Biotechnol. Bioeng.*, **77**, 420 (2002). Hybrid Model Building Methodology Using Unsupervised Fuzzy Clustering and Supervised Neural Networks.

138. P. J. Woolf and Y. Wang, *Physiol Genomics*, **3**, 9 (2000). A Fuzzy Logic Approach to Analyzing Gene Expression Data.

139. T. R. Cundari and M. Russo, *J. Chem. Inf. Comput. Sci.*, **41**, 281 (2001). Database Mining Using Soft Computing Techniques. An Integrated Neural Network-Fuzzy Logic-Genetic Algorithm Approach.

140. D. H. Rouvray, Ed., *Fuzzy Logic in Chemistry*, Academic, San Diego, 1997.

141. F. Ehrentreich, in *Encyclopedia of Computational Chemistry*, P. Schleyer, Ed., Wiley, Chichester, 1998, pp. 1090–1103. Fuzzy Methods in Chemistry.

Development of Computational Models for Enzymes, Transporters, Channels, and Receptors Relevant to ADME/Tox

Sean Ekins*[a] and Peter W. Swaan[†]

*GeneGo, 500 Renaissance Drive, Suite 106, St. Joseph, MI 49085
[†]Department of Pharmaceutical Sciences, University of Maryland, HSF2 20 Penn Street, Baltimore, MD 21201

INTRODUCTION

ADME/Tox Modeling: An Expansive Vision

Proteins may be classified primarily by their sequence or by their function, which may include acting as enzymes, transporters, channels, and receptors (a comprehensive and detailed review would be well beyond the scope of a single book chapter). An alternative way of classifying proteins is to consider the influence they have on drug *A*bsorption, *M*etabolism, *D*istribution, *E*xcretion, and *Tox*icology (ADME/Tox). A complete picture of any one protein system from expression, regulation, substrate and inhibitor selectivity, or protein–protein interaction is not currently feasible. We are therefore left

[a]Author for correspondence. Phone: 269-983-7649, Fax: 269-983-7654, Email: ekinssean@yahoo.com

Table 1 Characteristics of Enzymes Involved in Drug Metabolism

Enzyme	Location	Reaction	Cofactor[a]	Phase	Modeled
Cytochrome P450	Microsomal	Oxidation and reduction	NADPH	1	Yes
Flavin-containing monooxygenase	Microsomal	Oxidation	NADPH	1	No
Monoamine–diamine oxidases	Mitochondrial	Oxidation		1	Yes
Alcohol–aldehyde dehydrogenases	Cytosolic	Oxidation	NAD	1	
Prostaglandin synthetase–lipoxygenase	Microsomal	Oxidation	NADPH	1	
Polyamine oxidase	Cytosol	Oxidation	FAD	1	
Xanthine oxidase	Mitochondrial	Oxidation		1	
Aromatases	Mitochondrial	Oxidation	FAD	1	Yes
Alkylhydrazine oxidase	Unknown	Oxidation		1	
Azo and nitro reductases	Cytosolic	Reduction	FAD, FMN	1	
Carbonyl reductase	Microsomal and cytosolic	Reduction	NADPH	1	
Dihydropyrimidine dehydrogenase	Cytosolic	Reduction	NADPH	1	
Esterases	Microsomal and Cytosolic	Hydrolysis		1	Yes
Epoxide hydrolases	Microsomal and cytosolic	Hydration		1	Yes
UDP–glucuronosyl-transferases	glucuronidation	Microsomal	UDPGA	2	Yes
Sulfotransferases	Sulfation	Cytosolic	PAPS	2	Yes
Glutathione *S*-transferases	Glutathione conjugation	Cytosolic and Microsomal	Glutathione	2	Yes
Acyltransferases	Amino acid conjugation	Mitochondrial	Glycine	2	
N-Acetyltransferases	Acetylation	Cytosolic	Acetyl-coenzyme A	2	
Methyltransferase	Methylation	Cytosolic	*S*-Adenosyl-methionine	2	
Acyl-CoA-synthetases	Amino acid conjugation	Mitochondrial	Coenzyme A, ATP	2	

[a]Abbreviations: NADPH, β-nicotinamide adenine dinucleotide phosphate reduced form; NAD, β-nicotinamide adenine dinucleotide; FAD, flavin adenine dinucleotide; FMN, flavin mononucleotide; ATP, adenosine triphosphate; PAPS, 3′-phosphoadenosine 5′-phosphosulfate; UDP, uridine diphosphate; UDPGA, uridine diphosphate-glucuronic acid.

with a fragmented research area containing many individual proteins from which limited inferences can be drawn. What follows is an admittedly selective review on the current status of ADME/Tox for several intensely studied proteins in the hope that it will stimulate other investigators to think beyond individual proteins and adopt a more unified and holistic perspective in their research. In many cases, there may exist fundamental linkages between each class of protein for which the same computational tools can be applied to unravel the intricacies of each individual system; this will become the common thread interweaving through the fabric of this chapter. To our knowledge, no single laboratory has developed computational models for each ADME/Tox system described herein (although this may be currently underway). Without models for every system an initial barrier exists to their successful integration and the genesis of a complete prediction for ADME/Tox. To date, there have been many reviews on ADME/Tox modeling,[1–4] which should be refered to for more details on modeling general processes like blood–brain barrier (BBB) transport, absorption, and bioavailability.

The Concerted Actions of Transport and Metabolism

It is generally accepted that mammalian physiology has evolved mechanisms to specifically uptake essential nutrients and to remove hydrophobic xenobiotic and endobiotic molecules to prevent their accumulation and eventual toxicity. Important components of this process are *metabolism* and *transport*. There has been a dramatic increase in our understanding of these fields over the past decade, predominantly influenced by molecular biology, the isolation and expression of these proteins, and improvements in both the sensitivity and throughput of analytical and experimental technologies.

Metabolism

Metabolism can be defined as what the body does to convert a molecule to a more readily excreted one. Such molecules can actually become more biologically active via metabolism (which occurs for some pro-carcinogens, for example) and this kind of activation may be taken advantage of when designing prodrugs. In many species, metabolism is specifically enzymatic in nature such that a protein other than the desired target may bind the drug, and thereafter a cofactor-catalyzed reaction can remove or add a functional group to the drug molecule. Table 1 compiles the majority of enzymes, and describes their intracellular localization, cofactors, and functionalization pathways. The major enzymes involved in drug metabolism, like cytochromes P450 (CYP) and UDP-glucuronosyl transferases (UDPGT), are predominantly localized within the endoplasmic reticulum of cells and are relatively straightforward to study in vitro (reviewed in Ref. 5). These types of enzyme-catalyzed drug metabolism pathways may occur within many tissues in the body or they may be localized in just one cell type. Where these pathways exist is very

much dependent on the relative expression levels of the enzymes in a particular tissue although, in general, the liver and intestine contain the highest levels of most drug metabolizing enzymes.

The CYPs represent a very large superfamily of heme-containing enzymes that can either oxidize or reduce a large number of structurally different endogenous and exogenous molecules because of their broad substrate specificity and their regio- and stereoselectivity. These enzymes are ubiquitously expressed and they may be induced by drugs and endobiotics as well as by other environmental xenobiotics. Of increasing importance to our understanding of ADME/Tox is the role of enzymes in drug–drug interactions, in which one drug may interfere with the metabolism of another drug if they compete to fit (preferably) within the same ligand-binding site of the same enzyme. Among the endobiotics are the abundant steroids, and the bile acids that have essential roles as hormones, signaling molecules, and as detergents. However, we are now beginning to further understand how multiple endobiotics, xenobiotics, therapeutic, and environmental agents may interfere with the removal and metabolic mechanisms in vivo having potentially undesirable toxic consequences. The role of CYPs probably began first as a functional response for regulation of intracellular signals and further evolved to remove environmental molecules. In more popular terminology, it is believed that CYPs have evolved from plant versus animal warfare.[6]

Transporters

The transport of a molecule into and out of cells, by both active transport and passive diffusion, is integral to xenobiotic and endobiotic metabolism. It is now well appreciated that organic solutes such as physiologically critical nutrients (amino acids, sugars, vitamins, and bile acids), as well as neurotransmitters and drugs, are transferred across cellular membranes by specialized transport systems.[7] These systems encompass integral membrane proteins that shuttle substrates across the membrane, which is done by either a passive process through channels (facilitated transporters) or by an active process (via carriers). The latter is energized directly by the hydrolysis of ATP or indirectly by coupling to the cotransport of a counterion down its electrochemical gradient formed by Na^+, H^+, or Cl^-.

Our understanding of the biochemistry and molecular biology of mammalian transport proteins has significantly advanced because of the development of expression cloning techniques. Initial studies in *Xenopus laevis* oocytes by Hediger et al.[8,9] resulted in the isolation of the intestinal sodium-dependent glucose transporter, SGLT1. To date, sequence information and functional data derived from numerous transporters have revealed unifying designs, similar energy-coupling mechanisms, and common evolutionary origins.[10] The plethora of isolated transporters motivated the human gene nomenclature committee to classify these proteins into a distinct genetic superfamily

named SLC (for SoLute Carrier). Currently, the SLC class contains 37 families with 205 members and is rapidly expanding (http://www.gene.ucl.ac.uk/nomenclature/). The ABC superfamily contains 7 families with 48 members;[11] class B contains the well-known multidrug resistance gene (MDR1) derived P-glycoprotein (ABCB1), while class C comprises members of the multidrug resistance protein (MRP) subfamily. With the completion of the human genome project, it can be anticipated that a vast number of membrane transport proteins will be identified without known physiological function. This clearly raises questions that may be answered using computational technologies.

Transporters have a critical role in maintaining cellular homeostasis, and interference with this delicate balance by xenobiotics including therapeutics may have an undesirable effect. On the other hand, the efficacy of drugs may be improved by leveraging affinity for the transporters such that a drug can piggyback with the physiological substrate, or at the very least, mimic its critical molecular features.[12–14] Efflux of molecules from cells therefore can occur via transporters that would usually function to clear toxic endogenous metabolites such as conjugated bile acids from the cell. One can therefore envision that the enzymes involved in metabolism and the transporters have a very close linkage and functional regulation, working in concert to maintain the cellular steady state. Similarly, ion channels are key to maintaining cellular homeostasis. Ion channels have important roles in cellular communication and are critical to life. The up and down regulation of these proteins may be under the control of many receptors that themselves can bind the same (or similar) molecules. These receptors likely have endogenous functions. Also, there are receptors with unrelated functions, such as those in the central nervous system (CNS), which in some cases may have the same binding requirements as those of desirable non-CNS therapeutic targets. This, in turn, can lead to interactions that manifest as a neurological side effect, but this area has been poorly explored. In its simplest sense, the common binding requirement across numerous proteins of different function and in multiple locations represents a multidimensional problem that prevents our understanding of whether or not a drug will impact each of these processes. However, there are many transporters and enzymes of relevance for both metabolism and transport of drugs; understanding the effect a drug has on all of them represents a major challenge. This complicated ligand affinity profile determination is further compounded by the absence of freely available crystal structures for any of these membrane-bound proteins that are known to bind drugs. If anything, our understanding of drug metabolism, transport, ion channel function, and the role of receptors (both CNS and non-CNS) is now more complex than envisaged decades ago when far fewer of these proteins had been identified, sequenced, expressed, or analyzed in vitro or in vivo.

Consequently, the assessment of in vitro ADME/Tox parameters has been moved much earlier in the pharmaceutical discovery process such that large amounts of protein-specific data are generated. This data needs interpretation

and that knowledge, in turn, may provide a valuable resource for generating computational models in the future. These ADME/Tox specific proteins can be viewed as "antitargets" in that they may need to be avoided to some extent while the selection of molecules with a high affinity for the therapeutic target(s), on the other hand, is critical. This chapter aims to show novice molecular modelers what tools exist today for visualizing and modeling enzymes, transporters, channels, and receptors that are relevant to ADME/Tox with the goals of being able to design molecules that can leverage or avoid these antitargets as desired.

APPROACHES TO MODELING ENZYMES, TRANSPORTERS, CHANNELS, AND RECEPTORS

There have been considerable advances in the development of strategies for structure-based drug design. De novo molecule design, docking, and virtual combinatorial library generation have been recent hot topics in the literature. Many publications in the mid-1990s outlined the successes and limitations of all of these technologies.[15–21] Computational approaches needed for understanding metabolism and toxicology began to appear approximately a decade after the evolution of computational tools used for assisting in target prediction and optimization. Recently, several journal monographs have been devoted to in silico modeling of ADME/Tox properties. In those monographs are numerous reviews providing useful information on the subject.[1–3,22–30] During the past few years, we have seen researchers indicating that they can now predict a molecule's probability of success in vivo from simple chemico-physical descriptors.[31,32] The development of in vitro assays, computational protocols, and the development of cheminformatics in the past decade have also yielded data sets used to build specific computational models (Figure 1)
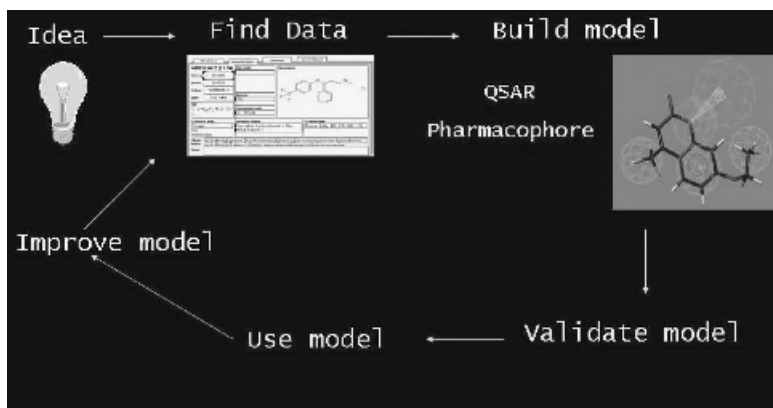
Figure 1 The in silico model building paradigm.

to predict a multitude of phenomena including BBB penetration,[33–36] solubility,[32,37] lipophilicity,[38,39] plasma protein binding,[40,41] volume of distribution,[42] half-life,[43] intrinsic clearance,[44,45] absorption,[46–50] metabolism,[51–53] and drug–drug interactions.[22,23] Computational models have also been generated for P-glycoprotein,[54–58] other drug transporters,[7] and toxicity end-points[2,25–27,29,30,59] such as mutagenicity data.[60–62] These examples represent just a small sample of the many computational studies of relevance to ADME/Tox performed in recent years and that may be used in a filter hierarchy (Figure 2). The toxicology papers[26,27,29,30,59] have in most cases either compared available software that contain built-in toxicology models or they have attempted to build QSAR models for various toxicology end-points. For more details, the reader is referred to these papers.

Some in silico studies have generated additional general rules comparable to Lipinski's "rule of 5" or they have resulted in the development of triage filters from large commercially available databases (CMC, MDDR, WDI, etc.) or from internal company data useful for predicting solubility and absorption potential.[31,32,63] A simple rule for rat bioavailability, for example, was
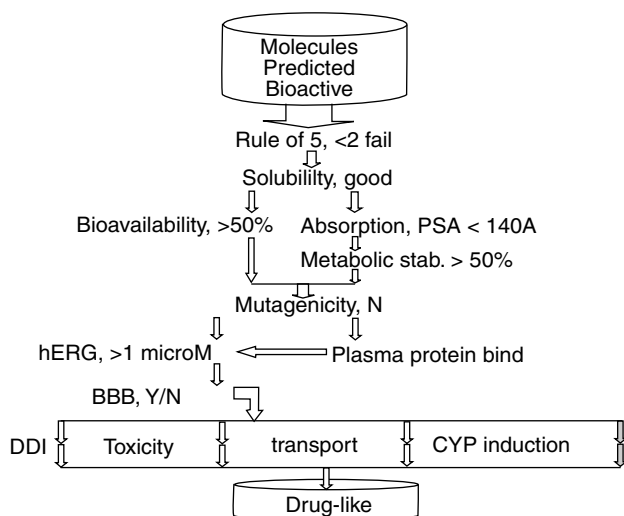
Figure 2 In silico ADME/Tox filter model placement hierarchy with suggested pass–fail criteria. Molecules predicted as having bioactivity are first passed through simple rules (like the Rule of 5) before prediction by first-level models like solubility. If models are predicted as soluble they can then pass onto bioavailability and/or separate filters for absorption and metabolism. Toxicity filters such as those for mutagenicity could then be implemented, while a filter for hERG may require inputs from a filter for protein binding to be meaningful. If the drug is desired to cross or not to cross the BBB barrier, a further filter could be used. Additional filters for numerous toxicity, drug–drug interaction, transporter, and induction models could then be used. Ultimately, more drug-like molecules should result.

described as being dependent on the polar surface area and number of rotatable bonds of the administered drug.[64] Similarly, there have been reasonably successful studies directed at discriminating between drug-like and non-drug-like molecules,[65,66] differentiating between leads and drugs,[67] and describing common structural features of known drugs,[68,69] as well as identifying molecules that are frequent or promiscuous hitters in high-throughput screens.[70,71] The above mentioned triage-type filters represent an adequate first-level in silico screen, but they have some limitations and they do not adequately deal with the overall ADME/Tox picture. These virtual approaches, however, represent an effective and rapid means to filter and prioritize molecules based on desirable structural descriptors or predicted simple physico-chemical properties. When combined with other computational or statistical approaches for selecting molecules in a multivariate–multiobjective optimization[22,25,72–74] one can avoid suboptimal molecules[31] and shorten lead generation and lead optimization times.[25] Ultimately these in silico models will enable us to increase the number of compounds that can be screened, if we use large virtual libraries[72,75,76] that can be scored for ADME/Tox and bioactivity. Now, we can consider classical QSAR, pharmacophore, and homology modeling techniques that have been applied to modeling some of the proteins involved in ADME/Tox.

Classical QSAR

The fundamentals, history, and methodology of QSAR and 3D-QSAR have been reviewed in considerable detail by Kubinyi, Waller and Oprea, as well as by others. The reader is referred to these general overviews.[77–79] As early as the 1960s it was appreciated that one could apply a mathematical model to understand metabolic actions in order to design new or improved drugs.[80] One of the limitations of the QSAR method is the availability of large, adequate data sets. In the 1960s, the log P term alone was used in all equations as a measure of hydrophobicity. It was found to be 2 for each system, suggesting that hydrophobicity was important for membrane penetration by a drug to reach the site of metabolism. Such studies were carried considerably further by Hansch's group,[81–84] as well as by Lewis et al.[85–93] in the metabolic field. By adding other descriptors such as HOMO and LUMO (highest occupied and lowest unoccupied molecular orbitals, respectively), pK_a, log $D_{7.4}$, dipole moment, solvent accessible surface area, volume of solvent accessible area, molecular length/width ratio, and molecular area/depth squared ratio, it became possible to further generate rough rules for the prediction of general properties displayed by substrates and inhibitors of each CYP.[85,86] These classical QSAR approaches for ADME/Tox properties have been updated to some extent by the utilization of newer three-dimensional (3D)-descriptors such as MS-WHIM.[94–100] These and other developments now present us with a rich source of molecular descriptors for use with various QSAR technologies.

Finally, we should point out that while classical QSAR approaches generally result in a single equation with statistical terms, modern 3D-QSAR methods generally produce graphically intensive models that may aid in the interpretation of important features in molecular 3D space and the mapping back of these features onto the molecules of interest.

Pharmacophore Models

One of the alternatives to direct protein modeling is the determination of a pharmacophore describing the features present within a ligand required for bioactivity. A pharmacophore is thus a representation of the spatial arrangement of structural features for a series of molecules (obtained after structure alignment and superposition) that show activity and affinity toward a protein. In some cases, the pharmacophore may be translated as a template for the actual binding site (though, depending on the software used, doing this is questionable). The alignment of molecules based on chemical functionality allows for diverse and structurally unique molecules to be grouped together without the need to perform an atom-by-atom comparison. A pharmacophore thus provides a straightforward method for representing drug–enzyme interactions that does not directly represent the active site of the protein but instead implicates only the key features necessary for a particular biological response. The prediction of interaction or activity for a novel molecule by a pharmacophore hypothesis is thus based on the geometric fit to the chemical features in that pharmacophore. A recent book and a number of reviews describing pharmacophore models exist.[101–103] In our experience we have most frequently used K_m, K_i, IC$_{50}$ (and less preferably percent inhibition) data when building pharmacophore models for ADME/Tox properties, although other valid types of kinetic experimental values could also be used, such as dissociation constants. According to the literature, the two most commonly used programs for pharmacophore development are DISCO (DIStance COmparisons) and Catalyst. They are part of commercially available software suites and will be described along with other programs below. Note that public domain and pharmaceutical company specific proprietary softwares also exist.

Catalyst
Catalyst (Accelrys, San Diego, CA) is an integrated environment for conformer generation using the poling technique (ConFirm),[104] and pharmacophore alignment, automated hypothesis generation (HypoGen),[105] pharmacophore, or molecular-shape based 3D searches. The software also provides a useful way to generate simple initial models (HipHop) based on a limited number of structures that could either be derived from X-ray conformations or from low-energy conformers covering conformational space.[106] The HipHop algorithm finds these models after a pruned exhaustive search where it begins with a small set of features and then extends those features
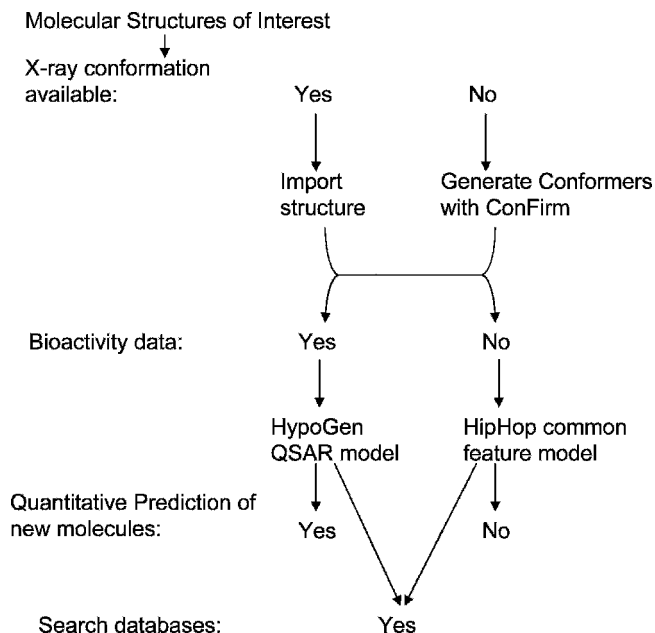
Figure 3 A schematic for Catalyst pharmacophore generation.

until it cannot find a larger common configuration.[106,107] The training set members must then map completely or partially on to the features in some configuration that the user can select. This technique is further described in two detailed reviews,[101,102] a schematic outlining these pharmacophore approaches is depicted in Figure 3.

To generate ADME/Tox pharmacophore models within Catalyst, our research groups have mainly used the HypoGen function. Following the generation of multiple conformers with ConFirm, HypoGen enables the generation of structure–activity relationship pharmacophore (hypothesis) models from a defined set of molecules that possess biological activity values. The hypotheses generated by HypoGen represent chemical features in 3D space that fit the features of the training set and are correlated with the biological data within certain tolerances and weights. The hypotheses created by the algorithm are pharmacophores that are generally common among the active molecules but not among the inactive ones in the training set. The hypotheses are created after constructive, subtractive, and optimization phases.[105] The constructive phase generates hypotheses common to the active molecules, by identifying the actives, generating and storing all the hypotheses present in the two most active molecules, and then retaining the hypotheses that fit the remainder of the actives. In the subtractive phase, hypotheses are removed that are unlikely to be useful if they are also found to be present in the inactive

compounds. A compound is deemed to be inactive if its activity is *n* orders of magnitude less active than the most active compound (where *n* is user determined). Hypothesis optimization is performed using simulated annealing, which perturbs the hypotheses by rotating vector features and translating other features at random in an attempt to improve the cost function. This algorithm accepts all improvements and some detrimental steps based on a probability function and retains the 10 unique best scoring pharmacophores. For each of these 10 hypotheses, the activity of each training set molecule is regressed after fitting to the pharmacophore versus the observed activity. A selected HypoGen hypothesis provides a means of predicting the biological activity for additional molecules that have yet to be synthesized as well as a 3D search query for databases.[105]

The creation of a pharmacophore model requires first generating multiple conformers of each molecule in an attempt to gather an extensive and diverse coverage of conformational space. Initially, we have used up to 255 conformers with an energy range up to 20 kcal/mol with the ''best conformer generation'' (i.e., poling algorithm) and the remaining default settings. More recently, we have started to utilize the ''fast conformer generation'' due to the time savings and the similar conformer coverage that this algorithm now provides. The same conformer generation routine is used for molecules in the training and test sets. After selecting required pharmacophore features that typically include hydrogen-bond acceptor, hydrogen-bond donor, hydrophobe, aromatic, and negative ionizable groups, the 10 hypotheses are generated for the training set using the conformers for each molecule. After assessment of all 10 hypotheses created, the lowest energy-cost hypothesis was frequently used as the representative pharmacophore. The quality of the structure–activity relationships (based on the observed and fitted data generated by Catalyst) are estimated by a correlation coefficient value (*r*). The ''total cost'' compared with the ''null cost'' has additional parameters evaluated to assess the model quality. Further testing of the model can be undertaken using the CatScramble routine where molecules in the data set can be permuted. This randomization, carried out multiple times, should always result in lower *r* values than for the real model. The Catalyst hypothesis generation procedure is repeated multiple times (typically 10) and the mean *r* value should be lower than the original model *r* value, if indeed the model is to be considered statistically significant.

The Catalyst hypothesis can be evaluated using a test set of molecules containing a similar level of diversity as that of the training set. The molecules in the test set have conformers generated the same way as those in the training set. The test set conformers are then fitted to the hypothesis deduced for each training data set in order to predict a binding or inhibition value. Catalyst provides two algorithms with this ability. These are ''best fit'' and ''fast fit''. ''Fast fit'' refers to the method of finding the optimum fit of the molecule to the hypothesis for all possible conformers of that molecule. The optimal fit

method involves the positioning of features on the molecule closest to the centroid of their corresponding pharmacophore features. The "best fit" procedure starts with "fast fit" and allows individual conformers to flex over a maximum energy range of 20 kcal/mol. This allows for examination of more conformational space and minimizes the distance between the hypothesis features and the atoms onto which they map. The predictions using either algorithm are generated from the hypothesis regression and can be compared by means of a residual that is calculated from the difference between predicted and observed value. The strength of Catalyst appears to be with relatively small and structurally diverse datasets containing from 10 to 40 molecules in our experience. Compared with other methods requiring structure alignment, Catalyst does not impart any user bias nor does it require much experience in modeling to begin with. One disadvantage of Catalyst is its lack of internal methods for model evaluation and cross-validation. To date, there have been no publications where the software has been used for even moderately large (>50 molecule) datasets to our knowledge.

DISCO

DISCO is a module within the SYBYL software suite (Tripos Associates, St. Louis, MO) that can be used to generate pharmacophore models.[108] The method is based on the assumption that the pharmacological potency of a compound can be represented by its structural points of potential pharmacological interest such as hydrophobic centers or hydrogen-bond donors. These structural points are called DISCO features. The pharmacophore is the maximum common feature among the set of molecules. To find the bioactive conformation instead of the energetically minimum conformation for each molecule, a maximum of 25 conformers within a 70-kcal/mol energy cutoff are usually generated for each molecule in a dataset using the "MultiSearch" function in DISCO. Subsequently, DISCO features are assigned to the various conformers. It is strongly recommended that the reference compound be the molecule having both the fewest features and conformers.[108] DISCO is run initially with all the possible "feature" points considered. Additional runs can then be performed with a specified minimum number of those features. The resulting pharmacophore models can be used to superimpose additional sets of molecules, which in turn can then serve as a structural overlap to be analyzed by a Comparative Molecular Field Analysis (CoMFA).

CoMFA

The CoMFA module within SYBYL is an especially useful QSAR technique that has been applied with considerable success in the areas of drug discovery and drug design as well as for enzyme and transporter kinetics.[109–112] It explains the gradual changes in observed biological properties by evaluating the electrostatic (Coulombic interactions) and steric (van der Waals interactions) fields at regularly spaced grid points surrounding a set of mutually

aligned ligands. A statistical algorithm, Partial Least Square (PLS), is used to correlate the field descriptors with biological activities. Both fields are usually calculated using an sp^3 hybridized carbon probe atom (with a +1 or −1 charge at 1.52 Å van der Waals radius) on a 2.0 Å spaced lattice, which extends beyond the dimensions of each aligned structure by 4.0 Å in all directions. An energy cutoff of 30.0 kcal/mol ensures that no extreme energy descriptors will distort the final model. The indicator fields[111] and hydrogen-bond fields[113] generated by the "advanced CoMFA" module can be included in the analysis as an option. To eliminate excessive noise, all electrostatic energies <1.0 kcal/mol and steric energies below 10.0 kcal/mol are set to zero in the indicator fields. The hydrogen-bond field descriptors are normally set to zero at sterically prohibited points. Sterically allowed points close to a hydrogen-bond acceptor are assigned a nominal steric potential, while the points close to a hydrogen-bond donor are assigned a nominal electrostatic potential. As a result, the steric field actually represents the acceptor component while the electrostatic field essentially indicates the donor component. Equal weights are assigned to these fields using the CoMFA standard scaling option. The CoMFA descriptors are used as independent variables. The dependent variable, usually a biological descriptor used in these studies, is derived from the type of experimental data obtained. The standard deviation of those experimental data can be used as a weighting factor in PLS analyses. Note that the weighting of columns can be assigned only from the command line of the program. The predictive ability of each model generated is evaluated by using a Leave-One-Out (LOO) cross-validation protocol. Subsequently, the cross-validated coefficient, q^2, is calculated as follows:

$$q^2 = 1 - \frac{\sum(Y_{predicted} - Y_{observed})^2}{\sum(Y_{observed} - Y_{mean})^2} \qquad [1]$$

where $Y_{predicted}$, $Y_{observed}$, and Y_{mean} are the predicted, observed, and mean values of the target property, respectively. The term $(Y_{predicted} - Y_{observed})^2$ is the predictive sum of squares (PRESS). The model with the optimum number of PLS components, corresponding to the lowest PRESS value is usually selected for deriving the final PLS regression models though other types of statistical measures can change this decision. In addition to the q^2, the conventional correlation coefficient r^2 and its standard error can be calculated. It is desirable to plot the predicted versus experimental activity to identify potential outliers. The process described above is repeated until no further improvements in q^2 is obtained or no outliers can be identified. Results from alternative descriptor fields (e.g., log P, calculated molecular refractivity, dipole moment) are compared and the model with the highest q^2 and lowest number of PLS components is usually accepted. The number of explanatory variables (descriptors) can be used as an additional guideline in selecting a model with

the lowest complexity. A simpler model is often considered to be a better model. In general, a contour plot of std * coefficients (the standard deviation times the value of the PLS coefficient at each grid point) enclosing the highest 20% value is created for each model to allow the user to visualize the CoMFA fields surrounding the molecules in the data set. Other options for visualizing the large number of CoMFA coefficients exist as well.

CoMSIA

Comparative Molecular Similarity Indices Analysis (CoMSIA) is an alternative 3D QSAR descriptor analysis tool developed by Klebe et al.[114] Hydrogen-bond acceptor and hydrophobic fields are considered in CoMSIA in addition to the steric and electrostatic features calculated for CoMFA. The CoMSIA similarity index descriptors are derived[114] using a lattice box as described above for CoMFA, typically with a grid spacing of 2 Å and using a negatively or positively charged sp^3 hybridized carbon atom probe. The CoMSIA similarity indices (A_F) for a molecule j with atoms i at a grid point q are calculated as follows:

$$A^q_{F,k}(j) = - \sum \omega_{probe,k} \omega_{ik} e_{iq}^{-\alpha r^2} \qquad [2]$$

Five physico-chemical properties k (steric, electrostatic, hydrophobic, hydrogen-bond donor, and hydrogen-bond acceptor) can be calculated using a single-probe atom. A Gaussian-type distance dependence is used between the grid point q and each atom i of the molecule so as to avoid extremely large values of field properties, k. A default attenuation factor (a) of 0.3 is often used. In COMSIA, the steric indices are related to the third power of the atomic radii, the electrostatic descriptors are derived from the assigned partial atomic charges, hydrophobic fields are derived from atom-based parameters,[115] and the hydrogen-bond donor and acceptor indices are obtained by a rule-based method derived from experimental values.[114] As in CoMFA, an optimal model is selected based on the following criteria: high q^2 (preferably >0.6), low number of PLS components, and minimal number of additional descriptors.

GOLPE

GOLPE (Generating Optimal Linear PLS Estimations) is an alternative QSAR method.[116] It performs multivariate regression analysis on the interaction fields around the molecules in the data set generated by the program GRID.[117] The type of field computed depends on the probe used. The probe in turn, should be selected based on the type of interaction one needs for the analysis. The phenolic hydroxyl (OH) probe is often selected in our laboratory because it can offer both donor and acceptor properties of a hydrogen-bond as well as locating sites of hydrophobic interaction. The interaction energies are calculated at 0.5 Å spaced grid points, which usually extend 4.0 Å beyond the

dimensions of all aligned substrates. The generated interaction fields are selected and then analyzed by GOLPE. Energy terms between 0.05 and −0.01 kcal/mol are usually set to zero to delete redundant descriptors in order to reduce the "noise". Field variables with standard deviation <0.1 kcal/mol are normally deactivated because they reveal very small variance in the data file. The variables that only take a few values and distribute themselves very unevenly among objects are removed because they force the model to explain the variance of a few objects with a high leverage. A Principle Component Analysis (PCA) is then performed to check the distribution of the objects and variables. The number of components is selected critically, keeping in mind that a low number of components yields a model with the lowest complexity. These settings are then applied to all ensuing analyses. A non-cross-validated PLS is subsequently performed followed by a LOO cross-validated PLS. One of the strengths of GOLPE is that a PLS plot of the components (called a T-U plot) can be generated to identify potential outliers, which can then be excluded in the next run. If no outliers are detected or if no improvements in q^2 can be achieved, iterations are stopped. If the resulting q^2 is too small (typically <0.3), further variable selections then need to be carried out. Subsequently, Smart Region Design (SRD)[118] is applied to generate Voronoi polyhedra for 1000 seed variables around one grid unit region of each seed variable. The polyhedra are then collapsed within two grid units of each seed variable. This maintains the 3D information and simplifies the variable selection process that follows. Based on SRD, variables that best span the multidimensional weight space are selected by D-Optimal preselection. Fractional Factorial Design (FFD) selection is carried out to further select only the most informative variables. The final non-cross-validated PLS is then performed followed by the cross-validated PLS. The resulting model is displayed visually by mapping the QSAR coefficient contour enclosing the top 20% value.

ALMOND

Most methods for performing 3D-QSAR rely upon an alignment step that can be time consuming and that can introduce user bias. The resultant model is thus dependent on and sensitive to the alignment routine used. ALMOND 2.0 is an alignment independent QSAR technique. It generates and analyzes GRid INdependent Descriptors (GRIND)[119] based on the interaction fields computed by GRID. Three probes: hydrophobic (DRY), carbonyl oxygen (O), and amide nitrogen (N1) are used by GRID at 0.5 Å spaced grid points to generate the interaction fields. ALMOND transforms these grid dependent and redundant variables into GRIND. These variables are then scaled by the program's Remove Baseline method. A PCA is performed to examine the variables and objects distribution and this is followed by a non-cross-validated PLS and/or a leave-one-out cross-validated PLS. Analogous to GOLPE, a PLS plot can be generated to identify outliers, which can then be

excluded in the next run. The FFD variable selection is performed after outliers are excluded and before generating the final model.

Homology Modeling

If a protein has a substantially high amino acid sequence homology (i.e., >40–60% identity) to one or more other proteins of known structure, it may then be assumed that this protein could adopt a similar 3D structure with respect to the known protein. This assumption provides the basis for homology modeling that enables us to build a hypothetical structure for a new protein. A recent review discussed this approach in considerable detail with regards to the CYPs and has shown the importance of using multiple template models (also suggested earlier by others[120]) to generate a model that was then validated against the known structure of crystallized CYP2C5.[121] There have been other excellent reviews describing the integration of homology models with site directed mutagenesis.[122,123]

The CYPs have been undoubtedly the most widely modeled protein using this technique compared to other proteins of interest in the ADME/Tox field. Transporters and some channels have likewise been modeled, but the low homology between them and the few crystallized membrane-bound proteins makes interpretation and extrapolation difficult (although several other approaches with promising results have been taken to understand the integral membrane-protein structure[7]). Homology models for channels have received considerable attention since the crystallization of KcsA and homology modeling may have utility beyond the potassium channels (described later). Models for receptors (generally GPCRs) have been hampered by the lack of crystal structures, although a number of structures exist for the ligand-binding domains of nuclear hormone receptors. Computational techniques such as threading offer some promise to increase the number of reliable structures of membrane bound proteins, as do combinations of intelligent approaches that take a one-dimensional (1D) sequence and convert it into a 3D structure.[124] The quality of the results derived from these techniques, and their utility for molecule design of key binding-site features is impacted by the resolution of the model, which in some cases may be low.

TRANSPORTER MODELING

Targeted delivery to transport systems in the gastrointestinal (GI) tract has emerged over the past 20 years as a successful strategy to increase oral availability of poorly absorbed drugs. In this approach, drug penetration is enhanced by coupling a given drug molecule to natural ligands known to target nutrient transporters. The toxicity and immunogenicity of drug–ligand conjugates is expected to be inherently low due to the use of endogenous

substrates. Alternatively, an approach called ''substrate mimicry'' can be used, which aims to create novel drug entities that mimic the 3D features of natural ligands. Both approaches should result in compounds that are recognized by a specific transport protein embedded in the enterocyte brush-border membrane, thereby facilitating transport across the intestinal wall.

Applications of Transporters

Oral absorption of a drug remains the favored route of administration from a patient comfort and compliance point of view. However, the development of orally administrable drugs and/or dosage forms poses a significant attrition threat to pharmacologically potent drug candidates. Despite intensive research in this area, oral drug delivery remains the greatest challenge to the pharmaceutical scientist, not only for the delivery of macromolecules, but also for small lead compounds with poor membrane permeability.

A promising approach for increasing oral bioavailability is targeting the intestinal solute transporter systems. Transporters are polytopic membrane proteins that are indispensable to the cellular uptake and homeostasis of many essential nutrients. During the past decade it has become clear that a vast number of drugs share transport pathways with nutrients. Moreover, a critical role has been recognized for transport proteins in the absorption, excretion, and toxicity of drug molecules, as well as in their pharmacokinetic and pharmacodynamic (PK/PD) profiles. Because cellular transporter expression is often regulated by nuclear orphan receptors that simultaneously regulate the translation and expression of metabolic enzymes in the cell (e.g., P-glycoprotein and cytochrome P450 regulation by the pregnane X receptor), they may indirectly control drug metabolism. Thus, transport proteins are involved in many facets of drug ADME/Tox, conferring an important field of study for pharmaceutical scientists involved in these areas. As a result, in-depth knowledge of membrane transport systems may be extremely useful in the design of new chemical entities (NCE). After all, it is now well appreciated that the most critical parameter for an NCE to survive the drug development pipeline on its way to the market is its ADME/Tox profile. Despite the involvement of solute transporters in fundamental cellular processes, most are poorly characterized at the molecular level. As a result, we are unable to accurately predict the interaction of drugs with this important class of membrane proteins a priori, and detection of drug–transporter interactions has been unacceptably serendipitous.

Transporter pathways can be exploited to increase oral drug absorption in two ways: (1) designing an NCE that mimics the molecular structure of the endogenous substrate to the intestinal transporter system or (2) piggybacking compounds through the cell by conjugation to substrates for transport systems. Both approaches require detailed knowledge of the 3D arrangement(s) between the substrate and transport protein. At the present time, with few

transport proteins crystallized, structural details and affinity requirements of transport proteins are generally unknown. The application of in silico techniques is finally gaining acceptance in the transporter field as more manuscripts appear that use a combined biology–molecular modeling approach to infer useful information on transporter structure–activity relationships. This represents an opportunity for optimizing molecules as substrates for the solute transporters and for providing an additional screening system for drug discovery. Clearly, the future growth in knowledge of transporter function will be lead by integrated in vitro and in silico approaches. The following section summarizes the major transporters that have been studied to date or deserve further attention with regard to computational modeling.

The Human Small Peptide Transporter, hPEPT1

In general, the intestinal small peptide carrier (PEPT1) is a proton-coupled, low-affinity, active, oligopeptide transport system with broad substrate specificity that enables transport of its natural substrates di- and tri-peptides occurring in food products.[125–129] The PEPT1 shows affinity toward a broad range of peptide-like pharmaceutically relevant compounds, such as β-lactam antibiotics[130,131] and angiotensin converting enzyme (ACE)-inhibitors.[132–142] In fact, these molecules can oftentimes be viewed as "peptide-like" in their molecular composition. For this reason, the transporter has been recognized as an important intermediate in the oral bioavailability of peptidomimetic compounds.[134] However, the lack of knowledge regarding structural specificity toward its substrates has prevented the use of this transporter on a more rational basis. In addition, its cellular localization to the apical membrane does not provide a mechanism for cellular exit into the basal compartment.[143,144] Currently, there exists a keen interest in understanding the structural determinants for substrates and inhibitors of this transport protein.

There have been numerous studies directed toward modeling peptide transporters using conformational analyses to imply the molecular determinants and the distances between functional groups in substrates critical for affinity.[145–148] By using β-lactam molecules, it was suggested that a carboxylic carbon (likely to position in a positively charged pocket), two carbonyl oxygen atoms (hydrogen-bond acceptors), a hydrophobic site and finally an amine nitrogen atom (hydrogen-bonding region) are important features of substrates.[109,149] Other studies using expressed rabbit PEPT1 or human PEPT1 (hPEPT1) indicate a peptide bond is not essential for substrates of these ortholog transport carriers. Instead, two ionized amino or carboxyl groups with at least four CH_2 units between them, or amino acid esters of nucleoside such as 5-aminopentanoic acid and valacyclovir, permit transport.[142,150–152] A recent meta-analysis of K_i values for 42 substrates using PEPT1 data from many sources provided a template consisting of an N-terminal NH_3 site, a

hydrogen-bond to the carbonyl group of the first peptide bond, a hydrophobic pocket and a carboxylate-binding site.[153] Other groups have confirmed these essential features for transport.[132,154] A more recent study[131] generated the first pharmacophore with 11 hPEPT inhibitors. This model agreed with the previous models for PEPT1 as a positive ionizable feature (aligns to amine groups) and two hydrogen-bonding regions that map-to-carbonyl groups were identified. This model provides us with a means of predicting computationally the EC_{50} values for other potential hPEPT1 inhibitors in the future. Ultimately, a much larger and more structurally diverse data set of hPEPT inhibitors and substrates would be useful for refined modeling studies. A comparison with the ligand specificity of the closely related transporter hPEPT2, which is expressed in other tissues such as the BBB, is also warranted. Numerous data sets have been published for species other than humans. There are likely differences in the binding specificity between species and between hPEPT1 and hPEPT2, which will require elucidation as they limit our ability to extrapolate from one system and species to another. We therefore await more definitive computational studies on these human transporters.

The Apical Sodium-Dependent Bile Acid Transporter

The high efficacy of the apical sodium-dependent bile acid transporter (ASBT) combined with its high capacity makes this system an interesting target for drug delivery purposes, including local drug targeting to the intestine and the improvement of intestinal absorption of poorly absorbable drugs. The ASBT has recently received much attention because of its pivotal role in cholesterol metabolism. Inhibition of intestinal bile acid reabsorption elicits increased hepatic bile acid synthesis from its precursor cholesterol, thereby lowering plasma cholesterol levels.[155] Application of this approach has met considerable clinical success using unspecific bile acid sequestrants, such as cholestyramine and colestipol.[156] Several novel ASBT inhibitors are currently in clinical trials for the treatment of hypercholesterolemia.[157]

Studies with endogenous bile acids have led to a physiological understanding of the function of bile acid and the enterohepatic circulation. The search for a deeper understanding of the molecular mechanism behind the affinity and for recognition of molecules by the bile acid carriers in both ileum and liver motivated groups to modify bile acids and to study the carrier affinity of these compounds. These modifications typically entail either the substitution of the hydroxyl groups at the 3, 7, or 12 positions by other functionalities, or the addition to or alterations at the C-17 side chain.

A QSAR approach using topological descriptors was developed by Lack and Weiner in the early 1970s and has been reviewed elsewhere.[13] From this and other studies the following basic aspects of bile salt absorption have been identified. (1) The parameter K_m is related to conjugation. In general, glyco- or tauro-conjugated bile acids have a twofold higher K_m value than their

unconjugated parent compounds. (2) The parameter V_{max} is independent of conjugation but appears to be related to the number of hydroxyl groups attached to the sterol nucleus: trihydroxy $\gg$ dihydroxy $>$ monohydroxy, however, no single hydroxy group is essential for transport. Triketo bile acids, such as taurodehydrocholic acid, are devoid of all hydroxyl groups and show considerably less transport capacity. (3) For efficient transport, a bile acid molecule must possess a single negative charge that should be located near the C-17 position of the sterol nucleus. (4) Although bile acids with two negative charges around the C-17 position have minimal active transport, the addition of an extra negative charge in the form of sulfonation at the C-3 position does not preclude active transport. The replacement of the anionic moiety from the C-17 side chain to the 3-position results in a complete loss of affinity. (5) Stereospecificity of the hydroxyl groups on the sterol nucleus exists as shown by substitution of this group at the 3-position with a hydroxyethoxy moiety.[158] The 3α-isomer was able to inhibit transport of [³H]-taurocholate in rabbit ileal brush border membrane vesicles, whereas the 3β-isomer showed very weak affinity and was unable to inhibit taurocholic acid transport.

Lack et al.[159] proposed early on that the recognition site for bile acid transport consists of a hydrophobic pocket on the membrane surface that features three components: a recognition site for interaction with the steroid nucleus; a cationic site for Coulombic interaction with the negatively charged side chain; and an anionic site for interaction with Na^+. Supposedly, this anionic site could be responsible for the reduced affinity of bile acid derivatives with a dianionic side chain. Based on the earlier work and that of more recent studies, the structural requirements for ASBT affinity can be generalized as follows: (1) The presence of at least one hydroxyl group on the steroid nucleus at position 3, 7, or 12. (2) A single negative charge in the general vicinity of the C-17 side chain (however, an additional negative charge at the C-3 position does not prevent active transport). (3) Substitutions at the C-3 position (which do not interfere with active transport). (4) Substitutions at the C-17 position (which can be tolerated as long as a negative charge around the C-24 position is retained). and (5) A cis configuration of rings A and B which must exist within the sterol nucleus.

More recently, our group and researchers from the laboratories of Baringhaus and Kramer have reported on the 3D structural requirements of ASBT that will be of use in the development of novel substrates for this transport protein. Using a training set of 17 chemically diverse inhibitors of ASBT, Baringhaus et al.[160] used Catalyst to develop an enantiospecific pharmacophore that mapped the molecular features essential for ASBT affinity: one hydrogen-bond donor, one hydrogen-bond acceptor, and three hydrophobic features. For natural bile acids, they found that (a) ring D in combination with methyl-18 maps one hydrophobic site and methyl-21 maps a second; (b) an α-OH group at position 7 or 12 constitutes a hydrogen donor; (c) the negatively charged side chain comprises the hydrogen-bond acceptor; and

(d) the 3α-OH group does not necessarily map a hydrogen-bond functionality. The ASBT pharmacophore model is in good agreement with the 3D-QSAR model we previously developed using a series of 30 ASBT inhibitors and substrates.[109] In that study, the electrostatic and steric fields around bile acids were mapped using CoMFA to identify regions of putative interaction with ASBT. This model enabled the in silico design of substrates for ASBT, especially for conjugation at the C-17 position. It should be pointed out that our model was silent on biological diversity around the C-3 position because of limited molecular variability in this region; however, alterations at that position have been described in detail by Kramer et al.[161] The two indirect models outlined above should facilitate the rational design of (pro)drugs for targeting to ASBT. There may also be the possibility of combining models from different groups although this may create its own problems if the data were generated with different systems or experimental conditions.

One serious limitation of indirect structure–activity models is the inherent lack of information on substrate–transport protein interactions at the molecular level. Currently, no crystal structure exists for ASBT and it is anticipated that suitable methods for crystallizing intrinsic membrane proteins will not be available for several years. As an alternative to high–resolution molecular information, we have recently constructed a model for the ligand binding of the ASBT transport protein using knowledge-based homology modeling. By using the transmembrane domains of bacteriorhodopsin as a scaffold, the extracellular loop regions were superposed and optimized with molecular dynamics simulations.[162] By probing the protein surface with cholic acid, we identified five binding domains, three of which are located on the outer surface of the protein (Fig. 4). Another binding domain was located between two extracellular loops in close enough proximity to the first binding region to accommodate di-cholic acid conjugates; this observation explains the extreme inhibitory capacity of this class of compounds.[163] In addition to the previously described pharmacophore and 3D-QSAR models, the molecular representation of ASBT may provide a powerful tool in the design of novel substrates or inhibitors for this transporter.

P-Glycoprotein

The ABC (ATP binding cassette) efflux transporter, P-glycoprotein (P-gp) is a large membrane-bound protein highly expressed at the interface of many important organs and their environment where it acts as a barrier limiting exposure to xenobiotics.[164] In addition, P-gp expression in malignant cells has been associated with the multidrug resistance phenomenon resulting from the P-gp-mediated active transport of anticancer drugs from the intracellular to the extracellular compartment.[164] P-gp is present in the canalicular domain of hepatocytes, brush border of proximal tubule cells and capillary endothelial cells in the CNS.[164] Expression of P-gp in such locations results
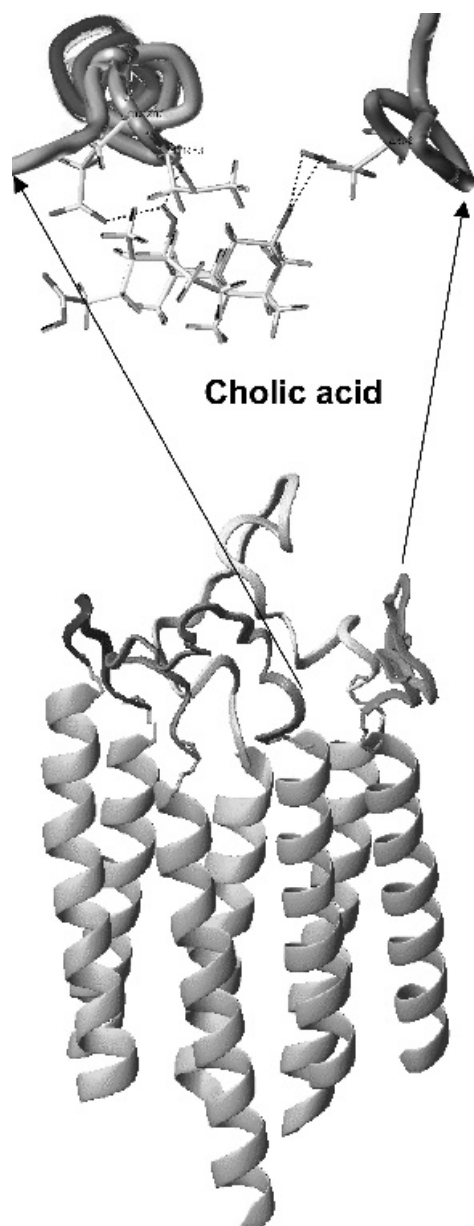
Figure 4 Homology model for ASBT and location of putative binding sites for cholic acid.

in reduced oral drug absorption and enhanced renal and biliary excretion of substrate drugs. Moreover, P-gp expression at the blood–brain barrier is a key factor in the limited CNS entry of many drugs. The expressed level of P-gp as well as altered functional activity of the protein due to genetic variability in the MDR1 gene appears to also impact the ability of this transporter to influence the disposition of drug substrates.[165]

In terms of P-gp structure–activity relationship elucidation, photoaffinity experiments have been valuable in defining the cyclosporin binding site in hamster P-gp[166] and indicating that trimethoxybenzoylyohimbine (TMBY) and verapamil bind either to a single or to overlapping sites in a human leukemic cell line.[167] Additional studies have shown that TMBY is a competitive inhibitor of vinblastine binding to P-gp.[168] The P-gp modulator LY 335979 has been shown to competitively block vinblastine binding[168] while vinblastine itself can competitively inhibit verapamil stimulation of P-gp-ATPase.[167] With the growth in knowledge derived from these and other studies using different probes and cell systems it would certainly be valuable to use structural information to define whether unrelated molecules are likely to interact with P-gp. Early computational studies using P-gp modulators such as verapamil, reserpine, 18-epireserpine, and TMBY showed that these structures could be aligned suggesting the importance of aromatic rings and a basic nitrogen atom in P-gp modulation.[169,170] A subsequent, more extensive study with 232 phenothiazines and structurally related compounds indicated that molecules with a carbonyl group were active P-gp inhibitors.[171] A model built with 21 molecules of various structural classes that modulate P-gp ATPase activity suggested these molecules compete for a single binding site.[172] Similarly, 19 propafenone-type P-gp inhibitors were then used to confirm the requirement for a carbonyl oxygen that is proposed to form a hydrogen bond with P-gp.[173] Klopman used MULTICASE to determine important substructural features like $CH_2—CH_2—N—CH_2—CH_2$,[174] while Jurs used linear discriminant analysis with topological descriptors[175] in an attempt to model this property. In 1997, the first 3D-QSAR analysis of phenothiazines and related drugs known to be P-gp inhibitors was described.[176] This was followed by Hansch-type QSAR studies using propafenone analogs,[177,178] CoMFA studies of phenothiazines and related drugs,[179] CoMFA studies of propafenone analogues[180] and simple regression models of propafenone analogues.[181,182] These latter models confirmed the relevance of hydrogen-bond acceptors and the basic nitrogen for inhibitors[181,182] and multiple hydrogen-bond donors in substrates being 2.5–4.6 Å apart.[183] One study utilizing a diverse array of inhibitors on P-gp ATPase activity noted that size of the molecular surface, polarizability and hydrogen bonding had the largest impact on the ATPase activity.[56] A number of computational approaches and models of P-gp have yielded useful information that is usually derived from a series of structurally related molecules. A recent experimental study suggested P-gp inhibitors with high lipophilicity

and polarizability are more likely to be high affinity ligands for the verapamil binding site.[184] A further example relied upon 2,4,5- and 2,3,4,5-substituted imidazoles as P-gp inhibitors to derive similar CoMFA and CoMSIA models that showed a sterically favored region around the phenyl substituent at the C-2 position of the imidazole ring.[185]

Interestingly, cytochrome P450 3A4 (CYP3A4), a drug metabolizing enzyme with a broad substrate specificity, appears to coexist with P-gp in organs such as the intestine and liver. These observations lead to the hypothesis that there may be an interrelationship between these two proteins in the drug disposition process. Wacher et al. described the overlapping substrate specificity and tissue distribution of CYP3A4[186] and P-gp. Schuetz et al.[187] found that modulators and substrates coordinate to up-regulate both proteins in human cell lines. Similarly, P-gp mediated transport was found to be important in influencing the extent of CYP3A induction in the same cell lines as well as in mice.[187] More recent data suggest that there may be a dissociation of inhibitory potencies for molecules against these proteins. Although some molecules can interact with CYP3A4 and P-gp to a similar extent, for the most part the potency of inhibition for CYP3A4 did not predict the potency of inhibition for P-gp, and vice versa.[164] Moreover, not all CYP3A substrates such as midazolam and nifedipine are P-gp substrates.[188] Thus, although there appears to be a relationship between the active sites of CYP3A4 and P-gp, this relationship is not by any means conclusive.

To account for the observed broad substrate specificities for both CYP3A4 and P-gp, the presence of multiple drug binding sites has been proposed.[189–192] The first experimentally determined signs of complex kinetic behavior for P-gp appeared in 1996 when cooperative, competitive, and noncompetitive interactions between modulators were found to interact with at least two binding sites in P-gp.[193] The multiple site hypothesis was confirmed by other groups.[194–196] Subsequent results have indicated there may actually be three or more binding sites.[197] Steady-state kinetic analyses of P-gp mediated ATPase activity using different substrates indicate these sites can show mixed-type or noncompetitive inhibition indicative of overlapping substrate specificities.[198] Other researchers have determined that immobilized P-gp demonstrates competitive behavior between vinblastine and doxorubicin, cooperative allosteric interactions between cyclosporin and vinblastine or ATP, and anticooperative allosteric interactions between ATP, vinblastine and verapamil.[199] Clearly, allosteric behavior by multiple substrates, inhibitors or modulators of CYP3A4, or P-gp complicates predicting the behavior and drug–drug interactions of new molecules in vivo. This has important implications for drug discovery. The computational modeling of P-gp has been extensively reviewed recently,[57] where it was suggested that although there are many datasets available for modeling, combining those data may be complicated by incompatibilities based on the assay and cell type used. Therefore our own modeling attempts have kept the data from different assays

separate so as to maintain this unique in vitro model-specific integrity and to allow for the production of computational models for specific, suggested binding sites.

Recently, we have described how computational approaches can be used to predict inhibition of P-gp by using in vitro data derived from structurally diverse inhibitors of digoxin transport in Caco-2 cells, vinblastine, and calcein accumulation in P-gp expressing LLC-PK1 (L-MDR1) cells or vinblastine binding in vesicles derived from CEM/VLB100 cells.[55] Using structurally divergent P-gp inhibitors and probe P-gp substrates, we have been able to generate distinct 3D-QSAR models that contain hydrogen-bond acceptors, hydrogen-bond donors, hydrophobes, and ring aromatic features. Some of our models rank order the data in other data sets quite well, indicating partial overlap for the binding sites probed by digoxin and vinblastine may exist. Models based on data for inhibition of vinblastine accumulation and vinblastine binding in different systems are not completely predictive for each other. Calcein accumulation data was not ranked to a statistically significant extent by either the vinblastine binding or the digoxin transport models. These different results may be indicative of some of the caveats associated with molecular modeling of each respective system in vitro. The assays for accumulation of substrates (vinblastine and calcein) involve inhibitors crossing the LLC-PK1 cell membrane, and then presumably binding at unspecified sites within the cells. This is clearly mechanistically different, from inhibition of vinblastine binding to plasma vesicles of CEM/VLB$_{100}$ cells where the inhibitors only interfere with binding. The data derived with calcein and LLC-PK1 cells may also indicate that we are dealing with binding to a separate site; however, the pharmacophore built with calcein data is able to rank the digoxin transport data, tentatively suggesting some degree of overlap of the pharmacophores. Overall vinblastine and calcein accumulation pharmacophores do not appear to be reliable for predicting the other P-gp data sets. This conclusion is based on the Spearman's rho ranking statistic, the small energy difference between null and final pharmacophores as well as the slight change in this value following permutation. The lack of success with these two models may be more a consequence of the limited structural diversity of the two training sets involved (large natural product structures), which in turn produce pharmacophores that explain less of the P-gp binding site(s) than from studies using structurally diverse training sets.

A Catalyst model constructed with 27 inhibitors of digoxin transport by P-gp appears to be the most useful and universal predictive model to date for both molecules known to inhibit digoxin transport or vinblastine binding.[55] This pharmacophore model contains one of the most potent inhibitors of P-gp previously reported, namely, LY-335979 (IC$_{50}$ 0.059 µM,[168]), which fits well to the model indicating that this may have potential for designing molecules that fit this pharmacophore with similar or greater affinity. The vinblastine inhibition pharmacophore was less predictive for the digoxin data as

judged by the model's r^2 value; however, the Spearman's rho coefficient suggested that both models are equivalent (0.68 and 0.70) at ranking the compounds in the other training set. Taken individually, we may have defined pharmacophores for what could be interpreted as multiple regions within the same binding site of P-gp as probed by the particular substrates used in the study. This hypothesis is based on each pharmacophore being slightly different in its feature content, as well as its angles and distances. However, these differences may actually be related to the structural diversity of molecules in each training set or the use of IC_{50} values in most cases rather than due to multiple-binding regions. This is a cautionary note, for novice and seasoned modelers alike. Naturally, K_i values relate more closely to competitive inhibitors and a true binding affinity for P-gp and would be the ideal measure for generating such models. The cross-predictivity of most data sets in this study provide a means of model validation between IC_{50} and K_i data sets.[55]

The findings described above based on these different probes and cell systems, is representative of similar computational studies commonly used in many laboratories. Such studies serve as an initial step toward characterization and prediction of P-gp-mediated drug transport both in vitro and in silico. From the above mentioned work, we hypothesized that vinblastine and digoxin are likely to bind to P-gp at a single site. This hypothesis was created because strong correlations between the two models were observed. The utility of the newly derived computational models was further tested using available literature data on verapamil-P-gp binding in vinblastine induced Caco-2 cells.[184] A new P-gp inhibition pharmacophore was constructed using this verapamil-binding data and tested with the previously generated data.[54] Analyses of data using these computational models confirmed that verapamil may interact with the vinblastine–digoxin binding site(s) in P-gp. All four previously generated pharmacophores for P-gp inhibition were useful in producing statistically significant rank ordering of the verapamil-binding inhibition data that was utilized in this second study. The Catalyst model (built with these 16 P-gp inhibitors of verapamil binding) was also predictive as confirmed by the Spearmans rho value for the data generated in our previous work that was based on inhibition of digoxin transport, vinblastine binding, and vinblastine accumulation.

Our findings suggested that vinblastine, verapamil, and digoxin have an overlapping affinity for similar or identical binding site(s) within P-gp. The presence of clearly defined regions in space occupied by clusters of identical features such as hydrophobes, hydrogen-bond acceptors, and ring aromatic features was apparent by merging all five Catalyst P-gp inhibitor pharmacophores (Figure 5). To some extent, the inhibition pharmacophore for calcein accumulation partially overlapped with the other four inhibition pharmacophores but its features did stand out. The initial P-gp pharmacophore, suggested by Pearce et al. in 1989[169] as consisting of aromatic rings and a basic nitrogen atom, can be extended by the pharmacophores for P-gp inhibitors.
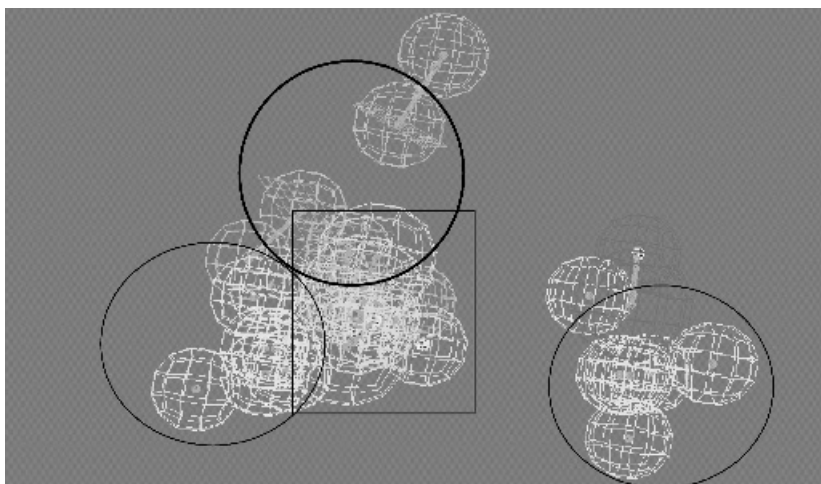
Figure 5 Five merged P-gp inhibition Catalyst pharmacophores defining areas of hydrophobicity = solid circles; aromatic rings = bold circle, and hydrogen-bond acceptors = square.

Using the digoxin transport model to predict 51 of the molecules from the vinblastine binding, vinblastine accumulation, and verapamil accumulation data sets results in a correlation of observed versus predicted values ($r^2 = 0.63$) and a Spearmans rho ranking correlation coefficient of 0.75 ($p = < 0.0001$, Figure 6). This is quite acceptable as a computational model for drug discovery where large databases need to be filtered in a cost-effective manner.
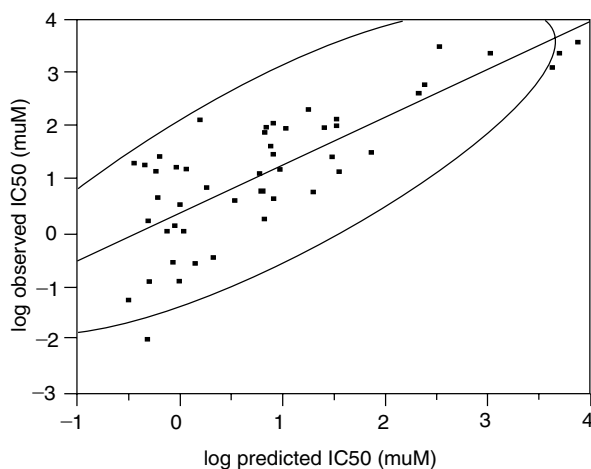
Figure 6 Evaluation of the digoxin transport P-glycoprotein pharmacophore tested on 51 molecules. Observed versus predicted IC_{50} $r^2 = 0.63$, Spearmans rho = 0.75, $p < 0.0001$, Elipse = 95% confidence interval.

The utility of the P-gp inhibitor pharmacophores produced to date was also assessed by using them to predict the rank order of other potential P-gp inhibitors not present in the data set used to create the models. A recent publication presented data for the varying potency of P-gp inhibition of verapamil metabolites.[200] We utilized each pharmacophore model to predict the likely IC_{50} of the four verapamil metabolites D-617, D-620, D-703, and norverapamil. All five pharmacophores were able to identify the least potent P-gp inhibitors correctly as being D-617 and D-620. These molecules are more likely to be hydrophilic as suggested previously for other low-affinity binding inhibitors at the verapamil site.[184] Two of the pharmacophores that are based on inhibitors of digoxin and verapamil binding provided useful quantitative predictions for the inhibition of verapamil transport with verapamil metabolites. The digoxin pharmacophore performed particularly well with the potent inhibitors D-703 and norverapamil because these molecules fit the majority of the features in the models. The third model, based on inhibitors of vinblastine binding, failed with D-703 (the prediction exceeded 1 log order of magnitude). These predictions for verapamil metabolites are perhaps not totally unexpected because all three of these models used verapamil as a training set member. However, the digoxin model used a much higher IC_{50} value for verapamil that makes it one of the least potent inhibitors. This in turn might explain its lower predicted value in this case. Our models for inhibition of vinblastine and calcein accumulation differed from one another in that the latter model was less quantitative in the nature of the predictions even though it could generate the correct rank order for the verapamil metabolites. Once again this lack of quantitative agreement may be a function of the complexity of the system requiring absorption prior to the inhibition that is measured. Future studies incorporating additional P-gp probes may define new binding sites or aid in the generation of more detailed pharmacophores that could prove valuable for both drug discovery and screening. Molecular-modeling studies like this have the potential to enhance our understanding of complex transporters such as P-gp without having a crystal structure, and such studies may be applied to other systems as well.

The hypothesis that some of the substrate probes for P-gp bind to similar sites was tested further. By alignment of verapamil and digoxin followed by fitting vinblastine, it was possible to identify possible common features across all three substrates. All three molecules have extended conformations with hydrophobic and hydrogen-bond acceptor features in common. These features are distributed toward the extremities of the molecules. This P-gp substrate pharmacophore therefore appears to be consistent with the features present in some of the inhibitor pharmacophores generated previously.[54,55] The alignment of other known P-gp modulators such as TMBY and reserpine was evaluated with this P-gp substrate model derived from the verapamil and digoxin alignment. Both TMBY and reserpine molecules could be fit to multiple features of the pharmacophore in the extended conformations and reserpine

was also fitted to similar pharmacophore features as verapamil. This finding is once again in agreement with previous work in which the reserpine analogues were aligned using different software[169] and provided additional support for our suggestion that vinblastine, verapamil and digoxin are likely to bind to similar sites in P-gp. Our findings are also consistent with available in vitro data for binding of substrates.[167,168] These recent in vitro and in silico approaches appear to confirm the chemical features deemed to be important for binding to this site as either substrates or as inhibitors. A recent pharmacophore model for P-gp substrates based on 144 molecules, generated 3 million pharmacophores (using in-house software).[58] Of those pharmacophores, an ensemble of 100 was used for predictions.[58] A threshold of 20 pharmacophores was set such that molecules matching less than this number would be indicated as nonsubstrates. This model correctly classified 80% of the training set but only 63% of the test set.[58] The pharmacophores used contained hydrogen-bond donors, hydrophobic, and aromatic ring features, but the hydrogen-bond acceptor was felt to be the most important feature. The utility of this model may be limited by its relatively poor predictivity, however, improvements could be made by increasing the amount of training data. Further pharmacophore-based approaches[201] using GASP alignments to vinblastine and to rhodamine 123 have been carried out to understand the verapamil binding site.[201] Those studies revealed similar pharmacophore requirements as proposed earlier. Multiple hydrophobic and hydrogen-bonding interactions were described.[201] A small number of P-gp ligands were superimposed with SYBYL and MOLCAD by Garrigues et al.[202] to generate two pharmacophores. The resulting models were validated with only two additional compounds, however. The generation of data for P-gp in other species including rat and mouse[203] will aid in our understanding of the binding sites of this transporter.

When the P-gp pharmacophores in previous studies[54,55] are compared with pharmacophores for inhibitors and substrates of CYP3A[97,204] (Figure 7), some similarity is found between them.[54,55] Both P-gp and CYP3A share pharmacophores with multiple hydrophobic features and at least one hydrogen-bond acceptor feature albeit in slightly different arrangements. This might explain why potent CYP3A4 inhibitors are not necessarily potent P-gp inhibitors[164] or substrates.[188] This slightly different arrangement helps clarify the independent nature of the relationship between ligands that bind to these two proteins.

Vitamin Transporters

The ascorbate transporter SVCT1 has been shown to be inhibited by some flavonols such as quercetin but less so by the related catechins.[205] The absence of the ketone at the 4-position of the C ring has a dramatic negative effect on the potency of inhibition, suggesting that a key hydrogen-bonding
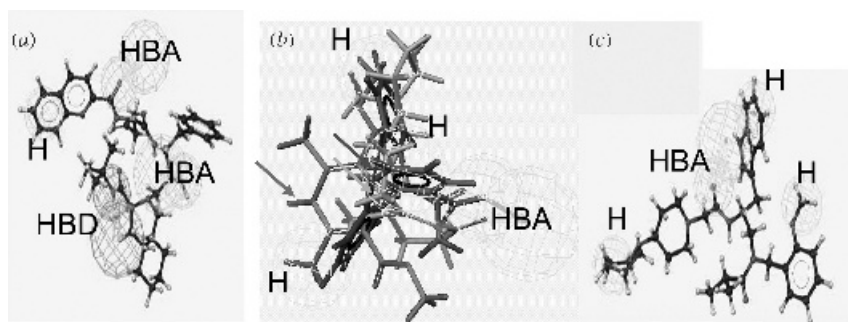
Figure 7 The partial similarities between a substrate pharmacophore for CYP3A4 (*a*), a CYP3A4 autoactivator pharmacophore (*b*), and a CYP3A4 inhibition pharmacophore (*c*). Legend: H = hydrophobe; HBA = hydrogen-bond acceptor; HBD = hydrogen-bond donor.

interaction is required for maximal inhibition. The addition of a glycone group on the C ring also affects inhibition suggesting that the transporter has some size limitation. Quercetin is a noncompetitive inhibitor of SVCT1 as well as the glucose transporter GLUT2.[205] No QSAR has been generated to our knowledge for the SVCT1 or GLUT2 transporter for either substrates or inhibitors to date. Development of a QSAR may be valuable for prodrug design as a viable means to improve membrane penetration of some drugs by addition of an ascorbic acid mimic.[206]

Organic Cation Transporter

The organic cation transporter, OCT1, is likely to play a role in the hepatic elimination of many cationic drugs.[207] A number of studies have described new molecules that interact with OCTs.[208,209] Understanding the 3D features fundamental to molecular interaction with the transporter would thus be valuable. Hydrophobicity and basicity may be important substrate requirements for interaction with the OC transporters on the apical and basolateral membranes of the rat renal proximal tubule[210] and on the apical and basolateral transporters in rabbit.[211–213] Structure–activity relationships have been developed for substrates of the OC^+/H^+ exchanger.[212] The binding site of the luminal transport step of rabbit renal proximal tubules, the OC^+/H^+ exchanger, includes a planar hydrophobic surface that is sufficiently accommodating so that no steric exclusion is evident when a planar (9×12Å) hydrophobic mass is rotated about an *N*-pyridinium center. A more recent study with OCT1 used a number of structurally diverse ligands to derive QSAR models with ClogP alone or with multiple descriptors in Cerius[2] and a pharmacophore model with Catalyst.[214] Future detailed computational studies undoubtedly will be required for both human OCT1 and OCT2 to understand their individual specificities.

Organic Anion Transporters

The rat kidney organic anion transporter (OAT) is characterized by its transport of *p*-aminohippurate, cAMP, and cGMP and by its inhibition by various anionic drugs. Although there have been many studies with rat OATs showing inhibition with beta-lactam antibiotics[215] and with other drugs, there have been no QSAR studies. A comprehensive review of transporters involved in organic anion transport[208] indicates there is little published on the topic of ligands for the human OATs. However, a recent study described the interactions of 12 NSAIDS with hOAT1, hOAT2, hOAT3, and hOAT4.[216] Both hOAT1 and hOAT3 demonstrated higher affinity binding with NSAIDS. It was suggested that this high affinity may explain some adverse physiological reactions. This small dataset might provide a viable starting point for a pharmacophore analysis of these transporters that in turn could be used for comparison with the hOCT pharmacophores generated to date.

Nucleoside Transporter

Nucleoside transporters (NTs) are important in mediating transport of nucleosides and nucleoside drugs (e.g., antiviral and anticancer drugs) across cell membranes.[217] These transporters can be classified into two broad categories: the Na^+-dependent concentrative (energy-dependent) transporters, which physiologically mediate influx of nucleosides, and the Na^+-independent equilibrative (or facilitative) transporters, which mediate both influx and efflux. Five principal Na^+-dependent concentrative nucleoside transporters (CNTs) have been identified so far. Of these, only two CNTs, CNT1 and CNT2, are found to be functionally present in the epithelial cells of organs important for drug absorption (intestine) and elimination (kidneys). Both CNT1 and CNT2 transport uridine and adenosine[218] and are insensitive to inhibition by nitrobenzylthioinosine (NBMPR). The equilibrative transporters mediate both the influx and efflux of nucleosides and exhibit broad substrate specificity, accepting both purine and pyrimidine nucleosides as permeants. Equilibrative nucleoside transporter 1 (ENT1, es) is inhibited by NBMPR concentrations as low as 0.1 nM (IC$_{50}$ ~0.4 nM), whereas the ENT2 (ei) transporter is insensitive to inhibition as high as 1 μM (IC$_{50}$ ~2.8 μM).[217] The ENT1 transporter is expressed in most, if not all, cell types while ENT2 is selectively expressed in some tissues such as muscles. By using a chimeric transporter T8 containing the rat N1 and N2 transporters, it was suggested that purine and pyrimidine nucleosides share a common binding site.[219] A structural inhibitory profile for the N1 and N2 transporters in human intestinal brush border membrane vesicles was produced using two concentrations of anticancer and antiviral drug analogues.[220] It was found that the 3′-oxygen in the ribose ring is required for inhibition. Further, the N2 transporter can tolerate substitution at the 5′-position, whereas the N1 transporter is more sensitive to substituents. The ribose or 2′-deoxyribose is necessary for

high-affinity interaction with both transporters. The 6 and 8 position on uracil and adenosine, respectively, are critical for inhibition of N1 and N2 transporters.[220]

Our laboratory has compared the relative and the unified structural requirements of nucleosides for high-affinity interaction with hCNT1, hCNT2, and hENT1.[221] By using nucleoside transporter inhibition data from a series of uridine and adenosine analogues (and a variety of nucleoside drugs),[219,220] a unique pharmacophore model for each transporter was generated with DISCO. Two multivariate regression analyses, CoMFA and GOLPE, were used to generate QSAR models that correlate substrate–inhibitor structural features with their binding affinities. The overall qualities of the resulting models were then used to construct more comprehensive models. It was found that both the hydrogen-bond acceptor and donor surrounding the 3′ carbon is required for hENT1 substrates. It was also found that a hydrogen-bond acceptor on the ribose next to the pentose ring is important for hCNT2 substrates, whereas hydrogen-bonding at the 5′ carbon is important for hCNT1 affinity. The CoMFA and (GOLPE) QSAR models with cross-validated r^2 values of 0.52 (0.69), 0.65 (0.69), 0.74 (0.70) were derived for hCNT1, hCNT2, and hENT1, respectively. The hCNT1 QSAR model displayed mainly hydrogen-bonding features, whereas hCNT2 and hENT1 exhibited electrostatic and steric features. Quantitative results correlated well with experimental analyses, suggesting subtle and unique structure–activity correlation for each nucleoside transporter. These QSAR models should now allow for the design of high-affinity nucleoside transporter inhibitors and substrates for both anticancer and antiviral therapy.

Breast Cancer Resistance Protein

The identification of a new ABC transporter termed the breast cancer resistance protein (BCRP, MXR, ABCG2) has revealed that increased expression of this transporter results in resistance to anticancer therapeutics. The recent suggestion that this transporter is also expressed in the intestine suggests that this transporter could also be important in limiting bioavailability and that Caco-2 cells express this at the level seen in the jejunum.[222] Understanding early in discovery how other drugs, and in particular new anticancer agents, are readily transported by this protein is important. To date, there are limited SAR type studies from which to initiate computational modeling. In fact, there exists only one with a large number of molecules, consisting of 42 diastereoisomeric mixtures of fumitremorgin-type indoyl diketopiperazine inhibitors of BCRP.[223] A further study focusing on the topoisomerase I drugs has described the affinity for BCRP (in decreasing order) as SN-38 > topotecan > 9-aminocamptothecin > CPT-11 > NX211 > DX8951f > BNP1350.[224] Future studies analogous to those with P-gp will be necessary in order to generate more generally predictive computational models for BCRP.
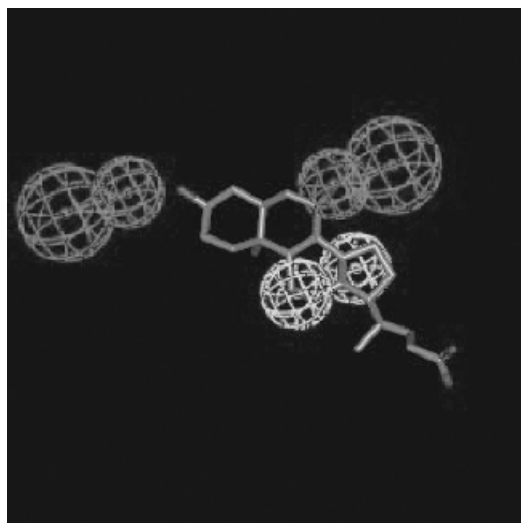
Figure 8 A pharmacophore for the human hepatic sodium-dependent bile acid transporter using eight molecules and IC_{50} values demonstrating two hydrophobic features (bottom right) and two hydrogen-bond donors (top left and top right). The observed versus predicted data resulted in a correlation $r = 0.97$. A training set member (ursodeoxycholic acid) is shown fitted to this pharmacophore.

Sodium Taurocholate Transporting Polypeptide

The transport of bile acids in the liver occurs via the sodium taurocholate transporting polypeptide (NTCP). Alterations in this activity contribute to cholestasis. A recent evaluation of 33 molecules (including commonly used drugs) to assess drug-induced cholestasis found that besides bile acids, propranolol, progesterone, cyclosporine, and a number of oligopeptides are potent inhibitors of taurocholate uptake.[225] Eight of these molecules demonstrated an IC_{50} between 1 and 264 µM and recently have been used to generate a pharmacophore that consists of two hydrophobic features and two hydrogen-bond donor features[226] (Figure 8). Interestingly, it has also been reported that class I antiarrhythmics can enhance bile acid uptake via this transporter, which to date has not been studied in detail.[225] A more complete QSAR analysis for this transporter is required in the future.

ENZYMES

Cytochrome P450

Since their discovery as heme thiolate proteins in the late-1950s, the cytochrome P450s have been recognized as the largest family of enzymes

known to be present across all organisms with CYP51 being present in every phyla.[6] The cytochrome P450 enzymes are considered by some to be the most important enzyme family in terms of endobiotic and xenobiotic metabolism because of their ubiquity and because they are expressed within many tissues such as the liver and intestine. By the 1970s, this superfamily started to grow, and through the 1980s–1990s many of them were purified, cloned, or expressed in other cell systems that allowed for a great deal of characterization and understanding of the requirements needed for substrate and inhibitor action. Some cytochrome members are human enzymes (families 1, 2, and 3) that were thought to be important for xenobiotic metabolism, and therefore were more widely studied than others. The use of in vitro systems to elucidate potential drug–drug interactions (DDI) became readily adopted by drug companies and the FDA. The cost of this research focus was offset by the lack of study of other enzymes, especially those outside of the CYPs involved in conjugative metabolism.

Unfavorable DDIs are clearly important and clinically relevant.[227] Even though in some populations the number of DDIs may seem small, they are an important factor in determining whether or not a new chemical entity will successfully make it beyond a drug discovery program to development. In addition, the late discovery of a clinically significant DDI could be costly in terms of the financial investment of a particular project. Therefore it is important to screen for potential interactions[228] early on, to aid in the selection of the most appropriate in vivo studies.[229,230] In this regard, drug interactions with cytochrome P450s (CYPs) are particularly important,[231] but ultimately avoidable (depending on the therapeutic index), even though drug metabolism is complex and to some extent predictable by careful assessment of structure–activity relationships. The enzymes CYP1A2, CYP2C9, CYP2C19, CYP2D6, and CYP3A4 represent > 90% of total hepatic P450[232] and nearly 80% of therapeutic drugs are metabolized by these same enzymes.[233] Interaction with one or more of these enzymes in vivo would thus pose a potentially relevant event, clinically. In recent years, in vitro systems have proved invaluable in predicting the likelihood of DDI[231] because they allow identification of the CYPs responsible for metabolism as well as determination of the relative contribution to overall elimination of the inhibited pathways.[234] Because the number of molecules synthesized by pharmaceutical companies has increased dramatically with the utilization of combinatorial chemistry, there is now a shift in emphasis toward earlier implementation of higher throughput in vitro studies for metabolism[235,236] or lead optimization.[237]

The CYPs may be involved in many DDIs because of their affinity for hydrophobic molecules of varying sizes. It is widely believed that an understanding of DDIs at the molecular level may lead to the development of more effective and safer therapeutics. In the absence of a freely available crystal structure for any of the human CYPs, there is an obvious need to build computational models in an attempt to predict drug metabolism and

interactions prospectively. Many approaches have been taken using various tools in this regard. Comprehensive analysis of existing physicochemical data, protein homology data, nuclear magnetic resonance (NMR) data, site directed mutagenesis results and insights from QSAR approaches have all been used. Recent reviews have described and compared the many pharmacophores for CYPs.[24,238] The foundation for those types of studies were laid in the late-1960s by Hansch et al. using mathematical approaches that include lipophilic character to describe metabolic characteristics of drugs. In the intervening years, there was a great emphasis on developing in vitro approaches for metabolism such that we are now aware that there exist many human CYPs of importance. The distribution of these enzymes, their expression in various tissues and the extent to which they metabolize commercially available drugs has also been widely studied. A major advance in technology for in vitro studies on drug-metabolizing enzymes involves the availability of recombinant enzymes both for CYPs and phase II enzymes. These recombinant CYPs have enabled the development of high throughput screens for DDIs and, concurrently, have provided increasingly large databases of molecules for computational modeling. This reductionist perspective may be problematic because removing molecules early in drug discovery based upon their poor performance in these screens may not account for molecules that may be dosed at significantly lower concentrations than usually assessed for CYP inhibition. Initially, 3D-QSAR models were built with CYP data derived from human liver microsomal data using a substrate probe shown to be relatively selective for the enzyme in question. This is likely not to be as clean a system as using the purified enzyme, hence models derived from such data are less desirable.

CoMFA models were first used with CYP1A2,[239] CYP2A5,[240] and CYP2C9,[241] using relevant conformers of inhibitors to suggest key functional groups, the geometry of selected structural features, and regions of electrostatic and steric interactions. Those studies typically used data from human liver microsomes and a probe substrate. More recently, QSAR models have been built after analysis of literature data including recombinant-derived kinetic values for enzymes such as CYP2B6,[100,242] CYP2C9,[241,243] and CYP2D6.[244] There have been a number of groups that have combined pharmacophores with homology models of either bacterial CYPs[241,245–247] or the recently crystallized rabbit CYP2C5/3.[242–244,248] One study generated a homology model of CYP2B6 based on CYP2C5 (48% sequence identity) and also modeled the missing F and G helices by unconstrained molecular dynamics.[249] This study[249] and others[242,250] have shown the importance of hydrophobic interactions with substrates using homology modeling that had also previously been suggested by a pharmacophore.[100] Because the CYP pharmacophores have been described previously, the reader is referred to the primary literature cited.

Members of the CYP3A family of enzymes are the most important in terms of human drug metabolism,[251] because they have wide substrate

specificity and are inducible by structurally unrelated compounds.[252] At present, we are aware of four differentially regulated CYP3A genes in humans: CYP3A4, CYP3A5, CYP3A7, and CYP3A43. The CYP3A4 gene is dominant in terms of hepatic expression and is inducible.[251] The CYP3A5 gene is polymorphically expressed in the liver and may constitute as much as 50% of hepatic CYP3A in a third of Caucasions and one-half of African Americans within the population.[253] The CYP3A7 gene is the fetal form of CYP3A and is believed to be of low abundance in adult liver[251] while CYP3A43 is newly identified with, at present, little understanding of its expression and catalytic activities.[254] One enzyme in particular, CYP3A4, has drawn considerable attention over the past decade because it metabolizes a large percentage of the molecules that are substrates for the CYPs.[251] Computational modeling of ligands for this enzyme has defined hydrogen bonding and hydrophobicity as important determinants of substrates.[204] (Figure 7). While computational inhibitor models of CYP3A4 differ slightly (depending on the substrate probe used in vitro) they maintain the trend of highlighting hydrophobic and hydrogen-bonding features.[97] More recently, there has been a focus on studying the regulation of human CYP3A with the intent to understand the expression of this enzyme and the variability in bioavailability and clearance of its substrates across the population[253] as well as for understanding drug–drug interactions.[255,256] One of the few early QSAR studies of inducers of CYPs based on in vitro and in vivo data assessed the rat CYP3A family and described the electrostatic potential maps for 16-substituted pregnenolones. From that QSAR, it was suggested that the length of the 16α substituent is related to the in vivo and in vitro induction while the steroidal skeleton of these molecules is involved in lipophilic (hydrophobic) interactions.[257] A QSAR study with 14 steroid inducers of rat CYP3A showed that the difference between frontier orbital energies, ΔE, correlated well with biological activity.[258] The authors also suggested that hydrogen bonding and hydrophobic interactions would be important in the receptors involved in induction. It was several years before we were able to predict induction of human CYP3A4, and it took the discovery of a new nuclear hormone receptor to catalyze that development (described later in this chapter as the pregnane X receptor).

Assessment of the inhibitory potency of CYP3A enzymes is often included as a first tier screen in early drug discovery alongside CYP2D6. Fluorescent probe substrates are now widely used for this screening purpose and offer the advantages over conventional compounds of being amenable to high throughput and being capable of real-time analysis.[259,260] Data from such front-line screening tests is often supplemented with that from traditional substrate probes.[261] The interaction between CYPs and their substrates in vitro is complex, as exemplified by CYP3A4.[189,190] Incubation buffer constituents appear to be able to alter the behavior of the enzyme[262] in addition to the conformation of the CYP3A4 active site.[263] Furthermore, inhibition of the CYP3A4 catalysis is substrate dependent.[259,264,265] In a study of CYP3A4

inhibition utilizing 10 substrates and 34 inhibitors, it was shown that CYP3A4 substrates could be clustered into more than three groups according to the effects of the inhibitors.[265] Data from various studies are consistent with the active site of CYP3A4 simultaneously accommodating two or more substrate molecules.[190,266,267] Kinetic models have been proposed for two substrate molecules binding simultaneously to the CYP3A4 active site.[190,268] Updated kinetic models for the interaction of these multiple molecules in the binding domains within the active site have also been developed.[269] Midazolam has been used to covalently modify a site occupied by triazolam in CYP3A4, in preference to a site occupied by testosterone.[270] Experimental evidence derived from substitution of substrate recognition residues in the CYP3A4 active site suggests that there exist two substrate-binding subpockets and one "effector–binding" region[266] similar to previous suggestions of a hydrophobic domain that is considered as being important for activation.[204,271]

An alternative hypothesis for the observations of substrate-dependent inhibition of CYP3A4 activity is that the enzyme exists in multiple conformations.[272] Another theoretical model proposes the concept of "nested allosterism", where multiple conformations of the enzyme exist both in the presence and absence of substrate, and where each conformer is sensitive to allosteric effects.[273] Mathematical and computational models have generated some useful information on ligand binding for CYP3A substrates[204] and CYP3A4 inhibitors.[97,274] Pharmacophore models in particular have offered the advantage of providing an interpretable visual representation of the structural features of compounds important for binding to CYPs as well as being able to provide a reasonably predictive model.[22,24] These models are unified in suggesting the importance of hydrophobicity for CYP3A4 substrates.

Because members of the CYP3A family of enzymes are the most important in terms of human drug metabolism,[251] have wide substrate specificities, and are inducible by structurally unrelated compounds,[252] it is of value to understand some of the important features of ligands that bind to these enzymes. Previously, we showed the utility of generating computational pharmacophores for CYP3A4 substrates[204] and inhibitors[97] using $K_{i\ (apparent)}$ and IC_{50} data (as summarized with other CYP pharmacophores,[24] Figure 7). This approach was also used to determine the important features of autoactivators of CYP3A4 that possess three hydrophobic features and one hydrogen-bond acceptor[204] (Figure 7b). This finding seems to agree well with site-directed mutagenesis data from another group.[271] A neural network has been applied in an attempt to differentiate between substrates and inhibitors of CYP3A4. In that study, literature data was collated from the human P450 metabolism database.[275] The model derived from that neural network was used to predict previously published data on structurally diverse CYP3A4 inhibitors,[97] but the model did not rank correctly the K_i data. The inhibitor LY024410 (K_i 701 μM) had the same score as most of the other molecules (K_i range

1.8 – 492.7 μM), while LY213829 was misclassified as a noninhibitor (K_i 6.6 μM). It remains to be seen whether such a wide classification of inhibitors is useful for drug discovery screening. The recent crystallization of CYP3A4 by researchers at Astex now presents an opportunity to validate all of the available computational models to date and to discern how activators and autoactivators behave in the active site of that protein. It is hoped that crystal structures for CYP3A5 and CYP3A7 will become available in the near future because such structures could provide some additional insight into the endogenous and developmental role of all of the members of the CYP3A family.

Epoxide Hydrolase

The epoxide hydrolases are known to catalyze the hydrolysis of epoxides or arene oxides to diols by addition of a water molecule. This process is thought to be a two-step process involving the formation and hydrolysis of a covalent acyl- or alkyl-enzyme intermediate. Both microsomal and soluble forms of the enzyme possess activity toward toxic xenobiotic epoxides. The soluble epoxide hydrolase (sEH) has an endogenous role in the hydrolysis of the epoxides of arachidonic and linoleic acid, known regulators of vascular permeability. The potential for therapeutic utility has been explored by generating numerous inhibitors of sEH. Several studies have generated QSAR models for sEH. A QSAR using Hansch substituents for 27 chalcone oxide inhibitors of mouse sEH suggested that steric and electronic features are important mediators of inhibition.[276] Human data with the same molecules produced a weaker correlation.[276] A CoMFA analysis of murine sEH inhibitors by molecules like benzoylureas, arylureas, and other analogues was performed using 37 molecules.[277] Large sterically unfavorable fields were found above the A ring and the urea bridge of benzoyl-phenylureas, while sterically favorable areas were found below the A and B rings of the 37 molecules analyzed. In addition, a number of negative electrostatic potential fields were present around the whole molecule along with a positively charged area beneath the carbonyl carbon atom that is important for activity.[277] These computational models complement the murine X-ray crystallographic data and site directed mutagenesis studies confirming key roles for Tyr465 and Tyr381 as hydrogen-bond donors to the urea carbonyl group and that Asp333 is involved in the nucleophillic attack.[278,279] Crystallization of the human sEH enzyme will be of value in the future to test QSAR models generated with human inhibitors. This in turn will allow us to predict the likelihood of epoxide hydrolysis for other xenobiotics that may not be as desirable.

Monoamine Oxidase

The monoamine oxidases are present in the outer membrane of mitochondria and are known to catalyze oxidation of many important

neurotransmitters. Monoamine oxidase A (MAO-A) inhibitors are valuable antidepressants and antianxiety molecules while monoamine oxidase B (MAO-B) inhibitors have found use in treating Alzheimers and Parkinsons disease. Consequently, there has been considerable interest in developing reversible inhibitors of these enzymes.[280] Besides their importance in the CNS as a therapeutic target, these enzymes are expressed in the liver (to some extent) and they may have a role in the metabolism of xenobiotics thus providing an opportunity for DDI.[281] Structure–activity data have been generated with either the rat brain[282] or rat liver[283] mitochondrial preparations for only a narrow chemical series to date. A study of 16 pirlindole inhibitors (IC_{50}) with MAO-A and MAO-B showed that most inhibitors were more potent against MAO-A. A CoMFA analysis used subsets of these molecules and indicated that the active site of MAO-A can accommodate long rigid molecules. Contrarily, with MAO-B, flexible and more hydrophobic molecules are preferred.[283] For a series of 19 condensed pyridazines and pyrimidines (IC_{50} values generated with MAO-B), a QSAR analysis using Hansch, electronic constants, enthalpic, and entropic contributions as well as volume descriptors also showed hydrophobicity being the most important parameter relating to inhibitor binding.[282] A CoMFA analysis based on 16 indolylmethylamine derivatives (K_i data is available for both MAO-A and MAO-B) showed there exist similar contributions from steric, electrostatic, and solvation terms for MAO-A and MAO-B and that the indole ring appears to act with different electrostatic responses toward each enzyme.[284] A large series of coumarin derivatives has also been evaluated and their IC_{50} values were used for deriving Hansch-type QSAR and CoMFA/GOLPE models with 41 and 44 molecules for MAO-A and MAO-B, respectively. Only the electrostatic field was able to explain the MAO-A data. Better statistics were derived for the MAO-B model using steric, electrostatic, and hydrophobic fields.[285] In general, the findings of this latter study are in agreement with those described previously by others, where hydrophobicity was found to be a factor leading to increased selectivity for MAO-B while the presence of a sulfonic ester at the 7-position of the molecule increased MAO-A activity.[285] A further study has relied upon Catalyst to correlate MAO inhibition with structure for five molecules.[286] The model contained a carbamate group, an aromatic hydrophobe, a hydrogen-bond donor–acceptor and a hydrogen-bond donor. When fitted to experimental binding data it suggested that 6-carbamoyl-N-propargylaminoindans are less potent than 6-carbamoylaminoindans.[286] The appearance of large diverse human MAO-A and MAO-B data sets in the literature appears to be some way off in the future. For now, models for the human enzymes will have to assume there is some similarity to the rat enzymes. The few examples where human enzyme have been used involve MAO-A. Structure–activity relationships (based on K_d values) have been generated for phenethylamines and benzylamines. The rate of substrate oxidation correlates best with electronic substituent effects for para substituted benzylamines,[287] while the Taft steric value

for alkyl side chains was found to be related linearly to the observed binding affinity.[288]

Flavin-Containing Monooxygenase

The flavin-containing monooxygenases FMOs are important in the N-oxidation of nucleophiles.[289] Few quantitative studies suitable for deriving a QSAR have been performed on this enzyme family, although one research group has suggested (after using a size analysis and in vitro K_m determination) that human FMO1, which is known to metabolize imipramine and orphenadrine, can also metabolize methimazole, thoiurea, and phenylthiourea, but not 1,3-diphenylthiourea. This and other members of the FMO superfamily may benefit from future QSAR studies once sufficient data is generated.

Sulfotransferases

The formation of sulfate conjugates of both endogenous and exogenous molecules occurs via the cytosolic enzyme sulfotransferase superfamily utilizing phosphoadenosine phosphosulfate (PAPS) as the donor. There may be 10 or more of these enzymes in humans one of which (SULT1A3) is expressed in the intestine and is important for the sulfation of amine neurotransmitters, drugs, and other xenobiotics. This enzyme was recently crystallized and experimental K_m data was used to derive a QSAR.[290] This stepwise regression QSAR suggested that hydrogen bonding and hydrophobicity are important for binding to the enzyme, which is consistent with the crystal structure that contains three hydrophobic phenylalanine residues creating a hydrophobic site. The expression of SULT1A3 in the breast and the potential for this enzyme to metabolically activate promutagenic derivatives of heterocyclic amines,[291] suggests that computational models of this or other related enzymes may also be useful.

Considerable amounts of K_m data have been generated for the rat hepatic aryl sulfotransferase (AST IV) that has a broad substrate specificity. These data provide some understanding of the influence of substrate structure and stereospecificity on catalysis.[292] One research group has also analyzed the kinetics of sulfation for primary[293] and secondary[294] alcohols, 1-aryl ethanols,[295] and N-alkyl-N-hydroxyanilines.[296] These data, in total, present a valuable starting point for QSAR analysis of this enzyme. It is presumed that hydrophobicity and steric effects play a large role in determining the specificity because there are clear limits to the size of molecules that can act as substrates.[293] Homology modeling has also played a role in interpreting binding of inhibitors as well as substrates and their proximity to PAPS.[296] A recent CoMFA and homology modeling study used 35 molecules as the training set and a six molecule test set, which were combined to predict K_{cat}/K_m.[297] Perhaps we can use the rat

data and use computational models for this and other rat sulfotransferases to eventually aid in predictions for human sulfotransferases.

Glucuronosyltransferases

Glucuronidation of small lipophillic molecules is an important metabolic process for the clearance of drugs, endobiotics and xenobiotics in all mammalian species.[298] In numerous instances, drugs azidothymidine (AZT), valproic acid, propofol, morphine, and others) are cleared extensively by direct glucuronidation,[299] although in many other cases the involvement of glucuronidation is restricted to the conjugation of glucuronic acid to metabolites of phase I oxidative metabolism. In cases where drugs are significantly glucuronidated independently of phase I metabolism, the functional group to which the glucuronic acid is transferred can be a hydroxyl group (phenolic or aliphatic), a carboxylic acid, or in some cases an amino group (primary, secondary, or tertiary).

The uridine diphospho-glucuronosyltransferases (UGT) family can be separated into two distinct subfamilies by sequence similarity. The UGT1 and UGT2 family of isoforms are known to be encoded by individual genes.[300] Characterization of cloned and expressed human UGT has demonstrated that many UGT family 1 isoforms are capable of glucuronidating phenols to varying degrees including UGT1A1,[301] UGT1A3,[302] UGT1A4,[303] UGT1A8, and UGT1A10.[304] The UGT family 2 isoforms also display activity toward phenols, although substrate acceptance and rate of glucuronidation appears to be more restricted for UGT2B15[305] and UGT2B7.[306] Two of the earliest UGT isoforms examined were done so on the basis of their ability to glucuronidate phenols. Both UGT1A6 and UGT1A9 were classified as phenol UGT isoforms due to the high turnover rates of these substrates.[307] The UGT1A9 demonstrated greater proficiency in glucuronidating bulky and complex phenols than UGT1A6, which was considered to be capable of glucuronidating only simple or planar phenols.[307] The high glucuronidation activity toward simple phenolic substrates has been shown to be present in human liver microsomes[308] and UGT1A6 comprises a significant proportion of liver UGT 1-naphthol glucuronidation capacity.[309]

Phenols have also been used as probe substrates for simple structure–activity relationship modeling, but very few reports of glucuronidation QSARs have been reported. Enzyme activity data sets for phenols and for benzoic acids incubated with rabbit and rat liver microsomes (published before UGT heterogeneity was recognized) have subsequently been used for QSAR modeling.[80,310,311] Since those original reports, much of the data contained within has been reanalyzed.[312] Kinetic constants for simple phenolic substrate glucuronidation were modeled by QSAR to characterize a partially purified rat UGT.[313] Using rat microsomal systems for this type of work further complicates any modeling of a heterogenous population of enzymes that can

display a considerable overlap in substrate specificity for different types of simple compounds. By accounting for these problematic assumptions, it seems likely that models derived from rat microsomes are limited in the information they provide. The generation of a QSAR for inhibitors in vitro and substrates in vivo has afforded us some degree of understanding of the rat UDPGT.[314,315] The benefit of studying isolated enzymes is that complications introduced by trying to predict the glucuronidation activities of a heterogenous population of isoforms are avoided, and, the substrate physicochemical parameters can be related directly to their influence on activity and affinity of a single active site.

A more recent study described the glucuronidation of simple 4-substituted phenols by the human UGT1A6 and UGT1A9 isoenzymes.[316] The Cerius[2] genetic function approximation software was used to produce models for these isoenzymes. Models to determine whether the K_m for phenol glucuronidation could be predicted were generated for UGT1A6 and UGT1A9 using a range of molecular surface (MS-WHIM) and atomic (AT-WHIM) descriptors. The models were used to compare the way these two isoforms glucuronidate phenols. These models were also used to determine the viability of developing QSAR models for more complex and diverse substrates in the future.

Although the molecules that were screened by testing with both isoforms vary only in the substituent at the 4-position, this position seems to be an especially important factor in determining whether a compound is or is not a substrate of UGT1A6. Again, UGT1A9 was shown to be proficient at glucuronidating a wide range of substituted phenols as reported previously.[307] This is the first indication of significant differences between the two isoforms. By comparing the K_m values for the set of phenol substrates that are glucuronidated by both isoforms, one finds substantially lower K_m values for UGT1A9 than for UGT1A6 even though the ranges of V_{max} are similar. Another point of interest is the observed trend between UGT1A6 V_{max} and the molecular volume of substrates. Even without the application of QSAR analysis it was clear that UGT1A6 V_{max} values decrease as the bulk of the para-substituent increases.

Glucuronidation of 19 indolocarbazoles in human liver microsomes was carried out in an attempt to assess substrate specificity.[317] Generation of molecular structures followed by semiempirical molecular orbital energy minimization showed that molecules with a diameter > 14.5 Å perpendicular to the phenolic O-position are not glucuronidated. Further studies with the recombinant enzyme suggested that UGT1A9 is responsible for this glucuronidation.[317] To date, datasets of UGT1A8 and UGT1A10 K_m values have not been used for QSAR generation.[318]

A recent study used new (unpublished) and published data together to generate 2D-QSAR (Cerius[2] and Dragon) and 3D-QSAR (Catalyst) pharmacophore models for human UGT1A1 and UGT1A9 inhibitors as well as for

UGT1A4 substrates.[319] A chemical feature was developed in Catalyst that could recognize the potential for glucuronidation by a nucleophilic atom. This feature was then used in subsequent HipHop and Hypogen models. These two latter types of models contain similar orientations of features and contain at least two hydrophobes and one glucuronidation feature.[319] The recent suggestion that UGT1A1 induction may arise via a novel signaling mechanism (as observed in HepG2 cells following treatment with a number of flavonoids)[320] raised some interesting SAR questions. Out of 22 molecules tested only acacetin, apigenin, luteolin, chrysin, and diosmetin produced greater than two-fold induction. Hydroxyl groups at the 5- and 7- position of the A ring and a 2,3 double bond in the C-ring were essential for induction.[320] It is likely that at least two hydrogen-bonding groups as well as hydrophobic interactions, determined by the shape of the flavonoid core structure, are required for the unidentified receptor.

The screening for high metabolic turnover early in development has enabled industrial drug designers to become adept at avoiding compounds that are likely to be highly metabolized by cytochrome P450 isozymes. If the successful circumvention of phase I metabolism leads to the development of additional molecules that are glucuronidated, then the next evolution in QSAR modeling for the pharmaceutical industry will require models for these enzymes. The generation of in vitro data for molecules where human UGTs contribute to clearance enables in vivo prediction of this[321] and could itself ultimately be used to generate a computational model once sufficient data is available.

Glutathione S-transferases

Glutathione S-transferases (GST) constitute a family of enzymes that catalyze addition of glutathione to various lipophilic substrates possessing an electrophilic functional group. To date, there have been limited QSAR studies on GST.[322–324] Most have used small homologous data sets and have shown to some extent that rat cytosolic fractions agree with human tissue since affinity increases with hydrophobicity.[322–324] By using 20 substrates for rat GST 4-4, a substrate template was derived using simple alignments of molecules to benzopyrene-7(R), 8(S)-diol-9(S), 10(R)-epoxide using the modeling program Chem-X. The final model derived from that alignment consisted of a flat aromatic (hydrophobic) interaction site and three electrostatic interaction sites. That model was further evaluated with six additional compounds as a test set.[325] This model was then extended by using four substituted 1-chloro-2-nitrobenzenes. Descriptors used included sterimol, the hydrophobic fragment constant and Hammet descriptors. This analysis showed the importance of electronic, steric, and lipophilic factors and added further dimensions to the substrate model of van der Aar.[326]

Another study was done using 122 diverse molecules with biological activity data for eight proteins including human GST (activity measured with the probe 1-chloro-2,4,-dinitrobenzene). Data from this study was used with a multivariate regression analysis to develop models capable of making predictions for new proteins.[327] This data, in itself, may also be valuable for building a computational model for the human GST in the future.

CHANNELS

There exists a wide array of ion channels within cells that perform fundamental physiological functions. Intervention with some of these ion channels represent validated therapeutic targets for major diseases. Some ion channels should not be interfered with by drugs used for other diseases, however, as life-threatening effects could result. Because of this, it is vitally important to understand the recognition process of ligands that may serve as therapeutic agents.

Human Ether-a-gogo Related Gene

Several drugs have been withdrawn from the market in recent years due to cardiovascular toxicity associated with alteration of the action potential. In particular prolongation of what is known as the "QT interval", which is the period between the start of ventricular depolarization and repolarization, is a major concern. Considerable interest in predicting QT prolongation induced by noncardiovascular drugs earlier in their development has occurred since the European pharmaceutical regulatory authority's Committee of Proprietary Medicinal Products (CPMP), issued a position on QT interval prolongation in 1997 (CPMP/986/96). The focus of many cardiac related in vitro studies to date has been the membrane bound inward (rapid activating delayed) rectifier potassium channel (I_{Kr}) [also known as the product of the Human Ether-a-GoGo Related Gene (hERG)]. This channel contributes to phase 3 repolarization by opposing the depolarizing Ca^{2+} influx during the plateau phase.[328] It is understood that drugs or their metabolites may block this channel thereby prolonging the QT interval and in some cases leading to potentially life-threatening ventricular arrhythmia. QT prolongation may frequently result in "torsades de pointes" (twisting of the points), which refers to the sinusoidal variation in the passage of the action potential through the ventricular muscle (commonly refered to as the "QRS axis") around the isoelectric line of an electrocardiogram. The ultimate result of torsades de pointes is a ventricular tachyarrhythmia, with the prolongation of the QT interval of the last sinus beat that precedes the onset of arrhythmia. Possession of a mutation in hERG[329] in the form of a single nucleotide polymorphism (SNP), may make carriers particularly sensitive to xenobiotics that in turn could affect potassium

currents and trigger arrhythmic events.[328] It would therefore be of considerable value in drug discovery to understand the structural requirements of inhibitors of this potassium channel. Knowing the important structural features (the pharmacophore) of molecules that inhibit hERG would enable the prediction of inhibition prior to molecule synthesis and reduce the likelihood of developing drugs that could lead to a life-threatening ventricular arrhythmia. At present, various in vivo and in vitro models for QT prolongation (and subsequent arrhythmia) exist but they may not be entirely predictive for humans. Perhaps the closest model to the human in vivo situation is healthy human-derived cardiac tissue, but data for this is not readily available.[330] However, various cell systems expressing the hERG channel have been developed using *Xenopus* oocytes[331] and mammalian cell lines such as HEK-293.[332] The latter are more amenable to higher throughput testing but are themselves beset with limitations due to the level of expression of the channel. However, HEK-293 cells expressing hERG have been used in patch clamping, binding studies with radiolabeled ligands, and in rubidium flux studies to date.

Because no crystal structure for hERG exists at present (due to its membrane bound nature) homology models based on the template bacterial KcsA channel and site-directed mutagenesis work[333] have instead been used to infer important amino acid residues likely to be involved in the inhibitor-channel interaction. The data collected to date using site directed mutagenesis work suggests that the amino acid residues located in the S6 transmembrane domain F656 and Y652, and, to a lesser extent V625 and G648, are important for interaction. The work of Mitcheson et al.[333] is therefore an important step forward in understanding the structural specificity for the hERG channel. However, the homology model itself may be of limited use in screening databases for molecules likely to interact with this domain because it is unlikely to provide a reliable and rapid prediction of the ability to bind and inhibit this channel.

Another computational approach, namely, 3D-QSAR, has also been used to evaluate potential hERG inhibitors. With the use of IC_{50} data generated previously with cDNA-expressed hERG channels in HEK-293 cells, a pharmacophore model was derived using 11 antipsychotic agents. This pharmacophore explained the likely structural features that are common between various potent inhibitors.[334] Eleven additional molecules were used to form a test set. Another 15 molecules with literature-derived hERG IC_{50} data were used as a second test set for this pharmacophore.[334] In both cases, these test sets were rank-ordered in a statistically significant manner using the antipsychotic derived pharmacophore (the Spearman's rho values were 0.71 for the 11 molecule and 0.74 for the 15 literature molecule test sets, respectively). Recall that a Spearman's rho value of 1 would be optimal and 0 corresponds to a random rank ordering. The literature set of 15 molecules was also used in an attempt to produce a more general model of hERG inhibition than that
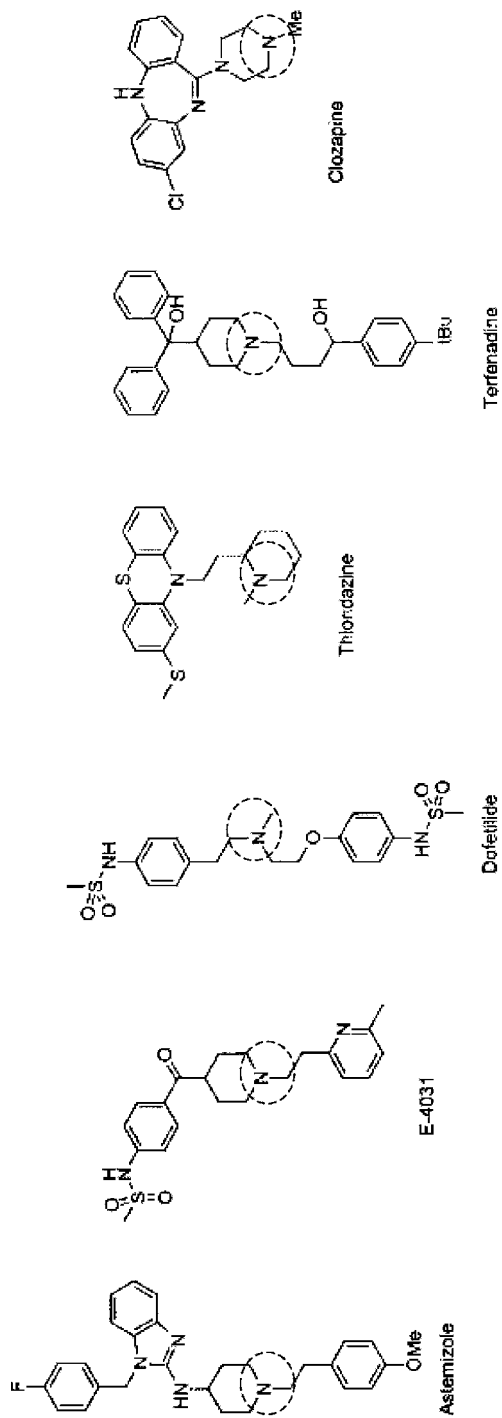
Figure 9 Structures of known potent hERG inhibitors with likely positive ionizable feature highlighted (dashed circle). Note that all of these molecules contain at least two aromatic rings and other areas of hydrophobicity.

obtained with the data from the antipsychotic agents.[334] The new pharmaco-phore generated with this literature data set contains four hydrophobes and one positive ionizable feature. This is somewhat different from the antipsychotic-derived pharmacophore in that the aromatic ring feature in the latter model is replaced with a positive ionizable feature, and, there are more hydrophobes in the new model. Agreement between the published homology model and the hydrophobic features in both hERG pharmacophores appears to coincide with the F656 and Y652 residues in the homology model that are involved in π–π stacking with aromatic residues of the inhibitors.[333]

The general hERG pharmacophore model based on literature data was also assessed using a test set of molecules excluded from the model. That data was generated in our own laboratories. In light of the work presented in our initial report, it appears that the pharmacophore is able to generate pre-dictions for the 22 molecules (predicted vs. observed $r^2 = 0.83$) and produces a statistically significant rank ordering as indicated by the Spearman's rho coefficient of 0.77. Also note that, on the whole, this model predicts some IC_{50} values to be higher than those observed experimentally but in a few cases, like terfenadine, this is reversed. However, it is important to understand that the model is able to correctly rank order the inhibition of parent molecules and metabolites. Indeed, the model can distinguish between thioridazine and its metabolite mesoridazine; clozapine and clozapine N-oxide and N-desmethyl-clozapine; risperidone and 9-hydroxyrisperidone as well as olanzapine and two of its metabolites. Furthermore, the general hERG model can distinguish potent inhibitors of hERG, such as thioridazine (Figure 9), cisapride, and ser-tindole from weaker inhibitors, such as nicotine, desmethyl olanzapine, and 2-hydroxymethyl olanzapine, therefore enabling a ranking of molecules, which may be valuable in early drug discovery.[334]

Protein binding and drug metabolism are also important factors to con-sider when selecting molecules in pharmaceutical design. Protein binding and drug metabolism are also expected to impact predictions for hERG inhibition. If the drug molecule is tightly bound or extensively metabolized, less of that parent drug will be available for inhibition of hERG (although in the case of metabolism the assessment of inhibitory potential of metabolites may be needed). It has been suggested by Kang et al. that hERG channel inhibition is not a class effect, at least in the case of fluoroquinolones.[335] In Kang's study of seven antibiotics for hERG inhibition in oocytes expressing the potassium channel, a range of IC_{50} values from 18 to 1420 μM was produced. This in vitro data was also used in conjunction with free plasma concentrations to cal-culate hERG IC_{50} / plasma concentration ratios. The results indicated that some molecules like grepafloxicin, which are known to prolong the QT inter-val in humans, possess low ratios while other molecules like ciprofloxacin have much higher ratios and, consequently, do not prolong the QT interval.

Our observations suggest there may be multiple binding interactions within the potassium channel ultimately making this difference difficult to

predict and could account for some of our poor predictions. Overcoming this limitation imposed by multiple-binding interactions may require multiple pharmacophores or platform-specific models (like the antipsychotic derived model described previously) that could detect subtle structural differences and account for the multiple conformations explored by software like Catalyst. To some extent, literature studies have explored platform-specific models. Kang et al.'s study of seven antibiotics with measured hERG IC$_{50}$ values[335] suggested the most potent hERG inhibitors contain C$_5$ substituents. It is unknown how this structure–activity relationship relates to other molecules from different therapeutic areas, thus limiting its applicability. It has been suggested by De Ponti et al., that some noncardiac drugs known to be hERG inhibitors contain the same structural feature pharmacophore as class-III antiarrhythmics (a para-substituted phenyl ring connected to a basic nitrogen by a variable chain) while others do not.[336]

In an attempt to predict classes of hERG inhibitors using data from Chinese hamster ovary (CHO) cells expressing the channel,[337] a computational analysis found a striking difference in ClogP between potent and nonpotent inhibitors. In agreement with the pharmacophore studies, hydrophobicity was found to be important for the potent inhibitors. In that study, neural network models were generated based on 244 proprietary structures. This neural network model performed better at identifying the less potent inhibitors because it misclassified some potent inhibitors.[337] In another pharmacophore study, literature data was used to build a CoMFA model for 31 inhibitors.[338] This model contained three aromatic functions as well as a central nitrogen function.[338] This CoMFA model was in good agreement with the earlier Catalyst pharmacophore as well as the aforementioned homology model for hERG. Some companies are generating inhibition of [^3H]-dofetilide binding data with hERG for use in a number of projects. For example, researchers at Merck have published two papers containing data for the 5HT$_{2A}$ class of molecules[339,340] and one relating to 3-aminopyrrolidinone farnesyltransferase inhibitors[341] in which hERG binding was reduced to some extent by structural modification. Ultimately, this data may also be used for computational model building for hERG although the structural diversity of the molecules is limited (Figure 10a–c). Alignment of Catalyst-derived pharmacophores (Figure 10d) generated with this Merck data suggested common areas of positive ionizable features, and hydrophobicity (aromatic rings).

We conclude the discussion on hERG by considering the ability of very large naturally occurring molecules like the scorpion toxin BeKm-1 (4092 Da), which acts as a potent and selective inhibitor of hERG (3.3 nM).[342] Perhaps large molecules like this peptide block multiple subunits on hERG, or, the N-terminal domain of the toxin contains a positively charged amino acid that acts like a stopper and blocks the channel in a single subunit. A recent paper suggested the most critical residues for binding are located on the alpha helix, which is in contrast to other known scorpion toxins.[343] It is interesting
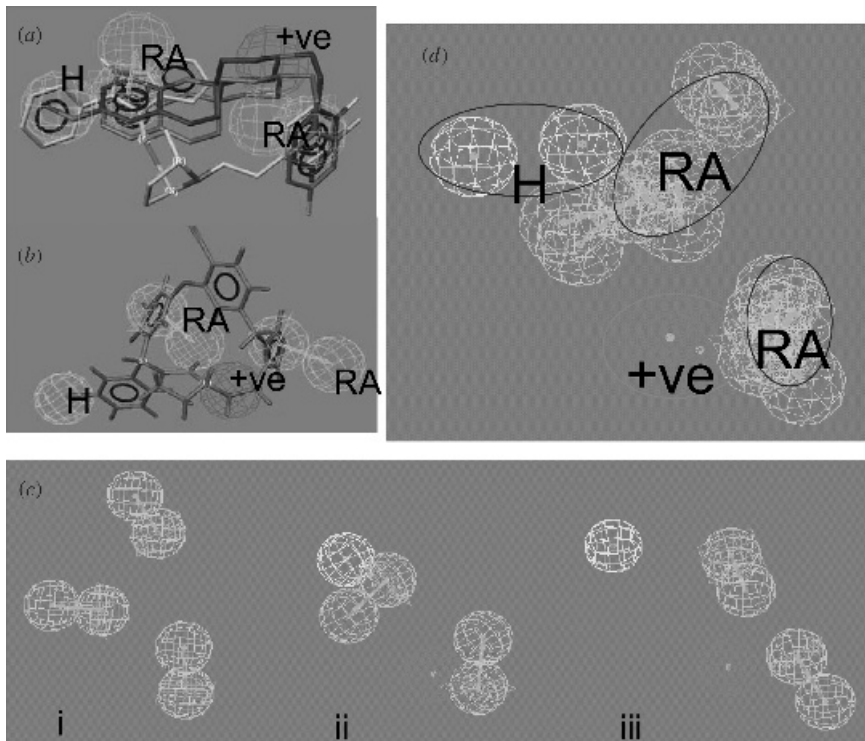
Figure 10 Catalyst pharmacophores. generated with Merck published data (H = hydrophobe; RA = ring aromatic; + ve = positive ionizable): (*a*) for 5HT$_{2A}$ inhibitors from Fletcher et al.[340] data, observed versus predicted $r = 0.93$. The figure shows inhibitors fitted to the features; (*b*) for farnesyltransferase inhibitors from Bell et al.[341] observed versus predicted $r = 0.87$; (*c*) comparison of pharmacophores from (*a*) and (*b*) as well as an additional pharmacophore (i) for 5HT$_{2A}$ inhibitors from Rowley et al.[339] observed versus predicted $r = 0.87$; (*d*) combination of all three hERG pharmacophores showing common regions.

to note that the surface of the protein clearly has an area of positive charge surrounded by multiple hydrophic areas, which mimics the pharmacophores defined for small molecule inhibitors described previously. Clearly, a molecule of the size of BeKm-1 is outside the scope of existing pharmacophores and other computational models generated to date for hERG, but this has implications for testing protein drugs in vitro as inhibitors of hERG. There is certainly a need for using a diverse array of computational approaches to better understand other ion channels that are important for cardiac function, cellular homeostasis and communication. To date, relatively few computational studies have been done although there are many SAR studies for inhibitors of calcium and sodium channels in the literature.

RECEPTORS

As with ion channels a wide diversity of receptors exists that play key roles in maintaining our physiology. Such receptors can also represent therapeutic targets. Examples include the α-adrenoreceptor, β-adrenoreceptor, AMPA, NMDA, GABA, serotonin, dopamine, glutamate, histamine, glycine, opiate, NMDA, cannabinoid, and steroid receptors. Nuclear receptors are a family of ligand-regulated transcription factors that include the glucocorticoid receptor, the vitamin D receptor, the estrogen receptor, and the so-called "orphan nuclear receptors". Interactions with these latter receptors may not be beneficial as we are now finding out.

Pregnane X-Receptor

Recently, it was discovered that the pregnane X receptor (PXR, also known as SXR or PAR) is a transcriptional regulator of the enzyme CYP3A[344–346] and is activated by many of the structurally diverse CYP3A inducers. This nuclear hormone receptor is just one member of a large family that acts as a transcription factor in order to regulate induction of numerous genes. The discovery of PXR provided some degree of understanding for modulation of CYP3A expression in response to endobiotics and xenobiotics. Three years after its discovery the role of PXR was expanded to include the regulation of expression of human MDR1 and CYP2C8/9.[347] These discoveries provided some insight as to how drugs could regulate not only their own metabolism but potentially their efflux too, as demonstrated for paclitaxel.[348] Adding to the complexity of understanding the interindividual variability in the expression and functional response was the identification of 38 SNPs. These SNPs were not found in the ligand binding site of human PXR. They could, nonetheless, have important physiological ramifications[349] as they suggest that PXR may have a crucial role in binding an endogenous ligand.[350] Recently, PXR was also shown to regulate many other genes involved in the transport, metabolism, and biosynthesis of bile acids.[351]

The impact of PXR on drug development is being felt in the pharmaceutical industry, which is advocating the use of high throughput assays to eliminate likely CYP3A inducers early in discovery.[352] The extent of use of assays for PXR depends on the screening paradigm instituted by each drug company at the discovery stage. The PXR reporter and functional assays represent a surrogate for the in vivo animal assays of induction. These assays have significantly higher throughput and avoid the complication of extrapolating animal in vivo data to human in vivo data. However, the availability of the PXR-null and SXR-transgenic mice represent in vivo models that incorporate human PXR with in vivo pharmacokinetics capabilities.[353,354] Hence, species differences in induction may be avoided to some degree. A diversity of molecules exist that bind to human PXR in vitro. These ligands include a selection

of bile acids,[351,355] statins,[356] components of herbal remedies such as hyperforin found in St. John's Wort,[357,358] human immunodeficiency virus (HIV) protease inhibitors,[359] calcium channel modulators,[360] steroids,[352] plasticizers and monomers,[361–363] organochlorine pesticides,[364] and a growing list of diverse xenobiotics.[344–347,352,357,365–368] To some extent, these in vitro findings explain in vivo DDIs that in some cases have been known for decades or in others may have only recently been recognized.

A growing list of PXR ligands now exists and one might think that virtually any suitable molecule could be added to this list because the ligand-binding domain is a large, flexible hydrophobic site with a few polar residues plus three distinct binding sites for SR12813 (as described by X-ray crystallography[354]). However, this structural information for the ligand-binding domain and structural information about ligands themselves can all be used to select molecules that avoid binding to this protein. The effect of different molecules binding uniquely to PXR was tested by mutating amino acids that form salt bridges adjacent to the binding cavity when CV-1 cells transfected with expression plasmids for PXR were incubated with SR12813 or rifampicin. When Asp205 is mutated to Ala, rifampicin becomes a more potent PXR activator in the reporter gene assay. Similarly, targeted mutants meant to confer a human-like response to mouse PXR confirmed the importance of these residues in other species. Rather than being responsible for direct binding with the ligand it is likely that these residues are altering the shape of the binding site significantly. Flexibility of the binding site probably enables the acceptance of more structurally diverse ligands that in turn may act as antagonists (like ecteinascidin) and possibly interact with the heterodimer RXR. There have been several reports from the same laboratory defining PXR binding in terms of EC_{50}.[352,355,357] These data for 12 molecules were used to generate a pharmacophore with Catalyst. That pharmacophore may define key features of ligands that bind to the PXR binding site[365] (Figure 11). The pharmacophore was also positioned in the human PXR ligand-binding domain. This pharmacophore was further tested with other PXR ligands for which activation–deactivation data was available. The pharmacophore was also aligned to match three binding positions to SR12813[365] as implicated from a crystallography study.[354] The PXR pharmacophore provided a good correlation between observed and predicted training set data derived from a single laboratory. It also enabled a qualitative assessment of 28 other molecules, some of which were PXR ligands (CYP3A4 inducers), by predicting EC_{50} data within the range of the training set. This pharmacophore may have defined the minimal set of molecular features needed for binding to this nuclear receptor. It implicates at least four hydrophobic features and at least one hydrogen-bonding feature that should be avoided in future drug candidate molecules. What might be difficult to understand from just a potential ligand structure alone is its binding orientation in the crystal structure. In addition to the three sites identified in SR12813, smaller ligands could have additional binding
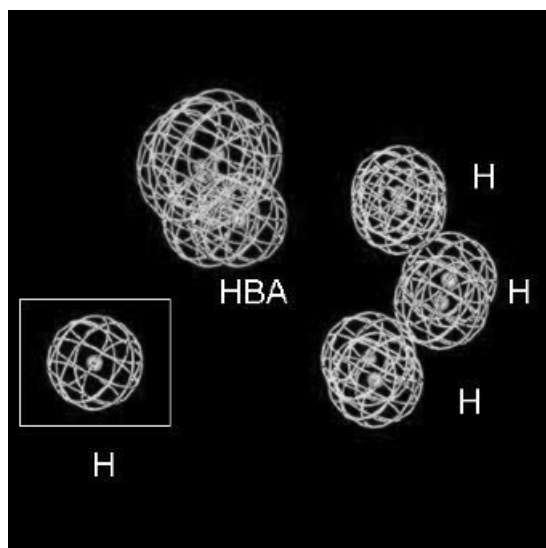
Figure 11 Alignment of the human PXR and human CAR pharmacophores showing the close alignment of three hydrophobes (H) and a hydrogen-bond acceptor feature (HBA). The PXR contains one hydrophobe (highlighted by a square) that is not present in the CAR pharmacophore.

orientations, and, multiple molecules may fit simultaneously into a single receptor site, thus obfuscating exactly how drug–receptor interactions take place. If each site is bound simultaneously, the question to ask is: Is the extent of activation additive? With large molecules like paclitaxel and ecteinascidin all binding contacts will clearly be complete. This may be the reason for the high-affinity antagonist response (low nM) observed for the latter ligand.[347] On the other hand, it may be difficult to determine if a small molecule is likely to be a potent or weak PXR are ligand in silico using only the crystal structure. Until cocrystals of the ligand bound to PXR are obtained for a selected number of molecules, in vitro reporter systems will continue to be used for evaluating computational predictions. From such a combined in vitro–in silico approach we are more likely to determine the important binding site and key ligand interactions as well as to enable iterative improvement of the in silico models.[24]

Because both P-gp and CYP3A4 are coregulated there must be features in common for these ligands that also translate into the binding site of PXR.[187,347] To some extent, we have already demonstrated this with multiple pharmacophores for inhibitors and substrates of P-gp, most of which contain multiple hydrophobic features and hydrogen-bond acceptor features.[54,55] Because CYP3A4 (as well as other CYPs)[189,190] and P-gp[369] appear to have multiple binding sites, it is not surprising that PXR may behave in a complex fashion, thus providing these proteins with the ability to simultaneously

handle diverse structures, some of which may result in up-regulation of trans-porters and enzymes to increase the rate of clearance.

The clinical implications from a complete understanding of PXR is becoming obvious. Our ability to predict potential DDIs that might occur as a result of coadministration of xenobiotic PXR ligands with molecules known to be metabolized or transported by any of the genes up-regulated at a parti-cular moment in time, becomes possible. Subsequently, the identification of other genes regulated by PXR has increased. The CYP2B6 enzyme is involved in the metabolism of many diverse structural classes of drugs,[370] and has more recently been shown to be directly regulated by PXR.[371] A further remarkable observation by Goodwin et al. is that similar levels of induction exist for CYP2B6 and CYP3A4 for four out of five molecules. Both CYP2C8 and CYP2C9 are involved in the regio- and stereoselective epoxidation of arachi-donic acid in the liver and kidney.[372] These enzymes have also been shown to be induced by calcium channel antagonists via PXR.[360] The intestinal trans-porter MDR1 induction by rifampicin and other xenobiotics has been shown to be mediated by PXR using the human colon carcinoma cell line LS174T as a model system.[373] Human MRP1 (ABCC1) and MRP2 (ABCC2), which are responsible for eliminating conjugates of toxic molecules and biliary efflux of endogenous molecules, respectively, have been shown to be induced by redox-active molecules as well as other types of compounds. However, it was unclear from one study exactly what role PXR might have in the induc-tion[374] of these proteins. The enzyme inducible nitric oxide synthase (iNOS) is up-regulated by PXR, thus explaining how steroids affect inflammation.[375] It is possible that genes previously thought to be regulated solely by alternative ligand-activated transcription factors may also be regulated partially via PXR. Endogenous hormones like estradiol are known to be PXR ligands.[344–346] They can regulate their own metabolism in hepatic tissues via CYP3A4 and conceivably in extrahepatic tissues via CYP1B1[376] or other CYPs simulta-neously. There may also be a developmental role of the orphan nuclear recep-tors (like PXR) in switching on genes at the appropriate time in response to endogenous ligands such as environmental pollutants that are teratogens under the right conditions.[377] This in turn may represent a point at which the gene can be interfered with by other molecules, thus preventing abnormal fetal growth. Predicting this activity computationally in the future is clearly of value.

Constitutive Androstane Receptor

A second orphan nuclear receptor, the constitutive androstane receptor (CAR), has $\sim 40\%$ identity with PXR in the ligand-binding domain. Murine CAR was found to be inhibited (EC$_{50}$ < 500 nM) by the androstane metabo-lites androstanol and androstenol,[378] which are most likely the endogenous repressors.[379] Following exposure to phenobarbital, CAR accumulates in the

nucleus, heterodimerizes with RXR, binds to the two phenobarbital responsive elements and ultimately activates transcription of the CYP2B genes.[380] Human CAR was found to be activated by the pesticide TCPOBOP, phenobarbital, chlorpromazine, O,P'-DDT, methoxychlor, and PCB. This activation corresponded well with the induction of the CYP2B6 gene.[381] Other ligands for human CAR including clotrimazole and the progesterone metabolite 5α-pregnane-3,20-dione have been described. Androstanol is a less potent activator for human CAR compared to mouse CAR.[382] Murine CAR is also activated by metyrapone and clotrimazole.[383] CAR appears to activate other genes besides CYP2B6 including CYP3A4[381] in a manner similar to how PXR can activate CYP2B6 as well as CYP3A4.[371] The induction of drug metabolizing enzymes via CAR has also been demonstrated in vivo in mice, while CAR knockout mice have an altered sensitivity to inducers.[384]

So far, it appears that the human PXR ligand-binding domain accomodates very large molecules that have the highest reported affinities (e.g., ecteinascidin $IC_{50} = 3$ nM[347]) while small planar molecules like steroids and bile acids bind with a much lower affinity.[355,382] In comparison large molecules like 1,4-bis[2-(3,5-dichloropyridyloxy)]benzene (TCPOBOP) do not bind effectively to human CAR but do bind to murine CAR,[382] while more compact molecules like clotrimazole bind well as a deactivator to human CAR but not to mouse CAR.[382] Interestingly, both the human PXR and CAR share only 70% amino acid identity with their homologues in other species[382,385,386] and alignments to the human crystal structure for the PXR ligand-binding domain clearly show there are some marked differences across the receptors and between species. This suggests that although there might be some perceived overlap in the binding affinity of both human CAR and PXR for the same ligands, there ultimately may be some significant cross-receptor differences in binding affinity. Therefore molecules like the bile acid metabolites that activate PXR with low affinity could have a higher affinity toward CAR or other nuclear hormone receptors. The ability for murine CAR to bind agonists and antagonists of differing size has not gone unnoticed[387] while the same facility for human CAR has not really been explored. The overlap between the receptors has an added functional consequence in sensing the level of ligand-binding and possibly responding to a different extent depending on the amount of ligand bound. Hence, the body retains high-affinity nuclear hormone receptors and low-affinity nuclear hormone receptors for structurally similar molecules to more efficiently regulate metabolism and efflux or to retain a steady state. The complexity of this system comes about when extrapolating to the in vivo state from the well-defined in vitro models. At this point in time the key question is: Does what we observe in vitro really translate to in vivo?

As more data is generated about CARs involvment in the induction of CYP2B,[388] CYP3A,[381] and possibly other genes, computational models will likely be generated for the ligands and inhibitors. At present a simple alignment of five molecules suggested to be mouse CAR activators

(chlorpromazine, clotrimazole, metyrapone, TCPOBOP, and phenobarbital[383]) yield a pharmacophore with two hydrophobic features and one hydrogen-bond acceptor.[226] This planar model appears to indicate that CAR is a less promiscuous receptor than PXR because it accommodates less flexibility in the ligands involved in activation. This hypothesis is based on the finding that CAR has high affinity for the rigid repressors and androstane metabolites that appear to also fit well within the confines of this model.[378] To some extent this in silico finding may help answer the question as to whether or not androstanes bind directly to CAR.[367] On the basis of this small pharmacophore the answer appears to be yes they do. When three molecules with known EC_{50} values for human CAR (clotrimazole, androstanol, and 5α-pregnane-3,20-dione[382]) were used to build a pharmacophore, a model consisting of three hydrophobes and one hydrogen-bond acceptor was generated.[226] This model parallels a previously described human CYP2B6 substrate pharmacophore,[100] which consists of the same features in a similar arrangement. When the human PXR pharmacophore (generated with Catalyst version 4.6 and fast conformer generation) and human CAR pharmacophores are merged together there exists some overlap of the hydrogen binding and hydrophobic features. But, there appears to be one less hydrophobe in the CAR model (Figure 11)[226] indicating a smaller binding site. A smaller binding site is consistent with a recent analysis of the binding cavity surface volumes of CAR (1170 Å^3) and PXR (1220 Å^3) using GRASP.[389] When the potent ligand 5α-pregnane-3,20 dione is fitted to the human CAR pharmacophore along with the bile acids that are identified as low-affinity PXR ligands[355] (e.g., lithocholic acid and ketolithocholic acid), it can be seen that there is some overlap between them.[226] This may imply that potent steroid ligands and related bile acids could be higher affinity ligands (activators or repressors) for CAR than for PXR. This speculation needs experimental verification, however. It is appropriate to relate this observation back to the major genes that each orphan nuclear receptor regulates, namely, CYP2B6 and CYP3A4. A molecule could potentially regulate both enzymes via different receptors, to differing extents simultaneously. The similarity of the pharmacophore for CAR with that of human CYP2B6[100] once again suggests that ligands for an enzyme (or transporter) have features in common with the ligands for the receptor responsible for regulating it as described for PXR.[365,390] By using the human PXR crystal structure as a template to align human CAR, it can be shown how a single amino acid, Phe161, can block SR12813 from binding, thus drastically reducing the volume of the CAR binding site compared with that of PXR in which Met243 is in the same position. The steric interactions that are described for SR12813 would ultimately suggest that binding to CAR is unfavorable, as actually found in vitro.[382] Four ligands have been docked in the homology model for CAR using GOLD. As with PXR it is found that there could be multiple binding modes.[389] In all cases, the ligands were suggested to interact with Phe161 as well as with other residues.

An impediment to our understanding of the roles of CAR and PXR comes in the form of submicromolar concentrations of glucocorticoids like dexamethasone, which increase PXR, CAR, and RXR expression in human cultured hepatocytes and ultimately result in increased CYP expression and response.[391–393] Pascussi et al. suggest that glucocorticoids may control hepatic expression of PXR and CAR and are responsible for basal CYP3A4 expression in the absence of inducers. Upon challenge with an inducer, these receptors are also activated and increase CYP3A4 expression.[391–393] The evidence Pascussi et al.[392] tender is that dexamethasone has been shown to be neither a CAR nor a PXR ligand at submicromolar levels. Those authors also propose instead that it acts via the glucocorticoid receptor to up-regulate PXR and CAR, which then acts on CYP3A4. This research group has also shown that a strong correlation exists between the expression levels of PXR, CAR, and CYP3A4 in human liver microsomes. This contrasts with the experimental data derived from CAR and PXR knockout animals that do not show any loss of CYP3A4,[353,355,384,394,395] indicative of dexamethasone playing no role in basal regulation for either of these receptors.

By limiting our discussion to just two nuclear receptors, we have avoided the complicated issue of how other nuclear receptors may be involved in the regulation of many key enzymes and transporters. Coming to terms with the complexity of the regulation of the many key proteins important for ADME/Tox processes can be accomplished with the help of molecular modeling.[226]

FUTURE DEVELOPMENTS

The increased level of interest in computational models for ADME/Tox is influenced by the need that multinational pharmaceutical companies now have to lower costs[396] and to increase the width of their discovery pipelines. The risks and expenses associated with developing drugs has increased to the point where companies have pulled forward to early development stages screens for ADME/Tox properties. These companies have started to utilize computational filters early on in their bid to lower costs and to improve the efficiency of developing molecules.[397]

Given the growing number of computational models for ADME/Tox properties as well as new data sets that are being published we may soon reach a point where other algorithmic technologies could be considered to create knowledge from those data sets. In addition to the various types of 3D-QSAR models already described in this chapter, there are those that have been developed using a genetic algorithm to simulate metabolic transformations.[398] Also, predictive models have been generated by taking into account the electronic properties of molecules like those with the tendency for oxidation (P450 mediated hydrogen-atom abstraction). These predictive models, based on this alternative modeling approach, have been used for both rat and

human enzymes.[51,399,400] In addition a number of rule-based tools have been developed to predict metabolism using the same concepts implemented for toxicity prediction.[53] One approach has used a metabolic fingerprint (META-PRINT) that uses a rule-based system (MetabolExpert) that outputs information on 179 metabolic transformations that can then be used for similarity searching and cassette dosing experiments.[401] The study initially describing this used a validation set of five compounds and it remains to be seen whether this type of rule based approach will become more widely used.

High throughput docking has recently been used with CYPcam and a homology model of CYP3A4. Using the GOLD, DOCK, PMF, and FlexX scoring functions an attempt was made to predict known substrates and inhibitors.[402] Of the 345 compounds evaluated, 334 had GOLD scores less than −100. However, this study was not able to differentiate between substrates and inhibitors of CYP3A4.[402] There have also been attempts to use an affinity fingerprint to train a QSAR.[327,403–405] The generation of protein affinity fingerprint models has the potential for use with ADME/Tox-related proteins.[405] The validity and utility of this method remains to be seen, however. The development[406–408] and evaluation[409–411] of various knowledge-based potentials for scoring ligand-binding within proteins combined with de novo design tools and ADME/Tox filters represents the next level of evolution for drug discovery. The simultaneous design of molecules within the target binding site along with optimally predicted ADME/Tox properties would have a considerable impact in molecular design.[412] With considerable interest in using numerous in vitro data sets and computational technologies for modeling and ultimately understanding G-protein-coupled receptors that are therapeutic targets,[413] we may better comprehend the structural features and dynamics of the many transporters and receptors that to date have eluded all efforts at crystallization. Some techniques have been developed recently to predict the tertiary structure of proteins from their amino acid sequence. Complementing this are new methods for predicting the binding site and binding energy of ligands to GPCRs.[124] Some success along these lines has been shown by Shacham et al.[414] who could reproduce the crystal structure of the only known example of a 7-transmembrane protein, rhodopsin. Such technology could be applied elsewhere. Complexity in ligand–protein interactions should not be underestimated and there is a shift toward thinking of some proteins as existing in a population of many conformations.[415] Clearly, the complexity of interactions and kinetics noted for CYP3A4, P-gp, and PXR and perhaps other ADME/Tox related proteins will require identifying these conformations. This may lead to computational predictions and algorithms that can be applied elsewhere.

New visualization technologies[416] and algorithms for descriptor selection for ADME/Tox models are also important in the development of the field. The recent description of ''particle swarms'' that explore the search space through a population of individuals that adapt and return to previously successful regions has been used for feature selection.[73] Although not yet fully

described in the literature, particle swarms may be combined with other algorithms for use in selecting appropriate (and potentially novel) ADME/Tox descriptors before model building. The relatively recent development of support vector machines (SVM) for classification problems may add another computational tool to the list available for ADME/Tox modeling. The theory behind this approach has been well described[417] and SVM has been applied to microarray gene expression data.[418,419] The use of SVM for pattern classification in QSAR has recently been described and compared with artificial neural networks for antistamine and antibacterial data sets.[420] SVM has also been used with drug discovery data sets in which the molecules were described with $> 100,000$ descriptors.[421] This approach may be useful for deriving ADME/Tox models from very large data sets although a careful evaluation of these approaches with well-known data sets may be necessary to show that they are better than existing and more commonly used technologies. This type of analysis could be facilitated by the creation of a publically available website for ADME/Tox datasets, molecular descriptors, and computational models that could be used by researchers in both academia and industry. Although efforts by the National Cancer Institute and the Environmental Protection Agency are being made to make available toxicity data sets, there has been no effort as yet to do this for ADME models. We could envision data sets for nonproprietary molecules with solubility, BBB, metabolism, and related data in a single location. It may be in the interest of the companies marketing computational software to sponsor these webpages as well as their working toward a standard for display and utilization of models in much the same way as various Markup languages have developed. As it stands now it would take a motivated and knowledgeable individual an enormous amount of time and many tens of thousands of dollars to start building ADME/Tox models just from literature data. Moreover, unless collaborators use the same software it is almost impossible to share models. If this barrier was removed, the threshold for entry into the drug discovery business could be dramatically lowered. At the same time we could be making all the pieces of virtual drug discovery from library generation, virtual screening, scoring, and selection algorithms available to the public (assuming that such tools will be used for the common good of society). At the same time that computational biologists are working toward standards for development of models, should not those of us in the field of computational chemistry and computational ADME/Tox be doing the same? Doing this may not be as unrealistic as it seems.

The future of computational ADME/Tox requires integrated approaches that automatically update computational models as data is being generated from the various in vitro assays. This needs to be done in such a way that the transition from data generation to data storage to computational modeling is seamless as depicted in Figure 1. This seamless interconnection is actually close to reality due to the database software now available. ADME/Tox model
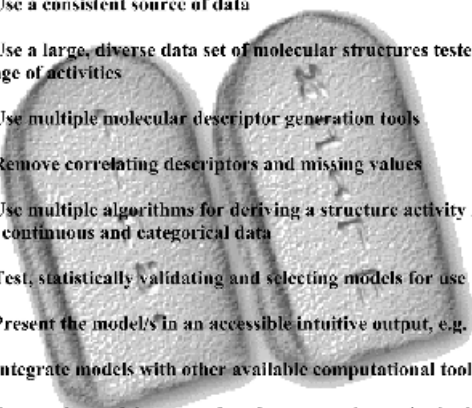
1. Use a consistent source of data

2. Use a large, diverse data set of molecular structures tested with a range of activities

3. Use multiple molecular descriptor generation tools

4. Remove correlating descriptors and missing values

5. Use multiple algorithms for deriving a structure activity relationship for continuous and categorical data

6. Test, statistically validating and selecting models for use

7. Present the model/s in an accessible intuitive output, e.g. webpage

8. Integrate models with other available computational tools

9. Ensure the models are used at the appropriate point in the drug discovery process

10. Continually update and refine models with new data

Figure 12 The 10 commandments of ADME/Tox model building.

building consists of a pathway in which several steps have equal importance. For successful ADME/Tox modeling, we list our "ten commandments" in Figure 12. This process and our commandments would be applicable to many ADME/Tox properties as well as for bioactivity models that at present both undergo multiple sequential screening cycles.[422] At some point, a limit will be reached in terms of the model's predictive ability. This depends on the structural diversity of the data set, its representation of chemistry space and that of the molecules it is predicting. There perhaps needs to be some investigation of how many molecules and what level of diversity a model should possess for maximum utility. Molecular descriptor-based models are developing alongside pharmacophore-based models for predicting DDI.[24,97–99] The latter models will have a greater viability within a structural series while the former models are more amenable to rapid screening of diverse chemotypes although there have been some successes in generating models from diverse structures and building pharmacophores with quite general predictivity. Even when there is some complexity in the kinetics or behavior of the enzyme, receptor, channel, or transporter, models built with data from different substrate probes and from in vitro studies may be used in combination to first score new molecules and then to generate some degree of consensus and classification.

Two areas are in urgent need of study. First, understanding how the predictions from multiple models may be combined or related in a logical fashion is important. There may be no single optimal way to combine the data for multiple predictions but as we have previously described there are tools available to do this.[25] How we weight the models may depend on the therapeutic area targeted and our confidence in the biological data and the models selected

(Figure 2). Second, we must find a way to evaluate cutoff criteria for model acceptability. This evaluation will depend to some extent on the biological, ADME/Tox antitarget under study.

The next generation of scientists must be able to communicate not only in the language of experimental biology but also that of computational biology and medicinal chemistry. The ability to do this depends very much on the support of academic institutions that need to introduce all of the available technologies that are now available as well as those that will be developed in the near future. The key skills we envision as being especially important to computational studies in ADME/Tox are:

1. Biological knowledge as applied to computational chemistry.
2. Some basic understanding of computational chemistry and biology software and operating systems.
3. Flexibility in switching between different modeling approaches (such as 3D-QSAR and statistical methods).
4. Awareness of the experimental implications of the ADME/Tox related protein being studied.
5. Understanding of ADME/Tox in vitro and in vivo models.
6. An ability to communicate with scientists in both ADME, drug safety, computational chemistry, discovery chemistry, discovery biology, biostatistics, and information technology groups.
7. An understanding that the quality of data being used is key to optimal model building.

The very existence of the pharmaceutical industry will become even more reliant on the computational approaches that have been developed over the past decade in addition to those that are being developed and applied now. We will rely on computational models to help understand how key proteins that determine ADME/Tox properties work and we will use that knowledge for the purposes of developing drugs with better biopharmaceutical properties.

ACKNOWLEDGMENTS

ABBREVIATIONS

QSAR, Quantitative structure–activity relationship; sEH, cytosolic epoxide hydrolase; CYP, cytochrome P450; CAR, constitutive androstane receptor; PXR, pregnane X receptor; hERG, human ether-a-gogo related gene; P-gp, P-glycoprotein; MAO, monoamine oxidase; FMO, Flavin-containing monooxygenase.

REFERENCES

1. S. Ekins, C. L. Waller, P. W. Swaan, G. Cruciani, S. A. Wrighton, and J. H. Wikel, *J. Pharmacol. Toxicol. Methods*, **44**, 251 (2000). Progress in Predicting Human ADME Parameters in Silico.

2. S. Ekins and J. P. Rose, *J. Mol. Graph.*, **20**, 305 (2002), in Silico ADME/TOX: The State of the Art at the 220th ACS Meeting.

3. M. D. Wessel and S. Mente, *Ann. Rep. Med. Chem.*, **36**, 257 (2001). ADME by Computer.

4. D. Butina, M. D. Segall, and K. Frankcombe, *Drug Disc. Today,* **7**, S83 (2002). Predicting ADME Properties in Silico: Methods and Models.

5. S. Ekins, J. Maenpaa, and S. A. Wrighton *Handbook of Drug Metabolism*; Marcel Dekker, New York, 1999; pp. 363–399. In Vitro Metabolism: Subcellular Fractions.

6. D. R. Nelson, L. Koymans, T. Kamataki, J. J. Stegeman, R. Feyereisen, D. J. Waxman, M. R. Waterman, O. Gotoh, M. J. Coon, R. W. Estabrook, I. C. Gunsalus, and D. W. Nebert, *Pharmacogenetics,* **6**, 1 (1996). P450 Superfamily: Update on New Sequences, Gene Mapping, Accession Numbers and Nomenclature.

7. E. Y. Zhang, M. A. Phelps, C. Cheng, S. Ekins, and P. W. Swaan, *Adv. Drug Del. Rev.,* **54**, 329 (2002). Modeling of Active Transport Systems.

8. M. A. Hediger, M. J. Coady, T. S. Ikeda, and E. M. Wright, *Nature (London)* **330**, 379 (1987). Expression Cloning and cDNA Sequencing of the Na + /Glucose Cotransporter.

9. M. A. Hediger, T. Ikeda, M. Coady, C. B. Gundersen, and E. M. Wright, *Proc. Natl. Acad. Sci. U.S.A.,* **84**, 2634 (1987). Expression of Size-Selected mRNA Encoding the Intestinal Na/Glucose Cotransporter in Xenopus laevis Oocytes.

10. M. H. Saier, Jr., *Int. Rev. Cytol.,* **190**, 61 (1999). Eukaryotic Transmembrane Solute Transport Systems.

11. M. Dean, A. Rzhetsky, and R. Allikmets, *Genome Res,* **11**, 1156 (2001). The Human ATP-Binding Cassette (ABC) Transporter Superfamily.

12. P. W. Swaan, S. Oie, and F. C. Szoka, Jr., *Adv. Drug. Del. Rev.*, **20**, 1 (1996). Carrier-Mediated Oral Drug Delivery—Preface.

13. P. W. Swaan, S. Oie, and F. C. Szoka, Jr., *Adv. Drug Del. Rev.*, **20**, 59, (1996). Use of the Intestinal and Hepatic Bile Acid Transporters for Drug Delivery.

14. P. W. Swaan, K. M. Hillgren, F. C. Szoka, Jr., and S. Oie, *Bioconjug. Chem.*, **8**, 520 (1997). Enhanced Transepithelial Transport of Peptides by Conjugation to Cholic Acid.

15. C. J. Blankley, *Pharm. Pharmacol. Commun.*, **4**, 139 (1998). Measuring Molecular Diversity: Evaluation of Alternative Subsets Selected from Reagent Building Block Libraries for Combinatorial Chemistry.

16. Y. C. Martin, M. G. Bures, and R. D. Brown, *Pharm. Pharmacol. Commun.,* **4**, 147 (1998). Validated Descriptors for Diversity Measurements and Optimization.

17. J. Sadowski, *Pharm. Pharmacol. Commun.,* **4**, 153 (1998). Methods for Selecting Compounds from Molecular Databases.

18. H. Kubinyi, *Pharmazie,* **50**, 647 (1995). Strategies and Recent Technologies in Drug Discovery.

19. H. Kubinyi, *Drug Disc. Develop.*, **1**, 4 (1998). Structure-Based Design of Enzyme Inhibitors and Receptor Ligands.

20. H. Kubinyi, *Drug Disc. Develop.*, **1**, 16 (1998). Combinatorial and Computational Approaches in Structure-Based Drug Design.

21. T. Fujita, *Quant. Struct. Act. Relat.*, **16**, 107 (1997). Recent Success Stories Leading to Commercializable Bioactive Compounds with the Aid of Traditional QSAR Procedures.

22. S. Ekins, B. J. Ring, G. Bravi, J. H. Wikel, and S. A. Wrighton, *Pharmacophore Perception, Development, and use in Drug Design*; IUL, San Diego, 2000, pp. 269–299. Predicting Drug–Drug Interactions in Silico Using Pharmacophores: A Paradigm for the Next Millennium.

23. S. Ekins and S. A. Wrighton, *J. Pharm. Tox. Methods,* **44**, 1 (2001). Application of in Silico Approaches to Predicting Drug–Drug Interactions: A Commentary.

24. S. Ekins, M. de Groot, and J. P. Jones, *Drug Metab. Dispos.,* **29**, 936 (2001). Pharmacophore and Three Dimensional Quantitative Structure Activity Relationship Methods for Modeling Cytochrome P450 Active Sites.

25. S. Ekins, B. Boulanger, P. W. Swaan, and M. A. Z. Hupcey, *J. Comput. Aided. Mol. Des.,* **16**, 381 (2002). Towards a New Age of Virtual ADME/TOX and Multidimensional Drug Discovery.

26. M. D. Barratt, *Environ. Health Perspectives,* **106**, 459 (1998). Integration of QSAR and In Vitro Toxicology.

27. M. D. Barratt and R. A. Rodford, *Curr. Opin. Chem. Biol.,* **5**, 383 (2001). The Computational Prediction of Toxicity.

28. M. T. Cronin, *Pharm. Pharmacol. Commun.,* **4**, 157 (1998). Computer-Aided Prediction of Drug Toxicity in High Throughput Screening.

29. D. E. Johnson, P. E. Blower, Jr., G. J. Myatt, and G. H. I. Wolfgang, *Curr. Opin. Drug Disc. Dev.,* **4** (2001). Chem-Tox Informatics: Data Mining Using a Medicinal Chemistry Block Approach.

30. D. E. Johnson and G. H. I. Wolfgang, *DDT,* **5**, 445 (2000). Predicting Human Safety: Screening and Computational Approaches.

31. C. A. Lipinski, *Curr. Drug Disc.,* **April**, 17 (2001). Avoiding Investment in Doomed Drugs. Is Poor Solubility an Industry Wide Problem?

32. C. A. Lipinski, F. Lombardo, B. W. Dominy, and P. J. Feeney, *Adv. Drug Del. Rev.,* **23**, 3 (1997). Experimental and Computational Approaches to Estimate Solubility and Permeability in Drug Discovery and Development Settings.

33. F. Lombardo, J. F. Blake, and W. J. Curatolo, *J. Med. Chem.,* **39**, 4750 (1996). Computation of Brain–Blood Partitioning of Organic Solutes via Free Energy Calculations.

34. U. Norinder and M. Haeberlein, *Adv. Drug Del. Rev.,* **54**, 291 (2002). Computational Approaches to the Prediction of the Blood–Brain Distribution.

35. U. Norinder, P. Sjoberg, and T. Osterberg, *J. Pharm. Sci.,* **87**, 952 (1998). Theoretical Calculation and Prediction of Brain–Blood Partitioning of Organic Solutes Using MolSurf Parameterization and PLS Statistics.

36. A. George, *Curr. Opinion Drug Disc. Dev.,* **2**, 286 (1999). The Design and Molecular Modeling of CNS Drugs.

37. T. Sanghvi, N. Ni, and S. H. Yalkowsky, *Pharm. Res.,* **18**, 1794 (2001). A Simple Modified Absorption Potential.

38. F. Lombardo, M. Y. Shalaeva, K. A. Tupper, and F. Gao, *J. Med. Chem.,* **44**, 2490 (2001). ElogDoct: A Tool for Lipophilicity Determination in Drug Discovery. 2. Basic and Neutral Compounds.

39. F. Lombardo, M. Y. Shalaeva, K. A. Tupper, F. Gao, and M. H. Abraham, *J. Med. Chem.,* **43**, 2922 (2000). ElogPoct A Tool for Lipophilicity Determination in Drug Discovery.

40. R. Saiakhov, L. R. Stefan, and G. Klopman, *Persp. Drug Disc. Design,* **19**, 133 (2000). Multiple Computer-Automated Structure Evaluation Model of the Plasma Protein Binding Affinity of Diverse Drugs.

41. G. Colmenarejo, A. Alvarez-Pedraglio, and J.-L. Lavandera, *J. Med. Chem.,* **44**, 4370 (2001). Cheminformatic Models to Predict Binding Affinities to Human Serum Albumin.

42. F. Lombardo, R. S. Obach, M. Y. Shalaeva, and F. Gao, *J. Med. Chem.,* **45**, 2867 (2002). Prediction of Volume of Distribution Values in Humans for Neutral and Basic Drugs Using Physicochemical Measurements and Plasma Protein Binding.

43. C. Quinones, J. Caceres., M. Stud, and A. Martinez, *Quant. Struct. Act Relationship,* **19**, 448 (2000). Prediction of Drug Half-Life Values of Antihistamines Based on the CODES/Neural Network Model.

44. S. Ekins and R. S. Obach, *J. Pharmacol. Exp. Thera.,* **295**, 463 (2000). Three Dimensional-Quantitative Structure Activity Relationship. Computational Approaches to Prediction of Human In Vitro Intrinsic Clearance.

45. C. L. Waller, M. V. Evans, and J. D. McKinney, *Drug Metabolism Disposition,* **24**, 203 (1996). Modeling the Cytochrome P450-Mediated Metabolism of Chlorinated Volatile Organic Compounds.

46. W. J. Egan, K. M. J. Merz, and J. J. Baldwin, *J. Med. Chem.,* **43**, 3867 (2000). Prediction of Drug Absorption Using Multivariate Statistics.

47. P. Stenberg, K. Luthman, and P. Artursson, *J. Controlled Release,* **65**, 231 (2000). Virtual Screening of Intestinal Permeability.

48. P. Stenberg, U. Norinder, K. Luthman, and P. Artursson, *J. Med. Chem.,* **44**, 1927 (2001). Experimental and Computational Screening Models for the Prediction of Intestinal Drug Absorption.

49. S. Ekins, G. L. Durst, R. E. Stratford, D. A. Thorner, R. Lewis, R. J. Loncharich, and J. H. Wikel, *J. Chem. Inf. Comput. Sci.,* **41**, 1578 (2001). Three Dimensional Quantitative Structure Permeability Relationship Analysis for a Series of Inhibitors of Rhinovirus Replication.

50. M. D. Wessel, P. C. Jurs, J. W. Tolan, and S. M. Muskal, *J. Chem. Inf. Comput. Sci.,* **38**, 726 (1998). Prediction of Human Intestinal Absorption of Drug Compounds from Molecular Structure.

51. J. P. Jones and K. R. Korzekwa, *Predicting the Rates and Regioselectivity of Reactions Mediated by the P450 Superfamily.*, Academic Press, Inc., New York, 1996, pp. 326–335.

52. J. P. Jones, M. Shou, and K. R. Korzekwa, *Biochemistry,* **34**, 6956 (1995). Stereospecific Activation of the Procarcinogen Benzo[*a*]pyrene: A Probe for the Active Sites of the Cytochrome P450 Superfamily.

53. J. Langowski and A. Long, *Adv. Drug Del. Rev.,* **54**, 407 (2002). Computer Systems for the Prediction of Xenobiotic Metabolism.

54. S. Ekins, R. B. Kim, B. F. Leake, A. H. Dantzig, E. Schuetz, L.-B. Lan, K. Yasuda, R. L. Shepard, M. A. Winter, J. D. Schuetz, J. H. Wikel, and S. A. Wrighton, *Mol. Pharmacol.,* **61**, 974 (2002). Application of Three Dimensional Quantitative Structure–Activity Relationships of P-Glycoprotein Inhibitors and Substrates.

55. S. Ekins, R. B. Kim, B. F. Leake, A. H. Dantzig, E. Schuetz, L.-B. Lan, K. Yasuda, R. L. Shepard, M. A. Winter, J. D. Schuetz, J. H. Wikel, and S. A. Wrighton, *Mol. Pharmacol.,* **61**, 964 (2002). Three Dimensional Quantitative Structure–Activity Relationships of Inhibitors of P-Glycoprotein.

56. T. Osterberg and U. Norinder, *Eur. J. Pharm. Sci.,* **10**, 295 (2000). Theoretical Calculation and Prediction of P-Glycoprotein-Interacting Drugs Using MolSurf Parameterization and PLS Statistics.

57. T. R. Stouch and O. Gudmundsson, *Adv. Drug Del. Rev.,* **54**, 315 (2002). Progress in Understanding the Structure–Activity Relationships of P-Glycoprotein.

58. J. E. Penzotti, M. L. Lamb, E. Evenson, and P. D. J. Grootenhuis, *J. Med. Chem.,* **45,** 1737 (2002). A Computational Ensemble Pharmacophore Model for Identifying Substrates of P-Glycoprotein.

59. N. Greene, *Adv. Drug Del. Rev.,* **54,** 417 (2002). Computer Systems for the Prediction of Toxicity: An Update.

60. O. Llorens, J. J. Perez, and H. O. Villar, *J. Med. Chem.,* **44,** 2793 (2001). Toward the Design of Chemical Libraries for the Mass Screening Biased Against Mutagenic Compounds.

61. S. S. Young, V. K. Gombar, M. R. Emptage, N. F. Cariello, and C. Lambert, *Chemo. Intell. Lab. Sys.,* **60,** 5 (2002). Mixture Deconvolution and Analysis of Ames Mutagenicity Data.

62. A. E. M. F. Soffers, M. G. Boersma, W. H. J. Vaes, J. Vervoort, B. Tyrakowska, J. L. M. Hermens, and I. M. C. M. Rietjens, *Toxicol. in vitro,* **15,** 539 (2001). Computer-Modeling-Based QSARs for Analyzing Experimental Data on Biotransformation and Toxicity.

63. C. A. Lipinski, *J. Pharm. Toxicol. Methods,* **44,** 235 (2000). Drug-Like Properties and the Causes of Poor Solubility and Poor Permeability.

64. D. F. Veber, S. R. Johnson, H.-Y. Cheng, B. R. Smith, K. W. Ward, and K. D. Kopple, *J. Med. Chem.,* **45,** 2615 (2002). Molecular Properties that Influence the Oral Bioavailability of Drug Candidates.

65. V. J. Gillet, P. Willett, and J. Bradshaw, *J. Chem. Inf. Comput. Sci.,* **38,** 165 (1998). Identification of Biological Activity Profiles Using Substructural Analysis and Genetic Algorithms.

66. J. Sadowski and H. Kubinyi, *J. Med. Chem.,* **41,** 3325 (1998). A Scoring Scheme for Discriminating Between Drugs and Nondrugs.

67. T. I. Oprea, A. M. Davis, S. J. Teague, and P. D. Leeson, *J. Chem. Inf. Comput. Sci.,* **41,** 1308 (2001). Is there a Difference between Leads and Drugs? A Historical Perspective.

68. G. W. Bemis and M. A. Murcko, *J. Med. Chem.,* **39,** 2887 (1996). The Properties of Known Drugs. 1. Molecular Frameworks.

69. G. W. Bemis and M. A. Murcko, *J. Med. Chem.,* **42,** 5095 (1999). Properties of Known Drugs. 2. Side Chains.

70. O. Roche, P. Schneider, J. Zuegge, W. Guba, M. Kansy, A. Alanine, K. Bleicher, F. Danel, E.-M. Gutknect, M. Rogers-Evans, W. Neidhart, H. Stalder, M. Dillon, E. Sjogren, N. Fotouhi, P. Gillespie, R. Goodnow, W. Harris, P. Jones, M. Taniguchi, S. Tsujii, W. von der Saal, G. Zimmermann, and G. Schneider, *J. Med. Chem.,* **45,** 137 (2002). Development of A Virtual Screening Method for Identification of "Frequent Hitters" in Compound Libraries.

71. S. L. McGovern, E. Caselli, N. Grigorieff, and B. K. Shoichet, *J. Med. Chem.,* **45,** 1712 (2002). A Common Mechanism Underlying Promiscuous Inhibitors from Virtual and High-Throughput Screening.

72. M. F. M. Engels and P. Venkatarangan, *Curr. Opin. Drug Disc. Dev.,* **4,** 275 (2001). Smart Screening: Approaches to Efficient HTS.

73. D. K. Agrafiotis and W. Cedeno, *J. Med. Chem.,* **45,** 1098 (2002). Feature Selection for Structure-Activity Correlation Using Binary Particle Swarms.

74. V. J. Gillet, W. Khatib, P. Willett, P. J. Fleming, and D. V. S. Green, *J. Chem. Inf. Comput. Sci.,* **42,** 375 (2002). Combinatorial Library Design Using a Multiobjective Genetic Algorithm.

75. W. P. Walters, M. T. Stahl, and M. A. Murcko, *Drug Disc. Today,* **3,** 160 (1998). Virtual Screening-an Overview.

76. A. R. Leach and M. M. Hann, *Drug Disc. Today,* **5,** 326 (2000). The in Silico World of Virtual Libraries.

77. H. Kubinyi, *Drug Discovery Today,* **2,** 457 (1997). QSAR and 3D QSAR in Drug Design. Part1: Methodology.

78. H. Kubinyi, *Drug Discovery Today,* **2,** 538–546 (1997). QSAR and 3D QSAR in Drug Design. Part 2: Applications and Problems.

79. T. I. Oprea and C. L. Waller in *Reviews in Computational Chemistry*; K. B. Lipkowitz, and D. B. Boyd, Eds.; Wiley-VCH, Wiley, New York, 1997, pp. 127–182. Theoretical and Practical Aspects of Three-Dimensional Quantitative Structure—Activity Relationships.

80. C. Hansch, E. J. Lien, and F. Helmer, *Arch. BioChem. Biophys.*, **128**, 319 (1968). Structure–Activity Correlations in the Metabolism of Drugs.

81. C. Hansch, *Drug Metab. Rev.*, **1**, 1 (1972). Quantitative Relationships between Lipophilic Character and Drug Metabolism.

82. C. Hansch, *Drug Metab. Rev.*, **15**, 1279 (1984). The QSAR Paradigm in the Design of Less Toxic Molecules.

83. C. Hansch, D. Hoekman, and H. Gao, *Chem. Rev.*, **96**, 1045 (1996). Comparative QSAR: Toward a Deeper Understanding of Chemicobiological Interactions.

84. C. Hansch and L. Zhang, *Drug Metab. Rev.*, **25**, 1 (1993). Quantitative Structure–Activity Relationships of Cytochrome P-450.

85. D. F. V. Lewis, *Toxicology*, **144**, 197 (2000). Structural Characteristics of Human P450s Involved in Drug Metabolism: QSARs and Lipophilicity Profiles.

86. D. F. V. Lewis, *Biochem. Pharmacol.*, **60**, 293 (2000). On the Recognition of Mammalian Microsomal Cytochrome P450 Substrates and Their Characteristics.

87. D. F. V. Lewis, P. J. Eddershaw, M. Dickins, M. H. Tarbit, and P. S. Goldfarb, *Chem. Bio. Interact.*, **115**, 175 (1998). Structural Determinants of Cytochrome P450 Substrate Specificity, Binding Affinity and Catalytic Rate.

88. D. F. V. Lewis, *Drug Metab. Rev.*, **29**, 589 (1997). Quantitative Structure Activity Relationships in Substrates, Inducers, and Inhibitors of Cytochrome P4501 (CYP1).

89. D. F. V. Lewis, P. J. Eddershaw, M. Dickins, M. H. Tarbit, and P. S. Goldfarb, *Chem. Biol. Interact.*, **117**, 187 (1999). Erratum to Structural Determinants of Cytochrome P450 Substrate Specificity, Binding Affinity and Catalytic Rate.

90. D. F. V. Lewis, C. Ioannides, and D. V. Parke, *Chem. Biol. Interact.*, **64**, 39 (1987). Structural Requirements for Substrates of Cytochromes P-450 and P-448.

91. D. F. V. Lewis, C. Ioannides, and D. V. Parke, *Biochem. Pharmacol.*, **35**, 2179 (1986). Molecular Dimensions of the Substrate Binding Site of Cytochrome P-448.

92. D. F. V. Lewis, C. Ioannides, and D. V. Parke, *Biochem. Pharmacol.*, **50**, 619 (1995). A Quantitative Structure–Activity Relationship Study on a Series of 10 para-Substituted Toluenes Binding to Cytochrome P4502B4 (CYP2B4), and Their Hydroxylation Rates.

93. D. F. V. Lewis, B. G. Lake, C. Ioannides, and D. V. Parke, *Xenobiotica*, **24**, 829 (1994). Inhibition of Rat Hepatic Aryl Hydrocarbon Hydroxylase Activity by a Series of 7-Hydroxycoumarins: QSAR Studies.

94. G. Bravi, E. Gancia, P. Mascani, M. Pegna, R. Todeschini, and A. Zaliani, *J. Comp.-Aided Mol. Des.*, **11**, 79 (1997). MS-WHIM, New 3D Theoretical Descriptors Derived from Molecular Surface Properties: A Comparative 3D QSAR Study in a Series of Steroids.

95. G. Bravi and J. H. Wikel, *Quant. Struct. Act. Rel.*, **19**, 29 (2000). Application of MS-WHIM Descriptors: 1. Introduction of New Molecular Surface Properties and 2. Prediction of Binding Affinity Data.

96. G. Bravi and J. H. Wikel, *Quant. Struct. Act. Rel.*, **19**, 39 (2000). Application of MS-WHIM Descriptors: 3. Prediction of Molecular Properties.

97. S. Ekins, G. Bravi, S. Binkley, J. S. Gillespie, B. J. Ring, J. H. Wikel, and S. A. Wrighton, *J. Pharmacol. Exper. Therap.*, **290**, 429 (1999). Three Dimensional-Quantitative Structure Activity Relationship (3D-QSAR) Analyses of Inhibitors for CYP3A4.

98. S. Ekins, G. Bravi, S. Binkley, J. S. Gillespie, B. J. Ring, J. H. Wikel, and S. A. Wrighton, *Pharmacogenetics*, **9**, 477 (1999). Three and Four Dimensional-Quantitative Structure Activity Relationship (3D / 4D-QSAR) Analyses of CYP2D6 Inhibitors.

99. S. Ekins, G. Bravi, S. Binkley, J. S. Gillespie, B. J. Ring, J. H. Wikel, and S. A. Wrighton, *Drug. Metab. Disp.*, **28**, 994 (2000). Three and Four Dimensional-Quantitative Structure Activity Relationship (3D/4D-QSAR) Analyses of CYP2C9 Inhibitors.

100. S. Ekins, G. Bravi, B. J. Ring, T. A. Gillespie, J. S. Gillespie, M. VandenBranden, S. A. Wrighton, and J. H. Wikel, *J. Pharmacol. Exper. Therap.*, **288**, 21 (1999). Three Dimensional-Quantitative Structure Activity Relationship (3D-QSAR) Analyses of Substrates for CYP2B6.

101. O. F. Guner, *Pharmacophore, Perception, Development, and Use in Drug Design*; University International Line, San Diego, 2000.

102. Y. Kurogi and O. F. Guner, *Curr. Med. Chem.*, **8**, 1035 (2001). Pharmacophore Modeling and Three-Dimensional Database Searching for Drug Design Using Catalyst.

103. O. F. Guner, *Curr. Topics Med. Chem.*, **2**, 1269 (2002). History and Evolution of the Pharmacophore Concept in Computer-Aided Drug Design.

104. A. Smellie, S. L. Teig, and P. Towbin, *J. Comput. Chem.*, **16**, 171 (1995). Poling: Promoting Conformational Coverage.

105. H. Li, J. Sutter and R. Hoffman, *Pharmacophore Perception, Development, and Use in Drug Design*; IUL: San Diego, 2000; pp. 173–189. HypoGen: An Automated System for Generating 3D Predictive Pharmacophore Models.

106. O. O. Clement and A. T. Mehl, *Pharmacophore Perception, Development, and Use in Drug Design*, IUL, San Diego, 2000, pp. 69–84. HipHop: Pharmacophore Based on Multiple Common-Feature Alignments.

107. D. Barnum, J. Greene, A. Smellie, and P. Sprague, *J. Chem. Inf. Comput. Sci.*, **36**, 563 (1996). Identification of Common Functional Configurations Among Molecules.

108. Y. C. Martin, M. G. Bures., E. A. Danaher, J. DeLazzer, I. Lico, and P. A. Pavlik, *J. Comput. Aided Mol. Des.*, **7**, 83 (1993). A Fast New Approach to Pharmacophore Mapping and Its Application to Dopaminergic and Benzodiazepine Agonists.

109. P. W. Swaan, F. C. Szoka, Jr., and S. Oie, *J. Comput. Aided Mol. Des.*, **11**, 581 (1997). Molecular Modeling of the Intestinal Bile Acid Carrier: A Comparative Molecular Field Analysis Study.

110. J. P. Horwitz, I. Massova, T. E. Wiese, B. H. Besler, and T. H. Corbett, *J. Med. Chem.*, **37**, 781 (1994). Comparative Molecular Field Analysis of the Antitumor Activity of 9H-Thioxanthen-9-one Derivatives Against Pancreatic Ductal Carcinoma 03.

111. R. T. Kroemer, E. Koutsilieri, P. Hecht, K. R. Liedl, P. Riederer, and J. Kornhuber, *J. Med. Chem.*, **41**, 393 (1998). Quantitative Analysis of the Structural Requirements for Blockade of the N-Methyl-D-aspartate Receptor at the Phencyclidine Binding Site.

112. W. Schaal, A. Karlsson, G. Ahlsen, J. Lindberg, H. O. Andersson, U. H. Danielson, B. Classon, T. Unge, B. Samuelsson, J. Hulten, A. Hallberg, and A. Karlen, *J. Med. Chem.*, **44**, 155 (2001). Synthesis and Comparative Molecular Field Analysis (CoMFA) of Symmetric and Nonsymmetric Cyclic Sulfamide HIV-1 Protease Inhibitors.

113. R. S. Bohacek and C. McMartin, *J. Med. Chem.*, **35**, 1671 (1992). Definition and Display of Steric, Hydrophobic, and Hydrogen-Bonding Properties of Ligand-Binding Sites in Proteins Using Lee and Richards Accessible Surface: Validation of a High-Resolution Graphical Tool for Drug Design.

114. G. Klebe, U. Abraham, and T. Mietzner, *J. Med. Chem.*, **37**, 4130 (1994). Molecular Similarity Indices in a Comparative Analysis (CoMSIA) of Drug Molecules to Correlate and Predict Their Biological Activity.

115. V. N. Viswanadhan, A. K. Ghose, G. R. Revankar, and R. K. Robins, *J. Chem. Inf. Comput. Sci.*, **29**, 163 (1989). Atomic and Physicochemical Parameters for Three-dimensional Structure-Directed Quantitative Structure–Activity Relationships. 4. Additional Parameters for Hydrophobic and Dispersive Interactions and Their Application for an Automated Superposition of Certain Naturally Occurring Antibiotics.

116. G. Cruciani and K. A. Watson, *J. Med. Chem.*, **37**, 2589 (1994). Comparative Molecular Field Analysis Using GRID Force-Field and GOLPE Variable Selection Methods in a Study of Inhibitors of Glycogen Phosphorylase b.

117. P. J. Goodford, *J. Med. Chem.*, **28**, 849 (1985). Computational Procedure for Determining Energetically Favourable Binding Sites on Biologically Important Macromolecules.

118. M. Pastor, G. Cruciani, and S. Clementi, *J. Med. Chem.,* **40**, 1455 (1997). Smart Region Definition: A New Way to Improve the Predictive Ability and Interpretability of Three-Dimensional Quantitative Structure Activity Relationships.

119. M. Pastor, G. Cruciani, I. McLay, S. Pickett, and S. Clementi, *J. Med. Chem.,* **43**, 3233 (2000). GRid-INdependent Descriptors (GRIND): A Novel Class of Alignment-Independent Three-Dimensional Molecular Descriptors.

120. K. R. Korzekwa and J. P. Jones, *Pharmacogenetics,* **3**, 1 (1993). Predicting the Cytochrome P450 Mediated Metabolism of Xenobiotics.

121. S. B. Kirton, C. A. Baxter, and M. J. Sutcliffe, *Adv. Drug Del. Rev.,* **54**, 385 (2002). Comparative Modelling of the Cytochromes P450.

122. G. D. Szklarz and J. R. Halpert, *Drug Metab. Dispos.,* **26**, 1179 (1998). Molecular Basis of P450 Inhibition and Activation Implications for Drug Development and Drug Therapy.

123. G. D. Szklarz and J. R. Halpert, *Life Sci.,* **61**, 2507 (1997). Use of Homology Modeling in Conjunction with Site-Directed Mutagenesis For Analysis of Structure–Function Relationships of Mammalian Cytochromes P450.

124. N. Vaidehi, W. B. Floriano, R. Trabanimo, S. E. Hall, P. Freddolino, E. J. Choi, G. Zamanakos, and W. A. I. Goddard, *Proc. Natl. Acad. Sci. U.S.A.* **99**, 12622 (2002). Prediction of Structure and Function of G Protein-Coupled Receptors.

125. G. K. Grimble, *Annu. Rev. Nutr.,* **14**, 419 (1994). The Significance of Peptides in Clinical Nutrition.

126. G. K. Grimble and D. B. A. Silk, *Nutr. Res. Rev.,* **2**, 87 (1989). Peptides in Human Nutrition.

127. S. A. Adibi, *Metabolism,* **36**, 1001 (1987). Experimental Basis for Use of Peptides as Substrates for Parenteral Nutrition: A Review.

128. P. Furst, S. Albers, and P. Stehle, *Proc. Nutr. Soc.,* **49**, 343 (1990). Dipeptides in Clinical Nutrition.

129. D. M. Mathews and S. A. Adibi, *Gastroenterology,* **71**, 151 (1976). Peptide Absorption.

130. N. J. Snyder, L. B. Tabas, D. M. Berry, D. C. Duckworth, D. O. Spry, and A. H. Dantzig, *Antimicrobial Agents Chemother,* **41**, 1649 (1997). Structure–Activity Relationship of Carbacephalosporins and Cephalosporins: Antibacterial Activity and Interaction with the Intestinal Proton-Dependent Dipeptide Transport Carrier of Caco-2 Cells.

131. H. Jiang, L. B. Tabas, S. Ekins, and A. H. Dantzig, *submitted for publication,* (2004). Transport of the β-Lactam Antibiotics, *para*-Hydroxy-Loracarbef and Cephalexin, by the Human Intestinal Peptide Transporter, hPEPT1.

132. V. A. Moore, W. J. Irwin, P. Timmins, P. A. Lambert, S. Chong, S. A. Dando, and R. A. Morrison, *Int. J. Pharm.,* **210**, 29 (2000). A Rapid Screening System to Determine Drug Affinities for the Intestinal Dipeptide Transporter 2: Affinities of ACE Inhibitors.

133. F. H. Leibach and V. Ganapathy, *Annu. Rev. Nutr.,* **16**, 99 (1996). Peptide Transporters in the Intestine and the Kidney.

134. H. K. Han, J. K. Rhie, D. M. Oh, G. Saito, C. P. Hsu, B. H. Stewart, and G. L. Amidon, *J. Pharm. Sci.,* **88**, 347 (1999). CHO/hPEPT1 Cells Overexpressing the Human Peptide Transporter (hPEPT1) as an Alternative In Vitro Model for Peptidomimetic Drugs.

135. K. M. Covitz, G. L. Amidon, and W. Sadee, *Pharm. Res.,* **13**, 1631 (1996). Human Dipeptide Transporter, hPEPT1, Stably Transfected Into Chinese Hamster Ovary Cells.

136. J. S. Kim, R. L. Oberle, D. A. Krummel, J. B. Dressman, and D. Fleisher, *J. Pharm. Sci.,* **83**, 1350 (1994). Absorption of ACE Inhibitors from Small Intestine and Colon.

137. J. P. Bai and G. L. Amidon, *Pharm. Res.,* **9**, 969 (1992). Structural Specificity of Mucosal-Cell Transport and Metabolism of Peptide Drugs: Implication for Oral Peptide Drug Delivery.

138. M. Hu, P. Subramanian, H. I. Mosberg, and G. L. Amidon, *Pharm. Res.,* **6**, 66 (1989). Use of the Peptide Carrier System to Improve the Intestinal Absorption of L-Alpha-Methyldopa: Carrier Kinetics, Intestinal Permeabilities, and In Vitro Hydrolysis of Dipeptidyl Derivatives of L-Alpha-Methyldopa.

139. D. M. Oh, H. K. Han, and G. L. Amidon, *Pharm. Biotechnol.*, **12**, 59 (1999). Drug Transport and Targeting Intestinal Transport.

140. M. Boll, D. Markovich, W. M. Weber, H. Korte, H. Daniel, and H. Murer, *Pflugers Arch. - Eur. J. Physiol.*, **429**, 146 (1994). Expression Cloning of a cDNA from Rabbit Small Intestine Related to Proton-Coupled Transport of Peptides, beta-Lactam Antibiotics and ACE-Inhibitors.

141. M. E. Ganapathy, M. Brandsch, P. D. Prasad, V. Ganapathy, and F. H. Leibach, *J. Biol. Chem.*, **270**, 25672 (1995). Differential Recognition of beta-Lactam Antibiotics by Intestinal and Renal Peptide Transporters, PEPT 1 and PEPT 2.

142. M. E. Ganapathy, W. Huang, H. Wang, V. Ganapathy, and F. H. Leibach, *Biochem. Biophys. Res. Commun.*, **246**, 470 (1998). Valacyclovir: A Substrate for the Intestinal and Renal Peptide Transporters PEPT1 and PEPT2.

143. H. Ogihara, T. Suzuki, Y. Nagamachi, K. Inui, and K. Takata, *HistoChem. J.,* **31**, 169 (1999). Peptide Transporter in the Rat Small Intestine: Ultrastructural Localization and the Effect of Starvation and Administration of Amino Acids.

144. H. Shen, D. E. Smith, T. Yang, Y. G. Huang, J. B. Schnermann, and F. C. Brosius, 3rd, *Am. J. Physiol.*, **276**, F658 (1999). Localization of PEPT1 and PEPT2 Proton-Coupled Oligopeptide Transporter mRNA and Protein in Rat Kidney.

145. P. W. Swaan and J. J. Tukker, *Pharm. Weekbl. Sci. Ed.,* **14M**, 4 (1992). Binding Site Mapping of the Intestinal Peptide Carrier.

146. P. W. Swaan and J. J. Tukker, *Pharm. Weekbl. Sci. Ed.,* **14F**, 62, (1992). Essential Molecular Requirements for Carrier-Mediated Peptide Transport.

147. J. Li and I. J. Hidalgo, *J. Drug Target,* **4**, 9 (1996). Molecular Modeling Study of Structural Requirements for the Oligopeptide Transporter.

148. P. W. Swaan and J. J. Tukker, *J. Pharm. Sci.,* **86**, 596 (1997). Molecular Determinants of Recognition for the Intestinal Peptide Carrier.

149. P. W. Swaan, B. C. Koops, E. E. Moret, and J. J. Tukker, *Receptors and Channels,* **6**, 189 (1998). Mapping the Binding Site of the Small Intestinal Peptide Carrier (PepT1) Using Comparative Molecular Field Analysis.

150. F. Doring, J. Will, S. Amasheh, W. Clauss, H. Ahlbrecht, and H. Daniel, *J. Biol. Chem.,* **273**, 23211 (1998). Minimal Molecular Determinants of Substrates for Recognition by the Intestinal Peptide Transporter.

151. H. Han, R. L. de Vrueh, J. K. Rhie, K. M. Covitz, P. L. Smith, C. P. Lee, D. M. Oh, W. Sadee, and G. L. Amidon, *Pharm. Res.,* **15**, 1154 (1998). 5'-Amino Acid Esters of Antiviral Nucleosides, Acyclovir, and AZT Are Absorbed by the Intestinal PEPT1 Peptide Transporter.

152. P. V. Balimane, I. Tamai, A. Guo, T. Nakanishi, H. Kitada, F. H. Leibach, A. Tsuji, and P. J. Sinko, *Biochem. Biophys. Res. Commun.,* **250**, 246 (1998). Direct Evidence for Peptide Transporter (PepT1)-Mediated Uptake of a Nonpeptide Prodrug, Valacyclovir.

153. P. D. Bailey, C. A. R. Boyd, J. R. Bronk, I. D. Collier, D. Meredith, K. M. Morgan, and C. S. Temple, *Angew. Chem. Int. Ed.,* **39**, 506 (2000). How to Make Drugs Orally Active: A Substrate Template for Peptide Transporter PepT1.

154. B. Bretschneider, M. Brandsch, and R. Neubert, *Pharm. Res.,* **16**, 55 (1999). Intestinal Transport of β-Lactam Antibiotics: Analysis of the Affinity at the H+/Peptide Symporter (PEPT1), the Uptake Into caco-2 Cell Monolayers and the Transepithelial Flux.

155. H. Buchwald, D. K. Stoller, C. T. Campos, J. P. Matts, and R. L. Varco, *Ann. Surg.,* **212**, 318 Discussion 329 (1990). Partial Ileal Bypass for Hypercholesterolemia. 20- to 26-Year Follow-up of the First 57 Consecutive Cases.

156. M. Ast and W. H. Frishman, *J. Clin. Pharmacol.,* **30**, 99 (1990). Bile Acid Sequestrants.

157. K. Takashima, T. Kohno, T. Mori, A. Ohtani, K. Hirakoso, and S. Takeyama, *Atherosclerosis,* **107**, 247 (1994). The Hypocholesterolemic Action of TA-7552 and Its Effects on Cholesterol Metabolism in the Rat.

158. G. Wess, W. Kramer, W. Bartmann, A. Enhsen, H. Glombik, S. Müllner, K. Bock, A. Dries, H. Kleine, and W. Schmitt, *Tetrahedron Lett.,* **33**, 195 (1992). Modified Bile Acids: Preparation

of 7α,12α-Dihydroxy-3β- and 7α,12α-Dihydroxy-3α-(2-hydroxyethoxy)-5β-cholanic Acid and Their Biological Activity.

159. L. Lack, J. T. Walker, and G. D. Singletary, *Am. J. Physiol.,* **219**, 487 (1970). Ileal Bile Salt Transport: In Vivo Studies of Effect of Substrate Ionization on Activity.

160. K. H. Baringhaus, H. Matter, S. Stengelin, and W. Kramer, *J. Lipid Res.,* **40**, 2158 (1999). Substrate Specificity of the Ileal and the Hepatic Na(+)/Bile Acid Cotransporters of the Rabbit. II. A Reliable 3D QSAR Pharmacophore model for the Ileal Na(+)/Bile Acid Cotransporter.

161. W. Kramer, S. Stengelin, K. H. Baringhaus, A. Enhsen, H. Heuer, W. Becker, D. Corsiero, F. Girbig, R. Noll, and C. Weyland, *J. Lipid Res.,* **40**, 1604 (1999). Substrate Specificity of the Ileal and the Hepatic Na(+)/Bile Acid Cotransporters of the Rabbit. I. Transport Studies with Membrane Vesicles and Cell Lines Expressing the Cloned Transporters.

162. E. H. Zhang, M. A. Phelps, F. Helsper, and P. W. Swaan, *submitted for publication* (2004). Membrane Topology and Structure of the Apical Sodium-Dependent Bile Acid Transporter (ASBT).

163. G. Wess, W. Kramer, A. Enhsen, H. Glombik, K. H. Baringhaus, G. Boger, M. Urmann, K. Bock, H. Kleine, G. Neckermann, A. Hoffmann, C. Pittius, E. Falk, H. W. Fehlhaber, H. Kogler, and M. Friedrich, *J. Med. Chem.,* **37**, 873 (1994). Specific Inhibitors Of Ileal Bile Acid Transport.

164. C. Wandell, R. B. Kim, S. Kajiji, F. P. Guengerich, G. R. Wilkinson, and A. J. J. Wood, *Cancer Res.,* **59**, 3944 (1999). P-Glycoprotein and Cytochrome P-450 3A Inhibition: Dissociation of Inhibitory Potencies.

165. S. Hoffmeyer, O. Burk, O. von Richter, H. P. Arnold, J. Brockmoller, A. Johne, I. Cascorbi, T. Gerloff, I. Roots, M. Eichelbaum, and U. Brinkmann, *Proc. Natl. Acad. Sci. U.S.A.,* **97**, 3473 (2000). Functional Polymorphisms of the Human Multidrug-Resistance Gene: Multiple Sequence Variations and Correlation of One Allele with P-Glycoprotein Expression and Activity In Vivo.

166. M. Demeule, A. Laplante, G. F. Murphy, R. M. Wenger, and R. Beliveau, *Biochemistry,* **37**, 18110 (1998). Identification of the Cyclosporin-Binding Site in P-Glycoprotein.

167. R. L. Shepard, M. A. Winter, S. C. Hsaio, H. L. Pearce, W. T. Beck, and A. H. Dantzig, *Biochem. Pharmacol.* **56**, 719 (1998). Effect of Modulators on the ATPase Activity and Vanadate Nucleotide Trapping of Human P-Glycoprotein.

168. A. H. Dantzig, R. L. Shephard, J. Cao, K. L. Law, W. J. Ehlhardt, T. M. Baughman, T. F. Bumol, and J. J. Starling, *Cancer Res.,* **56**, 4171 (1996). Reversal of P-Glycoprotein-Mediated Multidrug Resistance by a Potent Cyclopropyldibenzosuberane Modulator, LY335979.

169. H. L. Pearce, A. R. Safa, N. J. Bach, M. A. Winter, M. C. Cirtain, and W. T. Beck, *Proc. Natl. Acad. Sci. U.S.A.,* **86**, 5182 (1989). Essential Features of the P-Glycoprotein Pharmacophore as Defined by a Series of Reserpine Analogues that Modulate Multidrug Resistance.

170. H. L. Pearce, M. A. Winter, and W. T. Beck, *Adv. Enzyme. Regul.,* **30**, 357 (1990). Structural Characteristics of Compounds that Modulate P-Glycoprotein-Associated Multidrug Resistance.

171. A. Ramu and N. Ramu, *Cancer Chemother. Pharmacol.,* **30**, 165 (1992). Reversal of Multidrug Resistance by Phenothiazines and Structurally Related Compounds.

172. M. J. Borgnia, G. D. Eytan, and Y. G. Assaraf, *J. Biol. Chem.,* **271**, 3163 (1996). Competition of Hydrophobic Peptides, Cytotoxic Drugs, and Chemosensitizers on a Common P-Glyco-protein Pharmacophore as Revealed by Its ATPase Activity.

173. P. Chiba, G. Ecker, D. Schmid, J. Drach, B. Tell, S. Goldenberg, and V. Gekeler, *Mol. Pharmacol.,* **49**, 1122 (1996). Structural Requirements for Activty of Propafenone-Type Modulators in P-Glycoprotein-Mediated Multidrug Resistance.

174. G. Klopman, M. S. Leming, and A. Ramu, *J. Pharmacol. Exp. Ther.,* **52**, 323 (1997). Quantitative Structure-Activity Relationship of Multidrug Resisistance Reversal Agents.

175. G. A. Bakken and P. C. Jurs, *J. Med. Chem.,* **43**, 4534 (2000). Classification of Multidrug-Resistance Reversal Agents Using Structure-Based Descriptors and Linear Discriminant Analysis.

176. I. K. Pajeva and M. Wiese, *QSAR,* **16**, 1 (1997). QSAR and Molecular Modelling of Catamphiphilic Drugs Able to Modulate Multidrug Resistance in Tumors.

177. M. Salem, E. Richter, M. Hitzler, P. Chiba, and G. Ecker, *Sci. Pharm.,* **66**, 147 (1998). Studies on Propafenone-Type Modulators of Multidrug Resistance VIII: Synthesis and Pharmacological Activity of Indanon Analogues.

178. C. Tmej, P. Chiba, M. Huber, E. Richter, M. Hitzler, K.-J. Schaper, and G. Ecker, *Arch. Pharm. Med. Chem.,* **331**, 233 (1998). A Combined Hansch/free Wilson Approach as Predictive Tool in QSAR Studies on Propafenone-Type Modulators of Multidrug Resistance.

179. I. Pajeva and M. Wiese, *J. Med. Chem.,* **41**, 1815 (1998). Molecular Modeling of Phenothiazines and Related Drugs as Multidrug Resistance Modifiers: A Comparative Molecular Field Analysis Study.

180. I. K. Pajeva and M. Wiese, *QSAR,* **17**, 301 (1998). A Comparative Molecular Field Analysis of Propafenone-Type Modulators of Cancer Multidrug Resistance.

181. D. Schmid, G. Ecker, S. Kopp, M. Hitzler, and P. Chiba, *Biochem. Pharmacol.,* **58**, 1447 (1999). Structure–Activity Relationship Studies of Propafenone Analogues Based on P-Glycoprotein ATPase Activity Measurements.

182. G. Ecker, M. Huber, D. Schmid, and P. Chiba, *Mol. Pharmacol.,* **56** (1999). The Importance of a Nitrogen Atom in Modulators of Multidrug Resistance.

183. A. Seelig, *Int. J. Clin. Pharmacol. Ther.,* **36**, 50 (1998). How Does P-Glycoprotein Recognize Its Substrates?

184. S. Neuhoff, P. Langguth, C. Dressler, T. B. Andersson, C. G. Regardh, and H. Spahn-Langguth, *Int. J. Clin. Pharmacol. Ther.,* **38**, 168 (2000). Affinities at the Verapamil Binding Site of MDR1-Encoded P-Glycoprotein: Drugs and Analogues, Stereoisomers and Metabolites.

185. K. H. Kim, *Bioorg. Med. Chem.,* **9**, 1517 (2001). 3D-QSAR Analysis of 2,4,5- and 2,3,4,5-Substituted Imidazoles as Potent and Non Toxic Modulators of P-Glycoprotein Mediated MDR.

186. V. J. Wacher, C. Y. Wu, and L. Z. Benet, *Molecular Carcinogenesis,* **13**, 129 (1995). Overlapping Substrate Specificities and Tissue Distribution of Cytochrome P450 3A and P-Glycoprotein: Implications for Drug Delivery and Activity in Cancer Chemotherapy.

187. E. G. Schuetz, W. T. Beck, and J. D. Schuetz, *Mol. Pharmacol.,* **49**, 311 (1996). Modulators and Substrates of P-Glycoprotein and Cytochrome P4503A Coordinately Up-Regulate These Proteins in Human Colon Carcinoma Cells.

188. R. B. Kim, C. Wandel, B. Leake, M. Cvetkovic, M. F. Fromm, P. J. Dempsey, M. M. Roden, F. Belas, A. K. Chaudhary, D. M. Roden, A. J. J. Wood, and G. R. Wilkinson, *Pharm. Res.,* **16**, 408 (1999). Interrelationship between Substrates and Inhibitiors of Human CYP3A and P-Glycoprotein.

189. S. Ekins, B. J. Ring, S. N. Binkley, S. D. Hall, and S. A. Wrighton, *Inter. J. Clin. Pharmacol. Therap.,* **36**, 642 (1998). Autoactivation and Activation of Cytochrome P450s.

190. K. R. Korzekwa, N. Krishnamachary, M. Shou, A. Ogai, R. A. Parise, A. E. Rettie, and F. J. Gonzalez, *Biochemistry,* **37**, 4137 (1998). Evaluation of Atypical Cytochrome P450 Kinetics with Two-Substrate-Models: Evidence that Multiple Substrates Can Simultaneously Bind to Cytochrome P450 Active Sites.

191. J. B. Houston and K. E. Kenworthy, *Drug Metab. Dispos.,* **28**, 246 (2000). In Vitro-In Vivo Scaling of CYP Kinetic Data not Consistent with the Classical Michaelis-Menten Model.

192. L. M. Greenberger, C.-P. H. Yang, E. Gindin, and S. B. Horwitz, *J. Biol. Chem.,* **265**, 4394 (1990). Photoaffinity Probes for the α_1-Adrenergic Receptor and the Calcium Channel Bind to a Common Domain in P-Glycoprotein.

193. S. Ayesh, Y.-M. Shao, and W. D. Stein, *Bioch. Biophys. Acta,* **1316**, 8 (1996). Co-operative, Competitive and Non-Competitive Interactions between Modulators of P-Glycoprotein.

194. A. B. Shapiro and V. Ling, *Eur. J. Biochem.,* **250**, 130 (1997). Positively Cooperative Sites for Drug Transport by P-Glycoprotein with Distinct Drug Specificities.

195. S. Scala, N. Akhmed, U. S. Rao, K. Paull, L.-B. Lan, B. Dickstein, J.-S. Lee, G. H. Elgemeie, W. D. Stein, and S. E. Bates, *Mol. Pharmacol.,* **51**, 1024 (1997). P-Glycoprotein Substrates and Antagonists Cluster into two Distinct Groups.

196. S. Dey, M. Ramachandra, I. Pastan, M. M. Gottesman, and S. Ambudkar, *Proc. Natl. Acad. Sci. U.S.A.,* **94**, 10594 (1997). Evidence for Two Nonidentical Drug-Interaction Sites in the Human P-Glycoprotein.

197. A. B. Shapiro, K. Fox, P. Lam, and V. Ling, *Eur. J. Biochem.,* **259**, 841 (1999). Stimulation of P-Glycoprotein-Mediated Drug Transport by Prazosin and Progersterone. Evidence for a Third Site.

198. E. Wang, C. N. Casciano, R. P. Clement, and W. W. Johnson, *Biochim. Biophys. Acta,* **1481**, 63 (2000). Two Transport Binding Sites of P-Glycoprotein are Unequal Yet Contingent: Initial Rate Kinetic Analysis by ATP Hydrolysis Demonstrates Intersite Dependence.

199. L. Lu, F. Leonessa, R. Clarke, and I. W. Wainer, *Mol. Pharmacol.,* **59**, 62 (2001). Competitive and Allosteric Interactions in Ligand Binding to P-Glycoprotein as Observed on an Immobilized P-Glycoprotein Liquid Chromatographic Stationary Phase.

200. C. Pauli-Magnus, O. Von Richter, O. Burk, A. Ziegler, T. Mettang, M. Eichelbaum, and M. F. Fromm, *J. Pharmacol. Exp. Ther.,* **293**, 376 (2000). Characterization of the Major Metabolites of Verapamil as Substrates and Inhibitors of P-Glycoprotein.

201. I. K. Pajeva and M. Wiese, *J. Med. Chem.,* **45**, 5671 (2002). Pharmacophore Model of Drugs Involved in P-Glycoprotein Multidrug Resistance: Explanation of Structural Variety (Hypothesis).

202. A. Garrigues, N. Loiseau, M. Delaforge, J. Ferte, M. Garrigos, F. Andre, and S. Orlowski, *Mol. Pharmacol.,* **62**, 1288 (2002). Characterization of Two Pharmacophores on the Multidrug Transporter P-Glycoprotein.

203. K. Yasuda, L.-B. Lan, D. Sanglard, K. Furoya, J. D. Schuetz, and E. G. Schuetz, *J. Pharm. Exp. Thera.,* **303**, 323 (2002). Interaction of Cytochrome P450 3A Inhibitors with P-Glycoprotein.

204. S. Ekins, G. Bravi, J. H. Wikel, and S. A. Wrighton, *J. Pharmacol. Exp. Ther.,* **291**, 424 (1999). Three Dimensional Quantitative Structure Activty Relationship (3D-QSAR) Analysis of CYP3A4 Substrates.

205. J. Song, O. Kwon, S. Chen, R. Daruwala, P. Eck, J. B. Park, and M. Levine, *J. Biol. Chem.,* **277**, 15252 (2002). Flavonoid Inhibition of Sodium-Dependent Vitamin C Transporter 1 (SVCT1) and Glucose Transporter Isoform 2 (GLUT2), Intestinal Transporters for Vitamin C and Glucose.

206. S. Manfredi, B. Pavan, S. Vertuani, M. Scaglianti, D. Compagnone, C. Biondi, A. Scatturin, S. Tanganelli, L. Ferraro, P. Prasad, and A. Dalpiaz, *J. Med. Chem.,* **45**, 559 (2002). Design, Synthesis and Activity of Ascorbic Acid Prodrugs of Nipecotic, Kynurenic and Diclophenamic Acids, Liable to Increase Neurotropic Activity.

207. H. Koepsell, *Annu. Rev. Physiol.,* **60**, 243 (1998). Organic Cation Transporters in Intestine, Kidney, Liver, and Brain.

208. M. J. Dresser, M. K. Leabman, and K. M. Giacomini, *J. Pharm. Sci.,* **90**, 397 (2001). Transporters Involved in the Elimination of Drugs in the Kidney: Organic Anion Transporters and Organic Cation Transporters.

209. L. Zhang, W. Gorset, C. B. Washington, T. F. Blaschke, D. L. Kroetz, and K. M. Giacomini, *Drug Metabol. Disposition,* **28**, 329 (2000). Interactions of HIV Protease Inhibitors with a Human Organic Cation Transporter in a Mammalian Expression System.

210. K. J. Ullrich, F. Papavassiliou, C. David, G. Rumrich, and G. Fritzsch, *Pflugers Arch. -Eur. J. Physiol.,* **419**, 84 (1991). Contraluminal Transport of Organic Cations in the Proximal

Tubule of the Rat Kidney. I. Kinetics of N1-Methylnicotinamide and Tetraethylammonium, Influence of K+, HCO3, pH; Inhibition by Aliphatic Primary, Secondary and Tertiary Amines, and Mono- and Bisquaternary Compounds.

211. C. E. Groves, K. Evans, W. H. Dantzler, and S. H. Wright, *Am. J. Physiol.*, **266**, F450 (1994). Peritubular Organic Cation Transport in Isolated Rabbit Proximal Tubules.

212. S. H. Wright and T. M. Wunz, *Pflugers Arch.-Eur. J. Physiol.*, **437**, 603 (1999). Influence of Substrate Structure on Substrate Binding to the Renal Organic Cation/H+ Exchanger.

213. S. H. Wright, T. M. Wunz, and T. P. Wunz, *Pflugers Arch. -Eur. J. Physiol.*, **429**, 313 (1995). Structure and Interaction of Inhibitors with the TEA/H+ Exchanger of Rabbit Renal Brush Border Membranes.

214. D. Bednarczyk, S. Ekins, J. H. Wikel, and S. H. Wright, *Mol. Pharmacol.*, **63**, 489 (2003). Influence of Molecular Structure of Substrate Binding to the Human Organic Cation Transporter, hOCT1.

215. S. Jariyawat, T. Sekine, M. Takeda, N. Apiwattanakul, Y. Kanai, S. Sophasan, and H. Endou, *J. Pharmacol. Exp. Ther.*, **290**, 672 (1999). The Interaction and Transport of β-Lactam Antibiotics with the Cloned Rat Renal Organic Anion Transporter 1.

216. S. Khamdang, M. Takeda, R. Noshiro, S. Narikawa, A. Enomoto, N. Anzai, P. Piyachaturawat, and H. Endou, *J. Pharmacol. Exp. Ther.*, **303**, 534 (2002). Interactions of Human Organic Anion Transporters and Human Organic Cation Transporters with Non Steroidal Anti-inflammatory Drugs.

217. D. A. Griffith and S. M. Jarvis, *Biochim. Biophys. Acta*, **1286**, 153 (1996). Nucleoside and Nucleobase Transport Systems of Mammalian Cells.

218. D. Vijayalakshmi and J. A. Belt, *J. Biol. Chem.*, **263**, 19419 (1988). Sodium-Dependent Nucleoside Transport in Mouse Intestinal Epithelial Cells. Two Transport Systems with Differing Substrate Specificities.

219. J. Wang and K. M. Giacomini, *Mol. Pharmacol.*, **55**, 234 (1998). Characterization of a Bioengineered Chimeric Na+-Nucleoside Transporter.

220. S. D. Patil, L. Y. Ngo, and J. D. Unadkat, *Cancer Chemother. Pharmacol.*, **46**, 394 (2000). Structure-Inhibitory Profiles of Nucleosides for the Human Intestinal N1 and N2 Na+-Nucleoside Transporters.

221. C. Chang, P. W. Swaan, L. Y. Ngo, P. Y. Lum, S. D. Patel, and J. D. Unadkat, *Mol. Pharmacol.* (2004) **65** 558. Molecular Requirements of the Human Nucleoside Transporters hCNT1, hCNT2, and hENT1.

222. J. Taipalensuu, H. Tornblom, G. Lindberg, C. Einarsson, F. Sjoqvist, H. Melhus, P. Garberg, B. Lundgren, and P. Artursson, *J. Pharmacol. Exp. Ther.*, **299**, 164 (2001). Correlation of Gene Expression of Ten Drug Efflux Proteins of the ATP-Binding Cassette Transporter Family in Normal Human Jejunum and in Human Intestinal Epithelial Caco-2 Cell Monolayers.

223. A. van Loevezijn, J. D. Allen, A. H. Schinkel, and G.-J. Koomen, *Bioorg. Med. Chem. Lett.*, **11**, 29 (2001). Inhibition of BCRP-Mediated Drug Efflux by Fumitremorgin-Type Indolyl Diketopiperidines.

224. M. Maliepaard, M. A. van Gastelen, A. Tohgo, F. H. Hausheer, R. C. van Waardenburg, L. A. de Jong, D. Pluim, J. H. Beijnen, and J. H. Schellens, *Clin. Cancer Res.*, **7**, 935 (2001). Circumvention of Breast Cancer Resistance Protein (BCRP)-Mediated Resistance to Camptothecins In Vitro Using Non Substrate Drugs or the BCRP Inhibitor GF120918.

225. R. B. Kim, B. Leake, M. Cvetkovic, M. M. Roden, J. Nadeau, A. Walubo, and G. R. Wilkinson, *J. Pharmacol. Exp. Ther.*, **291**, 1204 (1999). Modulation by Drugs of Human Hepatic Sodium-Dependent Bile Acid Transporter (Sodium Taurocholate Cotransporting Polypeptide) Activity.

226. S. Ekins, L. Mirny, and E. G. Schuetz, *Pharm. Res.*, (2002) **19**, 1788. A Ligand-Based Approach to Understanding Selectivity of Nuclear Hormone Receptors PXR, CAR, FXR, LXRa and LXRb.

227. U. Fuhr, M. Weiss, H. K. Kroemer, G. Neugebauer, H. Rameis, W. Weber, and B. G. Woodcock, *Int. J. Clin. Pharmacol. Ther.*, **34**, 139 (1996). Systematic Screening for Pharmacokinetic Interactions During Drug Development.

228. S. A. Wrighton and P. M. Silber in *Scientific Stratergies for Accelerated Drug Discovery*; University of Wisconsin Press; Madison, WI, 1996. Screening Studies for Metabolism and Toxicology.

229. G. T. Tucker, *Int. J. Clin. Pharmacol. Ther.*, **30**, 550 (1992). The Rational Selection of Drug Interaction Studies: Implications of Recent Advances in Drug Metabolism.

230. G. T. Miwa, *Toxicol. Pathol.*, **23**, 131 (1995). Goals, Design, Timing, and Future Opportunities for Non Clinical Drug Metabolism Studies.

231. J. H. Lin and A. Y. H. Lu, *Ann. Rep. Med. Chem.*, **32**, 295 (1997). Inhibition of Cytochrome P-450 and Implications in Drug Development.

232. T. Shimada, H. Yamazaki, M. Mimura, Y. Inui, and F. P. Guengerich, *J. Pharmacol. Exp. Pharmacol.*, **270**, 414 (1994). Interindividual Variations in Human Liver Cytochrome P-450 Enzymes Involved in the Oxidation of Drugs, Carcinogens and Toxic Chemicals: Studies with Liver Microsomes of 30 Japanese and 30 Caucasians.

233. D. A. Smith, S. M. Abel, R. Hyland, and B. C. Jones, *Xenobiotica*, **28**, 1095 (1998). Human Cytochrome P450s: Selectivity and Measurement In Vivo.

234. J. H. Lin and A. Y. H. Lu, *Clin. Pharmacokinet.*, **35**, 361 (1998). Inhibition and Induction of Cytochrome P450 and the Clinical Implications.

235. G. C. Moody, S. J. Griffin, A. N. Mather, D. F. McGinnity, and R. J. Riley, *Xenobiotica*, **29**, 53 (1999). Fully Automated Analysis of Activities Catalysed by the Major Human Liver Cytochrome P450 (CYP) Enzymes: Assessment of Human CYP Inhibition Potential.

236. A. D. Rodrigues, *Pharmaceu. Res.*, **14**, 1504 (1997). Preclinical Drug Metabolism in the Age of High-Throughput Screening: An Industrial Perspective.

237. M. H. Tarbit and J. Berman, *Curr. Opin. Chem. Biol.*, **2**, 411 (1998). High-Throughput Approaches for Evaluating Absorption, Distribution, Metabolism and Excretion Properties of Lead Compounds.

238. M. J. de Groot and S. Ekins, *Adv. Drug Del. Rev.*, **54**, 367 (2002). Pharmacophore Modeling of Cytochromes P450.

239. U. Fuhr, G. Strobl, F. Manaut, E.-M. Anders, F. Sorgel, E. Lopez-de-brinas, D. T. W. Chu, A. G. Pernet, G. Mahr, F. Sanz, and A. H. Staib, *Mol. Pharmacol.*, **43**, 191 (1993). Quinolone Antibacterial Agents: Relationship between Structure and In Vitro Inhibition of Human Cytochrome P450 Isoform CYP1A2.

240. A. Poso, R. Juvonen, and J. Gynther, *Quant. Structure Activity Relationships*, **14**, 507 (1995). Comparative Molecular Field Analysis of Compounds with CYP2A5 Binding Affinity.

241. J. P. Jones, M. He, W. F. Trager, and A. E. Rettie, *Drug Metab. Dispos.*, **24**, 1 (1996). Three-Dimensional Quantitative Structure–Activity Relationship for Inhibitors of Cytochrome P4502C9.

242. Q. Wang and J. R. Halpert, *Drug Metab. Dispos.*, **30**, 86 (2002). Combined Three-Dimensional Quantitative Structure–Activity Relationship Analysis of Cytochrome P450 2B6 Substrates and Protein Homology Modeling.

243. L. Afzelius, I. Zamora, M. Ridderstrom, T. B. Andersson, A. Karlen, and C. M. Masimirembwa, *Mol. Pharmacol.*, **59**, 909 (2001). Competitive CYP2C9 Inhibitors: Enzyme Inhibition Studies, Protein Homology Modeling, and Three Dimensional Quantitative Structure Activity Relationship Analysis.

244. R. Snyder, R. Sangar, J. Wang, and S. Ekins, *Quant. Structure Activity Relationship*, **21**, 357 (2002). Three Dimensional Quantitative Structure Activity Relationship for CYP2D6 Substrates.

245. M. J. de Groot, M. J. Ackland, V. A. Horne, A. A. Alex, and B. C. Jones, *J. Med. Chem.*, **42**, 1515 (1999). Novel Approach to Predicting P450-Mediated Drug Metabolism: Development of a Combined Protein and Pharmacophore Model for CYP2D6.

246. M. J. de Groot, M. J. Ackland, V. A. Horne, A. A. Alex, and B. C. Jones, *J. Med. Chem.*, **42**, 4062 (1999). A Novel Approach to Predicting P450 Mediated Drug Metabolism. CYP2D6

Catalyzed N-Dealkylation Reactions and Qualitative Metabolite Predictions Using a Combined Protein and Pharmacophore Model for CYP2D6.

247. S. Rao, R. Aoyama, M. Schrag, W. F. Trager, A. Rettie, and J. P. Jones, *J. Med. Chem.,* **43,** 2789 (2000). A Refined 3-Dimensional QSAR of P4502C9.

248. M. J. de Groot, A. A. Alex, and B. C. Jones, *J. Med. Chem.,* **45,** 1983 (2002). Development of a Combined Protein and Pharmacophore Model for Cytochrome P4502C9.

249. C. Barhelt, R. D. Schmid, and J. Pleiss, *J. Mol. Model.,* **8,** 327 (2002). Regioselectivity of CYP2B6: Homology Modeling, Molecular Dynamics Simulation, Docking.

250. D. F. V. Lewis, B. G. Lake, M. Dickins, P. J. Eddershaw, M. H. Tarbit, and P. S. Goldfarb, *Xenobiotica,* **29,** 361 (1999). Molecular Modelling of CYP2B6, the Human CYP2B Isoform, by Homology with the Substrate-Bound CYP102 Crystal Structure: Evaluation of CYP2B6 Substrate Characteristics, the Cytochrome b5 Binding Site and Comparisons with CYP2B1 and CYP2B4.

251. S. A. Wrighton, E. G. Schuetz, K. E. Thummel, D. D. Shen, K. R. Korzekwa, and P. B. Watkins, *Drug Metab. Rev.,* **32,** 339 (2000). The Human CYP3A Subfamily: Practical Considerations.

252. S. A. Wrighton and J. C. Stevens, *Crit. Rev. Toxicol.,* **22,** 1 (1992). The Human Hepatic Cytochromes P450 Involved in Drug Metabolism.

253. P. Kuehl, J. Zhang, Y. Lin, J. Lamba, M. Assem, J. Schuetz, P. B. Watkins, A. Daly, S. A. Wrighton, S. D. Hall, P. Maurel, M. Relling, C. Brimer, K. Yasuda, R. Venkataramanan, S. Strom, K. Thummel, M. S. Boguski, and E. Schuetz, *Nature Genet.,* **27,** 383 (2001). Sequence Diversity in CYP3A Promotors and Characterization of the Genetic Basis of Polymorphic CYP3A5 Expression.

254. T. L. Domanski, C. Finta, J. R. Halpert, and P. G. Zachiropoulos, *Mol. Pharmacol.,* **59,** 386 (2001). cDNA Cloning and Initial Characterization of CYP3A43, a Novel Human Cytochrome P450.

255. S. C. Piscatelli, A. H. Burstern, D. Chaitt, R. M. Alfaro, and J. Falloon, *Lancet,* **355,** 547 (2000). Indinavir Concentrations and St. John's Wort.

256. F. Ruschitzka, P. J. Meier, M. Turina, T. F. Luscher, and G. Noll, *Lancet,* **355,** 548 (2000). Acute Heart Transplant Rejection Due to Saint John's Wort.

257. E. A. Rekka and P. N. Kourounakis, *European Journal of Drug Metabolism and Pharmacokinetics,* **21,** 7 (1996). An Approach to QSAR of 16-Substituted Pregnenolones as Microsomal Enzyme Inducers.

258. D. F. V. Lewis, C. Ioannides, D. V. Parke, and R. Schulte-Hermann, *J. Steroid BioChem. Mol Biol.,* **74,** 179 (2000). Quantitative Structure–Activity Relationships in a Series of Endogenous and Synthetic Steroids Exhibiting Induction of CYP3A Activity and Hepatomegaly Associated with Increased DNA Synthesis.

259. D. M. Stresser, A. P. Blanchard, S. D. Turner, J. C. L. Erve, A. A. Dandeneau, V. P. Miller, and C. L. Crespi, *Drug Metab. Dispos.,* **28,** 1440 (2000). Substrate-Dependent Modeulation of CYP3A4 Catalytic Activity: Analysis of 27 Test Compounds with Four Fluorimetric Substrates.

260. C. L. Crespi, V. P. Miller, and B. W. Penman, *Med. Chem. Res.,* **8,** 457 (1998). High Throughput Screening for Inhibition of Cytochrome P450 Metabolism.

261. S. Ekins, B. J. Ring, J. Grace, D. J. McRobie-Belle, and S. A. Wrighton, *J. Pharm. Tox. Methods.,* **44,** 313 (2000). Present and Future in Vitro Approaches for Drug Metabolism.

262. J. Maenpaa, S. D. Hall., B. J. Ring, S. C. Strom, and S. A. Wrighton, *Pharmacogenetics,* **8,** (1998). Human Cytochrome P4503A (CYP3A) Mediated Midazolam Metabolism: the Effect of Assay Conditions and Regioselective Stimulation by a-Napthoflavone, Terfenadine and Testosterone.

263. M. L. Schrag and L. C. Wienkers, *Drug Metab. Dispos.,* **28,** 1198 (2000). Topological Alteration of the P4503A4 Active Site by the Divalent Cation Mg^{2+}.

264. R. W. Wang, D. J. Newton, N. Liu, W. M. Atkins, and A. Y. H. Lu, *Drug Metab. Dispos.,* **28,** 360 (2000). Human Cytoch. P-4503A4: In Vitro Drug–Drug Interaction Patterns are Substrate-Dependent.

265. K. E. Kenworthy, J. C. Bloomer, S. E. Clarke, and J. B. Houston, *Br. J. Clin. Pharmacol.,* **48,** 716 (1999). CYP3A4 Drug Interactions: Correlation of Ten in Vitro Probe Substrates.

266. T. L. Domanski, Y.-A. He, K. K. Khan, F. Roussel, Q. Wang, and J. R. Halpert, *Biochemistry,* **40,** 10150 (2001). Phenylalanine and Tryptophan Scanning Mutagenesis of CYP3A4 Substrate Recognition Site Residues and Effect on Substrate Oxidation and Cooperativity.

267. N. A. Hosea, G. P. Miller, and F. P. Guengerich, *Biochemistry,* **39,** 5929 (2000). Elucidation of Distinct Ligand-Binding Sites for the Cytochrome P4503A4.

268. M. Shou, J. Grogan, J. A. Mancewicz, K. W. Krausz, F. J. Gonzalez, H. V. Gelboin, and K. R. Korzekwa, *Biochemistry,* **33,** 6450 (1994). Activation of CYP3A4: Evidence for the Simultaneous Binding of Two Substrates in a Cytochrome P450 Active Site.

269. M. Shou, R. Dai, D. Cui, K. R. Korzekwa, T. A. Baillie, and T. H. Rushmore, *J. Biol. Chem.,* **276,** 2256 (2001). A Kinetic Model for the Metabolic Interaction of the Two Substrates at the Active Site of Cytochrome P4503A4.

270. M. L. Schrag and L. C. Wienkers, *Arch. Biochem. Biophys.,* **391,** 49 (2001). Covalent Alteration of the CYP3A4 Active Site: Evidence For Multiple Substrate Binding Domains.

271. T. L. Domanski, J. Liu, G. R. Harlow, and J. R. Halpert, *Arch. Biochem. Biophys.,* **350,** 223 (1998). Analysis of Four Residues within Substrate Recognition Site 4 of Human Cytochrome P4503A4: Role in Steroid Hydroxylase Activity and a-Napthoflavone Stimulation.

272. A. P. Koley, R. C. Robinson, A. Markowitz, and F. K. Friedman, *Biochem. Pharmacol.,* **53,** 455 (1997). Drug–Drug Interactions: Effect of Quinidine on Nifedipine Binding to Human Cytochrome P4503A4.

273. W. M. Atkins, R. W. Wang, and A. Y. H. Lu, *Chem. Res. Toxicol.,* **14,** 338 (2001). Allosteric Behavior in Cytochrome P450-Dependent In Vitro Drug–Drug Interactions: A Prospective Based on Conformational Dyamics.

274. R. J. Riley, A. J. Parker, S. Trigg, and C. N. Manners, *Pharm. Res.,* **18,** 652 (2001). Development of a Generalized, Quantitative Physicochemical Model of CYP3A4 Inhibition for Use in Early Drug Discovery.

275. L. Molnar and G. M. Kesuru, *Bioorg. Med. Chem. Lett.,* **12,** 419 (2002). A Neural Network Based Virtual Screening of Cytochrome P4503A4 Inhibitors.

276. C. Morisseau, G. Du, J. W. Newman, and B. D. Hammock, *Arch. Biochem. Biophys.,* **356,** 214 (1998). Mechanism of Mammalian Soluble Epoxide Hydrolase Inhibition by Chalcone Oxide Derivatives.

277. Y. Nakagawa, C. E. Wheelock, C. Morisseau, M. H. Goodrow, B. G. Hammock, and B. D. Hammock, *Bioorg. Med. Chem.,* **8,** 2663 (2000). 3D-QSAR Analysis of Inhibition of Murine Soluble Epoxide Hydrolase (MsEH) by Benzoylureas, Arylureas, and Their Analogues.

278. T. Yamada, C. Morisseau, J. E. Maxwell, M. A. Argiriadi, D. W. Christianson, and B. D. Hammock, *J. Biol. Chem.,* **275,** 23082 (2000). Biochemical Evidence for the Involvement of Tyrosine in Epoxide Activation During the Catalytic Cycle of Epoxide Hydrolase.

279. M. A. Argiriadi, C. Morisseau, M. H. Goodrow, D. L. Dowdy, B. D. Hammock, and D. W. Christianson, *J. Biol. Chem.,* **275,** 15265 (2000). Binding of the Alkylurea Inhibitors to Epoxide Hydrolase Implicates Active Site Tyrosines in Substrate Activation.

280. S. Jegham and P. George, *Exp. Opin. Ther. Pat.,* **8,** 1143 (1998). Monoamine Oxidase A and B Inhibitors.

281. A. S. Kalgutkar, D. K. Dalvie, N. Castagnoli, Jr., and T. J. Taylor, *Chem. Res. Toxicol.,* **14,** 1139 (2001). Interactions of Nitrogen Containing Xenobiotics with Monoamine Oxidase (MAO) Isozymes A and B: SAR Studies on MAO Substrates and Inhibitors.

282. C. Altomare, S. Cellamare, L. Summo, M. Catto, A. Carotti, U. Thull, P.-A. Carrupt, B. Testa, and H. S. Evans, *J. Med. Chem.,* **41,** 3812 (1998). Inhibition of Monoamine Oxidase-B by Condensed Pyridazines and Pyrimidines: Effects of Lipophilicity and Structure–Activity Relationships.

283. A. E. Medvedev., A. V. Veselovsky, V. I. Shvedov, O. V. Tikhonova, T. A. Moskvitina, O. A. Fedotova, L. N. Axenova, N. S. Kamyshanskaya, A. Z. Kirkel, and A. S. Ivanov, *J. Chem. Inf.*

Comput. Sci., **38**, 1137 (1998). Inhibition of Monoamine Oxidase by Pirlindole Analogues: 3D-QSAR and CoMFA Analysis.

284. J. A. Moron, M. Campillo, V. Perez, M. Unzeta, and L. Pardo, J. Med. Chem., **43**, 1684 (2000). Molecular Determinants of MAO Selectivity in a Series of Indolylmethylamine Derivatives: Biological Activities, 3D-QSAR/CoMFA Analysis, and Computational Simulation of Ligand Recognition.

285. C. Gnerre, M. Catto, F. Leonetti, P. Weber, P.-A. Carrupt, C. Altomare, A. Carotti, and B. Testa, J. Med. Chem., **43**, 4747 (2000). Inhibition of Monoamine Oxidases by Functionalized Coumarin Derivatives: Biological Activities, QSARs, and 3D-QSARs.

286. J. Sterling, Y. Herzig, T. Goren, N. Finkelstein, D. Lerner, W. Goldenberg, I. Miskolczi, S. Molnar, F. Rantal, T. Tamas, G. Toth, A. Zagyva, A. Zekany, G. Lavian, A. Gross, R. Friedman, M. Razin, W. Huang, B. Krais, M. Chorev., M. B. Youdim, and M. Weinstock, J. Med. Chem., **45**, 5260 (2002). Novel Dual Inhibitors of AChE and MAO Derived from Hydroxy Aminoindan and Phenethylamine as Potential Treatment for Alzheimer's Disease.

287. J. R. Miller and D. E. Edmondson, Biochemistry, **38**, 13670 (1999). Structure–Activity Relationships in the Oxidation of para-Substituted Benzylamine Analogues by Recombinant Human Liver Monoamine Oxidase A.

288. R. Nandigama, and D. E. Edmondson, Biochemistry, **39**, 15258 (2000). Structure–Activity Relations in the Oxidation of Phenethylamine Analogues by Recombinant Human Liver Monoamine Oxidase A.

289. D. M. Ziegler, Annu. Rev. Pharmacol. Toxicol., **33**, 179 (1993). Recent Studies on the Structure and Function of Multisubstrate Flavin-Containing Monooxygenases.

290. R. Dajani, A. Cleasby, M. Neu, A. J. Wonacott, H. Jhoti, A. M. Hood, S. Modi, A. Hersey, J. Taskinen, R. M. Cooke, G. R. Manchee, and M. W. H. Coughtrie, J. Biol. Chem., **53**, 37862 (1999). X-Ray Crystal Structure of Human Dopamine Sulfotransferase, SULT1A3.

291. J. A. Williams, Carcinogenesis, **22**, 209 (2001). Single Nucleotide Polymorphisms, Metabolic Activation and Environmental Carcinogenesis: Why Molecular Epidemiologists Should Think about Enzyme Expression.

292. M. W. Duffel, A. D. Marshall, P. McPhie, V. Sharma, and W. B. Jakoby, Drug Metab. Rev., **33**, 369 (2001). Enzymatic Aspects of the Phenol (aryl) Sulfotransferases.

293. G. Chen, E. Banoglu, and M. W. Duffel, Chem. Res. Toxicol., **9**, 67 (1996). Influence of Substrate Structure on the Catalytic Efficiency of Hydroxysteroid Sulfotransferase STa in the Sulfation of Alcohols.

294. E. Banoglu and M. W. Duffel, Drug Metab. Dispos., **25**, 1304 (1997). Studies on the Interactions of Chiral Secondary Alcohols with Rat Hydroxysteroid Sulfotransfease STa.

295. E. Banoglu and M. W. Duffel, Chem. Res. Toxicol., **12**, 278 (1999). Importance of Peri-Interactions on the Stereospecificity of Rat Hydroxysteroid Sulfotransfease STa with 1-Arylethanols.

296. R. S. King, V. Sharma, L. C. Pedersen, Y. Kakuta, M. Negishi, and M. W. Duffel, Chem. Res. Toxicol., **13**, 1251 (2000). Structure-Function Modeling of the Interactions of the N-alkyl-N-Hydroxyanilines with Rat Hepatic Aryl Sulfotransferase IV.

297. V. Sharma and M. W. Duffel, J. Med. Chem., **45**, 5514 (2002). Comparative Molecular Field Analysis of Substrates for an Aryl Sulfotransferase Based on Catalytic Mechanism and Protein Homology Modeling.

298. R. H. Tukey and C. P. Strassburg, Annu. Rev. Pharmacol. Toxicol., **40**, 581 (2000). Human UDP-Glucuronosyltransferases: Metabolism, Expression, and Disease.

299. R. J. Bertz and R. G. Granneman, Clin. Pharmacokinet., **32**, 210 (1997). Use of In Vitro and In Vivo Data to Estimate the Likelihood of Metabolic Pharmacokinetic Interactions.

300. P. I. Mackenzie, I. S. Owens, B. Burchell, K. W. Bock, A. Bairoch, A. Belanger, S. Fournel-Gigleux, M. Green, D. W. Hum, T. Iyanagi, D. Lancet, P. Louisot, J. Magdalou, R. Chowdhury, J. K. Ritter, H. Schachter, T. R. Tephly, K. F. Tipton, and D. W. Nebert, Pharmacogenetics, **7** (1997). The UDP Glycosyltransferase Gene Superfamily: Recommended Nomenclature Based on Evolutionary Divergence.

301. S. Senafi, D. Clarke, and B. Burchell, *Biochem. J.,* **303**, 233 (1994). Investigation of the Substrate Specificity of a Cloned Expressed Human Bilirubin UDP-Glucuronosyltransferase: UDP-Sugar Specificity and Involvement in Steroid and Xenobiotic Glucuronidation.

302. M. D. Green, C. D. King, P. I. Mackenzie, and T. R. Tephly, *Drug Metab. Dispos.,* **26**, 507 (1998). Glucuronidation of Amines and Other Xenobiotics Catalyzed by Expressed Human UDP-Glucuronosyltransferase 1A3.

303. M. D. Green and T. R. Tephly, *Drug Metab. Dispos.,* **24**, 356 (1996). Glucuronidation of Amines and Hydroxylated Xenobiotics and Endobiotics Catalyzed by Expressed Human UGT1.4 Protein.

304. Z. Cheng, A. Radominska-Pandya, and T. R. Tephly, *Drug Metab. Dispos.,* **27**, 1165 (1999). Studies on the Substrate Specificity of Human Intestinal UDP-Glucuronosyltransferases 1A8 and 1A10.

305. M. D. Green, E. M. Oturu, and T. R. Tephly, *Drug Metab. Dispos.,* **22**, 799 (1994). Stable Expression of a Human Liver UDP-Glucuronosyltransferase (UGT2B15) with Activity Toward Steroids and Xenobiotics.

306. B. L. Coffman, C. D. King, G. R. Rios, and T. R. Tephly, *Drug Metab. Dispos.,* **26**, 73 (1998). The Glucuronidation of Opioids, Other Xenobiotics and Androgens by Human UGT2B7Y(268) and UGT2B7H(268).

307. T. Ebner and B. Burchell, *Drug Metab. Dispos.,* **20**, 50 (1993). Substrate Specificities of Two Stably Expressed Human Liver UDP-Glucuronosyltransferases of the UGT1 Gene Family.

308. A. Temellini, M. Franchi, L. Giuliani, and G. M. Pacifici, *Xenobiotica,* **21**, 171 (1991). Human Liver Sulphotransferase and UDP-Glucuronosyltransferase: Strucure–Activity Relationship for Phenolic Substrates.

309. M. Ouzzine, T. Pillot, S. Fournel-Gigleux, J. Magdalou, B. Burchell, and G. Siest, *Arch. Biochem. Biophys.,* **310**, 196 (1994). Expression of the Human Liver UDP-Glucuronosyltransferase UGT1*6 Analyzed by Specific Antibodies Raised Against a Hybrid Protein Produced in *Escherichia Coli.*

310. K. H. Kim, *J. Pharm. Sci.,* **80**, 966 (1991). Quantitative Structure–Activity Relationships of the Metabolism of Drugs by Uridine Diphosphate Glucuronsyltransferase.

311. M. Schaefer, I. Okulicz-Kozaryn, A. M. Batt, G. Siest, and V. Loppinet, *Eur. J. Med. Chem.,* **16**, 461 (1981). Structure–Activity Relationships in Glucuronidation of Substituted Phenols.

312. C. Hansch and A. Leo, *Exploring QSAR: Fundamentals and Applications in Chemistry and Biology*; American Chemical Society, Washington DC, 1995, 299–346.

313. H. Yin, G. Bennet, and J. P. Jones, *Chem. Biol. Interact.,* **90**, 47 (1994). Mechanistic Studies of Uridine Diphosphate Glucuronosyltransferase.

314. Z. G. Naydenova, K. C. Grancharov, D. K. Algarov, E. Golovinsky, V. I. M. Stanoeva, L. D. Shalamanova, and I. K. Pajeva, *Z. Naturforsch.,* **53c**, 173 (1998). Inhibition of UDP-Glucuronylsyltransferase by 5'-O-Amino Acid and Oligopeptide Derivatives of Uridine: Structure–Activity Relationships.

315. B. C. Cupid, E. Holmes, I. D. Wilson, J. C. Lindon, and J. K. Nicholson, *Xenobiotica,* **29**, 27 (1999). Quantitative Structure-Metabolism Relationships (QSMR) Using Computational Chemistry: Pattern Recognition Analysis and Statistical Prediction of Phase II Conjugation Reactions of Substituted Benzoic Acids in the Rat.

316. B. T. Ethell, S. Ekins, J. Wang, and B. Burchell, *Drug Metab. Dispos.,* **30**, 734 (2002). Quantitative Structure Activity Relationships for the Glucuronidation of Simple Phenols by Expressed Human UGT1A6 and UGT1A9.

317. N. Takenaga, M. Ishii, T. Kamei, and T. Yasumori, *Drug Metab. Dispos.,* **30**, 494 (2002). Structure–Activity Relationship in O-Glucuronidation of Indocarbazole Analogues.

318. Z. Cheng, A. Radominska-Pandya, and T. R. Tephly, *Drug Metab. Dispos.,* **27**, 1165 (1999). Studies on the Substrate Specificity of Human Intestinal UDP-Glucuronosyltransferases 1A8 and 1A10.

319. P. A. Smith, M. Sorich, R. McKinnon, and J. O. Miners, *Pharmacologist*, **44**, Suppl. (2002). QSAR and Pharmacophore Modelling Approaches for the Prediction of UDP-Glucuronosyltransferase Substrate Selectivity and Binding.

320. U. K. Walle and T. Walle, *Drug Metab. Dispos.*, **30**, 564 (2002). Induction of Human UDP-Glucuronosyltransferase UGT1A1 by Flavonoids-Structural Requirements.

321. M. G. Soars, B. Burchell, and R. J. Riley, *J. Pharmacol. Exp. Ther.*, **301**, 382 (2002). In Vitro Analysis of Human Drug Glucuronidation and Prediction of In Vivo Metabolic Clearance.

322. M. J. de Groot and N. P. E. Vermeulen, *Drug Metab. Rev.*, **29**, 747 (1997). Modeling the Active Site of Cytochrome P450s and Glutathione *S*-Transferases. Two of the Most Important Biotransformation Enzymes.

323. A. E. M. F. Soffers, J. H. T. M. Ploeman, M. J. H. Moonen, T. Wobbes, B. van Ommen, J. Vervoort, P. J. van Bladeren, and I. M. C. M. Rietjens, *Chem. Res. Toxicol.*, **9**, 638 (1996). Regioselectivity and Quantitative Structure–Activity Relationships for the Conjugation of a Series of Fluoronitrobenzenes by Purified Glutathione S-Transferase Enzymes from Rat and Man.

324. I. M. C. M. Rietjens, A. E. M. F. Soffers, G. J. E. J. Hooiveld, C. Veegar, and J. Vervoort, *Chem. Res. Toxicol.*, **8**, 481 (1995). Quantitative Structure–Activity Relationships Based on Computer Calculated Parameters for the Overall Rate of Glutathione S-Transferase Catalyzed Conjugation of a Series of Fluoronitrobenzenes.

325. M. J. de Groot, E. M. van der Aar, P. J. Niuwenhuizen, R. M. van der Plas, G. M. Donne-Op Kelder, J. N. M. Commandeur, and N. P. E. Vermeulen, *Chem. Res. Toxicol.*, **8**, 649 (1995). A Predictive Substrate Model for the Rat Glutathione S Transferase 4-4.

326. E. M. van der Aar, *Chem. Res. Toxicol.*, **10**, 439 (1997). 4-Sustituted 1-Chloro-2-Nitrobenzenes: Structure–Activity Relationships and Extension of the Substrate Model of Rat Glutathione S-Transferase 4-4.

327. L. M. Kauvar, D. L. Higgins, H. O. Villar, J. R. Sportsman, A. Engqvist-Goldstein, R. Bukar, K. E. Bauer, H. Dilley, and D. M. Rocke, *Chem. Biol.*, **2**, 107 (1995). Predicting Ligand Binding to Proteins by Affinity Fingerprinting.

328. W. Crumb and I. Cavero, *PSST*, **2**, 270 (1999). QT Interval Prolongation by Non-Cardiovascular Drugs: Issues and Solutions for Novel Drug Development.

329. M. E. Curran, I. Splawski, K. W. Timothy, G. M. Vincent, E. D. Green, and M. T. Keating, *Cell*, **80**, 795 (1995). A Molecular Basis for the Cardiac Arrhythmia: HERG Mutations Cause Long QT Syndrome.

330. S. Rees and M. J. Curtis, *Pharamcol. Ther.*, **69**, 199 (1996). Which Cardiac Potassium Channel Subtype Is the Preferable Target for Suppression of Ventricular Arrhythmias?

331. M. C. Sanguinetti, C. Jiang, M. E. Curran, and M. T. Keating, *Cell*, **81**, 299 (1995). A Mechanistic Link Between an Inherited and an Acquired Cardiac Arrhythmia: HERG Encodes the IKr Potassium Channel.

332. P. L. Smith, T. Baukrowitz, and G. Yellen, *Nature (London)*, **379**, 833 (1996). The Inward Rectification Mechanism of the HERG Cardiac Potassium Channel.

333. J. S. Mitcheson, J. Chen, M. Lin, C. Culberson, and M. C. Sanguinetti, *Proc. Natl. Acad. Sci. U.S.A.*, **97**, 12329 (2000). A Structural Basis for the Drug-Induced Log QT Syndrome.

334. S. Ekins, W. J. Crumb, R. D. Sarazan, J. H. Wikel, and S. A. Wrighton, *J. Pharmacol. Exp. Ther.*, **301**, 427 (2002). Three Dimensional Quantitative Structure Activity Relationship for the Inhibition of the hERG (human ether-a-gogo related gene) Potassium Channel.

335. J. Kang, L. Wang, X.-L. Chen, D. J. Triggle, and D. Rampe, *Mol. Pharmacol.*, **59**, 122 (2001). Interactions of a Series of Fluoroquinolone Antibacterial Drugs with the Human Cardiac K^+ Channel HERG.

336. F. De Ponti, E. Poluzzi, and N. Montanaro, *Eur. J. Clin. Pharmacol.*, **56**, 1 (2000). QT-Interval Prolongation by Non-Cardiac Drugs: Lessons to be Learned from Recent Experience.

337. O. Roche, G. Trube, J. Zuegge, P. Pflimlin, A. Alanine, and G. Schneider, *ChemBioChem*, **3**, 455 (2002). A Virtual Screening Method for the Prediction of the hERG Potassium Channel Liability of Compound Libraries.

338. A. Cavalli, E. Poluzzi, F. De Ponti, and M. Recanatini, *J. Med. Chem.*, **45**, 3844 (2002). Toward a Pharmacophore for Drugs Inducing the Long QT Syndrome: Insights from a CoMFA Study of HERG K+ Channel Blockers.

339. M. Rowley, D. J. Hallett, S. Goodacre, C. Moyes, J. Crawforth, T. J. Sparey, S. Patel, R. Marwood, S. Thomas, L. Hitzel, D. O'Connor, N. Szeto, J. L. Castro, P. H. Hutson, and A. M. MacLeod, *J. Med. Chem.*, **44**, 1603 (2002). 3-(4-Fluoropiperidin-3-yl)-2-phenylindoles as High Affinity, Selective, and Orally Bioavailable h5-HT2A Receptor Antagonists.

340. S. R. Fletcher, F. Burkhamp, P. Blurton, S. K. F. Cheng, R. Clarkson, D. O'Connor, D. Spinks, M. Tudge, M. B. van Niel, S. Patel, K. Chapman, R. Marwood, S. Shepheard, G. Bentley, G. P. Cook, L. J. Bristow, J. L. Castro, P. H. Hutson, and A. M. MacLeod, *J. Med. Chem.*, **45**, 492 (2002). 4-(Phenylsulfonyl)piperidines: Novel, Selective, and Bioavailable 5-HT2A Receptor Antagonists.

341. I. M. Bell, S. N. Gallicchio, M. Abrams, L. S. Beese, D. C. Beshore, H. Bhimnathwala, M. J. Bogusky, C. A. Buser, J. C. Culberson, J. Davide, M. Ellis-Hutchings, C. Fernandes, J. B. Gibbs, S. L. Graham, K. A. Hamilton, G. D. Hartman, D. C. Heimbrook, C. F. Homnick, H. E. Huber, J. R. Huff, K. Kassahun, K. S. Koblan, N. E. Kohl, R. B. Lobell, J. J. Lynch Jr, R. Robinson, A. D. Rodrigues, J. S. Taylor, E. S. Walsh, T. M. Williams, and C. B. Zartman, *J. Med. Chem.*, **45**, 2388 (2002). 3-Aminopyrrolidinone Farnesyltransferase Inhibitors: Design of Macrocyclic Compounds with Improved Pharmacokinetics and Excellent Cell Potency.

342. Y. V. Korolkova, S. A. Kozlov, A. V. Lipkin, K. A. Pluzhnikov, J. K. Hadley, A. K. Filippov, D. A. Brown, K. Angelo, D. Strobaek, T. Jespersen, S.-P. Olesen, B. S. Jensen, and E. V. Grishin, *J. Biol. Chem.*, **276**, 9868 (2001). An ERG Channel Inhibitor from the Scorpion Buthus Eupeus.

343. Y. V. Korolkova, E. V. Bocharov, K. Angelo, I. V. Maslennikov, O. V. Grinenko, A. V. Lipkin, E. D. Nosyreva, K. A. Pluzhnikov, S. P. Olesen, A. S. Areseniev, and E. V. Grishin, *J. Biol. Chem.*, **277**, 43104 (2002). New Binding Site on Common Molecular Scaffold Provides HERG Channel Specificity of Scorpion Toxin BeKm-1.

344. G. Bertilsson, J. Heidrich, K. Svensson, M. Asman, L. Jendeberg, M. Sydow-Backman, R. Ohlsson, H. Postlind, P. Blomquist, and A. Berkenstam, *Proc. Natl. Acad. Sci. U.S.A.*, **95**, 12208 (1998). Identification of a Human Nuclear Receptor Defines a New Signaling Pathway for CYP3A Induction.

345. B. Blumberg, W. Sabbagh, Jr., H. Juguilon, J. Bolado, Jr., C. M. van Meter, E. S. Ong, and R. M. Evans, *Genes Dev.*, **12**, 3195 (1998). SXR, a Novel Steroid and Xenobiotic-Sensing Nuclear Receptor.

346. S. A. Kliewer, J. T. Moore, L. Wade, J. L. Staudinger, M. A. Watson, S. A. Jones, D. D. McKee, B. B. Oliver, T. M. Willson, R. H. Zetterstrom, T. Perlmann, and J. M. Lehmann, *Cell*, **92**, 73 (1998). An Orphan Nuclear Receptor Activated by Pregnanes Defines a Novel Steroid Signalling Pathway.

347. T. W. Synold, I. Dussault, and B. M. Forman, *Nature Med.*, **7**, 584 (2001). The Orphan Nuclear Receptor SXR Coordinately Regulates Drug Metabolism and Efflux.

348. E. Schuetz and S. Strom, *Nature Med.*, **7**, 536 (2001). Promiscous Regulator of Xenobiotic Removal.

349. J. Zhang, P. Kuehl, E. D. Green, J. W. Touchman, P. B. Watkins, A. Daly, S. D. Hall, P. Maurel, M. Relling, C. Brimer, K. Yasuda, S. A. Wrighton, M. Hancock, R. B. Kim, S. Strom, K. Thummel, C. G. Russell, J. R. Hudson, Jr., E. G. Schuetz, and M. S. Boguski, *Pharmacogenetics*, **11**, 555 (2001). The Human Pregnane X Receptor: Genomic Structure and Identification and Functional Characterization of Natural Allelic Variants.

350. B. M. Forman, *Pharmacogenetics*, **11**, 551 (2001). Polymorphisms in Promiscuous PXR: An Explanation for Interindividual Differences in Drug Clearance?

351. J. Staudinger, Y. Liu, A. Madan, S. Habeebu, and C. D. Klaassen, *Drug Metab. Dispos.*, **29**, 1467 (2001). Coordinate Regulation of Xenobiotic and Bile Acid Homeostasis by Pregnane X Receptor.

352. J. T. Moore and S. A. Kliewer, *Toxicology,* **153**, 1 (2000). Use of the Nuclear Receptor PXR to Predict Drug Interactions.

353. W. Xie, J. L. Barwick, M. Downes, B. Blumberg, C. M. Simon, M. C. Nelson, B. A. Neuschwander-Tetri, E. M. Brunt, P. S. Guzelian, and R. M. Evans, *Nature (London),* **406**, 435 (2000). Humanized Xenobiotic Response in Mice Expressing Nuclear Receptor SXR.

354. R. E. Watkins, G. B. Wisely, L. B. Moore, J. L. Collins, M. H. Lambert, S. P. Williams, T. M. Willson, S. A. Kliewer, and M. R. Redinbo, *Science,* **292**, 2329 (2001). The Human Nuclear Xenobiotic Receptor PXR: Structural Determinants of Directed Promiscuity.

355. J. L. Staudinger, B. Goodwin, S. A. Jones, D. Hawkins-Brown, K. I. MacKenzie, A. LaTour, Y. Liu, C. D. Klaassen, K. K. Brown, J. Reinhard, T. M. Willson, B. H. Koller, and S. A. Kliewer, *Proc. Natl. Acad. Sci. U.S.A.,* **98**, 3369 (2001). The Nuclear Receptor PXR Is a Lithocholic Acid Sensor that Protects Against Liver Toxicity.

356. W. El-Sankary, G. G. Gibson, A. Ayrton, and N. Plant, *Drug Metab. Dispos.,* **29**, 1499 (2001). Use of a Reporter Gene Assay to Predict and Rank the Potency and Efficiency of CYP3A4 Inducers.

357. L. B. Moore, B. Goodwin, S. A. Jones, G. B. Wisely, C. J. Serabjit-Singh, T. M. Willson, J. L. Collins, and S. A. Kliewer, *Proc. Natl. Acad. Sci. U.S.A.,* **97**, 7500 (2000). St. John's Wort Induces Hepatic Drug Metabolism Through Activation of the Pregnane X Receptor.

358. J. M. Wentworth, M. Agostini, J. Love, J. W. Schwabe, and V. K. Chatterjee, *J. Endocrinol.,* **166**, R11 (2000). St. John's Wort, a Herbal Antidepressant, Activates the Steroid X Receptor.

359. I. Dussault, M. Lin, K. Hollister, E. H. Wang, T. W. Synold, and B. M. Forman, *J. Biol. Chem.,* **276**, 33309 (2001). Peptide Mimetic HIV Protease Inhibitors are Ligands for the Orphan Receptor SXR.

360. L. Drocourt, J. M. Pascussi, E. Assenat, J. M. Fabre, P. Maurel, and M. J. Vilarem, *Drug Metab. Dispos.,* **29**, 1325 (2001). Calcium Channel Modulators of the Dihydropyridine Family are Human Pregnane X Receptor Activators and Inducers of CYP3A, CYP2B, and CYP2C in Human Hepatocytes.

361. A. Takeshita, N. Koibuchi, J. Oka, M. Taguchi, Y. Shishiba, and Y. Ozawa, *Eur. J. Endocrinol.,* **145**, 513 (2001). Bisphenol-A, an Environmental Estrogen, Activates the Human Orphan Nuclear Receptor, Steroid and Xenobiotic Receptor-Mediated Transcription.

362. H. Masuyama, Y. Hiramatsu, M. Kunitomi, T. Kudo, and P. N. MacDonald, *Mol. Endocrinol.,* **14**, 421 (2000). Endocrine Disrupting Chemicals, Phthalic Acid and Nonylphenol, Activate Pregnane X Receptor-Mediated Transcription.

363. H. Masuyama, H. Inoshita, Y. Hiramatsu, and T. Kudo, *Endocrinology,* **143**, 55 (2002). Ligands Have Various Potential Effects on the Degradation of Pregnane X Receptor by Proteasome.

364. X. Coumol, M. Diry, and R. Barouki, *Biochem. Pharmacol.,* **64**, 1513 (2002). PXR-Dependent Induction of Human CYP3A4 Gene Expression by Organochlorine Pesticides.

365. S. Ekins and J. A. Erickson, *Drug Metab. Dispos.,* **30**, 96 (2002). A Pharmacophore for Human Pregnane-X-Receptor Ligands.

366. J. M. Lehmann, D. D. McKee, M. A. Watson, T. M. Wilson, J. T. Moore, and S. A. Kliewer, *J. Clin. Invest.,* **102**, 1 (1998). The Human Orphan Receptor PXR is Activated by Compounds that Regulate CYP3A4 Gene Expressionand Cause Drug Interactions.

367. D. J. Waxman, *Arch. Biochem. Biophys.,* **369**, 11 (1999). P450 Gene Induction by Structurally Diverse Xenochemicals: Central Role of Nuclear Receptors CAR, PXR, and PPAR.

368. R. E. Watkins, S. M. Noble, and M. R. Redinbo, *Curr. Opin. Drug Discov. Devel.,* **5**, 150 (2002). Structural Insights into the Promiscuity and Function of the Human Pregnane X Receptor.

369. C. Martin, G. Berridge, C. F. Higgins, P. Mistry, P. Charlton, and R. Callaghan, *Mol. Pharmacol.,* **58**, 624 (2000). Communication between Multiple Drug Binding Sites on P-Glycoprotein.

370. S. Ekins and S. A. Wrighton, *Drug Metab. Rev.,* **31**, 719 (1999). The Role of CYP2B6 in Human Xenobiotic Metabolism.

371. B. Goodwin, L. B. Moore, C. M. Stoltz, D. D. McKee, and S. A. Kliewer, *Mol. Pharmacol.,* **60**, 427 (2001). Regulation of the Human CYP2B6 Gene by the Nuclear Pregnane X Receptor.

372. B. E. Daikh, J. M. Lasker, J. Raucy, and D. R. Koop, *J. Pharm. Exp. Ther.,* **271**, 1427 (1994). Regio- and Stereoselective Epoxidation of Arachidonic Acid by Human Cytochromes P450 2C8 and 2C9.

373. A. Geick, M. Eichelbaum, and O. Burk, *J. Biol. Chem.,* **276**, 14581 (2001). Nuclear Receptor Response Elements Mediate Induction of Intestinal MDR1 by Rifampin.

374. H. M. Kauffmann, S. Pfannschmidt, H. Zoller, A. Benz, B. Vorderstemann, J. I. Webster, and D. Schrenk, *Toxicology,* **171**, 137 (2002). Influence of Redox-Active Compounds and PXR-Activators on Human MRP1 and MRP2 Gene Expression.

375. A. Toell, K. D. Kroncke, H. Kleinert, and C. Carlberg, *J. Cell Biochem.,* **85**, 72 (2002). Orphan Nuclear Receptor Binding Site in the Human Inducible Nitric Oxide Synthase Promoter Mediates Responsiveness to Steroid and Xenobiotic Ligands.

376. G. I. Murray, W. T. Melvin, W. F. Greenlee, and M. D. Burke, *Annu. Rev. Pharmacol. Toxicol.,* **41**, 297 (2001). Regulation, Function, and Tissue-Specific Expression of Cytochrome P450 CYP1B1.

377. I. Stoilov, *Trends Genet.,* **17**, 629 (2001). Cytochrome P450's: Coupling Development and Environment.

378. B. M. Forman, I. Tzameli, H.-S. Choi, J. Chen, D. Simha, W. Seol, R. M. Evans, and D. D. Moore, *Nature (London),* **395**, 612 (1998). Androstane Metabolites Bind to and Deactivate the Nuclear Receptor CAR-β.

379. D. Picard, *Nature (London),* **395**, 543 (1998). Two Orphans Find a Home.

380. I. Zelko and M. Negishi, *Biochem. Biophys. Res. Commun.,* **277**, 1 (2000). Phenobarbital-Elicited Activation of Nuclear Receptor CAR in Induction of Cytochrome P450 Genes.

381. T. Sueyoshi, T. Kawamato, I. Zelko, P. Honkakoski, and M. Negishi, *J. Biol. Chem.,* **274**, 6043 (1999). The Repressed Nuclear Receptor CAR Responds to Phenobarbital in Activating the Human CYP2B6 Gene.

382. L. B. Moore, D. J. Parks, S. A. Jones, R. K. Bledsoe, T. G. Consler, J. B. Stimmel, B. Goodwin, C. Liddle, S. G. Blanchard, T. M. Willson, J. L. Collins, and S. A. Kliewer, *J. Biol. Chem.,* **275**, 15122 (2000). Orphan Nuclear Receptors Constitutive Androstane Receptor and Pregnane X Receptor Share Xenobiotic and Steroid Ligands.

383. P. Honkakoski, I. Jaaskelainen, M. Kortelahti, and A. Urtti, *Pharm. Res.,* **18**, 146 (2001). A Novel Drug-Regulated Gene Expression System Based on the Nuclear Receptor Constitutive Androstane Receptor (CAR).

384. P. Wei, J. Zhang, M. Egan-Hafley, S. Liang, and D. D. Moore, *Nature (London),* **407**, 920 (2000). The Nuclear Receptor CAR Mediates Specific Xenobiotic Induction of Drug Metabolism.

385. E. L. LeCluyse, *Chem. Biol. Interact.,* **134**, 283 (2001). Pregnane X Receptor: Molecular Basis for Species Differences in CYP3A Induction by Xenobiotics.

386. S. A. Jones, L. B. Moore, J. L. Shenk, G. B. Wisely, G. A. Hamilton, D. D. McKee, N. C. Tomkinson, E. L. LeCluyse, M. H. Lambert, T. M. Willson, S. A. Kliewer, and J. T. Moore, *Mol. Endocrinol.,* **14**, 27 (2000). The Pregnane X Receptor: A Promiscuous Xenobiotic Receptor that Has Diverged During Evolution.

387. I. Tzameli and D. D. Moore, *Trends Endocrinol. Metab.,* **12**, 7 (2001). Role Reversal: New Insights from New Ligands for the Xenobiotic Receptor CAR.

388. P. Honkakoski, I. Zelko, T. Sueyoshi, and M. Negishi, *Mol. Cell Biol.,* **18**, 5652 (1998). The Nuclear Orphan Receptor CAR-Retinoid x Receptor Heterodimer Activates the Phenobarbital-Responsive Enhancer Module of the CYP2B Gene.

389. L. Xiao, X. Cui, V. Madison, R. E. White, and K.-C. Cheng, *Drug Metab. Dispos.,* **30**, 951 (2002). Insights from a Three-Dimensional Model into Ligand Binding to Constitutive Active Receptor.

390. S. Ekins and E. Schuetz, *TIPS* (2002). The PXR Crystal Structure: the End of the Beginning.

391. J. M. Pascussi, L. Drocourt, J. M. Fabre, P. Maurel, and M. J. Vilarem, *Mol. Pharmacol.,* **58**, 361 (2000). Dexamethasone Induces Pregnane X Receptor and Retinoid X Receptor-Alpha Expression in Human Hepatocytes: Synergistic Increase of CYP3A4 Induction by Pregnane X Receptor Activators.

392. J. M. Pascussi, L. Drocourt, S. Gerbal-Chaloin, J. M. Fabre, P. Maurel, and M. J. Vilarem, *Eur. J. Biochem.,* **268**, 6346 (2001). Dual Effect of Dexamethasone on CYP3A4 Gene Expression in Human Hepatocytes. Sequential Role of Glucocorticoid Receptor and Pregnane X Receptor.

393. J. M. Pascussi, S. Gerbal-Chaloin, J. M. Fabre, P. Maurel, and M. J. Vilarem, *Mol. Pharmacol.,* **58**, 1441 (2000). Dexamethasone Enhances Constitutive Androstane Receptor Expression in Human Hepatocytes: Consequences on Cytochrome P450 Gene Regulation.

394. A. Chawla, J. J. Repa, R. M. Evans, and D. J. Mangelsdorf, *Science,* **294**, 1866 (2001). Nuclear Receptors and Lipid Physiology: Opening the X-Files.

395. W. Xie, J. L. Barwick, C. M. Simon, A. M. Pierce, S. Safe, B. Blumberg, P. S. Guzelian, and R. M. Evans, *Genes Dev.,* **14**, 3014 (2000). Reciprocal Activation of Xenobiotic Response Genes by Nuclear Receptors SXR/PXR and CAR.

396. B. M. Bolten and T. DeGregorio, *Nature Rev. Drug Disc.,* **1**, 335 (2002). Trends in Development Cycles.

397. S. Ekins, C. L. Waller, P. W. Swaan, G. Cruciani, S. A. Wrighton, and J. H. Wikel, *J. Pharm. Tox. Methods,* **44**, 251 (2000). Progress in Predicting Human ADME Parameters In Silico.

398. G. Klopman, M. Tu, and J. Talafous, *J. Chem. Inf. Comput. Sci.,* **37**, 329 (1997). META. 3. A Genetic Algorithm for Metabolic Transform Priorities Optimization.

399. J. P. Jones, M. Mysinger, and K. R. Korzekwa, *Drug Metab. Dispos.,* **30**, 7 (2002). Computational Models for Cytochrome P450: A Predictive Electronic Model for Aromatic Oxidation and Hydrogen Abstraction.

400. H. Yin, M. W. Anders, K. R. Korzekwa, L. Higgins, K. E. Thummel, E. D. Kharasch, and J. P. Jones, *Proc. Natl. Acad. Sci. U.S.A.,* **92**, 11076 (1995). Designing Safer Chemicals: Predicting the Rates of Metabolism of Halogenated Alkanes.

401. G. M. Kesuru and L. Molnar, *J. Chem. Inf. Comput. Sci.,* **42**, 437 (2002). METAPRINT: A Metabolic Fingerprint. Application to Cassette Design for High-Throughput ADME Screening.

402. G. M. Kesuru, *J. Comput. Aided. Mol. Des.,* **15**, 649 (2001). A Virtual High Throughput Screen for High Affinity Cytochrome P450cam Substrates. Implications for In Silico Prediction of Drug Metabolism.

403. L. M. Kauvar, H. O. Villar, J. R. Sportsman, D. L. Higgins, and D. E. J. Schmidt, *J. Chromatogr. B,* **715**, 93 (1998). Protein Affinity Map of Chemical Space.

404. S. L. Dixon and H. O. Villar, *J. Chem. Inf. Comput. Sci.,* **38**, 1192 (1998). Bioactive Diversity and Screening Library Selection via Affinity Fingerprinting.

405. L. M. Kauvar and E. Laborde, *Curr. Opin. Drug Disc. Dev.,* **1**, 66 (1998). The Diversity Challenge in Combinatorial Chemistry.

406. A. V. Ishchenko and E. I. Shakhnovich, *J. Med. Chem.,* **45**, 2770 (2002). Small Molecule Growth (SMoG2001): An Improved Knowledge-Based Scoring Function for Protein–Ligand Interactions.

407. B. A. Grzybowski, A. V. Ishchenko, J. Shimada, and E. I. Shakhnovich, *Acc. Chem. Res.,* **35**, 261 (2002). From Knowledge-Based Potentials to Combinatorial Lead Design in Silico.

408. J. Shimada, A. V. Ishchenko, and E. I. Shakhnovich, *Protein Sci.,* **9**, 765 (2000). Analysis of Knowledge-Based Protein–Ligand Potentials Using a Self-Consistent Method.

409. G. E. Terp, B. N. Johansen, I. T. Christensen, and F. S. Jorgensen, *J. Med. Chem.,* **44**, 2333 (2001). A New Concept for Multidimensional Selection of Ligand Conformations (Multiselect) and Multidimensional Scoring (Multiscore) of Protein–Ligand Binding Affinities.

410. C. A. Sotriffer, H. Gohlke, and G. Klebe, *J. Med. Chem.*, **45**, 1967 (2002). Docking into Knowledge-Based Potential Fields: A Comparative Evaluation of Drugscore.

411. I. Muegge, Y. C. Martin, P. J. Hajduk, and S. W. Fesik, *J. Med. Chem.*, **42**, 2498 (1999). Evaluation of PMF Scoring in Docking Weak Ligands to the FK506 Binding Protein.

412. J. Shimada, S. Ekins, C. Elkin, E. I. Shaknovich, and J.-P. Wery, *Targets,* **1**, 196 (2002). Integrating Computer-Based De Novo Drug Design and Multidimensional Filtering for Desirable Drugs.

413. D. R. Flower, *Biochim. Biophys. Acta,* **1422**, 207 (1999). Modeling of G-Protein Coupled Receptors for Drug Design.

414. S. Shacham, M. Topf, N. Avisar, F. Glaser, Y. Marantz, S. Bar-Heim, S. Noiman, Z. Naor, and O. M. Becker, *Med. Res. Rev.*, **21**, 472 (2001). Modeling the 3D Structure of GPCRs from Sequence.

415. B. Ma, M. Shatsky, H. J. Wolfson, and R. Nussinov, *Protein Sci.*, **11**, 184 (2002). Multiple Diverse Ligands Binding at a Single Protein Site: A Matter of Preexisting Populations.

416. P. Gedeck and P. Willett, *Curr. Opin. Chem. Biol.*, **5**, 389 (2001). Visual and Computational Analysis of Structure–Activity Relationships in High-Throughput Screening Data.

417. K. P. Bennet and C. Campbell, *SIGKDD Explorations,* **2**, 1 (2000). Support Vector Machines: Hype or Hallelujah?

418. M. P. S. Brown, W. N. Grundy, D. Lin, N. Christianini, C. W. Sugnet, T. S. Furey, M. Ares, Jr., and D. Haussler, *Proc. Natl. Acad. Sci. U.S.A.,* **97**, 262 (2000). Knowledge-Based Analysis of Microarray Gene Expression Data by Using Support Vector Machines.

419. T. S. Furey, N. Christianini, N. Duffy, D. W. Bednarski, M. Schummer, and D. Haussler, *Bioinformatics*, **16**, 906 (2000). Support Vector Machine Classification and Validation of Cancer Tissue Samples Using Microarray Expression Data.

420. R. Czerminski, A. Yasri, and D. Hartsough, *Quant. Struct. Act. Relationships,* **20**, 227 (2001). Use of Support Vector Machine in Pattern Classification: Application to QSAR Studies.

421. M. K. Warmuth, G. Rtsch, M. Mathieson, J. Liao, and C. Lemmen, *J. Chem. Inf. Comput. Sci.* (2003) **43** 667. Active Learning with the Support Vector Machines in the Drug Discovery Process.

422. C. J. Manly, S. Louise-May, and J. D. Hammer, *Drug Disc. Today,* **6**, 1101 (2001). The Impact of Informatics and Computational Chemistry on Synthesis and Screening.

Author Index

Abel, S. M., 405
Abonyi, J., 328
Abraham, M. H., 394
Abraham, U., 398
Abrams, M., 411
Ackland, M. J., 405
Adams, M. J., 329, 330
Adibi, S. A., 399
Adler, B., 330
Aerts, P. J. C., 146, 150
Afzelius, L., 405
Agapito, J. A., 330
Agapito, L., 330
Agostini, M., 412
Agrafiotis, D. K., 330, 396
Ågren, H., 152, 212, 217
Ahlbrecht, H., 400
Ahlrichs, R., 149, 215, 217, 218
Ahlsen, G., 398
Akhmed, N., 403
Alanine, A., 396, 411
Albers, S., 399
Albu, T., 93
Alekseyev, A. B., 150
Alex, A. A., 405, 406
Alexander, M. H., 150
Alfaro, R. M., 406
Algarov, D. K., 409
Allen, F. H., 327
Allen, J. D., 404
Allikmets, R., 393
Allinger, N. L., 97
Allsop, P., 331
Almlöf, J., 146, 148
Altomare, C., 407, 408

Alvarez-Pedraglio, A., 395
Amarouche, M., 99
Amasheh, S., 400
Ambudkar, S., 403
Amidon, G. L., 399, 400
Amirav, A., 212
Anders, E.-M., 405
Anders, M. W., 414
Andersson, K., 212, 214
Andersson, H. O., 398
Andersson, T. B., 402, 405
Andrae, D., 217
Andre, F., 403
Angelis, F. D., 217
Angelo, K., 411
Antes, I., 147
Anzai, N., 404
Aoyama, R., 406
Apiwattanakul, N., 404
Appliquist, D. E., 96
Aquilanti, V., 152
Archirel, P., 93
Ardelea, A., 246
Ares, Jr., M., 415
Areseniev, A. S., 411
Argiriadi, M. A., 407
Arimoto, S., 245
Armstrong, D. A., 99
Arnold, H. P., 401
Artursson, P., 395, 404
Asai, K., 329
Ascenzi, D., 150
Aschi, M., 149
Asman, M., 411
Assaraf, Y. G., 401

Assem, M., 406
Assenat, E., 412
Ast, M., 400
Astier, R., 217
Atashroo, T., 147, 148
Atkins, P. W., 213
Atkins, P., 89
Atkins, W. M., 406, 407
Atmar, W., 326
Audouze, K., 329
Auf der Heyde, P. E. T., 325
Avisar, N., 415
Axenova, L. N., 407
Ayesh, S., 403
Ayrton, A., 412

Bach, N. J., 401
Bacic, Z., 151
Bäck, T., 326
Bader, R. F. W., 98
Baerends, E.-J., 149, 217
Bai, J. P., 399
Bailey, P. D., 400
Baillie, T. A., 407
Bairoch, A., 408
Bakken, G. A., 402
Balakrishnan, N., 150
Balasubramanian, K., 150
Baldridge, K. K., 149
Baldwin, J. J., 395
Balimane, P. D., 400
Balint-Kurti, G. G., 92, 95, 150
Banasiewicz, M., 212
Bandemer, H., 329
Banoglu, E., 408
Bär, M., 218
Bar, R., 96
Barandiaran, Z., 148
Bargheer, M., 151, 152
Bar-Heim, S., 415
Barhelt, C., 406
Baringhaus, K. H., 401
Barkley, D., 244, 246
Barnum, D., 398
Baron, H.-P., 218
Barouki, R., 412
Barratt, M. D., 394
Bartlett, R. J., 215
Bartmann, W., 400
Bartuv, A., 94
Barwick, J. L., 412, 414
Barysz, M., 149

Basch, H., 99, 147
Bassett, H., 327
Bates, S. E., 403
Batt, A. M., 409
Bauer, R., 410
Bauernschmitt, R., 215, 218
Baughman, T. M., 401
Baukrowitz, T., 410
Bauschlicher, Jr., C. W., 99, 150, 213
Baxter, C. A., 399
Bearpark, M. A., 149
Beck, M. E., 216
Beck, W. T., 401, 402
Becke, A. D., 212, 215, 216
Becker, O. M., 415
Becker, W., 401
Bednarczyk, D., 404
Bednarski, D. W., 415
Beese, L. S., 411
Belanger, A., 408
Belas, F., 402
Beliveau, R., 401
Beljonne, D., 151, 404
Bell, A. J., 213
Bell, I. M., 411
Belletete, M., 213
Belmonte, A. L., 244
Belt, J. A., 404
Belusov, B. P., 244
Bemis, G. W., 396
Benet, L. Z., 402
Bennet, A. J., 415
Bennet, G., 98, 409
Bennyworth, P. R., 95
Benson, M. T., 147
Bentley, G., 411
Benz, A., 413
Berger, R., 214
Berkenstam, A., 411
Berman, J., 405
Bernardi, F., 91
Bernd, T., 327
Berova, N., 213
Berridge, G., 412
Berry, D. M., 399
Berson, J. A., 88, 97
Bersuker, I. B., 97
Bertilsson, G., 411
Bertran, J., 89
Bertz, R. J., 408
Beshore, D. C., 411
Besler, B. H., 398

Subject Index

Computer programs are denoted in boldface; databases and journals are in italics.

Ab initio, 187, 194, 202, 210
Ab initio calculations, 47, 58, 59, 66, 87
Ab initio MO theory, 11
Ab initio model core potential (AIMP), 127
Ab initio VB theory, 2, 42, 45, 69, 84
Absolute configuration, 171
Absorption band, 164
Absorption spectra, 188
Acetaldehyde, 168
Acetone, 188, 191
Achiral, 65
Achiral chromophores, 203
Activation function, 254, 255
Activation value, 254
Activator variable, 225
Active bonds, 44
Active subspaces, 15
Active transport, 336
Acyl-CoA-synthetases, 334
Acyltransferases, 334
Adaptive knowledge representation scheme, 263
Adiabatic approximation, 183
Adiabatic BO approximation, 171
Adiabatic profile, 51
Adiabatic reaction path, 102
Adiabatic states, 45
ADME/Tox (Adsorption, Metabolism, Distribution, Excretions, and Toxicology), vii, 333
Agglomerative clustering, 251
Alcohol-aldehyde dehydrogenases, 334
Alcohols, 75, 76

Algebraic methods, 249
Alignment independent QSAR, 347
Alkali dimers, 43
Alkanes, 49
Alkoxide anion, 75
Alkyl groups, 54
Alkyl radicals, 49, 62
Alkylhydrazine oxidase, 334
Allosteric behavior, 356
Allosteric effects, 369
Allosteric interactions, 356
Allyl anion, 57
Allyl cation, 57
Allyl radical, 57, 78
ALMOND, 347
Alzheimer's disease, 371
AM1, 187
Amide, 76
Amino acid sequence homology, 348
a-N_2O_2, 142
Analytical methods, 249
Angiotensin converting enzyme (ACE) inhibitors, 350
Annihilation operators, 178, 180
Annulenes, 59, 60
Anthracene, 164, 166, 205
Antianxiety molecules, 371
Antiaromatic molecules, 42
Antiaromaticity, 6, 12, 14
Antiarrhythmics, 365
Antibiotics, 379
Anticancer drugs, 363, 364
Anticooperative allosteric interactions, 356